

Thermodynamic modelling as applied to the development of TRIP-Matrix-Composite materials: The Fe–Mg–Mn–Ti–Zr–O system

Der Fakultät für Werkstoffwissenschaft und Werkstofftechnologie
der Technischen Universität Bergakademie Freiberg

genehmigte

DISSERTATION

zur Erlangung des akademischen Grades

Doktor-Ingenieur
(akademischer Grad)

Dr.-Ing.
(Kurzform)

vorgelegt

von Dipl.-Ing. Ivan Saenko
geboren am 10.08.1992 in Jaroslawl

Gutachter: Dr. Dr. rer. nat. Olga Fabrichnaya, TU Bergakademie Freiberg
Prof. Dr. rer. nat. Florian Mertens, TU Bergakademie Freiberg
Stellungnahme: Prof. Dr. rer. nat. habil. Andreas Leineweber, TU Bergakademie Freiberg

Freiberg, den 16.12.2020
(Tag der Verleihung)

«Прочитай сначала инструкцию!»
Сергей Саенко

«Read the instructions first!»
Sergej Saenko

Acknowledgements

The present thesis was accomplished at the Institute of Materials Science of TU Bergakademie within the Collaborative Research Centre 799 “TRIP-Matrix Composite” (CRC799).

I am very thankful to Prof. David Rafaja and Prof. Andreas Leineweber for giving me an opportunity to become a part of a team of the Institute of Materials Science at the TU Bergakademie Freiberg. I would like to acknowledge Prof. Andreas Leineweber for critical reading of the manuscript and discussion.

My deepest thanks goes to Prof. Horst Biermann for providing me a chance to be involved to the CRC 799 and the financial support of my study. Thereby, I thank also the Deutsche Forschungsgemeinschaft (German Research Foundation) for funding the sub-project C2.

I would like to express my sincere gratitude to Dr. Olga Fabrichnaya for supervision, encouragement and support of my PhD study, for fruitful scientific discussions and sharing her knowledge and experience.

Furthermore, I am especially indebted to Dr. Mario J. Kriegel and Alexander Walnsch for staying together in a front of technical challenges, valuable suggestions during the work and proofreading the manuscript.

I am also grateful to many people contributed to this work and I would like to acknowledge their support: Prof. Alexander Udovsky for scientific discussions; Alexander Kuprava for the contribution during his diploma work; Dr. Boburjon Mukhamedov for the contribution during his stay in Freiberg and involving me in the *ab-initio* calculation. I appreciated very much the fruitful discussions with Mariia Ilatovskaia, Dr. Tilo Zienert, Dr. Stefan Martin and Dr. Anton Salomon. I would like to thank Galina Savinykh and Beate Wahl for sample preparation and DTA measurements; Dr. Christian Schimpf for XRD measurements; Brigitte Bleiber for technical support in SEM/EDX.

I would like to thank all colleagues of the Institute of Materials Science and the CRC 799 project for their willingness to support me during various challenges and the great working atmosphere.

Last but not the least, I am deeply grateful to my wife and family for their moral and emotional support.

Abstract

This thesis performed within the Collaborative Research Center 799 describes a development of the metal-ceramic thermodynamic databases as applied to the design of the TRIP-Matrix-Composite materials. A wide range of theoretical and experimental investigations have been carried out in the relevant systems of Fe–Mg–Zr–O, Mg–Ti–Zr–O and Mg–Mn–Zr–O. Thermodynamic data were obtained using experimental methods of calorimetry and *ab-initio* calculations. Phase relations in the constituent binary and ternary systems have been studied using different types of static and dynamic methods. The obtained results allowed an assessment of thermodynamic parameters of the aforementioned systems using CALPHAD approach. The thermodynamic calculations have been performed to predict interfacial reactions within the composite material as well as to made recommendations for the design and further development of production processes for TRIP-Matrix-Composite materials.

Table of contents

List of publications.....	2
Publications not included in this thesis	3
List of abbreviations and symbols.....	4
1. Introduction	5
2. Thermodynamic modelling	7
2.2. Optimization and database development.....	10
3. Materials and methods	14
3.1. Sample preparation.....	14
3.2. Phase equilibrium studies.....	15
3.2.1. X-ray diffraction.....	15
3.2.2. Microstructural investigation	16
3.2.3. Thermal analysis	16
3.3. Determination of thermodynamic properties	17
3.3.1. Differential scanning calorimetry.....	17
3.3.2. Drop solution calorimetry	18
3.3.3. First-principle calculations.....	18
4. Fe–Mg–Zr–O system.....	20
4.1. State of the art	20
4.2. Results and discussion.....	22
4.2.1. Fe–Zr system	22
4.2.2. Fe–Zr–O system	23
4.2.3. Fe–Mg–O system	26
4.2.4. Fe–Mg–Zr–O system.....	30
5. Mg–Ti–Zr–O system	33
5.1. State of the art	33
5.2. Results and discussion.....	35
5.2.1. TiO ₂ –ZrO ₂ system.....	35
5.2.2. MgO–TiO ₂ –ZrO ₂ system.....	36
5.2.3. Thermodynamic modelling of the Mg–Ti–Zr–O system	38
6. Mg–Mn–Zr–O system	39
6.1. State of the art	39
6.2. Results and discussion.....	41
6.2.1. Mn–Zr system	41
6.2.2. Mg–Mn–Zr–O system	41
7. Implication of thermodynamic modelling for the development of the TRIP-Matrix-Composites.....	43
7.1. Manganese as an adhesion promoter for TRIP-Matrix-Composite.....	46
7.2. Titanium as an adhesion promoter for TRIP-Matrix-Composite	48
7.3. Titania as an alternative for promotion of adhesion.....	49
8. Summary, conclusions and outlook	52
References	54
Appendix	63

List of publications

This thesis is based on the following papers, which will be referred to in the text in the form of [P#] (where # is a corresponding number). These publications can be found in the Appendix where my contribution and the contribution of the authors are detailed.

[P1] B.O. Mukhamedov, I. Saenko, A.V. Ponomareva, M.J. Kriegel, A. Chugreev, A. Udovsky, O. Fabrichnaya, I.A. Abrikosov, Thermodynamic and physical properties of Zr_3Fe and $ZrFe_2$ intermetallic compounds, *Intermetallics* 109 (2019) 189.

[P2] I. Saenko, A. Kuprava, A. Udovsky, O. Fabrichnaya, Heat capacity measurement of Zr_2Fe and thermodynamic re-assessment of the Fe–Zr system, *CALPHAD* 66 (2019) 101625.

[P3] I. Saenko, M. Ilatovskaia, G. Savinykh, O. Fabrichnaya, Experimental investigation of phase relations and thermodynamic properties in the ZrO_2 – TiO_2 system, *Journal of the American Ceramic Society* 101 (2018) 386.

[P4] I. Saenko, V. Tsukrenko, M. Ilatovskaia, D. Pavlyuchkov, G. Savinykh, O. Fabrichnaya, Experimental Investigation of Phase Equilibria in the ZrO_2 – TiO_2 –MgO System, *Advanced Engineering Materials* 21 (2019) 1800655.

[P5] I. Saenko, O. Fabrichnaya, Heat capacity measurements of the δ -phase $Mg_2Zr_{4.2}Ti_{0.8}O_{12}$ and thermodynamic modelling of the ZrO_2 – TiO_2 –MgO System, *Journal of the European Ceramic Society* 40 (2020) 3304.

[P6] A. Kuprava, I. Saenko, O. Fabrichnaya, Heat capacity measurement of $C14$ – $ZrMn_2$ and thermodynamic re-assessment of the Mn–Zr system, *CALPHAD* 68 (2020) 101745.

[P7] I. Saenko, O. Fabrichnaya, Thermodynamic database development for the ZrO_2 –MgO– MnO_x system, *Journal of Phase Equilibria and Diffusion* 41 (2020) 654.

Publications not included in this thesis

The author has contributed to the following publications which are outside the scope of this thesis. These will be referred to in the text by P and a corresponding number. These publications are not included in the Appendix.

[P8] O. Fabrichnaya, I. Saenko, M.J. Kriegel, J. Seidel, T. Zienert, G. Savinykh, G. Schreiber, Experimental investigation of phase relations and thermodynamic properties in the system $\text{ZrO}_2\text{--Eu}_2\text{O}_3\text{--Al}_2\text{O}_3$, *Journal of the European Ceramic Society* 36 (2016) 1455.

[P9] I. Saenko, O. Fabrichnaya, A. Udovsky, New Thermodynamic Assessment of the Fe–Y System, *Journal of Phase Equilibria and Diffusion* 38 (2017) 684.

[P10] M. Ilatovskaia, I. Saenko, G. Savinykh, O. Fabrichnaya, Experimental study of phase equilibria in the $\text{Al}_2\text{O}_3\text{--MgO--TiO}_2$ system and thermodynamic assessment of the binary MgO--TiO_2 system, *Journal of the American Ceramic Society* 101 (2018) 5198.

[P11] C. Baumgart, C. Weigelt, M. Wendler, I. Saenko, C.G. Aneziris, O. Volkova, L. Krüger, Challenges in Pressureless Sintering of Interstitially Alloyed TRIP Steel and Resulting Mechanical Properties, *Advanced Engineering Materials* 21 (2019) 1800700.

[P12] S. Borrmann, C. Kratzsch, L. Halbauer, A. Buchwalder, H. Biermann, I. Saenko, K. Chattopadhyay, R. Schwarze, Electron beam welding of CrMnNi-steels: CFD–modeling with temperature sensitive thermophysical properties, *International Journal of Heat and Mass Transfer* 139 (2019) 442.

[P13] M. Stopyra, I. Saenko, M. Ilatovskaia, G. Savinykh, O. Fabrichnaya, Phase relations in the $\text{ZrO}_2\text{--La}_2\text{O}_3\text{--Gd}_2\text{O}_3$ system: Experimental studies and phase modeling, *Journal of the American Ceramic Society* 102 (2019) 7628.

[P14] F. Qayyum, S. Guk, S. Prüger, M. Schmidtchen, I. Saenko, B. Kiefer, R. Kawalla, U. Prahl, Investigating the local deformation and transformation behavior of sintered X3CrMnNi16-7-6 TRIP steel using a calibrated crystal plasticity-based numerical simulation model, *International Journal of Materials Research* 111 (2020) 392.

[P15] G. Roncallo, G. Cacciamani, E. Vacchieri, M. Ilatovskaia, I. Saenko, O. Fabrichnaya, Thermodynamic modeling and experimental investigation of the $\text{MgO--Y}_2\text{O}_3\text{--ZrO}_2$ system, *Journal of the American Ceramic Society* (2020).

[P16] I. Saenko, O. Fabrichnaya, Thermodynamic Modelling in the Frames of the TRIP-Matrix-Composite Development, *Springer Series in Materials Science* 298 (2020) 621.

List of abbreviations and symbols

Abbreviations

BSE	Backscattered electrons
CALPHAD	Calculation of phase diagrams
DFT	Density functional theory
DTA	Differential thermal analysis
DSC	Differential scanning calorimetry
EMPA	Electron micro probe analysis
EDX	Energy dispersive X-ray spectrometry
Mg-PSZ	Zirconia partially stabilized by MgO
fcc	Face-centered cubic structure
bcc	Body-centered cubic structure
hcp	Hexagonal close-packed structure
OQMD	The open quantum materials database
PAW	Projector augmented wave
VASP	Vienna ab-initio simulation package
ICP-OES	Inductively coupled plasma – optical emission spectrometry
QHA	Quasiharmonic approximation
TRIP	Transformation induced plasticity
TMC	TRIP-Matrix-Composite
TGA	Thermogravimetric analysis
SGTE	Scientific group thermodata europe
SEM	Scanning electron microscopy
SE 1750/2400	DTA device Setsys Evolution 1750 or 2400
r.t.	Room temperature
XRD	X-ray diffraction
THXRD	High temperature x-ray diffraction

Symbols

a, b, c, d, e, f...	Polynomial coefficients
$\alpha, \gamma, \beta, \delta, \eta, \eta'$	Greek symbols to name phases
Sp	A phase with the spinel crystal structure (α – tetragonal; β – cubic)
Hal	Halite – a phase with the crystal structure of sodium chloride
M-ZrO ₂	Monoclinic zirconia
T-ZrO ₂	Tetragonal zirconia
C-ZrO ₂	Cubic zirconia
Liq	Liquid phase
ln	Natural logarithm
lg	Decimal logarithm
β_0	Average magnetic moment per atom
C_P	Specific heat capacity ($\text{J} \cdot \text{mol}^{-1} \cdot \text{K}^{-1}$)
$\Delta_f H_{298}^0$	Enthalpy of formation at RT ($\text{J} \cdot \text{mol}^{-1}$)
N_A	Avogadro constant
$G(T)$	Gibbs energy function
mol. %	Mole percent
G_P^{mag}	Magnetic contribution to the Gibbs energy
T	Temperature (K)
S_{298}^0	Standard entropy ($\text{J} \cdot \text{mol}^{-1} \cdot \text{K}^{-1}$)
θ	Half of the diffraction angle (°)
R	Gas constant ($\text{J} \cdot \text{mol}^{-1} \cdot \text{K}^{-1}$)
wt. %	Weight percent
x	Molar fraction

1. Introduction

Current strict ecological requirements for emission reduction, high-priced materials and energy costs as well as intensified international competitive have set under an immense pressure many industrial sectors, such as automotive industry, civil engineering, as well as aerospace manufacturing. Thus, continuous development of new materials and existing technologies became an essential need of the 21st century. In this context, composite materials have a great potential for application in terms of resource and energy efficiency as well as high potential to weight reduction due to extraordinary mechanical properties and high wear resistance.

An example of a high-tech innovative composite materials are the TRIP-Matrix-Composites (TMC), which is based on high-alloyed austenitic TRIP-steel and reinforcing ceramic particles of zirconia partially stabilized by MgO (Mg-PSZ) [1]. Under compressive loading, metastable austenite of the steel matrix transforms into martensite increasing strength. Thereby, ceramic particles of Mg-PSZ undergo a stress-induced transformation from tetragonal into monoclinic structure resulting in an additional increase of strength [2]. The particular composite materials exhibit excellent mechanical properties such as ductility, plasticity, damage resistance and extraordinary high values of specific energy absorption in compression [3]. Therefore, TMC have a wide range of possible technological applications especially in automotive production in the context of the weight reduction of automobile chassis contributing to an exhaust emissions decrease.

However, a development of such complex composite materials requires a wide range of investigations in the field of applied science, as well as fundamental material science. Both components of TMC, namely the steel matrix and ceramic particles should be well studied separately first. Then, compatibility of components and possible interfacial reactions should be considered in order to estimate and to optimize their interactions within the composite material. Thereby, knowledge of phase equilibria and the underlying thermodynamics play a crucial role. In this case, phase diagrams represent a kind of roadmaps for the material development and provide important information for understanding of technological aspects of its design and usage. However, similar to the most of the modern materials, TMC presents combination of multicomponent alloys and oxide systems, what makes the graphical representation of the phase diagrams of these systems challenging and complex. Except of an issue of the data representation, available information for many multicomponent systems are limited due to high costs of such prolonged fundamental experiments.

The methods of modelling and simulations make it possible to reduce amount of experimental investigations substantially. In particular, computational thermodynamics has become a necessary and very powerful tool for prediction and extrapolation helping to fulfil the gaps due to an absence of the experimental information and to reduce time for experimental work [4]. For the development of an innovative composite material such as TMC, thermodynamic simulation using the CALPHAD method [5] (CALculation of PHase Diagrams) can be used to support an optimization of chemical composition of the alloy, as well as to help in the development of the production process. Thereby, thermodynamic calculations provide essential information about the stable and metastable phase formation in the material of TMC as well as

the accompanying energetic effects and basic information of the physicochemical parameters of the manufacturing processes.

Thus, the development of TMC requires a multicomponent thermodynamic description, which would include all alloying elements of the matrix, as well as components of ceramics such as ZrO_2 and MgO as well as oxides appearing due to steel oxidation and impurities. Consequently, both types of materials had to be investigated, not only the steel matrix but also ceramic components. In the beginning of the development of TMC, an extensive thermodynamic database for the steel-based materials (Fe, Mn, Cr, Ni, Ti, Mo, W, V, Si, C and N) was created by Franke using the CALPHAD method [6]. In order to be able to simulate interfacial reaction of ceramic particles with the steel matrix, a ceramic database had to be implemented into the database for the steel-based materials. Thereby, it was necessary to include zirconium, magnesium and oxygen into the available thermodynamic description. Therefore, this thesis was focused on two different directions - investigations of steel and ceramic systems. First of all, the Fe–Mg–Zr–O system came into focus as the main bridge from the metal systems to the ceramics.

The second main part of this work deals with the ceramic components. Since, most of such composite materials are produced by powder-metallurgical techniques, no crystallographic coherent interface between the components can be formed due to the random particle orientation. Therefore, the interface bounding in such composite materials is one of the main manufacturing issues [7]. In order to achieve a satisfying connection between both components and to obtain desired mechanical properties, possible adhesion promoters should be applied. Based on the experimental studies [7–10], titanium and manganese were suggested as promising elements, that could serve as an adhesion promoter for the TMC manufacturing. Thus, optimizing of these additives, as well as estimation of all possible impacts of adhesion promoters on the Mg-PSZ ceramics as well as on the steel matrix became an important task for thermodynamic modelling. Therefore, the Mg–Ti–Zr–O and Mg–Mn–Zr–O systems were taken into focus with the main priority.

The studies behind this thesis have been cumulated in seven papers describing the main results (referred as P1 – P7). Chapter 2 describes the CALPHAD approach, which was applied in the present work for development of thermodynamic databases and assessment of thermodynamic parameters. Chapter 3 considers experimental techniques to study of phase equilibria as well as measurement methods and DFT calculations of thermodynamic properties. Chapters 4–6 are focused on the Fe–Mg–Zr–O, Mg–Ti–Zr–O and Mg–Mn–Zr–O systems, respectively, including short reviews of available literature data, as well as summarizing the results obtained in the present work, critical evaluations and thermodynamic assessments. Implication of thermodynamic modelling for the development of TMC are presented in Chapter 7. Summary, conclusions and outlook are given in Chapter 8.

2. Thermodynamic modelling

The CALPHAD method [5] was applied in order to obtain thermodynamic descriptions of systems related to TMC based on different kind of experimental data, which were obtained in this work, as well as all literature data. This approach has been pioneered by American metallurgist Larry Kaufman since the 1970s [5,11,12]. In the base of the CALPHAD modelling, there are mathematical expressions representing the Gibbs energies of individual phases, phase equilibrium data and experimental thermodynamic values, which should be in mutual agreement. The Gibbs energy of an individual phase is presented as function of temperature, pressure and composition [11]. Thereby, the stable phase equilibrium at given pressure, temperature and bulk composition of the system is determined by the global minimum of the Gibbs energy of a system. The Gibbs energy of the system represents a sum of the Gibbs energies of individual phases multiplied to their molar amount. If some phases do not exist in calculated equilibrium, their molar amount is equal to zero. A phase diagram is a representation of stability fields for various phase assemblages separated by boundaries between them at various conditions e.g. temperature vs. pressure or temperature vs. composition. Therefore, phase diagrams can be calculated by global minimization of the Gibbs energy for the system at varying conditions [5].

Different kinds of data are used for optimization of thermodynamic parameters simultaneously to reproduce both, phase diagrams and thermodynamic properties measured by various experimental methods. An obtained set of thermodynamic functions of individual phases can be used to calculate different kinds of diagrams. However, thermodynamic databases derived using phase equilibria only, without taking into account any thermodynamic data, can contain physically unreasonable thermodynamic values or there can exist several datasets, which reproduce the phase diagram equally well but containing totally different thermodynamic values. Therefore, experimental measurements of thermodynamic properties of individual phases using methods of calorimetry, vapor pressure and electrochemical data measurements, etc. have to be considered in optimization procedure of the thermodynamic parameters. On the other side, the phase diagrams are quite sensitive to change of thermodynamic parameters of individual phases that use only experimentally measured thermodynamic values can cause contradictions with phase diagrams. Therefore, both phase diagram data and experimental thermodynamic values should be taken into account simultaneously to derive a self-consistent database for the system.

Methodology of the CALPHAD method and main principles of thermodynamic databases development are described in many text books [5,11,12] and review papers [4,13]. In this chapter, the main information about CALPHAD will be described very shortly.

2.1. Methodology of CALPHAD

The Gibbs energy of individual phases is described as a function of temperature, pressure and composition. Pressure dependence of the Gibbs energy can be described by the molar volume

as a function of pressure and temperature. In this thesis, no pressure dependence of the Gibbs energy was modelled. Therefore, this will not be discussed further. Detailed information about thermodynamic modelling in dependence of pressure can be found on the books of Lukas *et al.* [5], as well as Fabrichnaya *et al.* [14].

Temperature dependence of the Gibbs energy function of a stoichiometric phases or end members of solid solutions at a certain T referred to the enthalpy of its phase at room temperature 298 K (r.t.) are described in the form presented in Eq.1 (all temperatures along this thesis are given in Kelvin units, energy units are given in Joule per mole).

$$G(T) = \Delta_f H_{298}^0 + \int_{298}^T C_P dT - T \left(S_{298}^0 + \int_{298}^T (C_P/T) dT \right) \quad (1)$$

where S_{298}^0 is the standard entropy, $\Delta_f H_{298}^0$ is the enthalpy of formation at r.t. and C_P is the heat capacity given by:

$$C_P = a + bT + cT^{-2} + dT^2 + eT^{-3} + \dots \quad (2)$$

The magnetic contribution G_P^{mag} can be taken into account according to Inden–Hillert–Jarl [15] formalism (Eq. 3).

$$G_P^{mag} = RT \ln(\beta_0 + 1) g(\tau) \quad (3)$$

where $\tau = T/T^*$, T^* is the critical temperature (the Curie temperature T_C for ferromagnetic materials or the Neel temperature T_N for antiferromagnetic materials), β_0 the average magnetic moment per atom and $g(\tau)$ is a function depending on τ [16].

The Gibbs energy $G_{A_a B_b}(T)$ of a stoichiometric phase $A_a B_b$ in case of absence of heat capacity data was modeled using Neumann-Kopp rule as:

$$G_{A_a B_b} = aGHSER_A + bGHSER_B + \alpha + \beta T \quad (4)$$

where $GHSER_i$ is the Gibbs energy of the pure element i referred to the enthalpy of pure element i at 298 K in its standard element reference (SER) state, α and β are parameters to be optimized representing enthalpy and minus entropy of formation of phase from components, respectively. Adopting Eq. 4, the difference between heat capacity of the compound and a sum of heat capacities of components multiplied by their stoichiometric coefficients is assumed to be zero.

The simplest non-ideal solution model is the substitutional model with the Gibbs energy expressed as follows:

$$G = \sum_i^n x_i G_i + RT \sum_i^n x_i \ln x_i + \Delta G^{Ex} \quad (5)$$

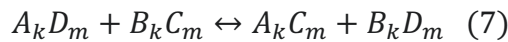
where x_i are the mole fractions, G_i is the Gibbs energy of an end-member i , $\sum_i^n x_i G_i$ are the surface of reference, $RT \sum_i^n x_i \ln x_i$ is the contribution to the Gibbs energy resulting from the configurational entropy of randomly mixing components, and ΔG^{Ex} is the excess Gibbs energy of mixing.

The excess Gibbs energy of mixing was modelled using Redlich–Kister polynomials [17], expressed as:

$$\Delta G^{Ex} = \sum_{i \neq j, i < j} x_i x_j \sum_{v=0} L_{i,j}^v (x_i - x_j)^v \quad (6)$$

where $L_{i,j}^v$ is the mixing parameter between end-members i and j while v are integer numbers. It should be noted that mixing parameters can be temperature dependent.

Solid solutions and compounds having a homogeneity range can have two or more different sites in the crystal structure (sublattices) which can be occupied by atoms or ions or more complex species. The composition dependence of the Gibbs energy of such phases can be described by the compound energy formalism developed by Hillert [18]. In this case, each sublattice can be related with specific atomic site in the crystal structure. The structure of the phase can be represented by the formula $(A,B)_k(C,D)_m$, indicating that A and B species mix on the first sublattice whereas C and D mix on the second sublattice. Coefficients k and m are stoichiometric numbers for the first and second sublattice, respectively. The constitution of the phase is described by site fractions Y_i^S (i.e. fraction of the species i occupying each sublattice S). The case when each sublattice is fully occupied by one species corresponds to the end-member compound e.g. $A_k D_m$ or $B_k C_m$. It should be noted that the end-member compounds are related with each other by reciprocal reaction (Eq.7).



The Gibbs energy of solution described by the sublattice model with three sublattices is given by

$$\Delta G^{mix} = \sum_i \sum_j \sum_k Y_i^s Y_j^t Y_k^u G_{ijk} + RT \sum_s \alpha_s \sum_i Y_i^s \ln(Y_i^s) + \Delta G^{Ex} \quad (8)$$

where Y_i^s is the mole fraction of constituent i on sublattice s , α_s is the number of sites on sublattice s per mole of formula unit of phase and ΔG^{Ex} is the excess Gibbs energy of mixing expressed as

$$\Delta G^E = \left(\sum_t y_j^t \right) \left(\sum_u y_k^u \right) \left(\sum_s y_i^s y_l^s L_{i,l}^s \right) + \left(\sum_s y_i^s \right) \left(\sum_t y_j^t \right) \left(\sum_u y_k^u y_m^u L_{k,m}^u \right) \\ + \left(\sum_s y_i^s \right) \left(\sum_u y_k^u \right) \left(\sum_t y_j^t y_n^t L_{j,n}^t \right) \quad (9)$$

$$L_{i,l}^s = \sum_n (Y_i^s - Y_l^s) {}^n L_{i,l} \quad (10)$$

where $L_{i,l}^s$ are binary interaction parameters between species i and l on sublattice s . Higher-order interaction parameters could also be included giving more complicated excess Gibbs energy terms.

A partially ionic liquid model [18] was used to describe liquid in multicomponent systems which contains complex charged species. In this work, the liquid was described by two sublattices: the first one is occupied by cations and the second one containing anions, vacancies and neutral species (see Eq. 11). The partially ionic liquid model makes it possible to have single liquid description for different kind of liquids namely, metallic liquid with the second sublattice mainly vacant, ionic liquid containing mainly anion species or polymeric liquid containing neutral species.

$$(C_i^{v_i+})_P (A_j^{v_j-}, Va, B_k^0)_Q \quad (11)$$

where C_i are cations v_i , A_j are anions with correspondent charge v_j , Va is vacancy and B_k are neutral species with covalent character of bonding. The coefficients P and Q are the number of sites on the cation and anion sublattices, respectively, which can be varied with the composition of liquid in terms of electroneutrality.

$$P = \sum_j v_j y_{A_j} + Q y_{Va} \quad (12)$$

$$Q = \sum_i v_i y_{C_i} \quad (13)$$

2.2. Optimization and database development

Thermodynamic databases derived by the CALPHAD method should be self-consistent. Thermodynamic descriptions of binary systems depend on the unary data for pure elements and on the models selected for the phases existing in the system. Thermodynamic descriptions of ternary and higher-order systems depend on the selected assessments of the corresponding lower-order systems [5]. The thermodynamic descriptions of Gibbs energy of the pure element was taken from UNARY database for pure elements and models established more than 20 years ago by the Scientific Group Thermodata Europe (SGTE) [19].

The mathematical descriptions for the Gibbs energies of the phases can be developed based on thermodynamic properties of the individual phases. However, the most of such experiments to determine thermodynamic properties are very time consuming and expensive. Sometimes it could be even impossible to perform that kind of experiments for example in the case of metastable phases. The expressions describing the Gibbs energies should contain adjustable parameters, which can be optimized to reproduce phase diagrams and thermodynamic values with minimal deviation from experimental data on phase relations, as well as available data on thermodynamic properties. The selection of a mathematical model describing the Gibbs energy of a phase depends on the nature of the system, crystal structure of the phase and types of atomic interactions. If thermodynamic data of some components are very well determined, they can be fixed during optimization procedure as “true” values of thermodynamic properties of a phase (thereby the measurement error has to be considered). Then, the other parameters such as mixing parameters of solution phases and metastable end-members of solid solutions should be optimized based on phase relations in a system. Finally, the aim of the CALPHAD method is to obtain a consistent description of all phases in the system reproducing the thermodynamic properties and phase diagrams within the uncertainty of the measurements. The self-consistent thermodynamic database allows predicting the phase relations and thermodynamic properties in regions where experimental information are not available as well as calculation of metastable phase diagrams, calculation of diffusion-less transformation and simulations of non-equilibrium processes assuming a local equilibration.

The optimization process is the most important step of the creation of a thermodynamic database, which gives the best representation of experimental data taking into account the error of every data point. These parameters are optimized using the least-squares method to obtain a description, which reproduces experimental data with minimal deviation. However, the least-squares method can work well only if the scatter of experimental data is completely random. Non-randomly distributed deviations of some data may completely destroy the validity of the least-squares method. They must be classified as systematic errors and excluded from the optimization. Therefore, judgements are required and decisions have to be made on the selection of data during the optimization process. From that point of view, the technique can also be called an assessment [5]. Unfortunately, including all available data in optimization does not necessarily lead to satisfactory results. Some experimental data could be in conflict to each other or can show large systematic errors. Thereby, setting different weights for these data points can help to recognize the influence of different experiments on the result of optimization. This procedure helps to identify which data are contradictory. However, it is usually impossible to optimize all parameters simultaneously. There are too many parameters and they have different influence on phase diagrams [13].

The optimization methodology of CALPHAD method can be subdivided into following stages:

1. Collection of various types of experimental information available in literature (crystallographic data for phases, phase equilibria, calorimetry, electrochemical data, vapor pressure measurements).
2. The selection of thermodynamic models based on crystallographic information for phases in the system under investigation. This implies selection of sub-lattices and their occupancies by constituents in agreement with crystal structure.
3. The consideration of temperature dependence of end-member parameters and introducing of mixing parameters for the Gibbs energy description of the phases.
4. The optimization of the thermodynamic parameters using all available experimental as well as theoretical data.
5. The storage of the optimized parameters in computer-readable thermodynamic datasets.
6. The calculation of phase diagrams and various phase equilibria using the obtained thermodynamic datasets in order to verify reliability of the results.

Assessment of thermodynamic parameters and calculation of phase diagram were performed using Thermo-Calc software package [20]. The principle of the CALPHAD approach is schematically presented in Fig. 1.

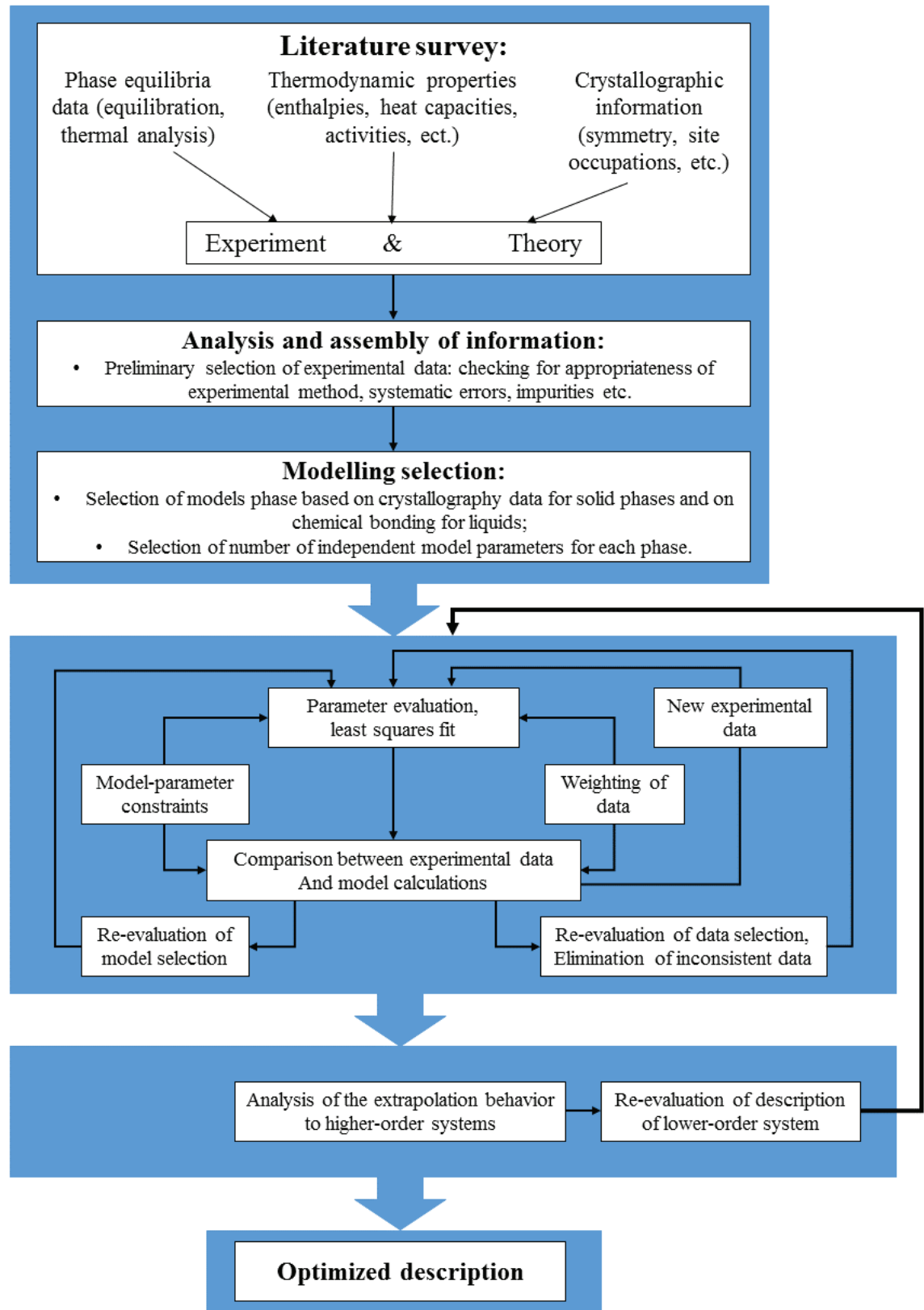


Fig. 1 – A schematic diagram of the CALPHAD assessment [5].

3. Materials and methods

3.1. Sample preparation

The development of TMC requires a multicomponent thermodynamic description, which includes all alloying elements of the steel matrix, as well as all components of ceramics. Consequently, this work was focused on both types of materials. Therefore, two different techniques of specimen preparation were applied for investigations of metal and ceramic systems.

In the case of metallic systems, two component alloys were prepared by arc-melting method in Ar-atmosphere. Chemically pure metals, slugs of Zr (99.5%, Alfa Aesar), pieces of Fe (99.99%, Alfa Aesar) and Mn (99.9 wt.%, Alfa Aesar) were used as initial materials. Precursors have been weighed in accordance to the nominal compositions using a laboratory scale ABJ 120-4M (KERN & Sohn GmbH). In the first step, the melting chamber was evacuated to $\sim 10^{-5}$ atm and refilled with argon at least three times. An ingot of Ti (ca. 3g) was placed in one of the molds and was melted before the melting of the samples in order to adsorb rest amount of oxygen and to prevent oxidation. In order to achieve a good homogeneity of the chemical composition, the samples were turned-over and re-melted three times during arc-melting process. The weight loss due to vaporization has been observed to be generally less than 1 mass%. In the end, samples obtained by arc melting were encapsulated in quartz tubes with Ar atmosphere. The pressure of Ar was chosen in order to reach 1 atm at the annealing temperature. The encapsulated samples were heat treated afterwards quenched into ice water.

For ceramic systems, the co-precipitation method was used for the sample preparation. Chemically pure salts of the desired elements have been used as the initial materials. The zirconium acetate solution in acetic acid $\text{Zr}(\text{CH}_3\text{COO})_4$ (99.99 %, Sigma-Aldrich), titanium (III) sulfate $\text{Ti}_2(\text{SO}_4)_3$ (99.99 %, Alfa Aesar), manganese nitrate $\text{Mn}(\text{NO}_3)_2$ (99.9 %, Alfa Aesar) and magnesium nitrate $\text{Mg}(\text{NO}_3)_2$ (99.97 %, Alfa Aesar) have been used as initial reagents. In the first step, the starting chemicals were diluted and dissolved in distilled water in order to obtain a more suitable consistence for the co-precipitation process (solutions: 1.14 mol/l for the zirconium acetate solution, 0.643 mol/l for the titanium (III) sulfate, 0.425 mol/l for the manganese nitrate and 0.494 mol/l for the magnesium nitrate). The concentration of the obtained initial solutions was measured by Inductively Coupled Plasma – Optical Emission Spectrometry (ICP-OES). Calculated volumes of the obtained solutions were mixed together in order to get around 2 grams of oxide powder of desired molar ratio. The obtained solution was dropped from a burette at a low speed (around 1 ml per minute) into a beaker containing about 500 ml of the aqueous solution of NH_4OH with pH value above 9.0. After evaporation at 333 K during 1 – 2 h, the obtained substance was dried at 353 K for 2 – 3 days. Finally, a pyrolysis of the dried powder was performed at 1073 K for 3 h in the air atmosphere. The obtained oxide powder was pressed into cylindrical pellets at 250 MPa and sintered in air atmosphere in Pt crucibles using a NABERTHERM furnace in order to reach equilibrium state. Annealing duration was chosen depending on sintering temperature.

3.2. Phase equilibrium studies

The quantities measured in phase diagrams are either temperatures of phase boundaries at fixed composition and invariant reaction determined by thermal analysis or phase compositions at fixed temperatures determined by sample equilibration. There are several experimental methods for measuring the phase-diagram data that could be divided into static and dynamic methods.

Static methods are different kinds of analysis such as X-ray powder diffraction (XRD), scanning electron microscopy combined with an energy dispersive X-ray spectrometry (SEM/EDX) or electron micro probe analysis (EMPA) for *ex-situ* phase identifications and for a determination of their chemical compositions after long time heat treatment (quasi-equilibrated state). The dynamic methods includes measurement techniques such as differential thermal analysis (DTA), differential scanning calorimetry (DSC), thermogravimetric analysis (TGA), high temperature X-ray diffraction (HTXRD) etc., that allow *in-situ* measuring different kinds of phase transformations in a system. They are described in detail by Lukas *et al.* [5]. In the current investigation, XRD, SEM/EDX and DTA/TGA were applied in order to obtain information about phase compositions, required for thermodynamic assessment of two and three component systems. Experimental data on phase compositions in multicomponent systems are usually not used directly during an assessment, but, if the extrapolation from the lower-order systems gives wrong results, these data could be used for modification of parameters describing the lower-order systems or by introducing high-order parameters and new phases. Additionally, if phases are not stable in a binary system the parameters of metastable phases can be assessed from a higher order system.

3.2.1. X-ray diffraction

After the long-time annealing, the phase assemblage of heat-treated samples have to be determined. The most powerful analytical techniques for identifying the phases is X-ray or neutron diffraction. Moreover, these techniques are also important for the determination of crystal structures. Lattice parameters and site occupancies as functions of composition and temperature can be obtained to provide detailed information about the Wyckoff positions of crystalline substances, including site occupancies, unit cell dimensions, bond-lengths and bond-angles. This information is necessary to find appropriate models for thermodynamic description.

In the current investigation, XRD was applied using an URD63 diffractometer (Seifert, FPM, Freiberg, Germany) equipped with a graphite monochromator and CuK α radiation ($\lambda = 1.5418$ Å). The goniometer of the diffractometer was working in Bragg-Brentano geometry. The measured samples in a powder form were placed on single crystalline silicon substrate with (510) orientation. In this case, the orientation of the substrate does not show any peak on the XRD patten in the range of $15 - 110^\circ$ of 2θ . The Rietveld refinement was applied for the evaluation of all measured diffraction patterns in order to obtain the volume fractions of present phases as well as lattice parameters. The program Maud [21] was applied.

3.2.2. Microstructural investigation

SEM/EDX allows measuring the chemical composition of the microstructural features. For example, boundaries in phase diagrams, which are often deduced from results of characterization of sample series with different compositions after equilibration at fixed temperatures, can be plotted as composition versus a temperature. Afterwards, these results can be applied for modelling of homogeneity ranges of e.g. solid phases.

The microstructures of the samples were analysed using Scanning Electron Microscope – LEO 1530 Gemini (Zeiss, Germany). The microscope was equipped with a field emission cathode, used at the acceleration voltage of 20 kV with working distance of 8 – 10.5 mm. Thereby, an EDX detector (Bruker AXS Mikroanalysis GmbH) was used in order to verify chemical compositions of samples, to determine chemical composition of the present phases, which was also used for identification of phases, as well as to estimate composition of liquid in eutectic reactions. The uncertainty of EDX measurements is around 2 – 4 at.%. For most of samples SEM images were recorded using back scattered electrons (BSE), while secondary electrons were considered only for few samples in order to distinguish phases from pores. Samples were grinded and polished to 1 μm .

For imaging in the SEM, samples must be electrically conductive, at least at their surface, and electrically grounded in order to prevent the accumulation of electrostatic charge at the surface at the interaction with the electron beam. Therefore, samples composed of oxides were coated with an graphite layer.

3.2.3. Thermal analysis

DTA was applied in order to detect temperatures of phase transitions and reactions occurring in the sample as well as melting temperatures. The technique of thermal analysis is based on the measuring of the temperature difference between the sample versus a reference as a function of time and temperature during programmed heating and cooling cycles. Any exothermic or endothermic changes occurring in the sample are registered by comparison with the reference as the temperature difference of the thermocouple signals in μV (thermal voltage). An inert material, which does not react with crucible and does not have phase transformations in the investigated temperature range can be used as a reference. However, it should be noted that empty crucibles are mostly used as reference at present.

In this work, DTA was performed using Setaram Setsys Evolution 1750 and Setaram Setsys Evolution 2400. The Setaram Setsys Evolution 1750 (SE 1750) device equipped with a type B thermocouple (Pt/Rh 70%/30% – Pt/Rh 94%/6%, by weight) works in an inert atmosphere of helium, argon or in air atmosphere in an interval between r.t. to 2023 K. The Setaram Setsys Evolution 2400 (SE 2400) device equipped with a type C thermocouple (W/Re 95%/5% – W/Re 74%/26%, by weight) works in an inert atmosphere of helium or argon up to 2673 K. As the crucible's materials, Pt/Rh10% was used for SE 1750 and pure W was used for SE 2400 in the case of ceramic materials. For metallic samples, ceramic crucibles e.g. Al_2O_3 should be used.

Thereby, corundum is the most common ceramic material. Both of these devices have an opportunity for TGA, which is very useful tool for measuring the mass change of a material as a function of temperature and time.

A temperature calibration procedure of the devices was systematically carried out by using pure reference elements with known melting temperatures. Measured temperatures were recalculated according to a correction function acquired at the last correction procedure. Temperature calibration of SE 1750 was performed using melting points of Al, Ag, Au, Cu and Ni. The correction procedure for SE 2400 was carried out using melting points of Al and Al_2O_3 as standard materials and solid phase transformation in LaYO_3 measured in SE 1750. These materials were chosen because of their inertness to crucible's materials. Correction polynomials were obtained by fitting derived points using the least-squares method. The temperatures of transformations were determined as on-set points i.e. intersection of the tangent line constructed in the point of highest slope and baseline. Since correction procedures were carried out using on-set point, temperatures of transformations have been also determined by on-set points.

3.3. Determination of thermodynamic properties

As mentioned above, thermodynamic properties of individual phases are necessary in order to achieve a reliable thermodynamic description of an evaluated system. There are many different techniques to determine thermodynamic properties of phases directly. Detailed description can be found in the books of Saunders and Miodovnik [12], Lukas *et al.* [5], review paper of Navrotsky [22] and others sources. In this chapter, only two types of measurements will be discussed further, namely drop solution and differential scanning calorimetry that were applied in the course of the current work.

Except of experimental methods, the predictive power of state-of-the-art first-principles simulations can be used efficiently to describe the thermodynamic properties of materials. This is very powerful tool to replace extremely difficult and time-consuming experiments or in a case if a performing of any measurements is impossible i.e. very low temperatures, extremely high pressures or metastable state of phases [23].

3.3.1. Differential scanning calorimetry

In the present work, differential scanning calorimetry (DSC) measurements were performed to obtain the heat capacity of individual phases of investigated systems. This information is essential for reliable thermodynamic assessments of binary and ternary systems and responsible modelling of multicomponent systems. The measurements in the temperature range from 100 to 675 K were carried out using a power-compensated device DSC 8000 (Perkin Elmer, Pt/Rh crucible, Ar or He flow, heating rate 10 K/min). For this type of measurements, the whole temperature range from 100 to 675 K was divided into small intervals of 100 – 150 K according to recommendation of the equipment supplier. The DSC measurements in the temperature range

from 623 to 1220 K were performed in one-step using a heat-flux device DSC Pegasus 404C (NETZSCH, Pt/Rh crucible, Ar flow, heating rate 10 K/min).

The classical three-step continuous method [24] with a constant heating rate was used as follows:

- The determination of the heat flow rate of the zero-line (with empty sample and reference sides). This step takes into account the heat capacity of inner parts of the device.
- The calibration step. At that, a sample of the material, for which heat capacity was precisely determined (for example synthetic sapphire), is measured in the sample crucible.
- Measurement of a sample with unknown heat capacity.

Calibration was performed using a certified sapphire standard in the case of ceramic materials. For metallic systems, calibration was performed using certified standard materials depending on the reliable temperature range of their heat capacity: copper standard was used in the temperature range from 100 to 320 K; molybdenum from 300 to 1073 K and platinum from 573 to 1473 K. The mass and radius of sample pellets were kept the same as for standard materials. The measurements of two different samples were repeated two times with a maximal uncertainty 3%. It should be mentioned that the C_p measurements at high temperatures using DSC equipment are becoming less reliable due to the increase of heat radiation which decreased registered signal. Thereby, the uncertainty of the measurement can reach up to 5% at high temperature (over 1273 K). This effect was considered during fitting of the experimental data. In order to exclude any phase transformation during the heat capacity measurement, XRD analyses of the samples were performed before the heat capacity measurements and afterwards.

3.3.2. Drop solution calorimetry

Drop solution calorimetry method was applied in order to determine the enthalpy of formation of oxide compounds. These measurements were performed using an Alexsys 800 heat-flux micro calorimeter (SETARAM, France). The samples pressed into pellets (\varnothing 1 mm, mass 3-9 mg) were dropped directly from r.t. into the calorimeter with a solvent at $T = 973$ K and the enthalpy increments of dropping and solution of a set of 9 pellets were measured. Sodium molybdate $3\text{Na}_2\text{O} \cdot 4\text{MoO}_3$ was used as the solvent. The calorimeter was calibrated using the molar enthalpy increment of dropping of 30 standard sapphire spheres. The error of the measurement was taken to be twice the standard deviation of the mean value.

3.3.3. First-principle calculations

In the current work, the density functional theory (DFT) and quasiharmonic approximation (QHA) were employed to calculate the free energy of the studied systems as a function of

volume and temperature. Thermodynamic properties were calculated using projector augmented wave (PAW) method [25] implemented in Vienna Ab-initio Simulation Package (VASP) [26]. Exchange-correlation effects were treated using the generalized gradient approximation [27]. Magnetic properties were accounted for within the collinear picture. The magnitudes and orientations of the collinear local moments were calculated self-consistently. The cut-off energies for plane waves and k-point grids were set based on the convergence test. The integration over the irreducible part of the Brillouin zone has been carried out using Monkhorst-Pack method [28]. The convergence criterion for electronic subsystem was set to be equal to 10^{-3} eV/atom for subsequent iterations. The relaxation of atomic positions was realized by calculation of Hellman-Feynman forces [29] and stress tensor by the conjugated gradient method. Relaxation was stopped when the forces became on the order of 10^{-3} eV/Å. The supercell approach was used for the phonon calculations. In order to calculate the interatomic forces in supercells, the values of atomic displacements was set to be equal to 0.01 Å. Postprocessing calculations of phonons was realized within the Phonopy code [30].

4. Fe–Mg–Zr–O system

4.1. State of the art

Thermodynamic modelling of the Fe–Mg–Zr–O system is essential for the understanding of possible interfacial reactions between steel and ceramic materials. As said above, the Fe–Mg–Zr–O system is a key sub-system for the development of the TRIP-Matrix-Composite.

Thermodynamic descriptions of all binary sub-systems of the Fe–Mg–Zr–O system were available [31–36]. Based on the available critical evaluation for the ternary Fe–Mg–Zr sub-system, an extrapolation from binaries would give reliable results due to absence ternary phases and significant ternary interactions [37].

According to available literature, the Fe–Mg–O system is well studied. There are many experimental data on phase relations, as well as on thermodynamic properties. A proper critical evaluation of all available experimental data and thermodynamic modelling of the Fe–Mg–O system have been presented by Jung *et al.* [38]. However, the authors have accepted thermodynamic models incompatible with the thermodynamic description of the current work. The last thermodynamic description of the Fe–Mg–O system has been presented by Dilner *et al.* [39]. Thermodynamic models of phases used in Ref. [39] are the same as in the present work but several parameters are different from the accepted parameters for the spinel phase assessed by Zienert and Fabrichnaya [40]. Therefore, thermodynamic parameters of the Fe–Mg–O system need to be re-assessed in order to obtain a self-consistent thermodynamic description.

Data on the phase relations in the Mg–Zr–O system were limited [41]. However, in the case of the development of TMC, the Mg–Zr–O system plays an essential role for the optimization of the ceramics Mg-PSZ. Concerning oxide sub-systems of the ternary Mg–Zr–O system, the first thermodynamic modelling of the MgO–ZrO₂ system was performed by Du and Jin [42] based on a critical evaluation of available experimental data. Later on, an optimization of the MgO–ZrO₂ system was done by Yin and Argent [43] using their own experimental thermodynamic data. The authors measured enthalpies of formation of the solid solution based on cubic ZrO₂ at different concentrations of the MgO stabilizer. The latest critical evaluation of the MgO–ZrO₂ system was made by Serena *et al.* [44] as a part of an assessment of the system CaO–MgO–ZrO₂. The last experimental investigation and thermodynamic modelling of the MgO–ZrO₂ system has been performed by Pavluchkov *et al.* [45], where the thermodynamic description was improved by using the compound energy formalism [18] for modelling of solid solutions of zirconia.

Experimental data for the Fe–Zr–O system were quite scarce due to difficulties in experimental studies of such systems. [1]. Since Fe can have several oxidation states, phase equilibria in this system depends on oxygen partial pressures and a requirement to control the partial pressure of oxygen during experiments becomes crucial for any experimental investigations of phase relations in this system. Substantial experimental difficulty is a possible reaction of samples with a crucible material [1]. For the first time, a thermodynamic database of the Fe–Zr–O system was derived by Huang [46]. The obtained thermodynamic description was based on

binary descriptions only. Moreover, presented calculations of the oxide part of the system were not fitted to reproduce experimental data of available literature [47,48]. The first thermodynamic assessment of the ternary area of the Fe–Zr–O system was performed by Fabrichnaya and Pavlyuchkov [49] to reproduce all available experimental data [47,48]. However, this work [49] was focused mostly on the oxide area of FeO–Fe₂O₃–ZrO₂. A preliminary description of Fe–Zr system [34] was introduced to calculate interaction between T–ZrO₂ and metallic liquid. However, in order to obtain a reliable thermodynamic description of the Fe–Zr–O system, the binary Fe–Zr sub-system should be re-assessed based on newly available data resolving existing inconsistencies.

The most recent systematic experimental study on binary Fe–Zr system was performed by Stein *et al.* [50]. In their work, Stein *et al.* succeeded in eliminating several contradictions and ambiguities. Namely, the Zr₆Fe₂₃ (ZrFe₃) phase was shown to be a non-equilibrium phase in the binary system. It was clearly demonstrated that this phase is stabilized by oxygen impurities. Additionally, the authors reported that there were four stable intermetallic compounds in the phase diagram: two polymorphic modifications of ZrFe₂ phase, Zr₃Fe and high-temperature Zr₂Fe. Cubic ZrFe₂ C15-Laves phase, which is stable up to 1503 K, transforms into the hexagonal C36 polymorph at 1563 K [50]. Intermetallic Zr₃Fe phase was found to be orthorhombic with Re₃B-type symmetry [50]. Zr₃Fe phase formed from a peritectoid reaction $\text{Zr}_2\text{Fe} + \beta\text{-Zr} \rightleftharpoons \text{Zr}_3\text{Fe}$; and the reported temperature of this reaction varied in several measurements: values of 1124 K [50], 1158 K [51], and 1213 K [52] were reported. Another intermetallic compound Zr₂Fe is a constituent of the above mentioned peritectoid reaction; it is a high-temperature phase with Al₂Cu-type crystalline structure. All stable intermetallic phases and their crystal structures are listed in Table 1.

According to the several thermodynamic assessments [53,54], there is limited information on thermodynamic properties of intermetallic compounds in binary Fe–Zr system at high temperatures. Regarding the heat capacity, Lück and Wang [55] performed the experimental measurements for C15–ZrFe₂ phase in the range of temperatures between 313 K and 653 K. Ali *et al.* [56] presented calculations of the heat capacity of Zr₂Fe and C15–ZrFe₂ by means of DFT methods. At the same time, there are no experimental data on the heat capacity of the Zr₂Fe and Zr₃Fe intermetallic phases. Moreover, it is worth noting that there is no available information on standard entropies for these intermetallic phases.

Summarizing the above discussion, it was necessary to resolve all existing inconsistencies, as well as to consider newly available thermodynamic data for the intermetallic compounds in order to achieve a reasonable thermodynamic description of the Fe–Zr system. Additionally, thermodynamic properties such as the specific heat capacity and the standard entropy for ZrFe₂, Zr₂Fe and Zr₃Fe should be obtained. Calculations of the heat capacity of Zr₂Fe presented in Ref. [56] should be verified and possibly extended by means of experimental studies. Moreover, the re-assessment of the Mg–Fe–O system is required in order to obtain a reliable thermodynamic description of the Fe–Mg–Zr–O system, which is essential for the implementation of the ceramics and steel databases.

Table 1. Data on crystal structures of solid phases of the Fe–Zr binary system.

Phase	Pearson symbol	Space group	Structure type
α -Fe	<i>cI2</i>	<i>Im$\bar{3}m$</i>	W
γ -Fe	<i>cF4</i>	<i>Fm$\bar{3}m$</i>	Cu
δ -Fe	<i>cI2</i>	<i>Im$\bar{3}m$</i>	W
Zr ₆ Fe ₂₃	<i>cF116</i>	<i>Fm$\bar{3}m$</i>	Mn ₂₃ Th ₆
C36-ZrFe ₂	<i>hP24</i>	<i>P6₃/mmc</i>	MgNi ₂
C15-ZrFe ₂	<i>cF24</i>	<i>Fd$\bar{3}m$</i>	MgCu ₂
Zr ₂ Fe	<i>tI12</i>	<i>I4/mcm</i>	Al ₂ Cu
Zr ₃ Fe	<i>oC16</i>	<i>Cmcm</i>	Re ₃ B
α -Zr	<i>hP2</i>	<i>P6₃/mmc</i>	Mg
β -Zr	<i>cI2</i>	<i>Im$\bar{3}m$</i>	W

4.2. Results and discussion

4.2.1. Fe–Zr system

As said above, the thermodynamic modelling of Fe–Zr system without any information on the thermodynamic properties of the phases becomes unreliable. At least, thermodynamics of the intermetallic compounds, that are stable in the wide temperature range, like Zr₃Fe and ZrFe₂, should be defined for further improvement of the thermodynamic description of the Fe–Zr system. Therefore, the DFT approach in combination with quasi-harmonic approximation (QHA) has been applied to determine the materials thermodynamic and thermal properties, such as heat capacity, entropy, etc. for orthorhombic Zr₃Fe and cubic C15-ZrFe₂ (Table 1). Since the QHA does not account anharmonic effects, which might be significant at high temperature [57], there is a limitation for this computational technique. Thus, in order to define the heat capacities of the investigated Zr₃Fe and C15-ZrFe₂ compounds at high temperatures, experimental measurements by DSC have been used as well.

Using the combination of DFT+QHA approach and experimental DSC analysis, a temperature dependence of the heat capacity $C_P(T)$, as well as the standard entropy S^{298} and enthalpy of formation ΔH^0 for the Zr₃Fe and ZrFe₂ intermetallic phases have been obtained from 0 K up to the temperature limits of their stability. Considering recent experimental data on the heat capacity and *ab-initio* calculations of the enthalpies of formation of the intermetallic compounds presented by Mukhamedov *et al.* [P1], Ali *et al.* [56] and values available in the databases of the Materials Project [58] and OQMD [59], the thermodynamics of the Fe–Zr system has been re-assessed in order to derive an up-dated set of Gibbs energies for all stable phases in the system. Liquid and solid solution phases such as bcc, fcc, and hcp have been described using a substitutional model. The compound energy formalism [18] has been used to describe homogeneity ranges of the C15- and C36-ZrFe₂ Laves phases. The magnetic properties of the solid phases have been considered using the Inden-Hiller-Jarl formalism [15]. The thermodynamic parameters derived in the present work reproduces the available experimental data on phase relations as well as on the thermodynamic properties [P2].

Within this thesis, the *ab-initio* calculations, experimental investigations and the thermodynamic modelling of the Fe–Zr system have been presented in detail in:

[P1] B.O. Mukhamedov, I. Saenko, A.V. Ponomareva, M.J. Kriegel, A. Chugreev, A. Udovsky, O. Fabrichnaya, I.A. Abrikosov, *Thermodynamic and physical properties of Zr₃Fe and ZrFe₂ intermetallic compounds*, *Intermetallics*, 109 (2019) 189.

[P2] I. Saenko, A. Kuprava, A. Udovsky, O. Fabrichnaya, *Heat capacity measurement of Zr₂Fe and thermodynamic re-assessment of the Fe–Zr system*, *CALPHAD*, 66 (2019) 101625.

4.2.2. Fe–Zr–O system

The obtained thermodynamic description of the Fe–Zr system was combined with the database of Fabrichnaya for the Fe–Zr–O system [49]. Afterwards, the thermodynamic model of the spinel phase in the Fe–Zr–O system has been re-assessed.

In the work of Fabrichnaya and Pavlyuchkov [49], the solubility of ZrO₂ in the Fe₃O₄ magnetite phase (spinel structure) was described by the following formula (Fe⁺²,Fe⁺³,Zr⁺⁴)_{T1}(Fe⁺²,Fe⁺³,Va)_{O2}(Fe⁺²,Va)_{I2}(O⁻²)₄, since there was no data in which the crystallographic site is occupied by Zr⁺⁴. However, based on crystallographic data for Mg₂TiO₄ and Fe₂TiO₄ it seems more reasonable that the large Zr⁺⁴ cation occupies the larger octahedral sites and, therefore, another formula should be used to describe magnetite i.e. (Fe⁺²,Fe⁺³)_{T1}(Fe⁺²,Fe⁺³,Zr⁺⁴,Va)_{O2}(Fe⁺²,Va)_{I2}(O⁻²)₄. Therefore, four end-members containing Zr⁺⁴ should appear Fe⁺²Zr⁺⁴₂Va₂O⁻²₄, Fe⁺³Zr⁺⁴₂Va₂O⁻²₄, Fe⁺²Zr⁺⁴₂Fe⁺²O⁻²₄ and Fe⁺³Zr⁺⁴₂Fe⁺²O⁻²₄. The Gibbs energy for two end-members can be derived using electro-neutrality conditions and the other two end-members using reciprocal reactions.

Fig. 2 shows the first two end-members together with Fe⁺²Fe⁺²₂Va₂O⁻²₄ and Fe⁺³Fe⁺²₂Va₂O⁻²₄ as well as electro-neutrality lines. Correspondingly, electro-neutrality reactions can be written as following:

- $\text{Fe}^{+2}\text{Zr}^{+4}_2\text{Va}_2\text{O}^{-2}_4 + \text{Fe}^{+2}\text{Fe}^{+2}_2\text{Va}_2\text{O}^{-2}_4 \rightleftharpoons 2 \cdot \text{Fe}^{+2}(\text{Fe}^{+2}_{0.5}\text{Zr}^{+4}_{0.5})_2\text{O}^{-2}_4$
- $\text{Fe}^{+3}\text{Zr}^{+4}_2\text{Va}_2\text{O}^{-2}_4 + 3 \cdot \text{Fe}^{+3}\text{Fe}^{+2}_2\text{Va}_2\text{O}^{-2}_4 \rightleftharpoons 4 \cdot \text{Fe}^{+3}(\text{Fe}^{+2}_{0.75}\text{Zr}^{+4}_{0.25})_2\text{O}^{-2}_4$

The Gibbs energy of inversed spinel Sp¹ (with Fe⁺²) is considered as sum of oxides ZrO₂ and FeO plus some positive parameter to be optimized:

- $G(\text{Fe}_2\text{ZrO}_4) = G(\text{ZrO}_2) + 2 \cdot G(\text{FeO}) + V1;$

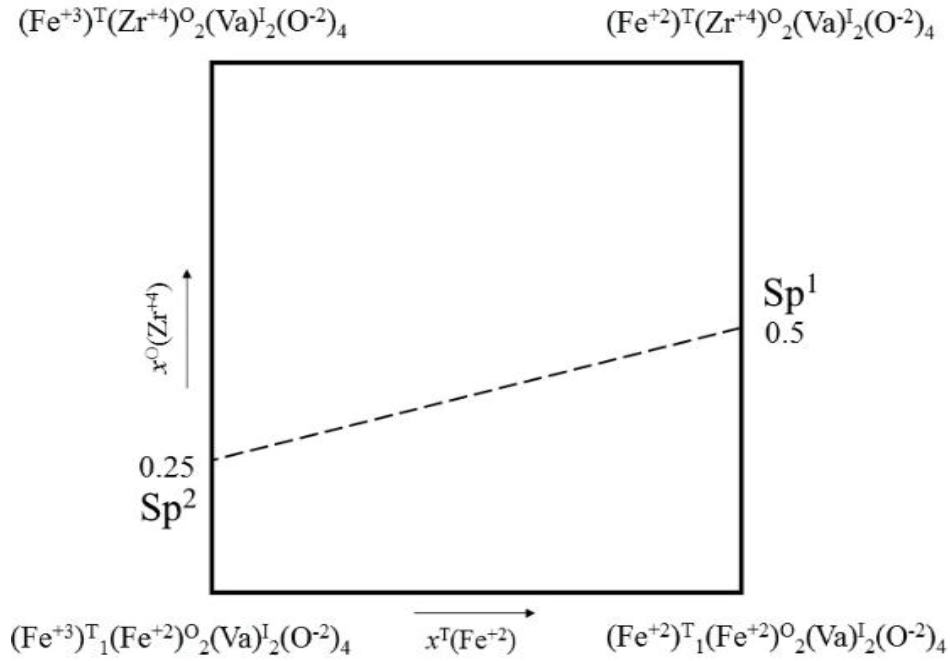


Fig. 2 – Electro-neutrality lines of the magnetite phase.

On the other hand, the Gibbs energy of inversed spinel Sp^1 is presented as:

- $2 \cdot G(Fe_2ZrO_4) = G(Fe^{+2}Zr_2Va_2O_4) + G(Fe^{+2}Fe^{+2}_2Va_2O_4) - 4 \cdot RT \ln(2);$

The Gibbs energy of inversed spinel Sp^2 (with Fe^{+3}) is considered as the sum of oxides ZrO_2 , FeO and Fe_2O_3 plus some positive parameter to be optimized:

- $4 \cdot GFe^{+3}(Zr^{+4}_{0.25}Fe^{+2}_{0.75})_2O_4 = 2 \cdot GZrO_2 + 6 \cdot GFeO + 2 \cdot GFe_2O_3 + V2$

On the other hand, the Gibbs energy of inversed spinel 2 is expressed as:

- $4 \cdot G(Fe^{+3}(Zr^{+4}_{0.25}Fe^{+2}_{0.75})_2O_4) = G(Fe^{+3}Zr_2Va_2O_4) + 3 \cdot G(Fe^{+3}Fe^{+2}_2Va_2O_4) + 8 \cdot R \cdot T \cdot (0.25 \cdot \ln(0.25) + 0.75 \cdot \ln(0.75));$

The Gibbs energies for the remaining two end-members $Fe^{+2}Zr^{+4}_2Fe^{+2}_2O_4$ and $Fe^{+3}Zr^{+4}_2Fe^{+2}_2O_4$ are obtained using the following reciprocal reactions:

- $Fe^{+2}Zr^{+4}_2Fe^{+2}_2O_4 + Fe^{+2}Fe^{+2}_2Va_2O_4 \rightleftharpoons Fe^{+2}Zr^{+4}_2Va_2O_4 + Fe^{+2}Fe^{+2}_2Fe^{+2}_2O_4;$
- $Fe^{+3}Zr^{+4}_2Fe^{+2}_2O_4 + Fe^{+3}Fe^{+2}_2Va_2O_4 \rightleftharpoons Fe^{+3}Zr^{+4}_2Va_2O_4 + Fe^{+3}Fe^{+2}_2Fe^{+2}_2O_4.$

The introduced changes into the description have not caused any substantial changes of the calculated phase diagram of the system presented in the work of Fabrichnaya and Pavlyuchkov [49].

The vertical section of $\text{ZrO}_2\text{--Fe}_2\text{O}_3$ calculated for air atmosphere and for $P(\text{O}_2) = 0.0021$ bar are presented in Fig. 3 together with experimental data. The isothermal section of $\text{ZrO}_2\text{--FeO--Fe}_2\text{O}_3$ is shown in Fig. 4.

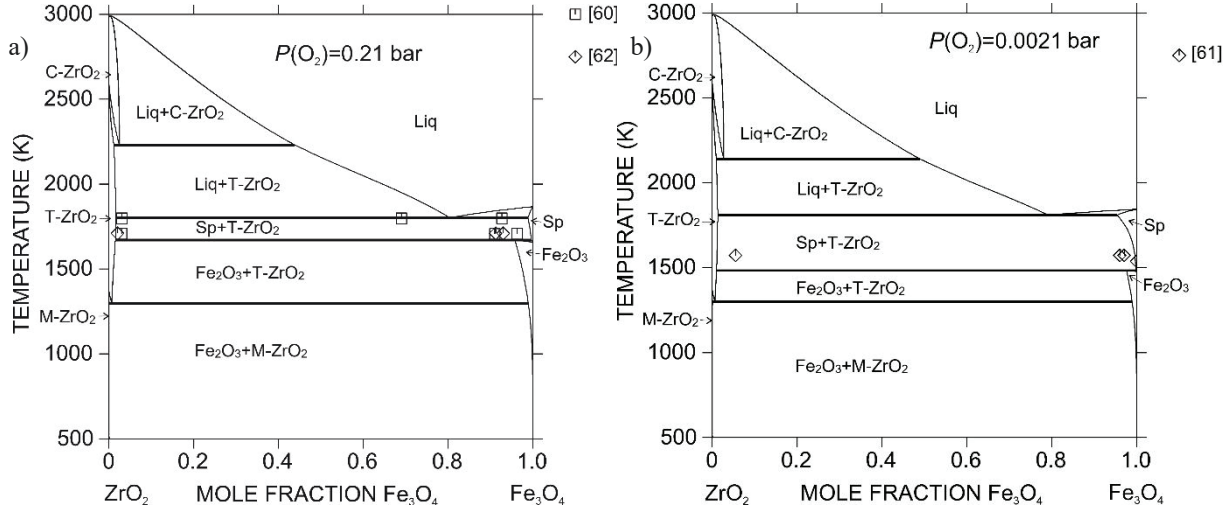


Fig. 3 – Calculated vertical section of $\text{ZrO}_2\text{--Fe}_2\text{O}_3$ at: a) air; b) $P(\text{O}_2) = 0.0021$ bar together with experimental data [60–62].

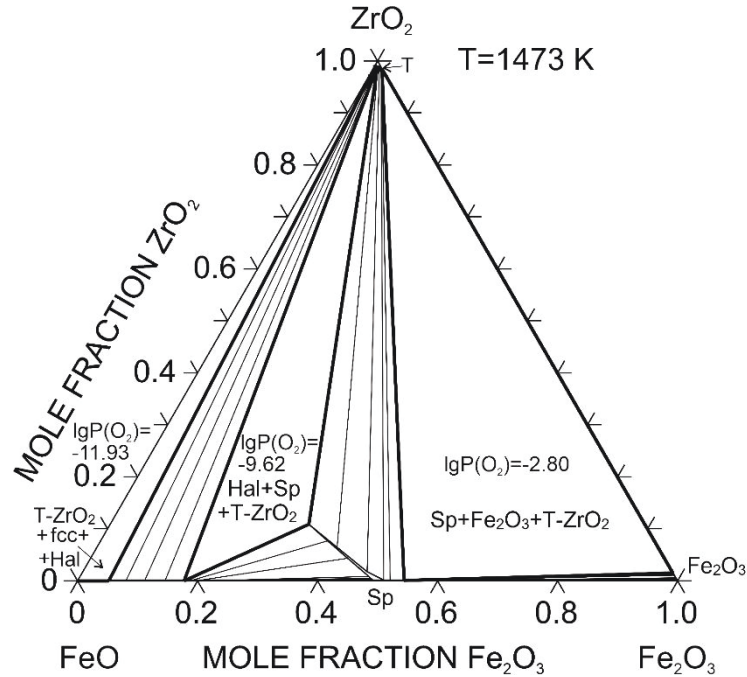


Fig. 4 – Calculated isothermal section of $\text{ZrO}_2\text{--FeO--Fe}_2\text{O}_3$ at 1473 K with calculated partial pressure conditions of three phase areas. According to experimental data from Ref. [47], partial pressure of the two phase field of $\text{Hal} + \text{T-ZrO}_2$ is in a range of $\lg P(\text{O}_2)$ from -11.82 to -9.21; $\text{Sp} + \text{T-ZrO}_2$ – $\lg P(\text{O}_2)$ from -9.09 to -3.36.

4.2.3 Fe–Mg–O system

Based on the available experimental results, a re-assessment of the Fe–Mg–O system has been performed in order to achieve the compatibility with the current thermodynamic database.

The magnesioferrite phase with spinel structure was modelled using the following formula $(\text{Fe}^{+2}, \text{Fe}^{+3}, \text{Mg}^{+2})_1(\text{Fe}^{+2}, \text{Fe}^{+3}, \text{Mg}^{+2}, \text{Va})_2(\text{Fe}^{+2}, \text{Mg}^{+2}, \text{Va})_2(\text{O}^{2-})_4$. The Gibbs energy for the spinel end-members in the Fe–O system were accepted from the description of Kjellqvist *et al.* [63] based on the description of Sundman [64]. The Gibbs energies of $\text{Mg}^{+2}(\text{Mg}^{+2})_2\text{Va}_2\text{O}^{2-}_4$ end-member were accepted from the work of Zienert and Fabrichnaya [40]. The Gibbs energies of $\text{Mg}^{+2}(\text{Fe}^{+3})_2\text{Va}_2(\text{O}^{2-})_4$ and $\text{Fe}^{+3}(\text{Mg}^{+2})_2\text{Va}_2\text{O}_4$ were optimized to reproduce experimental thermodynamic data for MgFe_2O_4 and the degree of inversion. The heat capacity is in a reasonable agreement with the data presented by Jung *et al.* [38], corresponding to the experimental data of King [65] and the adjusted data of Reznitskii *et al.* [66]. The heat capacity data were quite scattered. The heat capacity calculated from heat content measurements of Bonnickson [67] are incompatible with room temperature data of King [65]. Data on C_P from Barin [68] were lower at high temperature than calculated one from the measurements of Bonnickson [67]. The standard entropy of MgFe_2O_4 was determined by King [65] to be equal to $118.47 \text{ J}\cdot\text{mol}^{-1}\cdot\text{K}^{-1}$. However, later in book of Barin [68] a substantially higher value of $123.8 \text{ J}\cdot\text{mol}^{-1}\cdot\text{K}^{-1}$ was presented. It should be mentioned, that the value of standard entropy depends on the degree of inversion preserved in the measured substance and this phenomenon can explain the difference between different data.

In the present work a lower value of the standard entropy equal to $98.6 \text{ J}\cdot\text{mol}^{-1}\cdot\text{K}^{-1}$ was obtained as the result of the optimization procedure. It should be mentioned that the data on the enthalpy of formation of MgFe_2O_4 obtained by solution calorimetry present high uncertainty. The calculated value of the enthalpy of formation of $-19.293 \text{ kJ}\cdot\text{mol}^{-1}$ at room temperature reasonably agreed with value of Navrotsky [69] equal to $-20.64 \text{ kJ}\cdot\text{mol}^{-1}$ obtained at 973 K. It should be noted that value obtained using acid solution calorimetry by Koehler *et al.* [70] at 298 K was substantially higher $-2.52 \text{ kJ}\cdot\text{mol}^{-1}$. The temperature difference should not cause such a large difference in the enthalpy of formation from oxides. The main source of uncertainty is the enthalpy of dissolution of MgO. The latest data of Navrotsky [71] in combination with data of Majzlan *et al.* [72] for dissolution of Fe_2O_3 and data of Navrotsky [73] for dissolution of MgO resulted in $-2.22 \text{ kJ}\cdot\text{mol}^{-1}$ for the enthalpy of formation of MgFe_2O_4 at 973 K which is reproduced within the uncertainty range in the present work $-7.315 \text{ kJ}\cdot\text{mol}^{-1}$. To reproduce the degree of inversion, mixing parameters were introduced. The calculated degree of inversion along with experimental data are presented in Fig. 5.

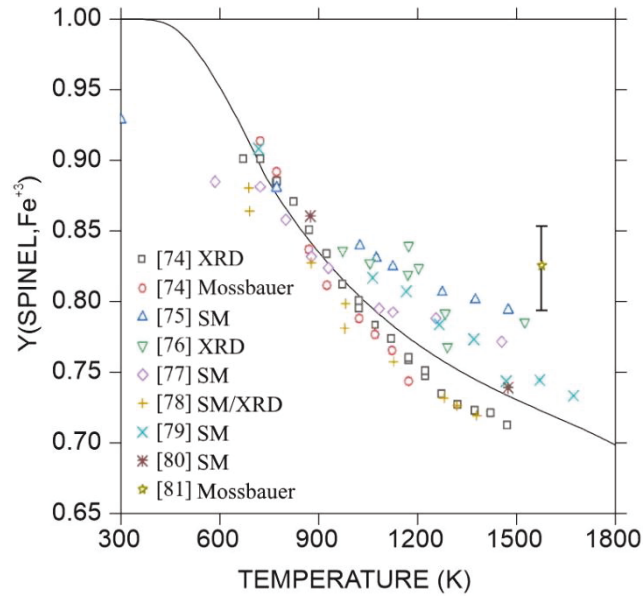


Fig. 5 – Inversion degree in the MgFe_2O_4 spinel with experimental data obtained by X-ray diffraction (XRD), Mossbauer and saturation magnetization (SM) measurements [74–81].

The experimental data on the Fe_2O_3 – MgO system at air pressure, the FeO – MgO system in presence of metallic iron, isothermal sections at varying partial pressures of oxygen, Fe^{+3} content in halite phase $(\text{Mg}^{+2}, \text{Fe}^{+2}, \text{Fe}^{+3}, \text{Va})_1(\text{O}^{2-})_1$ and other available data were used to optimise parameters of spinel, halite and liquid phases. A reasonable agreement between calculated and experimental data was obtained. The calculated phase diagram of the Fe_2O_3 – MgO system at air oxygen partial pressure is shown in Fig. 6. The calculated diagram for the FeO – MgO system in presence of metallic Fe is presented in Fig. 7.

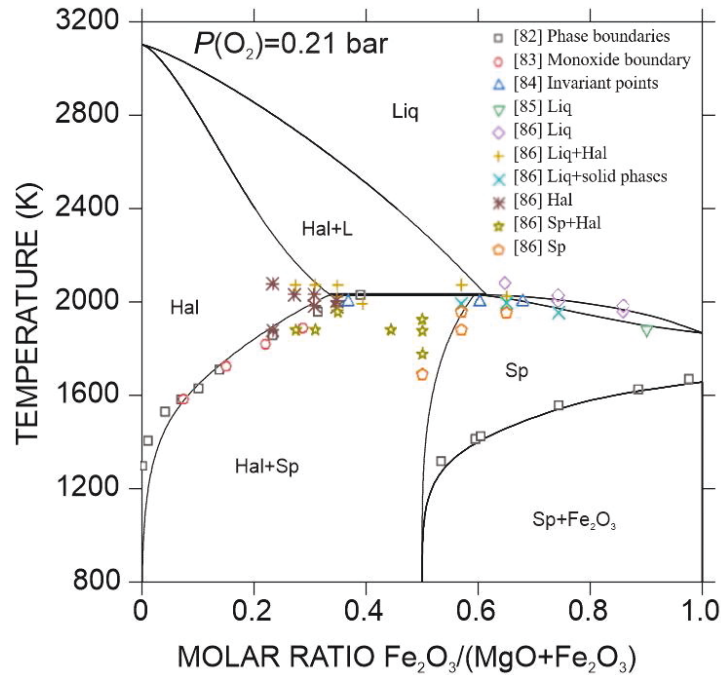


Fig. 6 – Calculated phase diagram of the Fe_2O_3 – MgO system in air corresponding to $P(\text{O}_2)=0.21$ bar in comparison with experimental data [82–86].

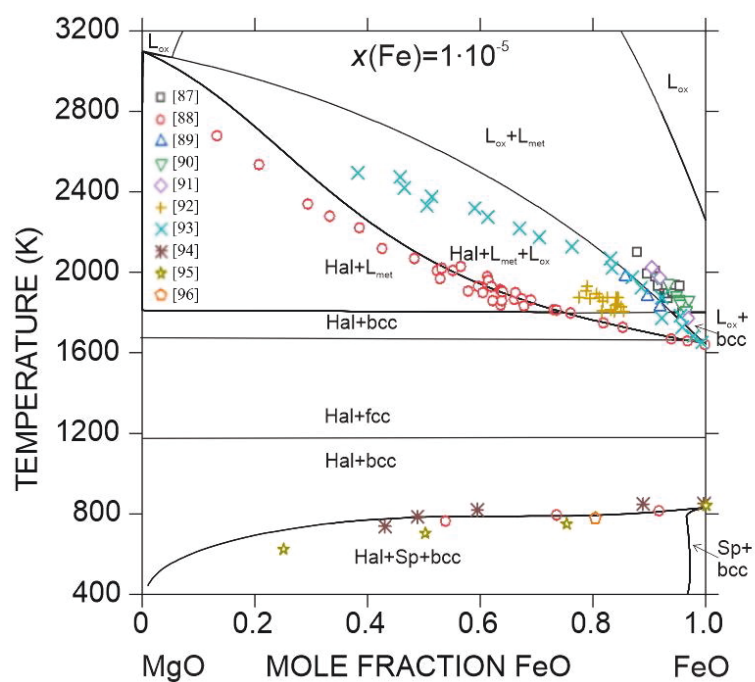


Fig. 7 – Calculated phase diagram of the FeO–MgO system in equilibrium in the presence of metallic Fe [87–96].

Isothermal sections at temperatures 1433, 1573 and 1673 K along with calculated isobars are compared with experimental data in Fig. 8.

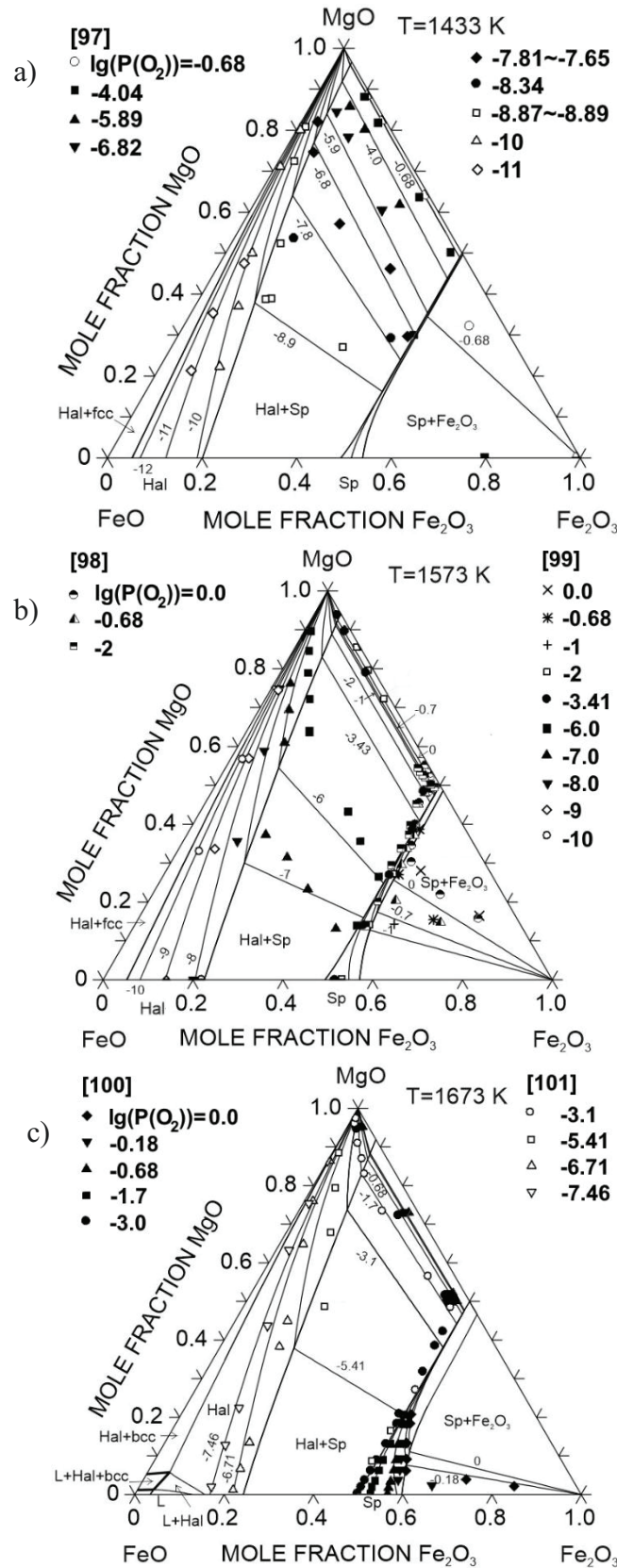


Fig. 8 – Calculated phase diagram section of the FeO–Fe₂O₃–MgO system along with calculated isobars at a) 1433, b) 1573 and c) 1673 K with experimental data on oxygen partial pressure in $\lg(P(\text{O}_2))$ in bar units [97–101].

The dependences of oxygen partial pressure on the metal ratio $\text{Mg}/(\text{Mg}+\text{Fe})$ at temperatures 1273, 1473, 1573 and 1773 K are presented in Fig 9.

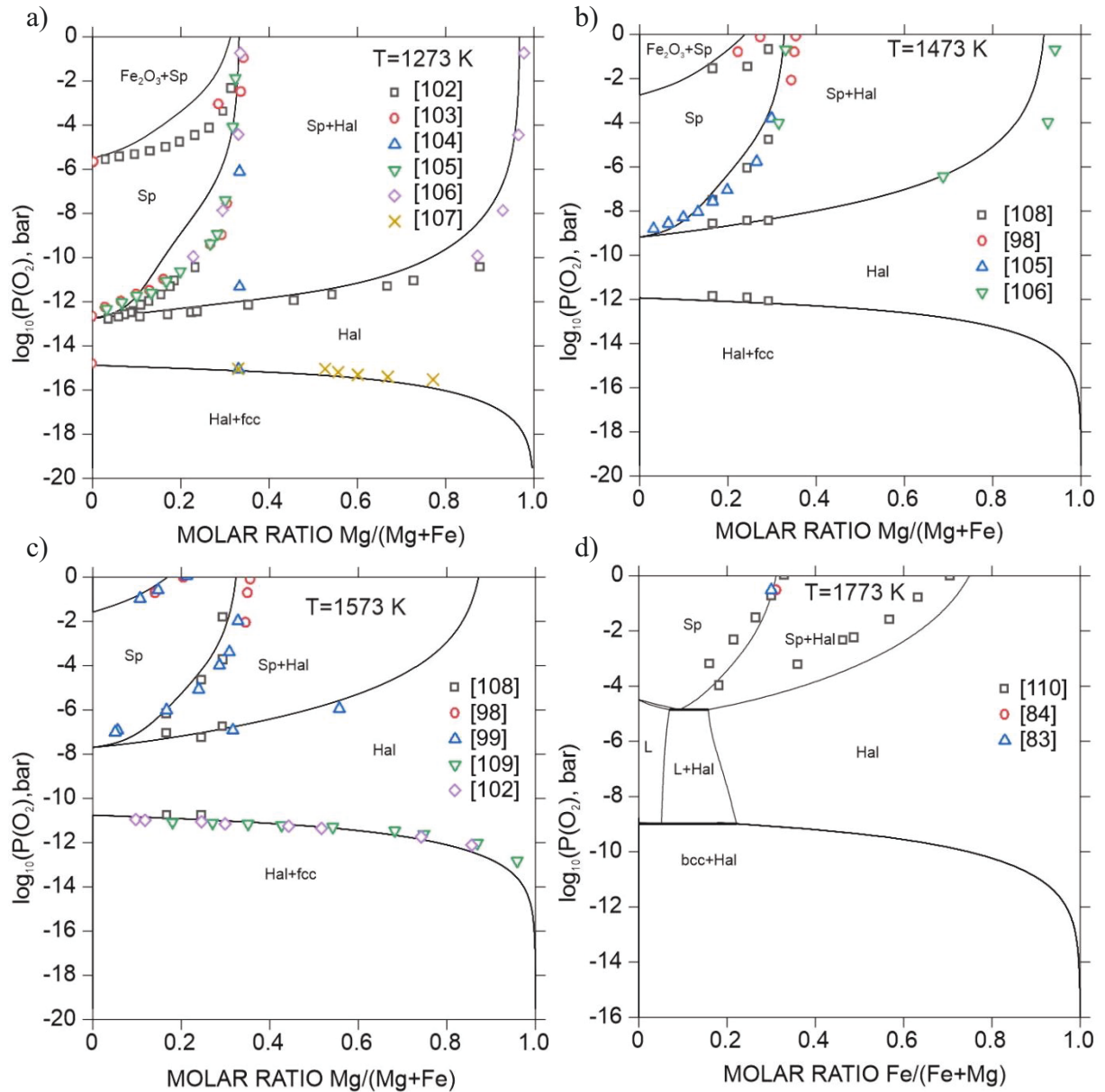


Fig. 9 – Calculated phase diagrams of the Fe–Mg–O system in dependence of oxygen partial pressure on metal ratio $\text{Mg}/(\text{Mg}+\text{Fe})$ at temperatures a) 1273, b) 1473, c) 1573 and d) 1773 K with experimental data [83,84,98,99,102–110].

4.2.4. Fe–Mg–Zr–O system

The thermodynamic description of the Mg–Zr–O system based on the work of Pavluchkov *et al.* [45], as well as obtained thermodynamic descriptions for the Fe–Zr–O and Fe–Mg–O systems have been combined with the available binary systems [31–36] in order to establish a thermodynamic database for the Fe–Mg–Zr–O system. The thermodynamic descriptions for Fe–O, Mg–O and Zr–O were accepted from the works of Kjellqvist [32], Hallstedt [36] and

unpublished description of Wang [33], respectively. According to recommendations of SGTE, the Mg–Zr system was accepted from the work of Härmäläinen and Zeng [35]. The Fe–Mg system was taken from Tibballs [111]. The Fe–Mg–Zr ternary system was accepted as an extrapolation from the binaries.

The introduction of the ZrO_2 solubility in the spinel phase for the $\text{FeO}_x\text{--MgO--ZrO}_2$ sub-system requires the definition of the Gibbs energies of four end-members: $\text{Mg}^{+2}(\text{Zr}^{+4})_2\text{Va}_2(\text{O}^{-2})_4$, $\text{Mg}^{+2}(\text{Zr}^{+4})_2(\text{Mg}^{+2})_2(\text{O}^{-2})_4$, $\text{Mg}^{+2}(\text{Zr}^{+4})_2(\text{Fe}^{+2})_2(\text{O}^{-2})_4$ and $\text{Fe}^{+2}(\text{Zr}^{+4})_2(\text{Mg}^{+2})_2(\text{O}^{-2})_4$.

The Gibbs energy of the Mg_2ZrO_4 metastable compound (inverse spinel $\text{Mg}(\text{Mg}_{0.5}\text{Zr}_{0.5})_2\text{Va}_2\text{O}_4$) was estimated to be $G(\text{Mg}_2\text{ZrO}_4)=2\cdot G(\text{MgO})+G(\text{ZrO}_2)+100000$. The Gibbs energy of end-member $\text{Mg}^{+2}(\text{Zr}^{+4})_2\text{Va}_2(\text{O}^{-2})_4$ was derived using electroneutrality condition:

- $\text{Mg}^{+2}(\text{Mg}^{+2})_2\text{Va}_2(\text{O}^{-2})_4+\text{Mg}^{+2}(\text{Zr}^{+4})_2\text{Va}_2(\text{O}^{-2})_4\rightleftharpoons 2\text{Mg}_2\text{ZrO}_4$ (inversed)
- $0.5\cdot G(\text{Mg}^{+2}\text{Zr}^{+4}_2\text{Va}_2\text{O}^{-2}_4)+0.5\cdot G(\text{Mg}^{+2}\text{Mg}^{+2}_2\text{Va}_2\text{O}^{-2}_4)-2\cdot RT\ln(2)=G(\text{Mg}_2\text{ZrO}_4)$

The Gibbs energies of other three end-members were obtained using reciprocal reactions

- $G(\text{Mg}^{+2}\text{Mg}^{+2}_2\text{Va}_2\text{O}^{-2}_4)=G(\text{Mg}^{+2}\text{Zr}^{+4}_2\text{Va}_2\text{O}^{-2}_4)+G(\text{Mg}^{+2}\text{Mg}^{+2}_2\text{Mg}^{+2}_2\text{O}^{-2}_4)-G(\text{Mg}^{+2}\text{Mg}^{+2}_2\text{Va}_2\text{O}^{-2}_4)$
- $G(\text{Mg}^{+2}\text{Zr}^{+4}_2\text{Fe}^{+2}_2\text{O}^{-2}_4)=G(\text{Mg}^{+2}\text{Zr}^{+4}_2\text{Va}_2\text{O}^{-2}_4)+G(\text{Fe}^{+2}\text{Zr}^{+4}_2\text{Fe}^{+2}_2\text{O}^{-2}_4)-G(\text{Fe}^{+2}\text{Zr}^{+4}_2\text{Va}_2\text{O}^{-2}_4)$
- $G(\text{Fe}^{+2}\text{Zr}^{+4}_2\text{Mg}^{+2}_2\text{O}^{-2}_4)=G(\text{Mg}^{+2}\text{Zr}^{+4}_2\text{Mg}^{+2}_2\text{O}^{-2}_4)+G(\text{Fe}^{+2}\text{Zr}^{+4}_2\text{Fe}^{+2}_2\text{O}^{-2}_4)-G(\text{Mg}^{+2}\text{Zr}^{+4}_2\text{Fe}^{+2}_2\text{O}^{-2}_4)$

The ternary solubility in ZrO_2 -based phases (cubic, tetragonal, monoclinic) and in the liquid phase were modelled based on binary extrapolations. Solubility of ZrO_2 in halite was not modelled due to absence of experimental data. Therefore, further experimental investigations are necessary. A calculated isothermal section at 1873 K is presented in Fig. 10.

The obtained thermodynamic description for the Fe–Mg–Zr–O system is presented in Appendix DTB1.

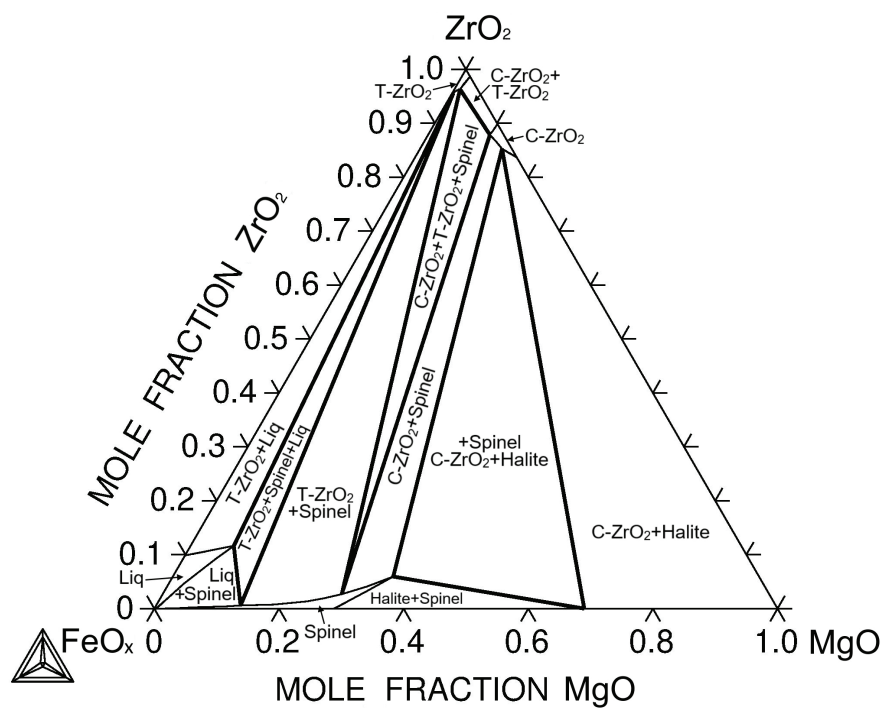


Fig. 10 – Calculated isothermal section of the FeO_x - MgO - ZrO_2 at 1873 K and air partial pressure of oxygen.

5. Mg–Ti–Zr–O system

5.1. State of the art

The interface bonding between the steel matrix and Mg-PSZ ceramic particles plays an important role for the development of TMC. Hereby, it was shown, that a coating of ceramic particles by a minor addition of TiO_2 improves bonding of the Mg-PSZ ceramics with the TRIP steel matrix [8]. Therefore, the thermodynamic modelling of the Mg–Ti–Zr–O system is a key subsystem for the optimization of the coating process of the Mg-PSZ for TMC.

All binary sub-systems of the Mg–Ti–Zr–O system are available from literature [35,36,49,112–114]. Based on the available critical evaluations for the ternary sub-systems, namely Ti–Zr–O [115], Mg–Zr–O [41], Mg–Ti–O [116] and Mg–Ti–Zr [117], data on the phase relations in ternary areas were limited and contradictory for thermodynamic modelling. However, in the case of the development of TMC, the Mg–Ti–Zr–O system plays essential role for optimization of the ceramics Mg-PSZ. Therefore, the MgO– TiO_2 – ZrO_2 system came into focus of this thesis.

For the oxide sub-systems of the ternary MgO– TiO_2 – ZrO_2 system, thermodynamic modelling of the MgO– ZrO_2 system was discussed earlier in Chapter 4.1. The last critical evaluation with a wide experimental investigation and the first consistent thermodynamic modelling of the MgO– TiO_2 system has have been performed by Ilatovskaia *et al.* [P9]. A new thermodynamic description of the MgO– TiO_2 system has been derived based on obtained heat capacity measurements of the Mg_2TiO_4 , MgTiO_3 , and MgTi_2O_5 compounds and considering the cation disordering in the intermediate compounds Mg_2TiO_4 and MgTi_2O_5 . The liquid phase was described by the two-sublattice partially ionic model [18]. All solid phase transitions, as well as all liquidus reactions were established and reproduced by the obtained thermodynamic description [P9]. A CALPHAD type assessment of the TiO_2 – ZrO_2 system has been performed using different models. Yokokawa *et al.* [118] used a substitutional model to describe the liquid and solid solutions. Cancarevic *et al.* [119] applied an associate model for the liquid and solid solutions. Schaedler *et al.* [120] and Arroyave [121] used the partially ionic liquid model for the liquid phase and the compound energy formalism for solid solutions. In comparison with other optimization, the thermodynamic description obtained by Cancarevic *et al.* [119] well reproduces most of experimental data and considers the homogeneity range of the high temperature $\beta\text{-(Zr}_x\text{Ti}_{1-x})_2\text{O}_4$ phase. However, it should be noted that the liquid phase description published in Ref. [119] shows an inversed miscibility gap above 2722 K and compositions of 60 mol% TiO_2 . Although there are still some contradictions in the published data on the phase equilibria, phase relations in the TiO_2 – ZrO_2 system were extensively studied. On the other hand, thermodynamic data for this system were scare. Therefore, in this work in order to obtain a self-consistent reliable thermodynamic description, verification of phase equilibria and additional thermodynamic measurements are necessary.

The phase relations in the MgO– TiO_2 – ZrO_2 system were first investigated by Coughanour *et al.* [122] in 1955. Based on obtained results, a tentative phase diagram of the ternary system has been constructed in the range between 1673 and 2023 K [122] (presented in Fig. 11). The ZrO_2 rich phases were not distinguished. Bayer [123] showed that up to 50 mol.% of ZrO_2 could

be replaced by TiO_2 in MgO -stabilized ZrO_2 in the temperature range of 1773–1873 K. Very limited data on phase relations were obtained in the MgTiO_3 – MgZrO_3 join (up to 30 mol.% MgZrO_3) at 1633–1693 K [124] indicating formation of secondary C- ZrO_2 phase starting from 5 mol.% of MgZrO_3 . The crystal structures of all solid phases of the quasi-binary oxide sub-systems of the MgO – TiO_2 – ZrO_2 system are listed in Table 2.

Table 2. Data on crystal structures of solid phases of the TiO_2 – ZrO_2 , MgO – ZrO_2 and MgO – TiO_2 quasi-binary systems.

Phase	Pearson symbol	Space group	Structure type
C- ZrO_2	<i>cF12</i>	$Fm\bar{3}m$	Fluorite- CaF_2
T- ZrO_2	<i>tP6</i>	$P4_2/nmc$	HgI_2
M- ZrO_2	<i>mP12</i>	$P2_1/c$	-
TiO_2	<i>tP6</i>	$P4_2/mnm$	Rutile
β -($\text{Zr}_x\text{Ti}_{1-x}$) $_2\text{O}_4$ (disordered)	<i>oP12</i>	$Pbcn$	α - PbO_2
α - TiZrO_4 (ordered)	-	$Pbcn$	-
α' - TiZrO_4 (Ti_2ZrO_6 -ordered)	<i>oP36</i>	$Pbcn$	-
MgO	<i>cF8</i>	$Fm\bar{3}m$	NaCl
MgTiO_3	<i>hR10</i>	$R\bar{3}$	Ilmenite- FeTiO_3
Mg_2TiO_4	<i>cF56</i>	$Fd\bar{3}m$	Spinel- Al_2MgO_4
MgTi_2O_5	<i>oS32</i>	$Ccmm$	Pseudobrookite- Fe_2TiO_5

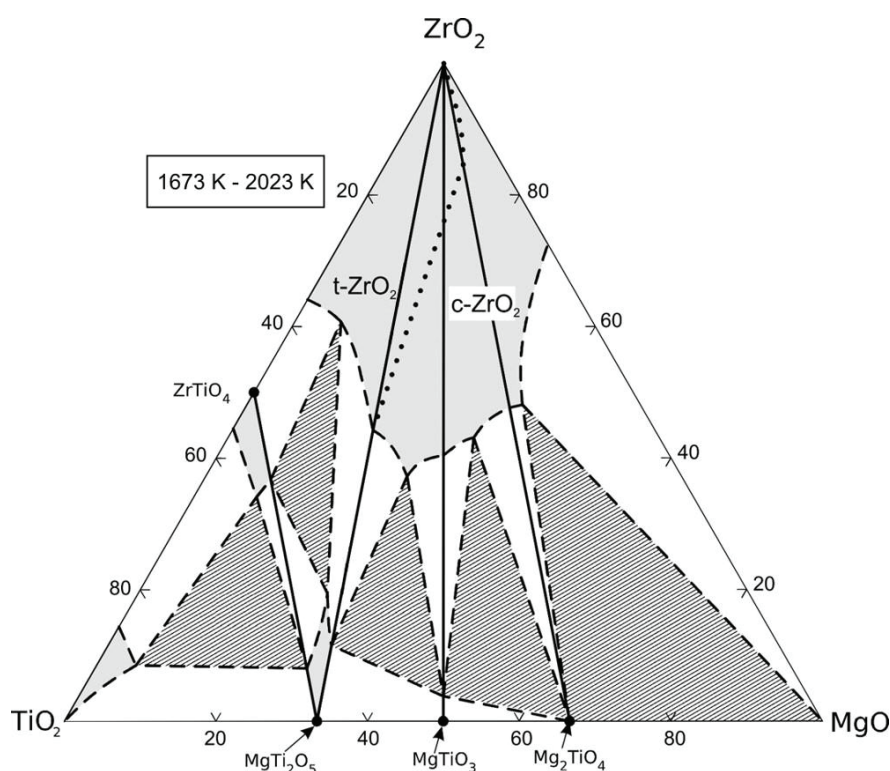


Fig. 11 – Preliminary phase diagram of the MgO – TiO_2 – ZrO_2 system [122].

Therefore, the aim of this work was the experimental investigation and thermodynamic modelling of the $\text{TiO}_2\text{--ZrO}_2$ system with further experimental studies of the phase relations in the $\text{MgO--TiO}_2\text{--ZrO}_2$ system to provide necessary information for the assessment of the thermodynamic parameters of the Mg--Ti--Zr--O system. The resulting thermodynamic description could be used for thermodynamic calculations of phase relations at the interface between Mg-PSZ particles and TRIP steel matrix.

5.2. Results and discussion

5.2.1. $\text{TiO}_2\text{--ZrO}_2$ system

In the first step of the re-assessment of the $\text{TiO}_2\text{--ZrO}_2$ system, heat capacity measurements of the disordered $\beta\text{-ZrTiO}_4$ compound (the $\beta\text{-(Zr}_x\text{Ti}_{1-x})_2\text{O}_4$ compound with the Zr:Ti molar ratio 1:1) have been performed in the wide temperature range of 235–1220 K. Moreover, the formation enthalpy of the $\beta\text{-ZrTiO}_4$ compound was determined by the drop solution calorimetry using the aforementioned Alexis 800 heat-flux microcalorimeter. The enthalpy of formation from oxides of $\beta\text{-ZrTiO}_4$ was measured to be $(-18.3 \pm 5.3) \text{ kJ}\cdot\text{mol}^{-1}$. The obtained experimental result was in a good agreement with experimental data of Hom *et al.* [125].

Phase relations in the $\text{TiO}_2\text{--ZrO}_2$ system has been investigated using XRD and SEM/EDX. The $\text{Liq} \rightleftharpoons \beta\text{-(Zr}_x\text{Ti}_{1-x})_2\text{O}_4 + \text{TiO}_2$ eutectic and the $\text{Liq} + \text{T-ZrO}_2 \rightleftharpoons \beta\text{-(Zr}_x\text{Ti}_{1-x})_2\text{O}_4$ peritectic reactions were determined using DTA at 2029 and 2117 K respectively. The compositions of the eutectic reaction was determined by SEM/EDX to be $83.2 \pm 1.0 \text{ mol\%}$ of TiO_2 . Experimental data on the phase relations obtained in this thesis were in a good agreements with available literature within the uncertainty limits [126–128].

The thermodynamic functions for pure oxides were available in literature [112,129]. Data for the Zr–O system were accepted from the work of Wang *et al.* [129]. The thermodynamic description of the Ti–O system published in the work of Hampl and Schmid-Fetzer [112] needed modification, namely re-modelling of liquid using the partially ionic liquid model to be compatible with other descriptions accepted in the present work. Therefore, thermodynamic descriptions of the liquid phase and $\text{Ti}_{20}\text{O}_{39}$ in the Ti–O system were re-assessed due to the application of the partially ionic liquid model [130]. Homogeneity ranges of solid solutions of ZrO_2 and TiO_2 , as well as $\beta\text{-(Zr}_x\text{Ti}_{1-x})_2\text{O}_4$ have been described using the compound energy formalism. The ordered compounds $\alpha\text{-TiZrO}_4$ and $\alpha'\text{-TiZrO}_4$ were modelled as stoichiometric compounds. The measured specific heat capacity, as well as the obtained value for enthalpy of formation of $\beta\text{-(Zr}_x\text{Ti}_{1-x})_2\text{O}_4$ were used for thermodynamic description directly. Using the obtained experimental results for the phase relations together with literature data, the thermodynamic parameters in the $\text{TiO}_2\text{--ZrO}_2$ system were derived. It can be concluded from this comparison, that reasonable consistency of the calculated and experimental data within uncertainty limits was achieved. Moreover, the reliability of obtained thermodynamic description was verified based on the reproducibility of experimental results in the ternary systems of our current studies [130]. Detailed information is given in:

[P3] I. Saenko, M. Ilatovskaia, G. Savinykh, O. Fabrichnaya, *Experimental investigation of phase relations and thermodynamic properties in the ZrO₂–TiO₂ system*, *Journal of the American Ceramic Society*, 101 (2018) 386.

5.2.2. MgO–TiO₂–ZrO₂ system

The MgO–TiO₂–ZrO₂ system has been experimentally investigated in the temperature range from 1530 K to the melting temperatures using XRD, SEM/EDX and DTA. Isothermal sections at 1475, 1530, 1555, 1680 and 1880 K were constructed based on corresponded experimental data. It has been determined that T-ZrO₂ phase can not be stabilized in the MgO–TiO₂–ZrO₂ system and transforms to monoclinic structure on cooling. A new ternary compound similar to δ -phase Y₄Zr₃O₁₂, which is the ordered phase of the fluorite structure (C-ZrO₂), so-called δ -phase, was found at 1530 K. Based on the SEM/EDX results, the δ -phase can be described by the formula Zr_{4.2}Ti_{0.8}Mg₂O₁₂. Homogeneity ranges of the compound were not established. However, based on the XRD results, it can be concluded that homogeneity ranges were negligible and, therefore, this compound can be considered as almost stoichiometric. The ternary compound has a trigonal structure of the Pr₇O₁₂-structure type. Results of XRD measurements are presented in Fig. 12. A temperature limit of the phase stability of the ternary compound has been determined to be 1535 – 1664 K using DTA.

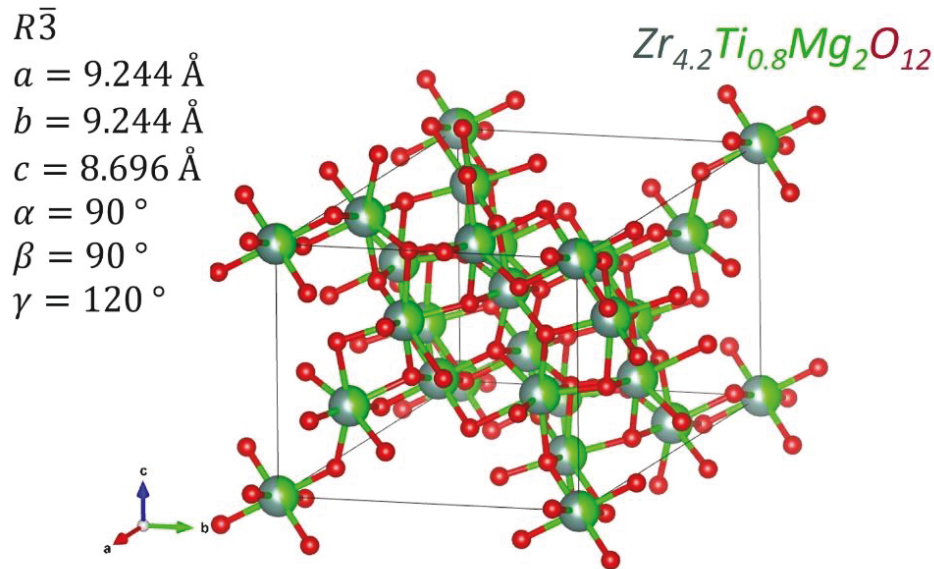


Fig. 12 – Crystal structure of the δ -phase with measured lattice parameters.

The heat capacity for the δ -phase was determined using DSC measurements and fitted using parameters of the Maier-Kelley equation. Using the mass effects suggested by Grimvall [131], the Einstein temperature of the new ternary compound was estimated to be $\theta_E^{\delta\text{-Phase}} = 571 \text{ K}$. By the application of an extended Einstein model [132], the standard entropy of the δ -phase was calculated to be $S^{298} = \int_0^{298} C_P \frac{dT}{T} = 12.3 \text{ J}\cdot\text{mol-at}^{-1}\cdot\text{K}^{-1}$.

The invariant reaction $\beta\text{-(Zr}_x\text{Ti}_{1-x})_2\text{O}_4 + \text{C-ZrO}_2 = \text{T-ZrO}_2 + \text{MgTi}_2\text{O}_5$ was experimentally found to occur at 1688 K based on DTA and microstructure investigation. The reaction is reversible and the high temperature phase assemblage could not be identified using XRD, while the SEM/EDX showed large grains of decomposed C-ZrO₂ phase [P4].

Using results obtained by DTA and SEM/EDX, the liquidus projection for the MgO–TiO₂–ZrO₂ system has been constructed. Three eutectic reactions have been found, namely:

- E₁: $\text{Liq} \rightleftharpoons \text{MgTi}_2\text{O}_5 + \text{C-ZrO}_2 + \text{MgTiO}_3$ at 1860 K; (8±1) mol% of ZrO₂, (50±2) mol% of TiO₂;
- E₂: $\text{Liq} \rightleftharpoons \text{TiO}_2 + \beta\text{-(Zr}_x\text{Ti}_{1-x})_2\text{O}_4 + \text{MgTi}_2\text{O}_5$ at 1851 K; (15±1) mol% of ZrO₂, (64±1) mol% of TiO₂;
- E₃: $\text{Liq} \rightleftharpoons \text{C-ZrO}_2 + \beta\text{-(Zr}_x\text{Ti}_{1-x})_2\text{O}_4 + \text{MgTi}_2\text{O}_5$ at 1800 K; (17±1) mol% of ZrO₂; (62±2) mol% of TiO₂;

Thereby, two reactions in the solid phases were determined: an eutectoid reaction of δ -phase $\rightleftharpoons \text{Mg}_2\text{TiO}_4 + \text{T-ZrO}_2 + \text{MgO}$ and the solid-state reaction of δ -phase + MgTiO₃ $\rightleftharpoons \text{Mg}_2\text{TiO}_4 + \text{T-ZrO}_2$.

Based on the obtained experimental data, thermodynamic parameters of the MgO–TiO₂–ZrO₂ system were optimized. Individual weights were given to every type of experimental data considering possible deviations and the accuracy of each experimental method. Thermodynamic descriptions of the binary sub-systems MgO–ZrO₂ and MgO–TiO₂ were accepted from the works of Pavlyuchkov *et al.* [45] and Ilatovskaya *et al.* [P9], respectively. A wide ternary extension of C-ZrO₂ in the ternary system, as well as less substantial ternary solubility of Mg₂TiO₄, MgTiO₃ and MgTi₂O₅ were modelled by the sublattice model using the compound energy formalism [18] described in Chapter 2.1. A very limited solubility of MgO found in $\beta\text{-(Zr}_x\text{Ti}_{1-x})_2\text{O}_4$ was considered to be insignificant and was not modelled in the current thermodynamic description. The ternary δ -phase was described as stoichiometric compound (ZrO₂)_{4.2}(TiO₂)_{0.8}(MgO)₂. The liquid phase was described by the two-sublattice partially ionic model. The Gibbs energies of charged end-members were calculated using electroneutrality conditions and reciprocal reactions [133].

All available experimental data on the phase relations in the MgO–TiO₂–ZrO₂ system, as well as the measured results of the high temperature heat capacity for the δ -phase are perfectly reproduced by the obtained thermodynamic description. Detailed information about all experimental investigations and the thermodynamic modelling of the MgO–TiO₂–ZrO₂ system can be found in:

[P4] I. Saenko, V. Tsukrenko, M. Ilatovskaia, D. Pavlyuchkov, G. Savinykh, O. Fabrichnaya, *Experimental Investigation of Phase Equilibria in the ZrO₂–TiO₂–MgO System*, *Advanced Engineering Materials*, 21 (2019) 1800655.

[P5] I. Saenko, O. Fabrichnaya, *Heat capacity measurements of the δ -phase $\text{Mg}_2\text{Zr}_{4.2}\text{Ti}_{0.8}\text{O}_{12}$ and thermodynamic modelling of the $\text{ZrO}_2\text{--TiO}_2\text{--MgO}$ System*, *Journal of the European Ceramic Society* 40 (2020) 3304.

5.2.3. Thermodynamic modelling of the Mg–Ti–Zr–O system

The obtained thermodynamic description of the $\text{MgO--TiO}_2\text{--ZrO}_2$ system was extended to a Mg–Ti–Zr–O database by applying descriptions for binary systems published in literature. Descriptions of the binary sub-systems Ti–Zr, Mg–Ti and Mg–O were accepted from available studies of Sridar *et al.* [113], Murray [114] and Hallstedt [36], respectively. According to recommendations of SGTE, the Zr–Mg system was accepted from the work of Hämäläinen and Zeng [35]. The same database for the Zr–O system [33] was applied in order to stay consistent with the Fe–Zr–O system. The Ti–O description was accepted from a work of Ilatovskaya *et al.* [130]. The finally established thermodynamic database for the Mg–Ti–Zr–O system is listed in Appendix as *TDB2*.

6. Mg–Mn–Zr–O system

6.1. State of the art

Since Mn is the second candidate for the improvement of the interface bounding between the steel and ceramics, thermodynamic modelling of the Mg–Mn–Zr–O system presents special interest for the development of TMC as well.

All binary sub-systems of the Mg–Mn–Zr–O system are available in literature. The sub-systems Mg–Zr, Zr–O, Mg–O were discussed earlier (Chapter 4 and 5). The previous descriptions of the Mn–O system by Kjellqvist and Selleby [63] and the Mg–Mn system by Tiaballs [111] have been accepted for this work. The Mn–Zr system has been modelled twice by Flandorfer *et al.* [134] and Hack [135]. Unfortunately, there is no reasonable thermodynamic description of the Mn–Zr system, that could be accepted in current work.

Hack [135] performed thermodynamic assessment based on phase diagram published by Massalski [136] indicating wide homogeneity range of the C14-ZrMn₂ phase. The phase diagram of the Mn–Zr system has widely studied by Flandorfer *et al.* [134] using DTA and EPMA for the first time. Thermodynamic parameters of the system were assessed by Flandorfer *et al.* [134] based on own experimental results and literature data. However, there were some contradictions between thermodynamic calculations of Flandorfer *et al.* [134] and available data on phase relations and thermodynamic properties in the system.

Thermodynamic studies in the Mn–Zr system, the enthalpy of formation of C14-ZrMn₂ was measured by Smetana *et al.* [137] to be (-16.6 ± 5.1) kJ·mol⁻¹ using the vapour pressure method. In the novel work of Rotter *et al.* [138] a value of (-22.66 ± 0.82) kJ·mol⁻¹ was obtained using drop solution calorimetry, which agreed well with the DFT calculation resulting in -20.3 kJ·mol⁻¹ presented in the same work [138]. In the work of Flandorfer *et al.* [134], the enthalpy of formation was set to be -40 kJ·mol⁻¹, what was significantly lower than experimental values. Moreover, Rotter *et al.* [138] have presented new data on heat capacity of the C14-ZrMn₂ phase in the range 3–170 K, which have to be considered for re-assessment of the Mn–Zr system. Unfortunately, no data at high temperatures is available so far. These data are necessary in order to obtain a reliable thermodynamic description.

In the work of Flandorfer *et al.* [134] the C14 phase was modelled with two sublattices: the first one occupied exclusively by atoms of Mn and the second one occupied by atoms of Zr and vacancies. Such a description implies that the homogeneity range is relevant due to the change of Zr occupation of a crystallographic site. However, a nonstoichiometry in AB₂ Laves phases with C14 structure occurs usually at specific ratio of radii of atoms R_A/R_B in a range of 1.12–1.26 and typically characterized by anti-site substitution defects [139]. An anti-site substitution mechanism is shown to be the dominant nonstoichiometry point defect mechanism in Laves phases [140], which is applied as common practice in thermodynamic modelling [141–144]. Therefore, the model applied in the assessment of Flandorfer *et al.* [134] needs to be revised.

The ternary Mg–Zr–O sub-system has been discussed in Chapter 4.1. Concerning the Mn–Zr–O and Mg–Mn–Zr systems, there is not enough information about phase relations in the ternary areas, which can be used for a proper thermodynamic assessment. The Mg–Mn–O ternary sub-system has been experimentally investigated and modelled by Dilner *et al.* [145] during the development of TMC [3]. Moreover, MnO_x – ZrO_2 and MgO – ZrO_2 oxide sub-systems of corresponding ternary sub-systems have been well studied within the TMC development [45,146].

The phase relations in the MgO – MnO_x – ZrO_2 system were experimentally studied by Pavlyuchkov *et al.* [147] for the first time. The investigations were carried out in air and inert gas atmosphere. It was shown that relatively small additions of ZrO_2 -stabilized cubic spinel in the ternary system in air at temperatures exceeding its stability range in the MgO – MnO_x bounding system and compositions substantially enriched by MgO . The addition of ZrO_2 also substantially expounds the homogeneity range of halite (MgO – MnO_x solid solution) toward MnO_x in air. It should be also noted that cubic ZrO_2 -based solid solutions are stabilized in the MgO – MnO_x – ZrO_2 system down to lower temperatures in comparison with the bounding systems, both in air and inert gas atmosphere.

The thermodynamic descriptions of the boundary systems are available in literature [45,145,146]. However the description of the MnO_x – ZrO_2 system needs to be modified since the description of Mn–O system accepted by Dilner *et al.* [145] was from the work of Kjellqvist and Selleby [63], while the one accepted by Pavlyuchkov *et al.* [146] was from a work of Grundy *et al.* [148]. Though the phase diagram of Mn–O system was very similar in both works, the description of Kjellqvist and Selleby [63] is more advanced taking into account the species distribution in the tetragonal and cubic Mn_3O_4 spinel. Special attention should be given to the fact that the thermodynamic description of the bounding systems MnO_x – ZrO_2 and MgO – ZrO_2 will be modified due to introducing Zr^{+4} in the spinel and halite models, which should cause only minimal changes of phase diagrams in the boundary system. It should be also noted, that stabilization of spinel and cubic ZrO_2 in the quaternary system outside its stability ranges in the boundary system will require introduction of Zr containing end-members in spinel and halite as well as ternary interaction parameters in all above mentioned phases to reproduce experimental data. Though the thermodynamic description for bounding systems are available, the MgO – MnO_x – ZrO_2 system was not modelled so far.

Summarizing, the aims of the present work were to revise the Mn–Zr system, as well as to develop a thermodynamic description of the MgO – MnO_x – ZrO_2 system which reproduces experimental data for the system. Some key DTA experiments were conducted to verify the thermodynamic description.

6.2. Results and discussion

6.2.1. Mn–Zr system

In order to improve the thermodynamic assessment of the Mn–Zr system, the heat capacity of the Laves C14-ZrMn₂ phase was measured in the range 200–980 K by means of DSC. The obtained data were applied to describe the Gibbs energy of the C14-ZrMn₂ phase. An extended Einstein model was applied for the description of heat capacity in the range from 0 to 1000 K and was used to calculate the standard entropy as 32.6 J·mol⁻¹·K⁻¹. The melting temperature of C14-ZrMn₂ phase was measured at 1765 K using the DTA method. The thermodynamic parameters of the Mn–Zr system were re-assessed considering newly available data presented by Rotter *et al.* [138]. The applied sublattice model of the C14-ZrMn₂ phase set to (Mn,Zr)₂(Mn,Zr)₁ was based on antisite substitution.

The re-assessment of the Mn–Zr system has been performed based on the obtained experimental results using the DSC and literature data. Liquid and solid solution phases have been described by a substitutional model. For the description of the C14-ZrMn₂ phase homogeneity range, the compound energy formalism for anti-site substitution was applied [18]. The presented description reproduces well the experimental data on phase equilibria and the thermodynamic properties of the phases. Details of the study can be found in Ref. [P6].

[P6] A. Kuprava, I. Saenko, O. Fabrichnaya, *Heat capacity measurement of C14-ZrMn₂ and thermodynamic re-assessment of the Mn–Zr system, CALPHAD*, 68 (2020) 101745.

6.2.2. Mg–Mn–Zr–O system

The thermodynamic database for the MgO–MnO_x–ZrO₂ system was derived based on the experimental data of Pavlyuchkov *et al.* [147]. The liquid phase is described by a two-sublattice partially ionic liquid model, while the solid solutions are described by the compound energy formalism [18]. The Zr⁺⁴ ions were introduced in the liquid phase, cubic spinel and halite phase. Due to introducing Zr⁺⁴ in halite and cubic spinel (βSp) phases the solubility of ZrO₂ should be very small in the MnO_x–ZrO₂ system. All polymorphic modifications of ZrO₂ have been modelled using two-sublattices. An extrapolation from bounding binary systems of the solubility of Mg⁺², Mn⁺³ and Mn⁺² in the C-ZrO₂ solid solutions has been extended by ternary interaction parameters. The solubilities of ZrO₂ in βSp and the halite phase in the ternary oxide system were experimentally established by Pavlyuchkov *et al.* [147]. The measured solubility of MgO and MnO_x was rather small in T-ZrO₂ and M-ZrO₂. Therefore, thermodynamic descriptions of these phases were combined based on descriptions of boundary systems and no ternary parameters were necessary to reproduce the phase relations involving these phases. Ternary mixing parameters and the Gibbs energy of end-members containing Zr⁺⁴ were necessary to model the solubility of ZrO₂ in βSp and the halite phase and to reproduce the phase relations involving these phases. Ternary mixing parameters were also introduced into the C-ZrO₂ description. The description of the liquid was based on extrapolations from boundary

systems. This was sufficient to reproduce all available data on phase relations involving the liquid. The description of other phases such as α -spinel, Mn_2O_3 , MnO_2 and Mg_6MnO_8 were accepted from the work of Dilner *et al.* [145] and were not modified further because phase equilibria studied in the paper of Pavlyuchkov *et al.* [147] did not involve these phases.

A thermodynamic modelling of the $\text{MgO-MnO}_x\text{-ZrO}_2$ oxide system has been performed for the first time. The obtained thermodynamic description was applied for the interpretation of DTA-TG results. The calculated phase fraction diagrams were used to relate the observed heat effects and mass losses. Detailed information can be found in:

[P7] I. Saenko, O. Fabrichnaya, *Thermodynamic database development for the $\text{ZrO}_2\text{-MgO-MnO}_x$ system*, *Journal of Phase Equilibria and Diffusion* 41 (2020) 654.

As said above, the obtained thermodynamic descriptions of ceramic systems have been combined with available descriptions of binary and ternary sub-systems into the Mg-Mn-Zr-O database (Appendix *TDB3*). The current database can be used for further thermodynamic modelling of the high-order systems for the development of the TRIP-Matrix-Composite [3,7]. Besides application for TMC, the obtained thermodynamic description has potential as a tool to predict the phase composition in directionally solidified eutectic materials based on the $\text{MgO-MnO}_x\text{-ZrO}_2$ system.

7. Implication of thermodynamic modelling for the development of the TRIP-Matrix-Composites

TMC containing highly alloyed austenitic TRIP-steel as a metal matrix and Mg-PSZ as a reinforcing ceramic component is considered as a promising new construction material with a high specific energy absorption during deformation. Under compression, the metastable austenite transforms into a martensitic phase resulting in an increasing strength. Besides this, Mg-PSZ undergoes a stress-induced transformation from tetragonal into monoclinic phase. Under compressive loading an increasing strength is observed by generation of additional stresses in the surrounding steel matrix of the composite material [2]. Furthermore, the martensitic transformation of the zirconia enables a certain plastic deformation of the rigid ceramic reinforcement, providing a remarkable toughness of the composite. Complexity of TMC requires the application of computational thermodynamics methods in order to reduce costs for the materials design and development process. Therefore, the CALPHAD method was applied for TMC development being a valuable tool for materials design. It was widely applied for:

- Optimization of chemical composition of steel matrix followed by annealing, which improves its microstructure [149];
- Study of pressureless sintering of TMC [P11];
- Prediction and understanding of the local deformation mechanisms [150];
- Modelling of interfacial reactions between steel matrix and ceramic particles [151];
- Understanding of phase transformations of the metastable austenite into martensite in the CrMnNi–N–C model alloy [152].

Additionally, the CALPHAD method provided a basis for application of further simulation methods used for the development of TMC i.e. thermo-mechanical modelling [153], simulation of electron beam welding [P12], the simulation of crystal plasticity [P14] and phase field modelling.

For the simulation of interfacial reactions between ceramic particles and the steel matrix as well as for the evaluation of the compatibility of materials, a thermodynamic database for the major sub-system Fe–Mg–Zr–O has been derived. TMC was developed to be produced by the method of the powder-metallurgical conventional sintering in a temperature range of 1623 – 1673 K in technical argon with a very low partial pressure of oxygen of $P(\text{O}_2) \approx 1 \times 10^{-4}$ bar. A more suitable technique to produce such types of composite materials is the Spark Plasma Sintering (SPS), which includes the application of the Joule heating and high pressure at sintering condition. Such complex conditions of the SPS production is very challenging for the thermodynamic simulation and requires at least more advance modelling of the pressure dependence of the Gibbs energies. Since no pressure dependence was not modelled in this work, the derived databases are not applicable to simulate the conditions at SPS production. Therefore, this method will not be discussed further in this chapter. However, due to the oxidized surface of the metal powder, a local equilibrium with an increased partial pressure of oxygen should be considered. Therefore, isothermal sections of the FeO–MgO–ZrO₂ system

were calculated at the temperatures of the sintering process, i.e. at 1623 and 1673 K in a presence of a small amount of iron (iron mole fraction $x(\text{Fe})=10^{-5}$) in order to consider possible reactions in the ceramic material. Calculated results are presented in Figs. 13 and 14. Based on the performed calculations, it can be concluded, that the solubility of the FeO in the T-ZrO₂ is insignificant and reaches around 2 mol%.

Further thermodynamic calculations have been performed in order to estimate possible reactions between Mg-PSZ and pure iron accounting the partial pressure of oxygen. During the conventional sintering of TMC, the atmosphere of the technical argon ($P(\text{O}_2) = 1 \times 10^{-4}$ bar) should be taken into account, as well as the ideal conditions of sintering where $P(\text{O}_2) \rightarrow 0$. The calculated vertical section between Mg-PSZ and pure Fe at $P(\text{O}_2)=10^{-4}$ bar and $P(\text{O}_2) \rightarrow 0$ are presented in Fig. 15. Based on the calculated diagram shown at Fig. 15 a, it can be concluded that even low partial pressure of oxygen ($P(\text{O}_2)=10^{-4}$ bar) is enough for the oxidation of iron and the appearance of the spinel phase. Thermodynamic calculations showed that the spinel phase dissolves ZrO₂ in the range from 1.2 to 1.8 mol.% at the temperatures of the sintering. Moreover, a significant amount of MgO (up to 5 mol.%) could be dissolved in the spinel phase. Such substantial diffusion of MgO from Mg-PSZ to the spinel phase could cause a destabilization of the Mg-PSZ ceramics. At the same time, T-ZrO₂ provides a very limited solubility of iron cations, which reaches only 1.3 mol.%. In the case of $P(\text{O}_2) \rightarrow 0$, the solubility of iron oxides in T-ZrO₂ is insignificant.

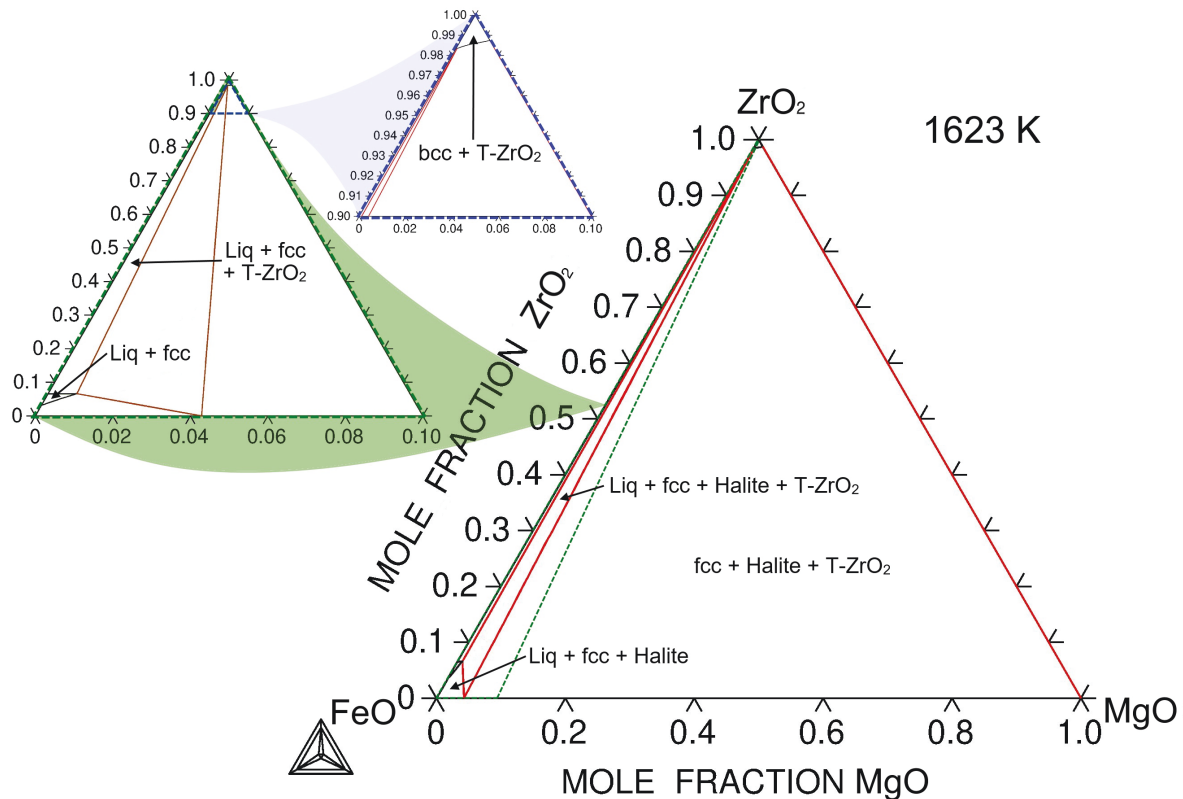


Fig. 13 – Calculated isothermal sections of the FeO–MgO–ZrO₂ system at 1623 K in presence of iron $x(\text{Fe})=10^{-5}$. Enlarged part of the diagram is labelled by green. ZrO₂-rich corner is labelled by blue.

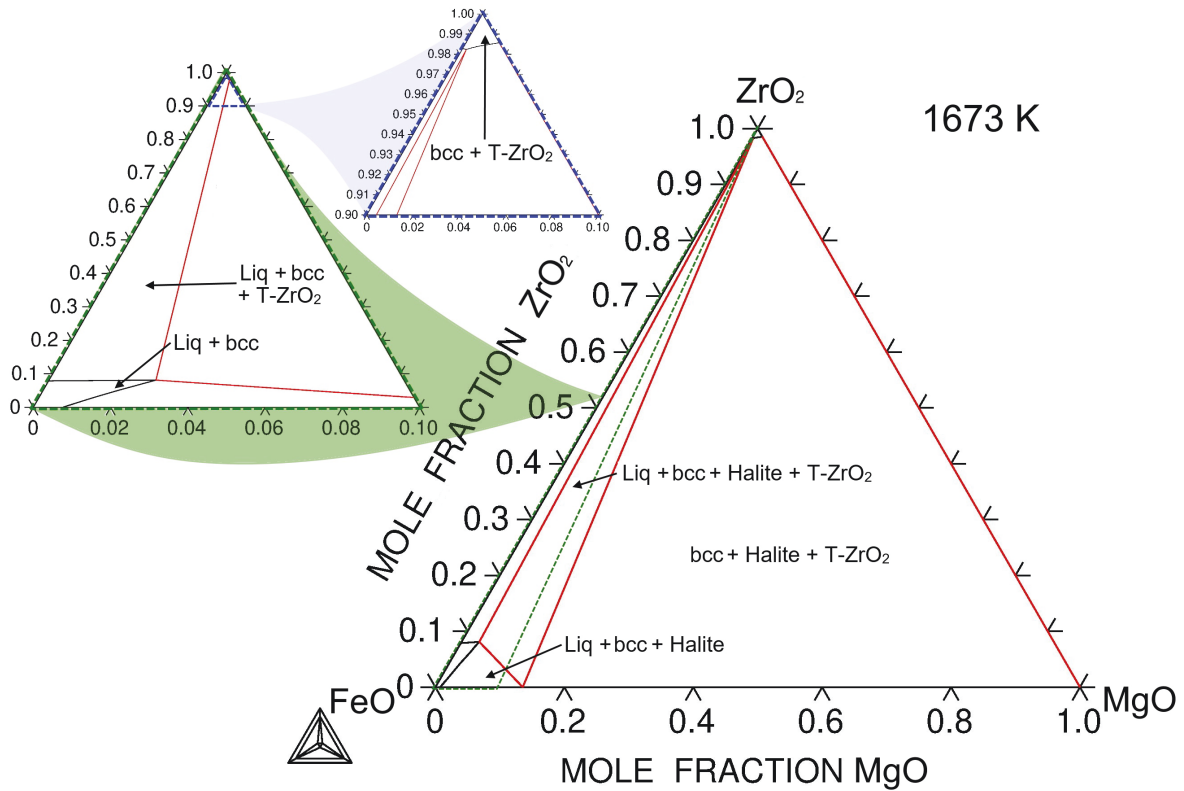


Fig. 14 – Calculated isothermal sections of the FeO–MgO–ZrO₂ system at 1673 K in presence of iron $x(\text{Fe})=10^{-5}$. Enlarged part of the diagram is labelled by green. ZrO₂-rich corner is labelled by blue.

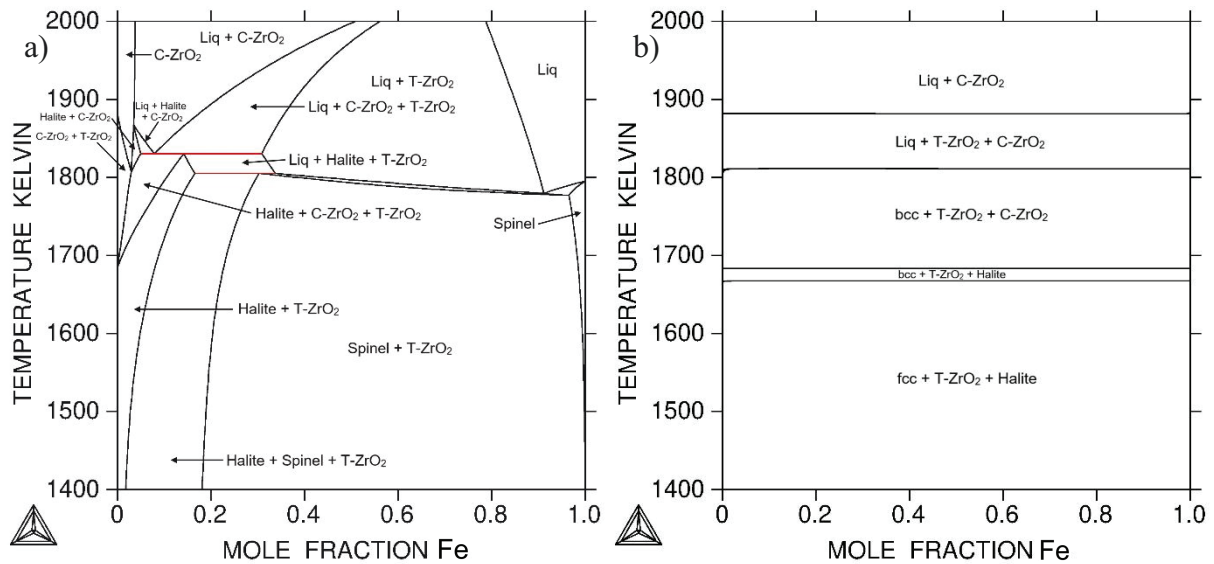


Fig. 15 – Calculated vertical section of Mg-PSZ (ZrO₂-10 mol.% MgO)–Fe at: a) $P(\text{O}_2)=10^{-4}$ bar; b) $P(\text{O}_2) \rightarrow 0$.

For a good performance of TMC, a strong adhesion between the metallic and the ceramic components is required in order to transmit stresses between different phases. As stated above, powder-metallurgical techniques i.e. conventional sintering applied for TMC production provide no crystallographic coherent interface between the components due to the random particle orientation [154]. Therefore, based on experimental results, titanium and manganese

have been suggested as promising elements that could serve as adhesion promoters by compound formation at the interface for TMC manufacturing [8–10,154]. Moreover, for a good performance most of the reinforcing zirconia should be present in tetragonal phase after the sintering process. Therefore, a certain thermal stability of the tetragonal phase at the sintering conditions need to be achieved, so that the phase transformation can occur during mechanical loading of the composite material. In order to attain the best adhesion between the metallic matrix and ceramics, an optimization of the adhesion promoters should be performed based on thermodynamic calculations. Thereby, possible interfacial reaction between matrix and the ceramics could be revealed.

7.1. Manganese as an adhesion promoter for TRIP-Marix-Composite

Experimental investigations of the interfacial reaction between Mg-PSZ and the steel matrix have shown that manganese provided a good adhesion bonding between the steel matrix and the Mg-PSZ ceramics [10,154]. Moreover, manganese is one of the main alloying elements of the steel matrix and can substitute Mg in Mg-PSZ during processing of this metal matrix composite [1,2,7], thus influencing the stabilities of the cubic and tetragonal phase. On the one hand, it was stated by Weigelt [155] that an incorporation of manganese ions into the zirconia lattice largely raised stabilization effects on the cubic phase. On the other hand, destabilization of Mg-PSZ occurs due to the diffusion of magnesium and the formation of Mg/Mn-rich compounds, such as spinel phases $(\text{Mg,Mn})\text{Al}_2\text{O}_4$ and silicates $(\text{Mg,Mn})_2\text{SiO}_4$, especially at the interfaces [9]. In order to avoid the formation of the undesirable phases at the boundary between the matrix and ceramics, an alloy with low silicon content was suggested. However, no sufficient results were achieved [156]. Consequently, in order to understand the nature of possible interfacial reactions between manganese and Mg-PSZ, thermodynamic calculations should be performed.

As said above, due to a significant surface oxidation of the metal powder during its production and storage, the local equilibrium with the manganese oxide should be considered. Since Mn can have oxidation state from Mn^{+2} to Mn^{+4} depending on the temperature and the partial pressure of oxygen [148], the formula of MnO_x is used for the representation of manganese oxide existing at the given conditions (i.e. T and $P(\text{O}_2)$). In order to present phase relations possible during TMC production, vertical sections of ZrO_2 with 10 mol.% MgO-MnO_x and isothermal sections of the $\text{MgO-MnO}_x\text{-ZrO}_2$ system were calculated at $P(\text{O}_2) = 1 \times 10^{-4}$ bar corresponding to the sintering condition in inert gas atmosphere and at air condition ($P(\text{O}_2) = 0.21$ bar) corresponding to the worst case of the local equilibrium appeared due to steel oxidation. The results of the calculations are presented in Fig. 16.

Thermodynamic calculations based on experimental results [146] have shown that the solubility of MnO_x is low in T- ZrO_2 and significantly higher in C- ZrO_2 . Thereby, a decreasing of the partial pressure of oxygen results in increase of the stability range of C- ZrO_2 (Fig. 16 a,b). However, due to wide homogeneity ranges of halite and spinel (Fig. 16 c,d), the interaction between Mg-PSZ and MnO_x would occur by a side diffusion of MgO along the MgO-MnO_x system into single phase fields of halite or spinel resulting in the destabilization of T- ZrO_2 or

C-ZrO₂. In other words, manganese in the form of MnO_x at the surface of the metal powder would react with Mg-PSZ forming solid solutions of (Mg,Mn)O halite and/or spinel phases during the conventional sintering leading to the destabilization of tetragonal phase of Mg-PSZ. Formation of the spinel or halite solid solutions will occur at the interface between the steel matrix and ceramics resulting in a crack formation at the phase boundaries. Thus, it is not possible to satisfy both requirements to achieve a proper bounding between steel matrix and ceramics and to keep the stabilized tetragonal zirconia at the same time. Based on the results of thermodynamic calculations, except of the adhesion promoters, a diffusion barrier on the surface of ceramic particles is necessary to inhibit the interaction of manganese with magnesium from the Mg-PSZ.

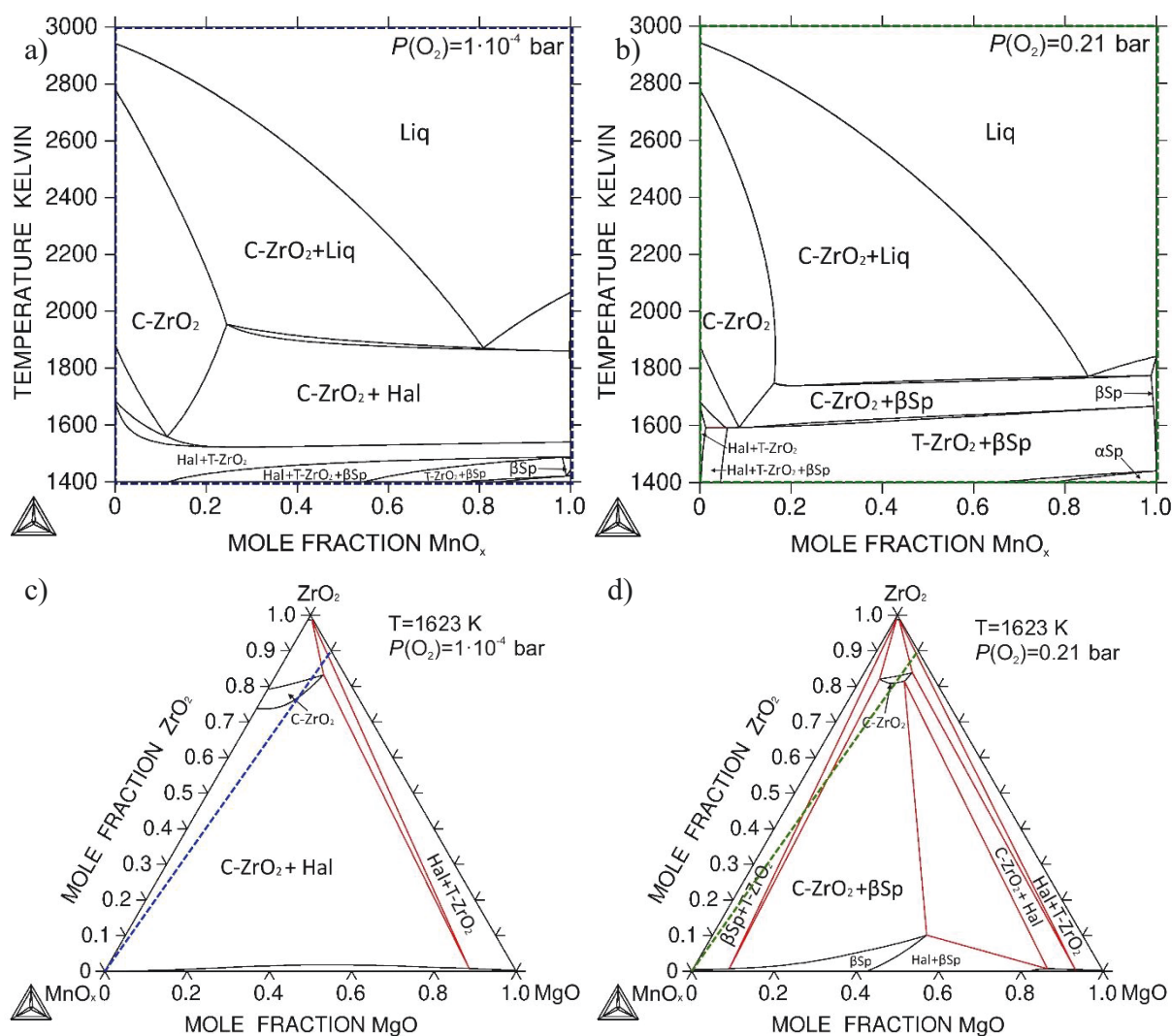


Fig. 16 – Calculated vertical section of Mg-PSZ (ZrO₂-10 mol.% MgO)–MnO_x at: a) $P(\text{O}_2)=10^{-4}$ bar; b) Air. Calculated isothermal sections of the ZrO₂–MgO–MnO_x system at 1623 K: c) $P(\text{O}_2)=10^{-4}$ bar; d) Air.

7.2. Titanium as an adhesion promoter for TRIP-Marix-Composite

The second promising approach to enhance the bounding between metal and ceramics was the minor addition of titanium [8]. The presence of titanium provides surface activation leading to sufficient infiltration during casting processes of ceramic preforms. Thereby, the addition of titanium improves the densification of the matrix material and the firm incorporation of the zirconia particles to the TRIP steel matrix [157]. However, in the case of an infiltration production presented by Wittig *et al.* [157], the addition of 20 wt.% of metal titanium powder to the Mg-PSZ ceramics lead to an enhanced brittleness of the TMC due to the appearance of Ti-rich phases. Based on further experimental results, Weigelt *et al.* [8] suggested an optimum of titanium additives existing in the range of 1 – 2 wt.%. In order to optimize the titanium content for the steel matrix, a vertical section between the TRIP steel matrix and titanium, as well as phase fraction diagrams have been calculated (Figs. 17 and 18).

Based on the performed thermodynamic calculations (Fig. 17), it can be seen that even small amounts of Ti in the matrix could result in the appearance of the titanium carbonitrides. Due to their small amount (up to 2.4 mol.% or 1.4 wt.%, see Fig. 18) this could be acceptable for the conventional sintering. However, in the case of the infiltration, titanium carbonitrides will appear as primary crystals from the melted steel (Fig. 17). Moreover, the formation of the C14 Laves phase could lead to high brittleness of the matrix above 4.8 wt.% of titanium. Moreover, titanium as a bcc-phase stabilizer would negatively influence to the steel matrix as well. This sets certain limits for the application of titanium as the adhesion promoter, i.e. based on thermodynamic modelling, titanium is unacceptable for infiltration at all.

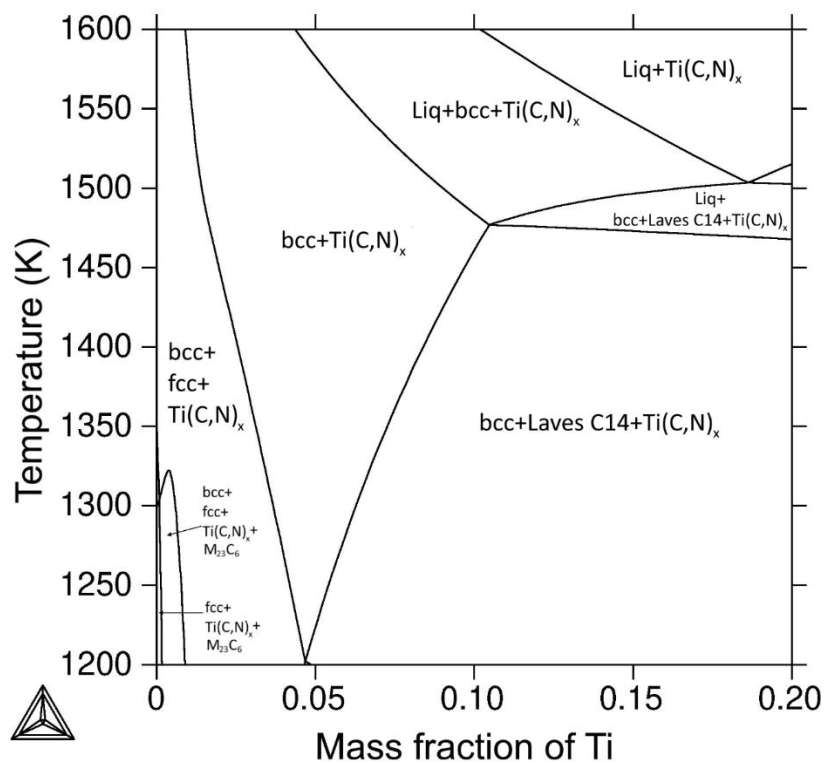


Fig. 17 – Vertical section of a TRIP steel (Fe-0.16C-0.14N-19Cr-4Ni-3Mn-0.45Si in wt.%)–20 wt.% of titanium.

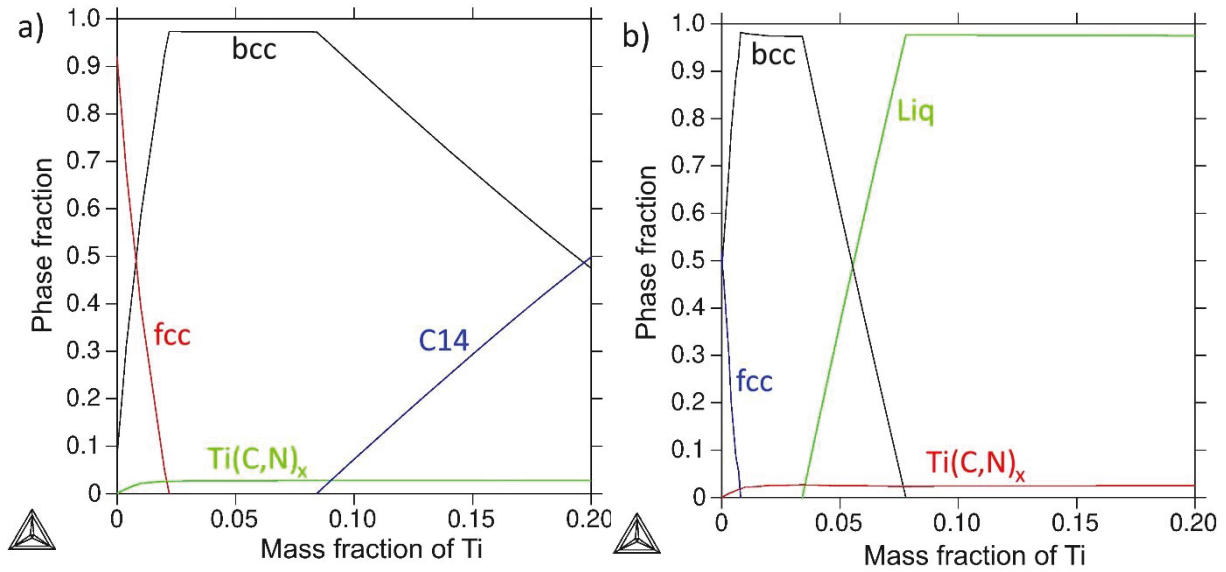


Fig. 18 – Phase fraction diagrams at: a) 1423 and b) 1623 K in dependence on the content of Ti related to the vertical section presented in Fig. 17.

7.3. Titania as an alternative for promotion of adhesion

To avoid the formation of Ti-rich phases, a solid-state coating process using high intensity milling was suggested in order to obtain a Ti-reaction layer on the surface of the Mg-PSZ ceramic particles. According to experimental results, the Mg-PSZ powder was covered by titanium oxides after the long-time milling process with small addition of the metal titanium. $\text{TiO}_x/\text{TiO}_2$ layer at the surface of the ceramic powder led to an enhancement of the bounding between metal and ceramics during the conventional sintering at 1623 K in technical argon atmosphere [156]. Thereby, destabilization of T-ZrO₂ and stabilization of C-ZrO₂ have been experimentally observed. For the understanding of all possible interactions between TiO₂ and Mg-PSZ, a vertical section for compositions between ZrO₂ with 10 mol.% MgO and TiO₂ was calculated. Calculated isothermal sections of the ZrO₂–TiO₂–MgO system as well as a calculated vertical section of Mg-PSZ–TiO₂ are presented in Fig. 19 a-g.

Based on the calculated results, it can be seen, that TiO₂ interacts with Mg-PSZ providing a good adhesion due to the formation of wide solid solutions in the ZrO₂–TiO₂ side system. Thereby, there is no or only very limited mutual solubility of MgO and TiO₂. However, an appearance of the intermediate phases of the MgO–TiO₂ system, as well as presence of the δ -phase could be possible at the grain boundary, especially at low temperatures (below 1606 K), which can cause problems of the bounding between steel and ceramics. It should be noted that the composition line between Mg-PSZ and TiO₂ intersects two tie-lines namely, between T-ZrO₂ + MgTi₂O₅ as well as zirconium titanate (β -(Zr_xTi_{1-x})₂O₄) + pseudoboorkite (MgTi₂O₅). Three-phase assemblages including the T-ZrO₂-solid solution and MgTi₂O₅ in equilibrium with C-ZrO₂ or zirconium titanate are possible up to 1688 K, which presents the temperature of the solid-state reaction β -(Zr_xTi_{1-x})₂O₄+C-ZrO₂=T-ZrO₂+MgTi₂O₅. At temperatures above this reaction, the composition line intersects β -(Zr_xTi_{1-x})₂O₄+C-ZrO₂ tie-line and corresponding three-phase tie-triangles including T-ZrO₂ or MgTi₂O₅. It should be noted, that occurrence of a

reversible solid-state reaction is not desirable in ceramic material. The vertical section for compositions between Mg-PSZ (10 mol.% MgO) and TiO_2 presented at Fig. 19 e allows the restriction of the amount of TiO_2 and the definition of the temperature range for sintering of composite material. It can be seen from the enlarged part of the diagram (Fig. 19 g) that, if a given concentration of TiO_2 would not overreach an amount of 12 mol.% and temperature of sintering is in the range 1610-1690 K, a formation of zirconia based solid solutions is the most probable result of the interaction between Mg-PSZ with TiO_2 , due to a significant solubility of TiO_2 in T- ZrO_2 and C- ZrO_2 .

Based on the thermodynamic calculations, the most suitable temperatures for the conventional sintering is stated to be in a range of 1606–1687 K (Fig. 19 e). As said above, the δ -phase and other intermediate compounds would appear at the interface between the steel matrix and ceramics below 1606 K (Figs. 19 a and b) that would increase possible cracking of the TMC. It should be noted that the formation of the C- ZrO_2 solid solution could be a dominating mechanism of the interaction between TiO_2 and Mg-PSZ due to the wide extension of cubic zirconia into the ternary area. Moreover, based on the experimental results [P3], no stabilization of the T- ZrO_2 by TiO_2 has been observed. T- ZrO_2 solid solution containing MgO and TiO_2 decomposes on cooling. Thereby, C- ZrO_2 is more stable in the ternary area and for some compositions can be preserved in cubic structure during cooling. Samples with 100 vol.% of cubic zirconia have been observed even upon slow cooling after heat treatment at 1673 K [P4].

On the other hand, the wide ternary extension of the cubic zirconia has great potential for an enhancement of the bonding between TRIP steel and Mg-PSZ ceramic. Experimentally observed interfacial layers around the ceramic particles indicate that the appeared cubic zirconia phase prevented decomposition of the tetragonal phase by the interruption of the reaction of Mg-PSZ with MnO_x described above [156]. Residual tetragonal zirconia grains surrounded by a cubic ZrO_2 area have been detected [156]. Therefore, covering of the Mg-PSZ particles by TiO_2 up to 10 mol.% (Fig. 19 f) should yield a strong connection between the individual phase constituents of the composite without the appearance of any detrimental phases at the grain boundaries with the steel matrix. Unfortunately, the technique of milling the Mg-PSZ powder with an addition of the metal titanium is not suitable to achieve that high amount of titania at the surface of the oxide powder. Consequently, a new satisfying technique the preparation of Mg-PSZ ceramics i.e. for titania deposition on the surface of the ceramic particles should be found.

8. Summary, conclusions and outlook

In this thesis, a wide range of theoretical and experimental investigations for the Fe–Mg–Zr–O, Mg–Ti–Zr–O and Mg–Mn–Zr–O systems have been performed. Thermodynamic data of studied intermetallic and ceramic compounds were received based on DSC and drop solution calorimetry methods, as well as by the means of Ab-initio calculations. Furthermore, phase relations have been studied by a wide range of static and dynamic methods.

Summing up, the following new results were obtained in the binary metallic systems:

- Zero temperature DFT calculations for the Zr_3Fe and $C15-ZrFe_2$ intermetallic compounds have been performed by VASP Software. A good agreement of theoretical results with available experimental data has been obtained;
- Effect of finite-temperatures was described within quasi-harmonic approximation (QHA). Heat capacities at constant volume (C_V) and at constant pressure (C_P) were calculated;
- Heat capacities of Zr_3Fe , Zr_2Fe were experimentally measured for the first time. Experimental data were obtained in a wide temperature range of 100 – 1023 K and 200 – 600 K, respectively;
- Available experimental data on the heat capacities of the Laves phases of $C15-ZrFe_2$ and $C14-ZrMn_2$ have been extended by the DSC measurement within a temperature ranges of 100 – 1473 K and 200 – 980 K, respectively;
- Based on the obtained results, using a combination of Ab-initio calculations and experimental data, temperature dependence functions of heat capacity $C_P(T)$, as well as thermodynamic parameters such as standard entropy S^{298} and enthalpy of formation ΔH^0 for intermetallic phases have been obtained from 0 K up to temperatures of their stability limit and described by an extended Einstein model [132];
- Thermodynamic parameters of the Fe–Zr and Mn–Zr systems have been re-assessed based on the obtained results.

New results for binary ceramic systems can be emphasized as follows:

- Formation enthalpy of the $\beta-ZrTiO_4$ compound from oxides was measured using drop solution calorimetry.
- Molar heat capacity of the $\beta-(Zr_xTi_{1-x})_2O_4$ compound was measured using DSC in the range 235–1220 K.
- The phase relations in the TiO_2 – ZrO_2 system were investigated in the temperature range from 1300 to 1900 K using XRD and SEM/EDX.
- Temperatures of invariant reactions in the TiO_2 – ZrO_2 system have been determined by means of DTA.
- Using the obtained experimental results together with literature data, the thermodynamic parameters in the TiO_2 – ZrO_2 system were derived.

For the ternary ceramic systems, following results have been obtained:

- MgO–TiO₂–ZrO₂ system was experimentally investigated in the temperature range from 1475 K to melting temperatures using XRD, SEM/EDX and DTA.
- Isothermal sections of the system at 1475, 1530, 1555, 1680 and 1880 K were constructed based on corresponding experimental data.
- According to experimental data of this work, T-ZrO₂ phase was not stabilized in the MgO–TiO₂–ZrO₂ system and transformed to monoclinic structure on cooling.
- A new ternary compound, i.e. the δ -phase with a trigonal structure of the Pr₇O₁₂-structure type with composition described by formula Mg₂Zr_{4.2}Ti_{0.8}O₁₂ has been found.
- Temperature range of stability has been determined between 1527 and 1664 K for the δ -phase.
- Heat capacities of the δ -phase was measured in the range 210–1370 K.
- Einstein temperature of the δ -phase was estimated to be 516 K using the mass effects suggested by Grimvall [131].
- Standard entropy for the δ -phase was evaluated to be 12.3 J·mol⁻¹·K⁻¹.
- Solid state transformations and invariant reactions have been experimentally defined.
- Liquidus projection for the MgO–TiO₂–ZrO₂ system has been constructed.
- Thermodynamic description of the MgO–TiO₂–ZrO₂ system has been derived.
- Based on the available experimental data, thermodynamic parameters of the MgO–MnO_x–ZrO₂ system were assessed.
- The obtained thermodynamic description was used for interpretation of DTA-TG results.

Based on the thermodynamic assessments of present study combined with data from literature, thermodynamic descriptions of the Fe–Zr–Mg–O, Mg–Ti–Zr–O and Mg–Mn–Zr–O systems have been derived. Thermodynamic calculations allow a prediction of interfacial reactions, consider the interactions between steel matrix and ceramics as well as to recommend conditions for production and development of the TMC (Chapter 7). Furthermore, the current thermodynamic description presents a basis for modelling of high-order systems. Moreover, the obtained thermodynamic description can be applied for the design and development of production processes for TMC, as well as other metal–ceramic–composite materials.

With regard to future work, thermodynamic parameters of other ternary sub-systems related to TMC need to be assessed for further development of the current thermodynamic description. Thereby, the most interesting aspect is an experimental investigation in atmosphere with controlled partial pressure of oxygen for study of oxide systems including element with different oxidation states.

Thermodynamic properties at temperatures below r.t. are essential for the distribution of the stressed induced transformation in TMC. Therefore, future works have to deal with the modelling in application of the 3rd Generation of CALPHAD databases which include extended description of the Gibbs energies from 0 K. In this work, the first steps for the 3rd Generation of CALPHAD have been accomplished by heat capacity measurements and calculations below room temperature.

References

- [1] H. Biermann, U. Martin, C.G. Aneziris, A. Kolbe, A. Müller, W. Schärfl, M. Herrmann, Microstructure and Compression Strength of Novel TRIP-Steel/Mg-PSZ Composites, *Adv. Eng. Mater.* 43 (2009) 1000.
- [2] S. Martin, S. Richter, S. Decker, U. Martin, L. Krüger, D. Rafaja, Reinforcing Mechanism of Mg-PSZ Particles in Highly-Alloyed TRIP Steel, *steel research int.* 82 (2011) 1133.
- [3] H. Biermann, TRIP-Matrix-Composites, *Adv. Eng. Mater.* 21 (2019) 1900126.
- [4] U.R. Kattner, The Calphad Method and its Role in Material and Process Development, *Tecnologia em metalurgia, materiais e mineracao* 13 (2016) 3.
- [5] H.L. Lukas, S.G. Fries and B. Sundman, Computational Thermodynamics The Calphad Method, Cambridge University Press, New York, 2007.
- [6] P. Franke, H.J. Seifert, The influence of magnetic and chemical ordering on the phase diagram of Cr–Fe–Ni, *Calphad* 35 (2011) 148.
- [7] S. Martin. private communication, 2020.
- [8] C. Weigelt, H. Berek, C.G. Aneziris, S. Wolf, R. Eckner, L. Krüger, Effect of minor titanium additions on the phase composition of TRIP steel/magnesia partially stabilised zirconia composite materials, *Ceram. Int.* 41 (2015) 2328.
- [9] H. Berek, A. Yanina, C. Weigelt, C.G. Aneziris, Determination of the Phase Distribution in Sintered TRIP-Matrix/Mg-PSZ Composites using EBSD, *steel research int.* 82 (2011) 1094.
- [10] M. Kirschner, S. Martin, S. Guk, U. Prahl, R. Kawalla, Forming Complex Graded and Homogeneous Components by Joining Simple Presintered Parts of TRIP-Matrix Composite through Powder Forging, *Metals* 10 (2020) 543.
- [11] L. Kaufman, H. Bernstein, Computer calculation of phase diagrams with special reference to refractory metals, Academic Press Inc, New York, 1970.
- [12] N. Saunders, A.P. Miodownik, Calphad: A comprehensive guide, Pergamon, Oxford, 1998.
- [13] R. Schmid-Fetzer, D. Andersson, P.Y. Chevalier, L. Eleno, O. Fabrichnaya, U.R. Kattner, B. Sundman, C. Wang, A. Watson, L. Zabdyr, M. Zinkevich, Assessment techniques, database design and software facilities for thermodynamics and diffusion, *Calphad* 31 (2007) 38.
- [14] O.B. Fabrichnaya, S.K. Saxena, P. Richet, E.F. Westrum, Thermodynamic Data, Models, and Phase Diagrams in Multicomponent Oxide Systems: An Assessment for Materials and Planetary Scientists Based on Calorimetric, Volumetric and Phase Equilibrium Data, Springer Berlin Heidelberg, 2004.
- [15] M. Hillert, M. Jarl, A model for alloying in ferromagnetic metals, *Calphad* 2 (1978) 227.
- [16] A.T. Dinsdale, SGTE data for pure elements, *Calphad* 15 (1991) 317.
- [17] O. Redlich, A.T. Kister, Algebraic Representation of Thermodynamic Properties and the Classification of Solutions, *Ind. Eng. Chem.* 40 (1948) 345.
- [18] M. Hillert, The compound energy formalism, *J. Alloys Comp.* 320 (2001) 161.
- [19] UNARY Database SGTE, <https://www.sgte.net/>, accessed 24 June 2020.

- [20] J.-O. Andersson, T. Helander, L. Höglund, P. Shi, B. Sundman, Thermo-Calc & DICTRA, computational tools for materials science, *Calphad* 26 (2002) 273.
- [21] L. Lutterotti, Total pattern fitting for the combined size–strain–stress–texture determination in thin film diffraction, *Nucl. Instrum. Methods Phys. Res., B* 268 (2010) 334.
- [22] A. Navrotsky, Progress and New Directions in Calorimetry: A 2014 Perspective, *J. Am. Ceram. Soc.* 97 (2014) 3349.
- [23] R.M. Dreizler, E.K.U. Gross, Density Functional Theory: An Approach to the Quantum Many-Body Problem, Springer Berlin Heidelberg, Berlin, Heidelberg, 1990.
- [24] G. Della Gatta, M.J. Richardson, S.M. Sarge, S. Stølen, Standards, calibration, and guidelines in microcalorimetry. Part 2. Calibration standards for differential scanning calorimetry (IUPAC Technical Report), *Pure Appl. Chem.* 78 (2006) 1455.
- [25] P.E. Blöchl, Projector augmented-wave method, *Phys. Rev. B Condens. Matter* 50 (1994) 17953.
- [26] G.G. Kresse, J. Furthmüller, Efficient iterative schemes for ab initio total-energy calculations using a plane-wave basis set, *Phys. Rev. B Condens. Matter* 54 (1996) 11169.
- [27] J.P. Perdew, K. Burke, M. Ernzerhof, Generalized Gradient Approximation Made Simple, *Phys. Rev. Lett.* 77 (1996) 3865.
- [28] H.J. Monkhorst, J.D. Pack, Special points for Brillouin-zone integrations, *Phys. Rev. B* 13 (1976) 5188.
- [29] R.P. Feynman, Forces in Molecules, *Phys. Rev.* 56 (1939) 340.
- [30] A. Togo, I. Tanaka, First principles phonon calculations in materials science, *Scr. Mater.* 108 (2015) 1.
- [31] S. Cui, I.-H. Jung, Thermodynamic Assessments of the Fe–Si–Cr and Fe–Si–Mg Systems, *Metall. and Mat. Trans. A* 48 (2017) 4342.
- [32] L. Kjellqvist, M. Selleby, B. Sundman, Thermodynamic modelling of the Cr–Fe–Ni–O system, *Calphad* 32 (2008) 577.
- [33] C. Wang. personal communication, 2006.
- [34] P.-Y. Chevalier and E. Fischer: Unpublished Research, 2003, cited by Landolt-Bernstein, Thermodynamic Properties of Inorganic Materials compiled by SGTE, Group IV (Physical Chemistry), Binary systems—subvolume B, Binary systems from Cs–K to Mg–Zr, Springer, Berlin, 2005.
- [35] M. Härmäläinen, K. Zeng, Thermodynamic evaluation of the Mg–Zr system, *Calphad* 22 (1998) 375.
- [36] B. Hallstedt, The Magnesium–Oxygen system, *Calphad* 17 (1993) 281.
- [37] G. Davignon, M. Giovannini, J. Gröbner, G. Haidemenopoulos, H.J. Seifert, Fe–Mg–Zr Ternary Phase Diagram Evaluation Ternary Evaluations, 2000, http://www.msi-eureka.com/full-html/10.16819.2.1/Fe-Mg-Zr_Ternary_Phase_Diagram_Evaluation.
- [38] I.-H. Jung, S.A. Decterov, A.D. Pelton, Critical thermodynamic evaluation and optimization of the Fe–Mg–O system, *J. Phys. Chem. Solids* 65 (2004) 1683.
- [39] D. Dilner, L. Kjellqvist, M. Selleby, Thermodynamic Assessment of the Fe–Ca–S, Fe–Mg–O and Fe–Mg–S Systems, *J. Phase Equilib. Diffus.* 37 (2016) 277.
- [40] T. Zienert, O. Fabrichnaya, Thermodynamic assessment and experiments in the system MgO–Al₂O₃, *Calphad* 40 (2013) 1.

- [41] N. Bochvar, L. Rokhlin, Mg–O–Zr Ternary Phase Diagram Evaluation Ternary Evaluations, 2001, http://www.msi-eureka.com/full-html/10.10317.1.3/Mg-O-Zr_Ternary_Phase_Diagram_Evaluation.
- [42] Du Yong, J. Zhanpeng, Optimization and calculation of the ZrO₂–MgO system, *Calphad* 15 (1991) 59.
- [43] Y. Yin, B.B. Argent, Phase diagrams and thermodynamics of the systems ZrO₂–CaO and ZrO₂–MgO, *J. Phase Equilib. Diffus.* 14 (1993) 439.
- [44] S. Serena, M.A. Sainz, S. de Aza, A. Caballero, Thermodynamic assessment of the system ZrO₂–CaO–MgO using new experimental results, *J. Eur. Ceram. Soc.* 25 (2005) 681.
- [45] D. Pavlyuchkov, G. Savinykh, O. Fabrichnaya, Experimental Investigation and Thermodynamic Modeling of the ZrO₂–MgO System, *Adv. Eng. Mater.* 15 (2013) 618.
- [46] W. Huang, Oxygen solubility in Fe–Zr–O liquid, *Calphad* 28 (2004) 153.
- [47] T. Katsura, M. Wakihara, S.-I. Hara, T. Sugihara, Some thermodynamic properties in spinel solid solutions with the Fe₃O₄ component, *J. Solid State Chem.* 13 (1975) 107.
- [48] Y.B. Petrov, Y.P. Udalov, J. Slovak, Y.G. Morozov, *Glass Phys. Chem.* 28 (2002) 139.
- [49] O. Fabrichnaya, D. Pavlyuchkov, Assessment of Experimental Data and Thermodynamic Modeling in the Zr–Fe–O System, *Metall. Mater. Trans. A* 47 (2016) 152.
- [50] F. Stein, G. Sauthoff, M. Palm, Experimental determination of intermetallic phases, phase equilibria, and invariant reaction temperatures in the Fe–Zr system, *J. Phase Equilib. Diffus.* 23 (2002) 480.
- [51] Malakhova, T.O., Kobylkin, A.N., Phase diagram for Zr–Fe(0–66,6 at.%Fe), *Izv. Akad. Nauk SSSR, Metall.* 14 (1982) 205.
- [52] K. Bhanumurthy, G.B. Kale, Modification of zirconium-iron phase diagram, *Scripta Metall. Mater.* 28 (1993) 753.
- [53] C. Guo, Z. Du, C. Li, B. Zhang, M. Tao, Thermodynamic description of the Al–Fe–Zr system, *Calphad* 32 (2008) 637.
- [54] Y. Yang, L. Tan, H. Bei, J.T. Busby, Thermodynamic modeling and experimental study of the Fe–Cr–Zr system, *J. Nucl. Mater.* 441 (2013) 190.
- [55] R. Lück, H. Wang, Heat capacity of the Fe₂Zr intermetallic compound, *J. Alloys Compd.* 191 (1993) L11.
- [56] K. Ali, P.S. Ghosh, A. Arya, A DFT study of structural, elastic and lattice dynamical properties of Fe₂Zr and FeZr₂ intermetallics, *J. Alloys Compd.* 723 (2017) 611.
- [57] B. Grabowski, L. Ismer, T. Hickel, J. Neugebauer, Ab initio up to the melting point: Anharmonicity and vacancies in aluminum, *Phys. Rev. B* 79 (2009) 597.
- [58] The Materials Project, <https://materialsproject.org/>, accessed 24 June 2020.
- [59] OQMD: The Open Quantum Materials Database, Chris Wolverton's group, <http://oqmd.org/>, accessed 24 June 2020.
- [60] T.S. Jones, S. Kimura, A. Muan, Phase Relations in the System FeO–Fe₂O₃–ZrO₂–SiO₂, *J. Am. Ceram. Soc.* 50 (1967) 137.
- [61] Kiminami, R. H. G. A, Study of the ZrO₂–FeO–Fe₂O₃ System by Thermogravimetry at Oxygen Partial Pressures 2.1·10² Pa and Temperatures up to 1380°C, *Ceramica* 34 (1988) 121.
- [62] A. Kiminami, A Thermogravimetric Analysis of The ZrO₂–FeO–Fe₂O₃ System at Partial Air Oxygen Pressure and Temperatures up to 1500°C, *Ceramica* 33 (1987) 207.
- [63] L. Kjellqvist, M. Selleby, Thermodynamic Assessment of the Fe–Mn–O System, *J. Phase Equilib. Diffus.* 31 (2010) 113.

- [64] B. Sundman, An assessment of the Fe–O system, *J. Phase. Equilibria. Diffus.* 12 (1991) 127.
- [65] E.G. King, Heat Capacities at Low Temperatures and Entropies at 298.16 K of Calcium and Magnesium Ferrites, *J. Am. Chem. Soc.* 76 (1954) 5849.
- [66] L.A. Reznitskii, K.G. Khomyakov, N.G. Korzhukov, S.E. Orel, Calorimeter for determining the true heat capacity of ferrites from 300 to 1000 K, *Zh. Fiz. Khim.* (1969) 2165.
- [67] K.R. Bonnickson, High Temperature Heat Contents of Calcium and Magnesium Ferrites, *J. Am. Chem. Soc.* 76 (1954) 1480.
- [68] I. Barin, G. Platzki, Thermochemical data of pure substances. 3rd ed., VCH, Weinheim, New York, 2008.
- [69] A. Navrotsky, O.J. Kleppa, Thermodynamics of formation of simple spinels, *J. Inorg. Nucl. Chem.* 30 (1968) 479.
- [70] M.F. Koehler, R. Barany, K.K. Kelley, Report of Investigation RI 5711: US Department of the Interior, Bureau of Mines, Washington (1961).
- [71] A. Navrotsky, Cation distribution energies and heats of mixing in MgFe_2O_4 – MgAl_2O_4 – ZnFe_2O_3 – ZnAl_2O_4 , and NiAl_2O_4 – ZnAl_2O_4 spinels: study by high-temperature calorimetry, *Am. Miner.* 71 (1986) 1160.
- [72] J. Majzlan, A. Navrotsky, B.J. Evans, Thermodynamics and crystal chemistry of the hematite-corundum solid solution and the FeAlO_3 phase, *Phys. Chem. Miner.* 29 (2002) 515.
- [73] W.C. A. Navrotsky, Thermochemistry of some pyroxenes and related compounds, *Geochim. Cosmochim. Acta* 40 (1976) 1281.
- [74] H. St. C. O'Neill, H. Annersten, D. Virgo, The temperature dependence of the cation distribution in magnesioferrite (MgFe_2O_4) from powder XRD structural refinements and Mössbauer spectroscopy, *Am. Mineral.* 77 (1992) 725.
- [75] J.C. Tellier, Substitution of trivalent, tetravalent, and pentavalent ions for the iron (III) ion in magnesium ferrite, *Rev. Chim. Miner.* 4 (1967) 325.
- [76] J.G. Faller, C.E. Birchenall, The temperature dependence of ordering in magnesium ferrite, *J. Appl. Crystallogr.* 3 (1970) 496.
- [77] R. Pauthenet, L. Bochirol, Aimantation spontanée des ferrites, *J. Phys. Radium.* 12 (1951) 249.
- [78] R.L. Mozzi, A.E. Paladino, Cation Distributions in Nonstoichiometric Magnesium Ferrite, *Int. J. Chem. Phys.* 39 (1963) 435.
- [79] C.J. Kriessman, S.E. Harrison, Cation Distributions in Ferrosinels. Magnesium–Manganese Ferrites, *Phys. Rev.* 103 (1956) 857.
- [80] D.J. Epstein, B. Frackiewicz, Some Properties of Quenched Magnesium Ferrites, *J. Appl. Phys.* 29 (1958) 376.
- [81] K. Seshan, A.S. Bommanavar, D.K. Chakrabarty, Mössbauer spectroscopic studies of magnesium nickel ferrites, *J. Solid State Chem.* 47 (1983) 107.
- [82] H.M. H.S. Roberts, The system MgO – FeO – Fe_2O_3 in air at one atmosphere, *Am. J. Sci.* 21 (1931) 145.
- [83] J.W. D. Woodhouse, Phase relationships of iron oxide-containing spinels: III, further investigations on the system Fe – Mg – O and Fe – Mg – Cr – O , *Trans. Br. Ceram. Soc.* 54 (1955) 333.
- [84] J.W. J.C. Willshee, An investigation of equilibrium relationships in the system MgO – FeO – Fe_2O_3 up to 1750°C in air, *Trans. Br. Ceram. Soc.* 66 (1967) 541.

- [85] I.K. E. Schurmann, Effect of the iron(III) oxide contents in steelmaking slags on the magnesia solubility at different oxygen partial pressures of the gas–slag equilibrium, *Steel Res.* 59 (1988) 185.
- [86] B. Phillips, S. Somiya, A. Muan, Melting Relations of Magnesium Oxide–Iron Oxide Mixtures in Air, *J. Am. Ceram. Soc.* 44 (1961) 167.
- [87] J.C. K.L. Fetters, Equilibria of liquid iron and slags of the system CaO–MgO–FeO–SiO₂, *Trans. AIME* 145 (1941) 95.
- [88] W.P. H. Schenck, Das System Eisen(II)-oxyd-Magnesiumoxyd und seine Verteilungsgleichgewichtemit flüssigem Eisen bei 1520 bis 1750°C, *Arch. Eisenhuettenwes.* 32 (1961) 741.
- [89] N.A. Gokcen, Equilibria in reactions of hydrogen, and carbon monoxide with dissolved oxygen in liquid iron; equilibrium in reduction of ferrous oxide with hydrogen, and solubility of oxygen in liquid iron, *J. Metals* 8 (1956) 1558.
- [90] W.A. Fischer, H. Vom Ende, Die Löslichkeit von Sauerstoff in Eisenschmelzen unter Eisenoxydul-, kieselsäure- und kalkgesättigten Eisenoxydulschlacken für Temperaturen von 1530 bis 1700°C, *Arch. Eisenhuettenwes.* 23 (1952) 21.
- [91] C.R. Taylor, J. Chipman, Thermodynamics of Oxygen in Liquid Iron under Simple Oxide Slag, *Trans. AIME* 154 (1943) 228.
- [92] J.D. Shim, S. Ban-Ya, The solubility of magnesia and ferric–ferrous equilibrium in liquid FeO–SiO₂–CaO–MgO slags, *Tetsu To Hagane* 67 (1981) 1735.
- [93] R. Scheel, Sprechsaal Keram., *Glas. Bautoffe* 108 (1975) 685.
- [94] O. Evrard, Thesis, University Nancy, France, 1970.
- [95] N.G. Schmahl, B. Frisch, G. Stock, *Arch. Eisenhuettenwes.* 32 (1961) 297.
- [96] S.Yu. Gurevich, Thesis, Ural Polytechnic Institute, Chelyabinsk, Russland, 1970.
- [97] R.A. Giddings, R.S. Gordon, Review of Oxygen Activities and Phase Boundaries in Wüstite as Determined by Electromotive-Force and Gravimetric Methods, *J. Am. Ceram. Soc.* 56 (1973) 111.
- [98] A.E. Paladino, Phase Equilibria in the Ferrite Region of the System FeO–MgO–Fe₂O₃, *J. Am. Ceram. Soc.* 43 (1960) 183.
- [99] D.H. Speidel, Phase Equilibria in the System MgO–FeO–Fe₂O₃: The 1300°C Isothermal Section and Extrapolations to Other Temperatures, *J. Am. Ceram. Soc.* 50 (1967) 243.
- [100] N.N. Oleinikov, Y.G. Saksonov, Y.D. Tret'yakov, A study of phase equilibria in the MgO–FeO–Fe₂O₃ system at 1400°C, *Izv. Akad. Nauk. SSSR, Neorg. Mater.* 1 (1965) 246.
- [101] H.F. J. Brynestad, The redox equilibrium in wüstite and solid solutions of wüstite and magnesium oxide, *Z. Elektrochem.* 62 (1958) 953.
- [102] I. Srecec, A. Ender, E. Woermann, W. Gans, E. Jacobsson, Activity–composition relations of the magnesiowüstite solid solution series in equilibrium with metallic iron in the temperature range 1050–1400 K, *Phys. Chem. Miner.* 14 (1987) 492.
- [103] Y.D. Tret'yakov, Thermodynamics of ferrites, *Khimiya, Leningrad* 59 (1967) 1299.
- [104] F.M. N. Wallet, Sur la Réduction Progressive des Ferrites de Magne'sium et de Nickel, *C. R. Hebd. Seances Acad. Sci.* 256 (1963) 1790.
- [105] J.T. H. Schmalzried, Fehlordnung in ferriten, *Ber. Bunsenges. Phys. Chem.* 70 (1966) 180.

- [106] M.M. N. Hilbrandt, High-temperature point defect equilibria in iron-doped MgO. An in situ Fe–K XAFS study on the valence and site distribution of iron in $(\text{Mg}_{1-x}\text{Fe}_x)\text{O}$, *Ber. Bunsen-Ges. Phys. Chem.* 102 (1998) 1747.
- [107] F.A. M. Maja, Caratteristiche termodinamiche del sistema Magnesia–Wustite, *Metall. Ital.* 10 (1973) 565.
- [108] S.-H. Kang, S.-H. Chang, H.-I. Yoo, Phase Stability of the System Mg–Fe–O, *J. Solid State Chem.* 149 (2000) 33.
- [109] A.M. W.C. Hahn, Activity measurements in oxide solid solutions: the system “FeO”–MgO in the temperature interval 1100°C to 1300°C, *Trans. Met. Soc. AIME.* 224 (1962) 416.
- [110] M. Wallace, S. Sun, S. Jahanshahi, Thermodynamic Constraints on Slag–Refractory Interaction: The Effect of Oxygen Potential on Spinel and Wustite Stability in the MgO–FeO–Fe₂O₃ System, *Sixth AusIMM Extractive Metallurgy Conference, Brisbane* (1994) 37.
- [111] J. Tibballs, in: I. Ansara, A.T. Dinsdale, M.H. Rand (eds.) (Ed.), COST 507, “Thermochemical database for light metal alloys” 2 (1998) 215.
- [112] M. Hampl, R. Schmid-Fetzer, Thermodynamic description of the Ti–O system, *Int. J. Mater. Res.* 106 (2015) 439.
- [113] S. Sridar, R. Kumar, K.C. Hari Kumar, Thermodynamic modelling of Ti–Zr–N system, *Calphad* 56 (2017) 102.
- [114] J.L. Murray, The Mg–Ti (Magnesium–Titanium) system, *Bulletin of Alloy Phase Diagrams* 7 (1986) 245.
- [115] O. Fabrichnaya, O–Ti–Zr Ternary Phase Diagram Evaluation Ternary Evaluations, 2010, http://www.msi-eureka.com/full-html/10.13037.1.6/O-Ti-Zr_Ternary_Phase_Diagram_Evaluation.
- [116] S. Wagner, I. Arpshofen, H.J. Seifert, Mg–O–Ti Ternary Phase Diagram Evaluation Ternary Evaluations, 2001, http://www.msi-eureka.com/full-html/10.10801.1.2/Mg-O-Ti_Ternary_Phase_Diagram_Evaluation.
- [117] N. Bochvar, Y. Liberov, Mg–Ti–Zr Ternary Phase Diagram Evaluation Ternary Evaluations, 2001, http://www.msi-eureka.com/full-html/10.25179.1.6/Mg-Ti-Zr_Ternary_Phase_Diagram_Evaluation.
- [118] Yokokawa, H., Sakai, N., Kawada, T., Dokiya, M., Phase diagram calculations for ZrO₂ based ceramics: Thermodynamic regularities in zirconate formation and solubilities of transition metal oxides, *Science and Technology of Zirconia V* (1992) 59.
- [119] M. Cancarevic, M. Zinkevich, F. Aldinger, Thermodynamic Assessment of the PZT System, *Nippon Seramikkusu Kyokai gakujutsu ronbunshi* 114 (2006) 937.
- [120] T.A. Schaedler, O. Fabrichnaya, C.G. Levi, Phase equilibria in the TiO₂–YO_{1.5}–ZrO₂ system, *J. Eur. Ceram. Soc.* 28 (2008) 2509.
- [121] Arroyave R., Thermodynamics and Kinetics of Ceramic/Metal Interfacial Interactions., Massachusetts Institute of Technology. (2004).
- [122] L.W. Coughanour, R.S. Roth, S. Marzullo, F.E. Sennett, Solid-state reactions and dielectric properties in the systems magnesia-zirconia-titania and lime-zirconia-titania, *J. Res. Natl. Bur. Stan.* 54 (1955) 191.
- [123] G. Bayer, Stabilization of Cubic ZrO₂ by MnO and Partial Substitution of Ti, Nb, or Ta for Zr, *J. Am. Ceram. Soc.* 53 (1970) 294.
- [124] C.-F. Tseng, Relationships between Zr substitution for Ti and microwave dielectric properties in Mg(Zr_xTi_{1-x})O₃ ceramics, *J. Alloys Compd.* 509 (2011) 9447.

- [125] B.K. Hom, R. Stevens, B.F. Woodfield, J. Boerio-Goates, R.L. Putnam, K.B. Helean, A. Navrotsky, The thermodynamics of formation, molar heat capacity, and thermodynamic functions of $\text{ZrTiO}_4(\text{cr})$, *J. Chem. Thermodyn.* 33 (2001) 165.
- [126] A.V. Shevchenko, L.M. Lopato, I.M. Maister et al., The $\text{TiO}_2\text{--ZrO}_2$ System, *Russ. J. Inorg. Chem.* (Engl. Transl.) 25 (1980) 1379.
- [127] L.W. Coughanour, R.S. Roth, V.A. DeProse, Phase equilibrium relations in the systems Lime-Titania and Zirconia-Titania, *J. Res. Natl. Bur. Stan.* 52 (1954) 37.
- [128] T. Noguchi, M. Mizuno, Phase Changes in the $\text{ZrO}_2\text{--TiO}_2$ System, *BCSJ* 41 (1968) 2895.
- [129] C. Wang, M. Zinkevich, F. Aldinger, The Zirconia–Hafnia System: DTA Measurements and Thermodynamic Calculations, *J. Am. Ceram. Soc.* 89 (2006) 3751.
- [130] M. Ilatovskaia, G. Savinykh, O. Fabrichnaya, Thermodynamic description of the $\text{ZrO}_2\text{--TiO}_2\text{--Al}_2\text{O}_3$ system based on experimental data, *J. Eur. Ceram. Soc.* 37 (2017) 3461.
- [131] G. Grimvall, Atomic-mass effects in phase diagrams and high-temperature thermodynamic properties, *J. Alloys Compd.* 233 (1996) 183.
- [132] M.W. Chase, I. Ansara, A. Dinsdale, G. Eriksson, G. Grimvall, L. Hoglund, and H. Yokokawa. Group 1: Heat capacity models for crystalline phases from 0 K to 6000 K, *CALPHAD* 19 (1995) 437.
- [133] M. Ilatovskaia, O. Fabrichnaya, Thermodynamic assessment of the $\text{Al}_2\text{O}_3\text{--MgO--TiO}_2$ system, *J. Alloys Compd.* 790 (2019) 1137.
- [134] H. Flandorfer, J. Groebner, A. Stamou, N. Hassiotis, Experimental investigation and thermodynamic calculation of the ternary system Mn--Y--Zr , *Z. Metall.* 88 (1997) 529.
- [135] K. Hack, System Mn--Zr , in: I. Ansara, A.T. Dinsdale, M.H. Rand (Eds.), Thermochemical database for light metal alloys. Ans1998, Office for Official Publications of the European Communities, Luxembourg, 245.
- [136] T.B. Massalski, Binary Alloy Phase Diagrams, Metals Park, Ohio, 1991.
- [137] F. Smetana, P. Entner, A. Neckel, Dampfdruckmessungen an festem $\beta\text{-Mn}$ und ZrMn_2 , *Monatshefte für Chemie* 101 (1970) 956.
- [138] M. Rotter, A. Grytsiv, X.-Q. Chen, P. Rogl, R. Podloucky, W. Wolf, V.T. Witusiewicz, A. Saccone, H. Noel, M. Doerr, A. Lindbaum, H. Michor, E. Bauer, S. Heathman, W. Kockelmann, J. Taylor, Structural, thermodynamic, and transport properties of Laves-phase ZrMn_2 from X-ray and neutron diffraction and first principles, *Phys. Rev. B* 74 (2006) 688.
- [139] D.J. Thoma, Intermetallics: Laves Phases, in: Encyclopedia of Materials: Science and Technology, Elsevier (2001) 4205.
- [140] J.H. Zhu, L.M. Pike, C.T. Liu, P.K. Liaw, Point defects in binary Laves phase alloys, *Acta Mater.* 47 (1999) 2003.
- [141] J. Pavlů, J. Vřešťál, M. Šob, Thermodynamic modeling of Laves phases in the Cr--Hf and Cr--Ti systems: Reassessment using first-principles results, *Calphad* 34 (2010) 215.
- [142] J. Pavlů, J. Vřešťál, X.-Q. Chen, P. Rogl, Thermodynamic modeling of Laves phases in the Ta--V system: Reassessment using first-principles results, *Calphad* 35 (2011) 103.
- [143] K. Zeng, H. Marko, L. Kaj, Thermodynamic modeling of the laves phases in the Cr--Zr system, *Calphad* 17 (1993) 101.
- [144] S. Liu, B. Hallstedt, D. Music, Y. Du, Ab initio calculations and thermodynamic modeling for the Fe--Mn--Nb system, *Calphad* 38 (2012) 43.

- [145] D. Dilner, D. Pavlyuchkov, T. Zienert, L. Kjellqvist, O. Fabrichnaya, Thermodynamics of the Mg–Mn–O system-modeling and heat capacity measurements, *J. Am. Ceram. Soc.* 100 (2017) 1661.
- [146] D. Pavlyuchkov, G. Savinykh, O. Fabrichnaya, Experimental investigation and thermodynamic modeling of the ZrO₂–MnO system, *J. Eur. Ceram. Soc.* 35 (2015) 3623.
- [147] D. Pavlyuchkov, D. Dilner, G. Savinykh, O. Fabrichnaya, Phase Equilibria in the ZrO₂–MgO–MnO_x System, *J. Am. Ceram. Soc.* 99 (2016) 3136.
- [148] A.N. Grundy, B. Hallstedt, L.J. Gauckler, Assessment of the Mn–O system, *J. Phase Equilibria Diffus.* 24 (2003) 21.
- [149] M. Wendler, B. Reichel, R. Eckner, O. Fabrichnaya, L. Krüger, A. Weiß, J. Mola, Effect of Vanadium Nitride Precipitation on Martensitic Transformation and Mechanical Properties of CrMnNi Cast Austenitic Steels, *Metall. Mater. Trans. A* 47 (2016) 139.
- [150] S. Martin, O. Fabrichnaya, D. Rafaja, Prediction of the local deformation mechanisms in metastable austenitic steels from the local concentration of the main alloying elements, *Mater. Lett.* 159 (2015) 484.
- [151] P. Franke, M. Ksyta, H.J. Seifert, Interfacial Reactions in TRIP-Steel/ZrO₂ Composites, *steel research int.* 82 (2011) 1149.
- [152] O. Fabrichnaya, C. Ullrich, M. Wendler, G. Savinykh, D. Rafaja, High-temperature phase transformations in strongly metastable austenitic-martensitic CrMnNi–N–C cast steels, *J. Alloys Compd.* 686 (2016) 511.
- [153] M. Hauser, M. Wendler, O. Fabrichnaya, O. Volkova, J. Mola, Anomalous stabilization of austenitic stainless steels at cryogenic temperatures, *Mater. Sci. Eng. A* 675 (2016) 415.
- [154] S. Martin. private communication, 2020.
- [155] C. Weigelt, Energy absorbing TRIP-steel/zirconia composite structures based on ceramic extrusion. Dissertation, 2012.
- [156] Internal results of SFB 799.
- [157] D. Wittig, A. Glauche, C.G. Aneziris, T. Minghetti, C. Schelle, T. Graule, J. Kuebler, Activated pressureless melt infiltration of zirconia-based metal matrix composites, *Mater. Sci. Eng. A* 488 (2008) 580.

Appendix

Publication P1.....	P1 - 1-18
Publication P2.....	P2 - 1-24
Publication P3.....	P3 - 1-20
Publication P4.....	P4 - 1-22
Publication P5.....	P5 - 1-18
Publication P6.....	P6 - 1-18
Publication P7.....	P7 - 1-22
Thermodynamic database Mg-Fe-Zr-O.....	TDB1 - 1-6
Thermodynamic database Mg-Ti-Zr-O.....	TDB2 - 1-6
Thermodynamic database Mg-Mn-Zr-O.....	TDB3 - 1-10

Publication P1: B.O. Mukhamedov, I. Saenko, A.V. Ponomareva, M.J. Kriegel, A. Chugreev, A. Udovsky, O. Fabrichnaya, I.A. Abrikosov, Thermodynamic and physical properties of Zr_3Fe and $ZrFe_2$ intermetallic compounds, *Intermetallics* 109 (2019) 189.
DOI: 10.1016/j.intermet.2019.01.018

Contributions to the paper:

Authors	Contribution [%]	Particular contribution
B.O. Mukhamedov	35	<ul style="list-style-type: none"> • First-principles calculations • Participation in C_p measurements • Evaluation of data • Magnetic modelling • Composition of the manuscript
I. Saenko	20	<ul style="list-style-type: none"> • Sample preparation and characterization • C_p measurements • Participation in first-principle calculations • Co-composition of the manuscript
Dr. A.V. Ponomareva	10	<ul style="list-style-type: none"> • Supervision of first-principle calculations • Work on the manuscript
Dr. M.J. Kriegel	3	<ul style="list-style-type: none"> • Dilatometer experiments
A. Chugreev	2	<ul style="list-style-type: none"> • Dilatometer experiments
Prof. A.L. Udovsky	10	<ul style="list-style-type: none"> • Supervision of the work • Work on the manuscript
Dr. rer. nat. habil. O. Fabrichnaya	10	<ul style="list-style-type: none"> • Supervision of the work • Work on the manuscript
Prof. I.A. Abrikosov	10	<ul style="list-style-type: none"> • Supervision of the work • Planning of first-principle calculations • Analysis of calculated results • Work on the manuscript

Thermodynamic and physical properties of Zr_3Fe and $ZrFe_2$ intermetallic compounds

B.O. Mukhamedov^{1,*}, I. Saenko^{2,3}, A.V. Ponomareva¹, M.J. Kriegel², A. Chugreev⁴, A. Udovsky^{3,5}, O. Fabrichnaya², I.A. Abrikosov⁶

¹ Materials Modeling and Development Laboratory, National University of Science and Technology ‘MISIS’, Moscow, 119049, Russia

² Freiberg University of Mining and Technology, Freiberg, Sachsen, 09599, Germany

³ Baikov Institute of Metallurgy and Material Science of the Russian Academy of Sciences, Moscow, 119991, Russia

⁴ IFUM - Institute of Forming Technology and Machines, Leibniz Universitaet Hannover, An der Universitaet 2, Garbsen 30823, Germany

⁵ National Research Nuclear University MEPhI, Moscow, 115409, Russia

⁶ Linköping University, Linköping, 581 83, Sweden

*Corresponding author:

B.O. Mukhamedov, Materials Modeling and Development Laboratory, National University of Science and Technology ‘MISIS’, Moscow, Russia, 119049

E-mail address: b.o.mukhamedov@gmail.com

Abstract

Experimental differential scanning calorimetry measurements and ab-initio simulations were carried out to define the heat capacities of Zr_3Fe and $C15-ZrFe_2$ compounds from 0 K up to their maximum stability temperatures. Experimental measurements of heat capacity of each compound were performed for the first time in wide range of temperatures. Density functional theory and quasi-harmonic approximation (QHA) were employed to calculate the free energy of the studied systems as a function of volume and temperature. A good agreement was observed between theoretical and experimental heat capacities within validity range of the QHA. This makes it possible to combine theoretical and experimental data to determine the standard entropies of intermetallic compounds.

1. Introduction

Zr-based alloys, so-called zircalloys, containing small amount of Fe and other alloying elements are widely used in nuclear industry due to their low absorption cross-section of thermal neutrons, high corrosion resistance and hardness [1–3]. Moreover, Zr–Fe intermetallic compounds in zircalloys are known to improve specific mechanical properties. Because of this, the Zr–Fe system plays an important role in modern steel design. For example, in the manufacturing of composite materials consisting of TRIP (transformation-induced plasticity) matrix and reinforcing ZrO_2 based ceramic, the phase relations in the Zr–Fe–O system are essential for the stability of ceramic particles [4]. In fact, both TRIP matrix and ceramic particles may undergo martensitic transformation during compression, which thereby improves the mechanical properties of composite material, such as strength and energy absorption during compression [5].

Therefore, Zr–Fe system is becoming the subject of intense research, and the detailed knowledge on its thermodynamic properties and phase relations is essential for the modern industry of composite and structural steels. A systematic experimental study on binary Zr–Fe system was performed in Ref. [2] for the whole range of compositions. The authors reported that there were four stable intermetallic compounds in the phase diagram: two polymorphic

modifications of ZrFe_2 phase, Zr_3Fe and high-temperature Zr_2Fe . Cubic ZrFe_2 C15-Laves phase, which is stable up to 1946 K, being in equilibrium with Fe at 24.7 at.% Zr transforms into hexagonal C36 polymorph at 1563 K [2]. Similar result was observed in Ref. [6], where the authors found the hexagonal Laves phase in $\text{Zr}_{22.5}\text{Fe}_{77.5}$ alloy after annealing at 1523 K. Intermetallic Zr_3Fe phase was found to be orthorhombic with Re_3B -type symmetry [2]. The Zr_3Fe phase is formed from peritectoid reaction $\text{Zr}_2\text{Fe} + \beta\text{-Zr} \rightleftharpoons \text{Zr}_3\text{Fe}$; and the reported temperature of this reaction varied in several measurements: values of 1124 K [2], 1158 K [7], and 1213 K [8] were reported. Another intermetallic compound Zr_2Fe is a constituent of above mentioned peritectoid reaction; it is a high-temperature phase with Ti_2Ni -type crystalline structure.

According to the several thermodynamic assessments [9,10], there is limited available information on thermodynamic properties of intermetallic compounds in binary Zr–Fe system. In Ref. [11] the enthalpy of formation ΔH_f of ZrFe_2 at 298 K was determined using direct reaction calorimetry. Enthalpy of formation of ZrFe_2 was also derived from indirect measurements by solution calorimetry in Refs. [12], [13] and levitation alloying calorimetry in Ref. [14]. The values of ΔH_f from Refs. [11] and [14] are quite consistent with each other, while the values of ΔH_f in Refs. [12] and [13] are more positive. Several *ab-initio* calculations predicted fairly consistent results on formation enthalpy of Zr–Fe intermetallics: for C15- ZrFe_2 phase the Density Functional Theory (DFT) calculations gave -0.280 eV/atom (-27.02 kJ/mol) [15] and -0.290 eV/atom (-27.98 kJ/mol) [16]. These results are in a good agreement with experimental data from Refs. [11] and [14]. For Zr_3Fe phase the theoretical enthalpy of formation ΔH_f was found to be equal to -0.140 eV/atom (-13.51 kJ/mol) [15] and -0.150 eV/atom (-14.47 kJ/mol) [16], however, there were no available experimental results. Regarding the heat capacity, in Ref. [17] the experimental measurements were performed for C15- ZrFe_2 phase in the range of temperatures between 313 K and 653 K. At the same time, we are not aware of any available experimental data on the heat capacity of Zr_3Fe intermetallic phase. Moreover, it is worth noting that there is no available information on standard entropies for these intermetallic phases.

Thermodynamic modeling of Zr–Fe system without information on the thermodynamic properties of the phases becomes unreliable. At least, thermodynamics of the intermetallic compounds, that are stable in the wide temperature range, like Zr_3Fe and ZrFe_2 , should be defined for further improvement of the thermodynamic description of the Zr–Fe system. In this respect, the topic of the next generation of databases of materials properties created based on CALPHAD approach in combination with reasonable description of thermodynamic properties starting from zero temperature attracts increasing attention. However, the experimental measurements of thermodynamic properties of materials at such low temperatures are rather difficult and time-consuming; and most of all they are very expensive. On the other hand, the predictive power of state-of-the-art first-principles simulations has greatly improved, and they can be used efficiently to describe the thermodynamic properties of materials [18]. For example, the DFT approach in combination with quasi-harmonic approximation allows one to simulate the materials thermodynamic and thermal properties, such as heat capacity, entropy, etc. However, the QHA has its limitation, since it does not account for the anharmonic effects, which might be significant at high temperature [19]. Thus, to define the heat capacities of studied Zr_3Fe and C15- ZrFe_2 compounds we apply DFT+QHA method for the low-temperature regions and experimental measurements for the high temperatures. The reliability of DFT+QHA results and the borders between low- and high-temperature regions are defined from the comparison between theoretical and experimental data. In addition to the heat capacity, we have determined the formation enthalpies and standard entropies of both compounds.

2. Methods

2.1. Calculation of thermodynamic properties

The total free energy $G_{\text{tot}}(V, T)$ of a system as a sum of electronic, vibrational and magnetic terms:

$$G_{\text{tot}}(V, T) = E_{\text{el}}(V) - TS_{\text{el}}(V, T) + G_{\text{vib}}(V, T) + G_{\text{magn}}(V, T) \quad (1)$$

considering each term as a function of volume V and temperature T . In Eq. 1, the terms $[E_{\text{el}}(V) - TS_{\text{el}}]$, $G_{\text{vib}}(V, T)$ and $G_{\text{magn}}(V, T)$ denote electronic, vibrational, and magnetic contributions to the total free energy, respectively. Zr₃Fe phase is non-magnetic; therefore, the last term in the right-hand side of Eq. 1 can be omitted in this case.

The electronic entropy can be estimated as:

$$S_{\text{el}} = -k_B \int_{-\infty}^{\infty} n(\varepsilon) [f \ln f + (1 - f) \ln(1 - f)] d\varepsilon \quad (2)$$

here, $n(\varepsilon)$ is the electronic density of states, and $f = f(\varepsilon, \varepsilon_F, T)$ is the Fermi distribution function.

Vibrational (or phonon) contribution $G_{\text{vib}}(V, T)$ to the free energy was simulated within quasi-harmonic approximation (QHA) where the phonon frequencies ω_q were derived from interatomic Hellmann-Feynman forces induced by finite atomic displacements. In QHA, the phonon frequencies are volume-dependent parameters, hence vibrational energy G_{vib} becomes volume-dependent, which makes it possible to account for the thermal expansion effects in the lattice. The vibrational energy as function of volume and temperature can be defined as:

$$G_{\text{vib}}(V, T) = \sum_q \left\{ \frac{\hbar \omega_q(V)}{2} + k_B T \ln \left[1 - \exp \left(- \frac{\hbar \omega_q(V)}{k_B T} \right) \right] \right\} \quad (3)$$

where ω_q is the phonon frequency with wave vector q , and k_B is the Boltzmann constant.

At low temperatures, which are of primary interest for theoretical simulations in this study, the dominant magnetic excitations are spin waves. A contribution from the spin-waves excitations to the total free energy of ZrFe₂ phase was taken into consideration within Heisenberg model with nearest neighbors interactions. According to the model, the magnon-dispersion relations can be calculated as:

$$\hbar \omega_k = 4JS[1 - \cos(ka)] \quad (4)$$

where J denotes an effective (pair) exchange interaction between the nearest neighbors; S is the on-site spin value of atom; ω_k is a magnon frequency with wave vector k ; and a is a lattice parameter. Computation of the J parameter has been performed using the Exact Muffin-Tin Orbitals (EMTO) method [20], where the exchange parameter J can be found analytically from the change in energy of embedding spins induced by rotation of them an infinitely small angle [21–23].

At the low temperatures, i.e. in the long wavelength limit $k \rightarrow 0$, the magnon dispersion has a parabolic form: $\hbar\omega_k = D_{stiff} k^2$, where $D_{stiff} = 2SJ a^2$ denotes the spin-wave stiffness at $T = 0$ K. According to Kittel [24], at the low temperatures the internal energy of magnons E_{mag} can be expressed as:

$$E_{mag}(V, T) = \frac{k_B T}{2\pi^2} \left(\frac{k_B T}{D_{stiff}} \right)^{\frac{3}{2}} \int_0^{x_{max}} \frac{x^{\frac{3}{2}}}{(e^x - 1)} dx \quad (5)$$

where $x = \hbar\omega_k/k_B T$. Since the effective exchange interaction J is volume-dependent parameter, the spin-wave frequency also becomes volume-dependent $\omega_k = \omega_k(V)$, which allows one to implicitly calculate the magnon energy E_{mag} as a function of volume V .

The evaluation of the spin-wave free energy $G_{mag}(V, T)$ can be done numerically by means of the internal energy $E_{mag}(V, T)$ via:

$$G_{mag}(V, T) = E_{mag}(V, 0) - T \int_0^T \frac{1}{T} \left(\frac{\partial E_{mag}(V, T)}{\partial T} \right) dT \quad (6)$$

By knowing the total free energy G_{tot} (see Eq. 1) as a function of volume V and temperature T it is possible to find the minimum free energy and corresponding volume V_{min} at each temperature. Thus, having the information on the ground state volume V_{min} as a function of the temperature we can determine the volumetric thermal expansion coefficient as:

$$\alpha_V = \frac{1}{V_0} \frac{dV_{min}}{dT} \quad (7)$$

where V_0 denotes the ground state volume at $T = 0$ K.

Bulk modulus as a function of the temperature can be expressed as:

$$B(T) = V_{min}(T) \left(\frac{\partial^2 G}{\partial V^2} \right)_T \quad (8)$$

Specific heat capacity at constant volume, i.e. isochoric heat capacity, can be defined by formula given below:

$$C_V = -T \left(\frac{\partial^2 G}{\partial T^2} \right)_{V_0} \quad (9)$$

Further, using the parameters obtained from Eqs. (7) – (10) one can determine the heat capacity at constant pressure, i.e. isobaric specific heat capacity, as:

$$C_P = C_V + \alpha_V^2 B_T V_m T \quad (10)$$

where V_m denotes the molar volume of the unit cell.

An electronic contribution to the heat capacity can be expressed from electronic entropy as:

$$C_{el} = T \left(\frac{\partial S_{el}}{\partial T} \right)_P \quad (11)$$

The spin-waves contribution to the heat capacity can be defined as the temperature derivative of $E_{mag}(V, T)$:

$$C_{mag} = \left(\frac{\partial E_{mag}}{\partial T} \right)_P \quad (12)$$

2.2. Calculations details

Based on the previous experimental data [2], the Zr_3Fe and $ZrFe_2$ phases were simulated as orthorhombic and cubic C15 crystals, respectively, with 16 and 6 atoms per unit cell. In Fig.1, we depict the unit cells of these intermetallic phases. Thermodynamic properties of Zr_3Fe and $ZrFe_2$ phases were calculated using projector augmented wave (PAW) [25] potentials implemented in Vienna Ab-initio Simulation Package (VASP) [26]. The exchange-correlation effects were treated using the generalized gradient approximation [27]. Magnetic properties were accounted for within the collinear picture. The magnitude and orientations of the collinear local moments were calculated self-consistently. The cutoff energies for plane waves were set to 700 and 500 eV for Zr_3Fe and $ZrFe_2$ compounds, correspondingly. The integration over the irreducible part of Brillouin zone has been carried out using Monkhorst-Pack method [28] on the grids of $18 \times 6 \times 6$ k-points for Zr_3Fe and $8 \times 8 \times 8$ for $ZrFe_2$. The convergence criterion for electronic subsystem was chosen to be equal to 10^{-3} eV/atom for subsequent iterations. The relaxation of atomic positions was realized by calculation of Hellman-Feynman forces [29,30] and stress tensor with using the conjugated gradient method. Relaxation was stopped when the forces became on the order of 10^{-3} eV/Å.

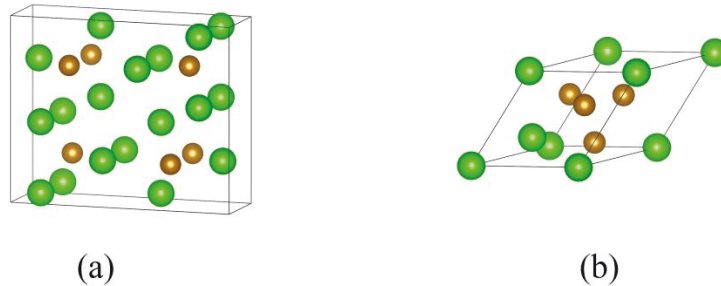


Fig. 1 – Unit cells of orthorhombic Zr_3Fe (a) and cubic C15- $ZrFe_2$ (b) intermetallic compounds.

Regarding to the phonon calculations, we applied supercells approach where Zr_3Fe and $ZrFe_2$ crystals were simulated as $3 \times 2 \times 2$ (192 atoms) and $2 \times 2 \times 2$ (48 atoms) supercells, respectively. To calculate the interatomic forces in supercells we set the values of atomic displacements to be equal to 0.01 Å. Postprocessing calculations of phonons was realized within Phonopy code [31]. To check the accuracy of phonon calculations we considered the larger in size supercells, $4 \times 2 \times 2$ for Zr_3Fe and $3 \times 3 \times 3$ for $ZrFe_2$, and performed convergence test of heat capacities at the ground state volume. The test revealed that difference in heat capacities C_V between larger and smaller supercells is about $\sim 1.5\%$ at low-temperatures between 0 and 5 K; and this difference gradually vanishes for the higher temperatures. Therefore, further phonon calculations were realized only for smaller in size supercells, e.i. $3 \times 2 \times 2$ for Zr_3Fe and $2 \times 2 \times 2$ for $ZrFe_2$ phase.

Total free energy G_{tot} from Eq. (1) was calculated for the 7 volume points in the range between -6 and $+6$ % with respect to the ground state volume at zero temperature.

Computation of effective exchange parameter J in cubic C15 phase was performed using the EMT method [20]. Simulations were carried out for a basis set including the valence s , p , d and f orbitals and by means of the frozen-core approximation, i.e. the core states were kept fixed. The integration over the irreducible part of the Brillouin zone has been performed using a grid of $6 \times 6 \times 6$ k-points. The energy integration has been carried out in the complex plane using a semi-elliptic contour comprising 12 energy points. The convergence of the energy with respect to the calculation parameters has been set to 10^{-4} eV.

2.3. Experimental methods

2.3.1. Sample preparation

Two binary Zr–Fe alloys with the nominal compositions of ZrFe_2 and Zr_3Fe were prepared by arc-melting method in the Ar-atmosphere. Pieces of Fe (99.99%, Alfa Aesar) and slugs of Zr (99.5%, Alfa Aesar) were weighed in accordance to the nominal compositions. In order to achieve a good homogeneity of the chemical composition in the bulks, the samples were turned-over and re-melted three times. The samples were sealed in the quartz tubes with the reduced Ar atmosphere. The pressure of the Ar in the quartz tubes was chosen in order to reach 1 atm. at the homogenization temperature. Afterwards, the samples were homogenized during 3 hours at 873 K for Zr_3Fe and 1123 K for ZrFe_2 .

2.3.2. Sample treatment and characterization

The samples were analysed by X-ray diffraction (XRD) and scanning electron microscopy combined with an energy dispersive X-ray spectrometry (SEM/EDX).

Phase assemblages of specimens after homogenization annealing have been identified by X-ray powder diffraction (XRD) using the URD63 diffractometer (Seifert, FPM, Freiberg, Germany) equipped with the graphite monochromator and the $\text{CuK}\alpha$ radiation ($\lambda = 1.5418$ Å). The goniometer of the diffractometer had the Bragg-Brentano geometry. The Rietveld refinement was applied for the characterisation of all measured diffraction patterns using Maud software [32].

We have investigated the sample microstructures after homogenization annealing using scanning electron microscopy combined with dispersive X-ray spectrometry (SEM/EDX; Leo1530, Carl Zeiss/ Bruker AXS Mikroanalysis GmbH). Chemical compositions of samples and present phases have been determined using a signal from EDX detector with an accuracy of ± 2 at. %.

Based on the XRD and SEM/EDX results the lattice parameters of Zr_3Fe were found to be $a = 3.322$ Å, $b = 10.973$ Å, $c = 8.822$ Å; and lattice parameter of C15- ZrFe_2 – $a = 7.075$ Å. XRD patterns are presented in the Fig.2. Measured lattice parameters exhibit a good agreement with the literature data [33–36]; and correspond to the stoichiometric intermetallic compounds. Microstructural analysis confirms the XRD results. Chemical composition of the samples measured by EDX method matches to the initial chemical composition within the error of the measurement. Chemical composition analysis shows that Zr_3Fe samples have 77 at.% of Zr;

and $ZrFe_2$ samples – 34 at.% of Zr. In both cases, we observed the deviations toward Zr side. However, the deviation was in the range of the reliable accuracy.

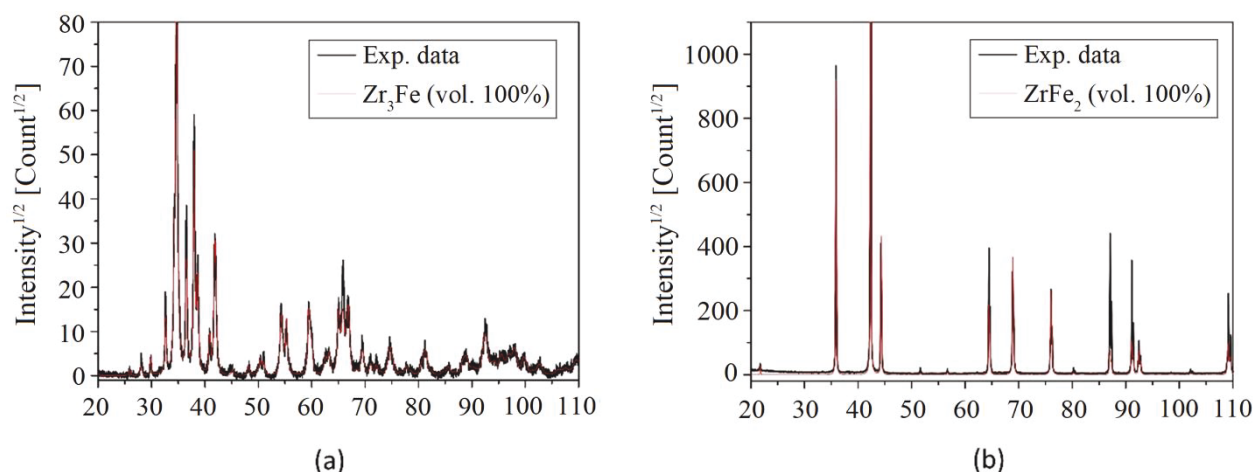


Fig. 2 – XRD results of Zr_3Fe (a) and C15- $ZrFe_2$ (b) intermetallic compounds.

2.3.3. Thermal expansion measurements

In order to verify thermal expansion coefficients calculated in the frame of the QHA, additional experimental measurements of the thermal expansion of the investigated compounds have been performed. The thermal expansion measurements were carried out in the temperature ranges: 353–1023 K for Zr_3Fe and 373–1523 K for $ZrFe_2$. In total, two different dilatometric devices were involved, namely DIL 802 (Netzsch GmbH, thermocouple type S, Ar flow, 10 K/min) and DIL 805A/D/T (TA Instruments Inc. formerly Bähr-Thermoanalyse GmbH, thermocouple type K, vacuum atmosphere, heating rate 300 K/min). Temperature correction of DIL 802 was performed using temperatures of magnetic and solid transformations in Fe (99.95% Alfa Aesar) and Co (99.995% Alfa Aesar). Certified reference material of sapphire (Bähr-Thermoanalyse GmbH) was used for calibration of linear temperature expansion. In the case of DIL 805A/D/T system, no additional calibration is required due to the specific design of the experimental procedure, since the thermocouple is placed directly onto the sample via spot welding. The measurements of two different samples were repeated two times with maximal uncertainty 6%. In order to avoid possible temperature gradients in the sample, we used quenching mode of DIL805A/D/T with hollow quartz push rods. Due to the principle of induction heating, only the sample is heated during the measurement.

2.3.4. Calorimetric measurements

For heat capacity measurements we used the classical three-step method (continuous method) with a constant heating rate [37]. The measurements were performed in the wide range of temperatures using two different devices. In the temperature range from 235 K to 675 K we have used DSC 8000 device (Perkin Elmer, Pt/Rh crucible, He/Ar flow, heating rate 10 K/min). The measurements in the temperature range from 235 K to 675 K were divided into smaller intervals 100–150 K. The heat capacity measurements in the temperature range from 623 K to 1220 K were performed in the one run using the device DSC Pegasus 404C (NETZSCH, Pt/Rh crucible, Ar flow, heating rate 10 K/min). Calibration was performed using the certified standard materials depending on the reliable temperature range of their heat capacity: copper standard was used in the temperature range from 100 to 320 K; molybdenum – 300 to 673 K and platinum – 573 to 1473 K. The measurements of two different samples were repeated two

times with maximal uncertainty value of 3 %. It should be mentioned that at high temperatures the C_P measurement with DSC equipment becomes less reliable due to increase of heat radiation which decreases a registered signal. This effect was considered during interpretation of the experimental data.

3. Results

3.1. Zero temperature electronic structure calculations

Let us start with calculations of thermodynamic properties of Zr_3Fe and $ZrFe_2$ phases at zero temperature. Theoretical data on lattice parameters, magnetic moments and formation energies for both phases are given in Table 1. Here, for comparison we also show the available experimental results at room temperature [34,35]. For orthorhombic Zr_3Fe phase, the calculated lattice parameters a and b are slightly underestimated, while parameter c is slightly overestimated compared to experimental data [34]. Simultaneously, the theoretical volume of Zr_3Fe is in excellent agreement with experiment. Zr_3Fe is found to be non-magnetic at zero temperature. For cubic C15- $ZrFe_2$ phase, the calculated lattice parameter a is 7.065 Å, while experiment gives $a = 7.061$ Å [35]. This compound is found to be ferrimagnetic with average magnetic moment 1.12 μ_B /atom, which is in good agreement with experimental result 1.04 μ_B /atom measured at the liquid helium temperature [38]. The calculated magnetic moments on Fe atoms with the average value of 1.924 μ_B are parallel to each other, but antiparallel to magnetic moments induced on Zr atoms with the values of -0.501 μ_B .

Formation enthalpies of the compounds are also listed in Table 1. They were calculated with respect to pure elements: non-magnetic hcp Zr and ferromagnetic bcc Fe. Our theoretical data on formation enthalpy -0.121 eV/at (-11.67 kJ/mol) and -0.288 eV/at (-27.79 kJ/mol) for Zr_3Fe and $ZrFe_2$ phases, respectively, are in good agreement with previous DTF calculations [15,16] and experimental results for $ZrFe_2$ [11–14].

Table1 – Ground state properties of Zr_3Fe and $ZrFe_2$ compounds at $T = 0$ K and available experimental data.

	Zr_3Fe		C15-$ZrFe_2$	
	Theory	Exp. [34]	Theory	Exp. [35]
Lattice parameter, Å	$a = 3.300$ $b = 10.900$ $c = 8.945$	$a = 3.321$ $b = 10.966$ $c = 8.825$	$a = 7.065$	$a = 7.061$
Volume, Å ³ /atom	20.100	20.087	14.694	14.669
Atomic basis coordinates	Fe1 [0.000 0.730 0.250] Zr1 [0.000 0.138 0.060] Zr2 [0.000 0.421 0.250]	Fe1 [0.000 0.744 0.250] Zr1 [0.000 0.135 0.062] Zr2 [0.000 0.426 0.250]	Fe1 [0.625 0.625 0.625] Zr1 [0.000 0.000 0.000]	Fe1 [0.625 0.625 0.625] Zr1 [0.000 0.000 0.000]
Magnetic moments, μ_B /atom	Non-magnetic	Non-magnetic	Total: 1.12 Fe: 1.924 Zr: -0.501	Total: 1.04 [38] - -
Formation energy, eV/at (kJ/mole)	-0.121 (-11.62)	-	-0.288 (-27.79)	-0.308 (-29.72) [11] -0.256 (-24.70) [12] -0.228 (-22.00) [13] -0.331 (-31.93) [14]

3.2. Finite-temperature effects

Because of the limitations of the experimental techniques to obtain data on the thermodynamic properties of the studied materials at low temperature, we calculate their thermodynamic properties in the temperature range from 0 K up to room temperature. We have accounted for the finite-temperature effects by determining the contributions of electronic entropy S_{el} , magnetic excitations G_{mag} and vibrational energy G_{vib} to the total free energy G_{tot} of the system. The electronic entropy S_{el} was estimated using Fermi distribution which depends on Fermi energy and temperature (see Eq. 2).

3.2.1 Magnetic excitations in ZrFe_2 phase

According to zero-temperature calculations, the ZrFe_2 phase is ferrimagnetic with opposite orientation of local magnetic moments on Zr and Fe atoms; and there are two types of magnetic moments in this phase. However, since the pure Zr atom on its own is non-magnetic, we assume that in ZrFe_2 phase the magnetic moment on Zr is induced by iron atoms in the local environment. Thus, for calculations of the magnon-dispersion relations we considered only the Fe-Fe pair exchange interactions.

The plot of magnon-dispersion relations as a function of wave vector k is shown in Fig. 3. Here, the value of effective exchange parameter J between Fe-Fe pair in the nearest neighborhood is $J_{\text{Fe-Fe}}^{\text{NN}} = 3.747$ meV. For the next nearest Fe-Fe pairs the exchange interaction becomes comparable too small $J_{\text{Fe-Fe}}^{\text{NNN}} = -0.194$ meV. The spin value for Fe atoms was chosen to be $S = 2$. Therefore, in the long wavelength limit $k \rightarrow 0$, the theoretical value of spin-waves stiffness for ZrFe_2 phase was found to be $D_{\text{stiff}} \approx 750$ meV·Å².

A simple estimation of the magnetic transition temperature T_C can be performed using pair exchange interactions within the mean-field approximation, $T_C^{\text{MFA}} = \frac{2}{3} \frac{1}{k_B} \sum_j J_{\text{Fe-Fe}} m_{\text{Fe}} m_{\text{Fe}}$, where summation runs over the first coordination shell and on-site magnetic moment is denoted as m_{Fe} . The obtained value for the Curie temperature T_C is 772 K. This result is overestimated as compared to the experimental value of 585 K [17], however, such a deviation is typical for the first-principles calculations of T_C .

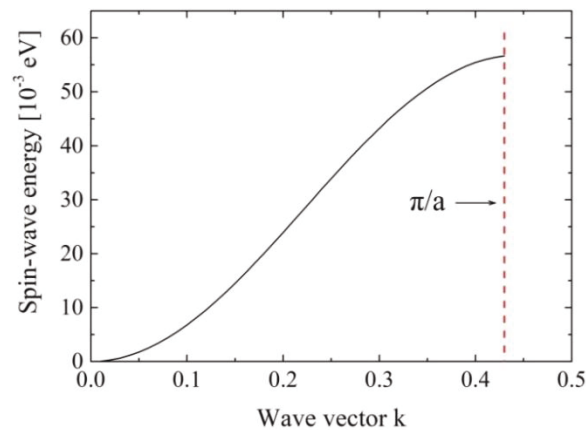


Fig. 3 – Magnon-dispersion relations of ZrFe_2 phase calculated for zero-temperature volume.

3.2.2. Phonon dispersion relations

Calculated phonon dispersion relations and corresponding phonon density of states of Zr_3Fe and ZrFe_2 compounds are plotted in Fig. 4 (a, b). The dispersion curves of Zr_3Fe and ZrFe_2 are shown along Γ -Z-T-Y-S-X-U-R and Γ -X-W-K- Γ -L directions of their Brillouin zones, respectively. The results confirm that both phases are dynamically stable since there are none imaginary frequencies for the whole set of wave vectors in the Brillouin zones. According to the calculated phonon density of states (PDOS), the vibrational frequencies are distributed in the range between 0 – 7 THz for Zr_3Fe and between 0 – 10 THz for ZrFe_2 . This is related to the difference in the masses between Zr and Fe atoms. Thus, in the Zr_2Fe , which contains larger amount of Fe atoms with lighter atomic mass, the distribution of phonon frequencies is broader compared to Zr_3Fe phase. By applying the Debye model to the calculated phonon frequencies we found the Debye frequency ω_D for each phase (see Fig. 4): $\omega_D(\text{Zr}_3\text{Fe}) = 5.43$ THz and $\omega_D(\text{ZrFe}_2) = 8.20$ THz. Consequently, the Debye temperatures are $\theta_D(\text{Zr}_3\text{Fe}) = 260.86$ K and $\theta_D(\text{ZrFe}_2) = 393.78$ K. The calculated values confirm our expectation on the reliability of the QHA for calculations of the thermodynamic properties of the studied systems in the temperature interval from 0 K to 300 K. However, in some cases they will be shown up to higher temperatures for methodological reasons.

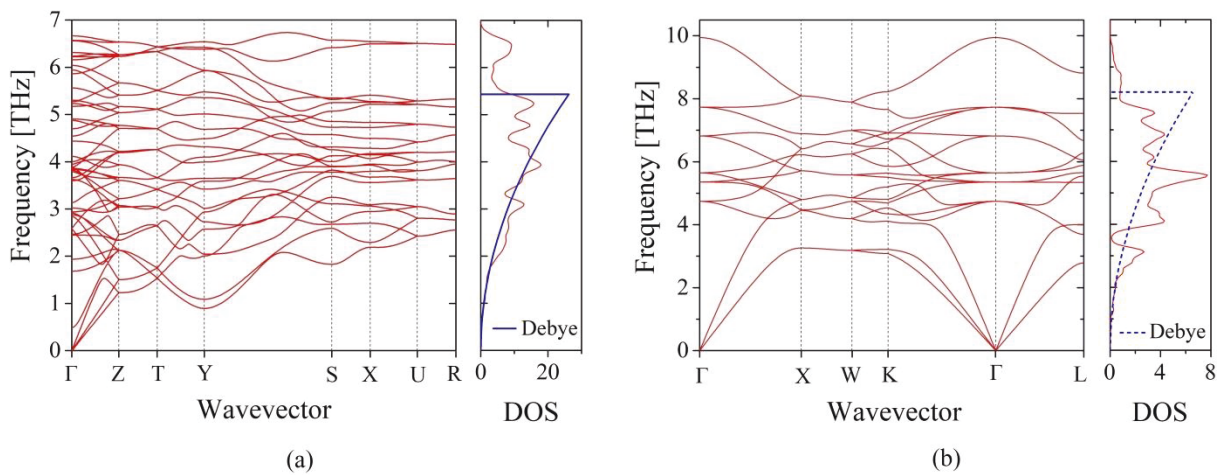


Fig. 4 – Phonon dispersion relations and phonon density of states of (a) Zr_3Fe and (b) ZrFe_2 compounds calculated for zero temperature volumes. Blue line represents the PDOS according to the Debye model.

Fig. 5 depicts calculated total free energies G_{tot} of both phases as the function of volume V and temperature T in the range between 0 K and 400 K. As can be seen from Fig. 5, the unit cell volumes, associated with the free energy minima, increase with the temperature. Dashed line, which connects the energy minima, shows the changes in ground state volume, viz. the thermal expansion of the lattices. Note that even at $T = 0$ K we observe the slight deviation of ground state volume compared to zero temperature DFT calculations due to the zero-point vibrations (see Tab. 1). The corresponding volumes are $20.163 \text{ \AA}^3/\text{atom}$ and $14.641 \text{ \AA}^3/\text{atom}$ for Zr_3Fe and ZrFe_2 , respectively. Interestingly, that the sign of this deviation is different for Zr_3Fe and ZrFe_2 phases.

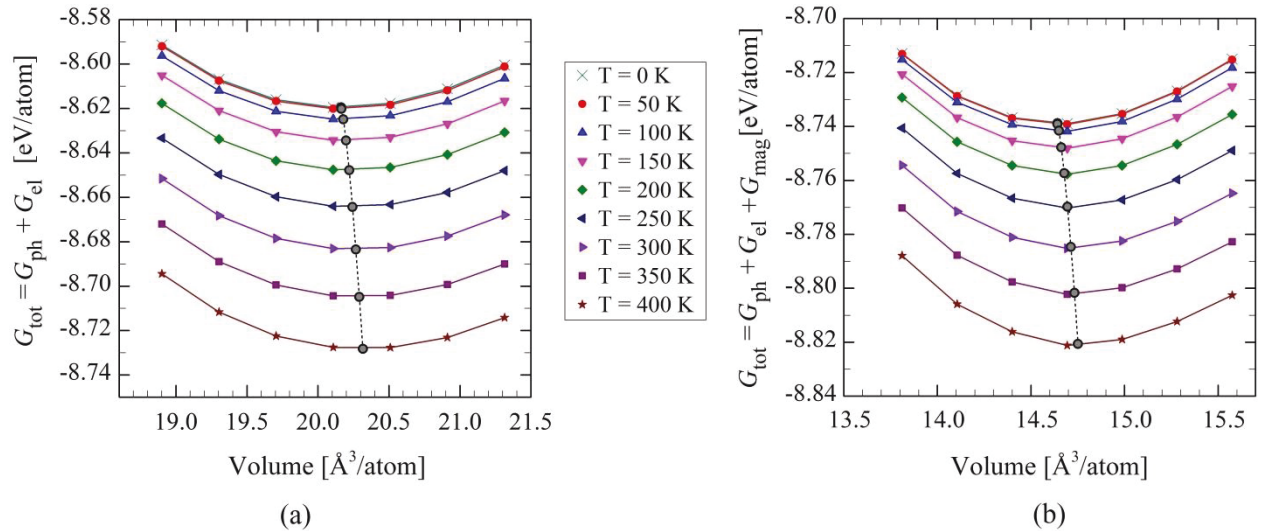


Fig. 5 – Total free energy G_{tot} of Zr_3Fe (a) and ZrFe_2 (b) phases plotted versus unit cell volume for the range of temperatures. The dashed black lines represent equilibrium volume and energy (curves minima) for the range of temperatures.

3.3. Thermal expansion coefficient

Let us now consider the properties that can be determined from the total free energy and compare them to our experiment. The experimental dilatometry results on Zr_3Fe and ZrFe_2 compounds obtained in this work and theoretical results on the volumetric thermal expansion coefficients calculated from Eq. 7 are summarized in Fig. 6. To find the volumetric thermal expansion coefficients from dilatometry results, it was assumed that both phases expand isotropically with temperature. Therefore, the volumetric coefficient is three times the linear coefficient: $\alpha_V = 3\alpha_L$.

According to the theoretical data, in the range of temperatures between 0 and 200 K the thermal expansion coefficient of Zr_3Fe is slightly higher than the one for ZrFe_2 phase. With further increasing of the temperature α_V of ZrFe_2 phase would become higher within QHA.

However, a comparison of calculated and experimental results shows that QHA significantly underestimates the values of α_V at temperatures above θ_D , where the contribution of anharmonic effects increases. Moreover, in the experiment we see that ZrFe_2 compound exhibits the magnetic transition. The Curie temperature measured by thermal expansion measurements is in a good agreement with our DCS results (reported below) and with data from literature, $T_c = 585$ K [17]. Because of this, for ZrFe_2 the magnetic contribution to thermal expansion becomes totally dominant, leading to well-developed λ -peculiarity at the magnetic phase transition. As will be seen from DSC results, the beginning of our thermal expansion measurements for ZrFe_2 is in the temperature range, where the magnetic transition already influences significantly on the thermodynamic properties of this compound. Therefore, the experimentally observed behavior of the thermal expansion coefficient of ZrFe_2 compound in the temperature range of 353–450 K cannot be directly compared with theory, justifying our decision to limit the simulations to low-temperatures. At the same time, one can see that the theoretical α_V of Zr_3Fe agrees well with experiment (within measurement uncertainty 6 %) at the temperatures close to the room temperature, confirming the reliability of the adopted theoretical scheme below $T \sim 300$ K.

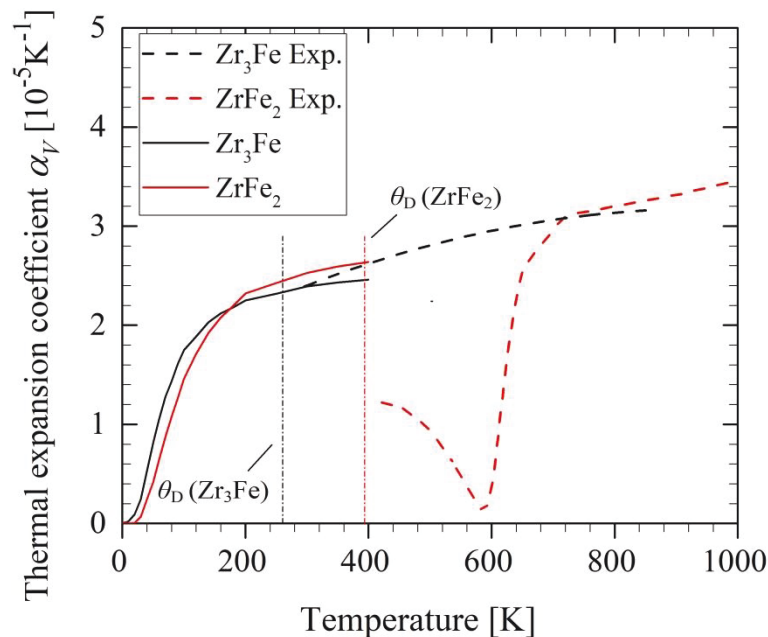


Fig. 6 – Experimental (dashed lines) and calculated (solid lines) volumetric coefficient of thermal expansion of Zr_3Fe (black) and ZrFe_2 (red). Vertical lines denote the Debye temperatures θ_D of both compounds.

3.4. Compressibility

In Fig. 7 we show the calculated results for bulk modulus B plotted as a function of temperature. In the range between 0 K and 300 K, each phase exhibits the reduction of bulk modulus with temperature: by $\sim 3\%$ for Zr_3Fe and by $\sim 2\%$ for ZrFe_2 . Unfortunately, there are no available experimental data on bulk modulus of Zr_3Fe and ZrFe_2 intermetallic compounds, however, our theoretical results are in good agreement with previous *ab-initio* calculations [15,39].

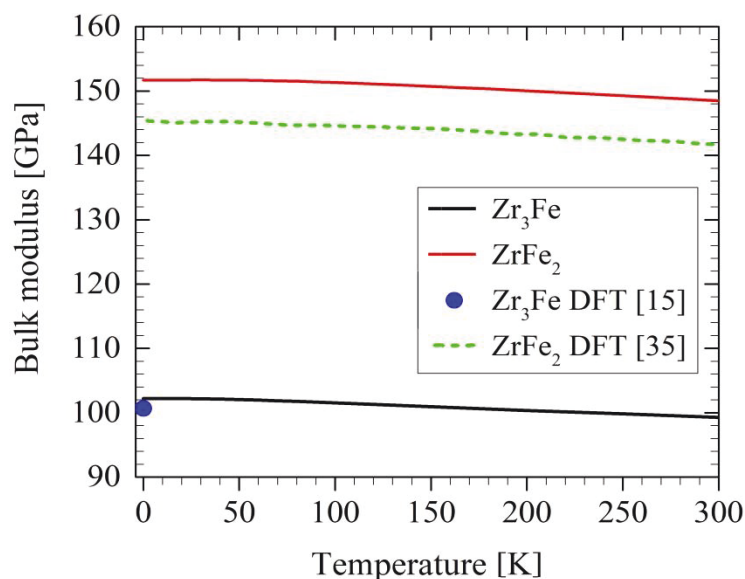


Fig. 7 – Bulk modulus of Zr_3Fe (black line) and ZrFe_2 (red line) compounds plotted versus temperature.

3.5. Heat capacity

The measurements of heat capacities C_P have been performed in range of temperatures between 100 and 1000 K for Zr_3Fe phase and in the range between 100 and 1480 K for ZrFe_2 phase. To the best of our knowledge, the measurements in such a broad temperature interval are reported for the first time. Results are plotted in Fig. 8. According to these data, the heat capacity C_P of ZrFe_2 phase exhibits a peak related to the magnetic transition at 585 K. Our C_P measurements of ZrFe_2 phase accurately reproduce previous experimental results in the range between 315 and 655 K from Ref. [17]. Experimental heat capacity of Zr_3Fe phase is plotted in Fig. 8a. Note that for orthorhombic Zr_3Fe phase the C_P was not studied before.

Theoretical calculations of total C_P are also shown in Fig. 8. In the case of orthorhombic Zr_3Fe phase (see Fig. 8a), at the low-temperature regions up to 300 K the theoretical heat capacity C_P agrees within $\pm 3\%$ with experimental data. For high temperatures the difference between theory (not shown) and experiment increases due to the increasing contribution from anharmonic effects. Regarding the ZrFe_2 phase (see Fig. 8b), one can see that the theory matches with experiment (within $\pm 3\%$ measurement error) in the range between 100 and 200 K. At higher temperatures the difference between theory and experiment significantly increases, most probably due to magnetic transition at $T_C = 585$ K. In fact, the contribution of magnetic excitations from Heisenberg model (reported below) weakly affects the calculated total heat capacity of ZrFe_2 phase. Moreover, we did not model the paramagnetic state of this compound, which strongly affects theoretical calculations of thermodynamic properties above T_C [40–42]. Nonetheless, in the low-temperature regions where the anharmonic and magnetic effects are small, we observe very good agreement between theory and experiment.

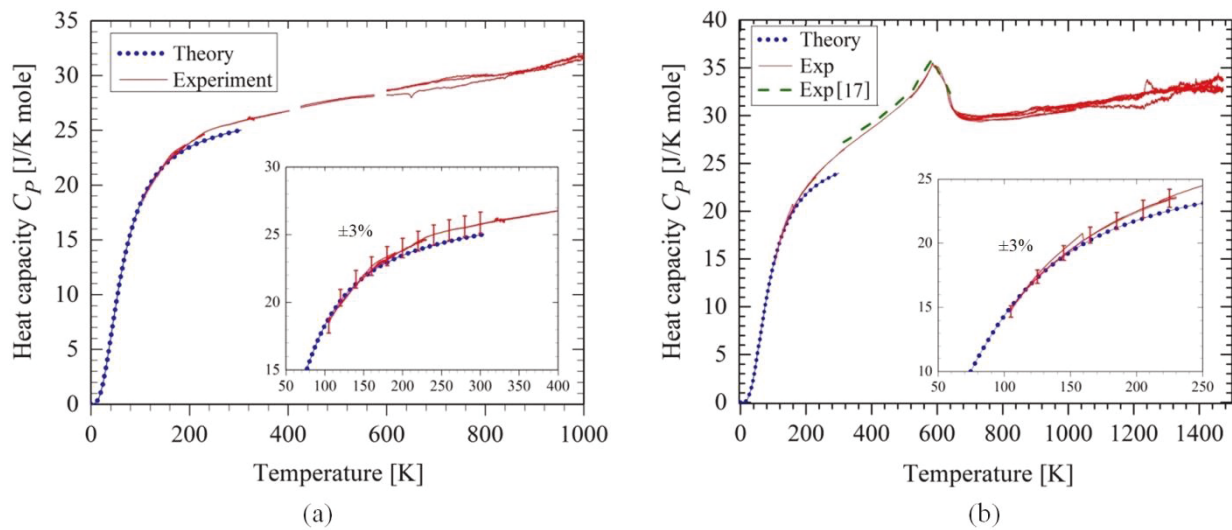


Fig. 8 – Theoretical and experimental results on heat capacity of Zr_3Fe (a) and ZrFe_2 (b) intermetallic compounds. Black and red lines respectfully represent our theoretical and experimental data. Green dashed line represents the available experimental data from Ref. [17]. The insets show the low temperature regions with information on the experimental error.

In Fig. 9 we plot the calculated contributions of phonons, electrons and magnons to the heat capacity. Fig. 9a represents the vibrational heat capacities at constant volume C_V^{ph} and pressure C_P^{ph} as well as electronic heat capacity C_P^{el} . One can see that with the temperature the isochoric heat capacity C_V^{el} (red dashed line) of Zr_3Fe phase reaches the saturation values $\sim 25 \text{ J} \cdot \text{mol}^{-1} \cdot \text{K}^{-1} = 3R$ faster than the one for ZrFe_2 phase. Isobaric heat capacity C_P^{ph} was calculated using Eq.

(10) and the information on $\alpha_V(T)$ and $B(T)$, discussed above. Regarding the electronic contribution, the Zr_3Fe phase exhibits higher values of C_p^{el} compared to the ZrFe_2 phase. In the low-temperature limit up to 100 K, calculated C_p^{el} of each phase changes linearly with temperature. This result is in accordance with the Sommerfeld model for electron heat capacity described as $C_V^{el} = \frac{\pi^2}{3} k_B^2 N(\epsilon_F) T = \gamma T$, where parameter γ is equal to 0.0025 and 0.0011 for Zr_3Fe and ZrFe_2 , respectively. Magnon heat capacity $C_p^{mag} \sim T^{3/2}$ for ZrFe_2 phase is plotted in Fig. 9b. Here, we compare C_p^{mag} with C_p^{el} for ZrFe_2 ; and as one can see, the spin-waves contribution to the total heat capacity is comparably too small.

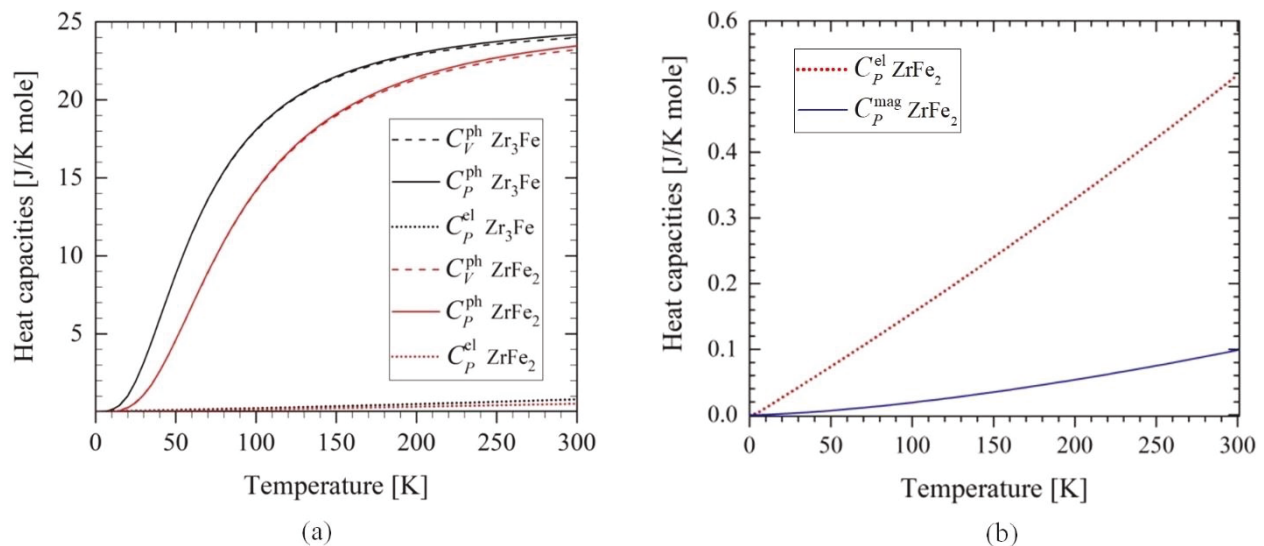


Fig. 9 – (a) Calculated vibrational (C_V^{ph} , C_p^{ph}) and electronic C_p^{el} contributions to heat capacity; as a function of temperature for Zr_3Fe (black lines) and ZrFe_2 (red lines) phases; and (b) comparison of spin-waves heat capacity C_p^{mag} with electronic heat capacity C_p^{el} in ferrimagnetic ZrFe_2 phase.

4. Discussion

For Zr_3Fe phase, where there is no magnetic transition, we observed a good agreement between theoretical and experimental heat capacities (see Fig. 8a). The most probable reason of deviation between theory and experiment might be the arising of anharmonic effects with the temperature. This assumption is supported by comparison of our theoretical and experimental data on thermal expansion coefficient (see Fig. 6a): QHA underestimates the thermal expansion of Zr_3Fe phase at the temperatures above ~ 300 K. The same assumption could be applied for ZrFe_2 phase according to data on thermal expansion and heat capacity (see Figs. 6b and 8b); however, the presence of magnetic transition makes it difficult to estimate the anharmonic effects on heat capacity of ZrFe_2 ; and it is obvious from Fig. 8b that the deviation between theoretical and experimental heat capacities mostly arises from magnetic transition in ZrFe_2 . Additionally, there are other factors that can influence on the deviation between theoretical and experimental C_p such as vacancies and other defects. However, their estimations are beyond the scope of the present work. From the comparison between DFT+QHA and DSC data on C_p we conclude that QHA results are reliable up to 300 K for Zr_3Fe and 200 K for ZrFe_2 .

So, in the low-temperature region the QHA gives fairly accurate information on thermodynamic properties of Zr_3Fe and ZrFe_2 intermetallic compounds. This allows us to extrapolate our experimentally measured heat capacity to zero temperature using our theoretical data. That is

to say, through the combination of theory and experiment we can accurately determine the heat capacity in the range from 0 K up to the highest studied temperature. To derive the equations for C_P we used RW-model [43], which is traditional for thermodynamic databases:

$$C_P^{RW}(T, \theta^{RW}) = C_V^{Deb}(T) + aT + bT^2 + C_P^{mag}(T) \quad (13)$$

where T is temperature, $\theta^{RW} = (\theta_D, a, b)$ is the vector of the unknown model parameters to be estimated, $C_P^{Deb}(T)$ is the heat capacity describing phonon contribution using Debye model, $C_P^{mag}(T)$ is magnetic contribution of the heat capacity.

Magnetic contribution to the thermodynamic properties was taken into account according to Hillert and Jarl [44] in the following form:

$$C_P^{mag} = R \ln(\beta_0 + 1) g(\tau) \quad (14)$$

where τ is T/T^* , T^* is the critical temperature (the Curie temperature T_C for ferromagnetic materials or the Neel temperature T_N for antiferromagnetic materials), β_0 the average magnetic moment per atom and $g(\tau)$ is a function depending on τ .

Obtained thermodynamic RW-models well reproduce the experimental data at high temperatures, as well as theoretical results at low temperatures. Thus, based on the obtained fitted models of C_P , it is possible to determine the standard entropies of both phases using the expression $S^{298} = \int_0^{298} C_P \frac{dT}{T}$. The data on C_P , S^{298} and ΔH_f for Zr₃Fe and ZrFe₂ phases are listed in Table 2.

Table 2 – Values of C_P fitting parameter, S^{298} and ΔH_f for Zr₃Fe and ZrFe₂ phases.

Parameters \ Compound	Zr ₃ Fe	ZrFe ₂
θ_D, K	260.86	393.78
$a \cdot 10^3$	5.62	6.85
$b \cdot 10^7$	10.52	–8.79
β_0	–	0.466
T_C, K	–	585
$S^{298}, J/mole \cdot K$	38.4	30.8
$\Delta H_f, kJ/mole$	–11.62	–27.79

5. Conclusions

In this work, using the combination of DFT+QHA approach and experimental DSC analysis we obtained the main thermodynamic parameters S^{298} and ΔH^0 and functions $C_P(T)$ for Zr₃Fe and ZrFe₂ intermetallic phases from 0 K up to temperatures of their stability. Experimental measurements of heat capacity of both phases have been performed for the first time in wide range of temperatures. Analysis of theoretical and experimental data on α_V and C_P shows that QHA remarkably underestimates the anharmonic and magnetic effects starting from temperatures ~ 200 –300 K. However, for low-temperature regions we observed very good agreement between theory and experiment. The new and complete information on the heat capacity and standard entropy and of Zr₃Fe and ZrFe₂ compounds is very important for future development of reliable thermodynamic description of the Zr–Fe binary system. The present study allows to perform the thermodynamic modeling in terms of the 3rd generation CALPHAD approach including the reasonable description of thermodynamic properties starting from zero temperature.

Acknowledgments

Theoretical calculations were supported by the Ministry of Science and High Education of the Russian Federation in the framework of Increase Competitiveness Program of NUST “MISIS” (No. K2-2019-001) implemented by a governmental decree dated 16 March 2013, No 211. We acknowledge support from the Strategic Research Areas the Swedish e-Science Research Centre (SeRC) and Advanced Functional Materials at Linköping University (Faculty Grant SFOMatLiU No. 2009 00971). The authors thank the German Research Foundation (DFG) for funding the sub-project C2 within the Collaborative Research Center SFB 799 Trip-Matrix Composites. A. Udovsky gratefully acknowledges Russian Foundation for Basic Research (No. 19-03-00530_a) for support in experimental measurements. In addition, we thank G. Savinykh and Dr. C. Schimpf (TU-Freiberg) for technical contribution.

References

- [1] M.S. Granovski, D. Arias, *J. Nucl. Mater.* 229 (1996) 29.
- [2] F. Stein, G. Sauthoff, and M. Palm, *J. Phase Equilib. Diff.* 23 (2002) 480.
- [3] X. Tao, J. Zhu, H. Guo, Yi. Ouyang, Yo. Du, *J. Nucl. Mater.* 440 (2013) 6.
- [4] H. Biermann et al., *Adv. Eng. Mater.* 11 (2009) 1000.
- [5] S. Martin et al., *Steel Research int.* 82 (2011) 1133.
- [6] L.N. Guseva, T.O. Malakhova, *Metallofiz. (Kiev)* 46 (1973) 111.
- [7] T.O. Malakhova and A.N. Kobylkin, *Russ. Metall.* (1982) 187.
- [8] K. Bhanumurthy and G.B. Kale, *Scr. Metall. Mater.* 28 (1993) 753.
- [9] C. Guo, Z. Du, C. Li, B. Zhang, M. Tao, *CALPHAD* 32 (2008) 637.
- [10] Yi. Yang, L. Tan, H. Bei, J.T. Busby, *J. Nucl. Mater.* 441 (2013) 190.
- [11] J.C. Gachon, J. Hertz, *CALPHAD* 7 (1983) 1.
- [12] A. Schneider, et al., *Pure Appl. Chem.* 2 (1961) 13.
- [13] O.Yu. Sidorov, et al., *Rasplavy* 3 (1989) 28.
- [14] M. Rosner-Kuhn, et al., *Z. Metallkd.* 86 (1995) 682.
- [15] K. Ali, A. Arya, P.S. Ghosh, G.K. Dey, *Comput. Mater. Sci.* 112 (2016) 52.
- [16] M. Mihalkovic, M. Widom, *Phys. Rev. B* 70 (2004) 144107.
- [17] R. Lück, H. Wang, *J. Alloys Compd.* 191 (1993) 11.
- [18] P.E.A. Turchi, I.A. Abrikosov, B. Burton, et al., *CALPHAD* 31 (2007) 4.
- [19] B. Grabowski, L. Ismer, T. Hickel, and J. Neugebauer, *Phys. Rev. B* 79 (2009) 134106.
- [20] L. Vitos, *Computational Quantum Mechanics for Materials Engineers: The EMT0 Method and Applications*, Springer-Verlag, London, (2007).
- [21] A.I. Liechtenstein, et al., *J. Phys. F Met. Phys.* 14 (1984) L125.
- [22] A.I. Liechtenstein, et al., *Solid State Commun.* 54 (1985) 327.
- [23] A.I. Liechtenstein, et al., *J. Magn. Magn. Mater.* 67 (1987) 65.
- [24] Ch. Kittel, *Quantum theory of solids*, 2nd Revised Edition (1987).
- [25] P. E. Blöchl, Projector augmented-wave method, *Phys. Rev. B* 50 (1994) 17953.
- [26] G. Kresse, J. Furthmüller, *Phys. Rev. B* 54 (1996) 11169.
- [27] J. P. Perdew, K. Burke, and M. Ernzerhof, *Phys. Rev. Lett.* 77 (1996) 3865.
- [28] H. J. Monkhorst and J. D. Pack, *Phys. Rev. B* 13 (1976) 5188.
- [29] H. Hellmann, *Einführung in die Quantumchemie*, Deuticke, Leipzig, 1937.
- [30] R.P. Feynman, *Phys. Rev.* 56 (1939) 340.
- [31] A. Togo and I. Tanaka, *Scr. Mater.* 108 (2015) 1.
- [32] L. Lutteroti, MAUD, *CPD Newsletter, IUCr* 24 (2000).
- [33] W. Brueckner, K. Kleinstueck, G.E.R. Schulze, *Physica Status Solidi.* 23 (1967) 475.
- [34] P. Matkovic, T. Matkovic, I. Vickovic, *Metallurgija, Croatia.* 29 (1990) 3.

- [35] E. Piegger, R.S. Craig, *J. Chemical Phys.* 39 (1963) 137.
- [36] H. Boller, *Monatshefte fuer Chemie* 104 (1973) 545.
- [37] G. Gatta, et al., *Pure Appl. Chem.* 78 (2006) 1455.
- [38] C.W. Kocher and P.J. Brown, *J. Appl. Phys.* 33 (1962) 1091.
- [39] K. Ali, P.S. Ghosh, A. Arya, *J. Alloy. Compd.* 723 (2017) 611.
- [40] B. Alling, T. Marten, and I. A. Abrikosov, *Nature Materials* 9 (2010) 283.
- [41] P. Steneteg, B. Alling, and I. A. Abrikosov, *Phys. Rev. B* 85 (2012) 144404.
- [42] N. Shulumba, et al., *Phys. Rev. B* 89 (2014) 174108.
- [43] M.W. Chase, et al., *CALPHAD* 19 (1995) 437.
- [44] M. Hillert, M. Jarl, *CALPHAD* 2 (1978) 227.

Publication P2: I. Saenko, A. Kuprava, A. Udovsky, O. Fabrichnaya, Heat capacity measurement of Zr_2Fe and thermodynamic re-assessment of the Fe–Zr system, *CALPHAD* 66 (2019) 101625.
DOI: 10.1016/j.calphad.2019.05.002

Contributions to the paper:

Authors	Contribution [%]	Particular contribution
I. Saenko	65	<ul style="list-style-type: none"> • Experimental work • Evaluation of data • Thermodynamic modelling • Composition of the manuscript
A. Kuprava	10	<ul style="list-style-type: none"> • Experimental assistance
Prof. A. Udovsky	5	<ul style="list-style-type: none"> • Proofreading of the manuscript
Dr. rer. nat. habil. O. Fabrichnaya	20	<ul style="list-style-type: none"> • Supervision of the work • Proofreading of the manuscript

Heat capacity measurement of Zr₂Fe and thermodynamic re-assessment of the Fe–Zr system

I. Saenko^{1,2}, A. Kuprava^{1,3}, A. Udovsky^{2,4}, O. Fabrichnaya^{1,*}

¹ Freiberg University of Mining and Technology, Freiberg, Sachsen, 09599, Germany

² Baikov Institute of Metallurgy and Material Science of the Russian Academy of Sciences, Moscow, 119991, Russia

³ National University of Science and Technology ‘MISIS’, Moscow, 119049, Russia

⁴ National Research Nuclear University MEPhI, Moscow, 115409, Russia

* Corresponding author:

Dr. rer.nat. habil. O. Fabrichnaya, Freiberg University of Mining and Technology, Freiberg, Sachsen, 09599, Germany

E-mail: fabrich@www.tu-freiberg.de

Abstract

Critical evaluation of the Fe–Zr binary system has been performed based on the available experimental and calculated data. New experimental data on the heat capacity of Zr₂Fe have been obtained using differential scanning calorimetry. Thermodynamic parameters have been optimized using the CALPHAD approach. New experimental results of specific heat capacity and ab-initio calculations for the ZrFe₂, Zr₂Fe and Zr₃Fe intermetallic compounds have been taken into account in the optimization of the thermodynamic parameters. A self-consistent thermodynamic description of the Fe–Zr system has been obtained. Using the generalized “ χ^2 ”-criterion, the results calculated using the thermodynamic descriptions derived in the present work are compared with those previously published.

1. Introduction

Zr-based alloys, the so-called zircaloys, containing small amounts of Fe and other alloying elements, are widely used in the nuclear industry because of their low absorption cross-section of thermal neutrons, high corrosion resistance and hardness [1–3]. Moreover, the Fe–Zr binary system plays an important role in the modern steel industry in the manufacture of novel composite materials. For example, composite materials based on high-alloyed steels, such as high-alloyed austenitic stainless TRIP-steel (Transformation Induced Plasticity) reinforced by Mg-PSZ (MgO-stabilized zirconia); the so-called TRIP-Matrix-Composite, is of particular interest owing to the wide range of technological applications, especially in the automotive sector [4]. In this composite, both the TRIP steel matrix and ceramic particles undergo martensitic transformations during compression thereby improving its mechanical properties, such as strength and energy absorption during compression [5]. The development of such complex materials requires a good understanding of their thermodynamic properties and phase relationships. The Fe–Zr system has become the subject of great interest, and a detailed knowledge of its thermodynamic properties is essential information for the modern composite materials and structural steels industries. Moreover, a thermodynamic description of the binary Fe–Zr system will play an important role in investigations and modelling of high-order systems containing these two elements. The most recent thermodynamic assessments of this system were carried out by Guo *et al.* [6] and Yang *et al.* [7]. More recently, the available information on the thermodynamic properties of the intermetallic compounds in the binary Fe–Zr system was extended by Ali *et al.* [8,9] and by Mukhamedov *et al.* [10]. Ali *et al.* [8] presented first-principles investigations of the intermetallic

compounds across the whole composition range of the Fe–Zr binary system. Subsequently, they reported plane-wave based density functional theory (DFT) investigations of structural, elastic and lattice dynamical properties of the Fe-rich C15-ZrFe₂ and Zr-rich Zr₂Fe intermetallic compounds, as well as calculated heat capacities of these phases [9]. Mukhamedov *et al.* [10] have performed detailed theoretical simulations and experimental investigations of the thermodynamic properties of the Zr₃Fe and C15-ZrFe₂ intermetallic compounds, where differential scanning calorimetry (DSC) measurements and *ab-initio* simulations were carried out to define descriptions of the Gibbs energies of these compounds from 0 K up to their maximum temperatures of stability. The methods applied by Ali *et al.* [9] and Mukhamedov *et al.* [10] for the heat capacity calculations were similar, namely the Density Functional Theory (DFT) approach was used in combination with quasi-harmonic approximations (QHA). However, in the work of Mukhamedov *et al.* [10], it was shown that the DFT-QHA method has limitations since it does not account for anharmonic effects that might be significant at high temperatures [11]. Thus, the DFT+QHA method can be applied only for low-temperature regions up to 250 – 300 K. Therefore, the reliability of the DFT+QHA results and borders between low- and high-temperature regions should be defined from a comparison of theoretical and experimental data [10]. Summarizing the above discussion, newly available thermodynamic properties for the intermetallic compounds in the Fe–Zr system should be taken into account for further improvement of the thermodynamic description of the Fe–Zr system. Furthermore, calculations of the heat capacity of Zr₂Fe presented by [9] should be verified and possibly extended by means of experimental studies. Therefore, the aim of the present work was to perform heat capacity measurements for Zr₂Fe and to assess thermodynamic parameters of the Fe–Zr system taking into account the newly available experimental results of Mukhamedov *et al.* [10] as well as *ab-initio* calculations from Mukhamedov *et al.* [10] and of Ali *et al.* [8,9]. The resulting thermodynamic description will be useful for further thermodynamic modelling of high-order systems.

2. Literature survey

Phase relationships in the Fe–Zr system have been studied on a number of occasions since the first experiments dedicated to constructing the phase diagram for the whole composition range was carried out by Svechnikov [12,13]. They found a cubic C15-ZrFe₂-phase as well as the Zr₃Fe phase, but no compounds in the Zr-rich composition range were identified. More recently, critical evaluations submitted by Arias and Abriata [14] have presented a phase diagram based on new experimental studies [12,13,15–20] where four compounds Zr₃Fe, C15-ZrFe₂, Zr₂Fe and Zr₆Fe₂₃ were shown to be stable. Subsequent thermodynamic assessments [6,21–23] reflected existing contradictions in the literature concerning phase stabilities. The most recent experimental studies relating to phase equilibria were carried out by Stein *et al.* [2]. In this work, Stein *et al.* succeeded in eliminating several contradictions and ambiguities. Namely, the Zr₆Fe₂₃ (ZrFe₃) phase was shown to be a non-equilibrium phase in the binary system. It was clearly demonstrated that this phase is stabilized by oxygen impurity. Additionally, it was shown in the work of Malakhova [24] and Malakhova and Alexeyeva [17] that the stability of the Zr₂Fe phase was limited to the temperature range from 1048 to 1247 K, and Zr₃Fe was stable below 1158 K. The stability ranges of these phases were verified and amended slightly by Stein *et al.* [2]. The phase diagram for the Fe–Zr binary system established by Stein [2] is presented in Fig. 1. All stable intermetallic phases and their crystal structures are listed in Table 1.

Table 1. Data on crystal structures of solid phases of the Fe–Zr system.

Phase	Pearson symbol	Space group	Prototype	Strukturbericht Designation	Reference
α -Fe	<i>cI2</i>	$Im\bar{3}m$	W	A2	[25]
γ -Fe	<i>cF4</i>	$Fm\bar{3}m$	Cu	A1	[25]
δ -Fe	<i>cI2</i>	$Im\bar{3}m$	W	A2	[25]
$\text{Zr}_6\text{Fe}_{23}$	<i>cF116</i>	$Fm\bar{3}m$	$\text{Mn}_{23}\text{Th}_6$	D8 _a	[2]
C36-ZrFe ₂	<i>hP24</i>	$P6_3/mmc$	MgNi_2	C36	[2]
C15-ZrFe ₂	<i>cF24</i>	$Fd\bar{3}m$	MgCu_2	C15	[2]
Zr_2Fe	<i>tI12</i>	$I4/mcm$	Al_2Cu	C16	[2]
Zr_3Fe	<i>oC16</i>	$Cmcm$	Re_3B	E1 _a	[2]
α -Zr	<i>hP2</i>	$P6_3/mmc$	Mg	A3	[25]
β -Zr	<i>cI2</i>	$Im\bar{3}m$	W	A2	[25]

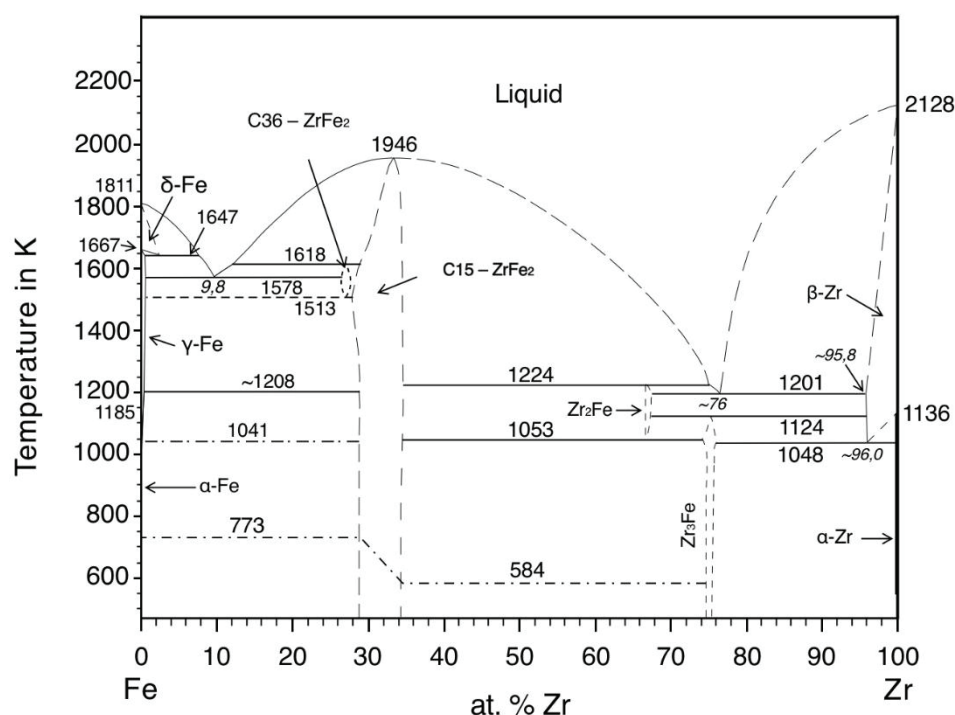


Fig. 1 – Fe–Zr phase diagram presented by Stein *et al.* [2].

The phase diagram derived from experiment [2] was accepted in two later optimizations that were conducted by Guo *et al.* [6] and Yang *et al.* [7]. The thermodynamic assessment by Guo [6] agrees better with the experimental results of Stein *et al.* [2], while Yang [7] gave more weight to the thermodynamic data and *ab-initio* calculations, which resulted in considerably worse agreement with the accepted phase diagram [2].

The enthalpy of formation of the C15-ZrFe₂ Laves phase was measured by Gachon *et al.* [26] using direct reaction calorimetry at 298 K. Additionally, the enthalpy of formation of C15-ZrFe₂ was derived from indirect solution calorimetry measurements undertaken by [27,28], and from levitation alloying calorimetry [29]. The values presented by Gachon *et al.* [26] and Rosner-Kuhnet *et al.* [29] are consistent with one another at $-29.7 \text{ kJ}\cdot\text{mol}^{-1}$ and $-31.93 \text{ kJ}\cdot\text{mol}^{-1}$, respectively, while values obtained by Schneider *et al.* [27] and Sidorov *et al.* [28] are more positive ($-22.0 \text{ kJ}\cdot\text{mol}^{-1}$ and $-24.69 \text{ kJ}\cdot\text{mol}^{-1}$, respectively). Enthalpies of formation of the Fe–Zr intermetallic compounds have been calculated by *ab-initio* methods: C15-ZrFe₂ [8,10,30], C36-ZrFe₂ [8,31], Zr_2Fe [3,8,30,31] and Zr_3Fe [8,10,30,31]. It should be

mentioned, that all results of *ab-initio* calculations for the C15- and C36-ZrFe₂ compounds are in good agreement with each other, and agree well with the experimental data of Gachon *et al.* [26] for C15-ZrFe₂ within the range of experimental uncertainty. Earlier results for Zr₃Fe and Zr₂Fe [3,30,31] are slightly more negative than newly presented data from Ali *et al.* [8] for Zr₃Fe and Zr₂Fe, and Mukhamedov *et al.* [10] for Zr₃Fe. It should be noted that *ab-initio* calculated data available in the databases of the Materials Project [32,33] and The Open Quantum Materials Database (OQMD) [34] agree perfectly with the calculations of Ali *et al.* [8] and Mukhamedov *et al.* [10] for all intermetallic compounds in the Fe–Zr system. However, it should be mentioned, that there are no experimental data available for the enthalpy of formation of C36-ZrFe₂, Zr₂Fe or Zr₃Fe. All available experimental and calculated enthalpies of formation of the intermetallic compounds in the Fe–Zr system are presented in Table 2.

The heat capacity of the C15-ZrFe₂ phase was measured over the temperature range from 313 K to 653 K by Lück and Wang [35]. Later, Mukhamedov *et al.* [10] measured the heat capacity of C15-ZrFe₂ and Zr₃Fe over a wide temperature range from 100 K to 1473 K, and from 100 to 1023 K, respectively. Moreover, in this work [10], a detailed theoretical simulation of the thermodynamic properties of C15-ZrFe₂ and Zr₃Fe was performed in the framework of DFT-QHA that allowed the extension of the experimentally derived heat capacity data down to 0 K, and in addition, calculation of standard entropies S^{298} and enthalpies of formation ΔH^0 for these two compounds. Earlier, the heat capacities of C15-ZrFe₂ and Zr₂Fe were estimated by Ali *et al.* [9] following plane-wave based DFT investigations. As indicated above, Mukhamedov [10] and Ali [9] used similar of *ab-initio* calculation methods, based on a combination of DFT and QHA. However, the calculations performed by Mukhamedov *et al.* [10] were improved by taking into account electronic contributions to the heat capacity and an evaluation of the magnetic excitation for the C15-ZrFe₂ phase. The calculated results for the heat capacity of C15-ZrFe₂ presented by Mukhamedov *et al.* [10] were in better agreement with experimental data than the results of Ali *et al.* [9]. Therefore, the calculated heat capacity data for C15-ZrFe₂ presented by Mukhamedov *et al.* [10] were accepted for the thermodynamic modelling of the system in this work.

The standard entropy of Zr₂Fe was calculated based on the work of Ali *et al.* [9] to be 33.4 J·K⁻¹·mol⁻¹. However, there are no available experimental data on the heat capacity for Zr₂Fe. All experimental and calculated standard entropies of the stable intermediate phases in the Fe–Zr system are presented in Table 3.

The enthalpy of melting of C15-ZrFe₂ was measured by Servant *et al.* [22] using DTA to be 20200 J·mol⁻¹ at 1932 K. The enthalpy of mixing in the liquid phase was measured at different temperatures using high-temperature calorimetry [28,36–40] and by levitation alloying calorimetry [29]. Despite the data being obtained at different temperatures in the range of 1900–2280 K, the values obtained are in a good agreement with each other within experimental uncertainty. The only exception is the results of [28] which are substantially less negative (maximal difference is ~10 kJ·mol⁻¹) than the others. All enthalpies of mixing are presented in Fig. 2.

Activities of iron were derived from high-temperature mass-spectrometry Knudsen effusion measurements [41] in the range of 1500 – 1850 K and 50 – 95 at.% Zr. The data were modified slightly by Chatain *et al.* [42]. The Fe activity measurements were used to calculate Zr activities using the Gibbs-Duhem equation. The calculated results for 1873 K [42] are presented in Fig. 3 together with experimental points.

Table 2. Comparison of the experimental and calculated data for the enthalpy of formation of the stable intermediate phases in the Fe–Zr system.

Intermetallic compounds	Temperature, K	Enthalpy of formation, kJ·(mol at) ⁻¹	Used method	Refs.
C15-ZrFe ₂	0	-27.79	<i>Ab initio</i>	[10]
		-28.07	<i>Ab initio</i>	[30]
		-27.0	<i>Ab initio</i>	[8]
		-27.40	<i>Ab initio</i>	[32,33]
		-26.98	<i>Ab initio</i>	[34]
	298.15	-29.7±1.7	Direct reaction cal.	[26]
		-31.93	Levitation alloying cal.	[29]
		-22.0	Solution calorimetry	[28]
		-24.69±1.4	Solution calorimetry	[27]
		-30.446	Optimization	[6]
		-28.954	Optimization	[7]
		-29.77	Optimization	This Work
C36-ZrFe ₂	0	-26.34	<i>Ab initio</i>	[8]
		-27.59	<i>Ab initio</i>	[31]
		-26.63	<i>Ab initio</i>	[32,33]
	298.15	-27.78	Optimization	[6]
		-28.23	Optimization	[7]
Zr ₂ Fe	0	-28.86	Optimization	This Work
		-16.07	<i>Ab initio</i>	[30]
		-18.76	<i>Ab initio</i>	[3]
		-16.02	<i>Ab initio</i>	[31]
		-13.51	<i>Ab initio</i>	[8]
		-13.70	<i>Ab initio</i>	[32,33]
	298.15	-13.49	<i>Ab initio</i>	[34]
		-12.81	Optimization	[6]
		-15.43	Optimization	[7]
		-11.70	Optimization	This Work
Zr ₃ Fe	0	-11.62	<i>Ab initio</i>	[10]
		-14.34	<i>Ab initio</i>	[30]
		-14.47	<i>Ab initio</i>	[31]
		-11.77	<i>Ab initio</i>	[8]
		-12.35	<i>Ab initio</i>	[32,33]
		-11.56	<i>Ab initio</i>	[34]
	298.15	-20.02	Optimization	[6]
		-14.46	Optimization	[7]
		-12.38	Optimization	This Work

Table 3. Comparison of the experimental and calculated data for the standard entropies of the stable intermediate phases in the Fe–Zr system.

Intermetallic compounds	Standard entropy, $\text{JK}^{-1}\cdot(\text{mol at})^{-1}$	Used method	Refs.
C15-ZrFe ₂	30.8	DFT,QHA,DSC	[10]
	30.0	DFT,QHA	[9]
	26.05	Optimization	[6]
	29.79	Optimization	[7]
	30.80	Optimization	This Work
C36-ZrFe ₂	30.47	Optimization	[6]
	30.70	Optimization	[7]
	32.47	Optimization	This Work
Zr ₂ Fe	35.2	DFT,QHA[9],DSC, RW-Debye	This Work
	33.8	DFT,QHA[9],DSC, RW-Einstein	This Work
	33.4	DFT,QHA	[9]
	37.48	Optimization	[6]
	34.52	Optimization	[7]
	39.32	Optimization	This Work
Zr ₃ Fe	38.4	DFT,QHA,DSC	[10]
	28.78	Optimization	[6]
	33.28	Optimization	[7]
	36.4	Optimization	This Work

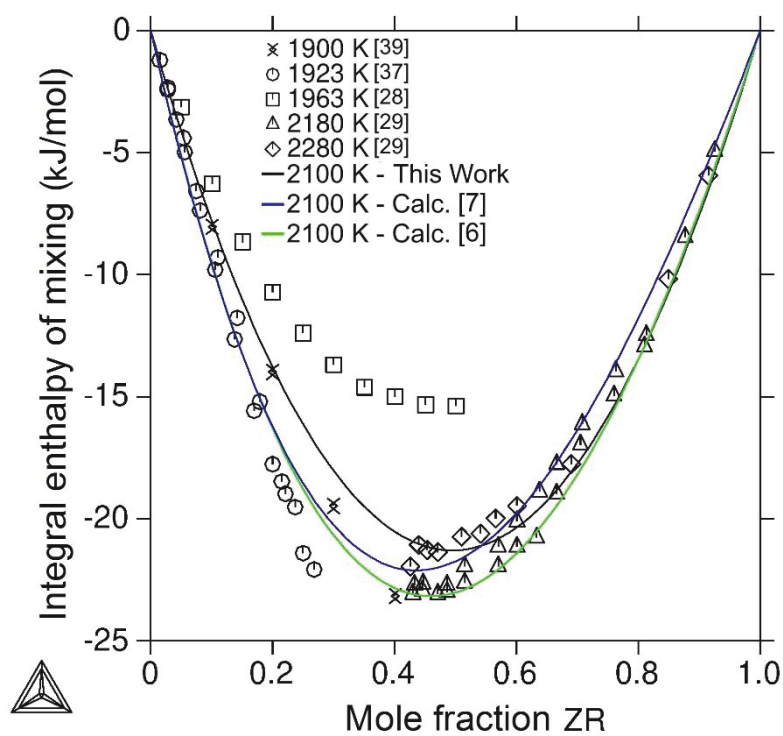


Fig. 2. Comparison of integral enthalpies of mixing of the liquid phase obtained in the present work (black line) and in the work of Guo *et al.* [6] (green line) and of Yang *et al.* [7] (blue line) together with experimental results [28,29,37,39].

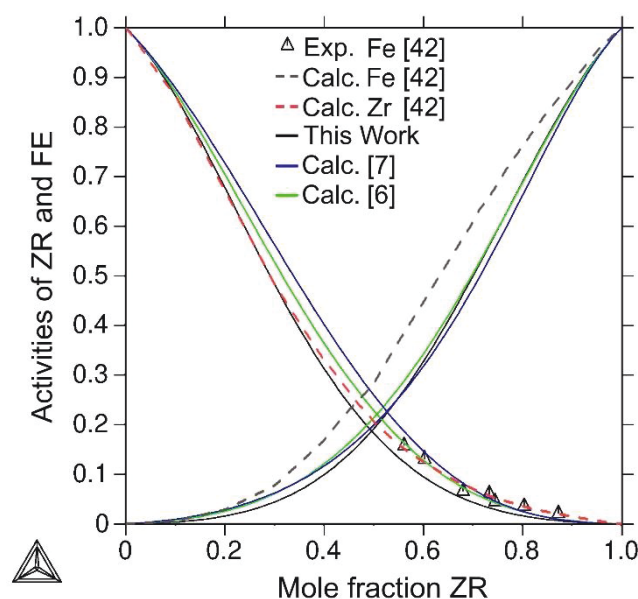


Fig. 3. Experimental activity data (hollow triangles) from [42] in comparison with calculations presented in the current work (black line), from the work of Guo *et al.* [6] (green line) and Yang *et al.* [7] (blue line). Dashed grey and red lines present calculated data from [42].

3. Experimental methods

3.1. Sample treatment and characterization

Binary Fe–Zr alloys were prepared by arc-melting under an Ar-atmosphere. Pieces of Fe (99.99%, Alfa Aesar) and slugs of Zr (99.5%, Alfa Aesar) were used as raw materials, weighed in appropriate amounts using a laboratory scale (ABJ 120-4M, KERN & Sohn GmbH). In order to achieve good chemical homogeneity in the bulk material, the samples were turned over and re-melted three times. The melting chamber was evacuated to a pressure of $\sim 10^{-5}$ atm and backfilled with argon 3 times. An ingot of pure Ti (c.a. 3g) was placed in one of the molds on the hearth of the melting chamber and was melted before the melting of the samples in order to adsorb residual oxygen and thus prevent possible oxidation. The weight losses owing to vaporization of Fe were generally less than 1 mass%. Solidified samples obtained by arc melting were then encapsulated in quartz tubes under an Ar atmosphere. The pressure of the Ar inside the tubes was chosen such that it would reach 1 atm. at the homogenization temperature. The samples were homogenized during 10–21 days at 1193 K. At the end of long-time annealing, the samples were quenched into ice-cold water. Quenched specimens were analysed by X-ray powder diffraction (XRD) and scanning electron microscopy combined with energy dispersive X-ray spectrometry (SEM/EDX).

XRD analysis was performed using an URD63 diffractometer (Seifert, FPM, Freiberg, Germany) equipped with a graphite monochromator and using $CuK\alpha$ radiation ($\lambda = 1.5418 \text{ \AA}$). The goniometer of the diffractometer had Bragg-Brentano geometry. Rietveld refinement using Maud software [43] was applied in order to characterise the diffraction patterns. SEM microstructural investigations were carried out using a Leo1530 (Carl Zeiss) microscope. Chemical compositions of the samples and phases present were determined using an EDX detector (Bruker AXS Microanalysis GmbH) with an accuracy of ± 2 at. %.

3.2 Calorimetric measurements

The classical three-step continuous method was used for heat capacity measurement [44]. The measurements were performed over the temperature range from 220 K to 600 K using a DSC 8000 (Perkin Elmer, Pt/Rh crucible, Ar flow 20 ml/min, heating rate 10 K/min). The measurements were taken over small temperature intervals of 150 –2 00 K. Calibration was achieved using certified standard materials over specified temperature ranges: a copper standard was used over the temperature range from 220 to 320 K, and molybdenum from 300 to 600 K. The mass and radius of the sample pellets were kept as close to those of the standards as possible, c.a. 135 mg and 5 mm. The measurement of two different samples was repeated twice giving a maximal uncertainty of 3%. In order to ensure that no phase transformation had taken place during the heat capacity measurement, XRD analysis of the samples was undertaken before and after each run.

4. Thermodynamic modelling

The thermodynamic description of the Gibbs energy of each a pure element i ($i = \text{Fe}, \text{Zr}$) in the Φ phase referred to the enthalpy of the phase at 298.15 K was taken from SGTE Unary database version 5.0 [45] in the following form:

$$GH\Phi_i = {}^0G_i^\Phi(T) - {}^0H_i^\Phi(298.15K) = a + bT + cT\ln T + dT^2 + eT^3 + fT^{-1} + gT^7 + hT^{-9} \quad (1)$$

The magnetic contribution to the thermodynamic properties of the element was taken into account according to the Inden–Hillert–Jarl [46] formalism (Eq.2).

$$G_m^{\Phi, mag} = RT\ln(\beta_0 + 1)g(\tau) \quad (2)$$

where $\tau = T/T^*$, T^* being the critical temperature (the Curie temperature T_C for ferromagnetic materials or the Neel temperature T_N for antiferromagnetic materials), β_0 the average magnetic moment per atom and $g(\tau)$ is a function depending on τ [47].

Substitutional solutions were modelled using following equation:

$$G_m^\Phi = G_m^{\Phi, srf} + G_m^{\Phi, conf} + G_m^{\Phi, Ex} = \sum_i^n x_i^0 G_i^\Phi + RT \sum_i^n x_i \ln x_i + G_m^{\Phi, Ex} \quad (3)$$

where $G_m^{\Phi, srf} = \sum_i^n x_i^0 G_i^\Phi$ is the surface of reference term, $G_m^{\Phi, conf} = RT \sum_i^n x_i \ln x_i$ is the Gibbs free energy resulting from the configurational entropy of mixing for a disordered solution, and $G_m^{\Phi, Ex}$ is the excess Gibbs free energy of mixing.

The excess Gibbs free energy of mixing was modelled using Redlich–Kister polynomials [48], expressed as:

$$G_m^{\Phi, Ex} = x_A x_B \sum_{v=0}^n {}^vL_{A,B}^\Phi (x_A - x_B)^v \quad (4)$$

The Gibbs energy $G_{A_a B_b}(T)$ of a stoichiometric compound $A_a B_b$ in the case where there is an absence of heat capacity data was modelled as:

$$G_{A_a B_b} - a \cdot {}^0H_A^\Phi(298.15K) - b \cdot {}^0H_B^\Phi(298.15K) = a + bT + cT\ln T + dT^2 + eT^{-1} \quad (5)$$

where parameters of the temperature dependence of Gibbs energies of stoichiometric compounds were optimized based on the literature data and the experimental results of the current investigation.

The homogeneity ranges of the BCC, FCC and HCP phases, as well as the liquid phase, were described using a substitutional model with one sublattice in the form of (Zr,Fe). Stable intermediate compounds in the Fe–Zr system that have homogeneity ranges were described by the compound energy formalism [49].

The optimization of the thermodynamic parameters and phase diagram calculations of the Fe–Zr system were performed using Thermo-Calc software; the PARROT module and the POLY-3 module, respectively. Individual weights were assigned to each type of experimental data considering the possible deviation and uncertainty in the experimental methods employed [50,51].

5. Optimization Strategy

In the first step of the optimization procedure, all intermetallic compounds C15-ZrFe₂, C36-ZrFe₂, Zr₂Fe and Zr₃Fe were modelled as stoichiometric phases. Using the information relating to enthalpy of formation, standard entropy and the temperature dependence of the heat capacity, descriptions for the Gibbs energies of all intermetallic compounds were defined. Experimentally determined heat capacities for the C15-ZrFe₂ and Zr₃Fe phases presented by Mukhamedov *et. al* [10] and Lück *et al.* [35] were described by a Maier-Kelly equation. The terms of the polynomial expressions obtained were then used as fixed parameters for the temperature dependence of Gibbs energies as follows:

$$C_p(T) = a' + b' \cdot T + c'/T^2 \quad (6)$$

$$\Delta H_m^\Phi = \Delta H_{298}^\Phi + \int_{298}^T C_p(T) dT \quad (7)$$

$$S_m^\Phi = S_{298}^\Phi + \int_{298}^T \frac{C_p(T)}{T} dT \quad (8)$$

$$\Delta G_m^\Phi = \Delta H_m^\Phi - TS_m^\Phi \quad (9)$$

The temperature dependence of the heat capacity of Zr₂Fe was described using a Neumann-Kopp approximation. In the case of the C36-ZrFe₂-phase, the data for C15-ZrFe₂ were used, taken from Mukhamedov *et. al* [10] but without the magnetic contribution.

There were no experimentally measured enthalpies of formation for C36-ZrFe₂, Zr₂Fe nor Zr₃Fe. Based on the experimental heat capacity data for Fe (bcc) and Zr (hcp) [52–54], the heat capacity of formation of these compounds was evaluated to be insignificantly small over the temperature range of 0 to 298.15 K. Consequently, *ab-initio* calculated enthalpies of formation for intermetallic compounds were treated as enthalpies of formation at 298.15 K.

The homogeneity ranges for the C15- and C36-ZrFe₂ Laves phases were modelled in the framework of the compound energy formalism [49] using a two-sublattice model with substitution in each sublattice, namely (Fe,Zr)(Zr,Fe)₂. Based on the experimentally

determined phase relationships from Stein *et al.* [2], the homogeneity ranges of Zr_2Fe and Zr_3Fe were assumed to be insignificant and therefore not modelled. The Zr_2Fe and Zr_3Fe -phases were described as stoichiometric compounds.

A substitutional model was used to describe the liquid phase in the system. In order to describe the temperature dependence of the interaction parameters ${}^{\circ}L_{A,B}^{\phi}$, two different models could be considered; a linear temperature dependence (LTD) $A - B \cdot T$, or a combined linear-exponential (CLE) model, as suggested by Kaptay [55], which could be applied if the LTD model was found to be insufficient to represent the experimental information simultaneously and at the same time, avoiding the appearance of any miscibility gaps. In the linear equation, the enthalpy of mixing and the excess entropy of mixing are related to the parameters A and B , respectively. In principle, more parameters can be included to model the temperature dependence of the excess heat capacity, but usually no such data are available. Moreover, increasing of number of interaction parameters and with the added complication of their temperature dependence does not always lead to the best agreement between experimental data and calculated results. Similar to previous assessments [56], the optimization strategy is to achieve the best agreement between the calculated and experimental data on phase relationships and thermodynamic properties using a minimum number of optimized parameters. The generalized “ χ^2 ”-criterion (Eq.10) [57] has been used during the optimization procedure in order to find optimal thermodynamic description and to compare it with earlier published thermodynamic assessments considering the number of independent optimized parameters.

$$\chi^2 = \sum_{i=1}^N \left[\frac{\alpha_{i.cal.} - \alpha_{i.exp.}}{\delta\alpha_{i.exp.}} \right]^2 \cdot (N - p - 1)^{-1} \quad (10)$$

where: $\alpha_{i.exp.}$ – an experimental value with an error $\delta\alpha_{i.exp.}$; $\alpha_{i.cal.}$ – a calculated value of a thermodynamic description; p – the number of independent optimized parameters; N – a general number of experimental values.

6. Results and discussion

6.1. Heat capacity measurement of Zr_2Fe

Two samples for heat capacity measurement were prepared using arc melting. Nominal and measured compositions of the samples are listed in Table 4. As-cast samples were analysed by SEM/EDX, annealed samples by XRD and SEM/EDX. The EDX results show that the chemical compositions match the initial chemical composition within the error of the measurement. Some enrichment in Zr can be observed. However, the deviation is within the range of reliable accuracy.

Table 4 – Sample compositions and results of sample characterization by XRD and SEM/EDX.

Sample	Initial sample composition [at.%]		Sample composition SEM-EDX results [at.%]		Temperature, [K] / Annealing time in days	Phases according to XRD&SEM/EDX results	Vol. %	Lattice parameters, [Å]				Phase composition SEM/EDX results [at.%]	
	Zr	Fe	Zr	Fe				a	b	c	β [°]	Zr	Fe
#1	66.7	33.3	68.8±0.4	31.2±0.4	cast	C15-ZrFe ₂	-	-	-	-	-	36.5	63.5
						Zr ₃ Fe	-	-	-	-	-	75.9	24.1
						Zr ₂ Fe	-	-	-	-	-	68.3	31.7
						Zr	-	-	-	-	-	93.4	6.6
						Eutectic	-	-	-	-	-	75.5	24.6
					1193 / 10	C15-ZrFe ₂	14	7.089	-	-	-	36.9	63.1
						Zr ₃ Fe	26	3.324	11.029	8.832	-	76.2	23.8
						Zr ₂ Fe	60	6.378	-	5.600	-	68.4	31.6
#2	68.0	32.0	70.3±1.0	29.7±1.0	Cast	Zr ₃ Fe	-	-	-	-	-	76.2	23.8
						Zr ₂ Fe	-	-	-	-	-	67.9	32.1
						Eutectic	-	-	-	-	-	74.7	25.3
					1193 / 21	Zr ₃ Fe	24	3.322	11.039	8.826	-	76.8	23.2
						Zr ₂ Fe	76	6.375	-	5.595	-	68.3	31.7
					DSC 220-320	Zr ₃ Fe	23	3.334	11.074	8.855	-	-	-
						Zr ₂ Fe	77	6.424	-	5.583	-	-	-
					DSC 300-450	Zr ₃ Fe	22	3.306	11.125	8.758	-	-	-
						Zr ₂ Fe	78	6.396	-	5.592	-	-	-
					DSC 420-620	C15-ZrFe ₂	11	7.044	-	-	-	-	-
						Zr ₃ Fe	19	3.302	11.094	8.727	-	-	-
						Zr ₂ Fe	70	6.385	-	5.588	-	-	-

Initially, sample #1 was prepared with a nominal chemical composition at the stoichiometry of the Zr_2Fe compound. Before long-time annealing at 1193 K, microstructural investigation of the as-cast sample has shown primary grains of the C15-ZrFe₂-phase (Fig. 4a). The microstructure of the as-cast sample #1 contained C15-ZrFe₂, Zr₂Fe, Zr₃Fe, eutectic areas (with composition of 75.5 at.% of Zr) and very small grains of β -Zr. After heat treatment for 10 days, the C15-ZrFe₂ grains have shown very small changes in size and shape (Fig. 4b). The eutectic areas, as well as small grains of β -Zr, were completely dissolved. The sample microstructure consisted of the C15-ZrFe₂, Zr₂Fe and Zr₃Fe-phases. Obviously, C15-ZrFe₂ is the most stable intermetallic compound in the system. An annealing temperature of 1193 K was not high enough to decompose the C15-ZrFe₂-phase after 10 days of heat treatment. The presence of C15-ZrFe₂ shifted the chemical composition of the rest sample to a higher zirconium content, i.e. to lie in the Zr_2Fe – β Zr two-phase region at that temperature (Fig.1). However, characterization of annealed sample #1, the sample contained the C15-ZrFe₂, Zr₂Fe and Zr₃Fe phases. Thus, it can be stated, that the $Zr_2Fe + \beta Zr \rightarrow Zr_3Fe$ reaction occurs quite quickly. Additionally, no obvious decomposition of Zr₂Fe can be seen in the microstructure of sample #1 (Fig.4b). Consequently, the Zr₂Fe compound can be quenched to room temperature. However, such sluggish kinetics of the decomposition of C15-ZrFe₂ would not allow an equilibrium state to be achieved at 66.7 at.% Zr and 1193 K. Therefore, the initial composition of the sample #2 was chosen to be shifted to the zirconium-rich side of the diagram in order to decrease the primary crystallization of the C15-ZrFe₂ Laves phase from the melt during arc melting.

As can be seen in Fig. 4c, no C15-ZrFe₂ is observed during microstructural analysis. The microstructure of as-cast sample #2 contained the Zr₂Fe primary phase, Zr₃Fe and eutectic areas. After long-time annealing, the quenched sample consisted of two phases: the main of Zr₂Fe-phase and a small amount of Zr₃Fe (Fig. 4d). XRD analysis suggests 76 vol.% of Zr₂Fe, which corresponds 81.4 mol.%. Since heat capacity is an additive function, the C_p of a sample consisting of two phases should equal the molar weighted sum of the heat capacities of the individual phases. Thus, the heat capacity of one of these two phases can be evaluated from the measured C_p of the sample, if the heat capacity of the second phase is well known. The heat capacity of the Zr₃Fe compound has been studied by Mukhamedov *et al.* [10]. Consequently, it was decided that sample #2 was suitable for further heat capacity measurements in order to derive the C_p for Zr₂Fe.

As indicated above, heat capacity measurements were made over small temperature intervals of 150–200 K. After each run, the samples were analysed using XRD in order to ensure that

there had been no phase change in the material during measurement. Temperature intervals and the corresponding XRD results are given in Table 4. It can be seen, that following measurements in the interval 420 to 620 K, the presence of C15-ZrFe₂ was identified. Consequently, the quenched Zr₂Fe compound partially decomposed in this temperature range. Therefore, the DSC data obtained in this interval were not considered further. Moreover, owing to the sluggish kinetics of the C15-ZrFe₂ + Zr₃Fe → Zr₂Fe reaction, it is not possible to make DSC measurements in the stability range of the Zr₂Fe compound at higher temperatures.

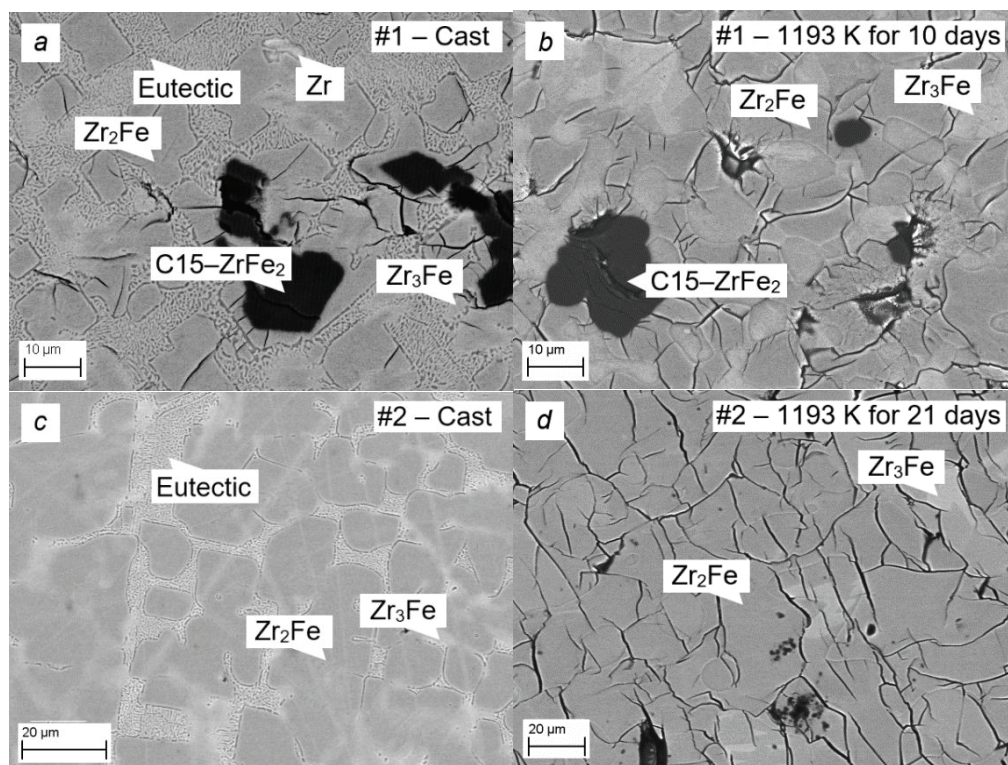


Fig. 4 – Sample microstructures (a) #1 as-cast; (b) #1 annealed at 1193 K for 10 days; (c) #2 as-cast; (d) #2 annealed at 1193 K for 21 days.

The evaluated heat capacity of Zr₂Fe is presented in Fig. 5a together with the Maier-Kelly expression

$$C_p(\text{Zr}_2\text{Fe}) = 25.525 + 0.0121 \cdot T - 133673.29/T^2 [\text{J/K} \cdot \text{mol} - \text{at}] \quad (11)$$

where temperature T is given in K.

Unfortunately, measurement in so limited a temperature range (220-460 K) cannot provide a good extrapolation to high temperatures and cannot be used for the description of the Gibbs energy of Zr₂Fe. Therefore, the data obtained, together with modelling at low temperatures, were used to estimate the standard entropy of the Zr₂Fe-phase, while at high temperature, the Neumann-Kopp rule was applied to estimate the heat capacity.

By combining the theoretical results of Ali *et al.* [9] and the current experimental data, a thermodynamic description for the heat capacity in the range from 0 K up to 450 K was obtained using a model that was proposed at the Ringberg Workshop in 1995 (RW-model) [39]:

$$C_P^{RW}(T, \theta^{RW}) = C_V^{Debye/Einstein}(T) + aT + bT^2 \quad (12)$$

where T is temperature, $\theta^{RW} = (\theta_{D/E}, a, b)$ is the vector of the unknown model parameters to be estimated, $C_V^{Debye/Einstein}(T)$ is the heat capacity describing the phonon contribution using the Debye or Einstein model.

The thermodynamic RW-models obtained reproduce the experimental data well in the given temperature range from 0 K up to 450 K. Traditionally, using an Einstein model to describe the phonon contribution gives slightly worse results at low temperatures as compared with the Debye model. The fitted model parameters obtained for C_P can be used to calculate the standard entropy of Zr₂Fe using the following equation: $S^{298} = \int_0^{298} C_P \frac{dT}{T}$. C_P and S^{298} for Zr₂Fe phase are listed in Table 5.

Table 5 – Values of C_P fitting parameter and calculated S^{298} for Zr₂Fe from 0 to 450 K using RW-models.

Parameters \ Compound	Debye	Einstein
$\theta_{D/E}, K$	278 [9]	252
$a \cdot 10^3$	10.37	13.20
$b \cdot 10^7$	56.87	-5.13
$S^{298}, J/K \cdot mol-at$	35.2	33.8

From a comparison of current experimental results with the calculated data of Ali *et al.* [9] (Fig 5b) it can be seen that the deviation between the data is even stronger than was presented in the work of Mukhamedov *et al.* [10] for other compounds in the system. This would suggest that the heat capacity calculations presented by Ali *et al.* [9] could be improved by considering electronic contributions giving a better agreement with experimental data. Moreover, to have a more accurate description in the low temperature range by the RW-model, further low temperature measurements are necessary in order to provide an intersection of the experimental and calculated data. Otherwise, the calculated standard entropy based on current results could be understated.

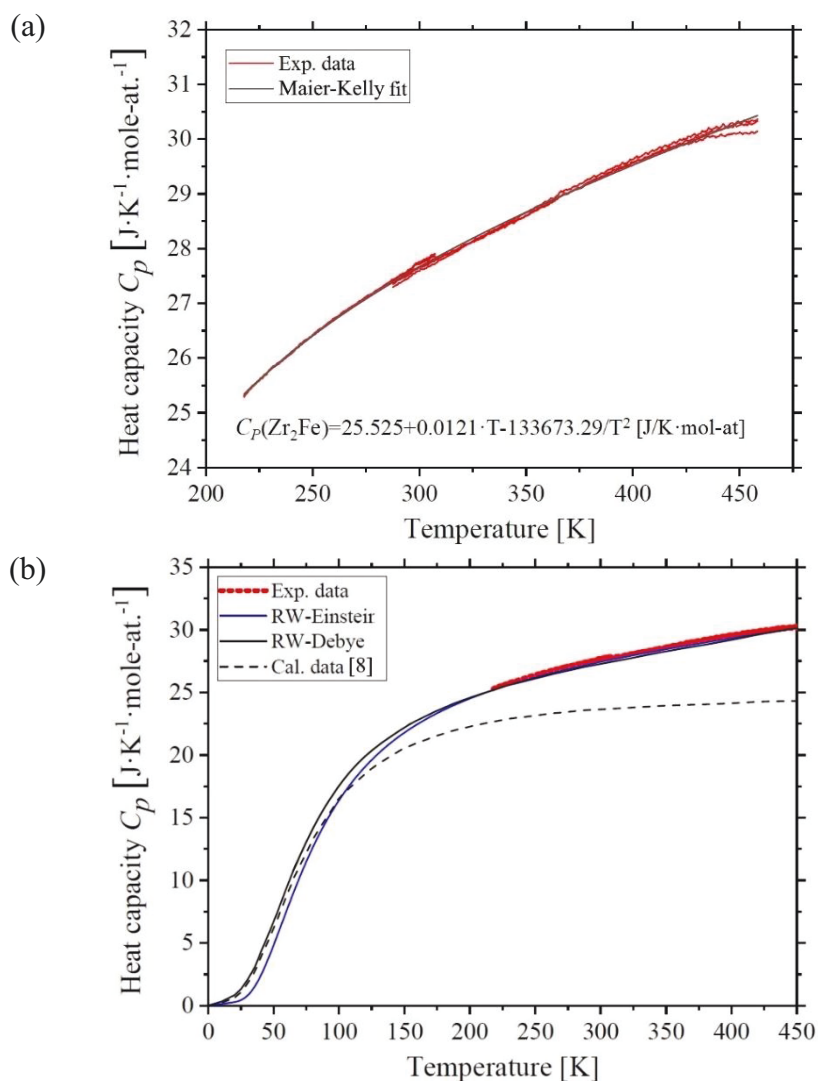


Fig. 5 – (a) Experimental DSC data together with the Maier-Kelly fit (b) Theoretical and experimental results of the heat capacity of the Zr_2Fe intermetallic compound. Red lines show the measured experimental data of this work. The dashed line corresponds to the available calculated data from [9]. Black and blue lines represent the fitted RW-model using Debye and Einstein models for phonon contribution, respectively.

6.2. Thermodynamic modelling

Optimized thermodynamic parameters are listed in Table 6. The Fe–Zr phase diagram calculated using the present dataset is presented in Fig. 6 along with experimental data from the work of Stein *et al.* [2] and Servant *et al.* [22]. Calculated invariant reactions, along with experimental data and results obtained in previous thermodynamic assessments [6,7], are presented in Table 7.

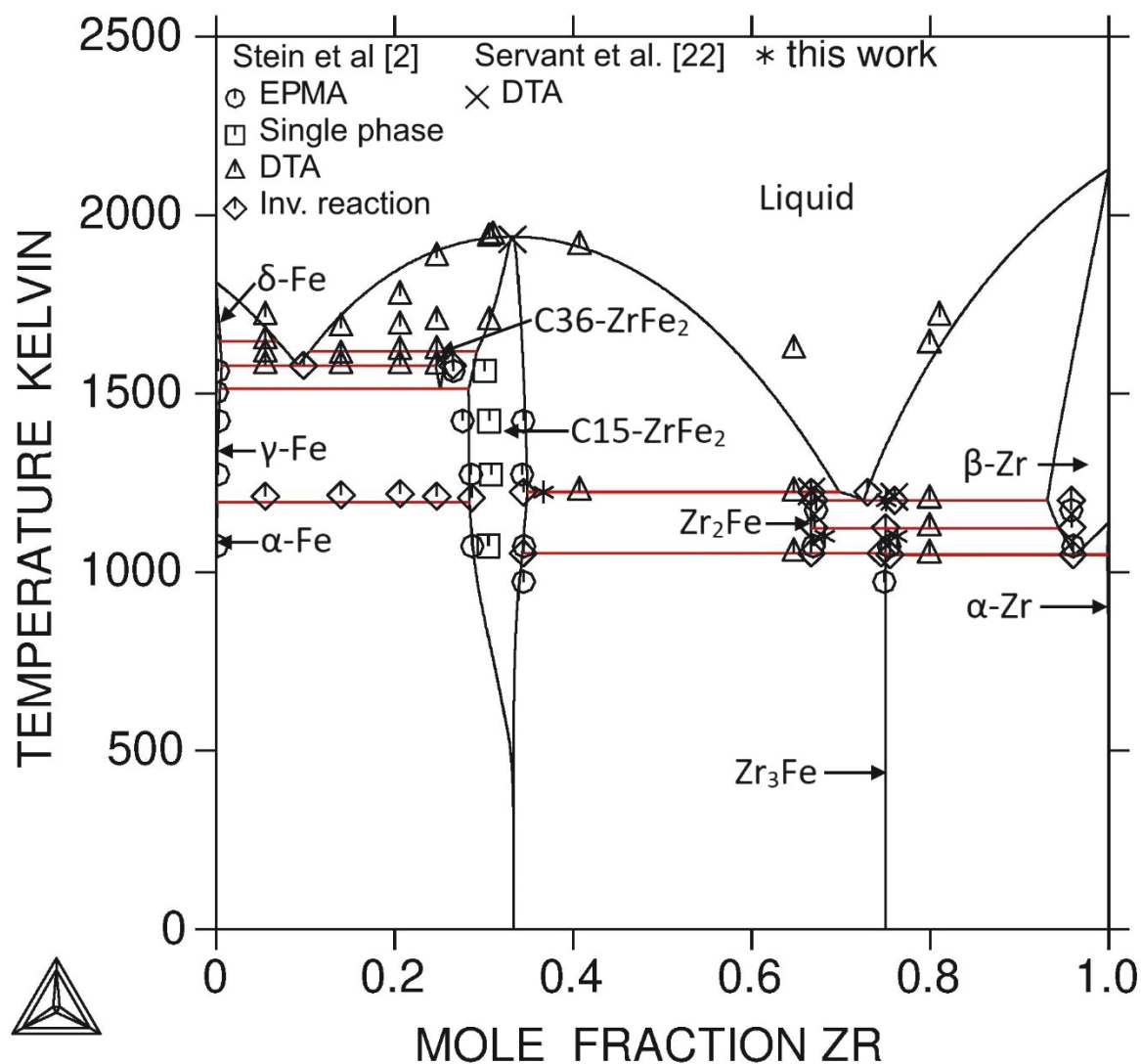


Fig. 6 – Calculated Fe–Zr phase diagram along with experimental data from the work of Stein *et al.* [2] and Servant *et al.* [22].

Table 6. Optimized thermodynamic parameters for the Fe–Zr system (J/mol)

Phase	Sublattice model	Optimized parameters
Liq	(Zr,Fe) ₁	${}^0L_{\text{Zr:Fe}}^{\text{Liq}} = -85196.3 + 12.83 \cdot T$ ${}^1L_{\text{Zr:Fe}}^{\text{Liq}} = -1655.5$
FCC_A1	(Zr,Fe) ₁ (Va) ₁	${}^0L_{\text{Zr:Fe}}^{\text{FCC_A1}} = -16847.9 - 3.56 \cdot T$
HCP_A3	(Zr,Fe) ₁ (Va) _{0.5}	${}^0L_{\text{Zr:Fe}}^{\text{HCP_A3}} = +5769.6$
BCC_A2	(Zr,Fe) ₁ (Va) ₃	${}^0L_{\text{Zr:Fe}}^{\text{BCC_A2}} = -33690.0 + 8.77 \cdot T$ ${}^1L_{\text{Zr:Fe}}^{\text{Liq}} = -11176.6 + 7.63 \cdot T$
C15-ZrFe ₂	(Zr,Fe) ₁ (Fe,Zr) ₂	${}^0G_{\text{Zr:Fe}}^{\text{C15-ZrFe2}} = -112156 + 438.6 \cdot T - 79.1 \cdot T \cdot \ln(T) - 6.8 \cdot 10^{-3} \cdot T^2$ $+ 330106 \cdot T^{-1}$ ${}^0G_{\text{Zr:Zr}}^{\text{C15-ZrFe2}} = +3 \cdot \text{GHSEZR} + 15000$ ${}^0G_{\text{Fe:Fe}}^{\text{C15-ZrFe2}} = +3 \cdot \text{GHSEFE} + 15000$ ${}^0G_{\text{Fe:Zr}}^{\text{C15-ZrFe2}} = -{}^0G_{\text{Zr:Fe}}^{\text{C15-ZrFe2}} + 30000$ ${}^0L_{\text{Zr:Fe:Fe}}^{\text{C15-ZrFe2}} = +56000$ ${}^0L_{\text{Zr:Fe:Zr}}^{\text{C15-ZrFe2}} = +56000$ ${}^0L_{\text{Fe:Fe,Zr}}^{\text{C15-ZrFe2}} = -23000 + 22.5 \cdot T$ ${}^0L_{\text{Zr:Fe,Zr}}^{\text{C15-ZrFe2}} = -23000 + 22.5 \cdot T$ $TC_{\text{Zr:Fe}}^{\text{C15-ZrFe2}} = 585$ $Bmag_{\text{Zr:Fe}}^{\text{C15-ZrFe2}} = 1.4$
C36-ZrFe ₂	(Zr,Fe) ₁ (Fe,Zr) ₂	${}^0G_{\text{Zr:Fe}}^{\text{C36-ZrFe2}} = -113000 + 440.2 \cdot T - 79.1 \cdot T \cdot \ln(T) - 6.8 \cdot 10^{-3} \cdot T^2$ $+ 330106 \cdot T^{-1}$ ${}^0G_{\text{Fe:Fe}}^{\text{C36-ZrFe2}} = +3 \cdot \text{GHSEFE} + 15000$ ${}^0L_{\text{Fe:Fe,Zr}}^{\text{C36-ZrFe2}} = -1533.1 + 3.095 \cdot T$ ${}^0L_{\text{Zr:Fe,Zr}}^{\text{C36-ZrFe2}} = -1533.1 + 3.095 \cdot T$
Zr ₂ Fe	(Zr) ₂ (Fe) ₁	${}^0G_{\text{Zr:Fe}}^{\text{Zr2Fe}} = +2 \cdot \text{GHSEZR} + \text{GHSEFE} - 44258.83 + 2.7322 \cdot T$
Zr ₃ Fe	(Zr) ₃ (Fe) ₁	${}^0G_{\text{Zr:Fe}}^{\text{Zr3Fe}} = -80910.01 + 519.9 \cdot T - 97.8 \cdot T \cdot \ln(T) - 1.41 \cdot 10^{-2} \cdot T^2$ $+ 144141 \cdot T^{-1}$

It should be mentioned that Stein did not present the congruent melting temperature of the C15-ZrFe₂-phase. The value of the melting point presented in the diagram (Fig.1) agrees with the previous experimental results of Svechnikov *et al.* [13] and differs slightly from later experimental results of Servant *et al.* [22]. Svechnikov *et al.* [13] used differential thermal analysis (DTA) in the construction of the phase diagram. The same technique was applied by Servant [22]. Since the difference between these two experimental results was within uncertainty limits (around 15 K), both experimental results were considered in the optimization procedure. From a comparison of the available experimental data and the calculated results of this work, it can be concluded that very good agreement between the two sets of data on phase relationships has been achieved within uncertainty limits.

Table 7. Invariant reactions in the Fe–Zr system: comparison between experimental data [2,22], calculations of [6,7] and current results.

Invariant Reaction	Type	Temp. (K)	Composition of Respective Phases (at.% Zr)			References
$Liq \leftrightarrow C15-ZrFe_2$	Congruent	~1946	n.d.	n.d.	-	Experimental [2]
		1932±15	n.d.	n.d.	-	Experimental [22]
		1946	33.07	33.07	-	Optimization [6]
		1945	33.5	33.5	-	Optimization [7]
		1939	33.2	33.2	-	Optimization of this work
$(\delta Fe) \leftrightarrow (\gamma Fe) + Liq$	Metatectic	1647±2	n.d.	n.d.	n.d.	Experimental [2]
		1647	1.35	1.27	7.77	Optimization [6]
		1646	1	1	7.2	Optimization [7]
		1647	0.5	0.5	6.7	Optimization of this work
$Liq + C15-ZrFe_2 \leftrightarrow C36-ZrFe_2$	Peritectic	1618±10	n.d.	n.d.	n.d.	Experimental [2]
		1618	11.30	29.22	27.30	Optimization [6]
		1628	11.3	28.2	26.8	Optimization [7]
		1618	10.5	29.2	25.7	Optimization of this work
$Liq \leftrightarrow (\gamma Fe) + C36-ZrFe_2$	Eutectic	1578±2	9.8±0.4	n.d.	26.5±0.5	Experimental [2]
		1579	10.24	1.63	26.64	Optimization [6]
		1572	9.8	1.3	26.1	Optimization [7]
		1578	9.2	0.7	24.6	Optimization of this work
$C36-ZrFe_2 \leftrightarrow (\gamma Fe) + C15-ZrFe_2$	Eutectoid	1513±10	n.d.	n.d.	n.d.	Experimental [2]
		1513	27.17	1.24	28.45	Optimization [6]
		1525	26.3	1.1	26.8	Optimization [7]
		1513	25.1	0.5	28.3	Optimization of this work
$(\gamma Fe) + C15-ZrFe_2 \leftrightarrow (\alpha Fe)$	Peritectoid	1208±10	n.d.	28.6±0.5	n.d.	Experimental [2]
		1208	0.21	28.45	0.39	Optimization [6]
		1196	0.2	27.1	0.3	Optimization [7]
		1196	0.1	28.4	0.2	Optimization of this work
$C15-ZrFe_2 + Liq \leftrightarrow Zr_2Fe$	Peritectic	1224±2	34.4±0.2	73±1	66.7±0.5	Experimental [2]
		1225±10	n.d.	n.d.	n.d.	Experimental [22]
		1224	34.53	67.17	66.93	Optimization [6]
		1212	35.9	70.73	69.2	Optimization [7]
		1224	34.8	69.8	66.67	Optimization of this work
$Zr_2Fe \leftrightarrow C15-ZrFe_2 + Zr_3Fe$	Eutectoid	1053±2	66.7±0.5	34.4±0.2	74.5±0.5	Experimental [2]
		1053	66.82	34.02	74.52	Optimization [6]
		1039	68.2	34.6	75.7	Optimization [7]
		1053	66.67	34.3	75.0	Optimization of this work
$Liq \leftrightarrow Zr_2Fe + (\beta Zr)$	Eutectic	1201±2	76±1	67.0±0.5	95.8±0.5	Experimental [2]
		1211±10	n.d.	n.d.	n.d.	Experimental [22]
		1201	72.19	67.27	91.11	Optimization [6]
		1211	71	69.5	93	Optimization [7]
		1201	72.5	66.67	93.1	Optimization of this work
$Zr_2Fe + (\beta Zr) \leftrightarrow Zr_3Fe$	Peritectoid	1124±2	67.0±0.5	95.9±0.5	75.0±0.5	Experimental [2]
		1124	67.21	92.88	74.96	Optimization [6]
		1129	69.5	94.6	76.5	Optimization [7]
		1123	66.67	94.3	75.0	Optimization of this work
$(\beta Zr) \leftrightarrow Zr_3Fe + (\alpha Zr)$	Metatectic	1048±4	96.0±0.5	75.5±0.5	n.d.	Experimental [2]
		1048	96.18	75.21	99.83	Optimization [6]
		1055	96.5	76.5	100	Optimization [7]
		1049	96.2	75.0	99.8	Optimization of this work

Fig. 2 shows the integral enthalpy of mixing of the liquid phase with respect to composition at a temperature of 2100 K that has been calculated in the present work and also in [6,7] in comparison with available experimental data [28,29,37,39]. The reference states are the pure elements in the liquid state at 2100 K. It is clearly evident that the calculated results of [6,7] better reproduce the experimental data of Wang *et al.* [39], while the results of the current work are closer to the data of Sudavtsova *et al.* [37]. However, all calculated results are in agreement with experiments within uncertainty limits. It should be mentioned that the results of Sidorov *et al.* [28] were not used in the optimization because their data strongly disagree with other works [29,37,39].

Fig. 3 presents the activities of zirconium and iron calculated using the thermodynamic description produced in this work compared with the measured data produced using Knudsen effusion mass spectrometry (KEMS) by Chatain *et al.* [42]. According to the experimental results, the activities of zirconium and iron have a strong negative deviation from ideal

behaviour. The calculated activities are consistent with the experimental data, as well as with the previous calculations [6,7].

The enthalpies of formation calculated in the present work are compared with experimental data and previous calculations [6,7] in Table 2. It can be seen that the current results are in reasonable agreement with experimental and *ab-initio* data for all solid phases. Moreover, in comparison to previous assessments [6,7], the results of the current calculations better reproduce the available experimental data and latest DFT calculations, including data presented by the Materials Project and OQMD. Additionally, current calculations of the standard entropy of C15- ZrFe_2 and Zr_3Fe agree well with data presented in the work of Mukhamedov *et al.* [10]. The calculated standard entropy for Zr_2Fe is slightly higher than the result obtained from *ab-initio* calculations by Ali *et al.* [9] and current experimental data. However, as indicated above, there are not enough experimental data for an accurate evaluation of the standard entropy of Zr_2Fe . Therefore, it can be concluded that the result obtained is in reasonable agreement, within uncertainty limits.

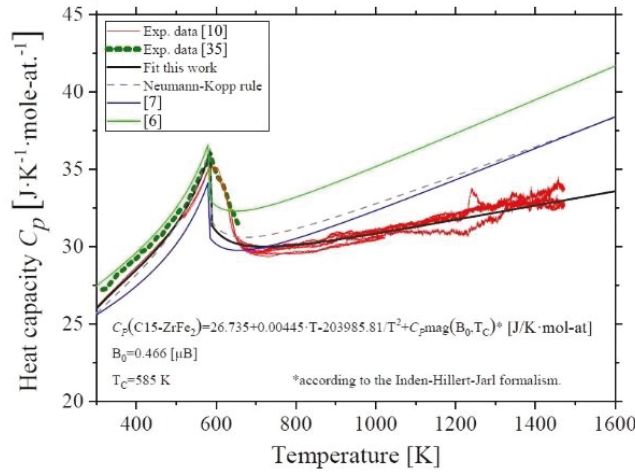
Experimental heat capacity results presented by Mukhamedov *et al.* [10] and Lück *et al.* [35], together with calculated results from the current work and previous assessments [6,7] are shown in Fig. 7a and 7b for the stoichiometric compositions of the C15- ZrFe_2 and Zr_3Fe phases, respectively. In the works of Guo *et al.* [6] and Yang *et al.* [7], only the data from [35] have been taken in account in the optimization of the Gibbs energy of the C15- Zr_2Fe -phase. It can be concluded for the comparison with experimental data that using experimental data over such a limited temperature range is not enough for extrapolation to high temperatures. For the thermodynamic description of the Zr_3Fe phase, Neumann–Kopp’s law was applied in the previous assessments of Guo *et al.* [6] and Yang *et al.* [7]. The experimental heat capacity results for Zr_3Fe are in good accordance with Neumann–Kopp’s law at low temperatures only, close to room temperature, while there is an insignificant deviation in the range of 400 – 500 K. Using the Thermo-Calc software, the calculated and experimental results obtained by Mukhamedov *et al.* [10] and Lück *et al.* [35] were fitted to a Maier–Kelley equation (6) in following form:

$$C_p(C15 - ZrFe_2) = 26.735 + 0.00445 \cdot T - \frac{203985.81}{T^2} + C_p mag(B_0, T_C) [J/K \cdot mol - at] \quad (13)$$

$$C_p(Zr_3Fe) = 24.466 + 0.00705 \cdot T - 72070.43/T^2 [J/K \cdot mol - at] \quad (14)$$

where: $C_p mag(B_0, T_C)$ is the magnetic contribution to the heat capacity calculated using the equation of Inden–Hillert–Jarl [46]; $B_0 = 0.466 [\mu B]$ and $T_C = 585 K$ accepted from the work Mukhamedov *et al.* [10].

(a)



(b)

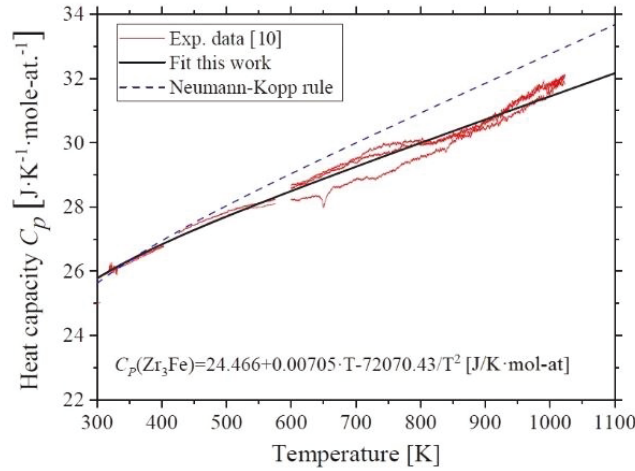


Fig. 7 – Experimental heat capacity data for C15-ZrFe₂ (a) and Zr₃Fe (b) intermetallic compounds presented in [10,35] in comparison with the Neumann–Kopp approximation, previous thermodynamic assessments [6,7] and the current work.

All available experimental and theoretical results, including information that was not considered earlier, were taken into account during the optimization of present thermodynamic description. The “ χ^2 ”-criterion (See Eq.10) was calculated for the present optimization and for the thermodynamic descriptions of Guo *et al.* [6] and Yang *et al.* [7]. The evaluated results are as follows: for the work of Guo *et al.* [6] $\chi^2 = 34.9$ ($\chi_{inv.}^2 = 32$ considering only experimental data on invariant reactions, the number of independent optimized parameters $p = 26$) and for the work of Yang *et al.* [7] $\chi^2 = 28.3$ ($\chi_{inv.}^2 = 4.1$, $p = 32$). The calculated result for the current optimization was $\chi^2 = 8.8$ ($\chi_{inv.}^2 = 3.1$, $p = 25$). The calculation of the

“ χ^2 ”-criterion for each thermodynamic description considered an identical number of experimental values of reliable literature data (244 experimental values including 30 points of phase equilibria). Errors in the experimental values were taken according to their accuracy. It can be concluded that the thermodynamic descriptions from Guo *et al.* [6], Yang *et al.* [7] and the current work reproduce well the phase diagram established by Stein *et al.* [2]. However, the thermodynamic description derived in the present work shows a better agreement with all available thermodynamic data than the descriptions published previously. Moreover, the number of optimized thermodynamic parameters in the present work is less than in previous assessments. The thermodynamic parameters of excess Gibbs energy of mixing of the liquid phase optimized using LTD model do not lead to a miscibility gap in the liquid phase across the whole range of temperatures of the SGTE functions of the pure elements. Therefore, the thermodynamic description obtained here is acceptable for use in the modelling of high-order metal-oxide systems.

7. Conclusions

Experimental heat capacity measurements of the Zr_2Fe compound were performed using a DSC over the temperature range from 220 to 450 K for the first time. The results obtained were compared with theoretical calculations of $C_P(T)$ presented by Ali *et al.* [9]. Using a combination of calculated [9] and experimental results, the temperature dependence of heat capacity $C_P(T)$ for Zr_2Fe was described by a RW-model over the temperature range of 0 to 450 K. The standard entropy S^{298} of Zr_2Fe was evaluated using the heat capacity data obtained. Taking into account recent experimental data on heat capacity and *ab-initio* calculations of the enthalpies of formation of the intermetallic compounds presented by Mukhamedov *et al.* [10], Ali *et al.* [8,9] and values available in the databases of the Materials Project [32,33] and OQMD [34], a thermodynamic re-assessment of the Fe–Zr system has been performed in order to derive an up-dated set of Gibbs energies for all stable phases in the system. Liquid and solid solution phases such as bcc, fcc, and hcp have been described using a substitutional model. The compound energy formalism [49] has been used to describe homogeneity ranges of the C15- and C36- ZrFe_2 Laves phases. The magnetic properties of the solid phases have been taken into account in the frame of Inden-Hiller-Jarl formalism [46]. The generalized “ χ^2 ”-criterion (Eq.10) [57] has been used as a method to compare the thermodynamic descriptions considering general number of optimized parameters. In the results, it has been demonstrated that the set of thermodynamic parameters derived in the present work describes the available experimental data better than thermodynamic descriptions published previously [6,7].

Acknowledgments

The authors gratefully acknowledge the German Research Foundation (DFG) for funding the sub-project C2 within the Collaborative Research Center SFB 799 Trip-Matrix Composites. Furthermore, the authors thank the RFBR for support within the grant 19-03-00530. We are grateful to G. Savinykh and Dr. C. Schimpf (TU-Freiberg) for technical contributions. We would like to thank B.O. Mukhamedov for scientific support and discussions. Additionally, authors would like to express their deepest gratitude to Dr. A. Watson for critical reading and help in improving English.

References

- [1] M.S. Granovsky, D. Arias, *J. Nucl. Mater.* 229 (1996) 29.
- [2] F. Stein, G. Sauthoff, M. Palm, *J. Phase Equilib. Diff.* 23 (2002) 480.
- [3] X. Tao, J. Zhu, H. Guo, Y. Ouyang, Y. Du, *J. Nucl. Mater.* 440 (2013) 6.
- [4] H. Biermann, U. Martin, C.G. Aneziris et al., *Adv. Eng. Mater.* 43 (2009) 1000.
- [5] S. Martin, S. Richter, S. Decker et al., *steel research int.* 82 (2011) 1133.
- [6] C. Guo, Z. Du, C. Li, B. Zhang, M. Tao, *CALPHAD* 32 (2008) 637.
- [7] Y. Yang, L. Tan, H. Bei, J.T. Busby, *J. Nucl. Mater.* 441 (2013) 190.
- [8] K. Ali, A. Arya, P.S. Ghosh, G.K. Dey, *Comp. Mater. Sci.* 112 (2016) 52.
- [9] K. Ali, P.S. Ghosh, A. Arya, *J. Alloy. Compd.* 723 (2017) 611.
- [10] B.O. Mukhamedov, I. Saenko, A. Ponomareva et al, *Intermetallics* 109 (2019) 189.
- [11] B. Grabowski, L. Ismer, T. Hickel, J. Neugebauer, *Phys. Rev. B* 79 (2009) 597.
- [12] V.N. Svechnikov, V.M. Pan, A.T. Spektor, *Zh. Neorg. Khim.* 8 (1963) 2118.
- [13] V.N. Svechnikov, A.T. Spektor, *Dokl. Akad. Nauk SSSR* 143 (1962) 613.
- [14] D. Arias, J.P. Abriata, *Bulletin of Alloy Phase Diagrams* 9 (1988) 597.
- [15] E.T. Hayes, A. H. Roberson, and W. L. Obrien, *Trans. ASM* 43 (1951) 888.
- [16] L.E. Tanner, D.W. Levinson, *Trans. Am. Inst. Min., Metall. Pet. Eng.* 215 (1959) 1066.
- [17] T.O. Malakhova, Z.M. Alekseyeva, *J. Less Common Met.* 81 (1981) 293.
- [18] T.O. Malakhova, A.N. Kobylkin, *Izv. Akad. Nauk SSSR, Metall* 2 (1982) 205.
- [19] F. Aubertin, U. Gonser, S.J. Campbell, H.-G. Wagner, *Z. Metallkd.* 76 (1985) 237.
- [20] M.M. Stupel, M. Bamberger, B.Z. Weiss, *Scripta Metall.* 19 (1985) 739.
- [21] A.D. Pelton, L. Leibowitz, R.A. Blomquist, *J. Nucl. Mater.* 201 (1993) 218.
- [22] C. Servant, C. Gueneau, I. Ansara, *J. Alloy. Compd.* 220 (1995) 19.
- [23] M. Jiang, K. Oikawa, T. Ikeshoji et al, *J. Phase Equilib. Diff.* 22 (2001) 406.
- [24] T.O. Malakhov, In: O.S. Ivanov, Z.M. Alekseeva (Eds.), *Alloys for Atomic Energy*, Nauka, Moscow, (1979) 123.
- [25] T.B. Massalski, *Binary Alloy Phase Diagrams*, Metals Park, Ohio, 1991.
- [26] J.C. Gachon, J. Hertz, *CALPHAD* 7 (1983) 1.
- [27] A. Schneider, H. Klotz, J. Stendel, G. Strauß, *Pure Appl. Chem.* 2 (1961) 13.
- [28] O.Yu. Sidorov, M.G. Valishev, Yu.O. Esin et al, *Izv. Akad. Nauk SSSR, Metall* 6 (1988) 23.
- [29] M. Rosner-Kuhn, J.P. Qin, K. Schaeffers et al, *Z. Metallkd.* 86 (1995) 682.
- [30] P.R. Ohodnicki, N.C. Cates, D.E. Laughlin et al, *J. Alloy. Compd.* 78 (2008) 207.
- [31] M. Mihalkovič, M. Widom, *Phys. Rev. B* 70 (2004) 177.
- [32] Materials Project. <https://materialsproject.org> (accessed 12 March 2019).
- [33] A. Jain, S.P. Ong, G. Hautier et al, *APL Materials* 1 (2013) 11002.
- [34] OQMD: The Open Quantum Materials Database, Chris Wolverton's group. <http://www.oqmd.org> (accessed 12 March 2019).
- [35] R. Lück, H. Wang, *J. Alloy. Compd.* 191 (1993) L11.
- [36] V.G. Dyubonov, A.Ya. Stomakhin, A.F. Filippov, *Izvest. Vyssh. Ucheb. Zaved., Chern. Metall.* 3 (1975) 5.
- [37] V.S. Sudavtsova, V.P. Kurach, G.I. Batalin, *Izv. Akad. Nauk, Metall* 3 (1987) 60.
- [38] M.G. Valishev, O.Yu. Sidorov, E.D. Pletneva et al, *Inorg. Mater. (Engl. Trans.)* 28 (1992) 1453.
- [39] H. Wang, R. Luck, B. Predel, *Z. Metallkd.* 81 (1990) 843.
- [40] M.A. Turchanin, P.G. Agraval, A.R. Abdulov, *Rasplavy* 6 (2006) 25.
- [41] S. Chatain, C. Guéneau, C. Chatillon, *J. Nucl. Mater.* 344 (2005) 281.
- [42] S. Chatain, B. Larousse, C. Maillault et al, *J. Alloy. Compd.* 457 (2008) 157.
- [43] L. Lutterotti, *Nuclear Inst. and Methods in Physics Research, B* 268 (2010) 334.
- [44] G. Della Gatta, M.J. Richardson, S.M. Sarge et al, *Pure Appl. Chem.* 78 (2006) 1455.

-
- [45] SGTE Pure Element Database (UNARY): 5.0, Scientific Group Thermodata Europe. <http://www.crct.polymtl.ca/sgte/unary50.tdb> (accessed 13 March 2019).
- [46] M. Hillert, M. Jarl, *CALPHAD* 2 (1978) 227.
- [47] A.T. Dinsdale, *CALPHAD* 15 (1991) 317.
- [48] O. Redlich, A.T. Kister, *Ind. Eng. Chem.* 40 (1948) 345.
- [49] M. Hillert, *J. Alloy. Comp.* 320 (2001) 161.
- [50] J.-O. Andersson, T. Helander, L. Höglund et al, *CALPHAD* 26 (2002) 273.
- [51] H.L. Lukas, S.G. Fries and B. Sundman, *Computational Thermodynamics The Calphad Method*, Cambridge University Press, New York, 2007.
- [52] R. Arroyave, A. van de Walle, Z.-K. Liu, *Acta Mater.* 54 (2006) 473.
- [53] Q. Chen, B. Sundman, *J. Phase Equilib. Diff.* 22 (2001) 631.
- [54] B.S. Gordon, L.J. Herrick, *J. Am. Chem. Soc.* 73 (1951) 4549.
- [55] G. Kaptay, *CALPHAD* 56 (2017) 169.
- [56] I. Saenko, O. Fabrichnaya, A. Udovsky, *J. Phase Equilib. Diff.* 38 (2017) 684.
- [57] A.L. Udovskii, *Izv. Akad. Nauk SSSR Met.* 2 (1990) 136.

Publication P3: I. Saenko, M. Ilatovskaia, G. Savinykh, O. Fabrichnaya, Experimental investigation of phase relations and thermodynamic properties in the $\text{ZrO}_2\text{--TiO}_2$ system, *Journal of the American Ceramic Society* 101 (2018) 386–399.
DOI: 10.1111/jace.15176

Contributions to the paper:

Authors	Contribution [%]	Particular contribution
I. Saenko	55	<ul style="list-style-type: none"> • Experimental work • Evaluation of data • Thermodynamic modelling • Composition of the manuscript
M. Ilatovskaia	10	<ul style="list-style-type: none"> • Experimental assistance
G. Savinykh	5	<ul style="list-style-type: none"> • Sample preparation • DTA measurements
Dr. rer. Nat. habil. O. Fabrichnaya	30	<ul style="list-style-type: none"> • Supervision of the work • Work on the manuscript

Experimental investigation of phase relations and thermodynamic properties in the ZrO₂–TiO₂ system

I. Saenko^{1*}, M. Ilatovskaia^{1,2}, G. Savinykh¹, O. Fabrichnaya¹

¹ Institute of Materials Science, Technical University Bergakademie Freiberg, Gustav-Zeuner-Str. 5, D-09599 Freiberg, Germany

² Institute of Metallurgy, Mechanical Engineering and Transport, Peter the Great St. Petersburg Polytechnic University, Politekhnikeskaya 29, 195251 Saint Petersburg, Russia

* Corresponding author:

I. Saenko, Institute of Materials Science, Technical University Bergakademie Freiberg, Gustav-Zeuner-Str. 5, D-09599 Freiberg, Germany

E-mail: ivan.saenko@iww.tu-freiberg.de

Abstract

Phase relations in the ZrO₂–TiO₂ system were studied experimentally using X-ray diffraction (XRD), scanning electron microscopy combined with dispersive X-ray spectrometry (SEM/EDX) and differential thermal analysis (DTA). The homogeneity ranges of ZrO₂ and TiO₂, as well as high temperature disordered β -(Zr_xTi_{1-x})₂O₄ compound were defined in the temperature range of 1700–2040 K. Temperature and composition of eutectic reaction were measured. The standard enthalpy of formation of the β -ZrTiO₄ compound was obtained by using high-temperature oxide-melt solution calorimetry. High temperature heat capacity measurement for the β -ZrTiO₄ compound was performed in the temperature range from 250 K to 1200 K. Thermodynamic description of ZrO₂–TiO₂ system has been derived based on obtained experimental results and data from literature.

1. Introduction

The ZrO₂-based ceramic materials are widely applied in industry. The β -ZrTiO₄ is well known compound in the field of electro-ceramics where it is used in the dielectric resonators and devices for telecommunications [1]. β -ZrTiO₄ show anisotropic thermal expansion and therefore has potential as thermal shock resistance application. In the work of E. López-López et al.[1] the thermomechanical properties of this compound were investigated and it was proposed for application as a constituent of thermal shock resistance materials. It should be mentioned, materials based on the ZrO₂–TiO₂ system are of interest due to their applications in electrical and optical devices such as capacitors, piezoelectric sensors, ultrasonic motors, and microwave dielectric resonators [2–7]. It is also useful as high temperature pigments and bi-functional catalyst [8, 9].

The materials based on Al₂TiO₅–ZrTiO₄–ZrO₂ system are new promising kinds of ceramic composite material with low thermal expansion coefficient and high-temperature stability [10]. The system ZrO₂–TiO₂ is part of the ZrO₂–Y₂O₃–TiO₂ system which presents interest for thermal barrier coating applications. It was shown that co-doping of ZrO₂ with Y₂O₃ and TiO₂ resulted in strong stabilization of tetragonal modification of YSZ (Yttria Stabilized Zirconia) which is used as TBC (Thermal Barrier Coating) [11].

The phase relations in the ZrO₂–TiO₂ system are important for application in metal matrix composite. High alloyed ductile TRIP-steel (Transformation Induced Plasticity) exhibited extraordinary high values of specific energy absorption due to reinforcing by Mg-PSZ-

ceramic (MgO Partially Stabilized Zirconia) [12]. Since, the Mg-PSZ-ceramic shows a martensitic transformation of tetragonal to monoclinic phase during deformation resulting in additional strength increase of the TRIP-steel [13]. In the work of C. Weigelt et al. [14], it was shown, that a minor addition of titanium improves the densification of the matrix material and the bonding between the zirconia particles and the TRIP steel matrix that improves mechanical properties of the composite [14]. Therefore, a thermodynamic description of the relevant $\text{ZrO}_2\text{--TiO}_2$ system used in combination with steel database would make it possible to calculate reactions at the interface of ceramic grains and TRIP steel and explain diffusion of Ti into ceramic component of metal matrix composite.

Phase equilibria in the $\text{ZrO}_2\text{--TiO}_2$ system were studied in several works [15-21] using various methods of sample preparation. However, there are some inconsistencies e.g. in eutectic composition. Intermediate phase was found in the system which is disordered at high temperature and ordered at temperatures below 1200 °C. Ordered phase $\alpha\text{-ZrTiO}_4$ has composition ZrTiO_4 in the range 1100-1200 °C and $\alpha'\text{-ZrTiO}_4$ (ZrTi_2O_6) from 1100 °C down to room temperature. Calorimetric investigations by adiabatic and high-temperature oxide melt solution methods allowed to determine standard entropy and enthalpy of formation of intermediate disordered phase with composition $\beta\text{-ZrTiO}_4$ [22]. Several thermodynamic descriptions are available for this system in the literature [11, 23-25]. The description of Cancarevic et al. [25] is the only one where homogeneity ranges in the disordered phase were taken into account and the liquid phase was described by associate model, while in the works of Schaedler et al. [11] and Arroyave [24] partially ionic liquid model was used for liquid, but homogeneity ranges in the $\beta\text{-ZrTiO}_4$ were not taken into account.

The aim of the present work is to measure heat capacity of $\beta\text{-(Zr}_x\text{Ti}_{1-x})_2\text{O}_4$ and investigate phase relations the $\text{ZrO}_2\text{--TiO}_2$ system in order to resolve present inconsistencies. Based on the measured heat capacity of intermediate compound at high temperatures in combination with literature data at room temperature, standard entropy and enthalpy of formation [22] together with phase equilibrium data from the present work and literature [15-21] thermodynamic database of the $\text{ZrO}_2\text{--TiO}_2$ system will be developed for further use in high-order systems.

2. Literature survey

Phase relations in the $\text{ZrO}_2\text{--TiO}_2$ system were experimentally investigated by several authors over many years [15-21, 26-32]. The high temperature regions (above 1473 K) of the $\text{ZrO}_2\text{--TiO}_2$ phase diagram were presented in the works [15, 16, 19]. Liquidus and solidus were studied by Shevchenko et al. [19], Coughanour et al. [15] and Noguchi and Mizuno [17]. According to these investigations, liquidus of the system has two inflections at 35 and 60 at.% of TiO_2 corresponding to metatectic and peritectic reactions [19] and one eutectic point at 73 at.% of TiO_2 and 1993 K [19] or 80 at.% and 2033 K [15]. Shevchenko et al. [19] stated that the first inflection corresponded to a metatectic reaction between cubic C- ZrO_2 and Liquid phase forming tetragonal T- ZrO_2 . However, there are contradictions in temperature and type of invariant reaction of phase equilibrium involving C- ZrO_2 , T- ZrO_2 and liquid for different experimental studies [17, 19, 33]. Polymorphic modifications of ZrO_2 and TiO_2 have homogeneity ranges up to 20 mol.% TiO_2 in tetragonal phase and 15mol. % ZrO_2 in TiO_2 . The homogeneity range of C- ZrO_2 was not determined. There are some disagreements between the phase diagrams obtained in the location of M- ZrO_2 +T- ZrO_2 two-phase field are due to a hysteresis effect for a transformation in the zirconia solid solutions upon cooling and heating [17, 18, 21, 26].

Three stable intermediate compounds were found in this quasi-binary system, namely the high-temperature disordered β -(Zr_xTi_{1-x})₂O₄ phase and two low-temperature ordered α -ZrTiO₄ and α' -ZrTiO₄ phases [20, 27, 30, 31, 34, 35], which have the same ordered structures of the β -(Zr_xTi_{1-x})₂O₄ phase with different stoichiometry (Zr:Ti molar ratio 1:1 and 1:2) [36]. The β -(Zr_xTi_{1-x})₂O₄ phase has an orthorhombic α -PbO₂ type structure, with the random distribution of Zr and Ti over the octahedral site [34, 37]. According to the work of Shevchenko et al. [19]; the inflection on the liquidus at 60 at.% of TiO₂ was defined to be the temperature of the peritectic reaction for the formation of the β -(Zr_xTi_{1-x})₂O₄ at 2103 K. This results is in the good accordance with experimental work of Coughanour et al. [15], where the melting temperature of β -(Zr_xTi_{1-x})₂O₄ phase was determined to be 2093 K [15]. The β -(Zr_xTi_{1-x})₂O₄ compound is stable above 1400 K [36]. Below this temperature, the β -(Zr_xTi_{1-x})₂O₄ polymorph undergoes structural ordering transition according to Park et al. [36] and Coughanour et al. [15]. Park et al. [36] suggested that the ordering transition occurs in several steps from the disordered β -Zr_xTi_{1-x}O₄ phase via an incommensurate state (partially ordered α -ZrTiO₄, $T > 1100$ K) to the commensurate phase (ordered α' -ZrTiO₄). The fully ordered α' -ZrTiO₄ has composition close to ZrTi₂O₆ [20]. It should be mentioned, that the samples in the work of McHale and Roth [20] were prepared using flux growth method. Growth of zirconium titanate crystals was carried out from a lithium molybdate flux melt [38]. In the works of Troitzsch et al. [21, 30], about 5 wt% of a flux, CuO or ammonium carbonate mixture was also added to samples in order to obtain ordered phases. According to Troitzsch et al. [39], the only sample that did not contain flux in the starting mix did not equilibrate completely due to sluggish kinetics and difficulty in performing experiments at relatively low temperatures (below 1473 K). In the work of Bordet et al. [34], the samples of the Zr₅Ti₇O₂₄ compound were prepared by solid-state reaction of the appropriate amounts of high-purity Y₂O₃, TiO₂ and ZrO₂ in the ration of 41.25 at% of ZrO₂, 57.75 at.% of TiO₂ and 1 at.% of Y₂O₃. Additionally, there is an inconsistency between different experimental data on the homogeneity ranges of the β -(Zr_xTi_{1-x})₂O₄ phase and stability ranges of ordered α -ZrTiO₄ and α' -ZrTiO₄ phases. The crystal structures of all solid phases are listed in Table 1.

The thermodynamic properties of β -ZrTiO₄ (disordered polymorph with Zr:Ti molar ratio 1:1) were studied by calorimetric methods [22]. The standard enthalpy of formation was obtained by using high-temperature oxide-melt solution calorimetry. The molar heat capacity was measured in the temperature range from 13 K to 400 K in an adiabatic calorimeter and extrapolated up to 1800 K by using the Debye and Einstein functions as well as fitting parameters to reproduce low-temperature results. There is no experimental data on molar heat capacity of β -ZrTiO₄ at high temperature. No other works concerning the thermodynamics of the phases in the ZrO₂–TiO₂ system are available.

Table 1. Data on crystal structures of solid phases of the ZrO₂–TiO₂ system.

Phase	Crystal system	Space group	Pearson Symbol	Structure type	References
C-ZrO ₂	Cubic	$Fm\bar{3}m$	cF12	CaF ₂	[40]
T-ZrO ₂	Tetragonal	$P4_2/nmc$	tP6	HgI ₂	[40]
M-ZrO ₂	Monoclinic	$P12_1/c1$	mP12	-	[41]
TiO ₂	Tetragonal	$P4_2/mnm$	tP6	Rutile	[42]
β -(Zr _x Ti _{1-x}) ₂ O ₄ (disordered)	Orthorhombic	$Pbcn$	oP12	α -PbO ₂	[34]
α -TiZrO ₄ (ordered)	Orthorhombic	$Pbcn$	-	-	[5, 35]
α' -TiZrO ₄ (Ti ₂ ZrO ₆ -ordered)	Orthorhombic	$Pbcn$	oP36	-	[34]

A CALPHAD type assessment of the $\text{ZrO}_2\text{--TiO}_2$ system has been performed using different models. Yokokawa et al. [23] used a substitutional model to describe liquid and solid solutions. Cancarevic et al. [25, 43] applied an associate model for liquid and solid solutions. Schaedler et al. [11] and Arroyave [24] used partially ionic liquid model for liquid phase and compound energy formalism for solid solutions. In comparison with other optimization, the thermodynamic description obtained by Cancarevic et al. [25] well reproduces most of experimental data and takes into account the homogeneity range of the high temperature $\beta\text{-(Zr}_x\text{Ti}_{1-x})_2\text{O}_4$ phase. Therefore, the optimization of Cancarevic et al. [25] was accepted as starting point for current work. However, as it was said above, the liquid phase was described by associate model in Ref. [25] while the partially ionic liquid model should be used in our thermodynamic description for consistency with previously published descriptions [44-46]. It should be also mentioned, that the thermodynamic description of the liquid phase published by Cancarevic et al. [25] shows an inversed miscibility gap at high temperatures above 2722 K at 60 mol.% of TiO_2 . Therefore, parameters of liquid should be re-assessed.

3. Experimental

3.1. Sample preparation

Samples were prepared using the co-precipitation method. The zirconium acetate solution in acetic acid, $\text{Zr}(\text{CH}_3\text{COO})_4$ (99.99 %, Sigma-Aldrich) and titanium (III) sulfate solution $\text{Ti}_2(\text{SO}_4)_3$ (99.99%, Alfa Aesar) have been used as the primary chemicals. In the first step, the titanium (III) sulfate and zirconium acetate solutions were diluted by water to obtain a concentration of 1.14 mol/l for the zirconium acetate solution and 0.643 mol/l for the titanium (III) sulfate solution in order to reach more suitable consistence for the co-precipitation process. The concentration of obtained initial solutions was determined by Inductively Coupled Plasma – Optical Emission Spectrometry (ICP-OES) spectrometry. The initial solutions were mixed to get ~2 g of oxide powder of specimens of required composition. The obtained solution was dropped from a buret at a low speed (around $1 \text{ ml}\cdot\text{min}^{-1}$) into a beaker containing about 500 ml of the aqueous solution of NH_4OH with the pH value above 9.0. In order to increase particles in the obtained suspension, it was heated up and held at 333 K for 1-2 hours before filtration. In order to perform an intermediate control of chemical composition of co-precipitated suspension and filtrates were analyzed by ICP-OES spectrometry. Then, filtrated substance was dried at 353 K for 2-3 days. Finally, pyrolysis of the dried precipitate powder was performed at 1073 K for 3 h in air. The obtained oxide powder was pressed into cylindrical pellets and sintered in air atmosphere in Pt-crucibles using NABERTHERM furnace in order to reach pseudo equilibrium state. Annealing duration was chosen depending on sintering temperature. The nominal sample compositions, as well as temperatures and annealing durations are listed in Table 2. Purity of the obtained samples was stated to be 99.99 % equal to the purity of initial reagents. However, the correspondence of real and initial chemical composition of samples was verified using ICP-OES and scanning electron microscopy combined with an energy dispersive X-ray spectrometry (SEM/EDX).

Table 2. Sample compositions and results its characterization by ICP-OES, XRD and SEM/EDX.

Sample	Initial sample composition [mol.%]		Sample composition ICP-OES/SEM-EDX results [mol.%]		Temperature, [K] / Annealing time in days	Phases according to XRD results	Vol. %	Lattice parameters, [nm]				Phase composition SEM/EDX results [mol.%]	
	ZrO ₂	TiO ₂	ZrO ₂	TiO ₂				a	b	c	β [°]	ZrO ₂	TiO ₂
TZ-1	70	30	67.8/ 67.7 ± 3.4	32.3/ 32.3 ± 3.4	1300 / 10	M-ZrO ₂	21	5.087	5.121	5.313	98.281	-	-
						β -(Zr _x Ti _{1-x}) ₂ O ₄	71	4.866	5.380	5.033	-	-	-
						T-ZrO ₂	7	3.578	5.152	-	-	-	-
						TiO ₂	1	4.594	2.959	-	-	-	-
					1370 / 10	M-ZrO ₂	27	5.092	5.126	5.314	98.441	-	-
						β -(Zr _x Ti _{1-x}) ₂ O ₄	66	4.850	5.377	5.028	-	-	-
						T-ZrO ₂	4	3.578	5.152	-	-	-	-
						TiO ₂	2	4.594	2.959	-	-	-	-
					1700 / 5	M-ZrO ₂	35	5.103	5.139	5.315	98.872	84.6 ± 0.3	15.4 ± 0.3
						β -(Zr _x Ti _{1-x}) ₂ O ₄	65	4.830	5.428	5.036	-	54.2 ± 0.2	45.8 ± 0.2
					1900 / 5	M-ZrO ₂	34	5.097	5.116	5.326	98.660	83.1 ± 0.2	16.9 ± 0.2
						β -(Zr _x Ti _{1-x}) ₂ O ₄	66	4.853	5.419	5.043	-	59.2 ± 0.1	40.8 ± 0.1
TZ-2	50	50	46.3/ 48.3 ± 0.4	53.7/ 51.7 ± 0.4	1300 / 10	M-ZrO ₂	3	5.109	5.135	5.351	98.783	-	-
						β -(Zr _x Ti _{1-x}) ₂ O ₄	83	4.798	5.412	5.026	-	-	-
						TiO ₂	14	4.606	2.975	-	-	-	-
						β -(Zr _x Ti _{1-x}) ₂ O ₄	17	5.107	5.151	5.315	98.824	-	-
					1370 / 10	M-ZrO ₂	58	4.796	5.397	5.027	-	-	-
						β -(Zr _x Ti _{1-x}) ₂ O ₄	24	4.604	2.974	-	-	-	-
						TiO ₂	100	4.793	5.456	5.025	-	-	-
						β -(Zr _x Ti _{1-x}) ₂ O ₄	100	4.787	5.441	5.022	-	-	-
					1473 / 5	M-ZrO ₂	100	4.787	5.432	5.022	-	-	-
						β -(Zr _x Ti _{1-x}) ₂ O ₄	100	4.787	5.432	5.022	-	-	-
						TiO ₂	100	4.796	5.403	5.024	-	-	-
						β -(Zr _x Ti _{1-x}) ₂ O ₄	100	4.796	5.403	5.024	-	-	-
TZ-3	30	70	27.4/ 27.1 ± 2.4	72.6/ 72.9 ± 2.4	1300 / 10	M-ZrO ₂	7	5.120	5.172	5.287	98.804	-	-
						β -(Zr _x Ti _{1-x}) ₂ O ₄	3	4.902	5.418	5.039	-	-	-
						α -ZrTiO ₄	28	14.410	5.396	5.027	-	-	-
						TiO ₂	62	4.603	2.973	-	-	-	-
					1370 / 10	M-ZrO ₂	22	5.112	5.156	5.311	98.912	-	-
						β -(Zr _x Ti _{1-x}) ₂ O ₄	2	4.875	5.402	5.052	-	-	-
						α -ZrTiO ₄	2	14.458	5.325	5.020	-	-	-
						TiO ₂	74	4.604	2.973	-	-	-	-
					1700 / 5	β -(Zr _x Ti _{1-x}) ₂ O ₄	44	4.777	5.431	5.017	-	43.9 ± 0.8	56.1 ± 0.8
						TiO ₂	56	4.617	2.990	-	-	10.4 ± 0.1	89.6 ± 0.1
					1900 / 5	β -(Zr _x Ti _{1-x}) ₂ O ₄	45	4.770	5.405	5.015	-	43.3 ± 0.1	56.2 ± 0.1
						TiO ₂	55	4.623	3.001	-	-	15.1 ± 0.1	84.9 ± 0.1

3.2. Sample treatment and characterization

The samples were analyzed by X-ray diffraction (XRD), scanning electron microscopy combined with an energy dispersive X-ray spectrometry (SEM/EDX) and differential thermal analysis (DTA).

Phase assemblages stable after long time annealing of specimens have been identified by X-ray powder diffraction (XRD) using the URD63 diffractometer (Seifert, FPM, Freiberg, Germany) equipped with the graphite monochromator and the CuK α radiation ($\lambda = 1.5418 \text{ \AA}$). The goniometer of the diffractometer has the Bragg-Brentano geometry. The Rietveld refinement was applied for the characterization of all measured diffraction patterns in order to obtain the volume fractions of present phases as well as lattice parameters. The programs BGMN [47] and Maud [48] were used.

In order to determine temperatures of invariant reactions, differential thermal analysis (DTA) was performed using SETARAM instruments SETSYS EVOLUTION 2400 (TG-DTA) in W crucibles in He atmosphere at temperatures up to 2373 K. The heating rate was of 20 K·min⁻¹ up to 1473 K and then of 10 K·min⁻¹; cooling rate was of 30 K·min⁻¹. Temperature calibration of SETSYS EVOLUTION 2400 was carried out using melting points of Al, Al₂O₃ and solid phase transformation in LaYO₃ as it was discussed in the work of Fabrichnaya et al. [49]. Temperature of transformation was accepted at on-set point, as well as at the calibrations procedure. Solid state transformations in the range between 298 and 1973 K were investigated

in SETSYS EVOLUTION 1750 (TG-DTA) device using PtRh10% crucible and Ar (or He) atmosphere.

Sample microstructures after sintering or after melting at DTA have been investigated using scanning electron microscopy combined with dispersive X-ray spectrometry (SEM/EDX; Leo1530, Carl Zeiss/ Bruker AXS Mikroanalysis GmbH). Chemical compositions of samples, phases and eutectic compositions have been determined using signal from EDX detector with an accuracy of ± 4 mol. %.

3.3. Calorimetric measurements

The sample for the heat capacity measurements of the β -($\text{Zr}_x\text{Ti}_{1-x}$) $_2\text{O}_4$ compound was prepared according to the nominal composition of about 50 at.% of TiO_2 (i.e. β - ZrTiO_4) and heat treated at 1873 K for 3 days. The heat capacity measurements in the temperature range from 235 K to 675 K were carried out using the device DSC 8000 (Perkin Elmer, Pt/Rh crucible, Ar flow, heating rate 10 K/min). The measurements in the temperature range from 235 K to 675 K were divided into small interval 100–150 K. The heat capacity measurements in the temperature range from 623 K to 1220 K were performed in the one temperature range using the device DSC Pegasus 404C (NETZSCH, Pt/Rh crucible, Ar flow, heating rate 10 K/min). The classical three-step method (continuous method) with a constant heating rate was used to measure specific heat capacity. The system was calibrated using a certified sapphire standard material. The mass and radius of sample pellets were kept the same as for standard material c.a. 85 mg and 5 mm. The measurements of two different samples were repeated two times with maximal uncertainty 3%. It should be mentioned that the C_p measurements at high temperatures using DSC equipment are becoming less reliable due to increase of heat radiation which decrease registered signal. This effect was considered during fitting of the experimental data. Fitting of the obtained results was performed using the Maier-Kelley equation. In order to exclude any phase transformation during the heat capacity measurement, XRD analysis of the obtained samples were performed before the heat capacity measurements and afterward.

Formation enthalpy of the β - ZrTiO_4 compound was determined on the Alexis 800 heat-flux microcalorimeter (SETARAM, France) using the “drop solution” method. The samples pressed into pellets (\varnothing 1 mm, mass 3-9 mg) were dropped directly from room temperature into the calorimeter with a solvent at $T = 973$ K and the enthalpy increments of dropping and solution of a set of 9 pellets were measured. The sodium molybdate $3\text{Na}_2\text{O} \cdot 4\text{MoO}_3$ was used as the solvent. The calorimeter was calibrated by using the molar enthalpy increment of dropping standard sapphire spheres. Error of the measurement was stated to be twice the standard deviation of the mean value.

4. Thermodynamic modelling

The thermodynamic functions for pure oxides were accepted from literature: data for the ZrO₂ polymorphic modifications from the work of Wang et al. [50], and TiO₂ from the work of M. Hampl and R. Schmid-Fetzer [51]. However, thermodynamic descriptions of the liquid phase and Ti₂₀O₃₉ were re-assessed for the case of the partially ionic liquid model [52]. Homogeneity ranges of polymorphic modifications of ZrO₂ and TiO₂, as well as the β -(Zr_xTi_{1-x})₂O₄ compound were described by the sublattice model in form of compound energy formalism [52]. Ordered compounds α -TiZrO₄ and α' -TiZrO₄ were modelled as stoichiometric compounds. Current thermodynamic description of the β -(Zr_xTi_{1-x})₂O₄ does not include the ZrTiO₄ species as an end member. Therefore, obtained experimental data on heat capacity were used in order to optimize C parameter of the mixing parameter of the β -(Zr_xTi_{1-x})₂O₄ phase expressed as ${}^0L_{\text{Ti+4,Zr+4;O-2}}=A+B\cdot T+C\cdot T\cdot \ln(T)$ which is related to heat capacity of β -ZrTiO₄. Parameters A and B were optimized based on experimental data for enthalpy of formation ([22] and present work), standard entropy [22] and phase equilibrium data. It should be noted that heat capacity calculated using Neumann-Kopp rule is very close to experimental results. Therefore, it was enough to fit only one parameter C to get satisfactory reproduction of experimental C_p data in the range 298.15–1220 K. The experimental C_p data fitted using Mayer-Kelly equation and calculations using correction parameter C to Neumann-Kopp are shown in the Figure 1. Heat capacity of the α' -TiZrO₄ phase was described using the Neumann-Kopp method. Monoclinic modification of ZrO₂ was used for the approximation of heat capacity of α' -TiZrO₄ phase as standard reference. The tetragonal modification of ZrO₂ was taken as standard reference for the high-temperature β -(Zr_xTi_{1-x})₂O₄ phase.

It was assumed, that the difference in the heat capacity of the ordered α -ZrTiO₄ and disordered β -(Zr_xTi_{1-x})₂O₄ compounds is insignificant. Therefore, the results of the heat capacity measurements of β -(Zr_xTi_{1-x})₂O₄ were used in the Gibbs energy description of the ordered α -ZrTiO₄ compound. The liquid phase is described by the two-sublattice partially ionic liquid model [52]. Thermodynamic function for oxygen was accepted from [53]. Thermodynamic parameters of the ZrO₂ and TiO₂ based solid solutions were assessed using phase equilibrium data of the present work and the literature data [15, 17, 19, 21] for the ZrO₂–TiO₂ system. Thermodynamic parameters for ordered α - and α' - ZrTiO₄ phases were optimized using experimental data [20, 21]. Moreover, reliability of obtained thermodynamic description was verified based on the reproducibility of experimental results in the ternary systems of our current studies [54]. Assessment of thermodynamic parameters and calculation of phase diagram were performed using Thermo-calc program set [55, 56].

5. Results and discussion

For current investigation, three chemical compositions were chosen 30, 50 and 70 mol.% of TiO₂ (TZ-1, TZ-2 and TZ-3 relatively). Annealing of the specimens was performed at 1300, 1370, 1700 and 1900 K. Chemical compositions of samples measured ICP-OES and scanning electron microscopy combined with an energy dispersive X-ray spectrometry (SEM/EDX) are presented in Table 2. Chemical analysis of specimens has shown good accordance to their nominal compositions. Phase assemblage and chemical composition of phases in the annealed samples were analyzed by XRD and SEM/EDX. In order to define temperatures of invariant reaction, differential thermal analysis (DTA) was performed. Additionally, calorimetric measurements have been performed for the TZ-2 samples containing only the β -(Zr_xTi_{1-x})₂O₄ phase using differential scanning calorimetry and drop solution calorimetry methods. Nominal

sample compositions, measured chemical compositions of co-precipitated samples using ICP-OES and SEM/EDX along with results of XRD examination after heat treatments are presented in Table 2.

5.1. Calorimetric measurements for disordered β -($\text{Zr}_x\text{Ti}_{1-x}$) $_2\text{O}_4$

The heat capacity measurements of the disordered β - ZrTiO_4 compound (the β -($\text{Zr}_x\text{Ti}_{1-x}$) $_2\text{O}_4$ compound at the Zr:Ti molar ratio 1:1) performed in the present work in the temperature range of 235-1220 K are compared with experimental results of Hom et al. [22] and calculation based on Neumann-Kopp rule [57] in the Figure 1. Experimental results obtained by Hom et al. [22] shows excellent agreement with current results. There is perfect overlap of the experimental data in the temperature range of 235-400 K. The calculations based on Neumann-Kopp rule show very good agreement with measured results at high temperature above 800 K. At the low temperature, measured results are slightly above calculations using Neumann-Kopp rule. However, the differences between experimental results and calculations are within limits of c.a. $\pm 3\%$. The experimental measurements of temperature dependence of heat capacity in 235-1220 K are fitted to following Mayer-Kelly expression

$$C_p(\text{J/mol} \cdot \text{K}) = 145.694 + 0.00801 \cdot T - 2.92 \cdot 10^6 / T^2$$

where temperature T is in K.

Measurements of drop solution calorimetry were performed using Alexis 800 heat-flux microcalorimeter (SETARAM, France) in order to determine the formation enthalpy of the β - ZrTiO_4 compound at $T = 973$ K. The sodium molybdate $3\text{Na}_2\text{O} \cdot 4\text{MoO}_3$ was used as the solvent. The obtained experimental result insignificantly differs from the value obtained by Hom et al. [22] within the uncertainty of measurements (see the Table 3). Therefore, it can be concluded, that there is good agreement between the present investigation and the work of Hom et al. [22].

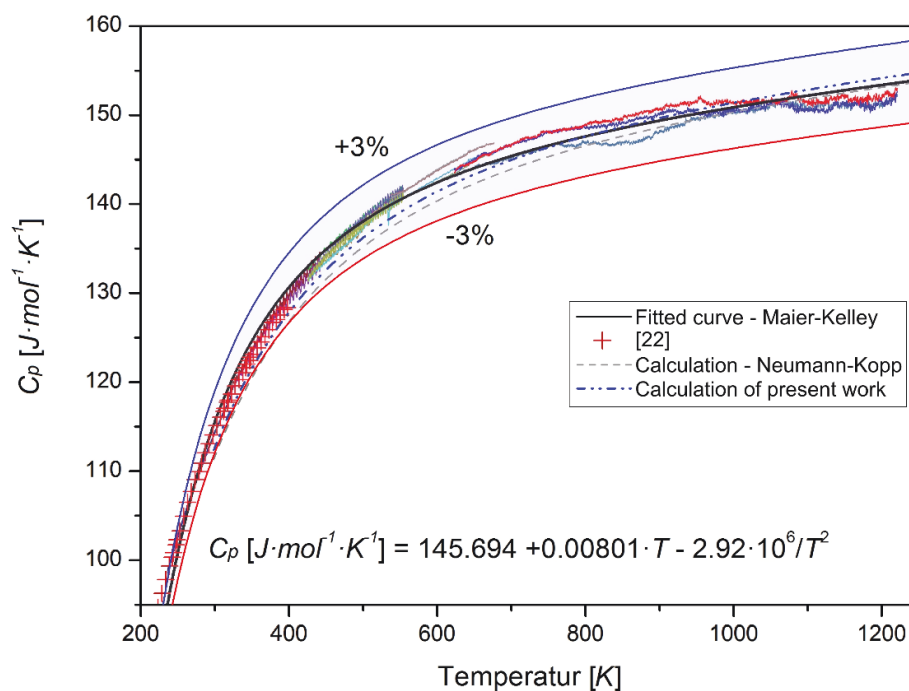


Fig. 1. Molar heat capacity of β - ZrTiO_4 .

Table 3. Calculated and experimentally measured formation enthalpy from oxides, Gibbs energy of formation and standard entropy of the β -(Zr_xTi_{1-x})₂O₄ compound at 298.15 K (where x = 0.5).

$\Delta_f H_m$ [kJ·mol ⁻¹]	$\Delta_f G_m$ [kJ·mol ⁻¹]	$\Delta S^{298.15}$ [J·mol ⁻¹ ·K ⁻¹]	References
24.0	19.0	116.7	Present work – cal.
18.3 ± 5.3			Present work – exp.
20.5 ± 4.1	15.9 ± 4.1	116.71 ± 0.31	[22]

5.2. Phase relations in the ZrO₂–TiO₂ system

The information for phase relations in the ZrO₂–TiO₂ system was obtained based on XRD, SEM/EDX and DTA investigations of the samples after annealing and/or melting in DTA performed in the present study. All data on invariant reactions occurring in the system are listed in the Table 4. As it can be seen from the Table 2, an ordered phase was detected in the TZ-3 samples at 1300 and 1370 K. It be noted, that superstructure reflections of the ordered phase overlap with reflection of monoclinic modification of zirconia. Therefore, it was very difficult in this case to distinguish superstructure reflections of the ordered structures in the XRD patterns and no ordered phases were evidently detected in XRD patterns. However, a splitting of the characteristic reflections of the structure of the β -(Zr_xTi_{1-x})₂O₄ compound was observed in the XRD pattern of the TZ-3 samples at 1300 and 1370 K (see Fig.2). It could mean existence of ordered phase in the phase assemblage of the sample. However, stoichiometry of this phase cannot be stated based on it result. As it was mentioned above, in the works of Troizch et al. [21, 39], where these two types of ordered phases were observed, the phases were grown from the melt using flux growth method.

Table 4. Invariant equilibria in the ZrO₂–TiO₂ system.

Reaction, mol.% TiO ₂				Type	T (K)	Reference
Liq	↔	β -(Zr _x Ti _{1-x}) ₂ O ₄	+	TiO ₂	Eutectic	
83.2±0.9		60.75		86.40	2029	Exp. this work
77.07		58.66		85.51	2024.34	Cal. this work
80.00		~60		~85	2033	[15]
75.30		-		-	1973	[17]
73.00		-		~82	1993±20	[19]
Liq	+	T-ZrO ₂	↔	β -(Zr _x Ti _{1-x}) ₂ O ₄	Peritectic	
-		-		-	2117	Exp. this work
63.65		18.92		40.24	2109.48	Cal. this work
55.00		-		50.00	2093	[15]
52.00		-		-	2093	[17]
60.00		-		-	2103	[19]
Liq	+	C-ZrO ₂	↔	T-ZrO ₂	Peritectic	
39.85		5.47		3.29	2439.10	Cal. this work
16.70		-		-	2616	[17]
35.00		-		-	2473	[19]
T-ZrO ₂	↔	M-ZrO ₂	+	α -ZrTiO ₄	Eutectoid	
8.99		6.81		50.00	1331.56	Cal. this work
-		12		(ZrTi ₂ O ₆)	923	[17]
-		5		(TiO ₂)	1354	[18]
~12		~9		~49	1357	[21]
TiO ₂	+	α -ZrTiO ₄	↔	α' -ZrTiO ₄	Peritectoid	
98.84		50.00		66.67	1329.28	Cal. this work
-		(β -(Zr _x Ti _{1-x}) ₂ O ₄)		~67	~1473	[20]
94.84		50.00		~61	~1340	[21]
β -(Zr _x Ti _{1-x}) ₂ O ₄	↔	α -ZrTiO ₄	+	TiO ₂	Eutectoid	
52.53		50.00		97.46	1461.32	Cal. this work
51.35		49.45		93.48	~1420	[21]
T-ZrO ₂	+	β -(Zr _x Ti _{1-x}) ₂ O ₄	↔	α -ZrTiO ₄	Peritectoid	
14.01		52.28		50.00	1461.71	Cal. this work
13.35		51.35		50.00	~1420	[21]
α -ZrTiO ₄	↔	M-ZrO ₂	+	α' -ZrTiO ₄	Eutectoid	
50.00		6.23		66.67	1296.81	Cal. this work
~50		7.66		~60	~1343	[21]

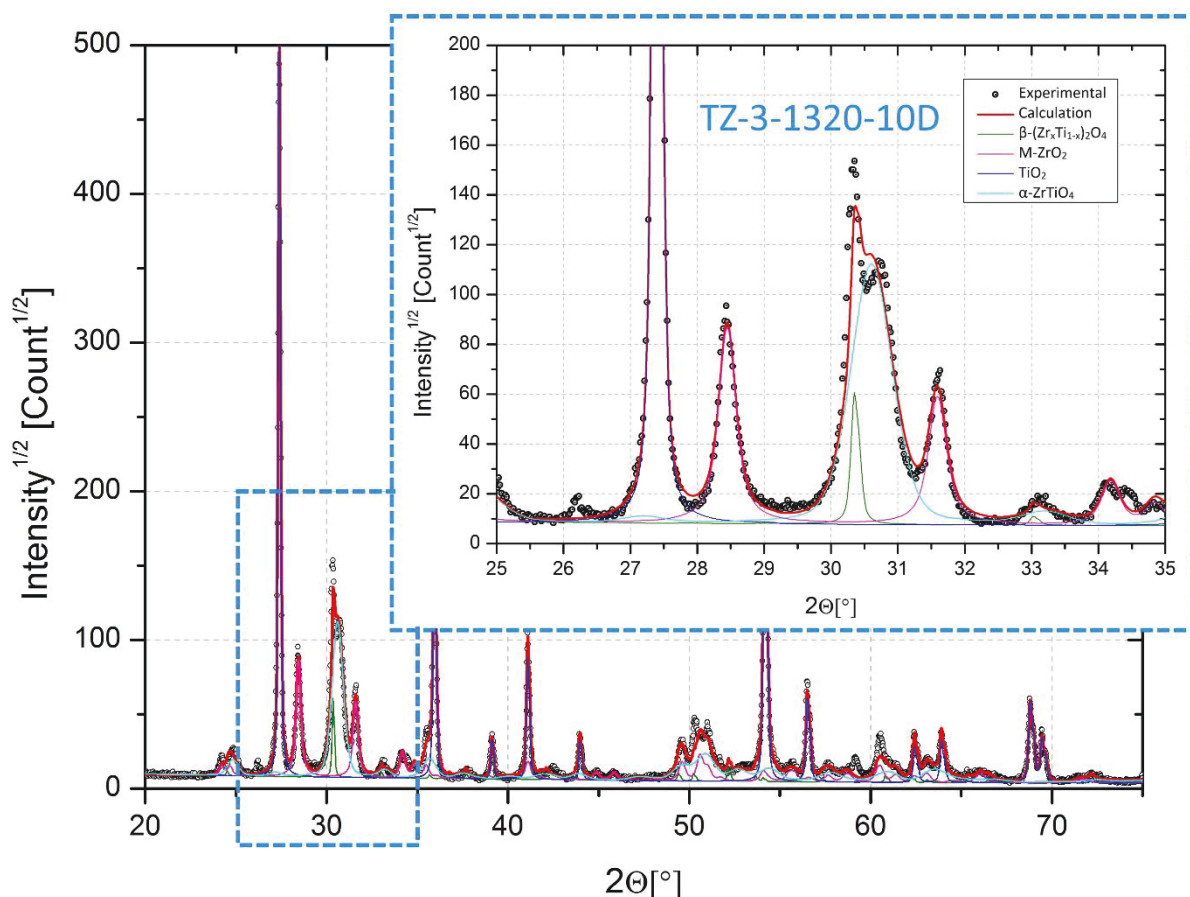


Fig.2. Splitting of the characteristic reflections of the structure of the β -(Zr_xTi_{1-x})₂O₄ compound.

Phase analysis results by XRD showed more than three phases in the binary experiments annealed at low temperatures (1300 and 1370 K). This is clear indication, according to Gibbs phase rule, that all those samples did not reach an equilibrium state. On the other hand, the SEM analysis of the samples annealed at high temperatures (1700 and 1900 K) showed well-developed microstructure (Figure 3). It can be concluded, that it is impossible to reach equilibrium state in the samples obtained by co-precipitation method at low-temperatures below 1370 K and therefore to get equilibrated ordered phases due to slow kinetics.

Although XRD results of all samples have shown the existence of monoclinic ZrO₂ instead of tetragonal ZrO₂, which is supposed to be the stable phase at the corresponding temperature and composition. Due to the nature of diffusionless transformation, the tetragonal modification of ZrO₂ transforms to monoclinic modification during cooling, which also observed in the literature [21].

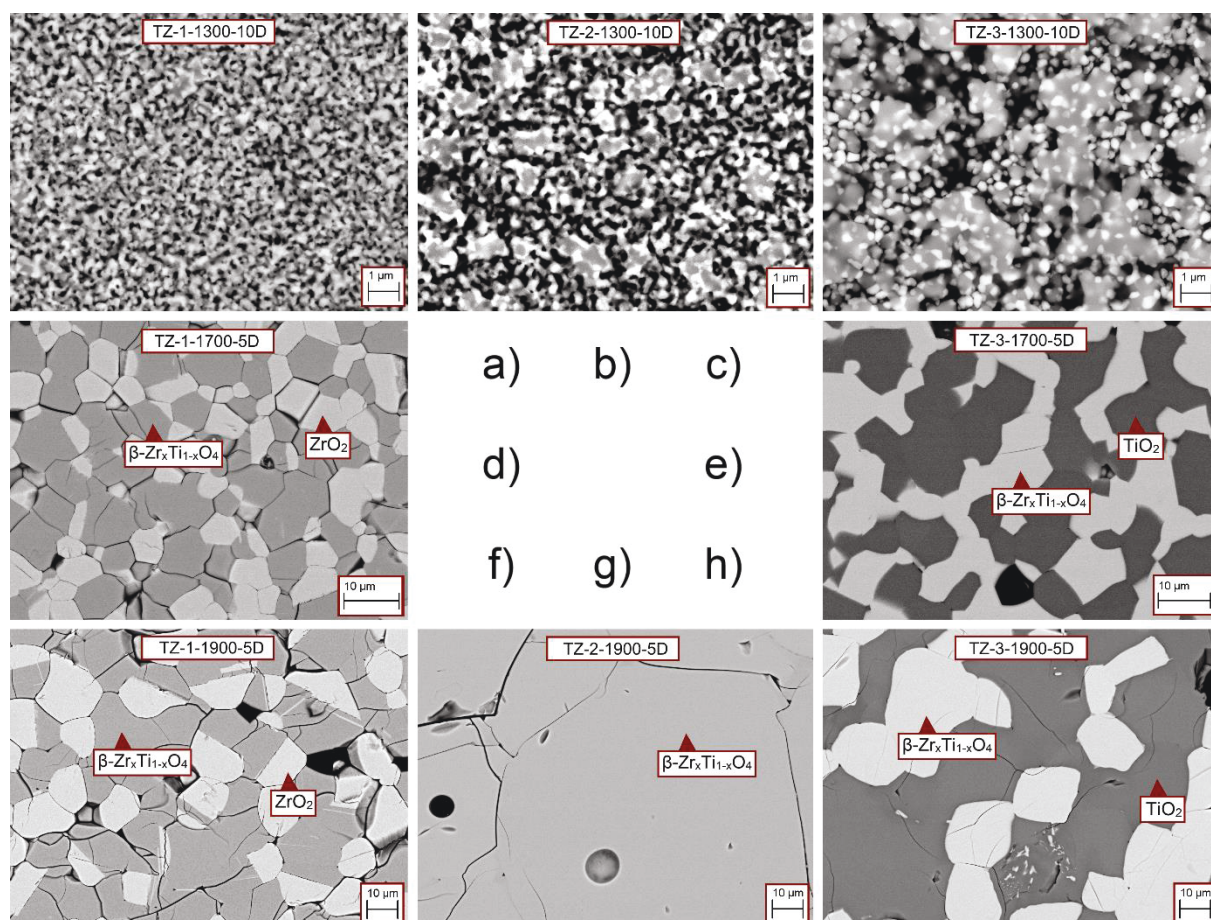


Fig. 3. Microstructures of annealed samples: a) TZ-1 at 1300 K for 10 days, b) TZ-2 at 1300 K for 10 days, c) TZ-3 at 1300 K for 10 days, d) TZ-1 at 1700 K for 5 days, e) TZ-3 at 1700 K for 5 days, f) TZ-1 at 1900 K for 5 days, g) TZ-2 at 1900 K for 5 days, h) TZ-3 at 1900 K for 5 days.

Based on the results reported by Troitzsch and Ellis [21], the solid-state transformation of the ordered- $\alpha\text{-ZrTiO}_4$ phase into disordered- $\beta\text{-(Zr}_x\text{Ti}_{1-x})_2\text{O}_4$ modification occurs above ~ 1420 K. Due to slow kinetics at these temperatures, it was impossible to measure this transformation using DTA. However, based on the long-time annealing (see Table 2), it was defined that the transition occurred below the temperature of 1473 K.

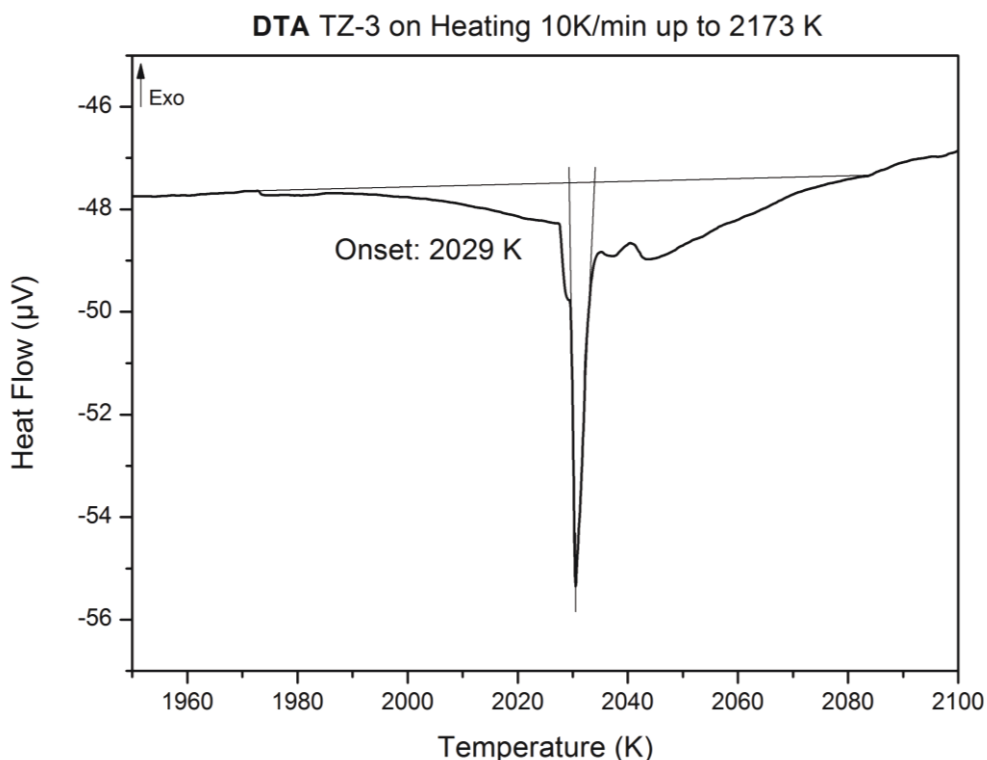


Fig.4. DTA on heating for sample TZ-3.

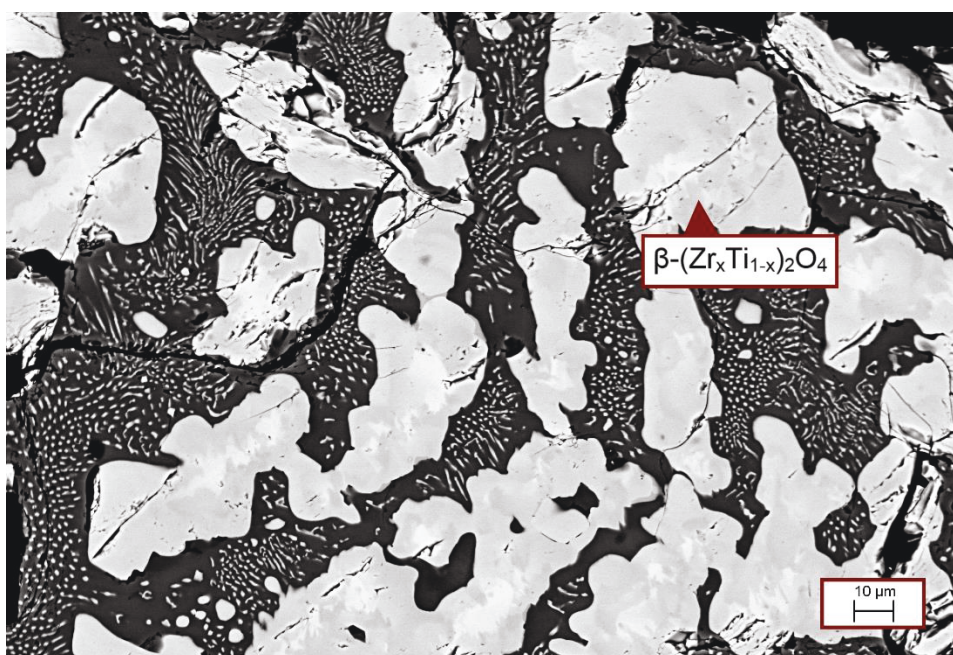


Fig. 5. Result of SEM/EDX investigation of the TZ-3 sample after melting in DTA.

The DTA heating curve for sample TZ-3 is shown in Fig. 4. The heat effect is observed at 2029 K. The microstructure presented at Fig.5 indicates the $\beta-(\text{Zr}_x\text{Ti}_{1-x})_2\text{O}_4$ to be primary crystallization phase and large areas of eutectic crystallization ($\text{L} \leftrightarrow \beta-(\text{Zr}_x\text{Ti}_{1-x})_2\text{O}_4 + \text{TiO}_2$). The measured composition of eutectic composition is (83.2 ± 1.0) mol.% TiO_2 . The obtained results are in a perfect agreement with data of Coughanour et al. [15], who defined this eutectic reaction to be at 80 mol.% of TiO_2 at 2033 K. Temperature measured using DTA is in good agreement with data of Shevchenko et al. [19] who observed this effect at 1993 K using DTA. However, the chemical compositions for the eutectic reaction stated by Shevchenko et

al. [19] and Noguchi and Mizuno [17] differ from current result. However, it should be mentioned, that Shevchenko et al. [19], as well as Coughanour et al. [15] and Noguchi and Mizuno [17] defined the chemical composition of the eutectic reaction by approximation from the obtained data on the solidus – liquidus temperatures. No microstructural investigations were performed [15, 17, 19]. Based on the DTA results for the TZ-1 sample, the $\text{Liq} + \text{T-ZrO}_2 = \beta\text{-(Zr}_x\text{Ti}_{1-x})_2\text{O}_4$ peritectic reaction was determined at 2117 K.

5.3. Assessment of thermodynamic parameters in the $\text{ZrO}_2\text{--TiO}_2$ system

The thermodynamic parameters of the $\text{ZrO}_2\text{--TiO}_2$ system were assessed based on the phase equilibrium data and DTA obtained in the present work. Data from other works [15-21, 26-32] were used in case of consistency with the results of present work. Experimental data for thermodynamic values (i.e. heat capacity and formation enthalpy of $\beta\text{-(Zr}_x\text{Ti}_{1-x})_2\text{O}_4$ compound) measured in the present work along with experimental data [22] were used in the present assessment. Experimental data on the molar heat capacity was used to describe heat capacity of $\alpha\text{-ZrTiO}_4$ and $\beta\text{-(Zr}_x\text{Ti}_{1-x})_2\text{O}_4$. Neumann-Kopp rule was used to describe heat capacity of the $\alpha'\text{-ZrTiO}_4$ (ZrTi_2O_6) phase. As it was said above, $\alpha\text{-ZrTiO}_4$ and $\alpha'\text{-ZrTiO}_4$ (ZrTi_2O_6) phases were not evidently distinguished in the phase assemblage of the samples due to slow kinetics at the low temperatures. Therefore, it was stated to model the $\alpha\text{-ZrTiO}_4$ and $\alpha'\text{-ZrTiO}_4$ (ZrTi_2O_6) phases as stoichiometric compounds. Parameters describing the homogeneity range of the T-ZrO_2 , M-ZrO_2 , $\beta\text{-(Zr}_x\text{Ti}_{1-x})_2\text{O}_4$ and TiO_2 phases were optimized based on present results and works of U.Troitzsch and D.J. Ellis [21] and F.H. Brown et al. [26]. Data on the phase relation in the area of equilibrium between T-ZrO_2 and M-ZrO_2 presented by T. Noguchi and M. Mizuno [17] were not accepted because of the absolute disagreement with other works. Parameters describing the homogeneity range of the C-ZrO_2 were optimized based on the temperature of the $\text{C-ZrO}_2 \leftrightarrow \text{Liq} + \text{T-ZrO}_2$ reaction, which was assumed by A.V. Shevchenko [19]. Parameters of the liquid phase were assessed based on obtained results of the eutectic and peritectic reactions and literature data [15-17, 19]. As it was described above, the reliability of obtained thermodynamic description was verified based on the reproducibility of experimental results in the ternary systems e.g. $\text{ZrO}_2\text{--TiO}_2\text{--Al}_2\text{O}_3$ [57]. In order to reproduce temperature of subsolidus invariant reactions in the $\text{ZrO}_2\text{--TiO}_2\text{--Al}_2\text{O}_3$ system [57] the temperature independent mixing parameter of the $\beta\text{-(Zr}_x\text{Ti}_{1-x})_2\text{O}_4$ compound was re-optimized along with mixing parameter of TiO_2 solid solution. The mixing parameter was adjusted to have better fit in the $\text{ZrO}_2\text{--TiO}_2$ system and again ternary description was checked for consistency with experimental data for invariant reactions. The calculated value of the formation enthalpy of $\beta\text{-(Zr}_x\text{Ti}_{1-x})_2\text{O}_4$ compound is slightly higher than experimental values (see Table 3). However, the deviation of the calculated value is still within the error of experimental measurements. Some deviation of the calculated homogeneity range of the TiO_2 from the experimental data can be observed in Figure 6. The thermodynamic description for the $\text{ZrO}_2\text{--TiO}_2$ system is presented in Table 5. The calculated phase diagram for the system $\text{ZrO}_2\text{--TiO}_2$ is presented in Figure 6 together with experimental data. Comparison of calculated invariant reactions (temperature and liquid composition) with experimental data obtained in the present work and literature is presented in Table 4. The temperature and chemical composition of eutectic reaction were determined. There is good accordance of obtained experimental results with the literature data and current optimization. It can be concluded from this comparison, that reasonable consistency of calculated and experimental data within uncertainty limits was achieved.

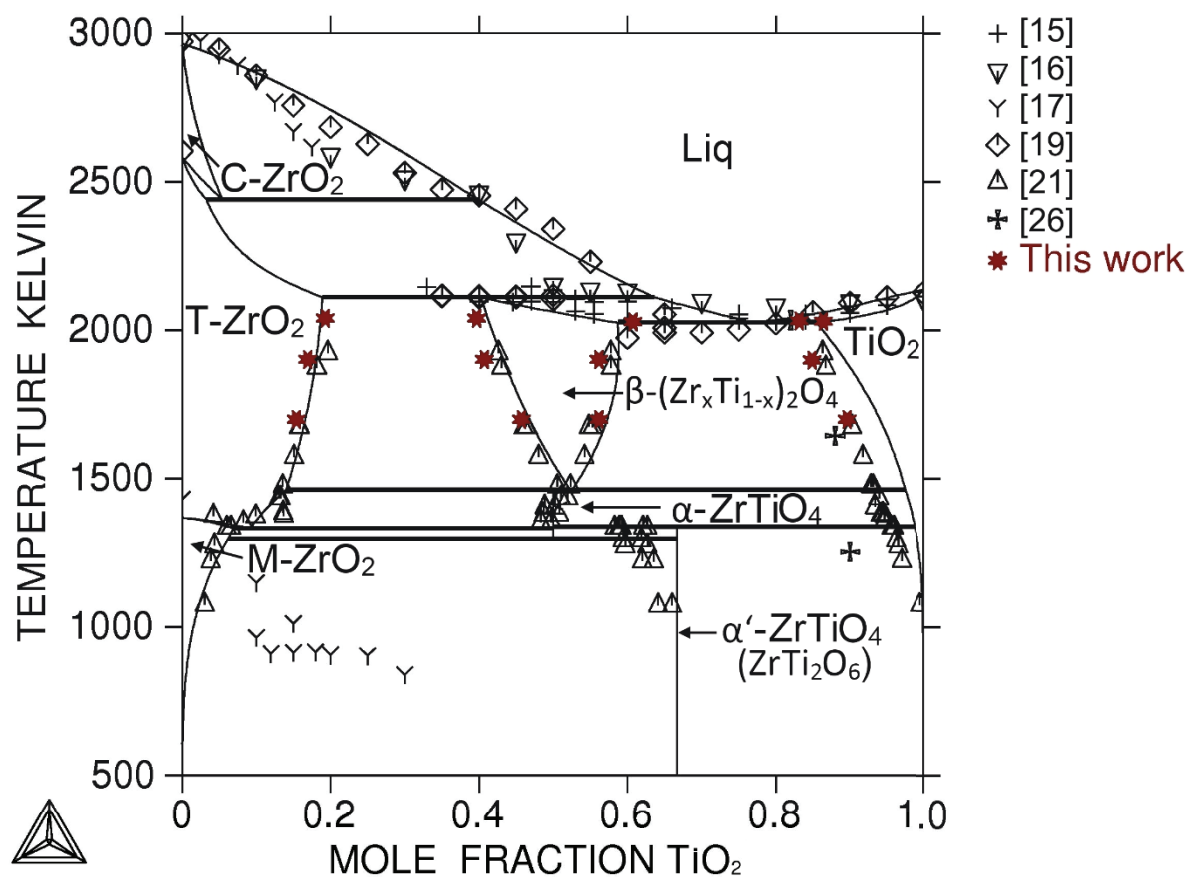


Fig. 6. Calculated phase diagram of the ZrO_2 - TiO_2 system along with experimental data of the present study and from Refs. [15-17, 19, 21, 26].

Table 5. Thermodynamic parameters for the phases of the $\text{ZrO}_2\text{--TiO}_2$ system. All values are given in SI units ($\text{J}, \text{mol}^{-1}, \text{K}$).

Phase/Model/Parameters, J/mol	Reference
Gas (O_2)	
$G(\text{GAS}, \text{O}_2; 0) + RT \ln P + 2 \cdot \text{GHSEEROO};$	[53]
Ionic Liquid ($\text{Ti}^{+2}, \text{Ti}^{+3}, \text{Zr}^{+4}$)($\text{O}^{2-}, \text{TiO}_2, \text{Va}, \text{O}$)	
${}^0G(\text{IONIC_LIQ}, \text{Ti}^{+2}; \text{O}^{2-}) = +2 \cdot \text{GTIIO1} + 141000 - 61.4 \cdot T;$	[51]
${}^0G(\text{IONIC_LIQ}, \text{Ti}^{+3}; \text{O}^{2-}) = +\text{GTI2O3} + 114147.4 - 45.6 \cdot T;$	[51]
${}^0G(\text{IONIC_LIQ}, \text{Zr}^{+4}; \text{O}^{2-}) = +2 \cdot \text{GZRO2L};$	[50]
${}^0G(\text{IONIC_LIQ}, \text{Ti}^{+2}; \text{VA}) = +\text{GLIQTI};$	[51]
${}^0G(\text{IONIC_LIQ}, \text{Ti}^{+3}; \text{VA}) = +\text{GLIQTI} + 200000;$	[51]
${}^0G(\text{IONIC_LIQ}, \text{Zr}^{+4}; \text{VA}) = +\text{GZRLIQ};$	[50]
${}^0G(\text{IONIC_LIQ}, \text{O}) = -2648.9 + 31.44 \cdot T + \text{GHSEEROO};$	[51]
${}^0G(\text{IONIC_LIQ}, \text{TiO}_2) = +\text{GTIO2} + 62222.4 - 28.2 \cdot T;$	This work
${}^0L(\text{IONIC_LIQ}, \text{Ti}^{+2}, \text{Ti}^{+3}; \text{O}^{2-}; 0) = +19431.27;$	[51]
${}^0L(\text{IONIC_LIQ}, \text{Ti}^{+2}; \text{O}^{2-}, \text{VA}; 0) = +168314.44 - 100 \cdot T;$	[51]
${}^1L(\text{IONIC_LIQ}, \text{Ti}^{+2}; \text{O}^{2-}, \text{VA}; 1) = +190655.57 - 95 \cdot T;$	[51]
${}^0L(\text{IONIC_LIQ}, \text{Ti}^{+3}; \text{O}^{2-}, \text{TiO}_2; 0) = -36682.45;$	[51]
${}^1L(\text{IONIC_LIQ}, \text{Ti}^{+3}; \text{O}^{2-}, \text{TiO}_2; 1) = +2382.5262;$	[50]
${}^0L(\text{IONIC_LIQ}, \text{Zr}^{+4}; \text{O}^{2-}, \text{VA}; 0) = +75166.0715 - 55.2382004 \cdot T;$	[50]
${}^1L(\text{IONIC_LIQ}, \text{Zr}^{+4}; \text{O}^{2-}, \text{VA}; 1) = +39057.4913;$	[50]
${}^0L(\text{IONIC_LIQ}, \text{Zr}^{+4}; \text{O}^{2-}, \text{TiO}_2) = +46371.394 - 30 \cdot T;$	This work
${}^1L(\text{IONIC_LIQ}, \text{Zr}^{+4}; \text{O}^{2-}, \text{TiO}_2) = -41079.6051;$	This work
${}^2L(\text{IONIC_LIQ}, \text{Zr}^{+4}; \text{O}^{2-}, \text{TiO}_2) = -33431.286.$	This work
C-ZrO ₂ Fluorite ($\text{Zr}^{+4}, \text{Ti}^{+4}$)(O^{2-}) ₂	
${}^0G(\text{C_ZRO}_2, \text{Ti}^{+4}; \text{O}^{2-}) = +\text{GTIO2} + 35000;$	[25]
${}^0G(\text{C_ZRO}_2, \text{Zr}^{+4}; \text{O}^{2-}) = +\text{GZRO2C};$	[50]
${}^0L(\text{C_ZRO}_2, \text{Ti}^{+4}, \text{Zr}^{+4}; \text{O}^{2-}) = +5600 - 8.89 \cdot T;$	This work
T-ZrO ₂ Tetragonal ($\text{Zr}^{+4}, \text{Ti}^{+4}$)(O^{2-}) ₂	
${}^0G(\text{T_ZRO}_2, \text{Ti}^{+4}; \text{O}^{2-}) = +\text{GTIO2} + 35000;$	[25]
${}^0G(\text{T_ZRO}_2, \text{Zr}^{+4}; \text{O}^{2-}) = +\text{GZRO2T};$	[50]
${}^0L(\text{T_ZRO}_2, \text{Ti}^{+4}, \text{Zr}^{+4}; \text{O}^{2-}) = -12883.4831 - 8.28911611 \cdot T;$	This work
${}^1L(\text{T_ZRO}_2, \text{Ti}^{+4}, \text{Zr}^{+4}; \text{O}^{2-}) = -4439.497 - 11.75 \cdot T;$	This work
M-ZrO ₂ Monoclinic ($\text{Zr}^{+4}, \text{Ti}^{+4}$)(O^{2-}) ₂	
${}^0G(\text{M_ZRO}_2, \text{Ti}^{+4}; \text{O}^{2-}) = +\text{GTIO2} + 7330;$	This work
${}^0G(\text{M_ZRO}_2, \text{Zr}^{+4}; \text{O}^{2-}) = +\text{GZRO2M};$	[50]
${}^0L(\text{M_ZRO}_2, \text{Ti}^{+4}, \text{Zr}^{+4}; \text{O}^{2-}) = +30245.15 - 4.0543 \cdot T;$	This work
TiO ₂ Rutile ($\text{Zr}^{+4}, \text{Ti}^{+4}$)($\text{O}^{2-}, \text{Va}^{2-}$) ₂	
${}^0G(\text{TiO}_2, \text{Ti}^{+4}; \text{O}^{2-}) = +\text{GTIO2};$	[51]
${}^0G(\text{TiO}_2, \text{Zr}^{+4}; \text{O}^{2-}) = +\text{GZRO2T} + 35000;$	[25]
${}^0G(\text{TiO}_2, \text{Ti}^{+4}; \text{VA}^{2-}) = +40000 + \text{GHSERTI};$	[51]
${}^0G(\text{TiO}_2, \text{Zr}^{+4}; \text{VA}^{2-}) = +40000 + \text{GHSERZR};$	[51]
${}^0L(\text{TiO}_2, \text{Ti}^{+4}, \text{Zr}^{+4}; \text{O}^{2-}) = +46400 - 33.445 \cdot T;$	This work
${}^1L(\text{TiO}_2, \text{Ti}^{+4}, \text{Zr}^{+4}; \text{O}^{2-}) = +3402.912 + 6.198 \cdot T;$	This work
${}^0L(\text{TiO}_2, \text{Ti}^{+4}, \text{Zr}^{+4}; \text{VA}^{2-}) = +46400 - 33.445 \cdot T;$	This work
${}^1L(\text{TiO}_2, \text{Ti}^{+4}, \text{Zr}^{+4}; \text{VA}^{2-}) = +3402.912 + 6.198 \cdot T;$	This work
${}^0L(\text{TiO}_2, \text{Ti}^{+4}; \text{O}^{2-}, \text{VA}^{2-}) = -90233.9 - 22.7954 \cdot T;$	[51]
${}^1L(\text{TiO}_2, \text{Ti}^{+4}; \text{O}^{2-}, \text{VA}^{2-}) = -89395.3 - 15.9034 \cdot T;$	[51]
${}^0L(\text{TiO}_2, \text{Zr}^{+4}; \text{O}^{2-}, \text{VA}^{2-}) = -100000;$	This work
αZrTiO_4 (ordered) (TiO_2)(ZrO_2)	
${}^0G(\text{TZ_LT}, \text{ZRO}_2; \text{TiO}_2) = -2095452.69 + 893.145297 \cdot T - 145.694 \cdot T \cdot \ln(T) - 0.004005 \cdot T^2 + 1461180 \cdot T^{-1}$	This work

βZrTiO_4 (disordered) ($\text{Zr}^{+4}, \text{Ti}^{+4}$) ₂ (O^{2-}) ₄	
${}^0G(\text{TIZRO4HT}, \text{Ti}^{+4}, \text{O}^{2-}) = +2 \cdot \text{GTIO2} + 13450;$	This work
${}^0G(\text{TIZRO4HT}, \text{Zr}^{+4}, \text{O}^{2-}) = +2 \cdot \text{GZRO2T} + 13450;$	This work
${}^0L(\text{TIZRO4HT}, \text{Ti}^{+4}, \text{Zr}^{+4}, \text{O}^{2-}) = +19200 + 22.0079 \cdot T - 4.15213 \cdot T \cdot \text{LN}(T);$	This work
$\alpha'\text{TiZrO}_4$ (ZrTi_2O_6 -ordered) (TiO_2) ₂ (ZrO_2)	
${}^0G(\text{ZRTI2O6}, \text{ZRO}_2; \text{TIO}_2) = -12100 + 7.9 \cdot T + \text{GZRO2M} + 2 \cdot \text{GTIO2};$	[25]
Symbols	
$\text{GHSEROO} (298.15 < T < 1000) = -3480.87 - 25.503038 \cdot T - 11.136 \cdot T \cdot \text{LN}(T) - 0.005098888 \cdot T^2 + 6.61846 \cdot 10^{-7} \cdot T^3 - 38365 \cdot T^{-1};$ $\text{GHSEROO} (1000 < T < 3300) = -6568.763 + 12.65988 \cdot T - 16.8138 \cdot T \cdot \text{LN}(T) - 5.95798 \cdot 10^{-4} \cdot T^2 + 6.781 \cdot 10^{-9} \cdot T^3 + 262905 \cdot T^{-1};$ $\text{GHSEROO} (3300 < T < 6000) = -13986.728 + 31.259625 \cdot T - 18.9536 \cdot T \cdot \text{LN}(T) - 4.25243 \cdot 10^{-4} \cdot T^2 + 1.0721 \cdot 10^{-8} \cdot T^3 + 4383200 \cdot T^{-1}.$	
$\text{GTIO1} (298.15 < T < 2500) = -551056.766 + 252.169378 \cdot T - 41.994808 \cdot T \cdot \text{LN}(T) + 327015.164 \cdot T^{-1} - 0.00889792452 \cdot T^2 + 1.0970448 \cdot 10^{-8} \cdot T^3;$	
$\text{GTI2O3} (298.15 < T < 470) = -1545045.78 + 185.96227 \cdot T - 30.3934128 \cdot T \cdot \text{LN}(T) - 0.099958898 \cdot T^2 - 5.93279345 \cdot 10^{-6} \cdot T^3 - 117799.056 \cdot T^{-1}$ $\text{GTI2O3} (470 < T < 2115) = -1586585.8 + 937.087 \cdot T - 147.673862 \cdot T \cdot \text{LN}(T) - 0.00173711312 \cdot T^2 - 1.53383348 \cdot 10^{-10} \cdot T^3 + 2395423.68 \cdot T^{-1};$	
$\text{GTIO2} (298.15 < T < 4000) = -976986.6 + 484.74037 \cdot T - 77.76175 \cdot T \cdot \text{LN}(T) - 67156800 \cdot T^2 + 1683920 \cdot T^{-1};$	
$\text{GZRO2C} (298.15 < T < 6000) = +10336 \cdot 4 \cdot T + \text{GZRO2T};$ $\text{GZRO2M} (298.15 < T < 6000) = -1126163.54 + 424.890806 \cdot T - 69.3875137 \cdot T \cdot \text{LN}(T) - 0.00375880141 \cdot T^2 + 683000 \cdot T^{-1};$ $\text{GZRO2T} (298.15 < T < 6000) = +5468 \cdot 4 \cdot T + \text{GZRO2M};$	
$\text{GHSERTI} (298.15 < T < 900) = -8059.921 + 133.615208 \cdot T - 23.9933 \cdot T \cdot \text{LN}(T) - 0.004777975 \cdot T^2 + 1.06716 \cdot 10^{-7} \cdot T^3 + 72636 \cdot T^{-1};$ $\text{GHSERTI} (900 < T < 1155) = -7811.815 + 132.988068 \cdot T - 23.9887 \cdot T \cdot \text{LN}(T) - 0.0042033 \cdot T^2 - 9.0876 \cdot 10^{-8} \cdot T^3 + 42680 \cdot T^{-1};$ $\text{GHSERTI} (1155 < T < 1940.99) = +908.837 + 66.976538 \cdot T - 14.9466 \cdot T \cdot \text{LN}(T) - 0.0081465 \cdot T^2 + 2.02715 \cdot 10^{-7} \cdot T^3 - 1477660 \cdot T^{-1};$ $\text{GHSERTI} (1940.99 < T < 6000) = -124526.786 + 638.806871 \cdot T - 87.2182461 \cdot T \cdot \text{LN}(T) + 0.008204849 \cdot T^2 - 3.04747 \cdot 10^{-7} \cdot T^3 + 36699805 \cdot T^{-1};$	
$\text{GHSEZR} (298.15 < T < 2128) = -7827.595 + 125.64905 \cdot T - 24.1618 \cdot T \cdot \text{LN}(T) - 0.00437791 \cdot T^2 + 34971 \cdot T^{-1};$ $\text{GHSEZR} (2128 < T < 6000) = -26085.921 + 262.724183 \cdot T - 42.144 \cdot T \cdot \text{LN}(T) - 1.342895 \cdot 10^{-31} \cdot T^9;$	
$\text{GLIQTI} (298.15 < T < 1300) = +12194.415 - 6.980938 \cdot T + \text{GHSERTI};$ $\text{GLIQTI} (1300 < T < 1940.99) = +368610.36 - 2620.99904 \cdot T + 357.005867 \cdot T \cdot \text{LN}(T) - 0.15526855 \cdot T^2 + 1.2254402 \cdot 10^{-5} \cdot T^3 - 65556856 \cdot T^{-1} + \text{GHSERTI};$ $\text{GLIQTI} (1940.99 < T < 6000) = +104639.72 - 340.070171 \cdot T + 40.9282461 \cdot T \cdot \text{LN}(T) - 0.008204849 \cdot T^2 + 3.04747 \cdot 10^{-7} \cdot T^3 - 36699805 \cdot T^{-1} + \text{GHSERTI};$	
$\text{GZRLIQ} (298.15 < T < 2128) = +18147.703 - 9.080762 \cdot T + 1.6275 \cdot 10^{-22} \cdot T^7 + \text{GHSEZR};$ $\text{GZRLIQ} (2128 < T < 6000) = +17804.649 - 8.91153 \cdot T + 1.343 \cdot 10^{-31} \cdot T^9 + \text{GHSEZR};$	

6. Conclusions

The phase relations in the ZrO_2 – TiO_2 system was investigated in the temperature range from 1300 to 1900 K using XRD and SEM/EDX. The $\text{Liq} \leftrightarrow \beta\text{-(Zr}_x\text{Ti}_{1-x})_2\text{O}_4 + \text{TiO}_2$ eutectic and the $\text{Liq} + \text{T-ZrO}_2 \leftrightarrow \beta\text{-(Zr}_x\text{Ti}_{1-x})_2\text{O}_4$ peritectic reactions were determined at 2029 and 2117 K respectively. Compositions of eutectic was determined by SEM/EDX as (83.2 ± 1.0) mol.%.

The temperature of eutectic reaction $\text{Liq} \leftrightarrow \beta\text{-(Zr}_x\text{Ti}_{1-x})_2\text{O}_4 + \text{TiO}_2$ determined in the present work is insignificantly higher as results obtained by [17] and accords perfectly with the data of [15] and [19]. Eutectic composition measured in the present work contained more TiO_2 compared to previous results [15, 17, 19]. However, the obtained results are within the uncertainty of the experimental techniques. Formation enthalpy of the $\beta\text{-ZrTiO}_4$ compound from oxides was measured to be $(-18.3 \pm 5.3) \text{ kJ} \cdot \text{mol}^{-1}$ using drop solution calorimetry. Molar heat capacities of the $\beta\text{-(Zr}_x\text{Ti}_{1-x})_2\text{O}_4$ compound was measured in the range 235–1220 K.

Experimental data for thermodynamic values (i.e. heat capacity and formation enthalpy of β -ZrTiO₄ compound) measured in the present work were used in order to optimize the description of heat capacity of α -ZrTiO₄ and β -(Zr_xTi_{1-x})₂O₄, as well as the contribution of the formation enthalpy of the β -Zr_xTi_{1-x}O₄ phase, respectively. Using the obtained experimental results together with literature data, the thermodynamic parameters in the ZrO₂–TiO₂ system were derived.

Acknowledgments

The authors thank the German Research Foundation (DFG) for funding within the Collaborative Research Center SFB 799 Trip-Matrix Composites. In addition, we thank B. Bleiber and Dr. C. Schimpf (TU-Freiberg) for technical contribution.

References

- [1] E. López-López, C. Baudin, R. Moreno, et al., *J. Eur. Ceram. Soc.* 32 (2012) 299.
- [2] G. Wolfram, H.E. Göbel, *Mater. Res. Bull.*, 16 (1981) 1455.
- [3] F. Azough, R. Freer, C.L. Wang, et al., *J. Mater. Sci.* 31 (1996) 2539.
- [4] C.L. Wang, H. Lee, F. Azough, et al., *J. Mater. Sci.* 32 (1997) 1693.
- [5] M. Dondi, F. Matteucci, G. Cruciani, *J. Solid. State. Chem.* 179 (2006) 233.
- [6] Y. Park, H.G. Kim, *Solid. State. Commun.* 102 (1997) 565.
- [7] S. Yamaguchi, K. Kobayashi, Y. Iguchi, et al., *Jpn. J. Appl. Phys.* 33 (1994) 5471.
- [8] F. Hund, *Z. Anorg. Allg. Chem.* 525 (1985) 221.
- [9] K. Arake, K. Tanabe, *Bulletin. Chem. Soc. Japan* 53 (1980) 299.
- [10] F.J. Parker, *J. Am. Ceram. Soc.* 73 (1990) 929.
- [11] T.A. Schaedler, O. Fabrichnaya, C.G. Levi, *J. Eur. Ceram. Soc.* 28 (2008) 2509.
- [12] H. Biermann, U. Martin, C.G. Aneziris, et al., *Adv. Eng. Mater.* 11 (2009) 1000.
- [13] S. Martin, S. Richter, S. Decker, et al., *Steel Research int.* 82 (2011) 1133.
- [14] C. Weigelt, H. Berek, C.G. Aneziris, et al., *Ceram. Int.* 41 (2015) 2328.
- [15] L.W. Coughanour, R.S. Roth, V.A. DeProse, *J. Res. Nat. Bur. Stand.* 52 (1954) 37.
- [16] T. Noguchi, M. Mizuno, *Sol. Energy* 11 (1966) 56.
- [17] T. Noguchi, M. Mizuno, *Bull. Chem. Soc. Jpn.* 41 (1968) 2895.
- [18] A. Ono, *Mineral. J.* 6 (1972) 433.
- [19] A.V. Shevchenko, L.M. Lopato, I.M. Maister, et al., *Russ. J. Inorg. Chem.* (Engl. Transl.) 25 (1980) 1379.
- [20] A.E. McHale, R.S. Roth, *J. Am. Ceram. Soc.* 69 (1986) 827.
- [21] U. Troitzsch, J. Ellis, *J. Mater. Sci.* 40 (2005) 4571.
- [22] B.K. Hom, R. Stevens, B.F. Woodfield, et al., *J. Chem. Thermodyn.* 33 (2001) 165.
- [23] H. Yokokawa, N. Sakai, T. Kawada, et al., *Sci. Technol. Zirconia* 5 (1992) 59.
- [24] R. Arroyave, *Thermodynamics and Kinetics of Ceramic/Metal Interfacial Interactions*. Diss. Massachusetts Inst. Techn. 2004.
- [25] M. Cancarevic, M. Zinkevich, F. Aldinger, *J. Ceram. Soc. Jpn.* 114 (2006) 937.
- [26] F.H. Brown, P. Duwez, *J. Am. Ceram. Soc.* 37 (1954) 129.
- [27] A.E. McHale, R.S. Roth, *J. Am. Ceram. Soc.* 66 (1983) 18.
- [28] M.J. Bannister, J.M. Barnes, *J. Am. Ceram. Soc.* 69 (1986) 269.
- [29] U. Troitzsch, J. Ellis, *Eur. J. Mineral.* 16 (2004) 577.
- [30] U. Troitzsch, A.G. Christy, J. Ellis, *J. Am. Ceram. Soc.* 87 (2004) 2058.
- [31] U. Troitzsch, A.G. Christy, D.J. Ellis, *Phys. Chem. Miner.* 32 (2005) 504.
- [32] U. Troitzsch, *J. Am. Ceram. Soc.* 89 (2006) 3201.
- [33] K. Kobayashi, K. Kato, K. Terabe, et al., *J. Ceram. Soc. Jap.* 106 (1998) 782.
- [34] P. Bordet, A. McHale, A. Santoro, et al., *J. Solid. State. Chem.* 64 (1986) 30.
- [35] R. Christofferson, P.K. Davies, *J. Am. Ceram. Soc.* 75 (1992) 563.

-
- [36] Y. Park, Y. Kim, *Mat. Res. Bullet.* 31 (1996) 7.
- [37] R.E. Newnham, *J. Am. Ceram. Soc.* 50 (1967) 216.
- [38] T. Sugai, S. Hasegawa, *J. Ceram. Soc. Jpn.* 76 (1968) 29.
- [39] U. Troitzsch, A.G. Christy, D.J. Ellis, *J. Solid. State. Chem.* 180 (2007) 2885.
- [40] P. Bouvier, E. Djurado, G. Lucazeau, et al., *Phys. Rev. B* 62 (2000) 8731.
- [41] M. Winterer, R. Delaplane, R. McGreevy, *J. Appl. Crystall.* 35 (2002) 434.
- [42] W. Gonschorek, *ZfKristall.* 160 (1982) 187.
- [43] M. Cancarevic, Thermodynamic Optimization of the PbO-ZrO₂-TiO₂ (PZT) System and its Application to the Processing of Composites of PZT Ceramics and Copper. Dissert. Univer. Stuttgart 2007.
- [44] D. Pavlyuchkov, G. Savinykh, O. Fabrichnaya, *Adv. Eng. Mater.* 15 (2013) 618.
- [45] D. Pavlyuchkov, G. Savinykh, O. Fabrichnaya, *J. Eur. Ceram. Soc.* 35 (2015) 3623.
- [46] D. Pavlyuchkov, D. Dilner, G. Savinykh, et al., *J. Am. Ceram. Soc.* 99 (2016) 3136.
- [47] BGMN <http://www.bgm.de> (accessed 11.04.17).
- [48] L. Lutterotti, *Nucl. Instr. Meth. Phys. Res. B* 268 (2010) 334.
- [49] O. Fabrichnaya, M.J. Kriegel, D. Pavlyuchkov, et al., *Thermochim. Acta* 558 (2013) 74.
- [50] C. Wang, M. Zinkevich, F. Aldinger, *J. Am. Ceram. Soc.* 89 (2006) 3751.
- [51] M. Hampl, R. Schmid-Fetzer, *Int. J. Mater. Res.* 106 (2015) 439.
- [52] M. Hillert, *J. Alloys. Compd.* 320 (2001) 161.
- [53] A.T. Dinsdale, *CALPHAD* 15 (1991) 317.
- [55] J.O. Andersson, T. Helander, L. Höglund, et al., *CALPHAD* 26 (2002) 273.
- [56] H.L. Lukas, S.G. Fries, B. Sundman, Computational Thermodynamics The Calphad Method. Cambridge University Press, New York, 2007.
- [57] J. Leitner, P. Vonka, D. Sedmidubsky, et al., *Thermochim. Acta* 497 (2010) 7.

Publication P4: I. Saenko, V. Tsukrenko, M. Ilatovskaia, D. Pavlyuchkov, G. Savinykh, O. Fabrichnaya, Experimental Investigation of Phase Equilibria in the $\text{ZrO}_2\text{--TiO}_2\text{--MgO}$ System, *Advanced Engineering Materials* 21 (2019) 1800655.
DOI: 10.1002/adem.201800655

Contributions to the paper:

Authors	Contribution [%]	Particular contribution
I. Saenko	35	<ul style="list-style-type: none"> • Experimental work • Evaluation of data • Thermodynamic modelling • Composition of the manuscript
V. Tsukrenko	20	<ul style="list-style-type: none"> • Experimental work • Evaluation of data
M. Ilatovskaia	10	<ul style="list-style-type: none"> • Experimental assistance
Dr. D. Pavlyuchkov	10	<ul style="list-style-type: none"> • Experimental work • Evaluation of data
G. Savinykh	5	<ul style="list-style-type: none"> • Sample preparation • DTA measurements
Dr. rer. nat. habil. O. Fabrichnaya	20	<ul style="list-style-type: none"> • Supervision of the work • Work on the manuscript

Experimental Investigation of Phase Equilibria in the ZrO₂–TiO₂–MgO System

I. Saenko^{1,*}, V. Tsukrenko², M. Ilatovskaia¹, D. Pavlyuchkov¹, G. Savinykh¹, O. Fabrichnaya¹

¹ Institute of Materials Science, Technical University Bergakademie Freiberg, Gustav-Zeuner-Str. 5, D-09599 Freiberg, Germany

² Frantsevich Institute for Problems in Materials Science, Akademika Krzhyzhanovs'koho St, 3, 03680 Kyiv, Ukraine

* Corresponding author:

I. Saenko, Institute of Materials Science, Technical University Bergakademie Freiberg, Gustav-Zeuner-Str. 5, D-09599 Freiberg, Germany

E-mail: ivan.saenko@iww.tu-freiberg.de

Abstract

Phase equilibria in the ZrO₂–TiO₂–MgO system are studied experimentally using X-ray diffraction (XRD), scanning electron microscopy combined with dispersive X-ray spectrometry (SEM/EDX) and differential thermal analysis (DTA). Based on the obtained experimental data, isothermal sections of the ZrO₂–TiO₂–MgO system at temperatures 1530, 1680 and 1880 K are established. Wide extension of stability of Zr_{1-x}Mg_xO_{2-x} phase with fluorite structure (C-ZrO₂) into ternary system is revealed. Very limited solubility of MgO is found in β-(Zr_xTi_{1-x})₂O₄ and tetragonal (Zr_{1-x}Ti_x)O₂ phase (T ZrO₂), while more substantial solubility of ZrO₂ is found in the intermediate compounds of the TiO₂–MgO system (Mg₂TiO₄, MgTiO₃ and MgTi₂O₅). Low temperature ternary compound similar to δ-phase Y₄Zr₃O₁₂ is revealed at 1530 K. Differential thermal analysis indicated that this δ-phase is stable up to 1664 K. Temperatures and compositions of three eutectic reactions are experimentally measured by DTA and ex-situ analysis of the sample microstructures after melting using SEM/EDX.

1. Introduction

Materials based on the ZrO₂–TiO₂–MgO system are of interest due to their dielectric properties [1, 2]. The MgTiO₃ ceramics are one among the leading materials for microwave frequency applications. Tseng [2] showed that small substitution of Zr for Ti increased density and grain size resulting in improvement of dielectric properties. Bayer [3] showed that substitution of TiO₂ in the MgO stabilized ZrO₂ with fluorite structure increased density and hardness of the materials. However the obtained fluorite structure was not stable and decomposed after prolonged heat treatment at 1373 and 1473 K. Moreover, the ZrO₂–TiO₂–MgO system is of interest for composite materials based on high-alloyed austenitic stainless TRIP-steel (Transformation Induced Plasticity) reinforced by MgO stabilized zirconia (Mg-PSZ). Present composite material exhibits extraordinary high values of specific energy absorption in compression [4] and is the base of TRIP-Matrix-Composite. The Mg-PSZ shows a martensitic transformation of tetragonal to monoclinic phase during deformation resulting in additional strength increase [5]. Minor addition of TiO₂ improves mechanical properties of the composite due to increase of bonding between the zirconia particles and the TRIP steel [6].

According to literature data, the quasi-binary sub-systems of the ternary system are well known. The last experimental investigation and thermodynamic modeling of the ZrO₂–MgO system has been performed by Pavlyuchkov et al [7]. The ZrO₂–TiO₂ and TiO₂–MgO systems have been

investigated and modeled by Saenko et al. [8] and Ilatovskaia et al. [9], respectively. The crystal structures of all solid phases of the quasi-binary sub-systems are listed in Table 1. Firstly, phase relations in the ZrO_2 – TiO_2 – MgO system have been investigated by Coughanour et al. [18] in 1955. Based on obtained results, tentative phase diagram of the ternary system has been constructed assuming to be valid in the range between 1673 and 2023 K [18] (presented in the Figure 1). The ZrO_2 rich phases were not distinguished. Bayer [3] showed that up to 50 mol.% ZrO_2 in Mg-stabilized ZrO_2 can be substituted by TiO_2 at 1773–1873 K. Very limited data on phase relations were obtained in the MgTiO_3 – MgZrO_3 join (up to 30 mol.% MgZrO_3) at 1633–1693 K [2] indicating formation of secondary fluorite phase starting from 5 mol.% of MgZrO_3 .

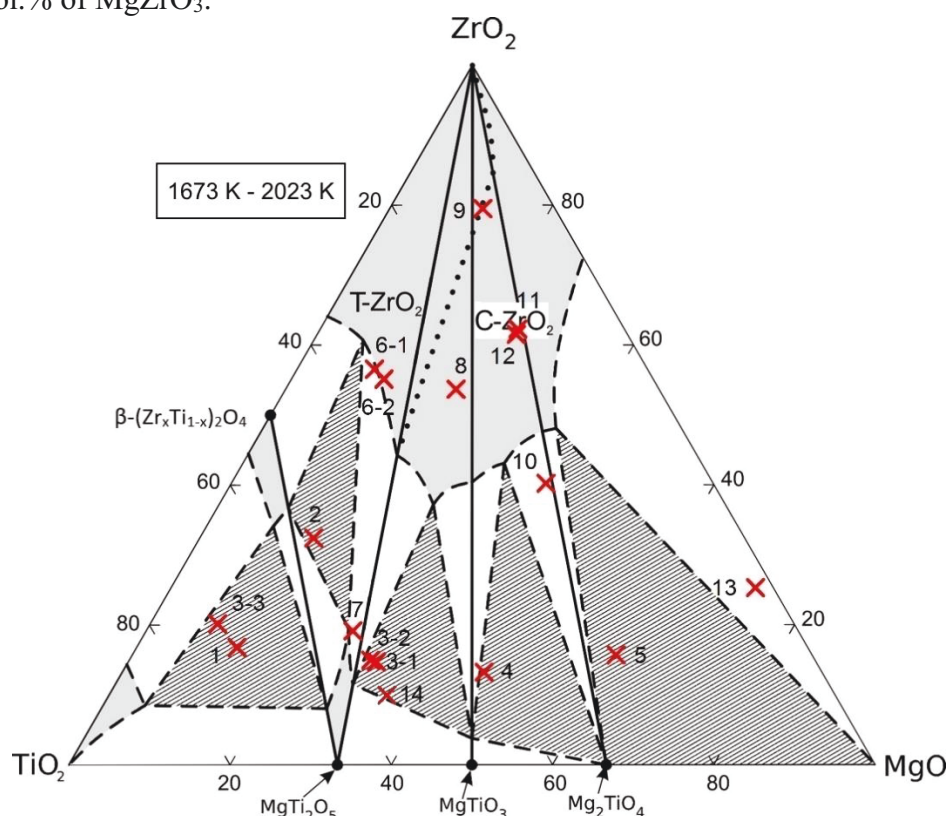


Fig. 1. Preliminary phase diagram of the ZrO_2 – TiO_2 – MgO system [18] with measured chemical compositions of the samples.

Table 1. Data on crystal structures of solid phases of the ZrO_2 – TiO_2 , ZrO_2 – MgO and TiO_2 – MgO quasi-binary systems.

Phase	Crystal system	Space group	Pearson Symbol	Structure type	References
C- ZrO_2	Cubic	$Fm\bar{3}m$	cF12	Fluorite- CaF_2	[10]
T- ZrO_2	Tetragonal	$P4_2/nmc$	tP6	HgI_2	[10]
M- ZrO_2	Monoclinic	$P12_1/c1$	mP12	-	[11]
TiO_2	Tetragonal	$P4_2/mnm$	tP6	Rutile	[12]
β -($\text{Zr}_x\text{Ti}_{1-x}$) $_2\text{O}_4$ (disordered)	Orthorhombic	$Pbcn$	oP12	α - PbO_2	[13]
α - TiZrO_4 (ordered)	Orthorhombic	$Pbcn$	-	-	[14,15]
α' - TiZrO_4 (Ti_2ZrO_6 -ordered)	Orthorhombic	$Pbcn$	oP36	-	[13]
MgO	Cubic	$Fm\bar{3}m$	cF8	NaCl	[16]
MgTiO_3	Trigonal	$R\bar{3}H$	hR10	Ilmenite- FeTiO_3	[17]
Mg_2TiO_4	Cubic	$Fd\bar{3}m$	cF56	Spinel- Al_2MgO_4	[17]
MgTi_2O_5	Orthorhombic	$Ccmm$	oS32	Pseudobrookite- Fe_2TiO_5	[17]

Therefore, the aim of this work is experimental study of phase relations in the $\text{ZrO}_2\text{--TiO}_2\text{--MgO}$ system to provide necessary information for assessment of thermodynamic parameters of this system.

2. Experimental

2.1. Sample preparation

Samples were prepared using the co-precipitation method. Along the paper, all samples were named in the way ZTM-##-temperature (K) –duration (days), where ZTM is the abbreviation of the investigated system, ## is the number of defined chemical composition. The zirconium acetate solution in acetic acid $\text{Zr}(\text{CH}_3\text{COO})_4$ (99.99 %, Sigma-Aldrich), titanium (III) sulfate solution $\text{Ti}_2(\text{SO}_4)_3$ (99.99%, Alfa Aesar) and magnesium nitrate hexahydrate $\text{Mg}(\text{NO}_3)_2 \cdot 6\text{H}_2\text{O}$ (99.97%, Alfa Aesar) have been used as the primary chemicals. In the first step, the starting chemicals were diluted and dissolved by the distilled water in order to obtain more suitable consistence for the co-precipitation process (solutions: 1.14 mol/l for the zirconium acetate solution, 0.643 mol/l for the titanium (III) sulfate solution and 0.494 mol/l for the magnesium nitrate hexahydrate).

The concentration of obtained initial solutions was determined by Inductively Coupled Plasma - Optical Emission Spectrometry (ICP-OES) spectrometry. Calculated volumes of initial solutions were mixed together in order to get ~2 g of oxide powder of desired molar ratio. The obtained solution was dropped from a burette at a low speed (around $1 \text{ ml} \cdot \text{min}^{-1}$) into a beaker containing about 500 ml of the aqueous solution of NH_4OH with the pH value above 9.0. In order to increase particles in the obtained suspension, it was heated up and held at 333 K for 1-2 hours before filtration. In order to control the chemical composition, co-precipitated suspension and filtrates were analyzed by ICP-OES. Since the composition of the samples obtained by ICP deviated significantly from nominal composition, an evaporation process was applied instead of filtration. Then, the substance obtained after filtration/evaporation was dried at 353 K for 2-3 days. Finally, pyrolysis of the dried precipitate powder was performed at 1073 K for 3 h in air. The obtained oxide powder was pressed into cylindrical pellets at 250 MPa and sintered in air atmosphere in Pt-crucibles using NABERTHERM furnace in order to reach pseudo equilibrium state. Annealing duration was chosen depending on sintering temperature and on development of microstructures. The nominal sample compositions, as well as temperatures and annealing durations are listed in Table 2. Purity of the obtained samples was stated to be 99.99 % equal to the purity of initial reagents. However, the correspondence of real and nominal chemical composition of samples was verified using scanning electron microscopy combined with an energy dispersive X-ray spectrometry (SEM/EDX). In order to verify sample preparation process, the accordance of the chemical compositions of co-precipitated materials to the nominal composition was measured for some samples by ICP-OES. Based on the ICP-OES results, it was revealed, that there was a loss of co-precipitated $\text{Mg}(\text{OH})_2$ from the mixture during filtration process due to relatively high solubility of this hydroxide. Afterwards, the filtration step was replaced by an evaporation process.

2.2. Sample treatment and characterization

The samples were analyzed by X-ray diffraction (XRD), scanning electron microscopy combined with energy dispersive X-ray spectrometry (SEM/EDX), and differential thermal analysis (DTA).

Phase assemblages of annealed specimens have been identified by X-ray powder diffraction (XRD) with $\text{CuK}\alpha$ radiation ($\lambda = 1.5418 \text{ \AA}$) using the URD63 diffractometer (Seifert, FPM, Freiberg, Germany) equipped by graphite monochromator. The goniometer of the diffractometer has Bragg-Brentano geometry. The Rietveld refinement was applied for the characterization of all measured diffraction patterns in order to obtain the volume fractions of present phases as well as lattice parameters. The program Maud [19] was used.

In order to determine temperatures of invariant reactions, differential thermal analysis (DTA) was performed using SETARAM instruments SETSYS EVOLUTION 2400 (TG-DTA) in W crucibles in He atmosphere at temperatures up to 2373 K. The heating rate was of $20 \text{ K}\cdot\text{min}^{-1}$ up to 1473 K and then $10 \text{ K}\cdot\text{min}^{-1}$; cooling rate was $30 \text{ K}\cdot\text{min}^{-1}$. Temperature calibration of SETSYS EVOLUTION 2400 was carried out using melting points of Al, Al_2O_3 and solid phase transformation in LaYO_3 as it was discussed in the work of Fabrichnaya et al. [20]. Temperature of transformation was accepted at on-set point, as well as at the calibrations procedure. Solid state transformations in the range between 298 and 1973 K were investigated in SETSYS EVOLUTION 1750 (TG-DTA) device using PtRh10% crucible and Ar (or He) atmosphere.

Sample microstructures after sintering or after melting at DTA have been investigated using scanning electron microscopy combined with dispersive X-ray spectrometry (SEM/EDX; Leo1530, Carl Zeiss/ Bruker AXS Mikroanalysis GmbH). Chemical compositions of samples, phases and eutectic compositions have been determined using signal from EDX detector with an accuracy of $\pm 4 \text{ mol. \%}$.

3. Results and discussion

Based on these preliminary results [18], assumed ternary areas and two compositions along the $\text{MgTi}_2\text{O}_5\text{--ZrO}_2$ join (40 and 80 mol.% of ZrO_2) were chosen for current investigation. During our study, the number of the samples increased due to several newly revealed facts. Experimentally measured chemical compositions of all samples are presented in the diagram as the red crosses (Fig.1). Heat treatment of the specimens was performed at 1530, 1600, 1680 and 1880 K. Nominal together with experimentally measured chemical compositions of samples are presented in Table 2 as well as results of Rietveld refinement and EDX measurements of chemical compositions of phases.

Table 2. Sample compositions and results of characterization by XRD and SEM/EDX.

Sample	Nominal / measured sample composition [mol.%]			Temperature, [K] / Annealing time in days	Phases according to XRD results	Vol. %	Lattice parameters, [Å]				Phase composition SEM/EDX results [mol.%]		
	ZrO ₂	TiO ₂	MgO				a	b	c	β [°]	ZrO ₂	TiO ₂	MgO
ZTM-1	17.0/16.7	71.0/71.0	12.0/12.3	1530 / 7	MgTi ₂ O ₅	37	9.774	10.025	3.746		4.33	63.34	32.33
					β-(Zr _x Ti _{1-x}) ₂ O ₄	23	4.782	5.453	5.021		37.38	60.8	1.82
					TiO ₂	40	4.612		2.986		11.09	88.36	0.55
				1680 / 5	MgTi ₂ O ₅	42	9.774	10.020	3.747		12.06	64.28	23.66
					β-(Zr _x Ti _{1-x}) ₂ O ₄	20	4.770	5.436	5.014		-	-	-
					TiO ₂	38	4.615		2.989		-	-	-
				1880 / 2	MgTi ₂ O ₅	43	9.797	10.042	3.754		5.8	63.7	30.5
					β-(Zr _x Ti _{1-x}) ₂ O ₄	15	4.764	5.438	5.015		41.3	58.7	0
					TiO ₂	42	4.628		3.004		17.7	80.1	2.2
ZTM-2	36.0/32.4	52.0/53.5	12.0/14.1	1530 / 7	MgTi ₂ O ₅	35	9.782	10.034	3.743		6.9	59.2	33.9
					β-(Zr _x Ti _{1-x}) ₂ O ₄	65	4.811	5.446	5.031		50.1	48.7	1.2
					MgTi ₂ O ₅	39	9.783	10.032	3.746		5.2	60.1	34.7
				1680 / 5	β-(Zr _x Ti _{1-x}) ₂ O ₄	61	4.807	5.433	5.027		46.0	51.8	2.2
					M-ZrO ₂	8	5.079	5.168	5.329	99.000	42.2	38.1	19.7
					MgTi ₂ O ₅	44	9.805	10.050	3.758		5.8	61.4	32.9
				1880 / 2	β-(Zr _x Ti _{1-x}) ₂ O ₄	48	4.814	5.428	5.030		41.9	56.8	1.3
					M-ZrO ₂	10	5.132	5.189	5.307	99.204	54.8	34.5	10.7
					MgTiO ₃	13	5.057		13.898		1.3	48.4	50.3
ZTM-3-1	15.0/14.9	52.0/55.3	33.0/29.8	1530 / 7	MgTi ₂ O ₅	77	9.821	10.053	3.762		5.7	61.6	32.7
					M-ZrO ₂	8	5.131	5.190	5.307	99.142	32.1	40.4	27.5
					MgTiO ₃	12	5.057		13.896		1.3	48.4	50.3
				1680 / 5	MgTi ₂ O ₅	79	9.818	10.049	3.761		8.2	57.7	34.1
					C-ZrO ₂	4	4.935				40.7	31.7	27.6
					MgTiO ₃	3	5.059		13.910		-	-	-
				1880 / 2	MgTi ₂ O ₅	93	9.843	10.071	3.765		12.0	56.7	31.3
					C-ZrO ₂	2	4.900				31.1	39.4	29.5
					MgTi ₂ O ₅	98	9.826	10.048	3.759		9.0	57.2	33.8
ZTM-3-2	15.0/14.6	52.0/54.7	33.0/30.7	1530 / 7	M-ZrO ₂	11	5.133	5.193	5.308	99.171	50.9	33.2	15.8
					MgTiO ₃	11	5.055		13.895		4.6	47.7	47.7
					MgTi ₂ O ₅	78	9.821	10.052	3.762		9.4	60.5	30.1
				1680 / 5	C-ZrO ₂	5	4.935				38.8	34.3	26.8
					MgTi ₂ O ₅	95	9.843	10.071	3.765		10.2	57.5	32.3
					C-ZrO ₂	8	4.900				32.1	38.8	29.1
				1880 / 2	MgTi ₂ O ₅	92	9.817	10.043	3.758		8.9	59.1	32.0
					MgTi ₂ O ₅	22	9.777	10.032	3.741		3.8	67.0	29.2
					β-(Zr _x Ti _{1-x}) ₂ O ₄	32	4.782	5.453	5.021		43.9	54.5	1.6
ZTM-3-3	15.0/20.1	52.0/71.7	33.0/8.2	1530 / 7	TiO ₂	46	4.612		2.986		9.3	90.1	0.6
					MgTi ₂ O ₅	31	9.773	10.020	3.747		4.6	62.4	33.0
					β-(Zr _x Ti _{1-x}) ₂ O ₄	27	4.771	5.434	5.014		42.1	57.0	0.8
				1680 / 5	TiO ₂	43	4.615		2.990		10.7	88.2	1.2
					MgTi ₂ O ₅	26	9.775	10.023	3.749		5.3	63.3	31.4
					β-(Zr _x Ti _{1-x}) ₂ O ₄	40	4.769	5.384	5.007		39.8	59.0	1.2
				1880 / 2	TiO ₂	34	4.620		3.000		14.0	85.2	0.8
					M-ZrO ₂	8	5.149	5.202	5.323	99.164	48.5	31.9	19.6
					MgTiO ₃	72	5.067		13.911		4.1	52.0	43.9
ZTM-4	12.5/13.2	39.5/42.0	48.0/44.8	1530 / 7	Mg ₂ TiO ₄	15	8.450				4.9	60.2	34.9
					Delta	5	9.246		8.701		-	-	-
					M-ZrO ₂	13	5.142	5.202	5.311	99.189	71.0	17.9	11.1
				1530 / 12	MgTiO ₃	68	5.066		13.905		5.6	48.3	46.2
					Mg ₂ TiO ₄	19	8.448				3.6	33.4	63.0
					C-ZrO ₂	8	4.950				41.1	27.5	31.4
				1680 / 5	MgTiO ₃	76	5.064		13.909		3.3	47.1	49.6
					Mg ₂ TiO ₄	16	8.443				2.2	32.9	64.9
					C-ZrO ₂	5	4.939				30.4	36.0	33.6
ZTM-5	15.0/15.7	19.0/24.4	66.0/59.9	1530 / 7	MgTiO ₃	92	5.062		13.897		3.3	47.9	48.7
					Mg ₂ TiO ₄	3	8.541				1.6	36.1	62.3
					M-ZrO ₂	5	5.133	5.202	5.312	99.234	46.8	20.4	32.8
				1530 / 12	MgO	18	4.213				3.8	4.1	92.1
					Mg ₂ TiO ₄	49	8.449				5.0	33.1	61.9
					Delta	28	9.256		8.704		-	-	-
				1680 / 5	M-ZrO ₂	16	5.144	5.202	5.311	99.206	96.6	2.0	1.4
					MgO	65	4.211				5.7	5.2	89.1
					Mg ₂ TiO ₄	18	8.449				8.5	30.5	61.0
ZTM-6-1	59.0/56.6	29.0/33.9	12.0/9.5	1530 / 7	Delta	1	9.246	8.702			53.5	18.1	28.4
					C-ZrO ₂	16	4.992				52.3	19.9	27.8
					MgO	25	4.211				3.0	2.3	94.7
				1680 / 5	Mg ₂ TiO ₄	59	8.443				3.4	32.9	63.7
					C-ZrO ₂	14	4.944				45.0	25.5	29.5
					MgO	30	4.211				0.3	0.4	99.3
				1880 / 2	Mg ₂ TiO ₄	56	8.452				2.5	34.2	63.3
					M-ZrO ₂	53	5.108	5.146	5.313	98.966	83.2	15.7	1.2
					MgTi ₂ O ₅	34	9.774	10.017	3.750		-	-	-
ZTM-6-2	59.0/55.2	29.0/33.4	12.0/11.4	1530 / 7	β-(Zr _x Ti _{1-x}) ₂ O ₄	13	4.819	5.444	5.033		51.8	47.3	0.9
					M-ZrO ₂	47	5.100	5.130	5.312	98.871	82.3	16.9	0.8
					MgTi ₂ O ₅	39	9.785	10.027	3.748		5.2	62.1	32.8
				1680 / 5	β-(Zr _x Ti _{1-x}) ₂ O ₄	14	4.828	5.424	5.033		50.7	47.5	1.8
					M-ZrO ₂	68	5.092	5.118	5.317	98.740	80.4	16.4	3.2
					MgTi ₂ O ₅	24	9.803	10.027	3.753		7.1	61.2	31.8
				1880 / 2	β-(Zr _x Ti _{1-x}) ₂ O ₄	8	4.806	5.464	5.046		57.2	40.8	2.0
					M-ZrO ₂	56	5.113	5.157	5.310	99.037	86.1	13.0	0.9
					MgTi ₂ O ₅	44	9.776	10.021	3.751		10.6	56.9	32.5
ZTM-7	20.0/19.1	55.0/55.4	25.0/25.5	1530 / 7	M-ZrO ₂	52	5.111	5.150	5.308	99.042	85.4	12.9	1.8
					MgO	48	9.788	10.033	3.752		6.0	61.3	32.7
					M-ZrO ₂	47	5.095	5.123	5.309	98.771	80.4	17.9	1.7
				1680 / 5	MgTi ₂ O ₅	47	9.798	10.029	3.753		6.1	62.9	31.1
					β-(Zr _x Ti _{1-x}) ₂ O ₄	6	4.872	5.414	5.014		52.7	46.6	0.7
					M-ZrO ₂	16	5.115	5.160	5.310	99.040	63.4	28.9	7.7
				1880 / 2	MgTi ₂ O ₅	82	9.774	10.023	3.751		7.6	55.5	36.9
					β-(Zr _x Ti _{1-x}) ₂ O ₄	2	4.769	5.464	5.046		42.4	56.1	1.5
					M-ZrO ₂	14	5.106	5.136	5.315	98.883	81.4	16.8	1.8
ZTM-8	20.0/19.1	55.0/55.4	25.0/25.5	1530 / 7	MgTi ₂ O ₅	83	9.788	10.035	3.753		5.1	61.9	33.1
					β-(Zr _x Ti _{1-x}) ₂ O ₄	3	4.800	5.464	5.046		-	-	-
					M-ZrO ₂	6	5.101	5.153	5.305	98.597	37.0	43.1	19.9
				1680 / 5	MgTi ₂ O ₅	92	9.799	10.033	3.757		6.3	63.5	30.2
					β-(Zr _x Ti _{1-x}) ₂ O ₄	2	4.805	5.465	5.047		-	-	-
					M-ZrO ₂	6	5.101	5.153	5.305	98.597	37.0	43.1	19.9
				1880 / 2	MgTi ₂ O ₅	92	9.799	10.033	3.757		6.3	63.5	30.2
					β-(Zr _x Ti _{1-x}) ₂ O ₄	2	4.805	5.465	5.047		-	-	-
					M-ZrO ₂	6	5.101	5.153	5.305	98.597	37.0	43.1	19.9

ZTM-8	80.0/79.6	10.0/9.0	10.0/11.4	1530 / 12	M-ZrO ₂	42	5.137	5.194	5.308	99.172	95.8	2.8	1.4
					MgTiO ₃	49	5.059		13.895		9.0	46.8	44.3
					MgTi ₂ O ₅	9	9.825	10.049	3.761	-	-	-	
				1680 / 5	M-ZrO ₂	10	5.133	5.184	5.311	99.108	83.1	14.6	2.3
					C-ZrO ₂	80	4.963				49.5	28.3	22.3
					MgTi ₂ O ₅	10	9.785	10.065	3.767		9.2	58.7	32.1
ZTM-9	51.0/53.8	25.0/25.2	24.0/21.0	1880 / 2	M-ZrO ₂	44	5.125	5.184	5.319	98.947	94.4	4.5	1.2
					C-ZrO ₂	56	5.046				78.6	9.5	11.9
				1530 / 12	M-ZrO ₂	70	5.141	5.198	5.310	99.208	93.0	5.6	1.4
					MgTiO ₃	18	5.061		13.891		3.0	49.6	45.9
					Mg ₂ TiO ₄	12	8.417				3.7	34.6	61.8
ZTM-10	40.0/40.3	20.0/20.8	40.0/38.9	1680 / 5	M-ZrO ₂	60	5.140	5.195	5.311	99.193	96.2	2.6	1.2
					C-ZrO ₂	40	5.004				69.3	12.2	18.5
				1880 / 2	C-ZrO ₂	100	4.970				54.3	23.8	21.9
ZTM-11	60.0/62.4	12.0/13.2	28.0/24.4	1530 / 7	M-ZrO ₂	21	5.144	5.201	5.311	99.214	91.7	3.2	5.0
					Delta	79	9.254		8.700		57.5	15.8	26.6
				1600 / 7	M-ZrO ₂	16	5.147	5.203	5.314	99.220	-	-	-
					Delta	84	9.258		8.705		-	-	-
				1680 / 5	C-ZrO ₂	90	5.003				64.3	12.1	23.7
					MgO	10	4.212				-	-	-
				1880 / 2	C-ZrO ₂	49	4.995				63.3	13.2	23.5
					Delta'	51	9.299		8.688		24.9	2.7	72.4
ZTM-12	59.0/61.6	14.0/13.8	27.0/24.6	1530 / 12	M-ZrO ₂	26	5.144	5.200	5.312	99.195	94.9	2.7	2.4
					Delta	74	9.238		8.694		58.6	14.7	26.7
				1600 / 7	M-ZrO ₂	16	5.143	5.201	5.312	99.207	96.5	2.2	1.3
					Delta	84	9.236		8.693		57.2	15.8	27.0
				1662 / 1	C-ZrO ₂	65	4.997				-	-	-
					Delta	35	9.244	8.700			-	-	-
				1677 / 1	C-ZrO ₂	100	4.992				-	-	-
				1680 / 5	C-ZrO ₂	100	4.994				62.1	14.7	23.2
					C-ZrO ₂	100	4.993				62.2	14.3	23.5
				DTA – 1643	M-ZrO ₂	18	5.141	5.198	5.310	99.172	-	-	-
					Delta	82	9.232		8.688		-	-	-
				DTA – 1683	M-ZrO ₂	18	5.145	5.194	5.309	99.127	-	-	-
					C-ZrO ₂	47	5.005				-	-	-
					Delta	35	9.244		8.696		-	-	-
ZTM-13	23.5/25.2	2.2/2.3	74.3/72.5	1530 / 12	M-ZrO ₂	24	5.145	5.203	5.311	99.196	-	-	-
					MgO	59	4.211				-	-	-
					Delta	17	9.260	8.702			-	-	-
				1680 / 5	C-ZrO ₂	39	5.039				72.9	6.8	20.4
					MgO	61	4.213				2.1	0.3	97.7
				1880 / 2	C-ZrO ₂	37	5.034				68.3	6.4	25.2
ZTM-14	10.0/10.1	50.0/55.5	40.0/34.4	1680 / 5	MgO	63	4.212				3.9	0.4	95.8
					C-ZrO ₂	2	4.947				42.7	32.2	25.1
					MgTiO ₃	24	5.058	13.903			1.5	52.6	45.9
				1880 / 10 m	MgTi ₂ O ₅	74	9.848	10.076	3.768		9.9	59.7	30.4
					C-ZrO ₂	2	4.947				26.2	41.3	32.5
					MgTiO ₃	26	5.063	13.906			2.2	52.1	45.7

Chemical analysis of specimens has shown good accordance to their nominal compositions except of the sample ZTM-3-3. The reason of such significant deviation was the problem with the filtration of co-precipitated mixture described above. The accordance of the measured chemical compositions of the samples to their nominal composition was sufficient for the investigation of the phase relations in the system. However, the samples corresponding to the pseudo binary system between MgTi₂O₅ and zirconia (ZTM-3 and ZTM-6) were produced one more time to get more reasonable accordance to their nominal compositions.

3.1. Solid phase relations

At 1530 K, samples were annealed for 7 days. Based on development of microstructures; samples ZTM-3-1, -4, -5, -10 were additionally heat treated for 12 days. Samples ZTM-8, -9, -12 and -13 were initially annealed 12 days long. Finally established isothermal section at 1530 K is presented in the Figure 2. It should be noted that the T-ZrO₂ phase, which was not stabilized by TiO₂ and MgO, transformed into M-ZrO₂ during cooling and identified by XRD.

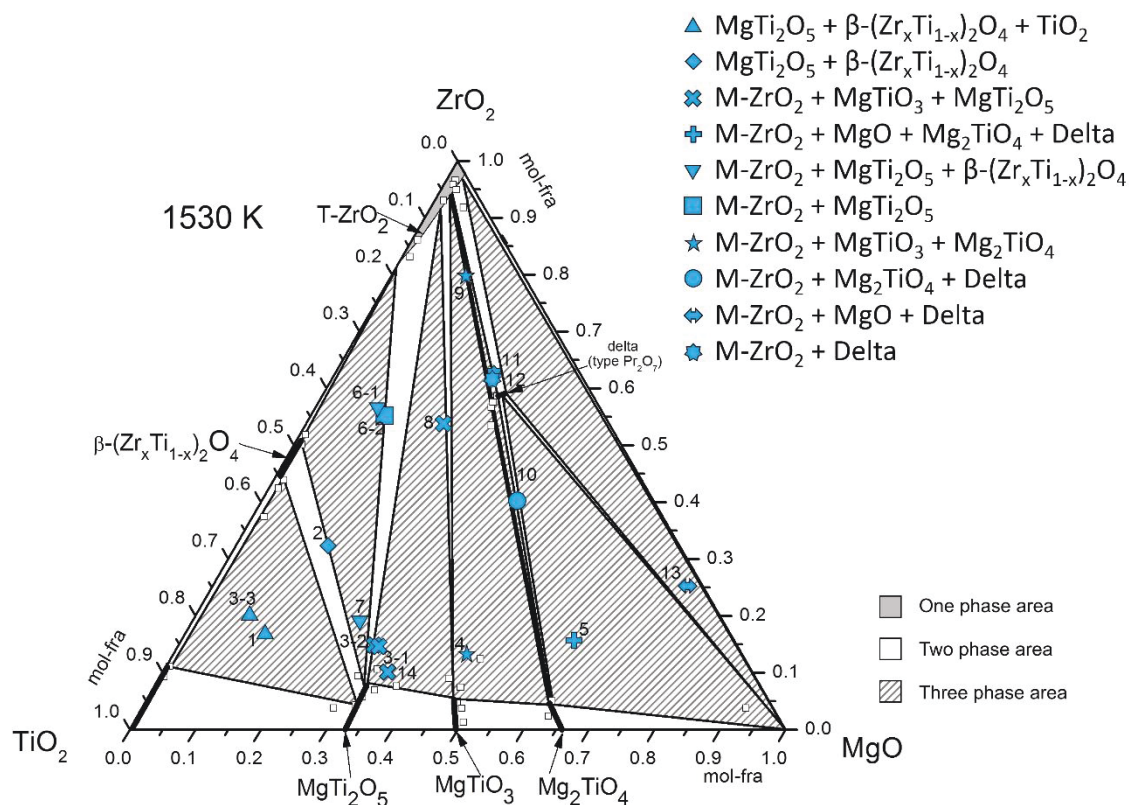


Fig.2. Constructed isothermal section of the ZrO_2 – TiO_2 – MgO system at 1530 K.

A new ternary compound similar to δ -phase $\text{Y}_4\text{Zr}_3\text{O}_{12}$, which is the ordered phase of fluorite structure (C-ZrO_2), so-called Delta phase, was discovered at 1530 K. The Delta phase was initially found in the phase assemblage of ZTM-4 and ZTM-5. Results of phase analysis by XRD showed more than three phases were present in the samples ZTM-4 and ZTM-5 annealed at 1530 K. Moreover, the SEM analysis of the samples ZTM-4 and ZTM-5 showed poorly-developed fine microstructure (Figure 3a and 3b). This is clear indication, that these samples did not reach an equilibrium state. The amount of the Delta phase in the microstructure of the samples ZTM-4 and ZTM-5 did not allow reliable measuring the chemical composition of the phase, only rough estimate. Therefore, the composition of sample ZTM-10 was selected with higher concentration of ZrO_2 and lower of MgO which is closer to estimated composition of Delta phase. The SEM analysis showed that the microstructure (Fig. 3c) of the sample ZTM-10 was too fine to measure chemical composition by EDX detector. However, XRD phase analysis of ZTM-10 indicated three phase assemblage $\text{MgTiO}_3 + \text{Mg}_2\text{TiO}_4 + \text{Delta}$ containing 59 vol.% of Delta phase. It allowed calculating possible chemical composition of the Delta phase using lever rule. According to this calculation, the sample ZTM-11 was produced in the assumed one-phase field of the Delta phase. XRD of ZTM-11 revealed the large amount of the Delta phase (79 mol.% of Delta) coexisting with M-ZrO_2 .

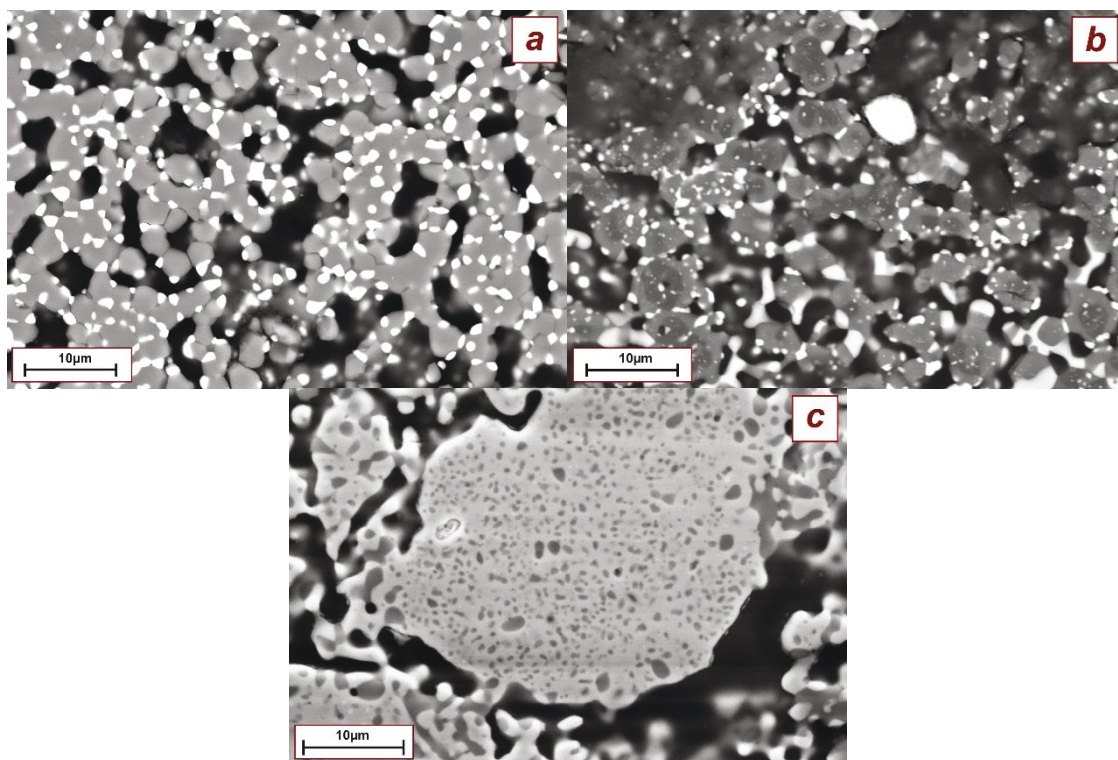


Fig. 3. Microstructures of annealed samples: a) ZTM-4 at 1530 K for 7 days, b) ZTM-5 at 1530 K for 7 days, c) ZTM-10 at 1530 K for 7 days.

Amount of the phase in the microstructure (Fig. 4a) was enough to measure the chemical composition of the phase. According to the measured EDX results, nominal chemical composition was chosen for the sample ZTM-12. Unfortunately, real chemical composition of the sample ZTM-12, as well as of sample ZTM-11 deviated from selected ratio. XRD results of sample ZTM-12 shown even less amount of the Delta phase (74 mol.% of Delta). According to the XRD results, this ternary compound had trigonal structure of the Pr_7O_{12} structure type with the average lattice parameters of $a=9.244 \text{ \AA}$, $c=8.696 \text{ \AA}$. Difference between experimental lattice parameters in different samples was very insignificant. Therefore, it can be concluded that this compound is almost stoichiometric. Additionally, it was confirmed by microstructural investigations. The experimentally measured chemical compositions of the Delta phase in different samples using SEM/EDX was practically the same within uncertainty of applied method (see Table 2). Average chemical composition was 57.5 mol.% of ZrO_2 , 15.7 mol.% of TiO_2 and 26.8 mol.% of MgO . Deviation from the average value was around $\pm 2 \text{ mol.}\%$. Microstructures of ZTM-11 and -12 are presented in the Figures 4a and 4b.

According to measured chemical composition of the Delta phase, this compound can be described by chemical formula as $\text{Zr}_4\text{TiMg}_2\text{O}_{12}$. Similarity between this compound and $\text{Y}_4\text{Zr}_3\text{O}_{12}$ can be seen as following. The $\text{TiO}_2\text{--MgO}$ and $\text{ZrO}_2\text{--MgO}$ couples in equimolar ratio are equivalent to substitute Y_2O_3 in the composition. It should be also mentioned that metastable phase $\text{Mg}_2\text{Zr}_5\text{O}_{12}$ with the sample structure was found in the $\text{ZrO}_2\text{--MgO}$ system^[21]. However, further structural investigations of the Delta phase are necessary to determine occupancies of crystallographic positions by cations in the structure.

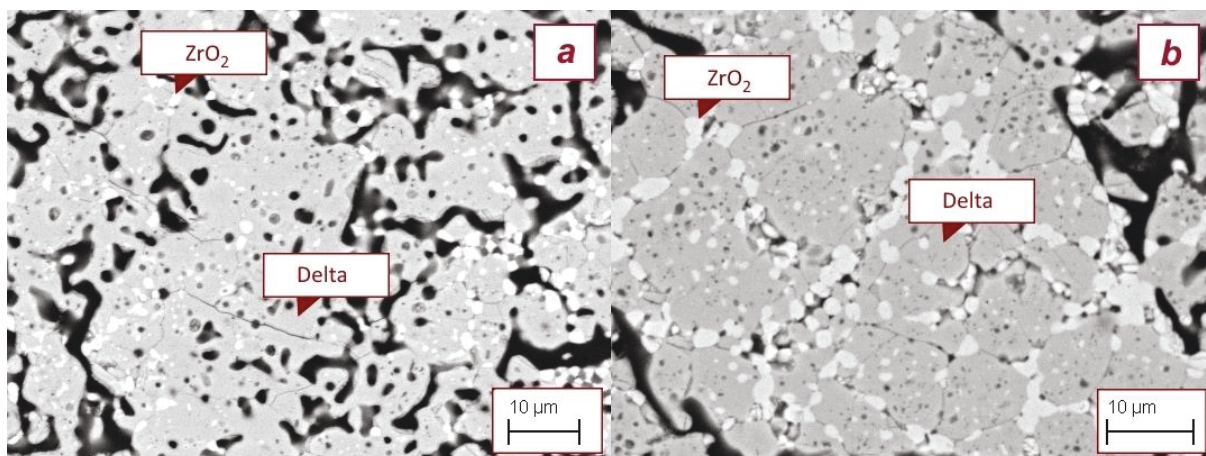


Fig.4. Microstructures of annealed samples: a) ZTM-11 at 1530 K for 7 days, b) ZTM-12 at 1530 K for 12 days.

In Figure 5a, there are results of differential thermal analysis of sample ZTM-12 with the large amount of the Delta phase. The first heat effect at 1403 K corresponds to the monoclinic-tetragonal transformation of zirconia. As mentioned above T- ZrO_2 phase was not stabilized by addition of TiO_2 and transformation into M- ZrO_2 was always observed on cooling of heat treated samples as well as in DTA. This should be kept in mind also while consider results of Table 2. The second peak was complex corresponding to several transformations. In order to distinguish all heat effects constituting this peak, we have performed a peak separation procedure using CALISTO software (SETARAM Inc). Based on the peak separation (Fig. 5b), additional DTA experiments were performed in combination with X-ray analysis. The sample ZTM-12 heat treated at 1530 K (Table 3) was divided into two parts and heated up to 1643 K and 1683 K in DTA. Afterwards, XRD analysis was performed (Table 3). Based on obtained results, it was established that the first deviation the red peak corresponded to increasing of the solubility of the T- ZrO_2 in the Delta phase. The green peak corresponded to the transformation of the Delta phase into C- ZrO_2 . Blue peak was assigned to transformation of the remaining T- ZrO_2 to C- ZrO_2 . It should be pointed out, that due to finite rate of the reaction the Delta phase was found in the phase assemblage after DTA up to 1683 K. However, it can be assumed that the destabilization of the Delta phase occurred at 1664 K, because the amount of Delta phase substantially decreased in comparison with results at 1643 K. In order to confirm this, additional annealing was performed at 1662 K and 1677 K. At 1662 K, 35 vol.% of Delta phase was found in the sample after long time annealing, while at 1677 K, no Delta phase was indicated by XRD. The XRD results for sample ZTM-12 are listed in the Table 3. Therefore it was concluded, that the Delta phase is stable up to 1664 K.

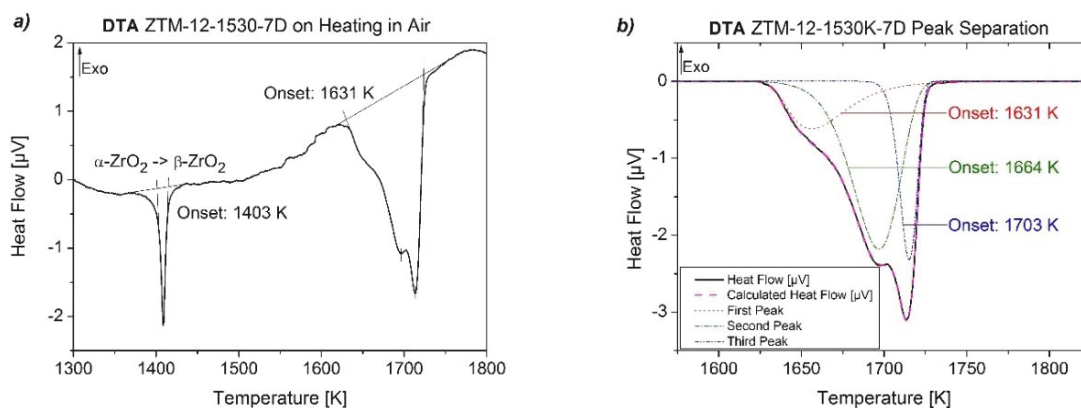


Fig.5. DTA on heating for sample ZTM-12: a) DTA curve from 1300 to 1800 K, b) Peak separation.

Table 3. XRD results after DTA and annealing of the sample ZTM-12.

Temperature, K	XRD / phase (vol.%)
1530, initial	Delta (74) + M-ZrO ₂ (26)
1643	Delta (82) + M-ZrO ₂ (18)
1683	Delta (35) + M-ZrO ₂ (18) + C-ZrO ₂ (47)
1750	C-ZrO ₂ (100)
1662 for 1 day	Delta (35) + C-ZrO ₂ (65)
1667 for 1 day	C-ZrO ₂ (100)

Additionally, there was an inconsistency between XRD results of some samples. As it was mentioned above, the XRD of the samples ZTM-4 and -5 indicated presence of more than three phases. In order to establish tie lines of the isothermal section, it was decided to anneal the samples ZTM-3-1, -4, -5, -10 at 1530 K for a longer time (12 days). XRD patterns of the annealed samples are presented in the Figures 6a and 6b. XRD results of samples ZTM-3-1, -4, -10 annealed for 12 days showed results that were consistent with other data. In accordance with other samples, MgO, Mg₂TiO₄ and Delta phase were expected in the sample ZTM-5 annealed for 12 days. However, more monoclinic phase than Delta was determined in comparison to the sample annealed for 7 days. In the microstructures of the sample ZTM-5 annealed duration of 7 and 12 days (Figures 7a and 7b), it was clearly seen, that the samples annealed for 12 days showed well developed microstructure in comparison to samples annealed for 7 days. To explain this inconsistency, it is assumed that a decomposition of the Delta phase into M-ZrO₂ could occur during cooling after heat treatment. Since, there was no contradictions between experimental data from other samples, the tie line of the sections at 1530 K were definitely established based on the phase assemblage of other samples as presented in Fig. 2.

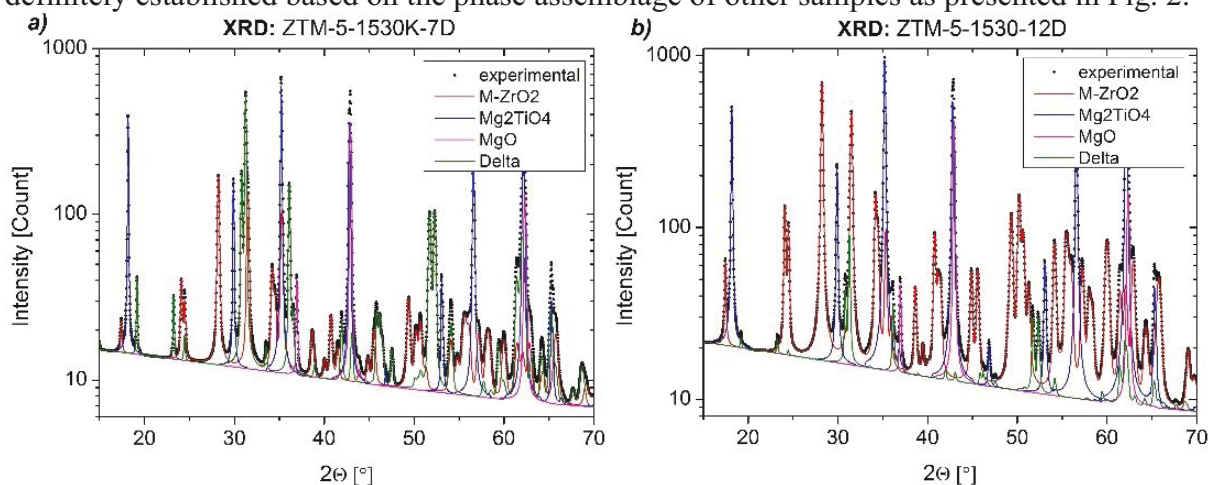


Fig.6. XRD result of the ZTM-5 sample annealed at 1530 K for: a) 7 days, b) 12 days.

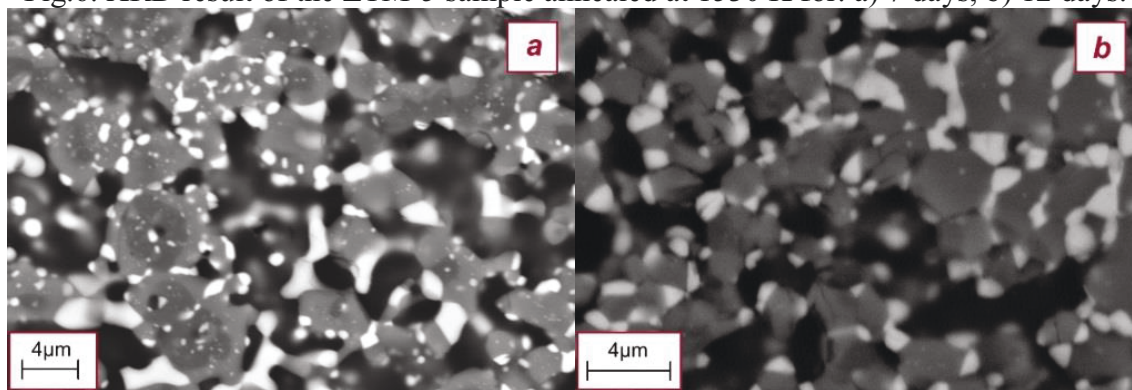


Fig.7. Microstructures of the ZTM-5 sample annealed at 1530 K for: a) 7 days, b) 12 days.

As it was mentioned above, the Delta phase is stable up to 1664 K. Therefore, samples ZTM-11 and ZTM-12 were annealed at 1600 K in order to get more equilibrated microstructure and to measure more precisely chemical composition of the Delta phase. However, there was insignificant deviation between EDX results of the samples annealed at 1530 K and 1600 K.

At 1680 K, there was no Delta phase in the samples ZTM-5, 10-13, that was in good agreement with the DTA results described above. Constructed isothermal section at 1680 K is presented in the Figure 8. A wide ternary extension of homogeneity range was found for C- ZrO_2 . Additionally, we have determined very limited solubility of MgO in β -($\text{Zr}_x\text{Ti}_{1-x}$) $_2\text{O}_4$, as well as in T- ZrO_2 phase and more substantial solubility of ZrO_2 in the intermediate compounds of the TiO_2 – MgO system (Mg_2TiO_4 , MgTiO_3 and MgTi_2O_5). SEM analysis of the samples annealed at 1680 K showed well equilibrated microstructure (Figures 9a-f). Based on SEM/EDX results, we have determined possible ranges of the ternary area of C- ZrO_2 phase and solubility ranges on the Mg_2TiO_4 , MgTiO_3 and MgTi_2O_5 compounds. It should be noted that SEM/EDX results were consistent with XRD and well equilibrated phase assemblages were observed. Measured solubility ranges of ZrO_2 in these compounds were 3.0, 3.4 and 5.2 mol.% respectively. It should be mentioned that the obtained results are in good agreement with data of Tseng ^[2] indicating formation of secondary C- ZrO_2 in mixtures with 2.5 mol.% ZrO_2 . The composition of fluorite phase 25.0 MgO –37.5 TiO_2 –37.5 ZrO_2 (in mol.%) determined by Tseng ^[2] is also in agreement with phase diagram constructed in the present work (see Fig. 8). However formation of TiO_2 in addition to fluorite phase at 5 and 15 mol.% of ZrO_2 is not compatible with equilibrium phase diagram.

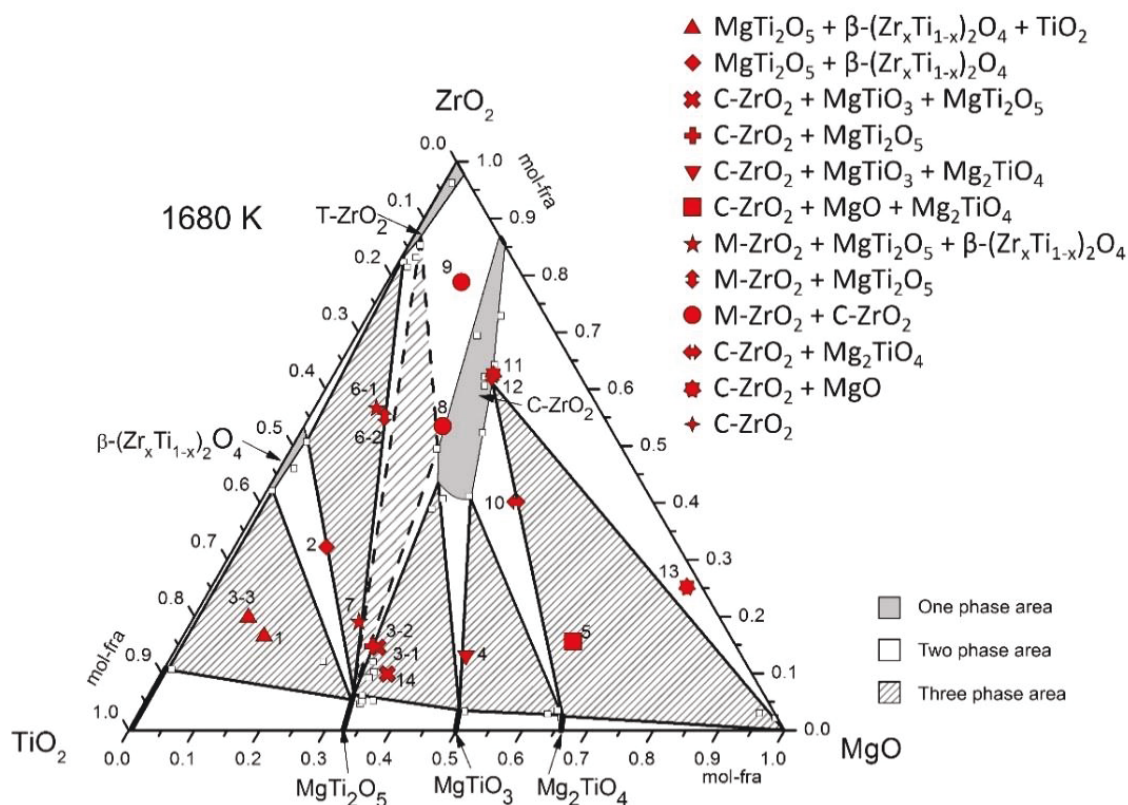


Fig.8. Constructed isothermal section of the ZrO_2 – TiO_2 – MgO system at 1680 K.

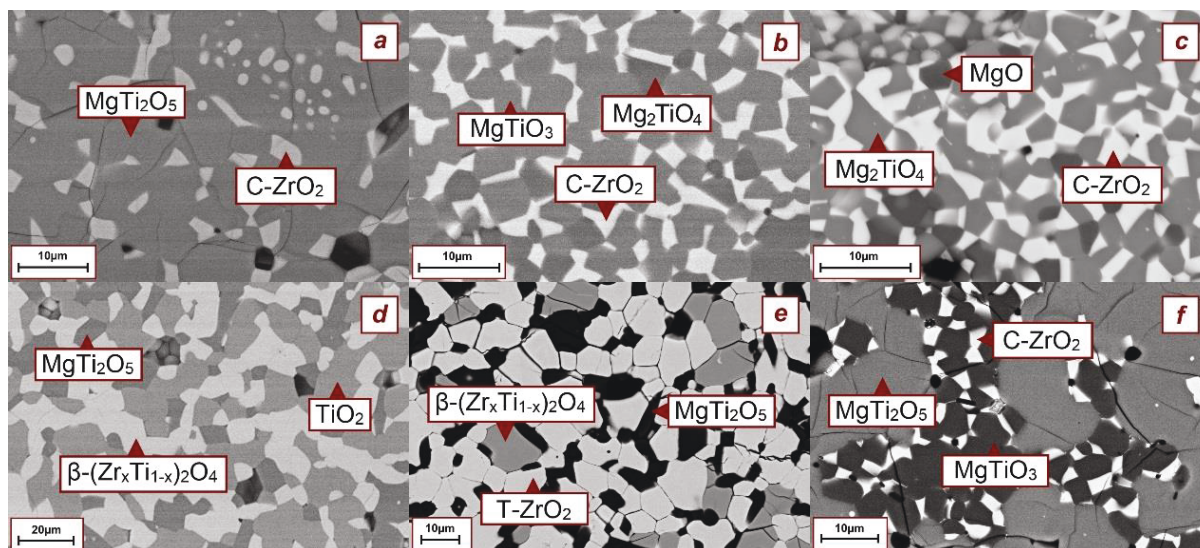


Fig.9. Microstructures of samples annealed at 1680 K for 5 days: a) ZTM-3-1, b) ZTM-4, c) ZTM-5; d) ZTM-3-3; e) ZTM-6-1; f) ZTM-14.

Constructed isothermal section at 1880 K is presented in the Figure 10. At this temperature, even larger extension of the C-ZrO₂ phase into ternary system was observed than at 1680 K while the similar solubility of the third component in the other binary compounds was determined. The measured compositions of C-ZrO₂ phase are in a good agreement with results of Bayer ^[3] synthesized cubic ZrO₂ with compositions of 33.3MgO-33.3ZrO₂-33.3TiO₂ and 25.0MgO-37.5ZrO₂-37.5TiO₂ (in mol.%) at 1773-1873 K. Moreover, unexpected, a phase with similar trigonal structure of the Pr₇O₁₂ structure type was found in the sample ZTM-11. In the Figure 11 (labeled as a Delta'), the plates of this phase in the C-ZrO₂ matrix can be seen. According to the XRD and SEM/EDX results, lattice parameters ($a=9.299 \text{ \AA}$, $c=8.688 \text{ \AA}$) of the phase, as well as the chemical composition (23.5 mol.% of ZrO₂, 2.2 mol.% of TiO₂) of this phase differed from the Delta phase, which was found at lower temperatures. The chemical composition of the sample ZTM-13 was chosen equal to the chemical composition of the indicated phase. However, no such phase was found in the sample after annealing at 1880 K. Therefore, this phase was metastable, and could appear during cooling after heat treatment.

Additionally, partial melting was already observed in the microstructure of several samples annealed at 1880 K. Fields corresponding to the liquid phase can be seen in the Figures 12a and 12b. Partial melting of the samples could be identified in the microstructure due to a rounded shape of the main grains and eutectic fields of frozen liquid phase in between. It should be noted that XRD indicated the same phase assemblage for samples ZTM-6-1 annealed at 1680 and 1880 K. However, microstructure of sample ZTM-6-1 annealed at 1880 K (Fig. 12c) showed large grains of C-ZrO₂ which were decomposed during cooling. Based on the microstructural study the solid state transformation $\text{C-ZrO}_2 + \beta\text{-(Zr}_x\text{Ti}_{1-x})_2\text{O}_4 \leftrightarrow \text{T-ZrO}_2 + \text{MgTi}_2\text{O}_5$ was assumed and tie-line C-ZrO₂ + $\beta\text{-(Zr}_x\text{Ti}_{1-x})_2\text{O}_4$ was shown at 1880 K in contrast with XRD data.

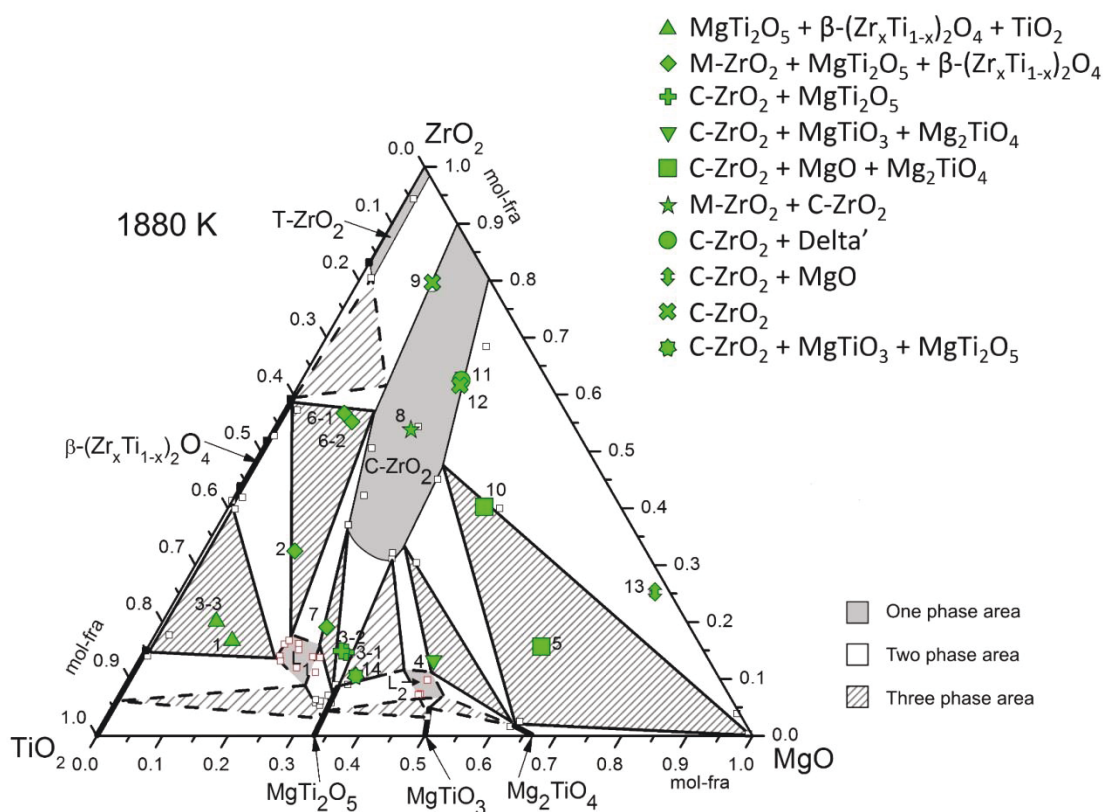


Fig.10. Constructed isothermal section of the ZrO_2 - TiO_2 - MgO system at 1880 K.

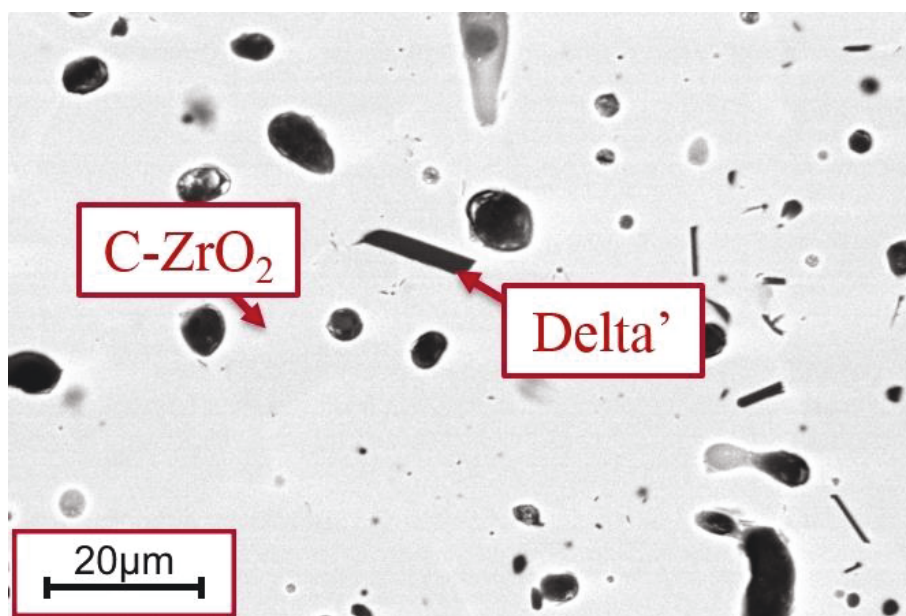


Fig.11. Microstructure of the ZTM-11 sample annealed at 1880 K during 7 days.

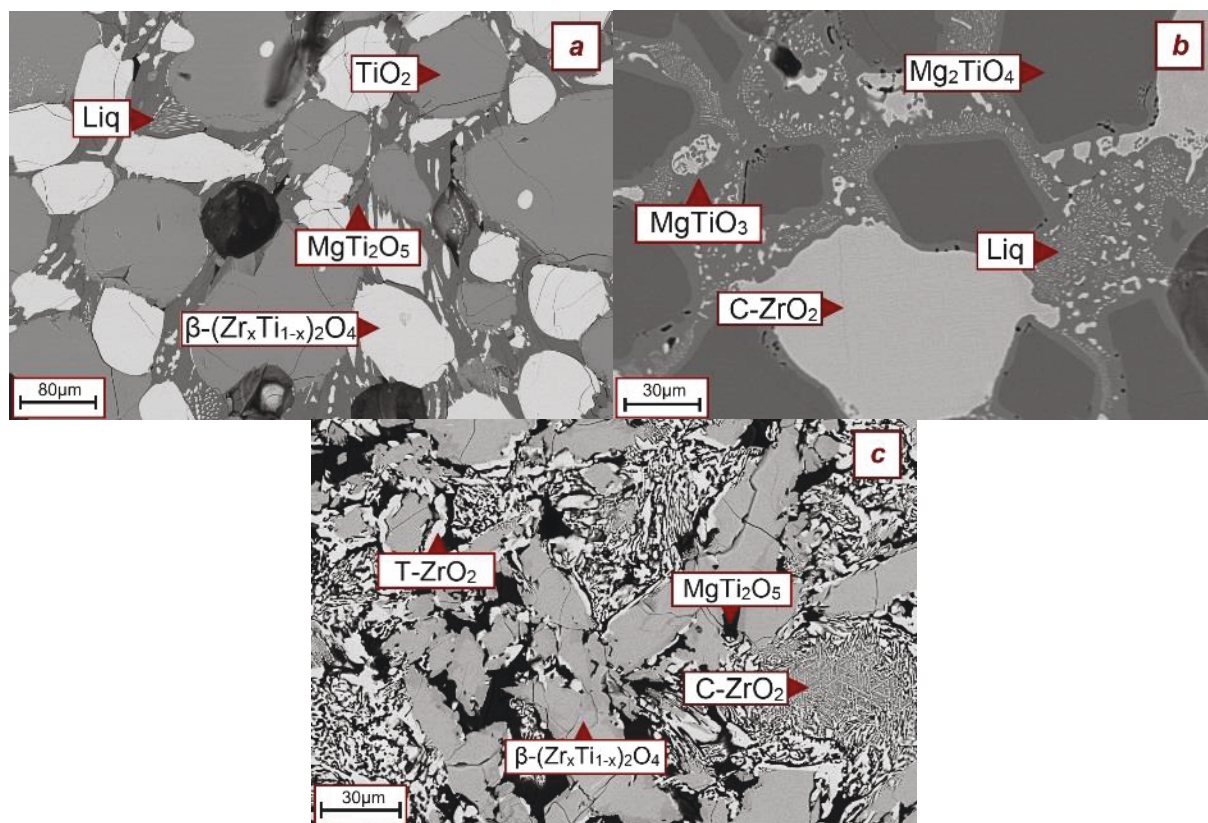


Fig.12. Microstructures of samples annealed at 1880 K for 2 days: a) ZTM-3-3, b) ZTM-4, c) ZTM-6-1.

3.2. Liquidus projection

Microstructural investigation of partially melted samples revealed, that in the $\text{ZrO}_2\text{--TiO}_2\text{--MgO}$ system there are three ternary eutectic reactions. Based on DTA and on the SEM/EDX results, temperatures and compositions of eutectics were determined to be:

- **E₁:** $\text{Liq} \leftrightarrow \text{MgTi}_2\text{O}_5 + \text{C-ZrO}_2 + \text{MgTiO}_3$ (1860 K; 8 ± 1 mol.% of ZrO_2 , 50 ± 2 mol.% of TiO_2 ; 42 ± 2 mol.% of MgO);
- **E₂:** $\text{Liq} \leftrightarrow \text{TiO}_2 + \beta\text{-(Zr}_x\text{Ti}_{1-x})_2\text{O}_4 + \text{MgTi}_2\text{O}_5$ (1851 K; 15 ± 1 mol.% of ZrO_2 , 64 ± 1 mol.% of TiO_2 ; 21 ± 2 mol.% of MgO);
- **E₃:** $\text{Liq} \leftrightarrow \text{C-ZrO}_2 + \beta\text{-(Zr}_x\text{Ti}_{1-x})_2\text{O}_4 + \text{MgTi}_2\text{O}_5$ (1800 K; 17 ± 1 mol.% of ZrO_2 , 62 ± 2 mol.% of TiO_2 ; 21 ± 2 mol.% of MgO);

It should be mentioned, the obtained results are in a good agreement with the established isothermal sections.

The melting temperatures of the samples ZTM-6-1, -3-3 and -4 were measured as 1800 K, 1851 K and 1872 K, respectively. The DTA curves on heating and cooling for these samples are shown in the Figures 13a, 13b and 13c. On heating of the sample ZTM-6-1 (Fig. 13a) several thermal effects were observed. The peak 1137 K corresponded to transformation of M-ZrO_2 to T-ZrO_2 . The effect at 1688 K was related to the transformation of the three phase assemblage $\text{T-ZrO}_2 + \beta\text{-(Zr}_x\text{Ti}_{1-x})_2\text{O}_4 + \text{MgTi}_2\text{O}_5$ into the assemblage $\text{C-ZrO}_2 + \beta\text{-(Zr}_x\text{Ti}_{1-x})_2\text{O}_4 + \text{MgTi}_2\text{O}_5$ due to reaction $\text{C-ZrO}_2 + \beta\text{-(Zr}_x\text{Ti}_{1-x})_2\text{O}_4 \leftrightarrow \text{T-ZrO}_2 + \text{MgTi}_2\text{O}_5$. It should be noted that this solid state reaction is reversible and corresponding effect can be seen on cooling (on-set 1582 K). The reversibility of solid state transformation explains why the same phase assemblage was found by XRD in sample ZTM-6-1 at 1680 and 1880 K. The effect at 1800 K was assigned to

the E_3 eutectic transformation. Peak at 1839 K showed the end of the melting. Microstructures of sample ZTM-6-1 after annealing at 1880 K and after DTA were very similar. In the microstructure of the samples ZTM-6-1 large areas of C- ZrO_2 decomposition was found, as well as phases β -($\text{Zr}_x\text{Ti}_{1-x}$) $_2\text{O}_4$, MgTi_2O_5 and T- ZrO_2 , while the E_3 eutectic was not observed (see Fig. 12c). Presence of decomposed C- ZrO_2 confirmed reversibility of solid state transformation. Chemical composition of the sample ZTM-6-1 lied far from the E_3 eutectic composition. The same phase assemblages were observed after heat treatment of sample ZTM-6-1 and ZTM-2 at 1880 K. However microstructure investigation of sample ZTM-2 annealed at 1880 K revealed the areas of the E_3 eutectic crystallization (Fig. 14a). Additionally, it should be mentioned, that a decomposition of the C- ZrO_2 phase observed in the microstructures of samples ZTM-6-1 and ZTM-2 was in a good accordance with the results of Bayer ^[3] who indicated that C- ZrO_2 decomposed during heat treatment at 1373 and 1473 K.

Microstructures of the samples ZTM-3-3 and -4 after DTA are presented in the Figures 14b and 14c. The heat effect observed at 1851 K in the sample ZTM-3-3 was assigned to eutectic reaction $L \leftrightarrow \beta$ -($\text{Zr}_x\text{Ti}_{1-x}$) $_2\text{O}_4$ + TiO_2 + MgTi_2O_5 (E_2). Microstructure of the sample ZTM-3-3 after melting in the DTA indicated primary crystals of β -($\text{Zr}_x\text{Ti}_{1-x}$) $_2\text{O}_4$, big grains of TiO_2 , matrix of MgTi_2O_5 and areas of E_2 eutectic. Microstructure of the sample ZTM-4 after DTA indicated primary crystals of C- ZrO_2 , big grains of Mg_2TiO_4 , matrix of MgTiO_3 and eutectic areas. It should be noted that measured composition of eutectic in sample ZTM-4 was outside the three-phase assemblage Mg_2TiO_4 + MgTiO_3 + C- ZrO_2 . This indicated to the non-equilibrium character of crystallization which probably finished by crystallization of eutectic $L \leftrightarrow \text{MgTiO}_3$ + C- ZrO_2 + MgTi_2O_5 (E_1). Therefore during heating in DTA the transition reaction $L + \text{Mg}_2\text{TiO}_4 \leftrightarrow \text{MgTiO}_3 + \text{C-}\text{ZrO}_2$ (U_2) occurred at 1872 K in the sample ZTM-4 (Fig. 14c). The microstructure of sample ZTM-4 after annealing at 1880 K also showed large grains of Mg_2TiO_4 and C- ZrO_2 , matrix MgTiO_3 and eutectic areas (Fig. 12b). In order to prove that liquid composition in the sample ZTM-4 corresponded to eutectic E_1 $L \leftrightarrow \text{MgTiO}_3 + \text{C-}\text{ZrO}_2 + \text{MgTi}_2\text{O}_5$, the sample ZTM-14 with composition corresponding to $\text{MgTiO}_3 + \text{C-}\text{ZrO}_2 + \text{MgTi}_2\text{O}_5$ phase assemblage was produced. The phase assemblage stable in samples ZTM-14 heat treated at 1680 and 1880 K was confirmed by XRD. DTA heating curve for ZTM-14 showed that the temperature of the melting was 1860 K (Fig. 13d). The E_1 eutectic areas were found in the sample ZTM-14 (Fig. 14d) and its composition was very close to the eutectic observed in the sample ZTM-4. Thus our assumption that eutectic E_1 crystalized in the sample ZTM-4 was confirmed. The fact that melting temperature of sample ZTM-14 was lower than of sample ZTM-4 is in agreement with our initial assumption that the reaction observed during heating of ZTM-4 sample was transitional while the reaction in the sample ZTM-14 was eutectic. In order to define the temperature of the transition reaction of $L + \text{MgO} \leftrightarrow \text{Mg}_2\text{TiO}_4 + \text{C-}\text{ZrO}_2$ (U_1), the samples ZTM-5 was investigated by DTA. The results are presented in Fig. 13e.

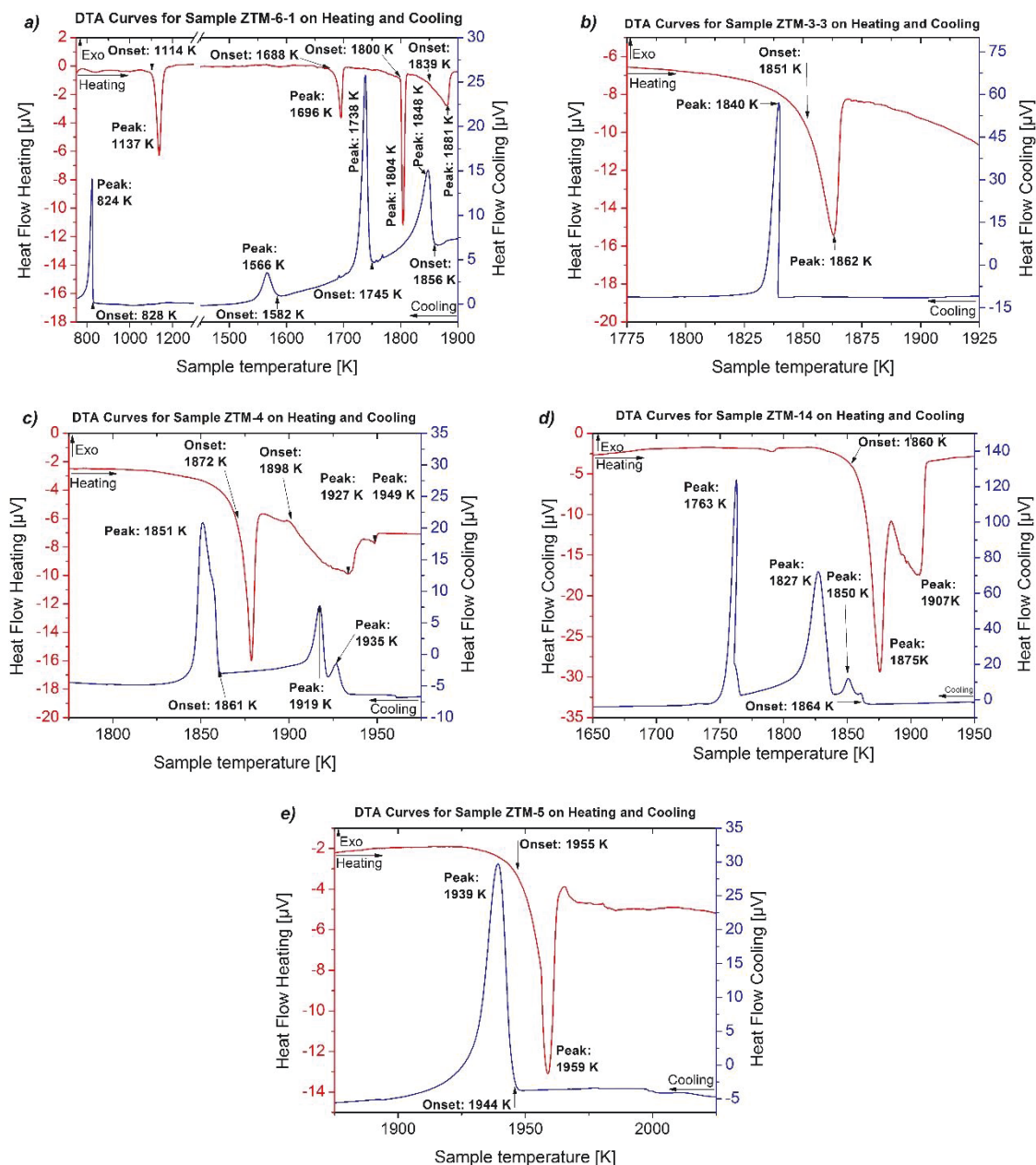


Fig.13. DTA on heating and cooling for samples: a) ZTM-6-1, b) ZTM-3-3, c) ZTM-4, d) ZTM-14 and e) ZTM-5.

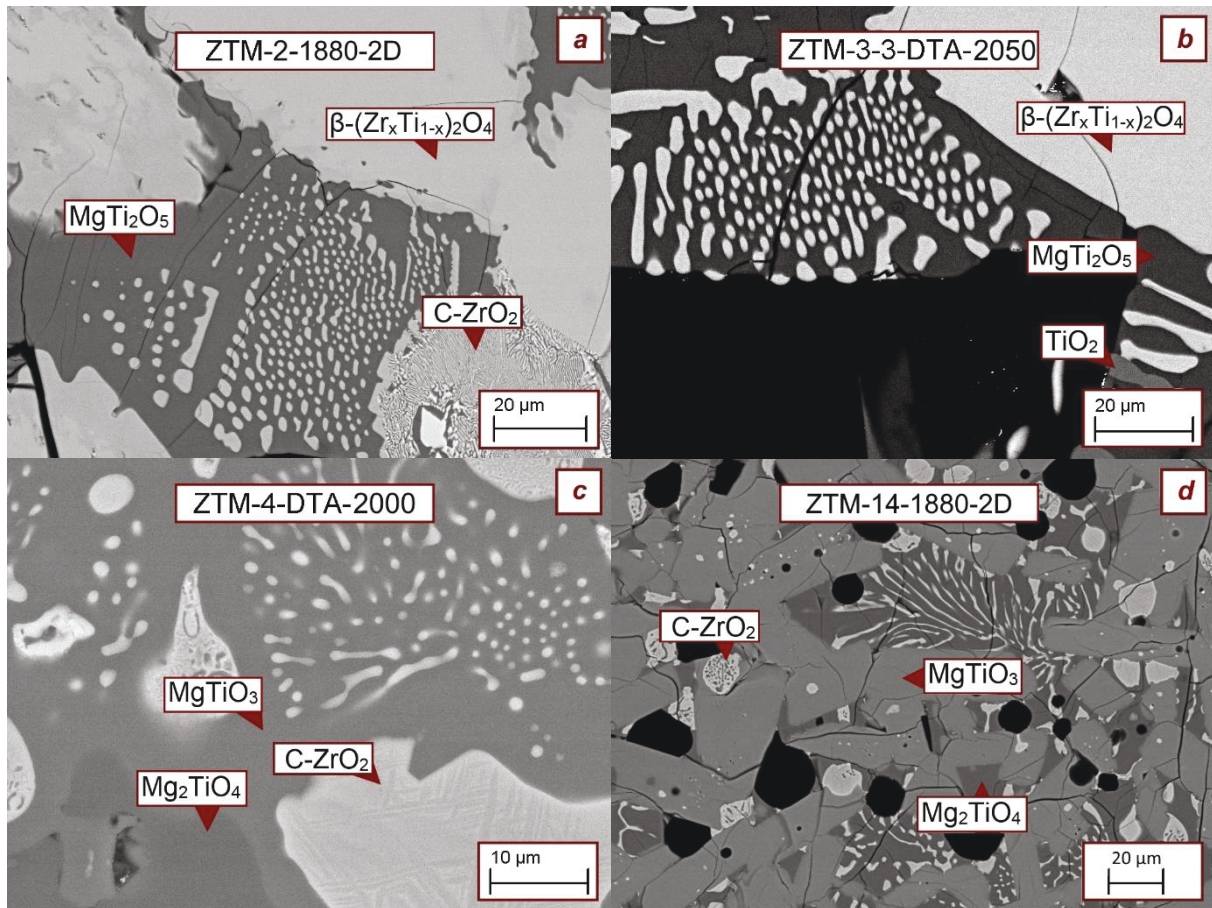


Fig.14. Microstructures of samples: a) ZTM-2 annealed at 1880 K, b) ZTM-3-3 after DTA, c) ZTM-4 after DTA and d) ZTM-14 annealed at 1880 K.

It should be mentioned, that XRD results of the sample ZTM-3-2 showed two phases: the pseudo-brookite MgTi_2O_5 and cubic zirconia C-ZrO_2 in the equilibrated state (Table 2). Moreover, no obvious partial melting was indicated in the microstructure of the sample ZTM-3-2 after annealing at 1880 K (Figure 15a). The DTA heating curve of this sample showed an effect at 1909 K (Figure 15b). Primary crystals of MgTi_2O_5 , small grains of C-ZrO_2 and eutectic with chemical composition of 20.3 mol.% ZrO_2 , 50.5 mol.% TiO_2 and 29.2 mol.% MgO were determined in the microstructure of the sample after DTA (Figure 15c).

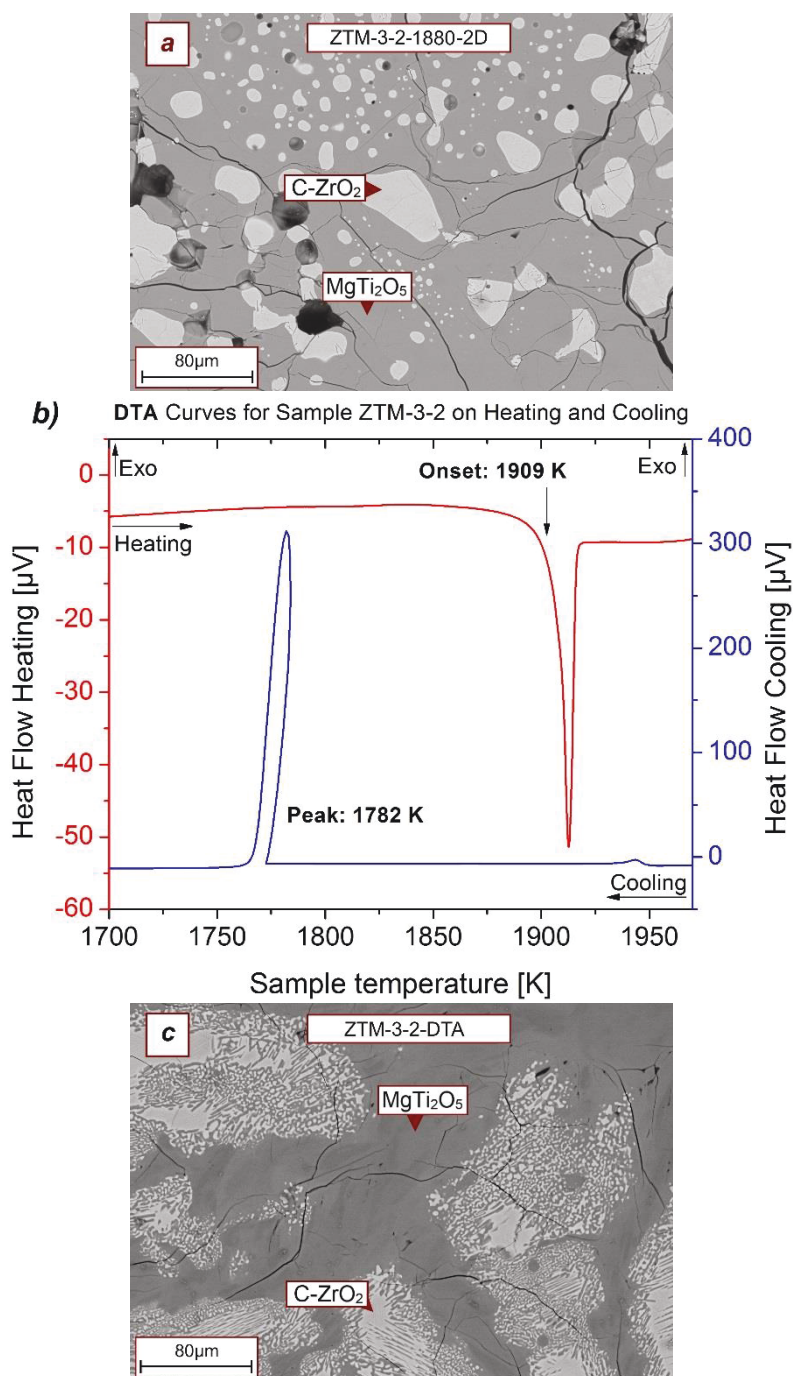


Fig.15. a) Microstructures of the sample ZTM-3-2 annealed at 1900 K for 2 days; b) DTA on heating and cooling of the sample ZTM-3-2; c) Microstructures of the sample ZTM-3-2 after DTA.

Since the chemical composition of the sample ZTM-3-2 lies on the pseudo-binary system between the pseudo-brookite MgTi₂O₅ and cubic zirconia C-ZrO₂, measured temperatures should correspond to the eutectic maximum ($e_{4\max}$) on the univariant line $L \leftrightarrow C\text{-ZrO}_2 + \text{MgTi}_2\text{O}_5$ in the ZrO₂–TiO₂–MgO system. Another eutectic maximum ($e_{5\max}$) should exist on the univariant line $L \leftrightarrow \beta\text{-(Zr}_x\text{Ti}_{1-x})_2\text{O}_4 + \text{MgTi}_2\text{O}_5$ between E₂ and E₃ eutectics corresponding to quasi-binary section $\beta\text{-(Zr}_x\text{Ti}_{1-x})_2\text{O}_4 + \text{MgTi}_2\text{O}_5$. However such composition would be difficult to get because compositions of E₂ and E₃ eutectics are close to each other.

Based on differential thermal analysis and microstructural investigations, liquidus projection of the $\text{ZrO}_2\text{--TiO}_2\text{--MgO}$ system was constructed (Figure 16). All invariant reactions in the ternary $\text{ZrO}_2\text{--TiO}_2\text{--MgO}$ system are presented in Table 4.

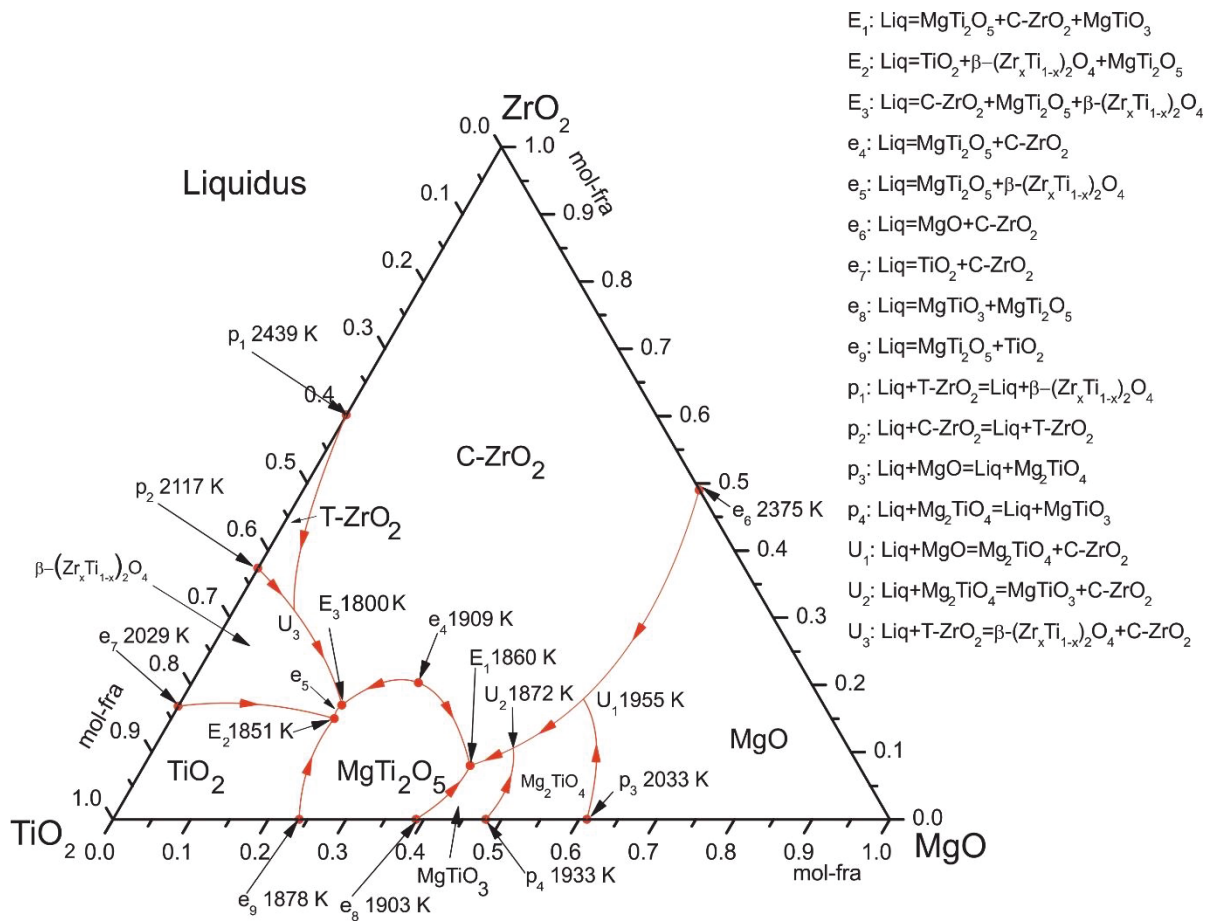


Fig.16. Constructed liquidus projection of the $\text{ZrO}_2\text{--TiO}_2\text{--MgO}$ system.

Table 4. Invariant equilibria in the $\text{ZrO}_2\text{--TiO}_2\text{--MgO}$ system.

Reaction	T (K)	Type	Phase	Composition, mol. %		
				ZrO_2	TiO_2	MgO
$\text{Liq} \leftrightarrow \text{MgTi}_2\text{O}_5 + \text{C-ZrO}_2 + \text{MgTiO}_3$	1860	Eutectic E_1	Liq	8	50	42
			MgTi_2O_5	-	-	-
			C-ZrO_2	2	36	62
			MgTiO_3	3	52	45
$\text{Liq} \leftrightarrow \text{TiO}_2 + \beta\text{-(Zr}_x\text{Ti}_{1-x})_2\text{O}_4 + \text{MgTi}_2\text{O}_5$	1851	Eutectic E_2	Liq	15	64	21
			TiO_2	14	85	1
			$\beta\text{-(Zr}_x\text{Ti}_{1-x})_2\text{O}_4$	43	56	1
			MgTi_2O_5	5	63	32
$\text{Liq} \leftrightarrow \text{C-ZrO}_2 + \text{MgTi}_2\text{O}_5 + \beta\text{-(Zr}_x\text{Ti}_{1-x})_2\text{O}_4$	1800	Eutectic E_3	Liq	17	62	21
			C-ZrO_2	23	49	28
			MgTi_2O_5	6	64	30
			$\beta\text{-(Zr}_x\text{Ti}_{1-x})_2\text{O}_4$	1	53	46
$\text{Liq} \leftrightarrow \text{MgTi}_2\text{O}_5 + \text{C-ZrO}_2$	1909	Eutectic max e_4	Liq	20	51	29
			MgTi_2O_5	11	59	30
			C-ZrO_2	31	41	28
$\text{Liq} \leftrightarrow \beta\text{-(Zr}_x\text{Ti}_{1-x})_2\text{O}_4 + \text{MgTi}_2\text{O}_5$	-	Eutectic max e_5	Liq	-	-	-
			$\beta\text{-(Zr}_x\text{Ti}_{1-x})_2\text{O}_4$	-	-	-
			MgTi_2O_5	-	-	-
$\text{Liq} + \text{MgO} \leftrightarrow \text{Mg}_2\text{TiO}_4 + \text{C-ZrO}_2$	1955	Transition reaction U_1	Liq	-	-	-
			MgO	-	-	-
			Mg_2TiO_4	-	-	-
			C-ZrO_2	-	-	-
$\text{Liq} + \text{Mg}_2\text{TiO}_4 \leftrightarrow \text{MgTiO}_3 + \text{C-ZrO}_2$	1872	Transition reaction U_2	Liq	-	-	-
			MgO	-	-	-
			Mg_2TiO_4	-	-	-
			C-ZrO_2	-	-	-
$\text{Liq} + \text{T-ZrO}_2 \leftrightarrow \beta\text{-(Zr}_x\text{Ti}_{1-x})_2\text{O}_4 + \text{C-ZrO}_2$	-	Transition reaction U_3	Liq	-	-	-
			T-ZrO_2	-	-	-
			$\beta\text{-(Zr}_x\text{Ti}_{1-x})_2\text{O}_4$	-	-	-
			C-ZrO_2	-	-	-

4. Conclusions

$\text{ZrO}_2\text{--TiO}_2\text{--MgO}$ system was experimentally investigated in the temperature range from 1530 K to melting temperatures using XRD, SEM/EDX and DTA. Isothermal sections of the system were constructed based on experimental data at 1530, 1680 and 1880 K. It has been determined that T-ZrO_2 phase is not stabilized in this system and transforms to monoclinic structure on cooling. Ternary compound described by formula $\text{Zr}_4\text{TiMg}_2\text{O}_{12}$ has been discovered. Homogeneity range of the compound was not established. However, based on experimental results, it can be stated that the homogeneity range is insignificant and this compound is almost stoichiometric. The ternary compound has a trigonal structure of the Pr_7O_{12} -structure type. Nevertheless, further crystallographic investigations are necessary to establish the cations position in the crystal structure of the phase. Temperature limit of the phase stability of the ternary compound has been determined to be 1664 K. Using results obtained by DTA and SEM/EDX, liquidus projection for the $\text{ZrO}_2\text{--TiO}_2\text{--MgO}$ system has been constructed. The eutectic reactions $\text{Liq} \leftrightarrow \text{C-ZrO}_2 + \beta\text{-(Zr}_x\text{Ti}_{1-x})_2\text{O}_4 + \text{MgTi}_2\text{O}_5$, $\text{Liq} \leftrightarrow \text{TiO}_2 + \beta\text{-(Zr}_x\text{Ti}_{1-x})_2\text{O}_4 + \text{MgTi}_2\text{O}_5$ and $\text{Liq} \leftrightarrow \text{MgTi}_2\text{O}_5 + \text{C-ZrO}_2 + \text{MgTiO}_3$ have been determined at 1800 K, 1851 K and 1872 K respectively. Established phase relations can be used to determine stability of materials used for industrial applications. Obtained experimental data will be applied for optimization of thermodynamic parameters of the $\text{ZrO}_2\text{--TiO}_2\text{--MgO}$ system. However, thermodynamic properties of the new ternary compound such as enthalpy of formation,

standard entropy and heat capacity are necessary in order to obtain a reliable thermodynamic description.

Acknowledgments

The authors thank the German Research Foundation (DFG) for funding within the Collaborative Research Center SFB 799 TRIP-Matrix Composite subproject C2. In addition, we thank B. Bleiber and Dr. C. Schimpf (Institute of Materials Science, TU Bergakademie Freiberg) for technical contribution.

References

- [1] R. Rieke, A. Ungewiss, *Ber. D. Deutschen Keram. Ges.* 17 (1936) 237.
- [2] C.-F. Tseng, *J. Alloys Compd.* 509 (2011) 9447.
- [3] G. Bayer, *J. Am. Ceram. Soc.* 53 (1970) 294.
- [4] H. Biermann, U. Martin, C.G. Aneziris et al., *Adv. Eng. Mater.* 11 (2009) 1000.
- [5] S. Martin, S. Richter, S. Decker et al., *Steel Research int.* 82 (2011) 1133.
- [6] C. Weigelt, H. Berek, C.G. Aneziris et al., *Ceram. Int.* 41 (2015) 2328.
- [7] D. Pavlyuchkov, G. Savinykh, O. Fabrichnaya, *Adv. Eng. Mater.* 15 (2013) 618.
- [8] I. Saenko, M. Ilatovskaia, G. Savinykh et al., *J. Am. Ceram. Soc.* 101 (2018) 386.
- [9] M. Ilatovskaia, I. Saenko, G. Savinykh et al., *J. Am. Ceram. Soc.* 101 (2018) 5198.
- [10] P. Bouvier, E. Djurado, G. Lucazeau, T. Le Bihan, *Phys. Rev. B* 62 (2000) 8731.
- [11] M. Winterer, R. Delaplane, R. McGreevy, *J. Appl. Crystall.* 35 (2002) 434.
- [12] W. Gonschorek, *Z. f. Kristall.* 160 (1982) 187.
- [13] P. Bordet, A. McHale, A. Santoro, R.S. Roth, *J. Solid State Chem.* 64 (1986) 30.
- [14] M. Dondi, F. Matteucci, G. Cruciani, *J. Solid State Chem.* 179 (2006) 233.
- [15] R. Christofferson, P.K. Davies, *J. Am. Ceram. Soc.* 75(1992) 563.
- [16] E. Schiebold, *Z. f. Kristall.* **1921**, 56, 430.
- [17] B.A. Wechsler, R.B. von Dreele, *Acta Cryst. Sec. B* 45 (1989) 542.
- [18] L.W. Coughanour, R.S. Roth, S. Marzullo et al., *J. Res. Nat. Bur. Stand.* 54 (1955) 191.
- [19] L. Lutterotti, *MAUD CPD Newsletter (IUCr)* 24 (2000).
- [20] O. Fabrichnaya, M.J. Kriegel, D. Pavlyuchkov et al., *Thermochim. Acta* 558 (2013) 74.
- [21] C. Howard, E.H. Kisi, R.B. Roberts, R.J. Hill, *J. Am. Ceram. Soc.* 73 (1990) 2828.

Publication P5: I. Saenko, O. Fabrichnaya, Heat capacity measurements of the δ -phase $\text{Mg}_2\text{Zr}_{4.2}\text{Ti}_{0.8}\text{O}_{12}$ and thermodynamic modelling of the $\text{ZrO}_2\text{--TiO}_2\text{--MgO}$ System, *Journal of the European Ceramic Society* 40 (2020) 3304–3313. DOI: 10.1016/j.jeurceramsoc.2020.02.047

Contributions to the paper:

Authors	Contribution [%]	Particular contribution
I. Saenko	65	<ul style="list-style-type: none"> • Experimental work • Evaluation of data • Thermodynamic modelling • Composition of the manuscript
Dr. rer. Nat. habil. O. Fabrichnaya	35	<ul style="list-style-type: none"> • Supervision of the work • Work on the manuscript

Heat capacity measurements and thermodynamic modelling of the ZrO_2 – TiO_2 – MgO System

I. Saenko and O. Fabrichnaya*

Institute of Materials Science, Technical University Bergakademie Freiberg, Gustav-Zeuner-Str. 5, 09599 Freiberg, Germany

*Corresponding author:

O.Fabrichnaya, Institute of Materials Science, Technical University Bergakademie Freiberg, Gustav-Zeuner-Str. 5, 09599 Freiberg, Germany

E-mail address: fabrich@ww.tu-freiberg.de

Abstract

Phase equilibria in the ZrO_2 – TiO_2 – MgO system have been studied experimentally using powder X-ray diffraction. Isothermal sections were constructed at 1475 K and 1555 K. The eutectoid reaction of δ -phase $\leftrightarrow \text{Mg}_2\text{TiO}_4 + \text{T-ZrO}_2 + \text{MgO}$ and the solid transition reaction of δ -phase + $\text{MgTiO}_3 \leftrightarrow \text{Mg}_2\text{TiO}_4 + \text{T-ZrO}_2$ were determined at temperatures of 1503 K and 1535 K, respectively. Heat capacity measurements for the δ -phase have been performed in the temperature range from 210 K to 1370 K. Debye temperature of the δ -phase was estimated. Standard entropy for the δ -phase was evaluated. Based on the obtained experimental data, a self-consistent thermodynamic description of the ZrO_2 – TiO_2 – MgO system has been developed.

1. Introduction

Materials based on the ZrO_2 – TiO_2 – MgO system exhibit high interest for industrial applications due to their dielectric properties [1,2]. The MgTiO_3 ceramics are one among the leading materials for microwave frequency applications. Thereby, a small substitution of Zr for Ti increases density of the material and improves dielectric properties [2]. All intermediate compounds of the TiO_2 – MgO sub-system, namely Mg_2TiO_4 , MgTiO_3 , and MgTi_2O_5 , are well-known minerals. Therefore, their thermodynamic properties are interesting for modelling of geological processes [3]. Moreover, the ZrO_2 – TiO_2 – MgO system plays an important role as a sub-system in the development of the manufacturing a novel composite material based on high-alloyed austenitic stainless TRIP-steel (Transformation Induced Plasticity) reinforced by MgO stabilized zirconia (Mg-PSZ) [4,5]. Such composite material undergoes a martensitic transformation of tetragonal modification of Mg-PSZ to monoclinic one during deformation resulting in additional strength increase [4]. Hereby, a coating of ceramic particles by minor addition of TiO_2 improves mechanical properties due to increase of bonding with the TRIP steel matrix [6].

According to literature data, the phase diagrams of binary sub-systems of the ternary ZrO_2 – TiO_2 – MgO system are well known. The last experimental investigation and thermodynamic modeling of the ZrO_2 – MgO system has been performed by Pavluchkov et al [7]. The ZrO_2 – TiO_2 and TiO_2 – MgO systems have been investigated and modelled last years by Saenko et al. [8] and Ilatovskaia et al. [3], respectively. Preliminary phase relations in the ZrO_2 – TiO_2 – MgO system were presented by Coughanour et al. [9] in 1955 for the first time. However, these data were scarce. Coughanour et al. have presented a tentative isothermal section in a temperature range between 1673 and 2023 K. Recently extensive investigation of phase relations in the ternary system was published by Saenko et al. [5]. Whereby, phase relations of the ZrO_2 – TiO_2 – MgO system were experimentally investigated in the temperature range from 1530 K to melting

temperatures using X-ray powder diffraction (XRD), scanning electron microscopy coupled with the energy-dispersive X-ray spectroscopy (SEM/EDX), and differential thermal analysis (DTA). Based on the obtained experimental data, isothermal sections at 1530 K, 1680 K and 1880 K as well as liquidus surface have been constructed. The eutectic reactions $\text{Liq} \leftrightarrow \text{C-ZrO}_2 + \beta\text{-(Zr}_x\text{Ti}_{1-x})_2\text{O}_4 + \text{MgTi}_2\text{O}_5$, $\text{Liq} \leftrightarrow \text{TiO}_2 + \beta\text{-(Zr}_x\text{Ti}_{1-x})_2\text{O}_4 + \text{MgTi}_2\text{O}_5$, and $\text{Liq} \leftrightarrow \text{MgTi}_2\text{O}_5 + \text{C-ZrO}_2 + \text{MgTiO}_3$ have been determined at 1800, 1851, and 1872 K, respectively. Additionally, it was shown, that tetragonal phase of zirconia (T-ZrO₂) could not be stabilized in this system and transforms back to monoclinic structure on cooling. However, the fluorite structure (C-ZrO₂) had a wide extension into ternary area and could be stabilized in a wide composition range [5].

Additionally, a new ternary compound with a crystal structure similar to $\delta\text{-Y}_4\text{Zr}_3\text{O}_{12}$ phase was revealed at 1530 K [5]. By analogy this new phase in the ZrO₂-TiO₂-MgO was called δ -phase [4]. The high temperature stability limit of this new δ -phase was determined to be 1664 K using DTA. The composition of this phase was measured using EDX 57.5 of ZrO₂, 15.7 of TiO₂ and 26.8 of MgO in molar percent. Based on the composition measurement for different samples it was found that the composition of δ -phase was not varied very much and it was assumed that the homogeneity range of the compound was quite limited [5]. The crystal structures of all solid phases of the ternary ZrO₂-TiO₂-MgO system based on the previous work [5] are listed in the Table 1. Experimental data obtained in work [4] are sufficient for thermodynamic parameters optimisation of the ZrO₂-TiO₂-MgO system except for thermodynamic properties of δ -phase such as enthalpy of formation, standard entropy and heat capacity which are necessary in order to obtain a reliable thermodynamic description. Moreover, further investigation of phase relations for compositions adjacent to the new δ -phase and at temperatures of its stability range of are important to understand all solid-state reactions and transitions involving δ -phase. Therefore, the aim of the present work is to measure the heat capacity of the δ -phase and investigate phase relations involving this phase. Based on the results of the preliminary calculations, additional selected experiments will be performed to verify calculated phase relations in the system. Afterwards, the thermodynamic parameters for the ZrO₂-TiO₂-MgO system will be optimized taking into account obtained experimental results of the present work. The resulting thermodynamic description is a part of large oxide system necessary for thermodynamic modelling of phase relations at the interface between ZrO₂-based particles and TRIP steel matrix.

Table 1. Data on crystal structures of solid phases of the ZrO_2 – TiO_2 – MgO system.

Phase	Crystal system	Space group	Pearson Symbol	Structure type	Ref.
C- ZrO_2	Cubic	$Fm\bar{3}m$	cF12	Fluorite- CaF_2	[10]
T- ZrO_2	Tetragonal	$P4_2/nmc$	tP6	HgI_2	[10]
M- ZrO_2	Monoclinic	$P12_1/c1$	mP12	-	[11]
TiO_2	Tetragonal	$P4_2/mnm$	tP6	Rutile	[12]
β -($\text{Zr}_x\text{Ti}_{1-x}$) $_2\text{O}_4$ (disordered)	Orthorhombic	$Pbcn$	oP12	α - PbO_2	[13]
α - TiZrO_4 (ordered)	Orthorhombic	$Pbcn$	-	-	[14,15]
α' - TiZrO_4 (Ti_2ZrO_6 -ordered)	Orthorhombic	$Pbcn$	oP36	-	[13]
MgO	Cubic	$Fm\bar{3}m$	cF8	NaCl	[16]
MgTiO_3	Trigonal	$R\bar{3}H$	hR10	Ilmenite- FeTiO_3	[17]
Mg_2TiO_4	Cubic	$Fd\bar{3}m$	cF56	Spinel- Al_2MgO_4	[17]
MgTi_2O_5	Orthorhombic	$Ccmm$	oS32	Pseudobrookite- Fe_2TiO_5	[17]
δ -phase	Trigonal	$R\bar{3}H$	hR19	Pr_7O_{12}	[5]

2. Materials and methods

2.1. Sample preparation

Samples were prepared using the co-precipitation method [5]. The zirconium acetate solution in acetic acid $\text{Zr}(\text{CH}_3\text{COO})_4$ (99.99 %, Sigma-Aldrich), titanium (III) sulfate solution $\text{Ti}_2(\text{SO}_4)_3 \cdot (99.99\%, \text{Alfa Aesar})$ and magnesium nitrate hexahydrate $\text{Mg}(\text{NO}_3)_2 \cdot 6\text{H}_2\text{O}$ (99.97%, Alfa Aesar) have been used as initial reagents. In the first step, the starting chemicals were diluted and dissolved by the distilled water in order to obtain a more suitable consistence for the co-precipitation process (solutions: 1.14 mol/l for the zirconium acetate solution, 0.643 mol/l for the titanium (III) sulfate solution and 0.494 mol/l for the magnesium nitrate hexahydrate). The concentration of obtained initial solutions was measured by Inductively Coupled Plasma - Optical Emission Spectrometry (ICP-OES) spectrometry. Calculated volumes of obtained solutions were mixed together in order to get ~2 g of oxide powder of desired molar ratio. The final mixture was dropped from a burette at a low speed (around 1 $\text{ml} \cdot \text{min}^{-1}$) into a beaker containing about 500 ml of the aqueous solution of NH_4OH with the pH value above 9.0. In order to control the chemical composition, co-precipitated suspension was analyzed by ICP-OES. After evaporation at 333 K during 1-2 h, the obtained substance was dried at 353 K for 2-3 days. Finally, a pyrolysis of the dried powder was performed at 1073 K for 3 h in the air atmosphere. The obtained oxide mixture was pressed into cylindrical pellets at 250 MPa and sintered in the air atmosphere in Pt-crucibles using NABERTHERM furnace in order to reach pseudo equilibrium state. Annealing duration was chosen based on data of the previous work [4] to be 16 days. Purity of the obtained samples was stated to be 99.99 % equal to the purity of initial reagents.

2.2. Sample treatment and characterization

Phase assemblages of annealed specimens have been identified by XRD with $\text{CuK}\alpha$ radiation ($\lambda = 1.5418 \text{ \AA}$) using the URD63 diffractometer (Seifert, FPM, Freiberg, Germany) equipped by graphite monochromator. The goniometer of the diffractometer has Bragg-Brentano geometry. The Rietveld refinement was applied using MAUD software [18] in order to characterize of all measured diffraction patterns. Based on the results of the Rietveld refinement, volume fractions of present phases as well as their lattice parameters were obtained.

2.3. Calorimetric measurements

Classical three-step continuous method [19] was used for heat capacity measurements by differential scanning calorimetry (DSC). The measurements were performed in the temperature range from 210 K up to 680 K using DSC 8000 device (Perkin Elmer, Pt/Rh crucible, Ar flow 20 ml/min, heating rate 10 K/min). The measurements were divided into small intervals of 150–200 K. The heat capacity measurements in the temperature range from 620 K to 1370 K were performed in the one step using the device DSC Pegasus 404C (NETZSCH, Pt/Rh crucible, Ar flow, heating rate 10 K/min). Calibration was performed using the certified standard sapphire material. The mass and radius of sample pellets were kept the close to standards c.a. 80 mg and 5 mm. The measurements of two different samples were repeated two times with maximal uncertainty 3%. In order to exclude any phase transformation during the heat capacity measurement, XRD analysis of the obtained samples were performed before the heat capacity measurements and afterward.

3. Thermodynamic modelling

The Thermo-Calc software was applied for the optimization of thermodynamic parameters based on the CALPHAD approach [20] and for phase diagram calculations using PARROT and POLY-3 modules, correspondently. Individual weights were given to every type of experimental data considering possible deviation and accuracy of the each experimental method [21]. Thermodynamic descriptions of binary sub-systems $\text{ZrO}_2\text{--MgO}$, $\text{ZrO}_2\text{--TiO}_2$ and $\text{TiO}_2\text{--MgO}$ were accepted from the works of Pavlyuchkov et al. [7], Saenko et al. [3] Ilatovskaya et al. [8], respectively.

Wide ternary extension of the fluorite structure (C--ZrO_2) into ternary system, as well as less substantial solubility of Mg_2TiO_4 , MgTiO_3 and MgTi_2O_5 were modelled by the sublattice model in form of the compound energy formalism described in detail by Hillert [22]. The compound energy formalism makes it possible to describe the Gibbs energy of solid solutions and compounds where two or more different sites in the crystal structure can be occupied by different atoms or ions or more complex species. Each Wyckoff positions in a crystal structure can be related to a specific sublattice in a phase model. Very limited solubility of MgO found in $\beta\text{-(Zr}_x\text{Ti}_{1-x})_2\text{O}_4$ was considered to be insignificant and was not modelled in the current thermodynamic description. The ternary δ -phase was described as stoichiometric compound $(\text{ZrO}_2)_{4.2}(\text{TiO}_2)_{0.8}(\text{MgO})_2$. This stoichiometry for the δ -phase was chosen based on the chemical composition measured in the previous work [5] and in order to reproduce all experimentally determined tie lines of isothermal sections of the present work and Ref. [5]. The liquid phase was described by the two-sublattice partially ionic model. Thermodynamic models for all stable phases in the $\text{ZrO}_2\text{--TiO}_2\text{--MgO}$ system are given in Table 2.

The experimental data on the temperature dependence of heat capacity for the δ -phase were fitted using the Mayer-Kelly equation (Eq.1). Obtained terms of the polynomial expression were used as fixed parameters for thermodynamic description of the Gibbs energy function of the δ -phase.

$$C_P(T) = a + b \cdot T - \frac{c}{T^2} \quad (1)$$

where a , b , c – fitted terms of the Mayer-Kelly equation.

In order to estimate standard entropy of the δ -phase, an extended Einstein (EE-model) model with physically motivated parameters was used to describe the temperature dependence of the heat capacity from 0 K. The EE-model was proposed at the Ringberg Workshop in 1995 [23]. The first term $C_V^{Einstein}(T)$ was proposed to describe the contribution from harmonic vibrations using the classical Einstein model (Eq.2) [23].

$$C_V^{Einstein}(T) = 3 \cdot R \cdot \left(\frac{\theta_E}{T}\right)^2 \cdot \frac{\exp\left(\frac{\theta_E}{T}\right)}{\left[\exp\left(\frac{\theta_E}{T}\right) - 1\right]^2} \quad (2)$$

where T is temperature, θ_E – Einstein temperature, R – the gas constant.

The second term of the EE-model was related to electronic excitations and low order anharmonic corrections (quasi-harmonic approximation). The third term contained the next order of anharmonic correction. In this work, the second and third terms of EE-model were chosen in accordance with the Mayer-Kelly equation (Eq.1) in the form of:

$$C_P^{EE}(T, \theta^{EE}) = C_V^{Einstein}(T) + aT + b/T^2 \quad (3)$$

where T is temperature, $\theta^{EE} = (\theta_E, a, b)$ is the vector of the unknown model parameters to be estimated, $C_V^{Einstein}(T)$ is the heat capacity describing phonon contribution using Einstein model, a and b are the second and third terms correspondently.

In the absence of the available data, Einstein temperature of new ternary compound was estimated based on the mass effects suggested by Grimvall [24] as follows.

$$\theta_E(A_aB_b) = \theta_E^A \cdot \frac{a}{a+b} + \theta_E^B \cdot \frac{b}{a+b} \quad (4)$$

where θ_E^A is the Einstein temperature of the component A, θ_E^B – Einstein temperature for the component B, a and b are stoichiometric coefficients.

Based on the EE model, it is possible to calculate standard entropy of the the δ -Phase by the integration from 0 K up to room temperature (RT).

$$S^{298} = \int_0^{RT} \frac{C_P^{EE}}{T} dT \quad (5)$$

Since this type of calculations includes only estimates, the obtained value of the standard entropy was taken into account as a start value for optimization of the thermodynamic description of the δ -phase.

Table 2. Thermodynamic models of phases in the ZrO₂–TiO₂–MgO system.

Phase	Thermodynamic model
C-ZrO ₂	(Mg ⁺² , Ti ⁺⁴ , Zr ⁺⁴) ₁ (O ⁻² , Va) ₂
T-ZrO ₂	(Mg ⁺² , Ti ⁺⁴ , Zr ⁺⁴) ₁ (O ⁻² , Va) ₂
M-ZrO ₂	(Mg ⁺² , Ti ⁺⁴ , Zr ⁺⁴) ₁ (O ⁻² , Va) ₂
TiO ₂	(Zr ⁺⁴ , Ti ⁺⁴) ₁ (O ⁻² , Va ⁻²) ₂
β-(Zr _x Ti _{1-x}) ₂ O ₄ (disordered)	(Zr ⁺⁴ , Ti ⁺⁴) ₂ (O ⁻²) ₄
α-TiZrO ₄ (ordered)	(TiO ₂)(ZrO ₂)
α'-TiZrO ₄ (Ti ₂ ZrO ₆ -ordered)	(TiO ₂) ₂ (ZrO ₂)
MgO	(MgO)
MgTiO ₃	(Mg ⁺²) ₁ (Ti ⁺⁴ , Zr ⁺⁴) ₁ (O ⁻²) ₃
Mg ₂ TiO ₄	(Mg ⁺² , Ti ⁺⁴) ₁ (Mg ⁺² , Ti ⁺⁴ , Zr ⁺⁴) ₂ (O ⁻²) ₄
MgTi ₂ O ₅	(Ti ⁺⁴ , Mg ⁺²) ₁ (Mg ⁺² , Ti ⁺⁴ , Zr ⁺⁴) ₂ (O ⁻²) ₅
δ-phase	(ZrO ₂) _{4.2} (TiO ₂) _{0.8} (MgO) ₂
Liquid	(Mg ⁺² , Ti ⁺² , Ti ⁺³ , Zr ⁺⁴)(O ⁻² , Va, O, TiO ₂)

4. Results and discussion

Samples #1–#5 were prepared using the co-precipitation method to obtain the most reliable sample for heat capacity measurements. Samples #6–#10 were produced in order to verify the thermodynamic description and to explain obtained inconsistencies observed during experiments that would be discussed in the section 4.2. Nominal and measured compositions of samples are listed in Table 3 as well as results of Rietveld refinement on phase assemblage in the annealed specimens. Raw samples were analysed by ICP-OES, annealed samples – by XRD. It should be noted that the T-ZrO₂ phase, which was not stabilized by TiO₂ and MgO, transformed into M-ZrO₂ during cooling and identified by XRD. Based on these ICP-OES results, it can be seen, that the chemical compositions match to the initial chemical composition within the error of the measurement.

4.1. Heat capacity

Based on XRD results measured after long time annealing, it was defined, that most of the five first samples contained three phases except of the sample #4, where only the δ-phase and M–ZrO₂ were found in the phase assemblage. The amount of the δ-phase was 79 vol.%, that corresponds 83 mol.%. Since the heat capacity is an additive function, C_P of a sample of two phases should represent a sum of their heat capacities in molar ratio. Similar to the previous work [5], the heat capacity for the δ-phase can be recalculated from experimental values of the sample #4 using the available heat capacity of M-ZrO₂ [25]. Consequently, it was decided that the obtained sample #4 was suitable for further heat capacity measurements.

Recalculated heat capacity data for the δ-phase were fitted by the Maier-Kelley equation (Eq.1). Polynomial expression is presented by following equation:

$$C_P \left(\frac{\text{J}}{\text{mol} \cdot \text{K}} \right) = 23.37 + 1.49 \cdot 10^{-3} T - 4.55 T^{-2} \quad (6)$$

Heat capacity calculated using Eq. 6 is presented in Fig. 1 together with experimental data and theoretical calculations by the Neumann-Kopp rule.

Table 3. Sample compositions and results of characterization by ICP-OES and XRD.

Sample	Nominal / measured sample composition [mol.%]			Temperature, [K] / Annealing time in days	XRD results	Vol. %	Lattice parameters, [Å]			
	ZrO ₂	TiO ₂	MgO				a	b	c	β [°]
#1	59.0/58.8	13.0/12.6	28.0/28.6	1475 / 16	M-ZrO ₂	65	5.149	5.201	5.317	99.211
					MgTiO ₃	4	5.054	13.898	-	-
					Mg ₂ TiO ₄	32	8.454	-	-	-
				1530 / 16	M-ZrO ₂	31	5.145	5.203	5.313	99.225
					MgO	3	4.210	-	-	-
					δ -phase	66	9.246	8.699	-	-
#2	61.0/60.8	8.0/7.4	31.0/31.8	1475 / 16	M-ZrO ₂	65	5.149	5.204	5.316	99.211
					Mg ₂ TiO ₄	27	8.449	-	-	-
					MgO	8	4.210	-	-	-
				1530 / 16	M-ZrO ₂	38	5.147	5.205	5.314	99.207
					MgO	15	4.212	-	-	-
					δ -phase	47	9.264	8.706	-	-
#3	58.6/58.3	14.3/11.7	27.1/30.0	1530 / 16	M-ZrO ₂	30	5.145	5.201	5.313	99.210
					MgTiO ₃	13	5.069	13.903	-	-
					δ -phase	57	9.236	8.698	-	-
#4	60.0/60.0	12.0/11.7	28.0/28.3	1475 / 16	M-ZrO ₂	65	5.151	5.204	5.318	99.211
					Mg ₂ TiO ₄	35	8.457	-	-	-
				1530 / 16	M-ZrO ₂	21	5.146	5.203	5.313	99.188
					δ -phase	79	9.254	8.703	-	-
				1530 / DSC	M-ZrO ₂	21	5.146	5.201	5.316	99.196
					δ -phase	79	9.253	8.703	-	-
#5	59.0/58.8	14.0/14.2	27.0/27.0	1475 / 16	M-ZrO ₂	47	5.150	5.202	5.318	99.200
					Mg ₂ TiO ₄	50	8.458	-	-	-
					MgTiO ₃	3	5.054	13.898	-	-
				1530 / 16	M-ZrO ₂	31	5.145	5.203	5.312	99.210
					MgTiO ₃	12	5.070	13.896	-	-
					δ -phase	57	9.246	8.698	-	-
#6	51.0/53.8	25.0/25.2	24.0/21.0	1475 / 16	M-ZrO ₂	58	5.141	5.194	5.314	99.183
					MgTiO ₃	42	5.060	13.906	-	-
				1555 / 16	M-ZrO ₂	52	5.139	5.196	5.312	99.187
					MgTiO ₃	48	5.060	13.901	-	-
#7	12.5/13.2	39.5/42.0	48.0/44.8	1475 / 16	M-ZrO ₂	13	5.146	5.201	5.314	99.166
					MgTiO ₃	69	5.067	13.912	-	-
					Mg ₂ TiO ₄	18	8.451	-	-	-
				1555 / 16	M-ZrO ₂	3	5.151	5.203	5.315	99.197
					MgTiO ₃	77	5.068	13.914	-	-
					Mg ₂ TiO ₄	10	8.452	-	-	-
#8	15.0/15.7	19.0/24.4	66.0/59.9	1475 / 16	δ -phase	10	9.244	8.702	-	-
					M-ZrO ₂	18	5.148	5.202	5.315	99.195
					Mg ₂ TiO ₄	64	8.452	-	-	-
					MgO	18	4.214	-	-	-
#9	40.0/40.3	20.0/20.8	40.0/38.9	1475 / 16	Mg ₂ TiO ₄	52	8.456	-	-	-
					M-ZrO ₂	44	5.148	5.199	5.316	99.189
					MgTiO ₃	4	5.054	13.898	-	-
				1555 / 16	Mg ₂ TiO ₄	40	8.451	-	-	-
					δ -phase	56	9.246	8.700	-	-
					MgTiO ₃	4	5.060	13.901	-	-
#10	23.5/25.2	2.2/2.3	74.3/72.5	1475 / 16	Mg ₂ TiO ₄	10	8.456	-	-	-
					M-ZrO ₂	37	5.150	5.202	5.316	99.181
					MgO	53	4.214	-	-	-

It can be seen that the heat capacity calculated using Neumann-Kopp rule deviates insignificantly at higher temperatures. Deviation reaches 4% at 1400 K with a tendency to grow even further. This fact underlines the importance of experimental measurement of heat capacity instead of using Neumann-Kopp rule for reliable thermodynamic description.

Using the mass effects suggested by Grimvall [24] (Eq.4), the Einstein temperature of new ternary compound was estimated to be $\theta_E^{\delta\text{-Phase}} = 516 \text{ K}$. All Einstein temperatures of compounds used for the calculation are presented in Table 4.

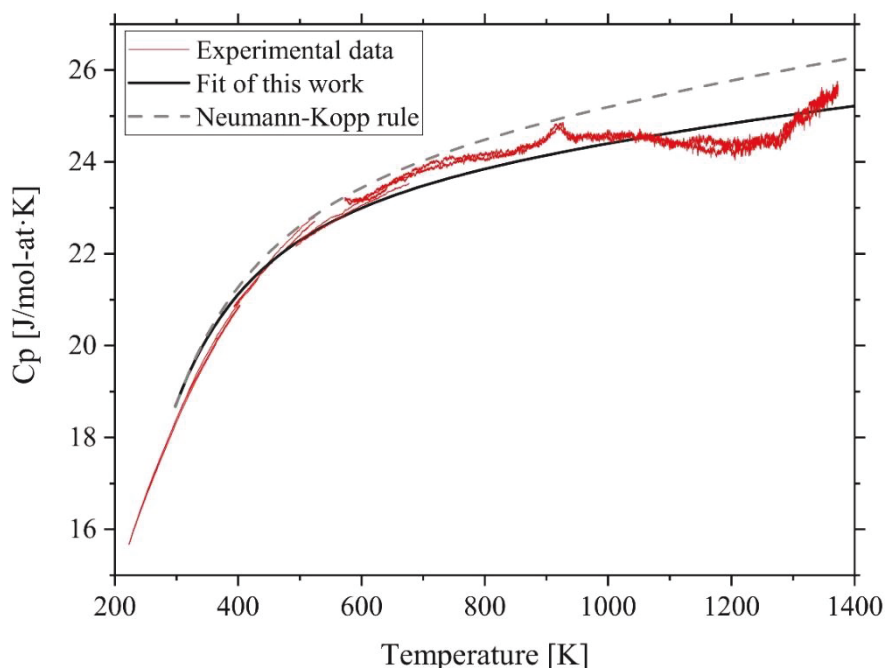


Fig. 1 – Experimental DSC data together with Maier-Kelly fit and Neumann-Kopp calculation.

Table 4. Einstein temperatures of main components and the δ -phase in the $\text{ZrO}_2\text{--TiO}_2\text{--MgO}$ system

Component	θ_E , K	Ref.
ZrO_2	439	[25]
TiO_2	670	[26,27]
MgO	589	[28]
δ -phase	516	Based on Grimvall's estimation [24], this work

Using calculated data of the Einstein temperature and DSC measurements enabled an application of an extended Einstein model (Eq.2) for the description from 0 K. Calculations based on obtained extended Einstein model (Eq.7) are presented in the Fig. 2 and coefficients of the equation are listed in Table 5. As it can be seen from the Fig. 5, both low and high temperature data are in excellent agreement and fitted together with low inaccuracy, which denotes relevance of the data.

$$C_p(T) = \frac{3 \cdot R \cdot \left(\frac{571}{T}\right)^2 \cdot e^{\frac{571}{T}}}{\left(e^{\frac{571}{T}} - 1\right)^2} + 1.3 \cdot 10^{-4} \cdot T + 1.04 \cdot 10^{-2} / T^2 \quad (7)$$

Based on the obtained fitted model of C_P , standard entropy of the δ -phase was calculated to be $S^{298} = \int_0^{298} C_P \frac{dT}{T} = 12.3 \text{ (J/mol – at} \cdot \text{K)}$.

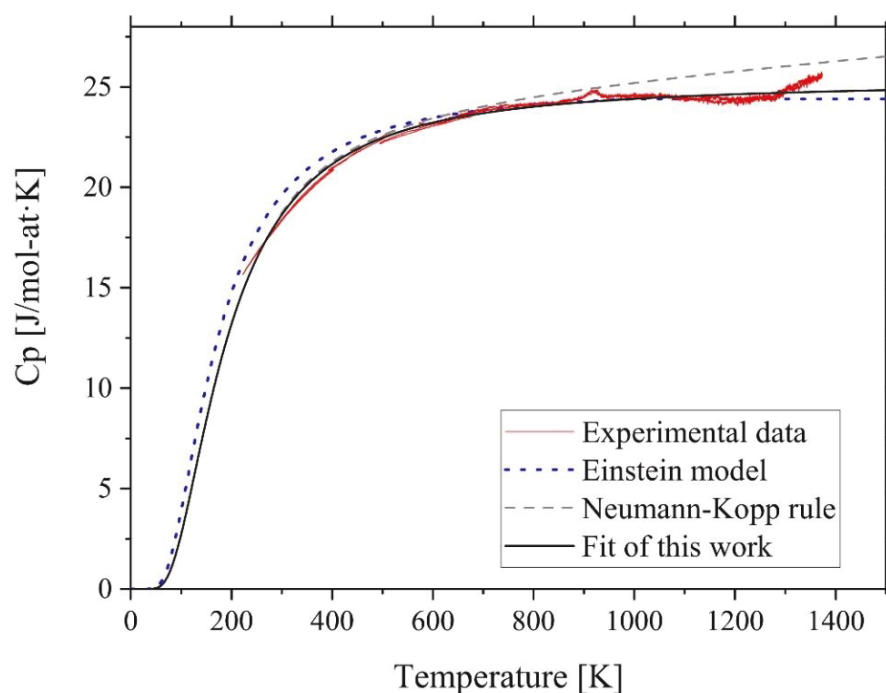


Fig. 2 – Result of the heat capacity measurements of the δ -phase fitted applying extended Einstein model.

Table 5 – Fitted parameters of the extended Einstein equation

Parameters	Value
θ_{Einstein} , (K)	571
$a \cdot 10^4$, ($\text{J} \cdot \text{mole}^{-1} \cdot \text{K}^{-2}$)	1.3
$b \cdot 10^2$, ($\text{J} \cdot \text{mole}^{-1} \cdot \text{K}$)	1.04
S^{298} , ($\text{J} \cdot \text{mole}^{-1} \cdot \text{K}^{-1}$)	12.3

Heat capacity and standard entropy were used for the preliminary description of the Gibbs energy for the δ -phase.

4.2. Phase relations and transitions

Samples #3 and #5 have shown a presence of M-ZrO_2 , MgTiO_3 and δ -phase after long time annealing. This contradicted the tie lines published earlier [5]. Based on the preliminary thermodynamic calculations it was revealed that the ternary area of M-ZrO_2 , MgTiO_3 and δ -phase exists at higher temperature above 1530 K. Moreover, based on the results of the previous work [5] it was assumed that a decomposition of the δ -phase into M-ZrO_2 occurred during cooling after the heat treatment. This assumption was also approved by the preliminary calculations. Therefore, in order to dissolve contradictions between the tie line, to verify possible solid phase reactions and to define the lowest limit of the stability of the δ -Phase, additional heat treatments have been performed at 1475 K and 1555 K. Chemical compositions of the samples were chosen in order to get sufficient information with a minimal of performed experiments. Based on the XRD results, the isothermal sections at 1475 K and 1555 K of the ZrO_2 - TiO_2 - MgO system were constructed. The established isothermal sections of the phase diagram are presented in Fig. 3.

At 1475 K, no δ -phase was found in the samples after the heat treatment. It was in a good agreement with the preliminary calculations, where the reaction of δ -phase $\leftrightarrow \text{Mg}_2\text{TiO}_4 + \text{T-}$

$\text{ZrO}_2 + \text{MgO}$ occurred at 1527 K. Based on the experimental results, it can be stated that the lowest limit of the temperature stability of the δ -phase lays between 1475 K and 1530 K. At 1555 K, the samples #6 has presented the binary phase field between the T- ZrO_2 and MgTiO_3 . The samples #7 and #9 consisted from the Mg_2TiO_4 , MgTiO_3 and δ -phase. Consequently, based on this fact, the solid phase transition of δ -phase + $\text{MgTiO}_3 \leftrightarrow \text{Mg}_2\text{TiO}_4$ + T- ZrO_2 occurs slightly above 1530 K. It should be also mentioned, that the sample #7 contained a small amount of ZrO_2 after the annealing. It can be explained by the decomposition of the δ -phase during cooling. On the other hand, the chemical composition of #7 is close to the phase field of T- ZrO_2 , MgTiO_3 and δ -phase. Therefore, due to the change of the solubility range of the MgTiO_3 , a transition between these two ternary areas could occur as well. However, this does not contradict the constructed tie lines in Fig. 3b.

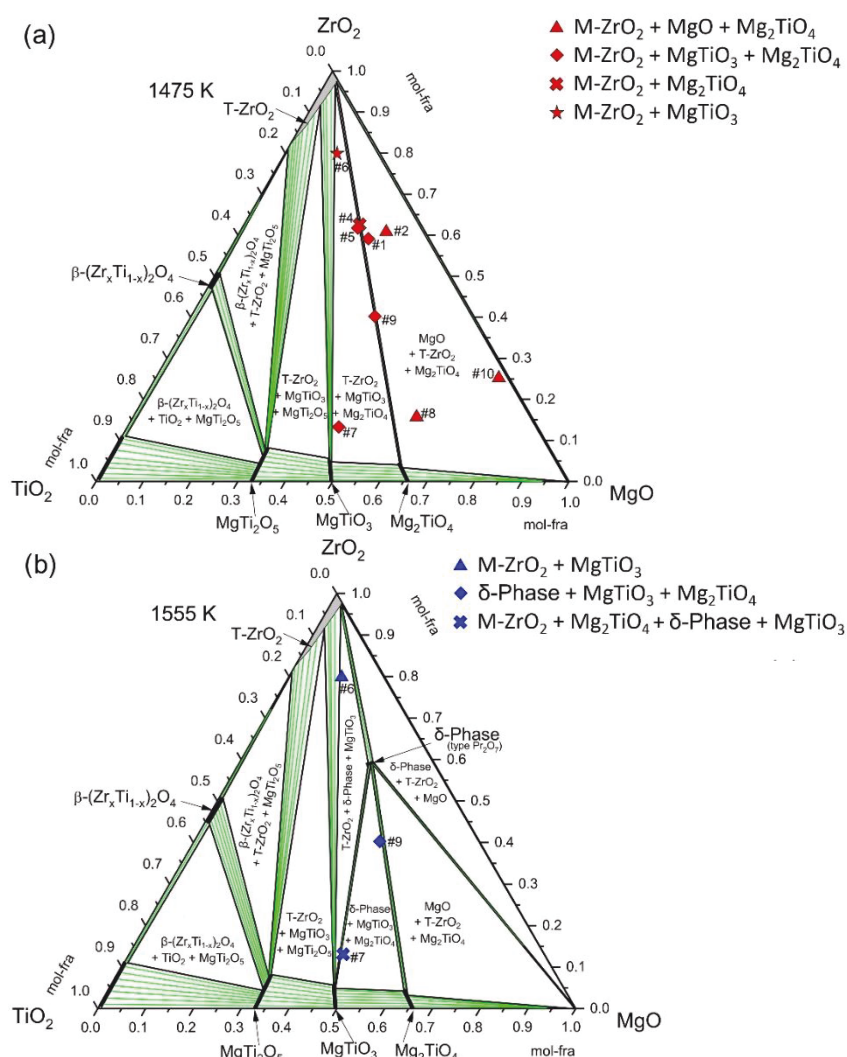


Fig. 3 – Experimental isothermal sections of the ZrO_2 - TiO_2 - MgO system at (a) 1475 K and (b) 1555 K.

4.3. Thermodynamic description

The thermodynamic parameters of the ZrO_2 – TiO_2 – MgO system were assessed based on the phase equilibrium data and DSC measurements obtained in the present work. Data obtained by XRD, DTA and SEM/EDX from the previous work [5] were used as well. Parameters describing wide ternary extension of C- ZrO_2 phase, as well as the parameters describing extension of Mg_2TiO_4 , MgTiO_3 and MgTi_2O_5 phases into ternary system were optimized based on the composition measurements of the previous study [5]. The Gibbs energies of charged end-members were calculated using electro-neutrality conditions and reciprocal reactions [29]:

- $\text{MgZr}_2\text{O}_4^{+2} + \text{MgMg}_2\text{O}_4^{-2} = 2 \cdot \text{Mg}(\text{Mg}_{0.5}\text{Zr}_{0.5})_2\text{O}_4$
- $\text{MgZr}_2\text{O}_4^{+2} + \text{TiTi}_2\text{O}_4^{+4} = \text{MgTi}_2\text{O}_4^{+2} + \text{TiZr}_2\text{O}_4^{+4}$
- $\text{MgZr}_2\text{O}_5 + \text{TiTi}_2\text{O}_5^{+2} = \text{Ti}_2\text{Zr}_2\text{O}_5^{+2} + \text{MgTi}_2\text{O}_5$.

The Gibbs energies of neutral end-members were calculated as sum of the Gibbs energies of oxides multiplied to corresponding stoichiometric number and optimized parameter.

Information about solid state transitions and data on reactions of the liquidus projection of the ZrO_2 – TiO_2 – MgO system measured by DTA [5] was taken into account as well. The fitted coefficients of heat capacity for the δ -phase were accepted as fixed parameters in the description of the temperature dependence of the Gibbs energy. The standard entropy of the δ -phase was used as a start value for optimization because there were only underlying theoretical assumptions and no experimental data for the low temperature range of the heat capacity. Optimized thermodynamic parameters for the ZrO_2 – TiO_2 – MgO system are presented in Table 6.

After completed optimization, the standard entropy of the δ -phase was calculated to be 18.68 J/K·mole-at, which is slightly higher than the value obtained from EE-model. Since, only estimated data on the low temperature heat capacity are available, obtained standard entropy was used for the optimization with a low weight. A priority was given to reproduce experimentally measured tie lines and temperature stability limits of the δ -phase. Consequently, further experimental investigations of the low temperature range of heat capacity, as well as measurements of the enthalpy of formation for the δ -phase are necessary in order to improve the Gibbs energy description of the δ -phase.

Table 6. Optimized thermodynamic parameters of the $\text{ZrO}_2\text{--TiO}_2\text{--MgO}$ system (J/mol)

Phase (Prototype)	Optimized parameters
Liquid phase	${}^0L_{\text{Mg}+2,\text{Zr}+4,\text{TiO}_2,\text{O}-2}^{\text{Liq}} = +26000;$
C-ZrO ₂ (Fluorite)	${}^0L_{\text{Mg}+2,\text{Ti}+4,\text{O}-2}^{\text{C-ZrO}_2} = -102000;$ ${}^0L_{\text{Ti}+4,\text{Zr}+4,\text{O}-2}^{\text{C-ZrO}_2} = +5600 - 8.89 \cdot T;$ ${}^0L_{\text{Mg}+2,\text{Zr}+4,\text{O}-2}^{\text{C-ZrO}_2} = +2550.15;$
Mg ₂ TiO ₄ (Spinel)	${}^0G_{\text{Mg}+2,\text{Zr}+4,\text{O}-2}^{\text{Spinel}} = +2 \cdot \text{ISPINZR} - \text{GMGMG} + 23.05244 \cdot T;$ ${}^0G_{\text{Ti}+4,\text{Zr}+4,\text{O}-2}^{\text{Spinel}} = +3 \cdot \text{SPINNORM} + 2 \cdot \text{INVSP} - 2 \cdot \text{GMGMG} + 23.05244 \cdot T + 2 \cdot \text{ISPINZR} - 2 \cdot \text{SPININV};$
MgTi ₂ O ₅ (Pseudobrookite)	${}^0G_{\text{Mg}+2,\text{Zr}+4,\text{O}-2}^{\text{Pseudobrookite}} = +2 \cdot \text{GZRO2M} + \text{GMGOSOL} + 40000;$ ${}^0G_{\text{Ti}+2,\text{Zr}+4,\text{O}-2}^{\text{Pseudobrookite}} = -\text{PSBNORM} + \text{GTI3O5} + 2 \cdot \text{GZRO2M} + \text{GMGOSOL} + 40000;$
MgTiO ₃ (Ilmenite)	${}^0G_{\text{Mg}+2,\text{Zr}+4,\text{O}-2}^{\text{Ilmenite}} = +\text{GZRO2M} + \text{GMGOSOL} + 20000;$
δ-phase	${}^0G_{\text{ZrO}_2,\text{TiO}_2,\text{MgO}}^{\text{Delta}} = -6651010 + 2645.465 \cdot T - 455.8 \cdot T \cdot \ln(T) - 1.487 \cdot 10^{-2} \cdot T^2 + 4133118 \cdot T^{-1};$
Functions	
ISPINZR	$+2 \cdot \text{GMGOSOL} + \text{GZRO2M} + 20000;$
GMGOSOL	
298-1700	$-619428.502 + 298.253571 \cdot T - 47.4817 \cdot T \cdot \ln(T) - 0.00232681 \cdot T^2 + 4.5043 \cdot 10^{-8} \cdot T^3 + 516900 \cdot T^{-1};$
1700-3100	$-655489.818 + 528.597187 \cdot T - 78.3772 \cdot T \cdot \ln(T) + 0.0097344 \cdot T^2 - 8.60338 \cdot 10^{-7} \cdot T^3 + 8591550 \cdot T^{-1};$
3100-5000	$-171490.159 - 1409.43369 \cdot T + 163.674142 \cdot T \cdot \ln(T) - 0.044009535 \cdot T^2 + 1.374896 \cdot 10^{-6} \cdot T^3 - 1.72665403 \cdot 10^{-8} \cdot T^{-1};$
5000-5100	$-722412.718 + 617.657452 \cdot T - 84 \cdot T \cdot \ln(T);$
GZRO2M	
298-6000	$-1126163.54 + 424.890806 \cdot T - 69.3875137 \cdot T \cdot \ln(T) - 0.00375880141 \cdot T^2 + 683000 \cdot T^{-1};$
SPININV	
298-6000	$+\text{SPINNORM} + \text{INVSP};$
SPINNORM	
298-6000	$-2211877.741 + 1017.950639 \cdot T - 160.88 \cdot T \cdot \ln(T) - 0.009985 \cdot T^2 + 1735500 \cdot T^{-1};$
INVSP	
298-6000	$-2824.083 - 28.335016 \cdot T;$
GMGMG	
298-6000	$+\text{NSPINEL} + 2 \cdot \text{ISPINEL} - 2 \cdot \text{GALAL} + 23.0525839 \cdot T;$
NSPINEL	
298-6000	$+\text{GMGOSOL} + \text{GCORUND} - 23204.5143 - 32.2303298 \cdot T + 4.31045184 \cdot T \cdot \ln(T);$
ISPINEL	
298-6000	$+\text{NSPINEL} + 18002.9059 - 0.398945666 \cdot T;$
GALAL	
298-6000	$+1.5 \cdot \text{GCORUND} - 0.5 \cdot \text{GHSEROO}$
PSBNORM	
298-6000	$-2580078.3886 + 1179.4171263 \cdot T - 190.76 \cdot T \cdot \ln(T) - 0.00608 \cdot T^2 + 2094000 \cdot T^{-1};$
GTI3O5	
298-6000	$+3 \cdot \text{GTIO2} - \text{GHSEROO}$
GTIO2	
298-4000	$-976986.6 + 484.74037 \cdot T - 77.76175 \cdot T \cdot \ln(T) - 67156800 \cdot T^{-2} + 1683920 \cdot T^{-1};$
GHSEROO	
298-1000	$-3480.87 - 25.503038 \cdot T - 11.136 \cdot T \cdot \ln(T) - 0.005098888 \cdot T^2 + 6.61846 \cdot 10^{-7} \cdot T^3 - 38365 \cdot T^{-1};$
1000-3300	$-6568.763 + 12.65988 \cdot T - 16.8138 \cdot T \cdot \ln(T) - 5.95798 \cdot 10^{-4} \cdot T^2 + 6.781 \cdot 10^{-9} \cdot T^3 + 262905 \cdot T^{-1};$
3300-6000	$-13986.728 + 31.259625 \cdot T - 18.9536 \cdot T \cdot \ln(T) - 4.25243 \cdot 10^{-4} \cdot T^2 + 1.0721 \cdot 10^{-8} \cdot T^3 + 4383200 \cdot T^{-1};$
GCORUND	
298-600	$-1707351.3 + 448.021092 \cdot T - 67.4804 \cdot T \cdot \ln(T) - 0.06747 \cdot T^2 + 1.4205433 \cdot 10^{-5} \cdot T^3 + 938780 \cdot T^{-1};$
600-1500	$-1724886.06 + 754.856573 \cdot T - 116.258 \cdot T \cdot \ln(T) - 0.0072257 \cdot T^2 + 2.78532 \cdot 20^{-7} \cdot T^3 + 2120700 \cdot T^{-1};$
1500-3000	$-1772163.19 + 1053.4548 \cdot T - 156.058 \cdot T \cdot \ln(T) + 0.00709105 \cdot T^2 - 6.29402 \cdot 10^{-7} \cdot T^3 + 12366650 \cdot T^{-1};$

There is good accordance of obtained experimental results [5] and current optimization. Calculations of isothermal sections at 1475 K, 1530 K and 1555 K (Fig. 4,5,6 correspondently)

have shown very good agreement in the tie lines and the solubility ranges of Mg_2TiO_4 , MgTiO_3 and MgTi_2O_5 with experimentally obtained diagrams [5]. However, there is quite strong deviation between calculations and experiments for the solubility range of the C- ZrO_2 phase at higher temperatures. Calculated and experimental isothermal sections at 1680 K and 1880 K are presented in Figs. 7 and 8. It can be seen, that the measured homogeneity range of the C- ZrO_2 phase is substantially wider. The attempt to get more extended homogeneity range leads to the shift of temperature of solid state transition reaction $\beta\text{-(Zr}_x\text{Ti}_{1-x})_2\text{O}_4 + \text{C-ZrO}_2 \leftrightarrow \text{MgTi}_2\text{O}_5 + \text{T-ZrO}_2$ below 1680 K that would cause inconsistency with experimental data [4]. It should be noted that present thermodynamic description reproduces the experimentally defined tie lines and phase fields very well.

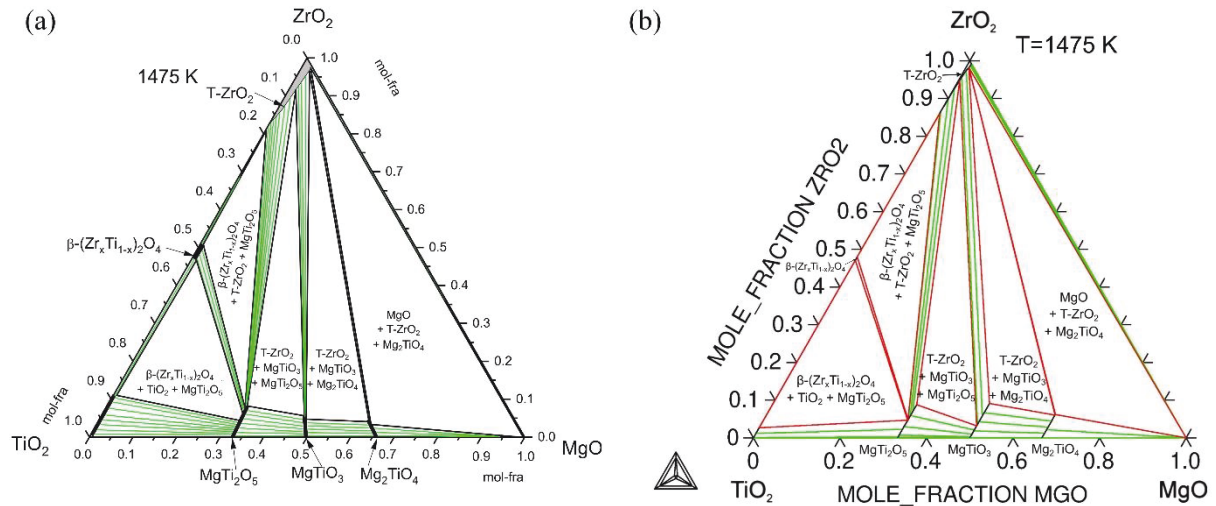


Fig. 4 – Isothermal section of the ZrO_2 – TiO_2 – MgO phase diagram at 1475 K: (a) experimentally determined, (b) calculated.

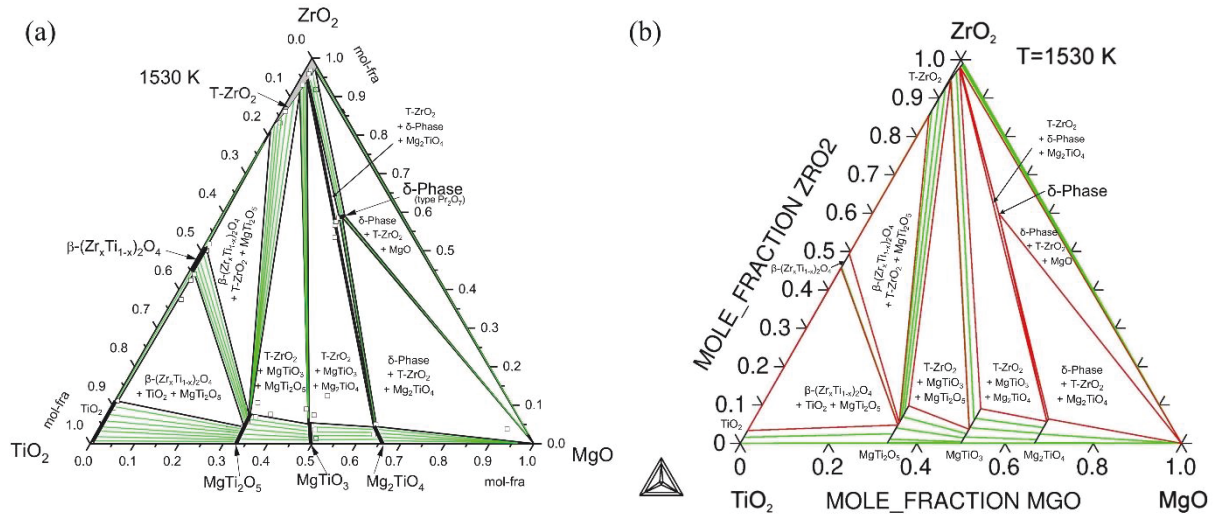


Fig. 5 – Isothermal section of the ZrO_2 – TiO_2 – MgO phase diagram at 1530 K: (a) experimentally determined, (b) calculated.

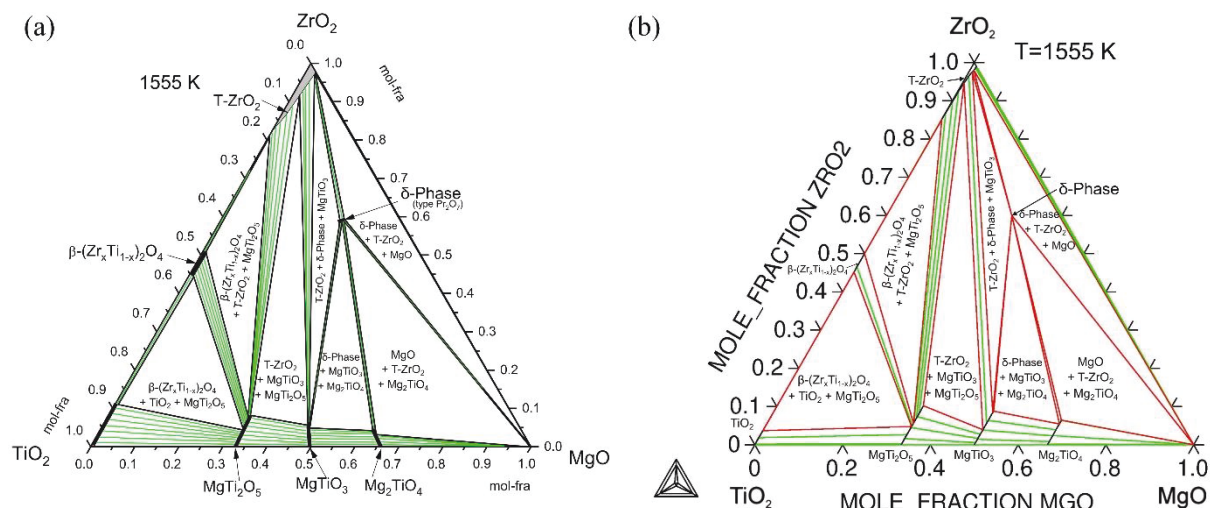


Fig. 6 – Isothermal section of the ZrO₂-TiO₂-MgO phase diagram at 1555 K: (a) experimentally determined, (b) calculated.

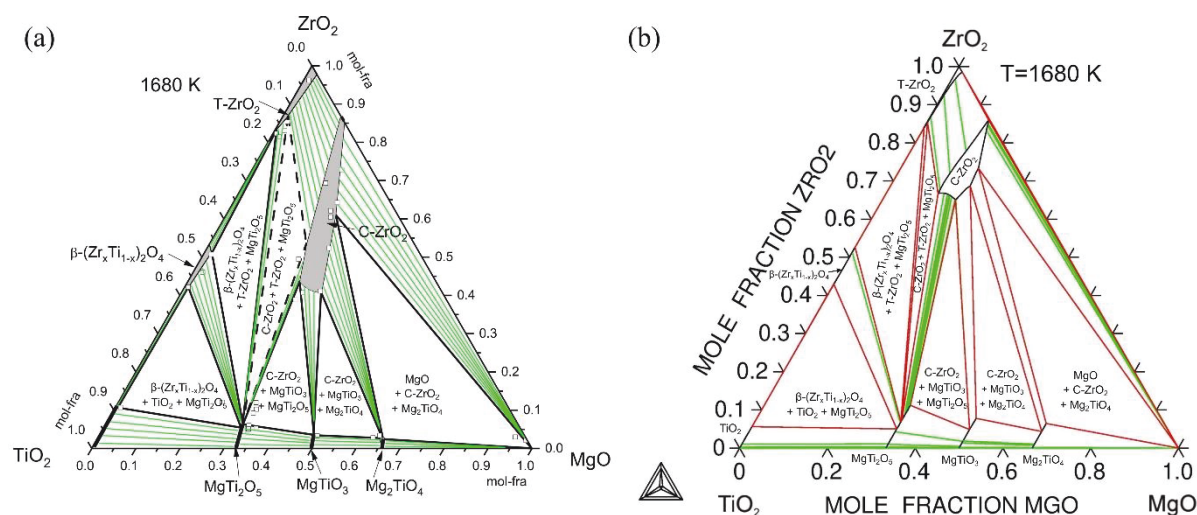


Fig. 7 – Isothermal section of the ZrO₂-TiO₂-MgO phase diagram at 1680 K: (a) experimentally determined, (b) calculated.

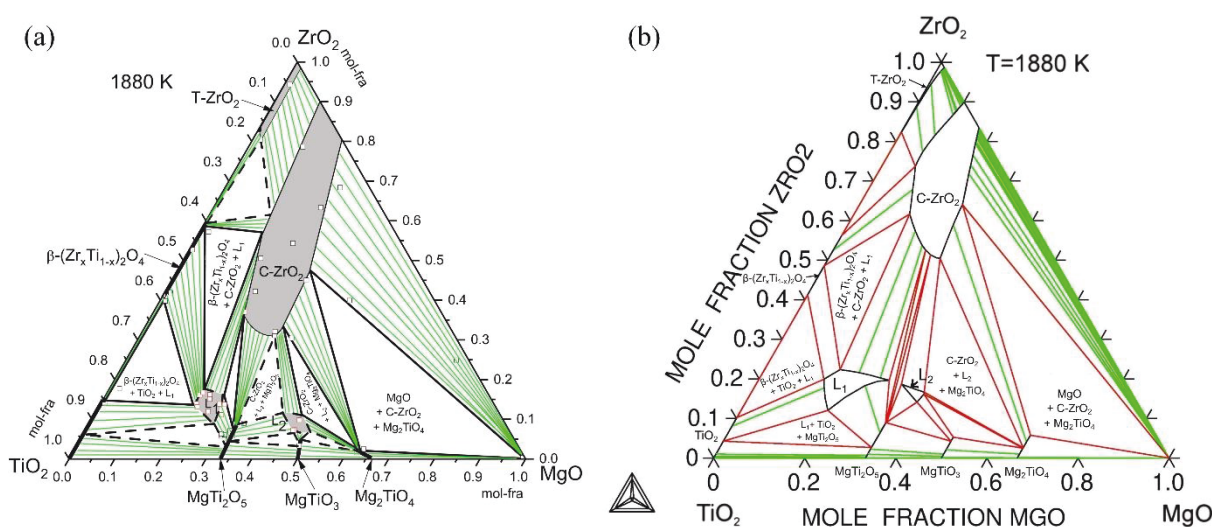


Fig. 8 – Isothermal section of the ZrO₂-TiO₂-MgO phase diagram at 1880 K: (a) experimentally determined, (b) calculated.

Thermodynamic parameter of the liquid phase were optimized based on the DTA and SEM/EDX results presented earlier [5]. Calculated and experimentally constructed [5] liquidus projections are presented in Fig. 9. It was stated, there are three eutectic reactions in the ZrO_2 – TiO_2 – MgO system:

- **E₁:** $\text{Liq} = \text{MgTi}_2\text{O}_5 + \text{C-ZrO}_2 + \text{MgTiO}_3$ (1860 K; 8 ± 1 mol.% of ZrO_2 , 50 ± 2 mol.% of TiO_2 ; 42 ± 2 mol.% of MgO);
- **E₂:** $\text{Liq} = \text{TiO}_2 + \beta\text{-(Zr}_x\text{Ti}_{1-x})_2\text{O}_4 + \text{MgTi}_2\text{O}_5$ (1851 K; 15 ± 1 mol.% of ZrO_2 , 64 ± 1 mol.% of TiO_2 ; 21 ± 2 mol.% of MgO);
- **E₃:** $\text{Liq} = \text{C-ZrO}_2 + \beta\text{-(Zr}_x\text{Ti}_{1-x})_2\text{O}_4 + \text{MgTi}_2\text{O}_5$ (1800 K; 17 ± 1 mol.% of ZrO_2 ; 62 ± 2 mol.% of TiO_2 ; 21 ± 2 mol.% of MgO);

The temperature of the transition reaction of $\text{L} + \text{MgO} \leftrightarrow \text{Mg}_2\text{TiO}_4 + \text{C-ZrO}_2$ (U_2) was defined by DTA to be 1955 K [5]. Comparison of calculated invariant reactions (temperatures and compositions) with experimental data from Ref. [5] is presented in Table 7. It should be noted that the type of reaction E_3 in calculations was obtained as transition reaction ($\text{C-ZrO}_2 + \text{L} = \beta\text{-(Zr}_x\text{Ti}_{1-x})_2\text{O}_4 + \text{MgTi}_2\text{O}_5$) while calculated temperature and liquid composition were in reasonable agreement with experimental data. All solid state transitions determined in the present work and Ref. [5] are perfectly reproduced by the obtained thermodynamic description, as well as the temperature stability range for the δ -phase. Based on this comparison it can be concluded, that reasonable consistency of calculated and experimental data within uncertainty limits was achieved.

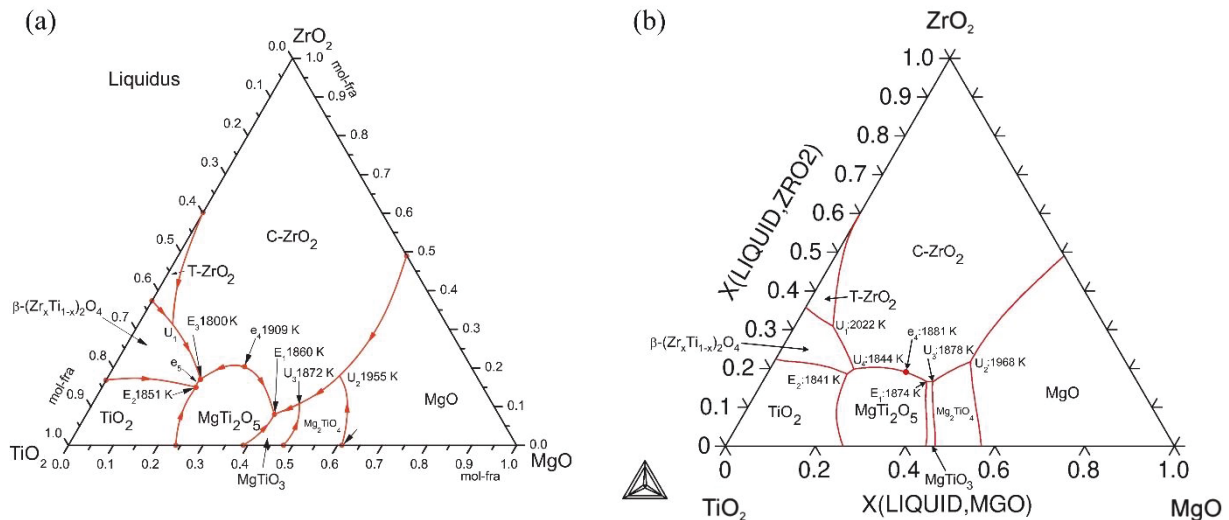


Fig. 9 – Liquidus projection of the ZrO_2 – TiO_2 – MgO phase diagram: (a) experimentally determined, (b) calculated.

Table 7. Invariant equilibria in the $\text{ZrO}_2\text{--TiO}_2\text{--MgO}$ system.

Reaction	T (K)	Type	Composition of the reaction in mol.%			Reference
			ZrO ₂	TiO ₂	MgO	
$\text{Liq} \leftrightarrow \text{MgTi}_2\text{O}_5 + \text{C-ZrO}_2 + \text{MgTiO}_3$	1860	Eutectic E ₁	8	50	42	Experiment [5]
	1874		16.3	47.2	36.5	Calc. this work
$\text{Liq} \leftrightarrow \text{TiO}_2 + \beta\text{-(Zr}_x\text{Ti}_{1-x})_2\text{O}_4 + \text{MgTi}_2\text{O}_5$	1851	Eutectic E ₂	15	64	21	Experiment [5]
	1841		18.6	63.6	17.8	Calc. this work
$\text{Liq} \leftrightarrow \text{C-ZrO}_2 + \text{MgTi}_2\text{O}_5 + \beta\text{-(Zr}_x\text{Ti}_{1-x})_2\text{O}_4$	1800	Eutectic E ₃	17	62	21	Experiment [5]
	1844	Transition reaction U ₄	19.8	61.5	18.7	Calc. this work
$\text{Liq} \leftrightarrow \text{MgTi}_2\text{O}_5 + \text{C-ZrO}_2$	1909	Eutectic max e ₄	20	51	29	Experiment [5]
	1881		19.2	50.6	30.2	Calc. this work
$\text{Liq} \leftrightarrow \beta\text{-(Zr}_x\text{Ti}_{1-x})_2\text{O}_4 + \text{MgTi}_2\text{O}_5$	-	Eutectic max e ₅	-	-	-	Experiment [5]
$\text{Liq} + \text{T-ZrO}_2 \leftrightarrow \beta\text{-(Zr}_x\text{Ti}_{1-x})_2\text{O}_4 + \text{C-ZrO}_2$	-	Transition reaction U ₁	-	-	-	Experiment [5]
	2022		30.8	60.6	8.6	Calc. this work
$\text{Liq} + \text{MgO} \leftrightarrow \text{Mg}_2\text{TiO}_4 + \text{C-ZrO}_2$	1955	Transition reaction U ₂	-	-	-	Experiment [5]
	1968		21.7	34.6	43.7	Calc. this work
$\text{Liq} + \text{Mg}_2\text{TiO}_4 \leftrightarrow \text{MgTiO}_3 + \text{C-ZrO}_2$	1872	Transition reaction U ₃	-	-	-	Experiment [5]
	1879		16.6	45.5	37.9	Calc. this work
$\text{Mg}_2\text{TiO}_4 + \text{C-ZrO}_2 + \text{MgO} \leftrightarrow \delta\text{-phase}$	1664	-	57.5	15.7	26.8	Experiment [5]
	1665		60.0	11.4	28.6	Calc. this work
$\delta\text{-phase} \leftrightarrow \text{Mg}_2\text{TiO}_4 + \text{T-ZrO}_2 + \text{MgO}$	~1503	-	57.5	15.7	26.8	Exp. This work
	1527		60.0	11.4	28.6	Calc. this work
$\text{C-ZrO}_2 \leftrightarrow \text{MgTiO}_3 + \text{Mg}_2\text{TiO}_4 + \text{T-ZrO}_2$	-	-	-	-	-	Experiment [5]
	1593		74.9	10.0	15.1	Calc. this work
$\beta\text{-(Zr}_x\text{Ti}_{1-x})_2\text{O}_4 + \text{C-ZrO}_2 \leftrightarrow \text{MgTi}_2\text{O}_5 + \text{T-ZrO}_2$	1688	Transition	-	-	-	Experiment [5]
	1688		63.1	27.9	9.0	Calc. this work
$\delta\text{-phase} + \text{MgTiO}_3 \leftrightarrow \text{Mg}_2\text{TiO}_4 + \text{T-ZrO}_2$	~1535	Transition	-	-	-	Exp. This work
	1530		57.5	12.9	29.6	Calc. this work

5. Conclusions

The phase relations in the $\text{ZrO}_2\text{--TiO}_2\text{--MgO}$ system were investigated in the temperature range between 1475 and 1555 K using XRD. Thereby, two reactions in the solid phases were determined: eutectoid reaction of $\delta\text{-phase} \leftrightarrow \text{Mg}_2\text{TiO}_4 + \text{T-ZrO}_2 + \text{MgO}$ and the solid state reaction of $\delta\text{-phase} + \text{MgTiO}_3 \leftrightarrow \text{Mg}_2\text{TiO}_4 + \text{T-ZrO}_2$. The isothermal sections at 1475 K and 1555 K were constructed based on experimental data. Heat capacities of the $\delta\text{-phase}$ was measured in the range 210–1370 K. Einstein temperature of the $\delta\text{-phase}$ was estimated to be 516 K using the mass effects suggested by Grimvall [24]. Based on the fitting of the estimated Einstein model and experimental data at high temperatures by EE-model, the Einstein temperature was found to be slightly higher i.e. 571 K. The evaluated standard entropy for the $\delta\text{-phase}$ was found to be 12.3 J/K·mol-at. Using all obtained experimental results including the data published earlier [5], the thermodynamic parameters for the $\text{ZrO}_2\text{--TiO}_2\text{--MgO}$ system were derived. However, in the lack of the experimental data on heat capacity at low temperature, the reproducibility of experimentally measured tie lines and temperature stability limits of the $\delta\text{-phase}$ was more sufficient. Thus, evaluated standard entropy was used for the optimization with a lower weight than the data on phase relations. Therefore, the standard entropy of the $\delta\text{-phase}$ calculated using the obtained thermodynamic database was slightly higher than the evaluated value i.e. 18.68 J/K·mole-at. However, all available experimental data on the phase relations in the $\text{ZrO}_2\text{--TiO}_2\text{--MgO}$ system, as well as the measured results of the high temperature heat capacity for the $\delta\text{-phase}$ are perfectly reproduced by the obtained thermodynamic description. Moreover, current database can be used for further thermodynamic modelling of the high-order systems. Nevertheless, results of current modelling can be applied for optimization of the coating process of the Mg-PSZ mentioned above, as well as for improving of dielectric materials based on the $\text{ZrO}_2\text{--TiO}_2\text{--MgO}$ system.

Acknowledgments

The authors thank the German Research Foundation (DFG) for funding Sub-project C2 within the Collaborative Research Center SFB 799 Trip-Matrix Composites. In addition, we thank G. Savinykh, B. Wahl and Dr. C. Schimpf (TU-Freiberg) for technical contribution.

References

- [1] E. López-López, I. Santacruz, L. Leon-Reina, et al., *J. Eur. Ceram. Soc.* 32 (2012) 1205.
- [2] C.-F. Tseng, *J. Alloy. Compd.* 509 (2011) 9447.
- [3] M. Ilatovskaia, I. Saenko, G. Savinykh et al., *J. Am. Ceram. Soc.* 101 (2018) 5198.
- [4] S. Martin, S. Richter, S. Decker, et al., *Steel Research int.* 82 (2011) 1133.
- [5] I. Saenko, V. Tsukrenko, M. Ilatovskaia, et al., *Adv. Eng. Mater.* 21 (2019) 1800655.
- [6] C. Weigelt, H. Berek, C.G. Aneziris, et al., *Ceram. Int.* 41 (2015) 2328.
- [7] D. Pavlyuchkov, G. Savinykh, O. Fabrichnaya, *Adv. Eng. Mater.* 15 (2013) 618.
- [8] I. Saenko, M. Ilatovskaia, G. Savinykh et al., *J. Am. Ceram. Soc.* 101 (2018) 386.
- [9] L.W. Coughanour, R.S. Roth, S. Marzullo et al., *J. Res. Nat. Bur. Stand.* (1955) 191.
- [10] P. Bouvier, E. Djurado, G. Lucazeau, T. Le Bihan, *Phys. Rev. B* 62 (2000) 8731.
- [11] M. Winterer, R. Delaplane, R. McGreevy, *J. Appl. Crystallogr.* 35 (2002) 434.
- [12] W. Gonschorek, *Z. f. Kristall.* 160 (1982) 187.
- [13] P. Bordet, A. McHale, A. Santoro, R.S. Roth, *J. Solid* 64 (1986) 30.
- [14] M. Dondi, F. Matteucci, G. Cruciani, *J. Solid* 179 (2006) 233.
- [15] R. Christoffersen, P.K. Davies, *J. Am. Ceram. Soc.* 75 (1992) 563.
- [16] E. Schiebold, *Z. f. Kristall* (1921) 430.
- [17] B.A. Wechsler, R.B. von Dreele, *Acta Crystallogr. B Struct. Sci.* 45 (1989) 542.
- [18] L. Lutterotti, *Nucl. Instrum. Methods Phys. Res., B* 268 (2010) 334.
- [19] G. Della Gatta, M.J. Richardson, S.M. Sarge et al., *Pure Appl. Chem.* 78 (2006) 1455.
- [20] H.L. Lukas, S.G. Fries and B. Sundman, *Computational Thermodynamics The Calphad Method*, Cambridge University Press, New York, 2007.
- [21] J.-O. Andersson, T. Helander, L. Höglund, et al., *CALPHAD* 26 (2002) 273.
- [22] M. Hillert, *J. Alloy. Compd.* 320 (2001) 161.
- [23] M.W. Chase, et al., *CALPHAD* 19 (1995) 437.
- [24] G. Grimvall, *J. Alloy. Compd.* 233 (1996) 183.
- [25] C. Degueldre, P. Tissot, H. Lartigue, M. Pouchon, *Thermochim. Acta* 403 (2003) 267.
- [26] D. de Ligny, P. Richet, E.F. Westrum Jr, *J. Roux, Phys. Chem. Miner.* 29 (2002) 267.
- [27] T. Mehmetoglu, *Acta Phys. Pol. A* 133 (2018) 126.
- [28] P.I. Dorogokupets, *J. Phys.: Conf. Ser.* 215 (2010) 12198.
- [29] M. Ilatovskaia, O. Fabrichnaya, *J. Alloy. Compd.* 790 (2019) 1137.

Publication P6: A. Kuprava, I. Saenko, O. Fabrichnaya, Heat capacity measurement of C14-ZrMn₂ and thermodynamic re-assessment of the Mn–Zr system, *CALPHAD* 68 (2020) 101745.
DOI: 10.1016/j.calphad.2020.101745

Contributions to the paper:

Authors	Contribution [%]	Particular contribution
A. Kuprava	40	<ul style="list-style-type: none"> • Experimental work • Evaluation of data
I. Saenko	35	<ul style="list-style-type: none"> • Composition of the manuscript • Thermodynamic modelling • Supervision of the work
Dr. rer. nat. habil. O. Fabrichnaya	25	<ul style="list-style-type: none"> • Co-composition of the manuscript • Supervision of the work • Proofreading of the manuscript

Heat capacity measurement of C14-ZrMn₂ and thermodynamic re-assessment of the Mn–Zr system

A. Kuprava, I. Saenko, O. Fabrichnaya*

Technical University Berakademie Freiberg, Institute of Materials Science, Gustav-Zeuner-Str. 5. D-09599, Germany

* Corresponding author:

O. Fabrichnaya, Technical University Berakademie Freiberg, Institute of Materials Science, Gustav-Zeuner-Str. 5. D-09599, Germany

E-mail: fabrich@ww.tu-freiberg.de

Abstract

The CALPHAD approach was used to derive thermodynamic parameters of the Mn – Zr system based on experimental results and critical evaluation of available data. Novel ab-initio calculations as well as experimental data on enthalpy of formation and heat capacity measurements for the C14-ZrMn₂ Laves phase were taken into account. The congruent melting point of the C14-ZrMn₂ Laves phase was determined using differential thermal analysis (DTA) at 1765 K. Data on heat capacity for the C14-ZrMn₂ phase were extended to high temperature range up to 980 K using differential scanning calorimetry (DSC). Standard entropy for C14-ZrMn₂ was calculated using an extended Einstein model based on newly obtained results. Additionally, the sublattice model based on antisite substitution in the C14-ZrMn₂ Laves phase has been used in order to describe its homogeneity range. Based on the currently obtained results and novel literature data, thermodynamic parameters for the Mn-Zr system were re-optimized. The self-consistent thermodynamic description derived in the present work reproduces all experimental data well.

1. Introduction

Zr-containing Laves phases including C14-ZrMn₂ have attracted attention as perspective hydrogen storage materials [1] due to fast kinetics, high storage capacity, easy activation and moderate working conditions [2]. C14-ZrMn₂ is able to absorb hydrogen up to the composition of ZrMn₂H₄ which gives promising potential of its utilization. Additionally, materials based on the Mn – Zr system play an important role in the development of modern composite materials such as the TRIP-matrix composite (TRIP-Transformation Induced Placticity) [3]. This metal-matrix composite is based on an austenitic stainless steel reinforced by ZrO₂-based ceramics, wherein manganese is one of the main alloying elements of steel [3]. Incorporation of ceramics into the steel matrix enhances martensitic transformation by inducing additional micro-stress under load [4]. Such composite material exhibits excellent strength and high specific energy absorption under compression [3]. Furthermore, thermodynamic description of the Mn–Zr system may become necessary when studying and modelling higher order systems containing this binary system.

The latest thermodynamic description of the Mn–Zr system was presented by Flandorfer et al. [5] coupled with experimental study. However, their thermodynamic description has a number disadvantages, namely an employment of an uncommon model for describing the C14-ZrMn₂ Laves phase as well as using Neumann-Kopp rule to describe the heat capacity of C14-ZrMn₂. Moreover, there are several inconsistencies in the system concerning the melting temperature of the C14-ZrMn₂ phase and eutectic reaction temperature. In the previous thermodynamic

description of Hack [6], a sublattice model with antisite substitution on the sublattices was used, but the data on the homogeneity range of C14-ZrMn₂ [5] were not taken into account.

Therefore, the aim of the current work is a re-assessment of the thermodynamic parameters of the Mn–Zr system using the data of Flandorfer et al. [5], novel literature data and own experimental results. Moreover, for further improvement of the thermodynamic description, high temperature heat capacity measurements of the C14-ZrMn₂ phase are necessary.

2. Literature survey

Mn–Zr phase diagram was constructed by Massalski [7] based on earlier works [8–11], focused mainly on the homogeneity range of C14-ZrMn₂ Laves phase. This phase diagram was later experimentally studied by Flandorfer et al. [5] using differential thermal analysis (DTA) and electron probe microanalysis (EPMA). Thermodynamic parameters of the system were assessed [5] based on the experimental results and literature data. In the work of Flandorfer et al. [5] the homogeneity range of the C14-ZrMn₂ phase was established, which appeared to be narrower than presented earlier. According to Massalski [7], the borders of the solubility range were proposed to be at ca. 21 and 40 at.% Zr. Based on EPMA measurement of Flandorfer et al., solubility ranges of C14 were between 28.5 and 34.1 at.% Zr, which implies larger extension of homogeneity range-towards Mn-rich compositions. Phase diagrams of the Mn–Zr system calculated by Flandorfer et al. [5] and published by Massalski [7] are presented in Fig. 1. Crystallographic information about all stable phases is presented in Table 1. Despite the fact that the phase diagram was studied throughout the whole composition range, it still retains contradictions and unclear details.

The first controversial point concerning the Mn–Zr system is the melting temperature of the C14-ZrMn₂, which has a great scatter in the literature. In the work of Savitskii and Kapetskii [12] it was measured at 1593 K, while according to Massalski [7] melting of C14-ZrMn₂ occurred at 1723 K. In another work on quasi-binary ZrMn₂–ZrFe₂ system by Pet'kov [13], the melting temperature was determined at 1843 K. Therefore the melting temperature of the C14-ZrMn₂ phase needs to be verified. The second controversial point is the temperature of the L = C14-ZrMn₂ + β -Zr eutectic reaction. According to Massalski [7] it occurs at 1363 K. The same temperature was calculated using the thermodynamic description of the system in the work of Flandorfer et al. [5]. However according to the DTA results from the same work [5], this reaction occurred between 1410 and 1421 K.

There are contradictions between phase relations in the Mn-rich compositions presented by Hellawell [9] and Savitskii and Kopetskii [12] (Fig.2). According to Hellawell's diagram, the eutectic reaction of δ -Mn and ZrMn₂ occurs at 1423 K, the eutectoid decomposition of δ -Mn to β -Mn and γ -Mn occurs at 1393 K and the peritectoid formation of β -Mn from δ -Mn and ZrMn₂ at 1413 K (Fig. 2 – right diagram). According to the phase diagram by Savitskii and Kopetskii [12] (Fig. 2 – left diagram), the eutectic reaction of δ -Mn and ZrMn₂ occurs at 1433 K, peritectic reaction of γ -Mn formation occurs at 1498 K and peritectoid reaction of β -Mn formation at 1398 K. As it is noted in the evaluation of Schlesinger [14], no true arbiter study has been performed. Although in the work of Svechnikov and Pet'kov [10] a partial phase diagram in the range between 50 and 80 at.% Mn was presented based on XRD investigation of annealed samples, DTA and microstructural studies. The temperatures of eutectic L=C14-ZrMn₂+ δ -Mn and peritectoid C14-ZrMn₂= β -Mn+ δ -Mn transformations obtained in the work [10] were the same as in the work of Hellawell [9]. Moreover, Svechnikov and Pet'kov [10] also confirmed that the eutectic solidification products were δ -Mn and C14-ZrMn₂. The melting point of C14-

ZrMn₂ reported by Svechnikov and Pet'kov [10] is more than 100 K higher than that determined by Savitskii and Kopetskii [12], but consistent with Refs. [5] and [7]. Therefore it can be assumed that alloys investigated by Savitskii and Kopetskii [12] could be contaminated thus being a source of the inaccurate phase equilibria determinations in the Mn-rich end [14]. As a result, the Mn-rich end of the diagram is accepted from the work of Hellawell [9] as it is more consistent with the assessment presented by Massalski [7].

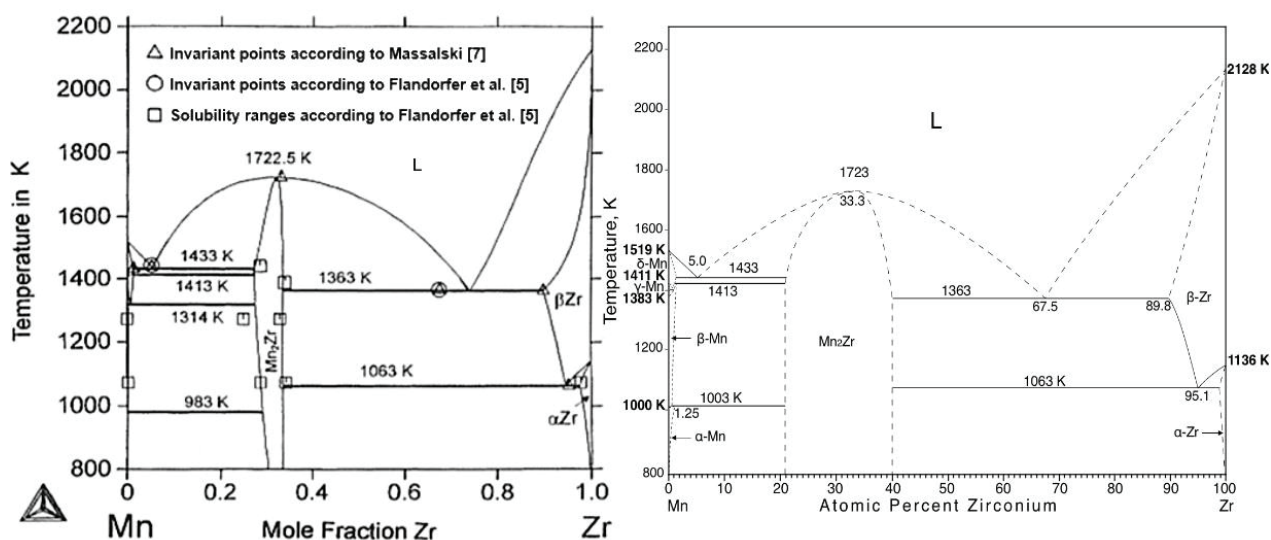


Fig. 1 – Mn–Zr phase diagram calculated by Flandorfer et al.[5] (left) and presented by Massalski [7] (right).

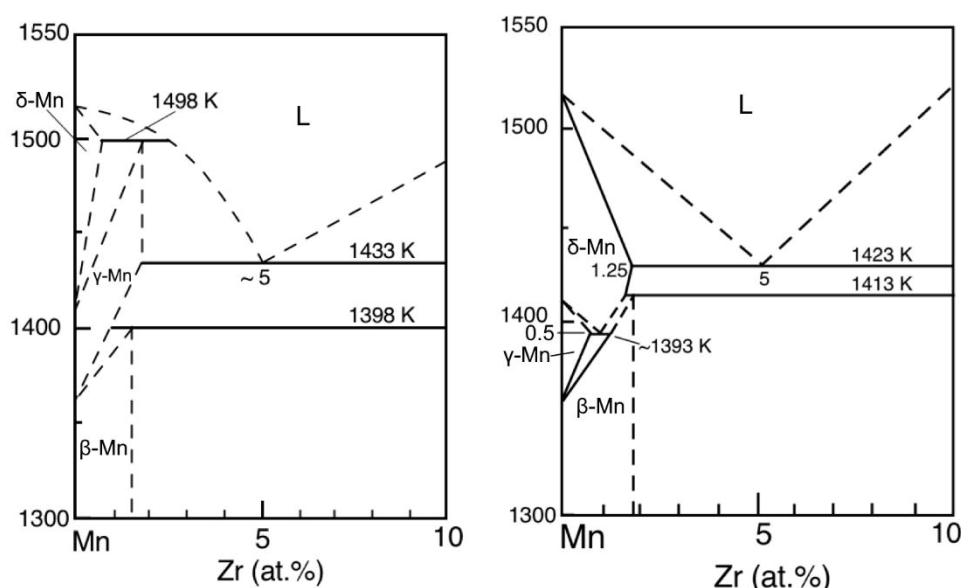


Fig. 2 – Mn-rich side of the Mn–Zr phase diagram according to Savitskii and Kopetskii [12] (left) and Hellawell [9] (right).

Concerning thermodynamic studies in the Mn – Zr system, experimental investigations [15–17] and a DFT [16] calculation have been reported. Enthalpy of formation of C14-ZrMn₂ was measured by Smetana et al. [15] to be -16.6 ± 5.1 kJ/mole-at by the vapour pressure method. In the novel work of Rotter et al. [16] a value of -22.66 ± 0.82 kJ/mole-at was obtained using drop solution calorimetry and agrees well with the DFT calculation resulting in -20.3 kJ/mole-at, performed in the same work. It should be mentioned that drop solution calorimetry provides more reliable results for enthalpy of formation in comparison with vapour pressure as it also pointed out in the work of Saenko et al. [18]. In the same work of Rotter et al. [16], heat capacity

of the C14-ZrMn₂ phase was measured in the range 3 – 170 K. However, no data at high temperatures is available so far. The enthalpy of mixing in the Mn-rich liquid alloys in the composition range 5 – 55 at.% was measured by Sidorov et al. [17] at 1846 K.

Thermodynamic descriptions of the Mn–Zr system were derived by Flandorfer et al. [5] and by Hack [6]. In the work of Flandorfer et al. [5] the C14 phase was modelled with two sublattices: the first one occupied exclusively by atoms of Mn and the second one occupied by atoms of Zr and vacancies. Such a description implies that the homogeneity range is relevant due to change of Zr occupation of a crystallographic site. However, a nonstoichiometry in AB₂ Laves phases with C14 structure occurs usually within specific R_A/R_B ratio range of 1.12–1.26. It is typically characterized by antisite substitution defects [19]. An antisite substitution mechanism is shown to be the dominant nonstoichiometry point defect mechanism in Laves phases [20], which is applied as common practice in modelling [18,21–24]. Therefore, the model applied in the assessment of Flandorfer et al. [5] needs to be revised. It should be noted that in the thermodynamic assessment of Hack [6] homogeneity ranges in Laves phase were modelled with the antisite substitution mechanism. However, the calculated homogeneity ranges were much wider than established by Flandorfer et al. [5]. According to Hack's [6] assessment, eutectic reaction L=C14-ZrMn₂ + β -Zr occurred at higher temperature (1424 K and 69.36 at.% Zr) than in work of Flandorfer et al. [5]. Phase relations in the Mn-rich composition range according to calculations of Hack [6] differ from the work of Flandorfer et al. [5] and both are different from experimental data of Refs. [9] and [12]. It should be noted that the phase diagram published by Massalski [7] (Fig. 1 – right diagram) in the Mn-rich composition is consistent with Hellawell [9]. Furthermore, heat capacity modelling of the intermetallic phase C14-ZrMn₂ was performed using the Neumann-Kopp rule in both works [5, 6] due to the absence of any experimental data on heat capacity.

Table 1 – Data on crystal structures of solid phases of the Mn–Zr system.

Phase	Pearson symbol	Space group	Prototype	Strukturbericht	Reference
α -Mn	cI58	$I\bar{4}3m$	Mn	A12	[25]
β -Mn	cP20	$P4_132$	Mn	A13	[26]
γ -Mn	cF4	$Fm\bar{3}m$	Cu	A1	[7]
δ -Mn	cI2	$Im\bar{3}m$	W	A2	[7]
α -Zr	hP2	$P6_3/mmc$	Mg	A3	[27]
β -Zr	cI2	$Im\bar{3}m$	W	A2	[28]
C14-ZrMn ₂	hP12	$P6_3/mmc$	MgZn ₂	C14	[29]

Besides C14-ZrMn₂, another intermetallic phase denoted as ZrMn was observed in two works [30,31], while this phase was not discussed or mentioned in the assessment of Flandorfer et al. [5]. According to the report of Gulay and Zaremba [31], it possesses cubic structure, though no crystallographic or phase equilibria investigations regarding this phase have been submitted so far. Based on the work of Kodama [30], Okamoto [32] proposed a diagram with the ZrMn phase (Fig. 3), but the stability of this phase is not confirmed yet. In the work of Gulay and Zaremba [31], the ZrMn phase is regarded to as a triple compound ZrMnX_(x) with X being O or N. As though this phase may contain amounts of oxygen or nitrogen, these elements are referred to as a contamination, suggesting the phase is able to dissolve these elements up to x atoms per formula.

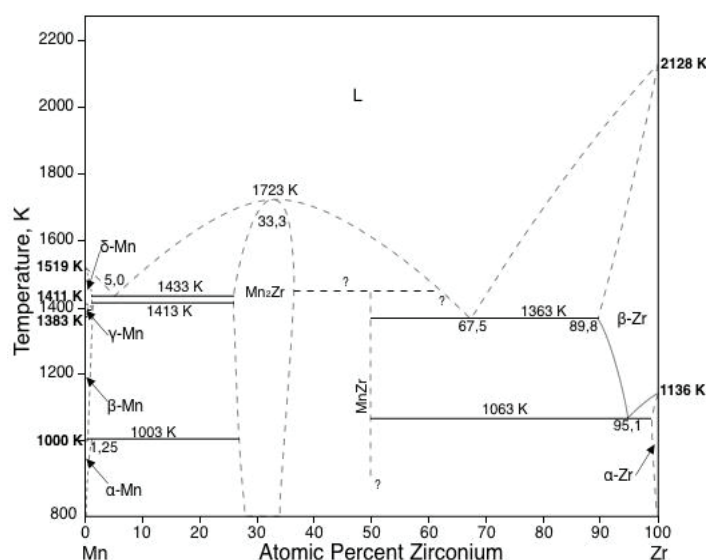


Fig. 3 – Phase diagram proposed by Okamoto [32].

3. Experimental

3.1. Sample preparation and characterization

Binary Mn–Zr alloys were prepared from pure Zr (99.99% wt.%, Alfa Aesar) and Mn (99.9 wt.%, Alfa Aesar) by arc-melting in an argon atmosphere. In order to achieve chemical homogeneity in the bulk material, all samples were turned over and re-melted three times. The melting chamber was evacuated to a pressure of $\sim 10^{-5}$ atm and backfilled with argon three times. Additionally, an ingot of Ti was placed in the melting chamber and was melted before the melting of the samples to eliminate remnants of oxygen and prevent possible oxidation. The weight losses of the samples did not exceed 2 weight %. Afterwards the obtained specimens were encapsulated in quartz tubes under an Ar atmosphere. The pressure of Ar inside the tubes was set to reach 1 atm at the annealing temperature. The samples were annealed for 7–10 days at 1073 and 1323 K. Immediately after the heat treatment, samples were quenched into the ice water. Quenched samples were analysed by X-ray powder diffraction (XRD) and scanning electron microscopy with energy dispersive X-ray spectrometry (SEM/EDX).

XRD measurements were performed on a URD63 diffractometer (Seifer, FPM, Freiberg) with Bragg-Brentano geometry. The device is equipped with a graphite monochromator using $\text{CuK}\alpha$ ($\lambda = 1.5418 \text{ \AA}$) radiation in a 2θ -range from 15 – 110° . For the characterization of the diffraction patterns, Rietveld refinements was used with the Maud [33] software. SEM microstructural investigations were carried out using LEO 1530 Gemini (Zeiss, Germany) microscope. Chemical compositions of the samples as well as of phases present were measured using an EDX detector (Bruker AXS Microanalysis GmbH) with an accuracy of $\pm 2 \text{ at.}\%$.

3.2. Thermo-analysis

The DTA measurements were carried out with a Setaram SETSYS Evolution 1750 (SETARAM, Caluire, France) at a heating rate 10 K/min under helium atmosphere flow of 20 l/min . Alumina crucibles were laid with a bed of yttria to prevent reaction between manganese and alumina. Crucibles were also covered with a lid to avoid evaporation of highly volatile

manganese. For more accurate temperature measurement, corresponding calibration was done using melting temperatures of Al, Au and Ni.

The heat capacity of the C14-ZrMn₂ phase was measured from 300 to 980 K on the Pegasus 404C device (Netzsch, Germany) with Pt/Rh crucibles in argon atmosphere. Measurements from 200 to 650 K were performed on the PerkinElmer DSC 8000 device. Experiments were carried at following the continuous three step method [34]. Copper, molybdenum and platinum were used as standard materials for calibration in corresponding temperature intervals.

4. Modelling

Calphad method was applied in this work for thermodynamic re-assessment of the Mn–Zr system using Thermo-Calc software.

The Gibbs energies of stable pure elements were taken from the SGTE database version 5 [35]. The Gibbs energy function is expressed in the following form:

$${}^oG_i^\Phi(T) = a_0 + a_1T + a_2T\ln(T) + a_3T^2 + a_4T^{-1} + \dots, \quad (1)$$

where $a_0 - a_n$ are polynomial coefficients.

For the description of a pure element i , Gibbs energy is referred to a Standard Reference State (SER) of the element and denoted as GHSER:

$$GHSER_i = {}^oG_i^\Phi(T) - H_i^{SER}(298.15K), \quad (2)$$

where H_i^{SER} is enthalpy of the i element at 298.15 K referred to its SER.

Magnetic influence on the equilibria is considered according to the Inden–Hillert–Jarl [36] formalism:

$$G_m^{\Phi, mag} = RT\ln(\beta_0 + 1)g(\tau) \quad (3)$$

where $\tau = T/T^*$, T^* is the critical temperature of the phase (the Curie temperature T_C for ferromagnetic materials or the Neel temperature T_N for antiferromagnetic materials), β_0 is the average magnetic moment per atom, $g(\tau)$ is a function depending on τ [35].

Substitutional solutions, such as liquid and HCP, BCC solid solutions were modelled according to the following equation:

$$G_m^\Phi = G_m^{\Phi, srf} + G_m^{\Phi, conf} + G_m^{\Phi, Ex} = \sum_{i=1}^n x_i {}^oG_i^\Phi + RT \sum_{i=1}^n x_i \ln x_i + G_m^{\Phi, Ex} \quad (4)$$

where $G_m^{\Phi, srf} = \sum_{i=1}^n x_i {}^oG_i^\Phi$ is the surface of the reference term, $G_m^{\Phi, conf} = RT \sum_{i=1}^n x_i \ln x_i$ is the Gibbs energy resulting from the configurational mixing entropy of a disordered solution ($n = 2$ for a binary system).

The excess Gibbs energy of mixing for a binary system is described by Redlich–Kister polynomials [37]:

$$G_m^{\Phi, Ex} = x_A x_B \sum_{v=0} {}^v L_{A,B}^{\Phi} (x_A - x_B)^v \quad (5)$$

where ${}^v L_{A,B}^{\Phi}$ is a binary interaction parameter. The temperature dependence of the interaction parameter is expressed as follows:

$${}^v L_{A,B}^{\Phi} = a_1 + a_2 \cdot T \quad (6)$$

Parameters a_1 and a_2 are related with excess enthalpy and minus excess entropy, respectively.

The Gibbs energy $G_{A_a B_b}(T)$ of a stoichiometric compound $A_a B_b$ in the case of heat capacity data being available is described as:

$$G_{A_a B_b} - aH_A^{\Phi}(298.15K) - bH_B^{\Phi}(298.15K) = a_1 + a_2 T + a_3 T \ln T + a_4 T^2 + a_5 T^{-1} \quad (7)$$

Coefficients a_1 to a_5 in the equation (7) are products of the integration of C_p and C_p/T where C_p is heat capacity described using the Maier-Kelley equation. Coefficient a_1 includes enthalpy of formation and a_2 includes standard entropy of the phase together with constants appeared due to integration. Coefficients a_3 to a_5 are related with parameters in the Maier-Kelly equation. All corresponding relations can be found in [38].

Homogeneity ranges of BCC, HCP, CUB and CBCC phases, as well as the liquid phase were described using of the substitutional model with one sublattice in the form of (Zr,Mn). Descriptions of magnetic properties of phases with the homogeneity range were taken unchanged from the SGTE database [35]. C14-ZrMn₂ was described using compound energy formalism as a non-magnetic phase [39]. In the present work, C14 is modelled with a compound energy formalism including two sublattices, where Mn and Zr atoms occupy sites on both first and second sublattices (Mn,Zr)₂(Mn,Zr)₁, implying the antisite defect mechanism of the nonstoichiometry. Three additional end members are added to the description of the phase. The Gibbs energies of Zr₂Zr and Mn₂Mn were described as for pure elements containing additional large positive terms (to make them unstable in the pure systems) which were optimized to reproduce homogeneity ranges of the C14 phase. The Gibbs energy of antisite end-member Zr₂Mn was calculated assuming that the Gibbs energy of the reciprocal reaction Zr₂Zr+Mn₂Mn=Zr₂Mn+Mn₂Zr is equal to zero.

The optimization of thermodynamic parameters and phase diagram calculations of the Mn–Zr system were performed using PARROT and POLY-3 modules in Thermo-Calc program set correspondingly [38,40]. Individual weights have been predetermined for every type of experimental data considering possible deviation and accuracy of each experimental method [38,40].

5. Results and discussion

Mn–Zr alloys with nominal contents of 31, 45, 50 and 68 at.% Zr were prepared and annealed at 1073 K for 10 days and at 1323 K for 7 days. XRD analysis results, as well as SEM/EDX measurements are presented in Table 2. It should be pointed out that due to the fast kinetics of polymorphous transformation β -Zr = α -Zr, *ex-situ* XRD measurements indicate the presence of α -Zr, which does not indicate an equilibrium state at the temperature of quenching.

Table 2 – Sample compositions and XRD & SEM/EDX results.

Sample	Sample composition [at.%]				Temperature[K] /Annealing duration[days]	Phases according to XRD& SEM/EDX	Vol. [%]	Lattice parameters, Å				Phase composition (SEM/EDX) [at.%]	
	Nominal		Measured with SEM/EDX					<i>a</i>	<i>b</i>	<i>c</i>	β [°]	Zr	Mn
	Zr	Mn	Zr	Mn									
#1	31	69	32.3	67.7	cast	C14-ZrMn ₂	100	5.031	—	8.265	—	34.5	65.5
					1073/10	C14-ZrMn ₂	100	5.046	—	8.295	—	35.2	64.8
					DSC 200-700	C14-ZrMn ₂	100	5.028	—	8.265	—	34.7	65.3
#2	45	55	45.6	54.4	cast	C14-ZrMn ₂	82	5.049	—	8.301	—	35.9	64.1
						(α-Zr)	12	3.235	—	5.19	—	95.1	4.9
						ZrMn	6	11.9	—	—	—	54.3	45.7
					1073/10	C14-ZrMn ₂	100	5.028	—	8.262	—	36.6	63.4
						(α-Zr)	—	—	—	—	—	97.2	2.8
					1323/7	C14-ZrMn ₂	84	5.047	—	8.293	—	34.7	65.3
						ZrMn	12	11.87	—	—	—	52.4	47.6
						(α-Zr)	4	3.232	—	5.146	—	97.8	2.2
#3	50	50	51.8	48.2	cast	C14-ZrMn ₂	70	5.055	—	8.308	—	36.5	63.5
						(α-Zr)	25	3.235	—	5.147	—	96.5	3.5
						ZrMn	5	11.9	—	—	—	54.6	45.4
						(Eutectic)	—	—	—	—	—	72	28
					1323/7	C14-ZrMn ₂	68	5.047	—	8.295	—	34.8	65.2
						(α-Zr)	22	3.239	—	5.162	—	98.4	1.6
	ZrMn	10	11.87	—	—	—	52.1	47.9					
#4	68	32	71.3	28.7	1323/7	C14-ZrMn ₂						35.4	64.6
						(α-Zr)							93.7

5.1. Heat capacity measurements of C14-ZrMn₂

Values presented in Table 2 confirmed that the sample #1 contained only single phase C14-ZrMn₂ before and after the DSC experiment.

Measured heat capacity data are fitted by the Maier-Kelley equation and are presented in Fig. 4 together with the theoretical calculation. Temperature dependence of heat capacity fitted using Maier-Kelley equation is presented as follows:

$$C_P(\text{C14} - \text{ZrMn}_2) = 25.75 + 0.0062 \cdot T - \frac{16.2 \cdot 10^4}{T^2} [\text{J} \cdot \text{K}^{-1} \cdot \text{mol} - \text{at}^{-1}] \quad (8)$$

Heat capacity calculated using the Neumann-Kopp rule deviates significantly at higher temperatures, as can be seen in Fig. 4. Deviation reaches 20% at 1000 K and is expected to grow even further. This fact underlines the importance of experimental measurement of heat capacity instead of using the Neumann-Kopp rule for reliable thermodynamic description.

Using measured data from the current work with the measurements of Rotter et al. [16] enabled application of an extended Einstein model presented at the Ringberg workshop [41] for the description from 0 K:

$$C_P(T, \theta) = C_V^{\text{Einstein}}(T) + aT + bT^2 \quad (9)$$

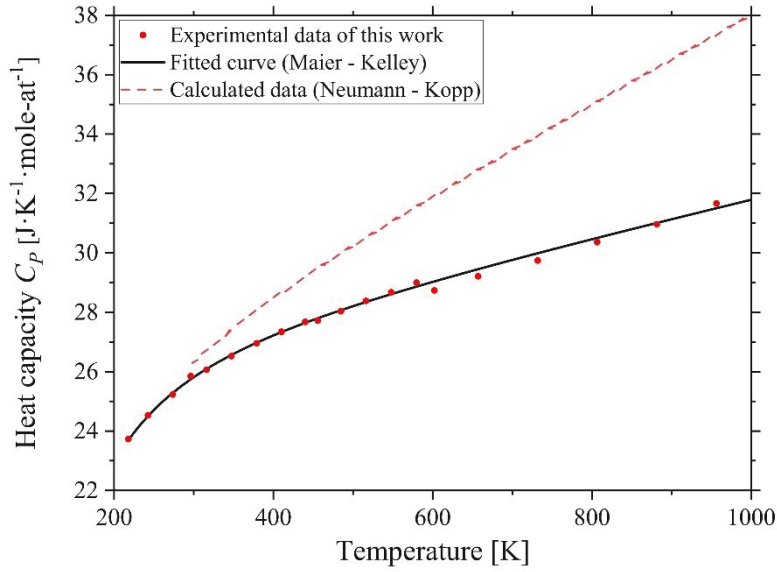


Fig. 4 – Result of the heat capacity measurements of the C14-ZrMn₂ phase.

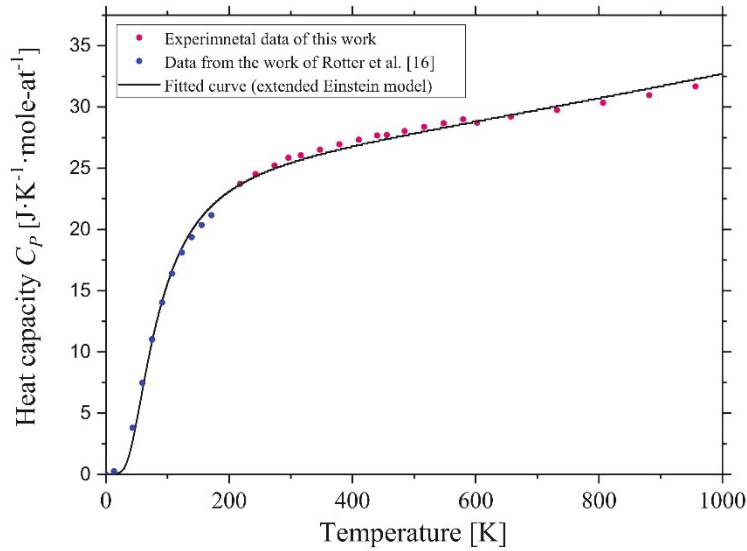


Fig. 5 – Result of the heat capacity measurements of the C14-ZrMn₂ fitted applying extended Einstein model. Fitting was done based on the data of this work combined with the data published by Rotter et al. [16].

Calculations based on the obtained extended Einstein model (Eq.10) are presented in Fig. 5 and coefficients of the equation are listed in Table 3. As can be seen from Fig. 5, both low and high temperature data are in excellent agreement and fit together with low inaccuracy, which denotes relevance of the data.

$$C_p(T) = \frac{3 \cdot R \cdot \left(\frac{253}{T}\right)^2 \cdot e^{\frac{253}{T}}}{\left(e^{\frac{253}{T}} - 1\right)^2} + 5.8 \cdot 10^{-3} \cdot T + 2.11 \cdot 10^{-6} \cdot T^2 \quad (10)$$

Based on the obtained fitted model of C_P , standard entropy of the C14-ZrMn₂ phase was calculated using the formula: $S^{298} = \int_0^{298} C_P \frac{dT}{T}$. Integration of the C_P/T expression resulted in 32.6 J·mole-at⁻¹·K⁻¹.

Table 3 – Fitted parameters of the extended Einstein equation.

Parameters	Value
$\theta_{\text{Einstein, K}}$	253
$a \cdot 10^3$	5.8
$b \cdot 10^6$	2.11
S^{298} , J·mole-at ⁻¹ ·K ⁻¹	32.6

5.2. Phase transformations

Samples #1 (1073/10) and #4 (1323/7), were studied by means of differential thermal analysis to determine melting temperatures of C14-ZrMn₂ and ZrMn as well as eutectic reaction temperature. DTA curves on heating are presented in Fig. 6.

The only heat effect in the single-phase sample #1 corresponding to the melting of C14-ZrMn₂ appeared at 1765 K. Compared with the values from other works, obtained value resides between those reported by Massalski (1723 K) [7] and Pet'kov (1843 K) [13]. Obtained melting temperature was used for further modelling of the C14-ZrMn₂ phase.

Eutectic reaction was observed in two other samples i.e. #2 (1323/7) and #3 (cast) studied by DTA both on heating and cooling. Observed values of 1414, 1405 and 1408 K are close to the temperatures experimentally determined by Flandorfer et al. [5], i.e. 1410 K and 1421 K. Therefore the temperature of the eutectic reaction $L = \text{C14-ZrMn}_2 + \beta\text{-Zr}$ reaction was accepted as an averaged value of 1409 K for optimization of the thermodynamic parameters. Microstructures of the sample #3 in cast state and after DTA are presented in Fig. 7.

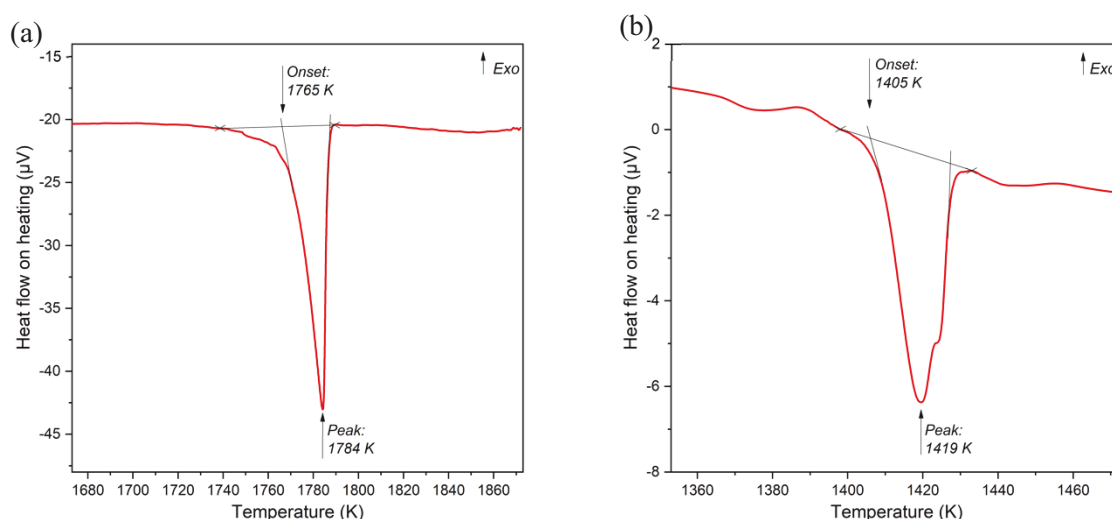


Fig. 6 – DTA curves of the cast samples #1 (a) and #4 (b).

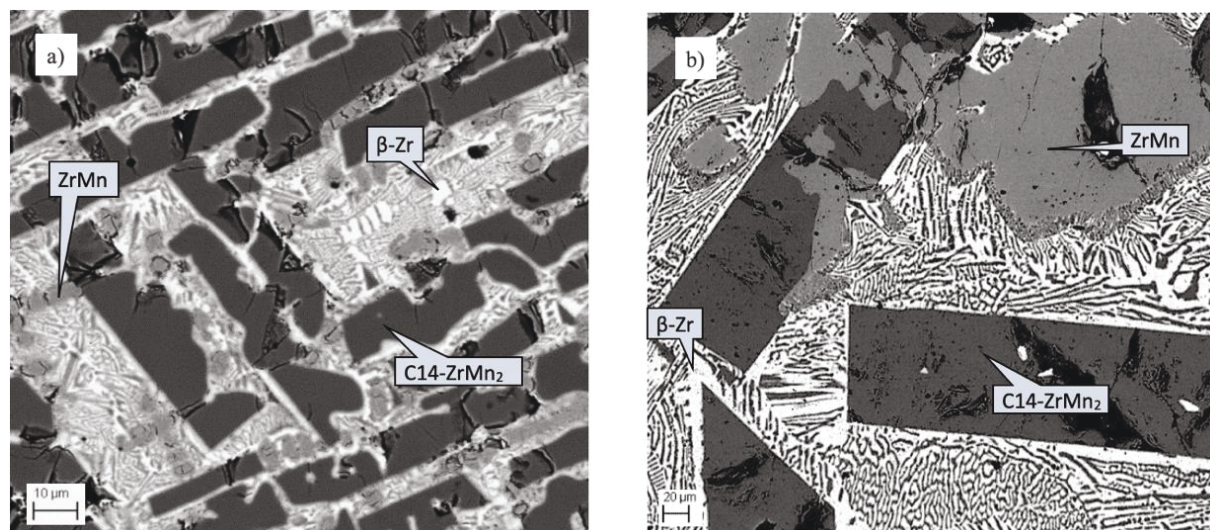


Fig. 7 – Microstructure of the sample #3 in cast state (a) and after DTA (b).

5.3. ZrMn phase

The phase with assigned 1:1 stoichiometry was rarely observed in the earlier works. In the present work, it appeared in significant quantities in the cast samples and after DTA experiments. The phase structure was identified to be the same as the Zr₃Mn₃O phase using XRD [42]. According to the literature [31] this phase can dissolve a limited amount of oxygen but less than in the Zr₃Mn₃O compound and thus it is denoted as ZrMn in the current work. Its melting temperature was determined at 1682 K. Based on the heat treatment results presented in Fig. 8a and 8b, it was concluded that the ZrMn phase was not stable down to room temperatures and decomposes between 1073 K and 1323 K. It should be noted that the decomposition of the ZrMn phase can be observed at the edges of the phase grains (Fig. 7) during cooling in the DTA experiment. Annealing of sample #4 (Fig. 8) at 1323 K did not lead to formation of the ZrMn phase, therefore contradicting the phase diagram of Okamoto [32] (Fig. 3). At the same time, ZrMn was present in sample #3 after annealing at the same temperature according to XRD (Fig. 9). Obviously equilibrium was not reached during annealing since three phases were observed in the sample. An eutectic structure with ZrMn was observed in as cast alloy sample #3 (72 at.% Zr eutectic) (Fig. 7a), though eutectic with C14-ZrMn₂ formed during cooling in DTA experiment (Fig. 7b). This can be explained by the fact stable eutectic was formed during relatively slow cooling in DTA. Since the protective gas contains some amount of oxygen, the presence of the ZrMn phase can be explained by stabilisation of this phase by oxygen impurities during DTA. Based on the observations it is suggested that the ZrMn phase most probably does not belong to the stable diagram. SEM/EDX measurements indicated an average 52 at.% Zr composition of the ZrMn phase. Although any presence of contamination by oxygen or nitrogen was not detected, a fairly small amount could be enough for ZrMn stabilization that is beyond EDX sensitivity.

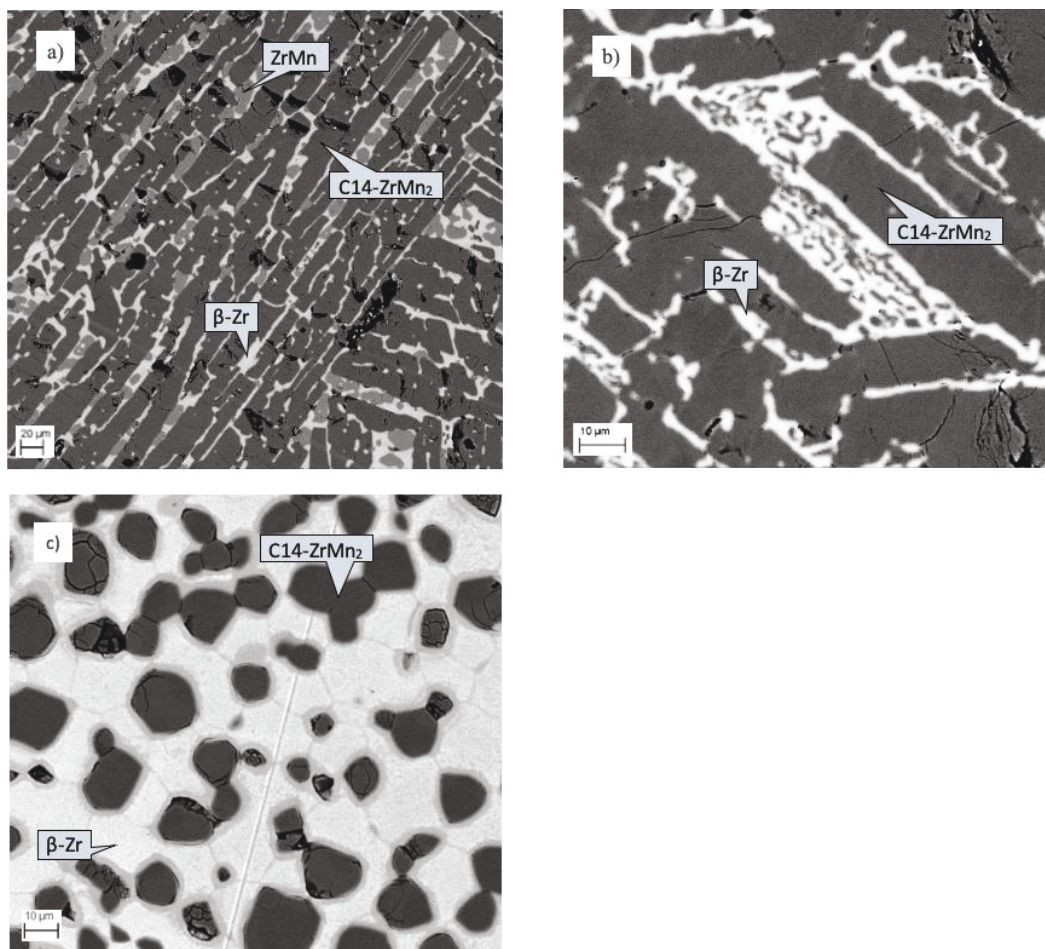


Fig. 8 – Sample #2 after annealing at 1323 K for 7 days (a) and after annealing at 1073 K for 10 days (b); sample #4 after annealing at 1323 K for 7 days (c).

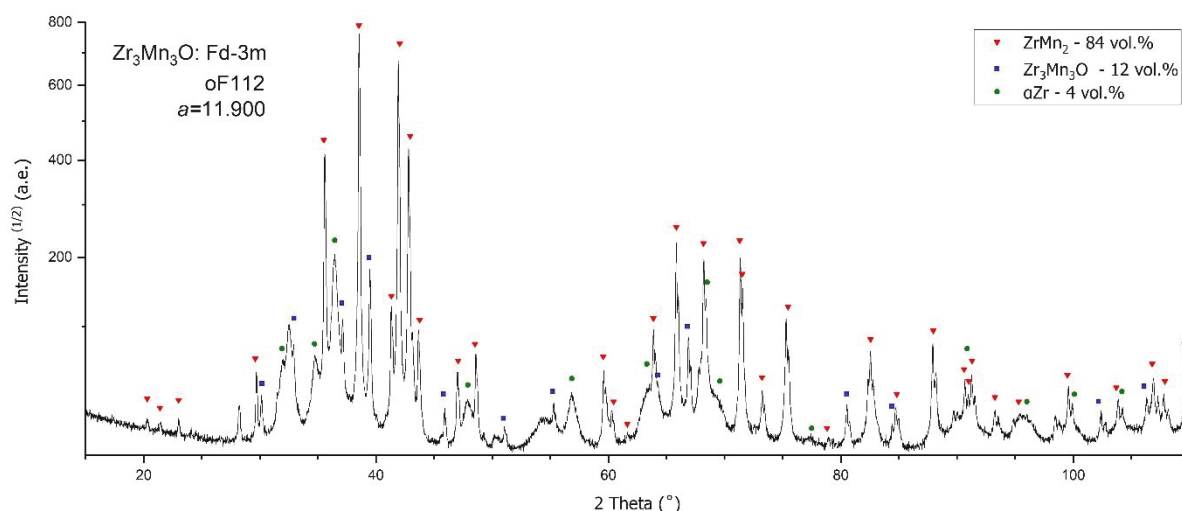


Fig. 9 – XRD pattern of the sample #3 annealed at 1323 K for 7 days.

Concerning the origin of the ZrMn phase, Zr is known to form AB compounds only with three metals of 4th period, namely Ni, Co and Cu. ZrNi possesses orthorhombic structure (oS8) while ZrCo and ZrCu possess cubic structure (cP2). Matching structure $\text{Zr}_3\text{Mn}_3\text{O}$ has 112 atoms per cell (Fig. 9). Assuming oxygen is a contamination in the phase [31], the phase with suggested ZrMn stoichiometry retains 96 atoms per cell. Taking into account that similar systems do not

contain a similar 1:1 stable phase, it can be concluded that probably the Mn–Zr system does not contain a stable ZrMn phase. An insight into the phase's nature may be found from also from another perspective. A wide family of carbides with the same A₃B₃C formula that share Fe₃W₃C structure type are isomorphous to Zr₃Mn₃O. According to the work of Karlsson [43], oxides isomorphous with the carbide Fe₃W₃C have been found to exist with the ideal composition Me₃Ti₃O, where Me is one of the transition metals manganese, iron, cobalt, nickel or copper. They were found to exhibit *Fd-3m* Space Group with 112 atoms per unit cell. The identified structure Zr₃Mn₃O is indeed isomorphous to Fe₃W₃C, exhibiting same space group and number of atoms pro unit cell as well as a group of other oxides Fe₃Ti₃O, Cu₃Ti₃O, Mn₃Ti₃O and Zr₃V₃O. Although crystal structure and its instability in the Mn–Zr system are suggested in the present work, it is recommended to perform a more detailed investigation of the structure of the ZrMn phase.

5.4. Thermodynamic modelling

The calculated phase diagram of the Mn–Zr system is presented in Fig. 10a with the Mn-rich corner (Fig. 10b). The calculated temperatures and phase compositions are compared with experimental data in Table 4. Optimized thermodynamic parameters are listed in Table 5.

At the first step of the optimization procedure the intermetallic compound C14-ZrMn₂ was modelled as a stoichiometric phase. Enthalpy of formation of the C14-ZrMn₂ and enthalpy of mixing of the liquid phase were used in the optimisation. Afterwards, thermodynamic descriptions of the homogeneity ranges of BCC, HCP, CUB, CBCC, as well as C14-ZrMn₂ were optimized based on the obtained experimental results and literature data published by Hellawell [9] and Flandorfer et al. [5].

Experimentally determined values of enthalpy of formation of the C14-ZrMn₂ phase are -16.3 ± 5.1 kJ/mole-at by Smetana et al. [15] and -22.66 ± 0.82 kJ/mole-at by Rotter et al. [16]. DFT calculation results performed by Rotter et al. [16] at -20.3 kJ/mole-at is close to experimental values. It should be pointed out that the value calculated based on the description of Flandorfer et al. [5] is equal to -13.33 kJ/mole-at and thus it is even lower than measured by Smetana et al. [15]. According to the thermodynamic description of the present work the value of enthalpy of formation of C14-ZrMn₂ is equal to -23.46 kJ/mole-at. This result is in a good accordance with Rotter et al. [16] accounting uncertainty limits of the measured value. Parameters describing the temperature dependence of heat capacity fitted by the Maier-Kelley equation were fixed according to Eq. (8). Standard entropy calculated in the current work was also fixed while enthalpy of formation of the C14-ZrMn₂ phase was optimized.

The thermodynamic dataset derived in the present work reproduces phase equilibria in the manganese-rich side according to Hellawell [9] in contrast with the assessment of Flandorfer et al. [5] which does not reproduce data of both works of Hellawell [9] and Savitskii and Kopetskii [12]. However, due to the lack of experimental data in that area, the phase diagram for Mn-rich compositions should be considered as a tentative calculation. In the assessment of Flandorfer et al. [5], the calculated temperature of eutectic reaction $L = \text{C14-ZrMn}_2 + \beta\text{-Zr}$ was in accordance with data of Massalski [7], though the DTA experiments [5] indicated a higher temperature. In the present assessment melting temperature of C14-ZrMn₂ and eutectic reaction were optimized based on our own DTA results. As said above, the melting of C14-ZrMn₂ was measured to be 1765 K at the chemical composition of about 32.3 at.% of Zr (sample #1). Calculations of the temperature and the chemical composition of invariant reaction $L = \text{C14-ZrMn}_2$ presented very good agreement with experimental results (Table 4).

Table 4 – Invariant equilibria in the Mn – Zr system.

Reaction, at.% Zr					Type	T (K)	Reference
Liq	↔	δ-Mn	+	C14-ZrMn ₂	Eutectic		
6		1.25		26		1433	Cal. this work
5		1.25		–		1428	[9]
4.9		–		25		–	[5]
5		1.25		20.83		1433	[7]
Liq	↔	β-Zr	+	C14-ZrMn ₂	Eutectic		
70.23		–		34.55		1409	Exp. This work
67.2		88		34.9		1405	Cal. this work
67.5		–		34		1363	[5]
67.5		89.8		40		1363	[7]
Liq	↔	C14-ZrMn ₂			Congruent		
		32.30				1765	Exp. this work
		32.88				1765	Cal. this work
		34				1613	[12]
		33.3				1843	[13]
		33.30				1723	[7]
δ-Mn	↔	γ-Mn	+	β-Mn	Eutectoid		
0.55		0.42		0.94		1399	Cal. this work
0.50		~0.15		~0.85		1393	[7]
δ-Mn	+	C14-ZrMn ₂	↔	β-Mn	Peritectoid		
0.11		26				1414	Cal. this work
~0.9		20.83		1.25		1413	[7]
β-Zr	↔	α-Zr	+	C14-ZrMn ₂	Eutectoid		
96.7		99		34		1066	Cal. this work
95.1		~99		40		1063	[7]
β-Mn	↔	C14-ZrMn ₂	+	α-Mn	Eutectoid		
0.13		28		0.01		975	Cal. this work

It should be mentioned, that the calculated homogeneity range of C14-ZrMn₂ at room temperature lays between 33.25 and 33.33 at.% of Zr. However, there were no experimental data for the solid solution of C14-ZrMn₂ at low temperatures.

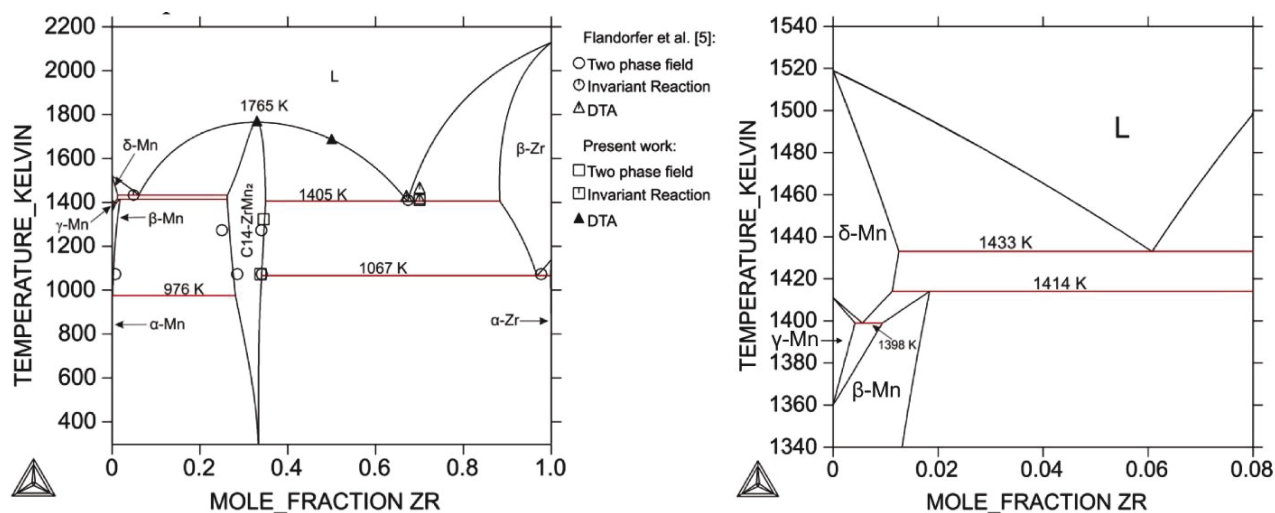


Fig. 10 – Calculated Mn – Zr phase diagram (left) and Mn-rich region of the diagram (right).

Table 5 – Optimized thermodynamic parameters of the Mn–Zr system.

Phase	Sublattice model	Optimized parameters*
Liquid	(Mn,Zr) ₁	${}^0L(\text{LIQUID}, \text{Mn}, \text{Zr}) = -73668.72 + 30.30 \cdot T$ ${}^1L(\text{LIQUID}, \text{Mn}, \text{Zr}) = -1991.63$
BCC_A2	(Mn,Zr) ₁ (Va) ₃	${}^0L(\text{BCC_A2}, \text{Mn}, \text{Zr}; \text{Va}) = -2135.3475 - 0.13258 \cdot T$ ${}^1L(\text{BCC_A2}, \text{Mn}, \text{Zr}; \text{Va}) = -1084$
CBCC_A12	(Mn,Zr) ₁ (Va) ₁	${}^0L(\text{CBCC_A12}, \text{Mn}, \text{Zr}; \text{Va}) = 20000$
CUB_A13	(Mn,Zr) ₁ (Va) ₁	${}^0L(\text{CUB_A13}, \text{Mn}, \text{Zr}; \text{Va}) = -18000$
FCC_A1	(Mn,Zr) ₁ (Va) ₁	${}^0L(\text{FCC_A1}, \text{Mn}, \text{Zr}; \text{Va}) = -7200$
HCP_A3	(Mn,Zr) ₁ (Va) _{0.5}	${}^0L(\text{HCP_A3}, \text{Mn}, \text{Zr}; \text{Va}) = 25000$
C14-ZrMn ₂	(Mn,Zr) ₁ (Mn,Zr) ₂	$G(\text{Mn}_2\text{Zr}, \text{Mn}; \text{Zr}) = -95954.93 + 427.95342 \cdot T - 9.295 \cdot 10^{-3} \cdot T^2 - 77.2627 \cdot T \cdot \ln(T) + 2.432485 \cdot 10^5 \cdot T^{-1}$ $G(\text{Mn}_2\text{Zr}, \text{Zr}; \text{Mn}) = 95954.93 - 427.95342 \cdot T + 9.295 \cdot 10^{-3} \cdot T^2 + 77.2627 \cdot T \cdot \ln(T) - 2.432485 \cdot 10^5 \cdot T^{-1} + 95000$ $G(\text{Mn}_2\text{Zr}, \text{Zr}; \text{Zr}) = 3 \cdot \text{GHSEZR} + 80000$ $G(\text{Mn}_2\text{Zr}, \text{Mn}; \text{Mn}) = 3 \cdot \text{GHSERMN} + 15000$

*Optimized parameters are given in the unit of Joule per mole of formula of with applied sublattice models.

Optimization was done using available experimental and theoretical data. For the description of the liquid phase, the only available data on mixing enthalpy from Sidorov et al. [17] were used for the optimization with a low weight. During the optimization, it was found that the data [17] were not well reproduced and consequently were inconsistent with the set of used experimental data. Additionally, the same method applied for measurements of enthalpy of mixing of iron-zirconium melts in another work of Sidorov et al. [44] resulted in more positive values than obtained in several independent measurements [18]. Calculated and experimental data on mixing enthalpy are presented in Fig. 11.

In comparison with the assessment of Flandorfer et al. [5] (Table 4), current re-assessment has the following improvements: the C14-ZrMn₂ phase was modelled using measured heat capacity data and calculated standard entropy; melting temperature of the C14-ZrMn₂ phase is in agreement with DTA results of the present work; temperature of the eutectic reaction $L = \text{C14-ZrMn}_2 + \beta\text{-Zr}$ is in better agreement with experimental data.

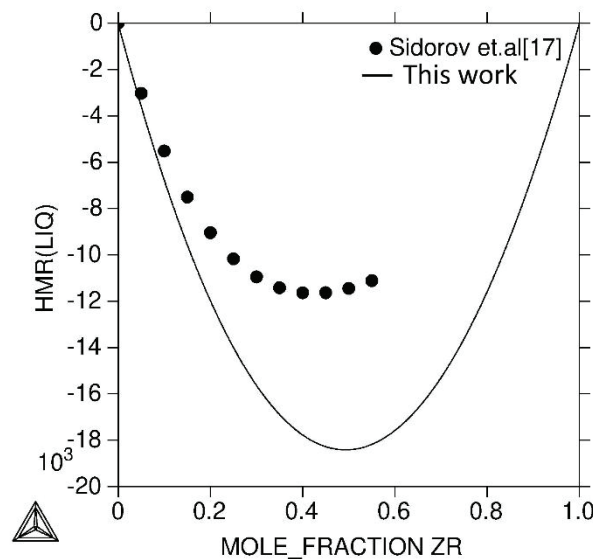


Fig. 11 – Mixing enthalpy of the liquid phase at 1846 K with the values after optimization.

Reproducing all available experimental data within uncertainty limits, obtained thermodynamic description reveals an inverted miscibility gap in the liquid phase at the temperatures above 5380 K. It should be noted that the boiling points of pure components are substantially lower (4650 K for zirconium and 2334 K for manganese) than temperature of the inverted miscibility gap and therefore the gas phase should be stable at 5380 K and above.

5. Conclusions

Heat capacity of the Laves C14-ZrMn₂ phase was measured in the range 200 – 980 K by means of DSC. Obtained data were applied for the Gibbs energy description of the C14-ZrMn₂ phase. An Extended Einstein model was applied for the description of heat capacity in the range from 0 to 1000 K and was used to calculate standard entropy as 32.6 J·mole⁻¹·K⁻¹. Melting temperature of C14-ZrMn₂ phase was measured at 1765 K using the DTA method.

The thermodynamic parameters of the Mn–Zr system were re-assessed taking into account new measurement of enthalpy of formation and DFT calculation by Rotter et al. [16]. Enthalpy of formation of C14-ZrMn₂ was calculated to be -23.46 kJ/mole-at, which agrees with the experimental value from Rotter et al. [16] within the uncertainty limits. The model of the C14-ZrMn₂ phase set to (Mn,Zr)₂(Mn,Zr)₁ was based on antisite substitution. The calculated temperature of the eutectic reaction $L = \text{C14-ZrMn}_2 + \beta\text{-Zr}$ was higher compared to Flandorfer et al. [5] and Massalski [7] since higher weight was given to experimental results of the present work and DTA data of Ref. [5]. The ZrMn melting temperature was determined at 1682 K using DTA and it was observed that this phase decomposed completely at 1073 K. It is assumed that ZrMn phase is metastable or stabilized by impurities based on the fact that this phase was absent in several alloys as well as on systematic considerations. The weight given to the data on mixing enthalpy of the liquid phase determined in the work of Sidorov et al. [17] were decreased during optimization because they deviated significantly from the calculated values of the present work.

The re-assessment of the Mn–Zr system has been performed in order to update set of the Gibbs energies for all phases in the system. Liquid and solid solution phases have been described by a substitutional model. For the description of the C14-ZrMn₂ phase homogeneity range, the compound energy formalism was applied [39]. Presented description reproduces well the experimental data on phase equilibria and thermodynamic properties of the phases.

Acknowledgments

The authors gratefully acknowledge the German Research Foundation (DFG) for funding the sub-project C2 within the Collaborative Research Center SFB 799 Trip-Matrix-Composites. We are grateful to G. Savinykh and Dr. C. Schimpf (TU-Freiberg) for technical contributions. We would like to thank D. Chebykin for scientific support.

References

- [1] G. Li, N. Nishimiya, *J. Alloy. Compd.* 375 (2004) 205.
- [2] L. Dai, S. Wang, L. Wang, et al., *Trans. Nonferrous Met. Soc. China* 24 (2014) 2883.
- [3] H. Biermann, U. Martin, C.G. Aneziris, et al., *Adv. Eng. Mater.* 43 (2009) 1000.
- [4] S. Martin, S. Richter, S. Decker, et al., *Steel Research int.* 82 (2011) 1133.
- [5] H. Flandorfer, J. Groebner, A. Stamou, N. Hassiotis, *Z. f. Metall.* 88 (1997) 529.

- [6] K. Hack, System Mn - Zr, in: I. Ansara, A.T. Dinsdale, M.H. Rand (Eds.), Thermochemical database for light metal alloys. Ans1998, Office for Official Publications of the European Communities, Luxembourg, (1998) 245.
- [7] T.B. Massalski, J.L. Murray, Binary alloy phase diagrams. Second print. 1987, American Society for Metals, Metals Park, Ohio, 1987.
- [8] Roberson A.H., E.T. Hayes, V.V. Donaldson, *ASM* (1953) 283.
- [9] A. Hellawell, *J. Less Common Met.* 1 (1959) 343.
- [10] V.N. Svechnikov, V.V. Pet'kov, *Metallofizika* 64 (1976) 24.
- [11] N. Nishimiya, *Mater. Res. Bull.* 21 (1986) 1025.
- [12] E.M. Savitskii, C.V. Kopetskii, *Russ. J. Inorg. Chem.* 5 (1960) 1173.
- [13] V.V. Pet'kov, *Izv. Akad.Nauk SSSR, Met.* 5 (1972) 155.
- [14] M.E. Schlesinger, *J. Phase Equilib. Diff.* 20 (1999) 79.
- [15] F. Smetana, P. Entner, A. Neckel, *Monatshefte fuer Chemie* 101 (1970) 956.
- [16] M. Rotter, A. Grytsiv, X.-Q. Chen, et al., *Phys. Rev. B* 74 (2006) 688.
- [17] O.Y. Sidorov, M.G. Valishev, S.V. Kolesnikov, et al., *Metally* 3 (1991) 58.
- [18] I. Saenko, A. Kuprava, A. Udovsky, O. Fabrichnaya, *CALPHAD* 66 (2019) 101625.
- [19] D.J. Thoma, Intermetallics: Laves Phases, in: Encyclopedia of Materials: Science and Technology, Elsevier, (2001) 4205.
- [20] J.H. Zhu, L.M. Pike, C.T. Liu, P.K. Liaw, *Acta Mater.* 47 (1999) 2003.
- [21] S. Liu, B. Hallstedt, D. Music, Y. Du, *CALPHAD* 38 (2012) 43.
- [22] K. Zeng, H. Marko, L. Kaj, *CALPHAD* 17 (1993) 101.
- [23] J. Pavlů, J. Vřešt'ál, M. Šob, *CALPHAD* 34 (2010) 215.
- [24] J. Pavlů, J. Vřešt'ál, X.-Q. Chen, P. Rogl, *CALPHAD* 35 (2011) 103.
- [25] C.P. Gazzara, R.M. Middleton, R.J. Weiss, E.O. Hall, *Acta Cryst.* 22 (1967) 859.
- [26] C.B. Shoemaker, D.P. Shoemaker, T.E. Hopkins, S. Yindepit, *Acta Crystall. B Struct. Sci.* 34 (1978) 3573.
- [27] J. Goldak, L.T. Lloyd, C.S. Barrett, *Phys. Rev.* 144 (1966) 478.
- [28] R.B. Russell, *JOM* 6 (1954) 1045.
- [29] H.J. Wallbaum, *Z. f. Kristall.* 103 (1941).
- [30] T. Kodama, *J. Alloy. Compd.* 256 (1997) 263.
- [31] L.D. Gulay, V.I. Zaremba, *J. Alloy. Compd.* 347 (2002) 184.
- [32] H. Okamoto, *J. Phase Equilib. Diff.* 19 (1998) 93.
- [33] L. Lutterotti, *Acta Crystall.* 56 (2000) 54.
- [34] G. Della Gatta, M.J. Richardson, S.M. Sarge, S. Stølen, *Pure Appl. Chem.* 78 (2006) 1455.
- [35] A.T. Dinsdale, *CALPHAD* 15 (1991) 317.
- [36] M. Hillert, M. Jarl, *CALPHAD* 2 (1978) 227.
- [37] O. Redlich, A.T. Kister, *Ind. Eng. Chem.* 40 (1948) 345.
- [38] H.L. Lukas, S.G. Fries, B. Sundman, Computational thermodynamics: The calphad method, Cambridge University Press, New York, 2007.
- [39] M. Hillert, *J. Alloy. Compd.* 320 (2001) 161.
- [40] J.-O. Andersson, T. Helander, L. Höglund, et al., *CALPHAD* 26 (2002) 273.
- [41] M.W. Chase, I. Ansara, A.T. Dinsdale, et al., *CALPHAD* 19 (1995) 437.
- [42] L.V. Zavalii, Riabov A.B, in: International Conference on Crystal Chemistry of Intermetallic Compounds, Lviv, 1995.
- [43] N. Karlson, *Nature* 168 (1951) 558.
- [44] O.Y. Sidorov, M.G. Valishev, Y.O. Esin, P.V. Gel'd, *Metally* 6 (1988) 19.

Publication P7: I. Saenko, O. Fabrichnaya, Thermodynamic database development for the $\text{ZrO}_2\text{--MgO--MnO}_x$ system, *Journal of Phase Equilibria and Diffusion* 41 (2020) 654–671.
DOI: 10.1007/s11669-020-00832-2

Contributions to the paper:

Authors	Contribution [%]	Particular contribution
I. Saenko	50	<ul style="list-style-type: none">• Evaluation of data• Co-composition of the manuscript
Dr. rer. nat. habil. O. Fabrichnaya	50	<ul style="list-style-type: none">• Thermodynamic modelling• Composition of the manuscript

Thermodynamic database development for the $\text{ZrO}_2\text{--MgO--MnO}_x$ system

I. Saenko*, O. Fabrichnaya

Technical University Berakademie Freiberg, Institute of Materials Science, Gustav-Zeuner-Str. 5. D-09599, Germany

* Corresponding author:

I. Saenko, Technical University Berakademie Freiberg, Institute of Materials Science, Gustav-Zeuner-Str. 5. D-09599, Germany

E-mail: i.saenko@iww.tu-freiberg.de

Abstract

Thermodynamic description of the $\text{ZrO}_2\text{--MgO--MnO}_x$ was derived for the first time using available experimental data on phase relations in air and protective gas atmosphere. Solid solution phases were modelled using compound energy formalism. The liquid phase was described by the modified two-sublattice model for ionic liquid. Solubility of ZrO_2 was modelled in cubic spinel and MgO--MnO solid solution (halite structure) and therefore the Gibbs energies of Zr-containing end-members were introduced. Ternary interaction parameters were introduced for halite, cubic spinel and cubic ZrO_2 in order to reproduce the stabilization of cubic ZrO_2 at temperatures below its stability in bounding systems and stabilization of cubic spinel at temperatures above its stability limit in the bounding systems. The obtained thermodynamic database was used to interpret results of differential thermal analysis.

1. Introduction

Phase equilibria in the $\text{ZrO}_2\text{--MgO--MnO}_x$ system are of interest due to several possible applications. One of them is development of TRIP steel metal matrix composite material strengthened by particles of MgO partially stabilized zirconia (Mg-PSZ)[1]. Manganese provides good adhesion bonding between the steel matrix and the Mg-PSZ ceramics[2,3]. On the other hand, manganese is one of the main alloying elements of the steel matrix and can substitute Mg in Mg-PSZ during processing of this metal matrix composite[2,4,5] thus influencing the stability of the Mg-PSZ structure. It was shown that due to Mg diffusion from Mg-PSZ into precipitate sites or the steel matrix the Mg-PSZ was destabilized and transformed into the monoclinic phase, while due to diffusion of Mn into ZrO_2 particles, grains at its boundary remained cubic or tetragonal[5]. Therefore, knowledge of phase relations in the $\text{ZrO}_2\text{--MgO--MnO}_x$ system is important to improve the stability of Mg-PSZ and its bonding to the steel matrix.

The other possible application of the $\text{ZrO}_2\text{--MgO--MnO}_x$ system is for directionally solidified eutectic materials since both bounding systems $\text{ZrO}_2\text{--MgO}$ and $\text{ZrO}_2\text{--MnO}_x$ are known to form directionally solidified eutectics[6,7].

The phase relations in the $\text{ZrO}_2\text{--MgO--MnO}_x$ system were experimentally studied by Pavlyuchkov et al.[8] for the first time. The investigations were carried out in air and inert gas atmosphere. It was shown that relatively small additions of ZrO_2 stabilize cubic spinel in the ternary system in air at temperatures exceeding its stability range in the MgO--MnO_x bounding system and compositions substantially enriched by MgO. The addition of ZrO_2 also significantly extends the homogeneity range of halite (MgO--MnO solid solution) toward MnO solubility in air. It should be also noted that cubic ZrO_2 -based solid solutions are stabilized in the $\text{ZrO}_2\text{--MgO--MnO}_x$ system down to lower temperatures in comparison with the bounding systems both in air and inert gas atmosphere.

The thermodynamic descriptions of the bounding systems are available in literature[9–11]. However the description of the $\text{ZrO}_2\text{--MnO}_x$ system needed to be modified since the description of the Mn–O system accepted by Dilner et al.[11] was from work of Kjellqvist and Selleby[12] while the one accepted by Pavlyuchkov et al. [10] was from work of Grundy et al.[13]. Though the phase diagram of the Mn–O system was very similar in both works, the description of Kjellqvist and Selleby[12] is more advanced as it takes into account species distribution in the Mn_3O_4 tetragonal and cubic spinel. Special attention should be given to the fact that the thermodynamic description of the bounding systems $\text{ZrO}_2\text{--MnO}_x$ and $\text{ZrO}_2\text{--MgO}$ will be modified due to introducing Zr^{+4} in spinel and halite models and this should cause only minimal change to the phase diagrams of the bounding systems. It should also be noted that stabilization of spinel and cubic ZrO_2 in the quaternary system outside its stability ranges in the bounding system would require introducing Zr containing end-members in spinel and halite as well as ternary interaction parameters in all above mentioned phases to reproduce experimental data. Though the thermodynamic descriptions of the bounding systems are available, the system $\text{ZrO}_2\text{--MgO--MnO}_x$ was not modelled so far.

The aim of the present work is to develop thermodynamic description of the $\text{ZrO}_2\text{--MgO--MnO}_x$ system which reproduces experimental data for the system. Some key DTA experiments are planned to verify the thermodynamic description.

2. Materials and methods

Samples were prepared using the co-precipitation method followed by evaporation procedure. The zirconium acetate solution in acetic acid $\text{Zr}(\text{CH}_3\text{COO})_4$ (99.99 %, Sigma-Aldrich), aqueous solution of manganese nitrate $\text{Mn}(\text{NO}_3)_2$ (99.9%, Alfa Aesar) and magnesium nitrate hexahydrate $\text{Mg}(\text{NO}_3)_2 \cdot 6\text{H}_2\text{O}$ (99.97%, Alfa Aesar) have been used as the primary chemicals. A detailed description of the sample preparation route was presented in Ref[8].

X-ray powder diffraction (XRD) was performed using the URD63 diffractometer (Seifert, FPM, Freiberg, Germany) equipped by graphite monochromator with $\text{CuK}\alpha$ radiation ($\alpha = 1.5418 \text{ \AA}$). The goniometer of the diffractometer had Bragg-Brentano geometry. Rietveld refinement was applied using the Maud software [14] for the characterization of all measured diffraction patterns in order to obtain the volume fractions of present phases as well as lattice parameters. Microstructural investigations have been carried out using scanning electron

microscopy combined with dispersive X-ray spectrometry (SEM/EDX; Leo1530, Carl Zeiss/Bruker AXS Mikroanalysis GmbH). Chemical compositions of samples, phases and eutectic compositions have been determined using an EDX detector with an accuracy of ± 4 mol. %. Differential thermal analysis coupled with thermogravimetry (DTA-TG) was performed using a Setsys Evolution 1750 device with PtRh10% crucibles, a heating rate of $10 \text{ K} \cdot \text{min}^{-1}$ and He atmosphere.

3. Thermodynamic modelling

As basis for the thermodynamic description of the $\text{ZrO}_2\text{--MgO--MnO}_x$ system, the modelling of the MgO--MnO_x boundary system was accepted according to the work of Dilner et al.[11]. The phase and their models are listed in Table 1. The liquid phase is described by modified two-sublattice model for ionic liquid[15,16], while solid solutions are described by compound energy formalism[17]. Zr^{+4} ions were introduced in the liquid phase, cubic spinel and halite phase. The thermodynamic descriptions of the $\text{ZrO}_2\text{--MgO}$ [9] and MgO--MnO_x [11] systems are compatible. Only due to the introduction of Zr^{+4} in the halite phase the boundary system should be checked to avoid noticeable solubility of ZrO_2 in halite. Due to using different species in the ionic liquid in the Mn--O system by Kjellqvist and Selleby[12] ($\text{MnO}_{1.5}$ neutral species in the anionic sublattice) and by Grundy et al.[13] (Mn^{+3} in the cationic sublattice) which were subsequently accepted in the work of Dilner et al.[11] for the MgO--MnO_x system and Pavlyuchkov et al.[10] for the $\text{ZrO}_2\text{--MnO}_x$ system, the liquid phase description appeared to be incompatible. Though there is no experimental evidence, which model is to be preferred the thermodynamic description of the liquid by Kjellqvist and Selleby[12] was accepted because of their advanced modelling of tetragonal and cubic spinel phases along with their good reproduction of the phase diagram and thermodynamic properties in the Mn--O system. Therefore, the description of the liquid phase should be modified in the $\text{ZrO}_2\text{--MnO}_x$ system. Due to the introduction of Zr^{+4} in halite and βSp phases the solubility of ZrO_2 should be very small in the $\text{ZrO}_2\text{--MnO}_x$ system.

The thermodynamic model assuming two-sublattices was accepted for the three modifications of ZrO_2 solid solutions as in the bounding systems. The solubility of Mg^{+2} , Mn^{+3} and Mn^{+2} in the ZrO_2 solid solutions were first based on extrapolations from bounding systems and then ternary interaction parameters were introduced to the cubic ZrO_2 based solid solution (c- ZrO_2). The solubilities of ZrO_2 in cubic spinel (βSp) and halite phases were experimentally established by Pavlyuchkov et al.[8] in the system $\text{ZrO}_2\text{--MgO--MnO}_x$. The thermodynamic description of t- ZrO_2 and m- ZrO_2 were combined based on descriptions of bounding systems because solubility of MgO and MnO_x was rather small in these phases and no ternary parameters were necessary to reproduce phase relations involving these phases. Thermodynamic descriptions of c- ZrO_2 , βSp and halite were modified in comparison with extrapolations from the bounding systems. Ternary parameters and the Gibbs energy of end-members involving Zr^{+4} were necessary to model the solubility of ZrO_2 in βSp and halite and to reproduce phase relations involving c- ZrO_2 , βSp and halite. The description of liquid was based on extrapolations from bounding systems. This was enough to reproduce phase relations involving liquid. The description of other phases such as α -spinel, Mn_2O_3 , MnO_2 and Mg_6MnO_8 were accepted from

Ref.[11] and were not modified further because phase equilibria studied in Ref.[8] did not involve only these phases.

Table 1. Phases in the Zr–Mn–Mg–O system.

Phase name and abbreviation	Space group	Thermodynamic model
ZrO ₂ based solid solutions		(Zr ⁺⁴ ,Mg ⁺² ,Mn ⁺² ,Mn ⁺³) ₁ (O ⁻² ,Va) ₂
cubic, c-ZrO ₂	<i>Fm</i> $\bar{3}$ <i>m</i>	
tetragonal, t-ZrO ₂	<i>P4</i> ₂ / <i>nmc</i>	
monoclinic, m-ZrO ₂	<i>P2</i> ₁ / <i>c</i>	
halite (H)	<i>Fm</i> $\bar{3}$ <i>m</i>	(Mg ⁺² ,Mn ⁺² ,Mn ⁺³ ,Zr ⁺⁴ ,Va) ₁ (O ⁻²) ₁
α -spinel (α Sp)	<i>I4</i> ₁ / <i>amd</i>	(Mg ⁺² ,Mn ⁺² ,Mn ⁺³) ₁ (Mg ⁺² ,Mn ⁺² ,Mn ⁺³ ,Va) ₂ (Mg ⁺² ,Mn ⁺² ,Va) ₂ (O ⁻²) ₄
β -spinel (β Sp)	*	(Mg ⁺² ,Mn ⁺²) ₁ (Mg ⁺² ,Mn ⁺² ,Mn ⁺³ ,Zr ⁺⁴ ,Va) ₂ (Mg ⁺² ,Mn ⁺² ,Va) ₂ (O ⁻²) ₄
Mn ₂ O ₃	<i>Ia</i> $\bar{3}$	(Mn ⁺³ ,Mn ⁺²) ₂ (O ⁻² ,Va) ₃ (O ⁻² ,Va) ₁
MnO ₂	<i>P4</i> ₂ / <i>mnm</i>	(Mn ⁺⁴) ₁ (O ⁻²) ₂
bcc	<i>Im</i> $\bar{3}$ <i>m</i>	(Mg,Mn,Zr) ₁ (O,Va) ₃
hcp	<i>P6</i> ₃ / <i>mnc</i>	(Mg,Mn,Zr) ₁ (O,Va) _{0.5}
fcc	<i>Fm</i> $\bar{3}$ <i>m</i>	(Mg,Mn,Zr) ₁ (O,Va) ₁
cbcc	<i>I</i> $\bar{4}$ <i>3m</i>	(Mg,Mn,Zr) ₁ (Va) ₁
cub_A13	<i>P4</i> ₁ <i>32</i>	(Mg,Mn,Zr) ₁ (Va) ₁
C14-ZrMn ₂ (C14)	<i>P6</i> ₃ / <i>mmc</i>	(Zr,Mn) ₂ (Zr,Mn) ₁

* β -spinel is supposed to have a cubic structure. However, in the work of Pavlyuchkov et al.[10], β -spinel has been identified by a tetragonal structure, which is very close to cubic symmetry.

It should be noted that phase equilibria were investigated in the field of stability of cubic spinel phase, while it transformed to tetragonal spinel during cooling. For most compositions cubic spinel is not quenchable (except Mg-rich compositions). Tetragonal ZrO₂ in the studied system is not quenchable transforming to the monoclinic phase. In order to get the preserved ZrO₂ with cubic structure also fast cooling was required. Therefore, in order to interpret experimental results, it was assumed that phases such as cubic spinel, tetragonal and cubic ZrO₂ solid solutions transformed to their low-temperature modifications without composition change.

3.1. Liquid

Liquid phase was described using the modified two sublattice model for ionic liquid [15,16] with the formula (Mg⁺²,Mn⁺²,Zr⁺⁴)_P(O⁻²,Va^{-Q},MnO_{1.5})_Q, where P and Q are stoichiometric parameters changing with composition to keep electro-neutrality.

3.2. Cubic spinel

Cubic spinel was described by the compound energy formalism assuming mixing in tetrahedral and octahedral sites also assuming that Mg⁺² and Mn⁺² can occupy part of octahedral sites which are normally vacant: (Mg⁺²,Mn⁺²)₁(Mg⁺²,Mn⁺²,Mn⁺³,Mn⁺⁴,Zr⁺⁴,Va)₂(Mg⁺²,Mn⁺²,Va)₂(O⁻²)₄. Therefore the model used in the work of Dilner et al.[11] was expanded by considering Zr⁺⁴ cations occupying the octahedral sites. It was assumed that smaller tetrahedral sites cannot be occupied by large Zr⁺⁴ cations. Therefore, six new end-members appeared. The Gibbs energy

of two of them can be derived using the electro-neutrality reactions between end-member compounds:



Mg₂ZrO₄ and Mn₂ZrO₄ are inversed spinel, Mg(Mg_{0.5}Zr_{0.5})₂O₄ and Mn(Mn_{0.5}Zr_{0.5})₂O₄ are fictive compounds, both unstable in the boundary systems. The Gibbs energy for these fictive compounds were described as the sum of the Gibbs energy of the oxides $G_{\text{ZrO}_2} + 2 \cdot G_{\text{MO}} + V_n$, where M=Mg⁺² or Mn⁺² and V_n (n=1,2) stands values to be optimized in both bounding systems. The calculated phase diagrams should show very limited solubility of ZrO₂ in spinel in the case of the ZrO₂–MnO_x system and avoid the spinel phase appearing in the ZrO₂–MgO system.

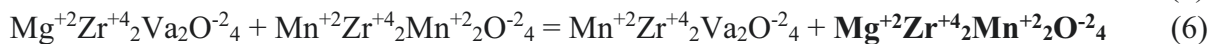
The Gibbs energy of inversed spinel in both systems can be written as following

$$G_{\text{M}_2\text{ZrO}_4} = 0.5 \cdot G_{\text{M}^{+2}\text{Zr}^{+4}\text{Va}_2\text{O}^{-2}_4} + 0.5 \cdot G_{\text{M}^{+2}\text{M}^{+2}\text{Va}_2\text{O}^{-2}_4} + 2 \cdot R \cdot T \cdot (0.5 \cdot \ln(0.5) + 0.5 \cdot \ln(0.5)) \quad (3)$$

Therefore, the Gibbs energy for the end-members $\mathbf{M}^{+2}\mathbf{Zr}^{+4}_2\mathbf{Va}_2\mathbf{O}^{-2}_4$ can be derived from equations 1 and 2:

$G_{\text{M}^{+2}\text{Zr}^{+4}\text{Va}_2\text{O}^{-2}_4} = 2 \cdot G_{\text{M}_2\text{ZrO}_4} - G_{\text{M}^{+2}\text{M}^{+2}\text{Va}_2\text{O}^{-2}_4} + 4 \cdot R \cdot T \cdot \ln(2)$, with the last term being the contribution from configurational entropy. The Gibbs energy of end-members $\mathbf{M}^{+2}\mathbf{M}^{+2}_2\mathbf{Va}_2\mathbf{O}^{-2}_4$ were accepted from Mn-Mg-O system [11].

For other four end-members (in bold) the Gibbs energy can be obtained from reciprocal reactions involving end-members with known Gibbs energy:



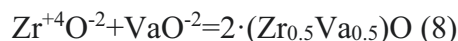
The Gibbs energies of reciprocal reactions were assumed to be zero. However, in case of necessity they can be considered as deviating from zero and adjusted to reproduce experimental data.

3.3. Halite

Halite is a monoxide solid solution with NaCl structure. The thermodynamic description of the halite phase was accepted from Dilner et al.[11] assuming that the cations Mg⁺², Mn⁺² and Mn⁺³ occupy the cationic sublattice together with vacancies that assure to keep electro-neutrality condition. To take into account the limited solubility of ZrO₂ (up to 4 mol.%) in halite the

determined by Pavlyuchkov et al.[8], Zr^{+4} was introduced into the cationic sublattice and thus the model for halite phase was presented by the formula $(Mg^{+2}, Mn^{+2}, Mn^{+3}, Zr^{+4}, Va)_1(O^{-2})_1$.

The electro-neutrality condition due to the hetero-valent substitution of divalent cation for Zr^{+4} was described by following reaction between end-members:



The Gibbs energy for VaO^{-2} fictive end-member was accepted to be equal to zero in accordance with Kjellqvist and Selleby[12]. The compound $Zr_{0.5}O$ is therefore the fictive end-member with the NaCl structure and its Gibbs energy is equal to $\frac{1}{2} (^{\circ}G_{ZrO_2_c} + V3)$, where V3 is the parameter to describe the very small solubility of ZrO_2 in the halite phase stable in both bounding systems ZrO_2 -MgO and ZrO_2 - MnO_x . Therefore, the Gibbs energy of the $Zr^{+4}O^{-2}$ fictive compound can be obtained from equation (6) as follows:

$$^{\circ}G_{Zr^{+4}:O^{-2}} = G_{ZrO_2_c} + V3 - ^{\circ}G_{Va:O^{-2}} + 2 \cdot R \cdot T \cdot \ln(2), \quad \text{which can be further rearranged to}$$

$$^{\circ}G_{Zr^{+4}:O^{-2}} = G_{ZrO_2_c} + V3 + 11.52622 \cdot T.$$

3.4. ZrO_2 based solid solutions

The same model described by the formula $(Zr^{+4}, Mg^{+2}, Mn^{+2}, Mn^{+3})_1(O^{-2}, Va)_2$ was applied for all three ZrO_2 -based solid solutions with the parameters accepted from bounding systems. Additional two ternary parameters describing interaction between $Zr^{+4}, Mg^{+2}, Mn^{+2}$ and $Zr^{+4}, Mg^{+2}, Mn^{+3}$ were introduced into C- ZrO_2 to describe experimentally determined stability ranges and homogeneity ranges.

Phases present in the system Zr-Mg-Mn-O are listed in Table 1 including crystallographic information and accepted thermodynamic models. It should be mentioned that in the thermodynamic description developed in the present work besides the already mentioned sub-systems like Mn-O, ZrO_2 - MnO_x , ZrO_2 -MgO and MgO- MnO_x , the binary descriptions for the systems of Zr-O[18], Mg-O[19], Zr-Mn[20], Zr-Mg[21] and Mg-Mn[22] were included.

4. Optimization procedure

First of all the thermodynamic description of Grundy et al.[13] was substituted by the thermodynamic description of Kjellqvist and Selleby[12]. It should be noted that this procedure did not substantially influence phase equilibria in sub-solidus region. The liquid phase description was modified by removing Mn^{+3} from the first sublattice and introducing the neutral species $MnO_{1.5}$ to the second sublattice. Correspondently, the mixing parameter in liquid ${}^0L(Zr^{+4}, Mn^{+3}:O^{-2})$ was substituted by ${}^0L(Zr^{+4}:O^{-2}, MnO_{1.5})$ which was then optimized to reproduce the phase diagram in air and in inert gas atmosphere assuming partial pressure of oxygen equal to $1 \cdot 10^{-4}$ bar.

As mentioned above, introducing Zr^{+4} into the halite and spinel phases should result in some solubility of ZrO_2 in halite in the $\text{ZrO}_2\text{--MgO}$ system (spinel should not appear as stable phase in this system) and in βSp and halite in the $\text{ZrO}_2\text{--MnO}_x$ system. Solubility of ZrO_2 in halite and βSp were not modelled in the assessments[8,9] because they were within experimental uncertainty. Therefore, for consistency with experimental data available for the bounding systems the calculated solubility of ZrO_2 in these phases should be small.

The next step was the optimization of the end-member parameters in cubic spinel and mixing parameters of the halite phase to reproduce the experimental data[8] for the $\text{ZrO}_2\text{--MgO--MnO}_x$ system. Optimized thermodynamic parameters are presented in Table 2.

Table 2. Optimized thermodynamic description for the $\text{ZrO}_2\text{--MgO--MnO}_x$ system (J/mol)

Phase	Sublattice model	Optimized parameters	Ref.
Ionic liquid	$(\text{Mg}^{+2}, \text{Mn}^{+2}, \text{Zr}^{+4})_P(\text{O}^{-2}, \text{MnO}_{3/2}, \text{Va})_Q$	${}^0G_{\text{Mg}+2:\text{Va}}^{\text{IonicLiquid}} = \text{GMGLIQ};$	[11]
		${}^0G_{\text{Mg}+2:\text{O}-2}^{\text{IonicLiquid}} = 2 \cdot \text{GMGOLIQ};$	[11]
		${}^0G_{\text{Mn}+2:\text{Va}}^{\text{IonicLiquid}} = \text{GLIQMN};$	[11]
		${}^0G_{\text{Mn}+2:\text{O}-2}^{\text{IonicLiquid}} = 2 \cdot \text{GMNOLIQ};$	[11]
		${}^0G_{\text{MnO}3/2}^{\text{IonicLiquid}} = 0.5 \cdot \text{GLMN2O3};$	[11]
		${}^0G_{\text{Zr}+4:\text{Va}}^{\text{IonicLiquid}} = \text{GZRLIQ};$	[9]
		${}^0G_{\text{Zr}+4:\text{O}-2}^{\text{IonicLiquid}} = 2 \cdot \text{GZRO2LIQ};$	[9]
		${}^0L_{\text{Mg}+2:\text{O}-2, \text{Va}}^{\text{IonicLiquid}} = +182000 + 26.8 \cdot T;$	[11]
		${}^0L_{\text{Mn}+2:\text{O}-2, \text{Va}}^{\text{IonicLiquid}} = +129519;$	[11]
		${}^1L_{\text{Mn}+2:\text{O}-2, \text{Va}}^{\text{IonicLiquid}} = -45459;$	[11]
		${}^0L_{\text{Mn}+2:\text{O}-2, \text{MnO}3/2}^{\text{IonicLiquid}} = -33859;$	[11]
		${}^0L_{\text{Mg}+2, \text{Mn}+2:\text{Va}}^{\text{IonicLiquid}} = +19125 + 12.5 \cdot T;$	[11]
		${}^0L_{\text{Mn}+2:\text{Va}, \text{MnO}3/2}^{\text{IonicLiquid}} = +110000;$	[11]
		${}^0L_{\text{Mg}+2:\text{O}-2, \text{MnO}3/2}^{\text{IonicLiquid}} = -1110000;$	[11]
		${}^0L_{\text{Mg}+2:\text{Va}, \text{MnO}3/2}^{\text{IonicLiquid}} = +110000;$	[11]
		${}^0L_{\text{Mg}+2, \text{Mn}+2:\text{O}-2}^{\text{IonicLiquid}} = +0;$	[11]
		${}^0L_{\text{Mn}+2, \text{Zr}+4:\text{O}-2}^{\text{IonicLiquid}} = -45000;$	this work
		${}^0L_{\text{Zr}+4:\text{O}-2, \text{Va}}^{\text{IonicLiquid}} = +75166.0715 - 55.2382004 \cdot T;$	[9]
		${}^1L_{\text{Zr}+4:\text{O}-2, \text{Va}}^{\text{IonicLiquid}} = +39057.4913;$	[9]
		${}^0L_{\text{Mn}+2, \text{Zr}+4:\text{Va}}^{\text{IonicLiquid}} = -73668.72 + 30.3 \cdot T;$	[10]
		${}^1L_{\text{Mn}+2, \text{Zr}+4:\text{Va}}^{\text{IonicLiquid}} = -1991.63;$	[10]
		${}^0L_{\text{Zr}+4:\text{O}-2, \text{MnO}3/2}^{\text{IonicLiquid}} = +19000;$	this work
		${}^0L_{\text{Mg}+2, \text{Zr}+4:\text{O}-2}^{\text{IonicLiquid}} = -68195.5443;$	[9]
		${}^1L_{\text{Mg}+2, \text{Zr}+4:\text{O}-2}^{\text{IonicLiquid}} = +35835.397;$	[9]
		${}^0L_{\text{Mg}+2, \text{Mn}+2:\text{Va}}^{\text{IonicLiquid}} = +19125 + 12.5 \cdot T;$	[11]
		${}^0L_{\text{Zr}+4, \text{Mg}+2:\text{Va}}^{\text{IonicLiquid}} = +14003.84 + 29.34205 \cdot T;$	[9]
Halite	$(\text{Mg}^{+2}, \text{Mn}^{+2}, \text{Mn}^{+3}, \text{Zr}^{+4}, \text{Va})_1(\text{O}^{-2})_1$	${}^0G_{\text{Mg}+2:\text{O}-2}^{\text{Halite}} = \text{GMGOSOL};$	[11]
		${}^0G_{\text{Mn}+2:\text{O}-2}^{\text{Halite}} = \text{GMN1O1};$	[11]
		${}^0G_{\text{Mn}+3:\text{O}-2}^{\text{Halite}} = -21884 + 22.185 \cdot T + \text{GMN1O1};$	this work
		${}^0G_{\text{Va}:\text{O}-2}^{\text{Halite}} = +0;$	[11]
		${}^0G_{\text{Zr}+4:\text{O}-2}^{\text{Halite}} = \text{GZRO2C} + 130000 + 11.5266 \cdot T;$	this work
		${}^0L_{\text{Mn}+2, \text{Mn}+3:\text{O}-2}^{\text{Halite}} = -42105;$	[11]
		${}^1L_{\text{Mn}+2, \text{Mn}+3:\text{O}-2}^{\text{Halite}} = +46513;$	[11]
		${}^0L_{\text{Mg}+2, \text{Mn}+2:\text{O}-2}^{\text{Halite}} = +11000;$	[11]
		${}^0L_{\text{Mg}+2, \text{Mn}+3:\text{O}-2}^{\text{Halite}} = +50000;$	[11]
		${}^0L_{\text{Mg}+2, \text{Mn}+3, \text{Zr}+4:\text{O}-2}^{\text{Halite}} = +0;$	this work
		${}^0L_{\text{Mg}+2, \text{Mn}+2, \text{Zr}+4:\text{O}-2}^{\text{Halite}} = -200000;$	this work
Cubic spinel	$(\text{Mg}^{+2}, \text{Mn}^{+2})_1(\text{Mg}^{+2}, \text{Mn}^{+2}, \text{Mn}^{+3}, \text{Mn}^{+4}, \text{Zr}^{+4}, \text{Va})_2(\text{Mg}^{+2}, \text{Mn}^{+2}, \text{Va})_2(\text{O}^{-2})_4$	${}^0G_{\text{Mg}+2:\text{Mg}+2:\text{Va}:\text{O}-2}^{\text{Cubic Spinel}} = +\text{GBMMV};$	[11]
		${}^0G_{\text{Mn}+2:\text{Mn}+2:\text{Va}:\text{O}-2}^{\text{Cubic Spinel}} = +\text{GB22V};$	[11]
		$T_C \text{ Mn}+2:\text{Mn}+2:\text{Va}:\text{O}-2 = 43.1;$	[11]
		${}^0G_{\text{Mn}+2:\text{Mn}+3:\text{Va}:\text{O}-2}^{\text{Cubic Spinel}} = +\text{GB23V};$	[11]
		$T_C \text{ Mn}+2:\text{Mn}+3:\text{Va}:\text{O}-2 = 43.1;$	[11]
		${}^0G_{\text{Mn}+2:\text{Mn}+4:\text{Va}:\text{O}-2}^{\text{Cubic Spinel}} = +\text{GB24V};$	[11]
		$T_C \text{ Mn}+2:\text{Mn}+4:\text{Va}:\text{O}-2 = 43.1;$	[11]
		${}^0G_{\text{Mg}+2:\text{Va}:\text{Va}:\text{O}-2}^{\text{Cubic Spinel}} = +\text{GBMVV};$	[11]
		${}^0G_{\text{Mn}+2:\text{Va}:\text{Va}:\text{O}-2}^{\text{Cubic Spinel}} = +\text{GB2VV};$	[11]
		$T_C \text{ Mn}+2:\text{Va}:\text{Va}:\text{O}-2 = 43.1;$	[11]
		${}^0G_{\text{Mg}+2:\text{Mn}+4:\text{Va}:\text{O}-2}^{\text{Cubic Spinel}} = +4 \cdot \text{GBM3V} - 2 \cdot \text{GB23V} - \text{GBMMV} - 60000;$	[11]
		${}^0G_{\text{Mg}+2:\text{Mn}+2:\text{Va}:\text{O}-2}^{\text{Cubic Spinel}} = +2 \cdot \text{GB23V} + \text{GBMMV} - 2 \cdot \text{GBM3V} + 60000;$	[11]

P7-9

$$\begin{aligned} {}^0G_{\text{Mg}+2;\text{Va}}^{\text{M--ZrO}_2} &= +\text{GMGOSOL} - \text{GHSEROO} + 120000 + 11.5263 \cdot T; & [9] \\ {}^0G_{\text{Mn}+2;\text{Va}}^{\text{M--ZrO}_2} &= +\text{GMN1O1} - \text{GHSEROO} + 11.5263 \cdot T + 120000; & [10] \\ {}^0G_{\text{Mn}+3;\text{Va}}^{\text{M--ZrO}_2} &= +0.5 \cdot \text{GMN2O3} - 1.5 \cdot \text{GHSEROO} + 9.35108255 \cdot T & [10] \\ &+ 100000; \\ {}^0G_{\text{Zr}+4;\text{Va}}^{\text{M--ZrO}_2} &= +\text{GZRO2M} - 2 \cdot \text{GHSEROO}; & [9] \end{aligned}$$

Functions	(Temperature limits)
GHSEROO	$(298\text{--}1000)$ $-3480.87 - 25.503038 \cdot T - 11.136 \cdot T \cdot \text{LN}(T) - 0.005098888 \cdot T^2$ $+ 6.61846 \cdot 10^{-7} \cdot T^3 - 38365 \cdot T^{-1};$ $(1000\text{--}3300)$ $-6568.763 + 12.65988 \cdot T - 16.8138 \cdot T \cdot \text{LN}(T) - 5.95798 \cdot 10^{-4} \cdot T^2$ $+ 6.781 \cdot 10^{-9} \cdot T^3 + 262905 \cdot T^{-1};$ $(3300\text{--}6000)$ $-13986.728 + 31.259625 \cdot T - 18.9536 \cdot T \cdot \text{LN}(T) - 4.25243 \cdot 10^{-4} \cdot T^2$ $+ 1.0721 \cdot 10^{-8} \cdot T^3 + 4383200 \cdot T^{-1};$
GHSERMG	$(298\text{--}923)$ $-8367.34 + 143.677875 \cdot T - 26.1849782 \cdot T \cdot \text{LN}(T) + 4.858 \cdot 10^{-4} \cdot T^2$ $- 1.393669 \cdot 10^{-6} \cdot T^3 + 78950 \cdot T^{-1};$ $(923\text{--}3000)$ $-14130.185 + 204.718543 \cdot T - 34.3088 \cdot T \cdot \text{LN}(T)$ $+ 1.038192 \cdot 10^{+28} \cdot T^{-9};$
GMGLIQ	$(298\text{--}923)$ $+8202.243 - 8.83693 \cdot T + \text{GHSERMG} - 8.0176 \cdot 10^{-20} \cdot T^7;$ $(923\text{--}3000)$ $+8690.316 - 9.392158 \cdot T + \text{GHSERMG} - 1.038192 \cdot 10^{+28} \cdot T^{-9};$
GMGOSOL	$(298\text{--}1700)$ $-619428.502 + 298.253571 \cdot T - 47.4817 \cdot T \cdot \text{LN}(T) - 0.00232681 \cdot T^2$ $+ 4.5043 \cdot 10^{-8} \cdot T^3 + 516900 \cdot T^{-1};$ $(1700\text{--}3100)$ $-655489.818 + 528.597187 \cdot T - 78.3772 \cdot T \cdot \text{LN}(T) + 0.0097344 \cdot T^2$ $- 8.60338 \cdot 10^{-7} \cdot T^3 + 8591550 \cdot T^{-1};$ $(3100\text{--}5000)$ $-171490.159 - 1409.43369 \cdot T + 163.674142 \cdot T \cdot \text{LN}(T)$ $- 0.044009535 \cdot T^2 + 1.374896 \cdot 10^{-6} \cdot T^3 - 1.72665403 \cdot 10^{-8} \cdot T^{-1};$ $(5000\text{--}5100)$ $-722412.718 + 617.657452 \cdot T - 84 \cdot T \cdot \text{LN}(T);$
GMGOLIQ	$(298\text{--}1700)$ $-549098.33 + 275.724634 \cdot T - 47.4817 \cdot T \cdot \text{LN}(T)$ $- 0.00232681 \cdot T^2 + 4.5043 \cdot 10^{-8} \cdot T^3 + 516900 \cdot T^{-1};$ $(1700\text{--}2450)$ $-585159.646 + 506.06825 \cdot T - 78.3772 \cdot T \cdot \text{LN}(T) + 0.0097344 \cdot T^2$ $- 8.60338 \cdot 10^{-7} \cdot T^3 + 8591550 \cdot T^{-1};$ $(2450\text{--}3100)$ $+9110429.75 - 42013.7634 \cdot T + 5298.548 \cdot T \cdot \text{LN}(T) - 1.30122485 \cdot T^2$ $+ 5.8262601 \cdot 10^{-5} \cdot T^3 - 3.24037416 \cdot 10^9 \cdot T^{-1};$ $(3100\text{--}5100)$ $-632664.468 + 589.239555 \cdot T - 84 \cdot T \cdot \text{LN}(T);$
GLIQMN	$(298\text{--}1519)$ $+17859.91 - 12.6208 \cdot T + \text{GHSERMN} - 4.41929 \cdot 10^{-21} \cdot T^7;$ $(1519\text{--}2000)$ $-9993.9 + 299.036 \cdot T - 48 \cdot T \cdot \text{LN}(T);$
GMN1O1	$(298\text{--}6000)$ $-402478 + 259.356 \cdot T - 46.835 \cdot T \cdot \text{LN}(T) - 0.00385 \cdot T^2 + 212922 \cdot T^{-1};$
GMNOLIQ	$(298\text{--}6000)$ $+ \text{GMN1O1} + 43947 - 20.628 \cdot T;$
GMN2O3	$(298\text{--}6000)$ $-998618 + 588.619 \cdot T - 101.956 \cdot T \cdot \text{LN}(T) - 0.018844 \cdot T^2$ $+ 589055 \cdot T^{-1};$
GLMN2O3	$(298\text{--}6000)$ $+ 2 \cdot \text{GMN1O1} + \text{GHSEROO} - 64953 + 43.144 \cdot T;$
GAMN3O4	$(298\text{--}6000)$ $-1439700 + 892.2 \cdot T - 154.748 \cdot T \cdot \text{LN}(T) - 0.017408 \cdot T^2 + 986139 \cdot T^{-1};$
GMN3O4B	$(298\text{--}6000)$ $+ 15270 + 7 \cdot T;$
GMNFE2O4	$(298\text{--}6000)$ $-182450 + 133 \cdot T - 23.099 \cdot T \cdot \text{LN}(T) - 0.0014 \cdot T^2 + 124000 \cdot T^{-1};$
GHSERZR	$(130\text{--}2128)$ $-7827.595 + 125.64905 \cdot T - 24.1618 \cdot T \cdot \text{LN}(T) - 0.00437791 \cdot T^2$ $+ 34971 \cdot T^{-1};$ $(2128\text{--}6000)$ $-26085.921 + 262.724183 \cdot T - 42.144 \cdot T \cdot \text{LN}(T) - 1.342896 \cdot 10^{31} \cdot T^{-9};$
GZRLIQ	$(130\text{--}2128)$ $+ 18147.69 - 9.080812 \cdot T + \text{GHSERZR} + 1.6275 \cdot 10^{-22} \cdot T^7;$ $(2128\text{--}6000)$ $-8281.26 + 253.812609 \cdot T - 42.144 \cdot T \cdot \text{LN}(T);$
GZRO2M	$(298\text{--}6000)$ $-1126163.54 + 424.890806 \cdot T - 69.3875137 \cdot T \cdot \text{LN}(T)$ $- 0.00375880141 \cdot T^2 + 683000 \cdot T^{-1};$

GZRO2T	(298–6000)	$+5468 - 4 \cdot T + \text{GZRO2M};$
GZRO2C	(298–6000)	$+10336 - 4 \cdot T + \text{GZRO2T};$
GZRO2LIQ	(298–6000)	$+87027 - 29.17432 \cdot T + \text{GZRO2C};$
NCUBIC SPINEL	(298–6000)	$+ \text{GMGOSOL} + \text{GCORUND} - 27600 - 62 \cdot T + 9 \cdot T \cdot \text{LN}(T);$
ICUBIC SPINEL	(298–6000)	$+ \text{NCUBIC SPINEL} + 51600 - 39 \cdot T;$
GCORUND	(298–600)	$-1707351.3 + 448.021092 \cdot T - 67.4804 \cdot T \cdot \text{LN}(T) - 0.06747 \cdot T^2$
	(600–1500)	$+1.4205433 \cdot 10^{-5} \cdot T^3 + 938780 \cdot T^{-1};$
	(1500–3000)	$-1724886.06 + 754.856573 \cdot T - 116.258 \cdot T \cdot \text{LN}(T) - 0.0072257 \cdot T^2$
		$+2.78532 \cdot 10^{-7} \cdot T^3 + 2120700 \cdot T^{-1};$
		$-1772163.19 + 1053.4548 \cdot T - 156.058 \cdot T \cdot \text{LN}(T) + 0.00709105 \cdot T^2 -$
		$6.29402 \cdot 10^{-7} \cdot T^3 + 12366650 \cdot T^{-1};$
GGAMMA	(298–600)	$-1689977.34 + 469.458181 \cdot T - 70.5452 \cdot T \cdot \text{LN}(T) - 0.070794 \cdot T^2$
	(600–1500)	$+1.491345 \cdot 10^{-5} \cdot T^3 + 981165 \cdot T^{-1};$
	(1500–3000)	$-1708389.72 + 791.591946 \cdot T - 121.754 \cdot T \cdot \text{LN}(T) - 0.0075467 \cdot T^2$
		$+2.89573 \cdot 10^{-7} \cdot T^3 + 2222750 \cdot T^{-1};$
		$-1758861.74 + 1110.41976 \cdot T - 164.253 \cdot T \cdot \text{LN}(T) + 0.00775305 \cdot T^2 -$
		$6.8247 \cdot 10^{-7} \cdot T^3 + 13162750 \cdot T^{-1};$
NSPFEAL	(298–6000)	$-287500 + 136 \cdot T - 22.1991 \cdot T \cdot \text{LN}(T) - 0.001867857 \cdot T^2$
		$+223844 \cdot T^{-1};$
BFE3O4	(298–3000)	$+46826 - 27.266 \cdot T;$
GFE3O4	(298–3000)	$-161731 + 144.873 \cdot T - 24.9879 \cdot T \cdot \text{LN}(T) - 0.0011952256 \cdot T^2$
		$+206520 \cdot T^{-1};$
G22V	(298–6000)	$+7 \cdot \text{GFE3O4} + \text{BFE3O4};$
G2AV	(298–6000)	$+7 \cdot \text{NSPFEAL};$
GB_JK	(298–6000)	$+0.142857143 \cdot \text{GAMN3O4} + 0.142857143 \cdot \text{GMN3O4B};$
KMN3O4B	(298–6000)	$+26210 - 17.46 \cdot T;$
REFSPAAV	(298–6000)	$+1.5 \cdot \text{G2AV} - 0.5 \cdot \text{G22V} + 32900;$
GGMN2O3B	(298–6000)	$+ \text{GMN2O3} + 192300 - 193.8 \cdot T + 0.05 \cdot T^2;$
MCUBIC SPINEL	(298–6000)	$+ \text{GMGOSOL} + 58000 - 18 \cdot T;$
BADDMG	(298–6000)	$+8 \cdot \text{MCUBIC SPINEL} - 2 \cdot \text{NCUBIC SPINEL} - 4 \cdot \text{ICUBIC SPINEL}$
		$-23.0527167 + 4 \cdot \text{REFSPAAV};$
GMGZ RVA	(298–6000)	$+4 \cdot \text{GMGOSOL} + 2 \cdot \text{GZRO2C} + 30000 + 23.05244 \cdot T - \text{GBMMV};$
		(this work)
GMNZ RVA	(298–6000)	$+4 \cdot \text{GMN1O1} + 2 \cdot \text{GZRO2C} + 70000 + 23.05244 \cdot T - \text{GB22V};$
		(this work)
GMN2MGO 4	(298–6000)	$-1629500 + 983.45 \cdot T - 166.1 \cdot T \cdot \text{LN}(T) + 2.97 \cdot 10^{-4} \cdot T^2 + 1470000 \cdot T^{-1};$
GBMMV	(298–6000)	$+ \text{NCUBIC SPINEL} + 2 \cdot \text{ICUBIC SPINEL} + 23.0527167 \cdot T$
		$- 2 \cdot \text{REFSPAAV};$
GB22V	(298–6000)	$+21 \cdot \text{GMNFE2O4} + 56000 - 14 \cdot \text{GFE3O4} + 2 \cdot \text{BFE3O4};$

GB23V	(298–6000)	+7·GB_JK;
GB24V	(298–6000)	+14·GB_JK –21·GMNFE2O4 –56000 +14·GFE3O4 –2·BFE3O4 +KMN3O4B;
GBMVV	(298–6000)	+8·GGAMMA +NCUBIC SPINEL +44.9543481·T +108000 – 6·REFSPAAY;
GB2VV	(298–6000)	+8·GGMN2O3B –56·GB_JK +63·GMNFE2O4 +168000 – 42·GFE3O4 +6·BFE3O4 –3·KMN3O4B +12·R·T·LN(6) – 6·R·T·LN(3) –4·R·T·LN(2);
GBM3V	(298–6000)	+GMN2MGO4 +52000 –18·T;

5. Results and discussions

The calculated phase diagrams of the $\text{ZrO}_2\text{--MgO}$ and $\text{ZrO}_2\text{--MnO}_x$ systems are presented in Figs. 1 a-d with experimental data[23–29]. The calculations were performed taking into account the gas phase which thermodynamic description was accepted SGTE Substance Database (SGSUB)[30]. The calculated data for invariant reactions are compared with the results from previous descriptions[8,9] in Table 3 and 4. Due to some uncertainty of oxygen partial pressure in inert gas atmosphere[11] calculations in the $\text{ZrO}_2\text{--MnO}_x$ system were performed at oxygen partial pressures equal to $1 \cdot 10^{-4}$ and $3.1 \cdot 10^{-3}$ bar. It can be seen that the phase diagrams only slightly deviate from previous descriptions due to the changes introduced in the present work, but the differences are within experimental uncertainty.

Table 3. Calculated and experimental data on invariant reactions in the $\text{ZrO}_2\text{--MgO}$ system.

		Reaction, mol.% MgO			Type	T (K)	Reference
L	↔	c-ZrO ₂	+	MgO	Eutectic		
50.78		22.90		98.51		2384	this work
51.29		23.17		100		2376	[9]
c-ZrO ₂	↔	t-ZrO ₂	+	MgO	Eutectoid		
13.68		1.47		99.58		1685	this work
13.71		1.47		100		1683	[9]
t-ZrO ₂	↔	m-ZrO ₂	+	MgO	Eutectoid		
0.55		0.34		99.87		1356	this work
0.55		0.35		100		1356	[9]

Table 4. Calculated and experimental data on invariant reactions in the $\text{ZrO}_2\text{--MnO}_x$ system.

Reaction, 100Mn/(Mn+Zr), mol.%					Type	T (K)	Reference
$P(\text{O}_2)=0.21$ bar							
L	\leftrightarrow	c-ZrO ₂	+	βSp	Eutectic		
86.38		22.83		98.92		1775	this work
86.5		23.5		100		1786	[10]
c-ZrO ₂	\leftrightarrow	t-ZrO ₂	+	βSp	Eutectoid		
17.40		1.17		99.40		1668	this work
17.4		1.15		100		1669	[10]
βSp	\leftrightarrow	t-ZrO ₂	+	αSp	Eutectoid		
99.91		0.44		100		1441	this work
-		-		-		1443	[10]
t-ZrO ₂	\leftrightarrow	m-ZrO ₂	+	αSp	Eutectoid		
0.55		0.34		100		1363	this work
-		-		-		1362	[10]
αSp	\leftrightarrow	Mn ₂ O ₃	+	m-ZrO ₂	Degenerated		
100		100		0.08		1159	this work
-		-		-		1133	[10]
Mn ₂ O ₃	\leftrightarrow	MnO ₂	+	m-ZrO ₂	Degenerated		
100		100		0		694	this work
$P(\text{O}_2)=3.16 \cdot 10^{-3}$ bar							
L	\leftrightarrow	c-ZrO ₂	+	H	Eutectic		
86.24		29.04		99.95		1782	this work
c-ZrO ₂	+	H	\leftrightarrow	βSp	Peritectoid		
25.26		99.98		98.23		1645	this work
c-ZrO ₂	\leftrightarrow	t-ZrO ₂	+	βSp	Eutectoid		
21.05		1.22		98.71		1590	this work
βSp	\leftrightarrow	t-ZrO ₂	+	αSp	Eutectoid		
99.67		0.60		100		1434	this work
t-ZrO ₂	\leftrightarrow	m-ZrO ₂	+	αSp	Eutectoid		
0.40		0.25		100		1358	this work
αSp	\leftrightarrow	Mn ₂ O ₃	+	m-ZrO ₂	Degenerated		
100		100		0.02		978	this work
Mn ₂ O ₃	\leftrightarrow	MnO ₂	+	m-ZrO ₂	Degenerated		
100		100		0		600	this work
$P(\text{O}_2)=1 \cdot 10^{-4}$ bar							
L	\leftrightarrow	c-ZrO ₂	+	H	Eutectic		
83.15		31.72		99.81		1860	this work
80.00		30.6		100		1805	[10]
c-ZrO ₂	\leftrightarrow	t-ZrO ₂	+	H	Eutectoid		
23.76		1.22		99.98		1540	this work
23.80		1.20		100		1540	[10]
t-ZrO ₂	+	H	\leftrightarrow	βSp	Peritectoid		
1.05		99.99		98.33		1488	this work
-		-		-		1487	[10]
βSp	\leftrightarrow	αSp	+	t-ZrO ₂	Eutectoid		
99.11		100		0.75		1421	this work
100		100		1.00		1443	[10]
t-ZrO ₂	\leftrightarrow	αSp	+	m-ZrO ₂	Eutectoid		
0.52		100		0.29		1354	this work
0.52		100		0.30		1354	[10]
αSp	\leftrightarrow	Mn ₂ O ₃	+	m-ZrO ₂	Degenerated		
100		100		0		869	this work
Mn ₂ O ₃	\leftrightarrow	MnO ₂	+	m-ZrO ₂	Degenerated		
100		100		0		540	this work

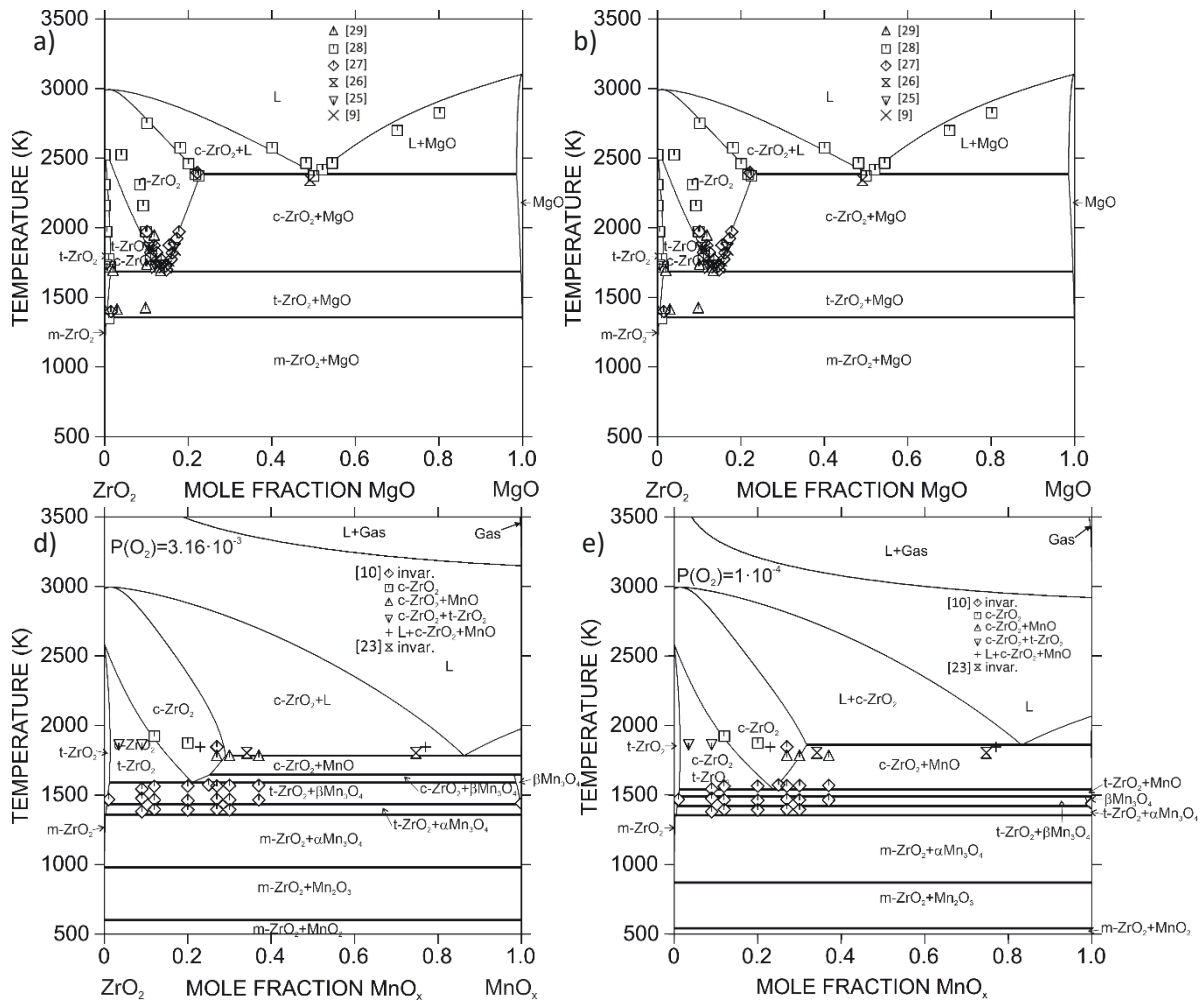


Fig. 1 – Calculated phase diagrams for a) the $\text{ZrO}_2\text{--MgO}$ system; b) the $\text{ZrO}_2\text{--MnO}_x$ system in air; c) the $\text{ZrO}_2\text{--MnO}_x$ system at $P(\text{O}_2)=3.16 \cdot 10^{-3}$; d) the $\text{ZrO}_2\text{--MnO}_x$ system at $P(\text{O}_2)=1 \cdot 10^{-4}$.

5.1. Isothermal sections of phase diagrams of the $\text{ZrO}_2\text{--MgO--MnO}_x$ system

The phase diagrams of the $\text{ZrO}_2\text{--MgO--MnO}_x$ system calculated in the present study at air oxygen partial pressure and fixed temperatures are compared with ones constructed based on experimental data[8] in Figs. 2 a-e. It should be noted that isothermal sections in the range between 1523 and 1713 K were reproduced quite well. The stabilization of cubic ZrO_2 at temperature of 1613 K, which is below its stability limit in the bounding systems was reproduced by calculations. Phase compositions for equilibrium $\text{t-ZrO}_2+\beta\text{Sp}+\text{H}$ at 1523 K and for $\text{c-ZrO}_2+\beta\text{Sp}+\text{H}$ at 1613 K were also quite well reproduced by calculations. However, with increasing temperature, the calculations indicated substantial manganese enrichment of halite in the equilibrium $\text{c-ZrO}_2+\beta\text{Sp}+\text{H}$ while experiments showed practically the same Mn content in halite at all studied temperatures. As a result the calculated three-phase equilibrium $\text{c-ZrO}_2+\beta\text{Sp}+\text{H}$ was shifted in the Mn rich composition range and is presented by a narrow triangle at temperatures between 1713 and 1913 K. The calculations reproduced the experimentally observed stabilization of the spinel at temperature of 1913 K, which was higher than the stability

limit of spinel in the MgO–MnO_x system. At 1813 K the calculations showed the formation of spinel at two different composition ranges: first enriched by MnO_x (95-100 mol.% MnO_x) and second one at ~40 mol.% of MnO_x. According to experimental data 2 mol.% of ZrO₂ was enough to stabilize β -spinel and form a separate phase in the ternary system, while according to calculations the ZrO₂ content in β Sp was substantially higher. It should be also noted that compositions of c-ZrO₂ in equilibrium with t-ZrO₂ were well reproduced as well as the increase of maximal solubility of stabilizers in c-ZrO₂ up to 27 mol. % of MgO and MnO_x together at intermediate compositions. This exceeded the stabilizer solubility in bounding systems ZrO₂–MgO and ZrO₂–MnO_x. Substantial contradictions between calculated and experimental phase equilibria involving liquid phase were observed at 1813 and 1913 K. Calculations indicated two equilibria c-ZrO₂+ β Sp+L and β Sp+H+L while according to experimental data analysis the stable assemblage involving liquid was c-ZrO₂+H+L at 1813 and 1913 K. Based on the experimental data[8] it was assumed that there were two three-phase equilibria c-ZrO₂+H+ β Sp with minimal and maximal content of MnO_x in β -spinel. The reason for inconsistency can be limitations in modelling as well as problems of experimental data interpretation due to transformations occurring in samples during cooling.

Phase diagrams calculated at oxygen partial pressures corresponding to protective gas atmosphere ($P(\text{O}_2)=1 \cdot 10^{-4}$ bar[8]) and temperatures of 1523 and 1913 K are compared with ones constructed based on experimental data[8] in Figs. 3 a,b. The stabilization of c-ZrO₂ below its stability ranges in bounding systems was reproduced by calculations at 1523 K though the homogeneity range of c-ZrO₂ at these conditions was very narrow and substantially shifted towards the ZrO₂-MnO_x bounding system. At 1913 K and $P(\text{O}_2)=1 \cdot 10^{-4}$ bar the phase relations were well reproduced indicating melting of c-ZrO₂+H assemblage in the vicinity of the ZrO₂–MnO_x bounding system. Calculations at 2003 K and $P(\text{O}_2)=1 \cdot 10^{-4}$ bar for composition ZrO₂–8.67MgO–61.03MnO_x indicated equilibrium of liquid phase with 16 mol.% of c-ZrO₂ phase. This result is consistent with the microstructure investigation of the sample with the above mentioned composition in protective gas atmosphere indicating small amount of primary c-ZrO₂ along with a wide eutectic area (Fig. 4).

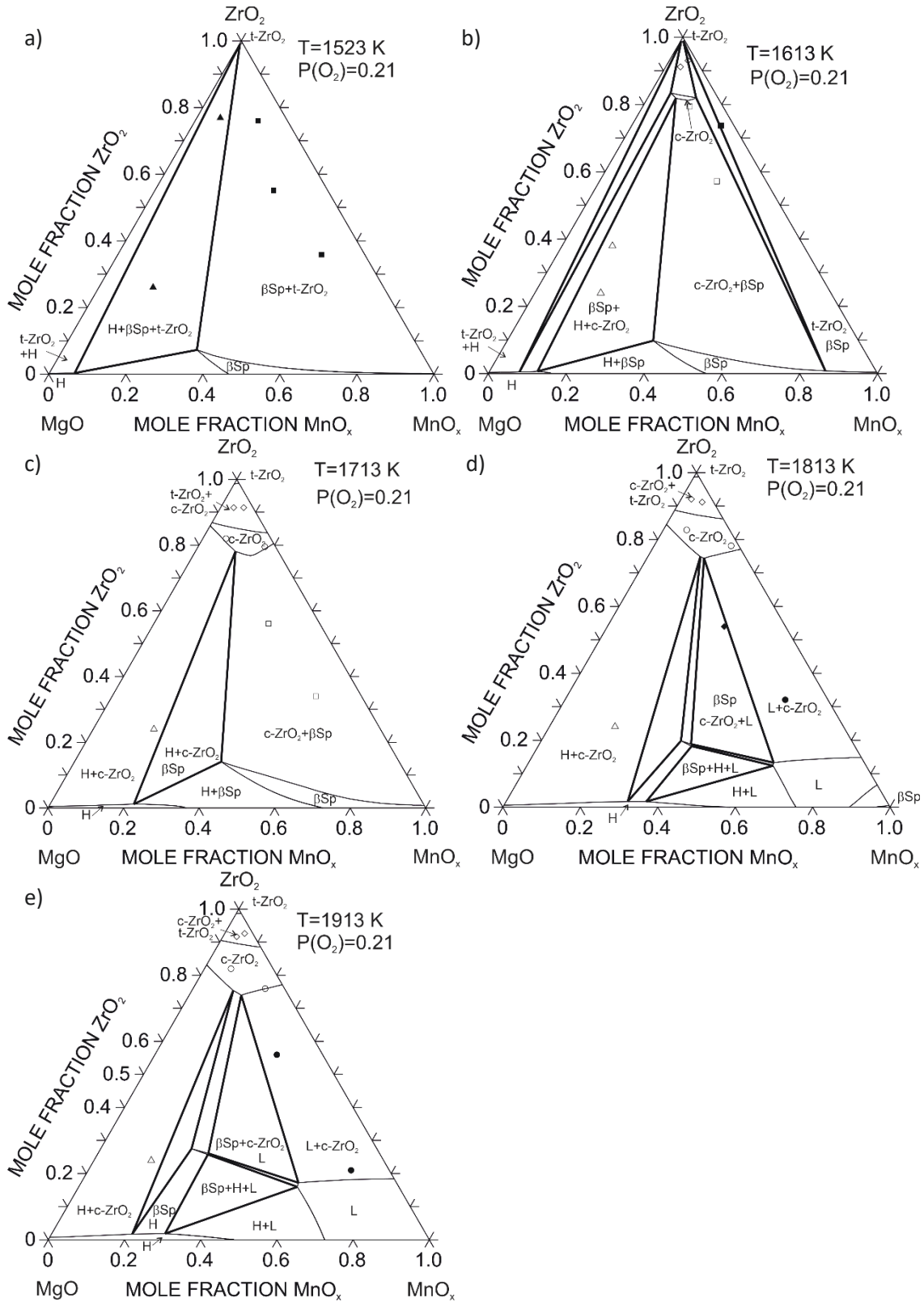


Fig. 2 – Calculated isothermal sections of the $\text{ZrO}_2\text{--MgO--MnO}_x$ system at: a) 1523; b) 1613 K; c) 1713 K; d) 1813 K; e) 1913 K in air with experimental data from Pavlyuchkov et al.[8].

Open circles – c-ZrO_2 ; closed circles – $\text{c-ZrO}_2 + \text{H} + \text{L}$; closed rectangles – $\text{t-ZrO}_2 + \beta\text{Sp}$; open rectangles – $\text{c-ZrO}_2 + \beta\text{Sp}$; closed triangles – $\text{t-ZrO}_2 + \beta\text{Sp} + \text{H}$; open triangles – $\text{c-ZrO}_2 + \beta\text{Sp} + \text{H}$; open rhombuses – $\text{t-ZrO}_2 + \text{c-ZrO}_2$; closed rhombuses – $\text{c-ZrO}_2 + \text{H}$.

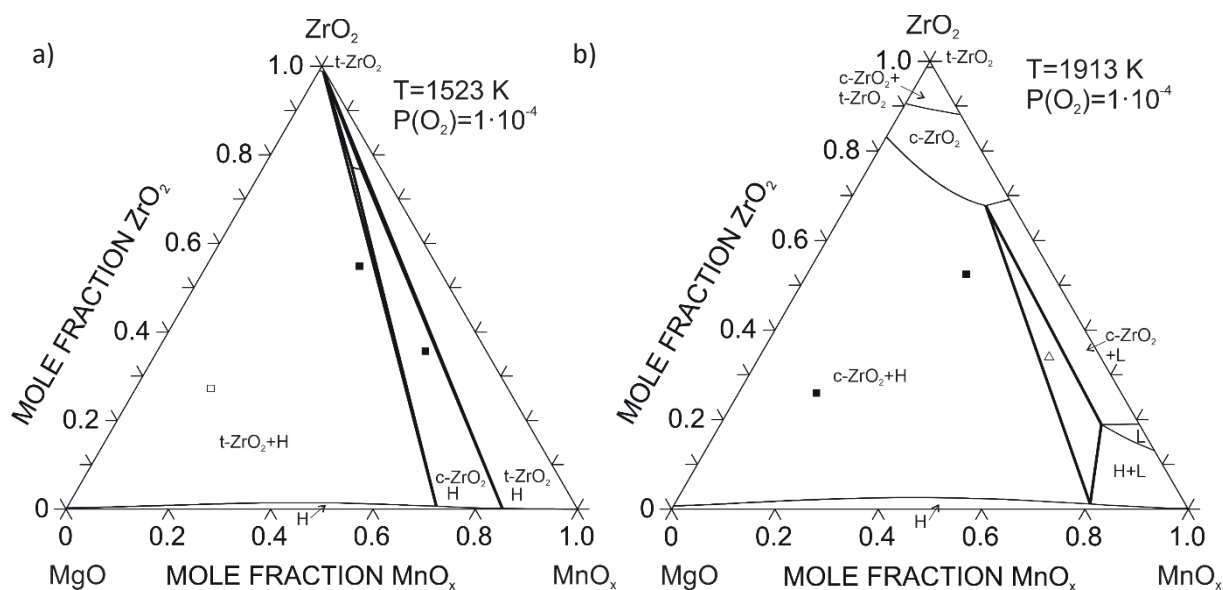


Fig. 3 – Calculated isothermal sections of the ZrO_2 - MgO - MnO_x system at oxygen partial pressure corresponding protective gas atmosphere ($P(\text{O}_2)=1\cdot 10^{-4}$ bar) at: a) 1523; b) 1913 K with experimental data from Pavlyuchkov et al.^[8]. Closed rectangles – $\text{c-ZrO}_2+\text{H}$; open rectangles – $\text{t-ZrO}_2+\text{H}$; open triangles – $\text{c-ZrO}_2+\text{H}+\text{L}$.

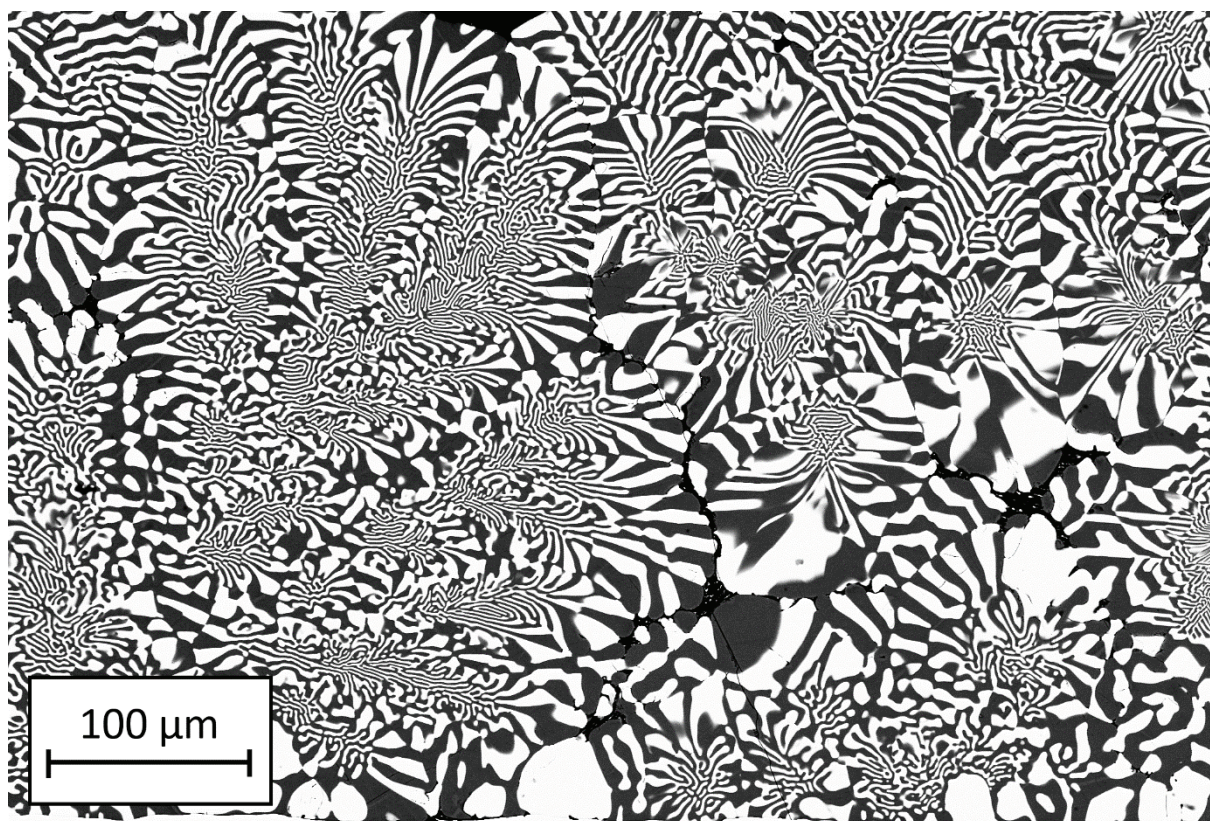


Fig. 4 – Microstructure of the sample ZrO_2 -8.67 MgO -61.03 MnO_x annealed at 1913 K during 15 minutes in He atmosphere (light phase – c-ZrO_2 , dark grey phase – halite).

5.2. Experimental investigations

Two samples with compositions $\text{ZrO}_2\text{--}8.67\text{MgO--}61.03\text{MnO}_x$ and $\text{ZrO}_2\text{--}58.33\text{MgO--}16.08\text{MnO}_x$ (in mol. %) after preliminary heat treatment in He atmosphere were investigated using DTA. The DTA-TG heating curves are presented in Figs. 5a,b together with calculated phase fraction diagrams. Though there were some inconsistencies between calculated and experimental phase diagrams, as discussed above the calculations help to interpret the obtained DTA results. It should be noted that there was an overheating effect for the m- ZrO_2 to t- ZrO_2 transformation indicated in pure ZrO_2 [31] as well as in the solid solutions[9].

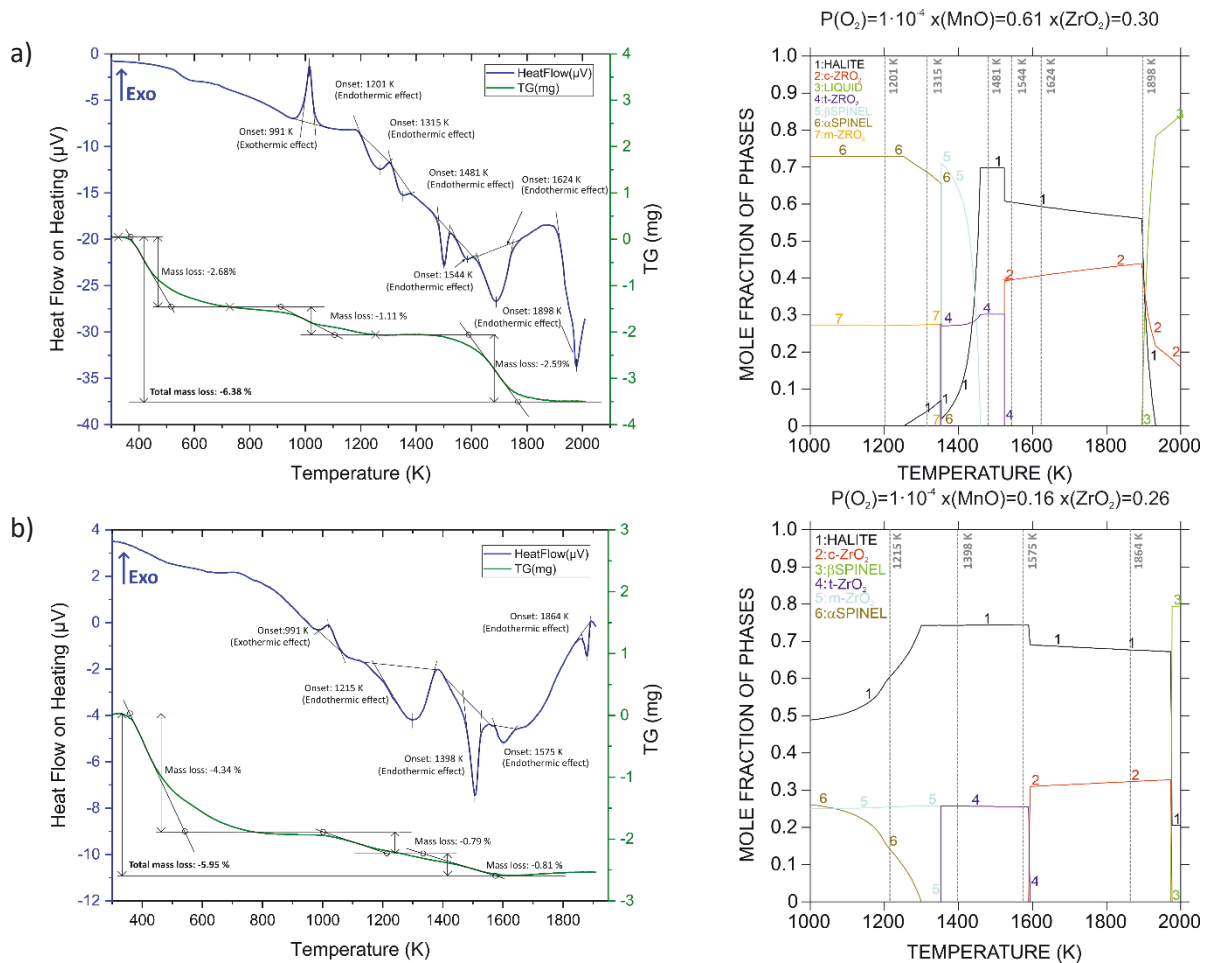


Fig. 5 – DTA-TG data in comparison with calculated phase fraction diagrams for compositions: a) $\text{ZrO}_2\text{--}8.67\text{MgO--}61.03\text{MnO}_x$ and b) $\text{ZrO}_2\text{--}58.33\text{MgO--}16.08\text{MnO}_x$ (in mol. %). Grey lines in the phase fraction diagrams label onset points of DTA results.

It should be noted that XRD indicated the presence of halite and cubic ZrO_2 in both samples after heat treatment at 1913 K. In both samples exothermic effects were observed at 991 K, indicating the transformations of the initial phase assemblage c- ZrO_2 +H into the stable assemblage.

According to calculations the stable assemblage for the sample of $\text{ZrO}_2\text{--}8.67\text{MgO--}61.03\text{MnO}_x$ (in mol. %) composition at 1000 K should be $\alpha\text{Sp}+\text{m-ZrO}_2$. The first heat effect at 1201 K can be related to the appearance of the halite phase observed in the calculated phase fraction

diagram at 1250 K. The formation of halite should be associated with a small mass loss since only a small fraction ~ 8 mol. % of halite phase should be formed according to the calculations. The effect observed at 1315 K can be related to the transformation of αSp into βSp . The next effect at 1481 K can be related to the transformation of $m\text{-ZrO}_2$ into $t\text{-ZrO}_2$. It should be noted that according to the calculations both transformations occurred at approximately the same temperature of 1350 K. As it was mentioned above monoclinic to tetragonal phase transformation usually occurs with a large overheating effect exceeding 100 K. The effect at 1544 K can be explained by the disappearance of βSp due to its transformation to the halite phase accompanied with mass loss which can be observed on the TG curve. According to the calculations this transformation occurs at 1460 K. The effect at 1624 K can be related to the transformation of $t\text{-ZrO}_2$ into $c\text{-ZrO}_2$ which can dissolve more stabilizer than $t\text{-ZrO}_2$. Therefore, the amount of halite phase should slightly decrease. The calculated temperature of the $t\text{-ZrO}_2$ to $c\text{-ZrO}_2$ transformation is 1525 K. The observed difference can be caused by an overheating effect due to kinetic reasons. The last effect at 1903 K can be explained by the melting of the $c\text{-ZrO}_2\text{+H}$ assemblage. This is in perfect agreement with the calculations, that indicates the beginning of melting at 1890 K. The shape of the peak indicates that there are two transformations. The calculations show that during melting the halite phase disappears at 1920 K. Therefore, the second effect in the melting peak can be related to the disappearance of halite.

The calculated stable assemblage for the sample with composition $\text{ZrO}_2\text{--}58.33\text{MgO--}16.08\text{MnO}_x$ (in mol. %) at 1000 K should be $\text{H}+\alpha\text{Sp}+m\text{-ZrO}_2$. The first effect in the heating curve was observed at 1214 K. It can be related to the transformation of αSp into the halite phase accompanied by mass loss. The mass loss was confirmed by the TG heating curve. The calculations show that a sharp decrease of αSp content starts at ~ 1200 K and finishes at 1300 K. However, in DTA this process occurs with some overheating due to kinetic reasons and finishes at substantially higher temperatures. Besides this there was an uncertainty concerning the oxygen partial pressure in the DTA. Calculations showed that if the partial pressure was $3.2 \cdot 10^{-3}$ bar as assumed by Dilner et al. [11] the stable phase will be βSp and it will disappear at higher temperatures. Next two heat effects at 1398 and 1575 K can be related to transformation of $m\text{-ZrO}_2$ to $t\text{-ZrO}_2$ which further transforms into $c\text{-ZrO}_2$. According to the calculations these transformations occurred at 1350 and 1589 K, respectively. The last transformation occurs in some temperature range until all $t\text{-ZrO}_2$ is transformed into $c\text{-ZrO}_2$ at 1594 K. It should be noted that according to the calculations the $t\text{-ZrO}_2$ dissolves a small amount of stabilizer ($\text{MnO}+\text{MgO}$), while $c\text{-ZrO}_2$ dissolved up to 25 mol.% of stabilizer that is also consistent with the experimental data of Pavlyuchkov et al. [2016Pav]. Therefore, the amount of halite phase decreases due to the dissolution of MgO and MnO in $c\text{-ZrO}_2$. According to the calculation the dissolution of MgO and MnO occurs simultaneously with formation of $c\text{-ZrO}_2$. However, in the DTA this process is substantially slower and finish at 1863 K which can be observed as the last heat effect on the heating curve.

Calculated mass loss for both compositions $\text{ZrO}_2\text{--}8.67\text{MgO--}61.03\text{MnO}_x$ and $\text{ZrO}_2\text{--}58.33\text{MgO--}16.08\text{MnO}_x$ (in mol.%) are compared with TG data in Fig. 6 a and b. In calculations, components were selected as MgO , MnO and O_2 . Mass.% of O_2 presented at the plots show the difference in mass between halite and spinel. Calculated mass loss is in reasonable agreement with TG though the temperature of the beginning and end of mass loss show deviation from

experimental data. The reason for these inconsistencies can be explained by the fact that the partial pressure of oxygen was not controlled in the experiments and by influence of kinetics from one side and uncertainty of calculations from another side. It should be noted that calculations show some small mass gain due to higher concentration of Mn^{+3} in βSp and in liquid. However, it is not clear if such effects can be observed in DTA/TG experiments.

Though the experiments have some uncertainties, such as oxygen partial pressure and kinetic effects, the derived thermodynamic description helps to relate observed heat effects with phase transformations and chemical reactions.

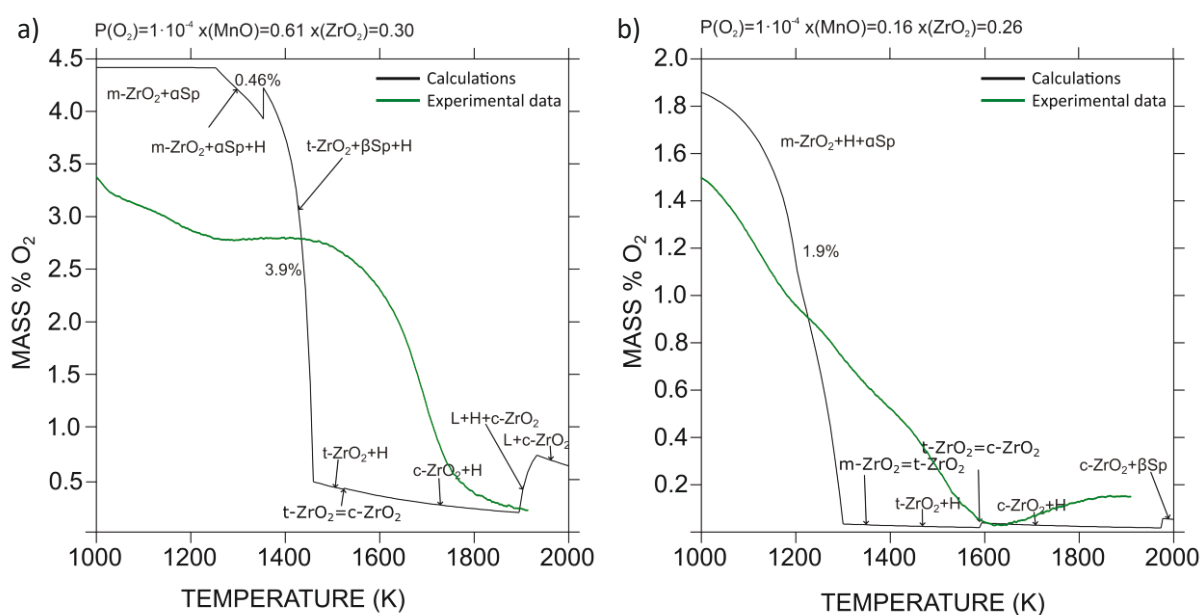


Fig. 6 – The calculated weight loss for compositions: a) $\text{ZrO}_2\text{--}8.67\text{MgO--}61.03\text{MnO}_x$ and b) $\text{ZrO}_2\text{--}58.33\text{MgO--}16.08\text{MnO}_x$ (in mol. %).

6. Conclusions

A thermodynamic database for the $\text{ZrO}_2\text{--MgO--MnO}_x$ system was derived based on experimental data of Pavlyuchkov et al.[8]. Thermodynamic modelling of the current oxide system has been performed for the first time. This work focused on the reproduction of the phase diagrams for oxide systems. The main features described are the stabilization of cubic ZrO_2 based solid solutions at temperatures below their stability limits in the bounding systems both in air and protective gas atmosphere as well as stabilization of cubic spinel ($\square\text{Sp}$) at temperatures above its stability limits in bounding systems. The thermodynamic description also incorporates all available descriptions of the binary subsystems. The obtained thermodynamic description was verified by interpretation of DTA-TG results obtained for two samples with compositions $\text{ZrO}_2\text{--}8.67\text{MgO--}61.03\text{MnO}_x$ and $\text{ZrO}_2\text{--}58.33\text{MgO--}16.08\text{MnO}_x$ (in mol. %). Calculated phase fraction diagrams were used to interpret observed heat effects and mass losses.

The current database can be used for further thermodynamic modelling of the high-order systems for the development of the TRIP-Matrix-Composites[3,32]. Thus, results of current

modelling can be applied for optimization of the coating process of the Mg-PSZ mentioned above. Moreover, the obtained thermodynamic description has potential for the study of directionally solidified eutectic materials based on the $\text{ZrO}_2\text{--MgO--MnO}_x$ system.

Acknowledgments

The authors thank the German Research Foundation (DFG) for funding Sub-project C2 within the Collaborative Research Center SFB 799 Trip-Matrix Composites. In addition, we thank G. Savinykh for technical contribution.

References

- [1] H. Biermann, U. Martin, C.G. Aneziris, et al., *Adv. Eng. Mater.* 43 (2009) 1000.
- [2] M. Kirschner, S. Martin, S. Guk, et al., *Metals* 10 (2020) 543.
- [3] S. Martin. private communication, 2020.
- [4] G. Bayer, *J. Am. Ceram. Soc.* 53 (1970) 294.
- [5] H. Berek, A. Yanina, C. Weigelt, C.G. Aneziris, *Steel Research int.* 82 (2011) 1094.
- [6] A. Orera, J.I. Peña, S. Serrano-Zabaleta, et al., *J. Eur. Ceram. Soc.* 35 (2015) 909.
- [7] W.J. Minford, R.C. Bradt, V.S. Stubican, *J. Am. Ceram. Soc.* 62 (1979) 154.
- [8] D. Pavlyuchkov, D. Dilner, G. Savinykh et al., *J. Am. Ceram. Soc.* 99 (2016) 3136.
- [9] D. Pavlyuchkov, G. Savinykh, O. Fabrichnaya, *Adv. Eng. Mater.* 15 (2013) 618.
- [10] D. Pavlyuchkov, G. Savinykh, O. Fabrichnaya, *J. Eur. Ceram. Soc.* 35 (2015) 3623.
- [11] D. Dilner, D. Pavlyuchkov, T. Zienert, et al., *J. Am. Ceram. Soc.* 100 (2017) 1661.
- [12] L. Kjellqvist, M. Selleby, *J. Phase Equilib. Diff.* 31 (2010) 113.
- [13] A.N. Grundy, B. Hallstedt, L.J. Gauckler, *J. Phase Equilib. Diff.* 24 (2003) 21.
- [14] L. Lutterotti, *Nucl. Instrum. Methods Phys. Res., B* 268 (2010) 334.
- [15] M. Hillert, B. Jansson, B. Sundman, J. Ågren, *Metall. and Mat. Trans. A* 16 (1985) 261.
- [16] B. Sundman, *CALPHAD* 15 (1991) 109.
- [17] M. Hillert, *J. Alloy. Compd.* 320 (2001) 161.
- [18] O. Fabrichnaya, D. Pavlyuchkov, *Metall. and Mat. Trans. A* 47 (2016) 152.
- [19] B. Hallstedt, *CALPHAD* 17 (1993) 281.
- [20] A. Kuprava, I. Saenko, O. Fabrichnaya, *CALPHAD* 68 (2020) 101745.
- [21] M. Härmäläinen, K. Zeng, *CALPHAD* 22 (1998) 375.
- [22] J. Tibballs, in: I. Ansara, A.T. Dinsdale, M.H. Rand (eds.) (Ed.), COST 507, “Thermochemical database for light metal alloys”, Vol. 2, EUR 18499 (1998) 215.
- [23] Y. Yin, B.B. Argent, *J. Phase Equilib. Diff.* 14 (1993) 439.
- [24] P. Duran, J.M. Rodriguez, P. Recio, *J. Mater. Sci.* 26 (1991) 467.
- [25] F. Ebert, E. Cohn, *Z. Anorg. Allg. Chem.* 213 (1933) 321.
- [26] C.F. Grain, *J. Am. Ceram. Soc.* 50 (1967) 288.
- [27] S.M.O. Sim, V.S. Stubican, *J. Am. Ceram. Soc.* 70 (1987) 521.
- [28] T. Kawashima, *JIM* 40 (1999) 967.
- [29] R.L. Shultz, A. Muan, *J. Am. Ceram. Soc.* 54 (1971) 504.
- [30] <https://www.sgte.net/>, accessed 24 June 2020.
- [31] C. Wang, M. Zinkevich, F. Aldinger, *J. Am. Ceram. Soc.* 89 (2006) 3751.
- [32] H. Biermann, *Adv. Eng. Mater.* 21 (2019) 1900126.

TDB1: Table of the optimized thermodynamic description for the Fe–Mg–Zr–O system (J/mol)

Phase	Sublattice model	Optimized parameters
Gas	(O ₂)	${}^0G_{O_2} = +2 \cdot \text{GHSEROO} + R \cdot T \cdot \ln(P)$;
Ionic Liquid	(Fe ⁺² , Mg ⁺² , Zr ⁺⁴) ₁ (O ⁻² , Va, FeO _{3/2}) ₁	${}^0G_{Fe+2;O-2}^{\text{IonicLiquid}} = +4 \cdot \text{GFEOLIQ}$;
		${}^0G_{Zr+4;O-2}^{\text{IonicLiquid}} = +2 \cdot \text{GZRO2LIQ}$;
		${}^0G_{Fe+2;Va}^{\text{IonicLiquid}} = +\text{GFELIQ}$;
		${}^0G_{Mg+2;Va}^{\text{IonicLiquid}} = +\text{GMGLIQ}$;
		${}^0G_{Mg+2;O-2}^{\text{IonicLiquid}} = +2 \cdot \text{GMGOLIQ}$;
		${}^0G_{Zr+4;Va}^{\text{IonicLiquid}} = +\text{GZRILIQ}$;
		${}^0G_{FeO3/2}^{\text{IonicLiquid}} = -89819 + 39.962 \cdot T + 2.5 \cdot \text{GFEOLIQ}$;
		${}^0L_{Fe+2,Zr+4;O-2}^{\text{IonicLiquid}} = -17320.87$;
		${}^1L_{Fe+2,Zr+4;O-2}^{\text{IonicLiquid}} = -3683$;
		${}^0L_{Fe+2;O-2,FeO3/2}^{\text{IonicLiquid}} = -26362$;
		${}^1L_{Fe+2;O-2,FeO3/2}^{\text{IonicLiquid}} = +13353$;
		${}^0L_{Fe+2;O-2,Va}^{\text{IonicLiquid}} = +176681 - 16.368 \cdot T$;
		${}^1L_{Fe+2;O-2,Va}^{\text{IonicLiquid}} = -65655 + 30.869 \cdot T$;
		${}^0L_{Zr+4;O-2,FeO3/2}^{\text{IonicLiquid}} = +41044.94$;
		${}^1L_{Zr+4;O-2,FeO3/2}^{\text{IonicLiquid}} = -17769.3$;
		${}^0L_{Zr+4;O-2,Va}^{\text{IonicLiquid}} = +75166.0715 - 55.2382004 \cdot T$;
		${}^1L_{Zr+4;O-2,Va}^{\text{IonicLiquid}} = +39057.4913$;
		${}^0L_{Fe+2,Zr+4;Va}^{\text{IonicLiquid}} = -85196.3 + 12.829 \cdot T$;
		${}^1L_{Fe+2,Zr+4;Va}^{\text{IonicLiquid}} = -1655.5$;
		${}^0L_{Fe+2;Va,FeO3/2}^{\text{IonicLiquid}} = +110000$;
		${}^0L_{Fe+2,Mg+2;Va}^{\text{IonicLiquid}} = +61343 + 1.5 \cdot T$;
		${}^1L_{Fe+2,Mg+2;Va}^{\text{IonicLiquid}} = -2700$;
		${}^0L_{Fe+2,Mg+2;O-2}^{\text{IonicLiquid}} = -20000$;
		${}^0L_{Mg+2;O-2,Va}^{\text{IonicLiquid}} = +182000 + 26.8 \cdot T$;
		${}^0L_{Mg+2;Va,FeO3/2}^{\text{IonicLiquid}} = -65000$;
		${}^0L_{Mg+2,Zr+4;O-2}^{\text{IonicLiquid}} = -68195.5443$;
		${}^1L_{Mg+2,Zr+4;O-2}^{\text{IonicLiquid}} = +35835.397$;
BCC	(Fe,Mg,Zr) ₁ (O,Va) ₃	${}^0G_{Fe;Va}^{\text{BCC}} = \text{GHSEFFE}$;
		${}^0G_{Fe;O}^{\text{BCC}} = \text{GHSEFFE} + 1.5 \cdot \text{GO2GAS} + 195 \cdot T$;
		${}^0G_{Zr;Va}^{\text{BCC}} = \text{GZRBCC}$;
		${}^0G_{Zr;O}^{\text{BCC}} = 3 \cdot \text{GHSEROO} + \text{GZRBCC} - 52652.008$;
		${}^0G_{Mg;Va}^{\text{BCC}} = \text{GHSERMG} + 3100 - 2.1 \cdot T$;
		${}^0G_{Mg;O}^{\text{BCC}} = \text{GHSERMG} + 1.5 \cdot \text{GO2GAS} + 10^6 + 195 \cdot T$;
		$T_{CFE;Va}^{\text{BCC}} = 1043$;
		$B_{OFe;Va}^{\text{BCC}} = 2.22$;
		${}^0L_{Fe;O;Va}^{\text{BCC}} = -517548 + 71.83 \cdot T$;
		${}^0L_{Fe;Zr;Va}^{\text{BCC}} = -33689.998 + 8.76457 \cdot T$;
		${}^1L_{Fe;Zr;Va}^{\text{BCC}} = -11176.623 + 7.6257 \cdot T$;
		${}^0L_{Zr;O;Va}^{\text{BCC}} = -1754239 + 336.32517 \cdot T$;
FCC	(Fe,Mg,Zr) ₁ (O,Va) ₁	${}^0G_{Fe;Va}^{\text{FCC}} = \text{GFEFFCC}$;
		${}^0G_{Fe;O}^{\text{FCC}} = \text{GFEFFCC} + 0.5 \cdot \text{GO2GAS} + 65 \cdot T$;
		${}^0G_{Zr;Va}^{\text{FCC}} = +7600 - 0.9 \cdot T + \text{GHSEZRZ}$;
		${}^0G_{Zr;O}^{\text{FCC}} = 0.5 \cdot \text{GHSEROO} + \text{GHSEZRZ} + 7600 - 0.9 \cdot T$;
		${}^0G_{Mg;Va}^{\text{FCC}} = +2600 - 0.9 \cdot T + \text{GHSERMG}$;
		${}^0G_{Mg;O}^{\text{FCC}} = 0.5 \cdot \text{GO2GAS} + \text{GHSERMG} + 65 \cdot T$;
		$T_{CFE;Va}^{\text{FCC}} = -201$;
		$B_{OFe;Va}^{\text{FCC}} = -2.1$;
		${}^0L_{Fe;O;Va}^{\text{FCC}} = -168758 + 19.17 \cdot T$;
		${}^0L_{Fe;Zr;Va}^{\text{FCC}} = -16847.9 - 3.5611 \cdot T$;
HCP	(Fe,Mg,Zr) ₁ (O,Va) _{0.5}	${}^0G_{Fe;Va}^{\text{HCP}} = \text{GFEHCP}$;
		${}^0G_{Fe;O}^{\text{HCP}} = \text{GFEHCP} + 0.5 \cdot \text{GHSEROO} + 32.5 \cdot T$;
		${}^0G_{Zr;Va}^{\text{HCP}} = \text{GHSEZRZ}$;
		${}^0G_{Zr;O}^{\text{HCP}} = 0.5 \cdot \text{GHSEROO} + \text{GHSEZRZ} - 286427.906 + 43.223 \cdot T$;
		${}^0G_{Mg;Va}^{\text{HCP}} = \text{GHSERMG}$;
		${}^0G_{Mg;O}^{\text{HCP}} = \text{GHSERMG} + 0.5 \cdot \text{GHSEROO} + 50 \cdot T$;
		${}^0L_{Zr;O;Va}^{\text{HCP}} = -37876.6552 + 17.2915 \cdot T$;
		${}^1L_{Zr;O;Va}^{\text{HCP}} = -4471.39$;
		${}^0L_{Fe;Zr;Va}^{\text{HCP}} = +57696$;
Fe ₂ Zr	(Fe,Zr) ₂ (Zr,Fe) ₁	${}^0G_{Fe;Zr}^{\text{Fe2Zr}} = -112156 + 438.584634 \cdot T - 79.10388 \cdot T \cdot \ln(T) - 0.006825 \cdot T^2 + 330106.042 \cdot T^{-1}$;
		${}^0G_{Fe;Fe}^{\text{Fe2Zr}} = +3 \cdot \text{GHSEFFE} + 15000$;
		${}^0G_{Zr;Zr}^{\text{Fe2Zr}} = +3 \cdot \text{GHSEZRZ} + 15000$;
		${}^0G_{Zr;Fe}^{\text{Fe2Zr}} = +112156 - 438.584634 \cdot T + 79.10388 \cdot T \cdot \ln(T) + 0.006825 \cdot T^2 - 330106.042 \cdot T^{-1} + 30000$;
		$T_{CFE;Va}^{\text{Fe2Zr}} = 585$;
		$B_{OFe;Va}^{\text{Fe2Zr}} = 1.4$;
		${}^0L_{Fe;Zr;Fe}^{\text{Fe2Zr}} = +56000$;
		${}^0L_{Fe;Zr;Zr}^{\text{Fe2Zr}} = +56000$;
		${}^0L_{Fe;Zr;Fe}^{\text{Fe2Zr}} = -23000 + 22.512 \cdot T$;
		${}^0L_{Zr;Zr;Fe}^{\text{Fe2Zr}} = -23000 + 22.512 \cdot T$;
hex.-Fe ₂ Zr	(Fe) ₂ (Zr,Fe) ₁	${}^0G_{Fe;Zr}^{\text{hex.-Fe2Zr}} = -113000 + 440.1791 \cdot T - 79.10388 \cdot T \cdot \ln(T) - 0.006825 \cdot T^2 + 330106.042 \cdot T^{-1}$;
		${}^0G_{Fe;Fe}^{\text{hex.-Fe2Zr}} = +3 \cdot \text{GHSEFFE} + 15000$;

		${}^0G_{\text{Fe:Zr:Fe}}^{\text{hex.-FeZr}} = -1533.1 + 3.095 \cdot T;$
FeZr ₂	(Fe) ₁ (Zr) ₂	${}^0G_{\text{Fe:Zr}}^{\text{FeZr2}} = +\text{GHSERFE} + 2 \cdot \text{GHSERZR} - 44258.83 - 2.7322 \cdot T;$
FeZr ₃	(Fe) ₁ (Zr) ₃	${}^0G_{\text{Fe:Zr}}^{\text{FeZr3}} = -80910.01 + 519.882937 \cdot T - 97.864 \cdot T \cdot \ln(T) - 0.0141 \cdot T^2 + 144140.86 \cdot T^{-1};$
M–ZrO ₂	(Fe ⁺² , Fe ⁺³ , Mg ⁺² , Zr ⁺⁴) ₁ (O ⁻² , Va) ₂	${}^0G_{\text{Fe+2:O-2}}^{\text{M-ZrO2}} = +\text{GWUSTITE} + \text{GHSEROO} + 120000 + 11.5263 \cdot T;$ ${}^0G_{\text{Fe+3:O-2}}^{\text{M-ZrO2}} = +0.5 \cdot \text{GFE2O3} + 0.5 \cdot \text{GHSEROO} + 100000 + 9.35108255 \cdot T;$ ${}^0G_{\text{Zr+4:O-2}}^{\text{M-ZrO2}} = +\text{GZRO2M};$ ${}^0G_{\text{Fe+2:Va}}^{\text{M-ZrO2}} = +\text{GWUSTITE} - \text{GHSEROO} + 120000 + 11.5263 \cdot T;$ ${}^0G_{\text{Fe+3:Va}}^{\text{M-ZrO2}} = +0.5 \cdot \text{GFE2O3} - 1.5 \cdot \text{GHSEROO} + 100000 + 9.35108255 \cdot T;$ ${}^0G_{\text{Zr+4:Va}}^{\text{M-ZrO2}} = +\text{GZRO2M} - 2 \cdot \text{GHSEROO};$ ${}^0G_{\text{Mg+2:O-2}}^{\text{M-ZrO2}} = +\text{GMGOSOL} + \text{GHSEROO} + 120000 + 11.5263 \cdot T;$ ${}^0G_{\text{Mg+2:Va}}^{\text{M-ZrO2}} = +\text{GMGOSOL} - \text{GHSEROO} + 120000 + 11.5263 \cdot T;$
T–ZrO ₂	(Fe ⁺² , Fe ⁺³ , Mg ⁺² , Zr ⁺⁴) ₁ (O ⁻² , Va) ₂	${}^0G_{\text{Fe+2:O-2}}^{\text{T-ZrO2}} = +\text{GWUSTITE} + \text{GHSEROO} + 60000 + 11.5263 \cdot T;$ ${}^0G_{\text{Fe+3:O-2}}^{\text{T-ZrO2}} = +0.5 \cdot \text{GFE2O3} + 0.5 \cdot \text{GHSEROO} + 9.35108255 \cdot T + 50000;$ ${}^0G_{\text{Zr+4:O-2}}^{\text{T-ZrO2}} = +\text{GZRO2T};$ ${}^0G_{\text{Fe+2:Va}}^{\text{T-ZrO2}} = +\text{GWUSTITE} - \text{GHSEROO} + 60000 + 11.5263 \cdot T;$ ${}^0G_{\text{Fe+3:Va}}^{\text{T-ZrO2}} = +0.5 \cdot \text{GFE2O3} - 1.5 \cdot \text{GHSEROO} + 9.5108255 \cdot T + 50000;$ ${}^0G_{\text{Zr+4:Va}}^{\text{T-ZrO2}} = +\text{GZRO2T} - 2 \cdot \text{GHSEROO};$ ${}^0G_{\text{Mg+2:O-2}}^{\text{T-ZrO2}} = +\text{GMGOSOL} + \text{GHSEROO} + 60000 + 11.5263 \cdot T;$ ${}^0G_{\text{Mg+2:Va}}^{\text{T-ZrO2}} = +\text{GMGOSOL} - \text{GHSEROO} + 60000 + 11.5263 \cdot T;$ ${}^0L_{\text{Mg+2,Zr+4:O-2}}^{\text{T-ZrO2}} = +50000;$ ${}^0L_{\text{Mg+2,Zr+4:Va}}^{\text{T-ZrO2}} = +50000;$ ${}^0L_{\text{Fe+2,Zr+4:O-2}}^{\text{T-ZrO2}} = +50000;$ ${}^0L_{\text{Fe+2,Zr+4:Va}}^{\text{T-ZrO2}} = +50000;$ ${}^0L_{\text{Fe+3,Zr+4:O-2}}^{\text{T-ZrO2}} = +10000;$ ${}^0L_{\text{Fe+3,Zr+4:Va}}^{\text{T-ZrO2}} = +10000;$
C–ZrO ₂ Fluorite	(Fe ⁺² , Fe ⁺³ , Mg ⁺² , Zr ⁺⁴) ₁ (O ⁻² , Va) ₂	${}^0G_{\text{Fe+2:O-2}}^{\text{C-ZrO2}} = +\text{GWUSTITE} + \text{GHSEROO} + 45000 + 11.5263 \cdot T;$ ${}^0G_{\text{Fe+3:O-2}}^{\text{C-ZrO2}} = +0.5 \cdot \text{GFE2O3} + 0.5 \cdot \text{GHSEROO} + 9.35108255 \cdot T + 50000;$ ${}^0G_{\text{Zr+4:O-2}}^{\text{C-ZrO2}} = +\text{GZRO2C};$ ${}^0G_{\text{Fe+2:Va}}^{\text{C-ZrO2}} = +\text{GWUSTITE} - \text{GHSEROO} + 45000 + 11.5263 \cdot T;$ ${}^0G_{\text{Fe+3:Va}}^{\text{C-ZrO2}} = +0.5 \cdot \text{GFE2O3} - 1.5 \cdot \text{GHSEROO} + 9.35108255 \cdot T + 50000;$ ${}^0G_{\text{Zr+4:Va}}^{\text{C-ZrO2}} = +\text{GZRO2C} - 2 \cdot \text{GHSEROO};$ ${}^0G_{\text{Zr+4:Va}}^{\text{C-ZrO2}} = +\text{GMGOSOL} - \text{GHSEROO} + 45000 + 11.5263 \cdot T;$ ${}^0G_{\text{Zr+4:Va}}^{\text{C-ZrO2}} = +\text{GMGOSOL} + \text{GHSEROO} + 45000 + 11.5263 \cdot T;$ ${}^0L_{\text{Mg+2,Zr+4:O-2}}^{\text{C-ZrO2}} = +2550.15;$ ${}^0L_{\text{Mg+2,Zr+4:Va}}^{\text{C-ZrO2}} = +2550.15;$ ${}^0L_{\text{Fe+2,Zr+4:O-2}}^{\text{C-ZrO2}} = +15000;$ ${}^0L_{\text{Fe+2,Zr+4:Va}}^{\text{C-ZrO2}} = +15000;$ ${}^0L_{\text{Fe+3,Zr+4:O-2}}^{\text{C-ZrO2}} = +9250;$ ${}^0L_{\text{Fe+3,Zr+4:Va}}^{\text{C-ZrO2}} = +9250;$
Halite	(Fe ⁺² , Fe ⁺³ , Mg ⁺² , Va) ₁ (O ⁻²) ₁	${}^0G_{\text{Fe+2:O-2}}^{\text{Halite}} = +\text{GWUSTITE};$ ${}^0G_{\text{Fe+3:O-2}}^{\text{Halite}} = +1.25 \cdot \text{AWUSTITE} + 1.25 \cdot \text{GWUSTITE};$ ${}^0G_{\text{Mg+2:O-2}}^{\text{Halite}} = +\text{GMGOSOL};$ ${}^0G_{\text{Va:O-2}}^{\text{Halite}} = +0;$ ${}^0L_{\text{Fe+2,Mg+2:O-2}}^{\text{Halite}} = +19369.9567 - 12 \cdot T;$ ${}^1L_{\text{Fe+2,Mg+2:O-2}}^{\text{Halite}} = -3758.04262;$ ${}^0L_{\text{Fe+3,Mg+2:O-2}}^{\text{Halite}} = +68236.7774 - 30 \cdot T;$ ${}^1L_{\text{Fe+3,Mg+2:O-2}}^{\text{Halite}} = -6748.0443;$ ${}^0L_{\text{Fe+2,Fe+3:O-2}}^{\text{Halite}} = -12324;$ ${}^1L_{\text{Fe+2,Fe+3:O-2}}^{\text{Halite}} = +20070;$
Spinel	(Fe ⁺² , Fe ⁺³ , Mg ⁺²) ₁ (Fe ⁺² , Fe ⁺³ , Mg ⁺² , Zr ⁺⁴ , Va) ₂ (Fe ⁺² , Mg ⁺² , Va) ₂ (O ⁻²) ₄	${}^0G_{\text{Fe+2:Fe+2:Fe+2:O-2}}^{\text{Spinel}} = +9 \cdot \text{GFE3O4} + \text{DFE3O4};$ $T_{\text{CFE+2:Fe+2:Fe+2:O-2}}^{\text{Spinel}} = 848;$ $B_{\text{OFe+2:Fe+2:Fe+2:O-2}}^{\text{Spinel}} = 44.54;$ ${}^0G_{\text{Fe+3:Fe+2:Fe+2:O-2}}^{\text{Spinel}} = +9 \cdot \text{GFE3O4} + \text{DFE3O4} - \text{BFE3O4};$ $T_{\text{CFE+3:Fe+2:Fe+2:O-2}}^{\text{Spinel}} = 848;$ $B_{\text{OFe+3:Fe+2:Fe+2:O-2}}^{\text{Spinel}} = 44.54;$ ${}^0G_{\text{Fe+2,Zr+4:Fe+2:O-2}}^{\text{Spinel}} = +2 \cdot \text{GZRO2C} + 4 \cdot \text{GWUSTITE} + 23.0524394 \cdot T + 10000 + \text{DFE3O4} - 5 \cdot \text{GFE3O4} - 2 \cdot \text{BFE3O4};$ ${}^0G_{\text{Fe+2:Fe+3:Fe+2:O-2}}^{\text{Spinel}} = +9 \cdot \text{GFE3O4} + \text{DFE3O4} - \text{BFE3O4};$ $T_{\text{CFE+2:Fe+3:Fe+2:O-2}}^{\text{Spinel}} = 848;$ $B_{\text{OFe+2:Fe+3:Fe+2:O-2}}^{\text{Spinel}} = 44.54;$ ${}^0G_{\text{Fe+3:Fe+3:Fe+2:O-2}}^{\text{Spinel}} = +9 \cdot \text{GFE3O4} + \text{DFE3O4} - 2 \cdot \text{BFE3O4};$ $T_{\text{CFE+3:Fe+3:Fe+2:O-2}}^{\text{Spinel}} = 848;$ $B_{\text{OFe+3:Fe+3:Fe+2:O-2}}^{\text{Spinel}} = 44.54;$ ${}^0G_{\text{Fe+3:Zr+4:Fe+2:O-2}}^{\text{Spinel}} = +2 \cdot \text{GZRO2C} + 2 \cdot \text{GFE2O3} + 6 \cdot \text{GWUSTITE} + 10000 + 37.40388 \cdot T - 19 \cdot \text{GFE3O4} + \text{DFE3O4} - \text{BFE3O4};$ ${}^0G_{\text{Fe+2:Va:Fe+2:O-2}}^{\text{Spinel}} = +7 \cdot \text{GFE3O4} + \text{DFE3O4} + \text{CFE3O4} - \text{BFE3O4};$ $T_{\text{CFE+2:Va:Fe+2:O-2}}^{\text{Spinel}} = 848;$ $B_{\text{OFe+2:Va:Fe+2:O-2}}^{\text{Spinel}} = 44.54;$ ${}^0G_{\text{Fe+3:Va:Fe+2:O-2}}^{\text{Spinel}} = +7 \cdot \text{GFE3O4} + \text{DFE3O4} + \text{CFE3O4} - 2 \cdot \text{BFE3O4};$ $T_{\text{CFE+3:Va:Fe+2:O-2}}^{\text{Spinel}} = 848;$ $B_{\text{OFe+3:Va:Fe+2:O-2}}^{\text{Spinel}} = 44.54;$ ${}^0G_{\text{Fe+2:Fe+2:Va:O-2}}^{\text{Spinel}} = +7 \cdot \text{GFE3O4} + \text{BFE3O4};$ $T_{\text{CFE+2:Fe+2:Va:O-2}}^{\text{Spinel}} = 848;$ $B_{\text{OFe+2:Fe+2:Va:O-2}}^{\text{Spinel}} = 44.54;$ ${}^0G_{\text{Fe+3:Fe+2:Va:O-2}}^{\text{Spinel}} = +7 \cdot \text{GFE3O4};$ $T_{\text{CFE+3:Fe+2:Va:O-2}}^{\text{Spinel}} = 848;$

		$B_{\text{Fe}^{+3}\text{Fe}^{+2}\text{Va}\text{O}_2}^{\text{Spinel}} = 44.54;$ ${}^0G_{\text{Fe}^{+2}\text{Zr}^{+4}\text{Va}\text{O}_2}^{\text{Spinel}} = +2 \cdot \text{GZRO2C} + 4 \cdot \text{GWUSTITE} + 10000 + 23.0524394 \cdot T$ $- 7 \cdot \text{GFE3O4} - \text{BFE3O4};$ ${}^0G_{\text{Fe}^{+2}\text{Fe}^{+3}\text{Va}\text{O}_2}^{\text{Spinel}} = +7 \cdot \text{GFE3O4};$ $T_{\text{CFe}^{+2}\text{Fe}^{+3}\text{Va}\text{O}_2}^{\text{Spinel}} = 848;$ $B_{\text{Fe}^{+2}\text{Fe}^{+3}\text{Va}\text{O}_2}^{\text{Spinel}} = 44.54;$ ${}^0G_{\text{Fe}^{+3}\text{Fe}^{+3}\text{Va}\text{O}_2}^{\text{Spinel}} = +7 \cdot \text{GFE3O4} - \text{BFE3O4};$ $T_{\text{CFe}^{+3}\text{Fe}^{+3}\text{Va}\text{O}_2}^{\text{Spinel}} = 848;$ $B_{\text{Fe}^{+3}\text{Fe}^{+3}\text{Va}\text{O}_2}^{\text{Spinel}} = 44.54;$ ${}^0G_{\text{Fe}^{+3}\text{Zr}^{+4}\text{Va}\text{O}_2}^{\text{Spinel}} = +2 \cdot \text{GZRO2C} + 2 \cdot \text{GFE2O3} + 6 \cdot \text{GWUSTITE} - 21 \cdot \text{GFE3O4}$ $+ 10000 + 37.40388 \cdot T;$ ${}^0G_{\text{Fe}^{+2}\text{Va}\text{Va}\text{O}_2}^{\text{Spinel}} = +5 \cdot \text{GFE3O4} + \text{CFE3O4};$ $T_{\text{CFe}^{+2}\text{Va}\text{Va}\text{O}_2}^{\text{Spinel}} = 848;$ $B_{\text{Fe}^{+2}\text{Va}\text{Va}\text{O}_2}^{\text{Spinel}} = 44.54;$ ${}^0G_{\text{Fe}^{+3}\text{Va}\text{Va}\text{O}_2}^{\text{Spinel}} = +5 \cdot \text{GFE3O4} + \text{CFE3O4} - \text{BFE3O4};$ $T_{\text{CFe}^{+3}\text{Va}\text{Va}\text{O}_2}^{\text{Spinel}} = 848;$ $B_{\text{Fe}^{+3}\text{Va}\text{Va}\text{O}_2}^{\text{Spinel}} = 44.54;$ ${}^0G_{\text{Mg}^{+2}\text{Mg}^{+2}\text{Mg}^{+2}\text{O}_2}^{\text{Spinel}} = +\text{GMGMGMG};$ ${}^0G_{\text{Mg}^{+2}\text{Va}\text{Mg}^{+2}\text{O}_2}^{\text{Spinel}} = +\text{GMGVAMG};$ ${}^0G_{\text{Mg}^{+2}\text{Mg}^{+2}\text{Va}\text{O}_2}^{\text{Spinel}} = +\text{GMGMG};$ ${}^0G_{\text{Mg}^{+2}\text{Va}\text{Va}\text{O}_2}^{\text{Spinel}} = +\text{GMGVA};$ ${}^0G_{\text{Mg}^{+2}\text{Fe}^{+3}\text{Va}\text{O}_2}^{\text{Spinel}} = +\text{GMGFE3NO};$ $T_{\text{CMg}^{+2}\text{Fe}^{+3}\text{Va}\text{O}_2}^{\text{Spinel}} = 689.5;$ $B_{\text{OMg}^{+2}\text{Fe}^{+3}\text{Va}\text{O}_2}^{\text{Spinel}} = 1.0;$ ${}^0G_{\text{Fe}^{+3}\text{Mg}^{+2}\text{Va}\text{O}_2}^{\text{Spinel}} = +2 \cdot \text{GMGFE3IN} - 7 \cdot \text{GFE3O4} + \text{BFE3O4} + 23.05244 \cdot T;$ $T_{\text{CFe}^{+3}\text{Mg}^{+2}\text{Va}\text{O}_2}^{\text{Spinel}} = 689.5;$ $B_{\text{OFe}^{+3}\text{Mg}^{+2}\text{Va}\text{O}_2}^{\text{Spinel}} = 1.0;$ ${}^0G_{\text{Fe}^{+2}\text{Mg}^{+2}\text{Va}\text{O}_2}^{\text{Spinel}} = +2 \cdot \text{GMGFE3IN} - 7 \cdot \text{GFE3O4} + 2 \cdot \text{BFE3O4} + 23.05244 \cdot T;$ ${}^0G_{\text{Mg}^{+2}\text{Fe}^{+2}\text{Va}\text{O}_2}^{\text{Spinel}} = +\text{GMGFE3NO} + \text{BFE3O4};$ ${}^0G_{\text{Mg}^{+2}\text{Fe}^{+2}\text{Mg}^{+2}\text{O}_2}^{\text{Spinel}} = +\text{GMGMGMG} + \text{GMGFE3NO} + \text{BFE3O4} - \text{GMGMG}$ $+ 500000;$ ${}^0G_{\text{Mg}^{+2}\text{Fe}^{+3}\text{Mg}^{+2}\text{O}_2}^{\text{Spinel}} = +\text{GMGMGMG} + \text{GMGFE3NO} - \text{GMGMG} + 500000;$ ${}^0G_{\text{Fe}^{+2}\text{Mg}^{+2}\text{Mg}^{+2}\text{O}_2}^{\text{Spinel}} = +\text{GMGMGMG} + 2 \cdot \text{GMGFE3IN} - 7 \cdot \text{GFE3O4} + 2 \cdot \text{BFE3O4}$ $+ 23.05244 \cdot T - \text{GMGMG};$ ${}^0G_{\text{Fe}^{+3}\text{Mg}^{+2}\text{Mg}^{+2}\text{O}_2}^{\text{Spinel}} = +\text{GMGMGMG} - 7 \cdot \text{GFE3O4} + \text{BFE3O4} + 23.05244 \cdot T$ $- \text{GMGMG} + 500000;$ ${}^0G_{\text{Mg}^{+2}\text{Fe}^{+2}\text{Fe}^{+2}\text{O}_2}^{\text{Spinel}} = +2 \cdot \text{GFE3O4} + \text{DFE3O4} + \text{GMGFE3NO} + 500000;$ ${}^0G_{\text{Fe}^{+2}\text{Mg}^{+2}\text{Fe}^{+2}\text{O}_2}^{\text{Spinel}} = +\text{DFE3O4} + 2 \cdot \text{GMGFE3IN} - 5 \cdot \text{GFE3O4} + 23.05244 \cdot T$ $+ 500000;$ ${}^0G_{\text{Mg}^{+2}\text{Fe}^{+3}\text{Fe}^{+2}\text{O}_2}^{\text{Spinel}} = +2 \cdot \text{GFE3O4} + \text{DFE3O4} - \text{BFE3O4} + \text{GMGFE3NO}$ $+ 500000;$ ${}^0G_{\text{Fe}^{+3}\text{Mg}^{+2}\text{Fe}^{+2}\text{O}_2}^{\text{Spinel}} = +\text{DFE3O4} + 2 \cdot \text{GMGFE3IN} - 5 \cdot \text{GFE3O4} + \text{BFE3O4}$ $+ 23.05244 \cdot T + 500000;$ ${}^0G_{\text{Fe}^{+2}\text{Fe}^{+3}\text{Mg}^{+2}\text{O}_2}^{\text{Spinel}} = +\text{GMGMGMG} + 2 \cdot \text{GMGFE3IN} - 7 \cdot \text{GFE3O4} + 2 \cdot \text{BFE3O4}$ $+ 23.05244 \cdot T - 2 \cdot \text{GMGMG} + \text{GMGFE3NO} + 1000000;$ ${}^0G_{\text{Fe}^{+3}\text{Fe}^{+2}\text{Mg}^{+2}\text{O}_2}^{\text{Spinel}} = +\text{GMGMGMG} - 7 \cdot \text{GFE3O4} + 2 \cdot \text{BFE3O4} + 23.05244 \cdot T$ $- 2 \cdot \text{GMGMG} + \text{GMGFE3NO} + 1000000;$ ${}^0G_{\text{Fe}^{+3}\text{Va}\text{Mg}^{+2}\text{O}_2}^{\text{Spinel}} = -7 \cdot \text{GFE3O4} + \text{BFE3O4} + 23.05244 \cdot T - \text{GMGMG}$ $+ \text{GMGVAMG} + 500000;$ ${}^0G_{\text{Fe}^{+2}\text{Va}\text{Mg}^{+2}\text{O}_2}^{\text{Spinel}} = +2 \cdot \text{GMGFE3IN} - 7 \cdot \text{GFE3O4} + 2 \cdot \text{BFE3O4} + 23.05244 \cdot T$ $- \text{GMGMG} + \text{GMGVAMG} + 500000;$ ${}^0G_{\text{Fe}^{+2}\text{Fe}^{+2}\text{Mg}^{+2}\text{O}_2}^{\text{Spinel}} = +\text{GMGMGMG} + 2 \cdot \text{GMGFE3IN} - 7 \cdot \text{GFE3O4} + 3 \cdot \text{BFE3O4}$ $+ 23.05244 \cdot T - \text{GMGMG} + \text{GMGFE3NO} + 1000000;$ ${}^0G_{\text{Fe}^{+3}\text{Fe}^{+3}\text{Mg}^{+2}\text{O}_2}^{\text{Spinel}} = +\text{GMGMGMG} - 7 \cdot \text{GFE3O4} + 3 \cdot \text{BFE3O4} + 23.05244 \cdot T$ $- 2 \cdot \text{GMGMG} + \text{GMGFE3NO} + 1000000;$ ${}^0G_{\text{Mg}^{+2}\text{Va}\text{Fe}^{+2}\text{O}_2}^{\text{Spinel}} = +\text{GMGVA} + 2 \cdot \text{GFE3O4} + \text{DFE3O4} - \text{BFE3O4} + 500000;$ ${}^0G_{\text{Mg}^{+2}\text{Mg}^{+2}\text{Fe}^{+2}\text{O}_2}^{\text{Spinel}} = +\text{GMGMG} + 2 \cdot \text{GFE3O4} + \text{DFE3O4} - \text{BFE3O4} + 500000;$ ${}^0G_{\text{Mg}^{+2}\text{Zr}^{+4}\text{Va}\text{O}_2}^{\text{Spinel}} = +2 \cdot \text{GMGZRO4} - \text{GMGMG} + 23.05244 \cdot T;$ ${}^0G_{\text{Mg}^{+2}\text{Zr}^{+4}\text{Mg}^{+2}\text{O}_2}^{\text{Spinel}} = +2 \cdot \text{GMGZRO4} - \text{GMGMG} + \text{GMGMGMG} + 23.05244 \cdot T;$ ${}^0G_{\text{Mg}^{+2}\text{Zr}^{+4}\text{Fe}^{+3}\text{O}_2}^{\text{Spinel}} = +2 \cdot \text{GMGZRO4} - \text{GMGMG} + 23.05244 \cdot T + 2 \cdot \text{GFE3O4}$ $+ \text{DFE3O4} - \text{BFE3O4};$ ${}^0G_{\text{Mg}^{+2}\text{Zr}^{+4}\text{Fe}^{+2}\text{O}_2}^{\text{Spinel}} = +2 \cdot \text{GZRO2C} - \text{GMGMG} + \text{GMGMGMG} + 23.05244 \cdot T$ $+ \text{GWUSTITE} + 1000 - 7 \cdot \text{GFE3O4} - \text{BFE3O4};$ ${}^0L_{\text{Fe}^{+3}\text{Mg}^{+2}\text{Mg}^{+2}\text{Va}\text{O}_2}^{\text{Spinel}} = -162358.584;$ ${}^0L_{\text{Fe}^{+3}\text{Mg}^{+2}\text{Fe}^{+3}\text{Va}\text{O}_2}^{\text{Spinel}} = -32110.6041;$ ${}^0L_{\text{Fe}^{+3}\text{Fe}^{+3}\text{Mg}^{+2}\text{Va}\text{O}_2}^{\text{Spinel}} = +44188.8675;$ ${}^0L_{\text{Mg}^{+2}\text{Fe}^{+3}\text{Mg}^{+2}\text{Va}\text{O}_2}^{\text{Spinel}} = +90042.1775;$
Corundum	$(\text{Fe}^{+3}, \text{Zr}^{+4})_2(\text{O}^{-2}, \text{Va})_1(\text{O}^{-2})_3$	${}^0G_{\text{Fe}^{+3}\text{O}_2\text{O}_2}^{\text{Corundum}} = +\text{GFE2O3} + \text{GHSEROO};$ ${}^0T_{\text{CFe}^{+3}\text{O}_2\text{O}_2}^{\text{Corundum}} = -2867;$ ${}^0B_{\text{OFe}^{+3}\text{O}_2\text{O}_2}^{\text{Corundum}} = -25.1;$ ${}^0G_{\text{Zr}^{+4}\text{O}_2\text{O}_2}^{\text{Corundum}} = +2 \cdot \text{GZRO2C} + 50000;$ ${}^0G_{\text{Fe}^{+3}\text{Va}\text{O}_2}^{\text{Corundum}} = +\text{GFE2O3};$ ${}^0G_{\text{Zr}^{+4}\text{Va}\text{O}_2}^{\text{Corundum}} = +2 \cdot \text{GZRO2C} - \text{GHSEROO} + 50000;$ ${}^0T_{\text{CFe}^{+3}\text{Va}\text{O}_2}^{\text{Corundum}} = -2867;$ ${}^0B_{\text{OFe}^{+3}\text{Va}\text{O}_2}^{\text{Corundum}} = -25.1;$ ${}^0L_{\text{Fe}^{+3}\text{Zr}^{+4}\text{Va}\text{O}_2}^{\text{Corundum}} = +120000;$ ${}^0L_{\text{Fe}^{+3}\text{Zr}^{+4}\text{O}_2\text{O}_2}^{\text{Corundum}} = +120000;$

Functions	(Temperature limits)	
GHSEROO	(298–1000)	$-3480.87 - 25.503038 \cdot T - 11.136 \cdot T \cdot \ln(T) - 0.005098888 \cdot T^2 + 6.61846 \cdot 10^{-7} \cdot T^3$ $- 38365 \cdot T^{-1}$
	(1000–3300)	$-6568.763 + 12.65988 \cdot T - 16.8138 \cdot T \cdot \ln(T) - 5.95798 \cdot 10^{-4} \cdot T^2 + 6.781 \cdot 10^{-9} \cdot T^3$ $+ 262905 \cdot T^{-1}$
	(3300–6000)	$-13986.728 + 31.259625 \cdot T - 18.9536 \cdot T \cdot \ln(T) - 4.25243 \cdot 10^{-4} \cdot T^2 + 1.0721 \cdot 10^{-8} \cdot T^3$ $+ 4383200 \cdot T^{-1}$
GO2GAS	(298–1000)	$-6961.74451 - 76729.7484 \cdot T^{-1} - 51.0057202 \cdot T - 22.2710136 \cdot T \cdot \ln(T)$ $- 0.0101977469 \cdot T^2 + 1.32369208 \cdot 10^{-6} \cdot T^3$
	(1000–3300)	$-13137.5203 + 525809.556 \cdot T^{-1} + 25.3200332 \cdot T - 33.627603 \cdot T \cdot \ln(T)$ $- 0.00119159274 \cdot T^2 + 1.35611111 \cdot 10^{-8} \cdot T^3$
	(3300–6000)	$-27973.4908 + 8766421.4 \cdot T^{-1} + 62.5195726 \cdot T - 37.9072074 \cdot T \cdot \ln(T)$ $- 8.50483772 \cdot 10^{-4} \cdot T^2 + 2.14409777 \cdot 10^{-8} \cdot T^3$
GHSERFE	(298–1811)	$+1225.7 + 124.134 \cdot T - 23.5143 \cdot T \cdot \ln(T) - 0.00439752 \cdot T^2 - 5.8927 \cdot 10^{-8} \cdot T^3$ $+ 77359 \cdot T^{-1}$
	(1811–6000)	$-25383.581 + 299.31255 \cdot T - 46 \cdot T \cdot \ln(T) + 2.29603 \cdot 10^{31} \cdot T^{-9}$
GFEFCC	(298–1811)	$-236.7 + 132.416 \cdot T - 24.6643 \cdot T \cdot \ln(T) - 0.00375752 \cdot T^2 - 5.8927 \cdot 10^{-8} \cdot T^3 + 77359 \cdot T^{-1}$
	(1811–6000)	$-27097.396 + 300.25256 \cdot T - 46 \cdot T \cdot \ln(T) + 2.78854 \cdot 10^{31} \cdot T^{-9}$
GFEHCP	(298–1811)	$-3705.78 + 12.591 \cdot T - 1.15 \cdot T \cdot \ln(T) + 6.4 \cdot 10^{-4} \cdot T^2 + \text{GHSERFE}$
	(1811–6000)	$-3957.195 + 5.249009 \cdot T + \text{GHSERFE} + 4.9251 \cdot 10^{30} \cdot T^{-9}$
GFELIQ	(298–1811)	$+12040.17 - 6.55843 \cdot T - 3.67516 \cdot 10^{-21} \cdot T^7 + \text{GHSERFE}$
	(1811–6000)	$+14544.751 - 8.01055 \cdot T + \text{GHSERFE} - 2.29603 \cdot 10^{31} \cdot T^{-9}$
GFEOLIQ	(298–6000)	$-137252 + 224.641 \cdot T - 37.1815 \cdot T \cdot \ln(T)$
GFE2O3	(298–3000)	$-858683 + 827.946 \cdot T - 137.0089 \cdot T \cdot \ln(T) + 1453810 \cdot T^{-1}$
GWUSTITE	(298–3000)	$-279318 + 252.848 \cdot T - 46.12826 \cdot T \cdot \ln(T) - 0.0057402984 \cdot T^2$
AWUSTITE	(298–3000)	$-55384 + 27.888 \cdot T$
GFE3O4	(298–3000)	$-161731 + 144.873 \cdot T - 24.9879 \cdot T \cdot \ln(T) - 0.0011952256 \cdot T^2 + 206520 \cdot T^{-1}$
DFE3O4	(298–3000)	$+402520 - 30.529 \cdot T$
BFE3O4	(298–3000)	$+46826 - 27.266 \cdot T$
CFE3O4	(298–3000)	$+120730 - 20.102 \cdot T$
GHSERZR	(130–2128)	$-7827.595 + 125.64905 \cdot T - 24.1618 \cdot T \cdot \ln(T) - 0.00437791 \cdot T^2 + 34971 \cdot T^{-1}$
	(2128–6000)	$-26085.921 + 262.724183 \cdot T - 42.144 \cdot T \cdot \ln(T) - 1.342896 \cdot 10^{31} \cdot T^{-9}$
GZRBCC	(130–2128)	$-525.539 + 124.9457 \cdot T - 25.607406 \cdot T \cdot \ln(T) - 3.40084 \cdot 10^{-4} \cdot T^2 - 9.729 \cdot 10^{-9} \cdot T^3$ $+ 25233 \cdot T^{-1} - 7.6143 \cdot 10^{-11} \cdot T^4$
	(2128–6000)	$-4620.034 + 1.55998 \cdot T + \text{GHSERZR} + 1.4103476 \cdot 10^{32} \cdot T^{-9}$
GZRLIQ	(130–2128)	$+18147.69 - 9.080812 \cdot T + \text{GHSERZR} + 1.6275 \cdot 10^{-22} \cdot T^7$
	(2128–6000)	$-8281.26 + 253.812609 \cdot T - 42.144 \cdot T \cdot \ln(T)$
GZRO2M	(298–6000)	$-1126163.54 + 424.890806 \cdot T - 69.3875137 \cdot T \cdot \ln(T) - 0.00375880141 \cdot T^2$ $+ 683000 \cdot T^{-1}$
GZRO2T	(298–6000)	$+5468 - 4 \cdot T + \text{GZRO2M}$
GZRO2C	(298–6000)	$+10336 - 4 \cdot T + \text{GZRO2T}$
GZRO2LIQ	(298–6000)	$+87027 - 29.17432 \cdot T + \text{GZRO2C}$
GCRUND	(298–600)	$-1707351.3 + 448.021092 \cdot T - 67.4804 \cdot T \cdot \ln(T) - 0.06747 \cdot T^2 + 1.4205433 \cdot 10^{-5} \cdot T^3$ $+ 938780 \cdot T^{-1}$
	(600–1500)	$-1724886.06 + 754.856573 \cdot T - 116.258 \cdot T \cdot \ln(T) - 0.0072257 \cdot T^2 + 2.78532 \cdot 10^{-7} \cdot T^3$ $+ 2120700 \cdot T^{-1}$
	(1500–3000)	$-1772163.19 + 1053.4548 \cdot T - 156.058 \cdot T \cdot \ln(T) + 0.00709105 \cdot T^2 - 6.29402 \cdot 10^{-7} \cdot T^3$ $+ 12366650 \cdot T^{-1}$
GHSERMG	(298–3000)	$-8367.34 + 143.677875 \cdot T - 26.1849782 \cdot T \cdot \ln(T) + 4.858 \cdot 10^{-4} \cdot T^2 - 1.393669 \cdot 10^{-6} \cdot T^3$ $+ 78950 \cdot T^{-1}$
		$-14130.185 + 204.718543 \cdot T - 34.3088 \cdot T \cdot \ln(T) + 1.038192 \cdot 10^{28} \cdot T^{-9}$

GMGLIQ	(298–923)	$+8202.243 - 8.83693 \cdot T + \text{GHSERMG} - 8.0176 \cdot 10^{-20} \cdot T^7$
	(923–3000)	$+8690.316 - 9.392158 \cdot T + \text{GHSERMG} - 1.038192 \cdot 10^{+28} \cdot T^{-9}$
GMGOLIQ	(298–1700)	$-549098.33 + 275.724634 \cdot T - 47.4817 \cdot T \cdot \ln(T) - 0.00232681 \cdot T^2 + 4.5043 \cdot 10^{-8} \cdot T^3$
	(1700–2450)	$+516900 \cdot T^{-1}$ $-585159.646 + 506.06825 \cdot T - 78.3772 \cdot T \cdot \ln(T) + 0.0097344 \cdot T^2 - 8.60338 \cdot 10^{-7} \cdot T^3$
	(2450–3100)	$+8591550 \cdot T^{-1}$ $+9110429.75 - 42013.7634 \cdot T + 5298.548 \cdot T \cdot \ln(T) - 1.30122485 \cdot T^2$
	(3100–5100)	$+5.8262601 \cdot 10^{-5} \cdot T^3 - 3.24037416 \cdot 10^9 \cdot T^{-1}$ $-632664.468 + 589.239555 \cdot T - 84 \cdot T \cdot \ln(T)$
GMGOSOL	(298–1700)	$-619428.502 + 298.253571 \cdot T - 47.4817 \cdot T \cdot \ln(T) - 0.00232681 \cdot T^2 + 4.5043 \cdot 10^{-8} \cdot T^3$
	(1700–3100)	$+516900 \cdot T^{-1}$ $-655489.818 + 528.597187 \cdot T - 78.3772 \cdot T \cdot \ln(T) + 0.0097344 \cdot T^2 - 8.60338 \cdot 10^{-7} \cdot T^3$
	(3100–5000)	$+8591550 \cdot T^{-1}$ $-171490.159 - 1409.43369 \cdot T + 163.674142 \cdot T \cdot \ln(T) - 0.044009535 \cdot T^2$
	(5000–5100)	$+1.374896 \cdot 10^{-6} \cdot T^3 - 1.72665403 \cdot 10^8 \cdot T^{-1}$ $-722412.718 + 617.657452 \cdot T - 84 \cdot T \cdot \ln(T)$
GALAL	(298–6000)	$+1.5 \cdot \text{GCORUND} - 0.5 \cdot \text{GHSEROO}$
NSPINEL	(298–6000)	$+ \text{GMGOSOL} + \text{GCORUND} - 23204.5143 - 32.2303298 \cdot T + 4.31045184 \cdot T \cdot \ln(T)$
ISPINEL	(298–6000)	$+ \text{NSPINEL} + 18002.9059 - 0.398945666 \cdot T$
GMGMG	(298–6000)	$+ \text{NSPINEL} + 2 \cdot \text{ISPINEL} - 2 \cdot \text{GALAL} + 23.0525839 \cdot T$
GMGVA	(298–6000)	$+ \text{NSPINEL} + 8 \cdot \text{GALGAMMA} - 6 \cdot \text{GALAL} + 44.9540891 \cdot T + 102792.122$
GMGGAMMA	(298–6000)	$+ \text{GMGOSOL} + 24319.9053$
GMGMGMG	(298–6000)	$+ 8 \cdot \text{GMGGAMMA} - \text{NSPINEL} - 2 \cdot \text{ISPINEL} + 2 \cdot \text{GALAL}$
GALGAMMA	(298–6000)	$+ \text{GCORUND} + 27140.4693 - 11.3005601 \cdot T$
GMGVAMG	(298–6000)	$+ 8 \cdot \text{GMGGAMMA} - \text{NSPINEL} - 4 \cdot \text{ISPINEL} + 8 \cdot \text{GALGAMMA} - 2 \cdot \text{GALAL}$ $- 23.0525839 \cdot T + 44.9540891 \cdot T + 102792.122$
GMGFE3IN	(298–6000)	$-1491536.06 + 847.138581 \cdot T - 139.0343 \cdot T \cdot \ln(T) - 0.04400522 \cdot T^2$ $+ 4.8464667 \cdot 10^{-7} \cdot T^3 + 1215870.5 \cdot T^{-1}$
GMGZRO4	(298–6000)	$+ \text{GZRO2C} + 2 \cdot \text{GMGOSOL} + 100000$
GANCA	(298–6000)	$+ 23000$
GMGFE3NO	(298–6000)	$+ \text{GMGFE3IN} + \text{GANCA}$

TDB2: Table of the optimized thermodynamic description for the Mg–Ti–Zr–O system (J/mol)

Phase	Sublattice model	Optimized parameters
Gas	(Mg, MgO, Mg ₂ , O, O ₂ , O ₃ , Ti, TiO, TiO ₂ , Zr, Zr ₂ , ZrO, ZrO ₂)	${}^0G_{\text{Mg}} = F13284T + R \cdot T \cdot \ln(P);$ ${}^0G_{\text{MgO}} = F13320T + R \cdot T \cdot \ln(P);$ ${}^0G_{\text{Mg}_2} = F13297T + R \cdot T \cdot \ln(P);$ ${}^0G_{\text{O}} = F12575T + R \cdot T \cdot \ln(P);$ ${}^0G_{\text{O}_2} = 2 \cdot \text{GHSEROO} + R \cdot T \cdot \ln(P);$ ${}^0G_{\text{O}_3} = F13204T + R \cdot T \cdot \ln(P);$ ${}^0G_{\text{Ti}} = F14590T + R \cdot T \cdot \ln(P);$ ${}^0G_{\text{TiO}} = F12867T + R \cdot T \cdot \ln(P);$ ${}^0G_{\text{TiO}_2} = F13212T + R \cdot T \cdot \ln(P);$ ${}^0G_{\text{Zr}} = \text{GZRGAS} + R \cdot T \cdot \ln(P);$ ${}^0G_{\text{Zr}_2} = \text{GZR2G} + R \cdot T \cdot \ln(P);$ ${}^0G_{\text{ZrO}} = F12964T + R \cdot T \cdot \ln(P);$ ${}^0G_{\text{ZrO}_2} = F13281T + R \cdot T \cdot \ln(P);$
Ionic Liquid	(Mg ⁺² , Ti ⁺² , Ti ⁺³ , Zr ⁺⁴) ₁ (O ⁻² , O, TiO ₂ , Va) ₁	${}^0G_{\text{Mg}+2,\text{Va}}^{\text{IonicLiquid}} = \text{GMGLIQ};$ ${}^0G_{\text{Mg}+2,\text{O}-2}^{\text{IonicLiquid}} = 2 \cdot \text{GMGOLIQ};$ ${}^0G_{\text{Ti}+2,\text{Va}}^{\text{IonicLiquid}} = \text{GTILIQ};$ ${}^0G_{\text{Ti}+3,\text{Va}}^{\text{IonicLiquid}} = \text{GTILIQ} + 200000;$ ${}^0G_{\text{Ti}+2,\text{O}-2}^{\text{IonicLiquid}} = 2 \cdot \text{GTIO} + 141000 - 61.42 \cdot T;$ ${}^0G_{\text{Ti}+3,\text{O}-2}^{\text{IonicLiquid}} = \text{GTIO}_3 + 114147.4 - 45.6 \cdot T;$ ${}^0G_{\text{TiO}_2}^{\text{IonicLiquid}} = \text{GTIO}_2 + 62222.4 - 28.2 \cdot T;$ ${}^0G_{\text{Zr}+4,\text{Va}}^{\text{IonicLiquid}} = \text{GZRLIQ};$ ${}^0G_{\text{Zr}+4,\text{O}-2}^{\text{IonicLiquid}} = 2 \cdot \text{GZRO}_2\text{LIQ};$ ${}^0G_{\text{O}}^{\text{IonicLiquid}} = \text{GHSEROO} - 648.9 + 31.44 \cdot T;$ ${}^0L_{\text{Mg}+2,\text{Zr}+4,\text{Va}}^{\text{IonicLiquid}} = +4961 + 38.18 \cdot T;$ ${}^0L_{\text{Mg}+2,\text{Ti}+2,\text{Va}}^{\text{IonicLiquid}} = +77020;$ ${}^0L_{\text{Ti}+2,\text{Zr}+4,\text{Va}}^{\text{IonicLiquid}} = -20278 + 8.427 \cdot T;$ ${}^0L_{\text{Mg}+2,\text{Zr}+4,\text{O}-2}^{\text{IonicLiquid}} = -68195.5443;$ ${}^1L_{\text{Mg}+2,\text{Zr}+4,\text{O}-2}^{\text{IonicLiquid}} = +35835.397;$ ${}^0L_{\text{Ti}+2,\text{Ti}+3,\text{O}-2}^{\text{IonicLiquid}} = +19431.27;$ ${}^0L_{\text{Mg}+2,\text{O}-2,\text{Va}}^{\text{IonicLiquid}} = +182000 + 26.8 \cdot T;$ ${}^0L_{\text{Mg}+2,\text{O}-2,\text{TiO}_2}^{\text{IonicLiquid}} = -181798.44 + 28.102167 \cdot T;$ ${}^1L_{\text{Mg}+2,\text{O}-2,\text{TiO}_2}^{\text{IonicLiquid}} = -29264.098;$ ${}^0L_{\text{Ti}+2,\text{O}-2,\text{Va}}^{\text{IonicLiquid}} = +168314.44 - 100 \cdot T;$ ${}^1L_{\text{Ti}+2,\text{O}-2,\text{Va}}^{\text{IonicLiquid}} = +190655.57 - 95 \cdot T;$ ${}^0L_{\text{Ti}+3,\text{O}-2,\text{TiO}_2}^{\text{IonicLiquid}} = -36682.45;$ ${}^1L_{\text{Ti}+3,\text{O}-2,\text{TiO}_2}^{\text{IonicLiquid}} = +2382.5262;$ ${}^0L_{\text{Zr}+4,\text{O}-2,\text{Va}}^{\text{IonicLiquid}} = +75166.0715 - 55.2382004 \cdot T;$ ${}^1L_{\text{Zr}+4,\text{O}-2,\text{Va}}^{\text{IonicLiquid}} = +39057.4913;$ ${}^0L_{\text{Zr}+4,\text{O}-2,\text{TiO}_2}^{\text{IonicLiquid}} = +46371.394 - 30 \cdot T;$ ${}^1L_{\text{Zr}+4,\text{O}-2,\text{TiO}_2}^{\text{IonicLiquid}} = -41079.6051;$ ${}^2L_{\text{Zr}+4,\text{O}-2,\text{TiO}_2}^{\text{IonicLiquid}} = -33431.286;$
BCC	(Mg, Ti, Zr) ₁ (O, Va) ₃	${}^0G_{\text{Mg,Va}}^{\text{BCC}} = \text{GMGBCC};$ ${}^0G_{\text{Mg,O}}^{\text{BCC}} = 0;$ ${}^0G_{\text{Ti,Va}}^{\text{BCC}} = \text{GTIBCC};$ ${}^0G_{\text{Ti,O}}^{\text{BCC}} = -984174.3 + 559.8598 \cdot T - 91.23 \cdot T \cdot \ln(T) - 0.007585 \cdot T^2 + 840000 \cdot T^{-1};$ ${}^0G_{\text{Zr,Va}}^{\text{BCC}} = \text{GZRBCC};$ ${}^0G_{\text{Zr,O}}^{\text{BCC}} = 3 \cdot \text{GHSEROO} + \text{GZRBCC} - 52652.008;$ ${}^0L_{\text{Ti,O,Va}}^{\text{BCC}} = -697161 + 38.155 \cdot T;$ ${}^0L_{\text{Zr,O,Va}}^{\text{BCC}} = -1754239 + 336.32517 \cdot T;$ ${}^0L_{\text{Mg,Ti,Va}}^{\text{BCC}} = +33608;$ ${}^0L_{\text{Mg,Zr,Va}}^{\text{BCC}} = +19512 + 31.816 \cdot T;$ ${}^0L_{\text{Ti,Zr,Va}}^{\text{BCC}} = -4100 + 3.47 \cdot T;$
HCP	(Mg, Ti, Zr) ₁ (O, Va) _{0.5}	${}^0G_{\text{Mg,Va}}^{\text{HCP}} = \text{GHSERMG};$ ${}^0G_{\text{Mg,O}}^{\text{HCP}} = 0;$ ${}^0G_{\text{Ti,Va}}^{\text{HCP}} = \text{GHSERTI};$ ${}^0G_{\text{Ti,O}}^{\text{HCP}} = -277514 + 40.6543 \cdot T + \text{GHSERTI} - 0.5 \cdot \text{GHSEROO};$ ${}^0G_{\text{Zr,Va}}^{\text{HCP}} = \text{GHSERZR};$ ${}^0G_{\text{Zr,O}}^{\text{HCP}} = 0.5 \cdot \text{GHSEROO} + \text{GHSERZR} - 286427.906 + 43.223 \cdot T;$ ${}^0L_{\text{Ti,O,Va}}^{\text{HCP}} = +817.9;$ ${}^0L_{\text{Zr,O,Va}}^{\text{HCP}} = -37876.6552 + 17.2915 \cdot T;$ ${}^1L_{\text{Zr,O,Va}}^{\text{HCP}} = -4471.39;$ ${}^0L_{\text{Mg,Ti,Va}}^{\text{HCP}} = +21779 + 22.165 \cdot T;$ ${}^1L_{\text{Mg,Ti,Va}}^{\text{HCP}} = +9467;$ ${}^0L_{\text{Mg,Zr,Va}}^{\text{HCP}} = +30384 + 13.723 \cdot T;$ ${}^1L_{\text{Mg,Zr,Va}}^{\text{HCP}} = +18589 - 25.175 \cdot T;$ ${}^0L_{\text{Ti,Zr,Va}}^{\text{HCP}} = +5707 - 2.403 \cdot T;$
Halite	(Mg ⁺² , Ti ⁺² , Ti ⁺³ , Zr ⁺⁴ , Va) ₁ (O ⁻² , Va) ₁	${}^0G_{\text{Mg}+2,\text{O}-2}^{\text{Halite}} = \text{GMGOSOL};$ ${}^0G_{\text{Ti}+2,\text{O}-2}^{\text{Halite}} = \text{GTIOX};$ ${}^0G_{\text{Ti}+3,\text{O}-2}^{\text{Halite}} = +15885.45 + 15.7134 \cdot T + 0.5 \cdot \text{GTIO}_3;$ ${}^0G_{\text{TiO}-2}^{\text{Halite}} = +3000 - 0.05 \cdot T + 0.5 \cdot \text{GHSERTI} + 0.5 \cdot \text{TIOX};$ ${}^0G_{\text{Va},\text{O}-2}^{\text{Halite}} = +0;$ ${}^0G_{\text{Mg}+2,\text{Va}}^{\text{Halite}} = +0;$ ${}^0G_{\text{Ti}+2,\text{Va}}^{\text{Halite}} = +3000 - 0.05 \cdot T + 0.5 \cdot \text{GHSERTI} + 0.5 \cdot \text{GTIOX};$ ${}^0G_{\text{Ti}+3,\text{Va}}^{\text{Halite}} = +6000 - 0.1 \cdot T + \text{GHSERTI};$

		${}^0G_{\text{Ti:Va}}^{\text{Halite}} = +6000 - 0.1 \cdot T + \text{GHSERTI};$ ${}^0G_{\text{Va:Va}}^{\text{Halite}} = +10 \cdot T;$ ${}^0L_{\text{Ti+2,Ti:O-2}}^{\text{Halite}} = -76218.3 + 18.1321 \cdot T;$ ${}^0L_{\text{Ti+2,Va:O-2}}^{\text{Halite}} = -334896 + 7.3928 \cdot T;$ ${}^0L_{\text{Ti+3,Va:O-2}}^{\text{Halite}} = -474650 - 9.8944 \cdot T;$ ${}^0L_{\text{Ti+3:O-2,Va}}^{\text{Halite}} = -438973 + 42.0674 \cdot T;$ ${}^0L_{\text{Ti,Va:Va}}^{\text{Halite}} = 70 \cdot T;$
Spinel	$(\text{Mg}^{+2}, \text{Ti}^{+4})_1(\text{Mg}^{+2}, \text{Ti}^{+4}, \text{Zr}^{+4})_2(\text{O}^{2-})_4$	${}^0G_{\text{Mg+2,Mg+2:O-2}}^{\text{Spinel}} = +\text{GMGMG};$ ${}^0G_{\text{Ti+4,Mg+2:O-2}}^{\text{Spinel}} = +\text{SPINNORM};$ ${}^0G_{\text{Mg+2,Ti+4:O-2}}^{\text{Spinel}} = +2 \cdot \text{SPININV} - \text{GMGMG} + 23.05244 \cdot T;$ ${}^0G_{\text{Ti+4,Ti+4:O-2}}^{\text{Spinel}} = +3 \cdot \text{SPINNORM} + 2 \cdot \text{INVSP} - 2 \cdot \text{GMGMG} + 23.05244 \cdot T;$ ${}^0G_{\text{Mg+2,Zr+4:O-2}}^{\text{Spinel}} = +2 \cdot \text{ISPINZR} - \text{GMGMG} + 23.05244 \cdot T;$ ${}^0G_{\text{Ti+4,Zr+4:O-2}}^{\text{Spinel}} = +3 \cdot \text{SPINNORM} + 2 \cdot \text{INVSP} - 2 \cdot \text{GMGMG} + 23.05244 \cdot T$ $+ 2 \cdot \text{ISPINZR} - 2 \cdot \text{SPININV};$
Pseudobrookite	$(\text{Ti}^{+4}, \text{Mg}^{+2})_1(\text{Mg}^{+2}, \text{Ti}^{+4}, \text{Zr}^{+4})_2(\text{O}^{2-})_5$	${}^0G_{\text{Mg+2,Mg+2:O-2}}^{\text{Pseudobrookite}} = +3 \cdot \text{PSBNORM} + 2 \cdot \text{INVPSB} - 2 \cdot \text{GTI3O5} + 23.05244 \cdot T;$ ${}^0G_{\text{Ti+4,Mg+2:O-2}}^{\text{Pseudobrookite}} = +2 \cdot \text{PSBINV} - \text{GTI3O5} + 23.0524439 \cdot T;$ ${}^0G_{\text{Mg+2,Ti+4:O-2}}^{\text{Pseudobrookite}} = +\text{PSBNORM};$ ${}^0G_{\text{Ti+4,Ti+4:O-2}}^{\text{Pseudobrookite}} = +\text{GTI3O5};$ ${}^0G_{\text{Ti+4,Ti+4:O-2}}^{\text{Pseudobrookite}} = +\text{GTI3O5};$ ${}^0G_{\text{Mg+2,Zr+4:O-2}}^{\text{Pseudobrookite}} = +2 \cdot \text{GZRO2M} + \text{GMGOSOL} + 40000;$ ${}^0G_{\text{Ti+2,Zr+4:O-2}}^{\text{Pseudobrookite}} = -\text{PSBNORM} + \text{GTI3O5} + 2 \cdot \text{GZRO2M} + \text{GMGOSOL} + 40000;$
Ilmenite	$(\text{Mg}^{+2})_1(\text{Ti}^{+4}, \text{Zr}^{+4})_1(\text{O}^{2-})_3$	${}^0G_{\text{Mg+2,Ti+4:O-2}}^{\text{Ilmenite}} = -1617341.75 + 744.617699 \cdot T - 119.39 \cdot T \cdot \ln(T) - 0.0045852 \cdot T^2 + 1499000 \cdot T^{-1};$ ${}^0G_{\text{Mg+2,Zr+4:O-2}}^{\text{Ilmenite}} = +\text{GZRO2M} + \text{GMGOSOL} + 20000;$
Rutile	$(\text{Ti}^{+4}, \text{Zr}^{+4})_1(\text{O}^{2-}, \text{Va}^{2-})_2$	${}^0G_{\text{Ti+4:O-2}}^{\text{Rutile}} = +\text{GTIO2};$ ${}^0G_{\text{Zr+4:O-2}}^{\text{Rutile}} = +\text{GZRO2} + 35000;$ ${}^0G_{\text{Ti+4,Va-2}}^{\text{Rutile}} = +\text{GHSERTI} + 40000;$ ${}^0G_{\text{Zr+4,Va-2}}^{\text{Rutile}} = +\text{GHSERZR} + 40000;$ ${}^0L_{\text{Zr+4,Ti+4:O-2}}^{\text{Rutile}} = +46400 - 33.445 \cdot T;$ ${}^1L_{\text{Zr+4,Ti+4:O-2}}^{\text{Rutile}} = +3402.912 - 6.198 \cdot T;$ ${}^0L_{\text{Ti+4:O-2,Va-2}}^{\text{Rutile}} = -90233.9 - 22.7954 \cdot T;$ ${}^1L_{\text{Ti+4:O-2,Va-2}}^{\text{Rutile}} = -89395.3 - 15.9034 \cdot T;$ ${}^0L_{\text{Ti+4,Zr+4:Va-2}}^{\text{Rutile}} = +46400 - 33.445 \cdot T;$ ${}^1L_{\text{Ti+4,Zr+4:Va-2}}^{\text{Rutile}} = +3402.912 + 6.198 \cdot T;$
HT–TiZrO ₄	$(\text{Ti}^{+4}, \text{Zr}^{+4})_2(\text{O}^{2-})_4$	${}^0G_{\text{Ti+4:O-2}}^{\text{HT-TiZrO4}} = +2 \cdot \text{GTIO2} + 13450;$ ${}^0G_{\text{Zr+4:O-2}}^{\text{HT-TiZrO4}} = +2 \cdot \text{GZRO2T} + 13450;$ ${}^0L_{\text{Zr+4,Ti+4:O-2}}^{\text{HT-TiZrO4}} = +19200 + 22.0079 \cdot T - 4.15213 \cdot T \cdot \ln(T);$
LT–TiZrO ₄	$(\text{TiO}_2)_1(\text{ZrO}_2)_1$	${}^0G_{\text{TiO2:ZrO2}}^{\text{LT-TiZrO4}} = -2095452.69 + 893.145297 \cdot T - 145.694 \cdot T \cdot \ln(T) - 0.004005 \cdot T^2 + 1461180 \cdot T^{-1};$
T ₂ ZrO ₆	$(\text{TiO}_2)_2(\text{ZrO}_2)_1$	${}^0G_{\text{TiO2:ZrO2}}^{\text{T2ZrO6}} = -12100 + 7.9 \cdot T \cdot \text{GZRO2} + 2 \cdot \text{GTIO2};$
M–ZrO ₂	$(\text{Mg}^{+2}, \text{Ti}^{+4}, \text{Zr}^{+4})_1(\text{O}^{2-}, \text{Va})_2$	${}^0G_{\text{Mg+2:O-2}}^{\text{M-ZrO2}} = +\text{GMGOSOL} + \text{GHSEROO} + 120000 + 11.5263 \cdot T;$ ${}^0G_{\text{Ti+4:O-2}}^{\text{M-ZrO2}} = +\text{GTIO2} + 7330;$ ${}^0G_{\text{Zr+4:O-2}}^{\text{M-ZrO2}} = +\text{GZRO2M};$ ${}^0G_{\text{Mg+2,Va}}^{\text{M-ZrO2}} = +\text{GMGOSOL} - \text{GHSEROO} + 120000 + 11.5263 \cdot T;$ ${}^0G_{\text{Ti+4,Va}}^{\text{M-ZrO2}} = +0;$ ${}^0G_{\text{Zr+4,Va}}^{\text{M-ZrO2}} = +\text{GZRO2M} - 2 \cdot \text{GHSEROO};$ ${}^0L_{\text{Ti+4,Zr+4:O-2}}^{\text{M-ZrO2}} = +30245.15 - 4.0543 \cdot T;$
T–ZrO ₂	$(\text{Mg}^{+2}, \text{Ti}^{+4}, \text{Zr}^{+4})_1(\text{O}^{2-}, \text{Va})_2$	${}^0G_{\text{Mg+2:O-2}}^{\text{T-ZrO2}} = +\text{GMGOSOL} + \text{GHSEROO} + 60000 + 11.5263 \cdot T;$ ${}^0G_{\text{Ti+4:O-2}}^{\text{T-ZrO2}} = +\text{GTIO2} + 35000;$ ${}^0G_{\text{Zr+4:O-2}}^{\text{T-ZrO2}} = +\text{GZRO2T};$ ${}^0G_{\text{Mg+2,Va}}^{\text{T-ZrO2}} = +\text{GMGOSOL} - \text{GHSEROO} + 60000 + 11.5263 \cdot T;$ ${}^0G_{\text{Ti+4,Va}}^{\text{T-ZrO2}} = +0;$ ${}^0G_{\text{Zr+4,Va}}^{\text{T-ZrO2}} = +\text{GZRO2T} - 2 \cdot \text{GHSEROO};$ ${}^0L_{\text{Ti+4,Zr+4:O-2}}^{\text{T-ZrO2}} = -12883.4831 - 8.28911611 \cdot T;$ ${}^1L_{\text{Ti+4,Zr+4:O-2}}^{\text{T-ZrO2}} = -4439.497 - 11.75 \cdot T;$ ${}^0L_{\text{Mg+2,Zr+4:O-2}}^{\text{T-ZrO2}} = +50000;$ ${}^0L_{\text{Mg+2,Zr+4,Va}}^{\text{T-ZrO2}} = +50000;$
C–ZrO ₂ Fluorite	$(\text{Mg}^{+2}, \text{Ti}^{+4}, \text{Zr}^{+4})_1(\text{O}^{2-}, \text{Va})_2$	${}^0G_{\text{Mg+2:O-2}}^{\text{C-ZrO2}} = +\text{GMGOSOL} + \text{GHSEROO} + 45000 + 11.5263 \cdot T;$ ${}^0G_{\text{Ti+4:O-2}}^{\text{C-ZrO2}} = +\text{GTIO2} + 35000;$ ${}^0G_{\text{Zr+4:O-2}}^{\text{C-ZrO2}} = +\text{GZRO2C};$ ${}^0G_{\text{Mg+2,Va}}^{\text{C-ZrO2}} = +\text{GMGOSOL} - \text{GHSEROO} + 45000 + 11.5263 \cdot T;$ ${}^0G_{\text{Ti+4,Va}}^{\text{C-ZrO2}} = +\text{GTIO2} - 2 \cdot \text{GHSEROO};$ ${}^0G_{\text{Zr+4,Va}}^{\text{C-ZrO2}} = +\text{GZRO2C} - 2 \cdot \text{GHSEROO};$ ${}^0L_{\text{Mg+2,Ti+4:O-2}}^{\text{C-ZrO2}} = +102000;$ ${}^0L_{\text{Ti+4,Zr+4:O-2}}^{\text{C-ZrO2}} = +5600 - 8.89 \cdot T;$ ${}^0L_{\text{Mg+2,Zr+4:O-2}}^{\text{C-ZrO2}} = +2550.15;$ ${}^0L_{\text{Mg+2,Zr+4,Va}}^{\text{C-ZrO2}} = +2550.15;$
δ–Phase	$(\text{ZrO}_2)_{4.1}(\text{TiO}_2)_{0.9}(\text{MgO})_2$	${}^0G_{\text{ZrO2:TiO2:MgO}}^{\text{Delta}} = -6651010 + 2645.465 \cdot T - 455.8 \cdot T \cdot \ln(T) - 1.487 \cdot 10^{-2} \cdot T^2 + 4133118 \cdot T^{-1};$
TiO	$(\text{Ti})_1(\text{O})_1$	${}^0G_{\text{Ti:O}}^{\text{TiO}} = +\text{GTIO} + 6687.759 + 0.9994 \cdot T;$
Ti ₁₀ O ₁₉	$(\text{Ti})_{10}(\text{O})_{19}$	${}^0G_{\text{Ti:O}}^{\text{Ti10O19}} = -9184010.72 + 5027.55 \cdot T - 795.20328 \cdot T \cdot \ln(T) - 0.0018836103 \cdot T^2 - 39646.1 \cdot \ln(T) + 8428269.7 \cdot T^{-1} - 2.8905886 \cdot 10^8 \cdot T^{-2};$
Ti ₂₀ O ₃₉	$(\text{Ti})_{20}(\text{O})_{39}$	${}^0G_{\text{Ti:O}}^{\text{Ti20O39}} = -18941502.7 + 9864.17839 \cdot T - 1573.582 \cdot T \cdot \ln(T) - 0.0018830976 \cdot T^2 - 39647.965 \cdot \ln(T) + 25267204 \cdot T^{-1} - 9.6061736 \cdot 10^8 \cdot T^{-2};$

Ti ₂ O ₃	(Ti) ₂ (O) ₃	${}^0G_{\text{Ti:O}}^{\text{Ti2O3}} = +\text{GTI2O3};$
Ti ₃ O ₂	(Ti) ₃ (O) ₂	${}^0G_{\text{Ti:O}}^{\text{Ti3O2}} = -1109130.7 + 195.8524 \cdot T + 3 \cdot \text{GHSERTI} + 2 \cdot \text{GHSEROO};$
Ti ₃ O ₅	(Ti) ₃ (O) ₅	${}^0G_{\text{Ti:O}}^{\text{Ti3O5}} = +\text{GTI3O5};$
Ti ₄ O ₇	(Ti) ₄ (O) ₇	${}^0G_{\text{Ti:O}}^{\text{Ti3O5}} = -3322872.12 + 2125.25 \cdot T - 328.12018 \cdot T \cdot \ln(T) - 0.0018905269 \cdot T^2 - 39565.448 \cdot \ln(T) - 1652281.1 \cdot T^{-1} + 1.1239302 \cdot 10^8 \cdot T^{-2};$
Ti ₅ O ₉	(Ti) ₅ (O) ₉	${}^0G_{\text{Ti:O}}^{\text{Ti5O9}} = -4300008.12 + 2608.25 \cdot T - 406.01398 \cdot T \cdot \ln(T) - 0.0018837486 \cdot T^2 - 39644.622 \cdot \ln(T) + 8971.0933 \cdot T^{-1} + 46713032 \cdot T^{-2};$
Ti ₆ O ₁₁	(Ti) ₆ (O) ₁₁	${}^0G_{\text{Ti:O}}^{\text{Ti6O11}} = -5276828.48 + 3091.68 \cdot T - 483.85327 \cdot T \cdot \ln(T) - 0.001883476 \cdot T^2 - 39646.437 \cdot \ln(T) + 1692471 \cdot T^{-1} - 20421628 \cdot T^{-2};$
Ti ₇ O ₁₃	(Ti) ₇ (O) ₁₃	${}^0G_{\text{Ti:O}}^{\text{Ti7O13}} = -6253637.01 + 3575.49 \cdot T - 561.69079 \cdot T \cdot \ln(T) - 0.0018834938 \cdot T^2 - 39646.136 \cdot \ln(T) + 3376516.5 \cdot T^{-1} - 87588297 \cdot T^{-2};$
Ti ₈ O ₁₅	(Ti) ₈ (O) ₁₅	${}^0G_{\text{Ti:O}}^{\text{Ti8O15}} = -7230525.75 + 4059.52 \cdot T - 639.52544 \cdot T \cdot \ln(T) - 0.0018839308 \cdot T^2 - 39642.745 \cdot \ln(T) + 5061210.6 \cdot T^{-1} - 1.5478406 \cdot 10^8 \cdot T^{-2};$
Ti ₉ O ₁₇	(Ti) ₉ (O) ₁₇	${}^0G_{\text{Ti:O}}^{\text{Ti9O17}} = -8207343.14 + 4543.61 \cdot T - 717.36806 \cdot T \cdot \ln(T) - 0.0018831257 \cdot T^2 - 39647.955 \cdot \ln(T) + 6744064.3 \cdot T^{-1} - 2.218912 \cdot 10^8 \cdot T^{-2};$
Functions	(Temperature limits)	
GHSEROO		
	(298–1000)	$-3480.87 - 25.503038 \cdot T - 11.136 \cdot T \cdot \ln(T) - 0.005098888 \cdot T^2 + 6.61846 \cdot 10^{-7} \cdot T^3 - 38365 \cdot T^{-1}$
	(1000–3300)	$-6568.763 + 12.65988 \cdot T - 16.8138 \cdot T \cdot \ln(T) - 5.95798 \cdot 10^{-4} \cdot T^2 + 6.781 \cdot 10^{-9} \cdot T^3 + 262905 \cdot T^{-1}$
	(3300–6000)	$-13986.728 + 31.259625 \cdot T - 18.9536 \cdot T \cdot \ln(T) - 4.25243 \cdot 10^{-4} \cdot T^2 + 1.0721 \cdot 10^{-8} \cdot T^3 + 4383200 \cdot T^{-1}$
GHSERMG		
	(298–923)	$-8367.34 + 143.677875 \cdot T - 26.1849782 \cdot T \cdot \ln(T) + 4.858 \cdot 10^{-4} \cdot T^2 - 1.393669 \cdot 10^{-6} \cdot T^3 + 78950 \cdot T^{-1}$
	(923–3000)	$-14130.185 + 204.718543 \cdot T - 34.3088 \cdot T \cdot \ln(T) + 1.038192 \cdot 10^{+28} \cdot T^{-9}$
GMGBCC		
	(298–3000)	$+3100 - 2.1 \cdot T + \text{GHSERMG}$
GMGLIQ		
	(298–923)	$+8202.243 - 8.83693 \cdot T + \text{GHSERMG} - 8.0176 \cdot 10^{-20} \cdot T^7$
	(923–3000)	$+8690.316 - 9.392158 \cdot T + \text{GHSERMG} - 1.038192 \cdot 10^{+28} \cdot T^{-9}$
MGGOSOL		
	(298–1700)	$-619428.502 + 298.253571 \cdot T - 47.4817 \cdot T \cdot \ln(T) - 0.00232681 \cdot T^2 + 4.5043 \cdot 10^{-8} \cdot T^3 + 516900 \cdot T^{-1}$
	(1700–3100)	$-655489.818 + 528.597187 \cdot T - 78.3772 \cdot T \cdot \ln(T) + 0.0097344 \cdot T^2 - 8.60338 \cdot 10^{-7} \cdot T^3 + 8591550 \cdot T^{-1}$
	(3100–5000)	$-171490.159 - 1409.43369 \cdot T + 163.674142 \cdot T \cdot \ln(T) - 0.044009535 \cdot T^2 + 1.374896 \cdot 10^{-6} \cdot T^3 - 1.72665403 \cdot 10^{+8} \cdot T^{-1}$
	(5000–5100)	$-722412.718 + 617.657452 \cdot T - 84 \cdot T \cdot \ln(T)$
MGGOLIQ		
	(298–1700)	$-549098.33 + 275.724634 \cdot T - 47.4817 \cdot T \cdot \ln(T) - 0.00232681 \cdot T^2 + 4.5043 \cdot 10^{-8} \cdot T^3 + 516900 \cdot T^{-1}$
	(1700–2450)	$-585159.646 + 506.06825 \cdot T - 78.3772 \cdot T \cdot \ln(T) + 0.0097344 \cdot T^2 - 8.60338 \cdot 10^{-7} \cdot T^3 + 8591550 \cdot T^{-1}$
	(2450–3100)	$+9110429.75 - 42013.7634 \cdot T + 5298.548 \cdot T \cdot \ln(T) - 1.30122485 \cdot T^2 + 5.8262601 \cdot 10^{-5} \cdot T^3 - 3.24037416 \cdot 10^9 \cdot T^{-1}$
	(3100–5100)	$-632664.468 + 589.239555 \cdot T - 84 \cdot T \cdot \ln(T)$
GHSERTI		
	(298–900)	$-8059.921 + 133.615208 \cdot T - 23.9933 \cdot T \cdot \ln(T) - 0.004777975 \cdot T^2 + 1.06716 \cdot 10^{-7} \cdot T^3 + 72636 \cdot T^{-1}$
	(900–1155)	$-7811.815 + 132.988068 \cdot T - 23.9887 \cdot T \cdot \ln(T) - 0.0042033 \cdot T^2 - 9.0876 \cdot 10^{-8} \cdot T^3 + 42680 \cdot T^{-1}$
	(1155–1940.99)	$+908.837 + 66.976538 \cdot T - 14.9466 \cdot T \cdot \ln(T) - 0.0081465 \cdot T^2 + 2.02715 \cdot 10^{-7} \cdot T^3 - 1477660 \cdot T^{-1}$
	(1940.99–6000)	$-124526.786 + 638.806871 \cdot T - 87.2182461 \cdot T \cdot \ln(T) + 0.008204849 \cdot T^2 - 3.04747 \cdot 10^{-7} \cdot T^3 + 36699805 \cdot T^{-1}$
GFCCTI		
	(298–6000)	$+6000 - 0.1 \cdot T + \text{GHSERTI}$
GTIBCC		
	(298–900)	$+6787.856 + 1.098972 \cdot T - 1.5835 \cdot T \cdot \ln(T) + 0.00411413 \cdot T^2 - 3.85519 \cdot 10^{-7} \cdot T^3 - 65428 \cdot T^{-1} + \text{GHSERTI}$
	(900–1155)	$+6539.75 + 1.726111 \cdot T - 1.5881 \cdot T \cdot \ln(T) + 0.003539455 \cdot T^2 - 1.87927 \cdot 10^{-7} \cdot T^3 - 35472 \cdot T^{-1} + \text{GHSERTI}$
	(1155–1940.99)	$+5758.548 + 38.389841 \cdot T - 7.4305 \cdot T \cdot \ln(T) + 0.00936357 \cdot T^2 - 1.048055 \cdot 10^{-6} \cdot T^3 - 525090 \cdot T^{-1} + \text{GHSERTI}$
	(1940.99–6000)	$+151010.046 - 821.233343 \cdot T + 106.308337 \cdot T \cdot \ln(T) - 0.030213169 \cdot T^2 + 1.533611 \cdot 10^{-6} \cdot T^3 - 35299304 \cdot T^{-1} + \text{GHSERTI}$

GTILIQ	(298–1300) (1300–1940.99) (1940.99–6000)	+12194.415 – 6.980938·T + GHSERTI +368610.36 – 2620.99904·T + 357.005867·T·ln(T) – 0.15526855·T ² +1.2254402·10 ⁻⁵ ·T ³ – 65556856·T ⁻¹ + GHSERTI +104639.72 – 340.070171·T + 40.9282461·T·ln(T) – 0.008204849·T ² +3.04747·10 ⁻⁷ ·T ³ – 36699805·T ⁻¹ + GHSERTI
GTIOX	(298–6000)	+GFCCTI + GHSEROO – 532988 + 179.403·T – 11·T·ln(T)
GTII01	(298–2500)	–551056.766 + 252.169378·T – 41.994808·T·ln(T) + 327015.164·T ⁻¹ – 0.00889792452·T ² + 1.0970448·10 ⁻⁸ ·T ³
GTI2O3	(298–470) (470–2115)	–1545045.78 + 185.96227·T – 30.3934128·T·ln(T) – 0.099958898·T ² – 5.93279345·10 ⁻⁶ ·T ³ – 117799.056·T ⁻¹ – 1586585.8 + 937.087·T – 147.673862·T·ln(T) – 0.00173711312·T ² – 1.53383348·10 ⁻¹⁰ ·T ³ + 2395423.68·T ⁻¹
GTIO2	(298–4000)	–976986.6 + 484.74037·T – 77.76175·T·ln(T) – 67156800·T ⁻² + 1683920·T ⁻¹
GTI3O5	(298–6000)	+3·GTIO2 – GHSEROO
GHSEZR	(130–2128) (2128–6000)	–7827.595 + 125.64905·T – 24.1618·T·ln(T) – 0.00437791·T ² + 34971·T ⁻¹ – 26085.921 + 262.724183·T – 42.144·T·ln(T) – 1.342896·10 ³¹ ·T ⁻⁹
GZRBCC	(130–2128) (2128–6000)	–525.539 + 124.9457·T – 25.607406·T·ln(T) – 3.40084·10 ⁻⁴ ·T ² – 9.729·10 ⁻⁹ ·T ³ + 25233·T ⁻¹ – 7.6143·10 ⁻¹¹ ·T ⁴ – 4620.034 + 1.55998·T + GHSEZR + 1.4103476·10 ³² ·T ⁻⁹
GZRLIQ	(130–2128) (2128–6000)	+18147.69 – 9.080812·T + GHSEZR + 1.6275·10 ⁻²² ·T ⁷ – 8281.26 + 253.812609·T – 42.144·T·ln(T)
GZRO2M	(298–6000)	–1126163.54 + 424.890806·T – 69.3875137·T·ln(T) – 0.00375880141·T ² + 683000·T ⁻¹
GZRO2T	(298–6000)	+5468 – 4·T + GZRO2M
GZRO2C	(298–6000)	+10336 – 4·T + GZRO2T
GZRO2LIQ	(298–6000)	+87027 – 29.17432·T + GZRO2C
NSPINEL	(298–6000)	+GMGOSOL + GCORUND – 23204.5143 – 32.2303298·T + 4.31045184·T·ln(T)
ISPINEL	(298–6000)	+NSPINEL + 18002.9059 – 0.398945666·T
SPINNORM	(298–6000)	–2211877.741 + 1017.95064·T – 160.88·T·ln(T) – 0.009985·T ² + 1735500·T ⁻¹
INVSP	(298–6000)	–2824.083 – 28.335016·T
SPININV	(298–6000)	+SPINNORM + INVSP
PSBNORM	(298–6000)	–2580078.389 + 1179.41713·T – 190.76·T·ln(T) – 0.00608·T ² + 2094000·T ⁻¹
INVPSB	(298–6000)	+13497.083 – 4.1090551·T
PSBINV	(298–6000)	+PSBNORM + INVPSB
ISPINZR	(298–6000)	+2·GMGOSOL + GZRO2M + 20000
GCORUND	(298–600) (600–1500) (1500–3000)	–1707351.3 + 448.021092·T – 67.4804·T·ln(T) – 0.06747·T ² + 1.4205433·10 ⁻⁵ ·T ³ + 938780·T ⁻¹ – 1724886.06 + 754.856573·T – 116.258·T·ln(T) – 0.0072257·T ² + 2.78532·10 ⁻⁷ ·T ³ + 2120700·T ⁻¹ – 1772163.19 + 1053.4548·T – 156.058·T·ln(T) + 0.00709105·T ²

		$-6.29402 \cdot 10^{-7} \cdot T^3 + 12366650 \cdot T^{-1}$
GALAL	(298–6000)	+1.5·GCORUND –0.5·GHSEROO
GMGMG	(298–6000)	+NSPINEL +2·ISPINEL –2·GALAL +23.0525839·T
F12575T	(298–2950)	+243206.494 –20.8612587·T –21.01555·T·ln(T) +1.2687055·10 ⁻⁴ ·T ² –1.23131283·10 ⁻⁸ ·T ³ –42897.09·T ⁻¹
	(2950–6000)	+252301.423 –52.0847285·T –17.21188·T·ln(T) –5.413565·10 ⁻⁴ ·T ² +7.64520667·10 ⁻⁹ ·T ³ –3973170.5·T ⁻¹
F12964T	(298–500)	+84650.2479 –322.816859·T +21.98592·T·ln(T) –0.10713165·T ² +2.81704·10 ⁻⁵ ·T ³ –333363.35·T ⁻¹
	(500–1100)	+42648.3264 +404.464721·T –93.37933·T·ln(T) +0.03332466·T ² –3.80849833·10 ⁻⁶ ·T ³ +2526299·T ⁻¹
	(1100–4100)	+84838.707 +11.527709·T –37.46259·T·ln(T) +9.16682·10 ⁻⁵ ·T ² –7.005105·10 ⁻⁸ ·T ³ –3491878·T ⁻¹
	(4100–9600)	+106867.647 –98.6658671·T –23.49987·T·ln(T) –0.00315689·T ² +5.93994·10 ⁻⁸ ·T ³ –6661880·T ⁻¹
	(9600–10000)	+255442.536 –262.961955·T –6.281221·T·ln(T) –0.0038787795·T ² +6.18786667·10 ⁻⁸ ·T ³ –2.2466925·10 ⁸ ·T ⁻¹
F12867T	(298–800)	+45279.4546 –44.8816797·T –27.20855·T·ln(T) –0.01130768·T ² +2.093465·10 ⁻⁶ ·T ³ +15817.82·T ⁻¹
	(800–2600)	+38441.7462 +44.9717334·T –40.8145·T·ln(T) +0.001204741·T ² –1.26287067·10 ⁻⁷ ·T ³ +690966.5·T ⁻¹
	(2600–4300)	+78758.7741 –116.513546·T –20.67482·T·ln(T) –0.0031585015·T ² +4.49507333·10 ⁻⁸ ·T ³ –14168070·T ⁻¹
	(4300–6000)	+107274.032 –220.71175·T –7.872196·T·ln(T) –0.00560405·T ² +1.29955033·10 ⁻⁷ ·T ³ –25273450·T ⁻¹
F13320T	(298–500)	+20088.935 +57.8131812·T –41.59562·T·ln(T) +0.020256165·T ² –1.10843517·10 ⁻⁵ ·T ³ +147497.95·T ⁻¹
	(500–800)	+55632.3032 –532.855703·T +51.361·T·ln(T) –0.08730415·T ² +1.2172605·10 ⁻⁵ ·T ³ –2387726.5·T ⁻¹
	(800–1100)	+15232.3188 –103.535483·T –10.94431·T·ln(T) –0.045568·T ² +7.08342667·10 ⁻⁶ ·T ³ +2434495·T ⁻¹
	(1100–1800)	–95453.5569 +949.198341·T –161.1372·T·ln(T) +0.04478888·T ² –3.083445·10 ⁻⁶ ·T ³ +17692215·T ⁻¹
	(1800–3900)	+57603.9158 +20.4842916·T –37.72359·T·ln(T) +2.619384·10 ⁻⁴ ·T ² –4.91653667·10 ⁻⁸ ·T ³ –18117370·T ⁻¹
	(3900–8000)	+42627.5732 +17.6963681·T –36.55545·T·ln(T) –0.001102706·T ² +3.13090167·10 ⁻⁸ ·T ³ –1887194·T ⁻¹
	(8000–10000)	–58764.2849 +233.649462·T –61.25933·T·ln(T) +0.001492504·T ² –1.85976333·10 ⁻⁸ ·T ³ +73112200·T ⁻¹
F13204T	(298–700)	+130696.944 –37.9096651·T –27.58118·T·ln(T) –0.02763076·T ² +4.60539333·10 ⁻⁶ ·T ³ +99530.45·T ⁻¹
	(700–1300)	+114760.623 +176.626736·T –60.10286·T·ln(T) +0.00206456·T ² –5.17486667·10 ⁻⁷ ·T ³ +1572175·T ⁻¹
	(1300–2100)	+49468.3958 +710.094819·T –134.3696·T·ln(T) +0.039707355·T ² –4.10457667·10 ⁻⁶ ·T ³ +12362250·T ⁻¹
	(2100–2800)	+866367.075 –3566.80563·T +421.2001·T·ln(T) –0.1284109·T ² +5.44768833·10 ⁻⁶ ·T ³ –2.1304835·10 ⁸ ·T ⁻¹
	(2800–3500)	+409416.384 –1950.70834·T +223.4437·T·ln(T) –0.0922361·T ² +4.306855·10 ⁻⁶ ·T ³ –21589870·T ⁻¹
	(3500–4900)	–1866338.6 +6101.13383·T –764.8435·T·ln(T) +0.09852775·T ² –2.59784667·10 ⁻⁶ ·T ³ +9.610855·10 ⁸ ·T ⁻¹
	(4900–6000)	+97590.0432 +890.79836·T –149.9608·T·ln(T) +0.01283575·T ² –3.555105·10 ⁻⁷ ·T ³ –2.1699975·10 ⁸ ·T ⁻¹
F13284T	(298–1900)	+136346.96 –4.82603167·T –20.78595·T·ln(T) –9.778455·10 ⁻⁸ ·T ²
	(1900–2700)	+131004.76 +25.2078895·T –24.73039·T·ln(T) +0.001300831·T ² –8.09592167·10 ⁻⁸ ·T ³ +1361843·T ⁻¹
	(2700–3640)	+108558.443 +123.736524·T –37.20356·T·ln(T) +0.004390735·T ² –2.24912·10 ⁻⁷ ·T ³ +8958715·T ⁻¹
	(3640–5400)	+137405.469 +24.8050173·T –25.1271·T·ln(T) +0.002179723·T ² –1.502275·10 ⁻⁷ ·T ³ –3744678·T ⁻¹
	(5400–9200)	+453901.917 –789.444217·T +70.54811·T·ln(T) –0.010649025·T ² +1.716475·10 ⁻⁷ ·T ³ –1.996814·10 ⁸ ·T ⁻¹
	(9200–10000)	–320526.4 +427.791915·T –63.73726·T·ln(T) –2.847232·10 ⁻⁴ ·T ² +2.15099667·10 ⁻⁸ ·T ³ +6.39436·10 ⁸ ·T ⁻¹

F13297T		
(298–1900)		$+265944.946 - 87.7878521 \cdot T - 20.93983 \cdot T \cdot \ln(T) + 1.552631 \cdot 10^{-4} \cdot T^2$ $- 2.450615 \cdot 10^{-8} \cdot T^3 - 152571.35 \cdot T^{-1}$
(1900–3100)		$+60639.4722 + 1067.97947 \cdot T - 172.7914 \cdot T \cdot \ln(T) + 0.05046705 \cdot T^2$ $- 3.17995833 \cdot 10^{-6} \cdot T^3 + 52217650 \cdot T^{-1}$
(3100–3800)		$+1258706.77 - 3439.78878 \cdot T + 385.2094 \cdot T \cdot \ln(T) - 0.06477725 \cdot T^2$ $+ 1.27170267 \cdot 10^{-6} \cdot T^3 - 4.2909405 \cdot 10^8 \cdot T^{-1}$
(3800–4800)		$+3667699.34 - 11556.5772 \cdot T + 1374.666 \cdot T \cdot \ln(T) - 0.24531065 \cdot T^2$ $+ 7.44476833 \cdot 10^{-6} \cdot T^3 - 1.5282495 \cdot 10^9 \cdot T^{-1}$
(4800–6000)		$-5340467.97 + 12291.2038 \cdot T - 1438.848 \cdot T \cdot \ln(T) + 0.1458377 \cdot T^2$ $- 2.76687 \cdot 10^{-6} \cdot T^3 + 3.8878475 \cdot 10^9 \cdot T^{-1}$
F13212T		
(298–600)		$-317236.334 - 34.3402542 \cdot T - 31.38 \cdot T \cdot \ln(T) - 0.02810811 \cdot T^2$ $+ 5.84100333 \cdot 10^{-6} \cdot T^3 + 38666.435 \cdot T^{-1}$
(600–1800)		$-326946.95 + 118.875263 \cdot T - 55.31666 \cdot T \cdot \ln(T) - 0.0013442355 \cdot T^2$ $+ 1.16887017 \cdot 10^{-7} \cdot T^3 + 791905.5 \cdot T^{-1}$
(1800–3900)		$-335731.446 + 173.772851 \cdot T - 62.65958 \cdot T \cdot \ln(T) + 0.001471994 \cdot T^2$ $- 9.15459167 \cdot 10^{-8} \cdot T^3 + 2826501 \cdot T^{-1}$
(3900–6000)		$-257501.28 - 63.897708 \cdot T - 34.08998 \cdot T \cdot \ln(T) - 0.0031802585 \cdot T^2$ $+ 5.10434 \cdot 10^{-8} \cdot T^3 - 37446800 \cdot T^{-1}$
F13281T		
(298–700)		$-332610.845 + 3.22325893 \cdot T - 38.10718 \cdot T \cdot \ln(T) - 0.01852473 \cdot T^2$ $+ 3.29626 \cdot 10^{-6} \cdot T^3 + 218721.05 \cdot T^{-1}$
(700–2600)		$-342836.09 + 140.579945 \cdot T - 58.93983 \cdot T \cdot \ln(T) + 6.65405 \cdot 10^{-4} \cdot T^2$ $- 8.11812167 \cdot 10^{-8} \cdot T^3 + 1173742 \cdot T^{-1}$
(2600–4900)		$-272800.105 - 96.5265444 \cdot T - 30.24766 \cdot T \cdot \ln(T) - 0.0038011495 \cdot T^2$ $- 1.83201667 \cdot 10^{-11} \cdot T^3 - 28436635 \cdot T^{-1}$
(4900–6000)		$-36436.1523 - 803.246487 \cdot T + 54.45089 \cdot T \cdot \ln(T) - 0.017172935 \cdot T^2$ $+ 3.92562833 \cdot 10^{-7} \cdot T^3 - 1.509956 \cdot 10^8 \cdot T^{-1}$
F14590T		
(298–1800)		$+467609.96 - 25.791683 \cdot T - 23.45359 \cdot T \cdot \ln(T) + 0.0026178525 \cdot T^2$ $- 4.83678833 \cdot 10^{-7} \cdot T^3 - 101456.95 \cdot T^{-1}$
(1800–4500)		$+492971.637 - 184.379174 \cdot T - 2.247876 \cdot T \cdot \ln(T) - 0.005476885 \cdot T^2$ $+ 1.10024367 \cdot 10^{-7} \cdot T^3 - 5945505 \cdot T^{-1}$
(4500–10000)		$+364869.208 + 112.534909 \cdot T - 36.55164 \cdot T \cdot \ln(T) - 0.0016270125 \cdot T^2$ $+ 3.69943667 \cdot 10^{-8} \cdot T^3 + 80422300 \cdot T^{-1}$
GZRGAS		
(298–700)		$+586876.841 + 74.4171195 \cdot T - 38.69111 \cdot T \cdot \ln(T) + 0.01152846 \cdot T^2$ $- 1.693255 \cdot 10^{-6} \cdot T^3 + 270638.8 \cdot T^{-1}$
(700–1300)		$+595990.293 - 26.0530509 \cdot T - 24.06106 \cdot T \cdot \ln(T) + 0.001743641 \cdot T^2$ $- 5.94312333 \cdot 10^{-7} \cdot T^3 - 748947.5 \cdot T^{-1}$
(1300–2700)		$+593841.673 - 46.0204551 \cdot T - 20.46361 \cdot T \cdot \ln(T) - 0.002961084 \cdot T^2$ $+ 1.08391433 \cdot 10^{-7} \cdot T^3 + 526352.5 \cdot T^{-1}$
(2700–6600)		$+630745.052 - 161.965371 \cdot T - 6.647343 \cdot T \cdot \ln(T) - 0.0046738955 \cdot T^2$ $+ 1.06833583 \cdot 10^{-7} \cdot T^3 - 15872340 \cdot T^{-1}$
(6600–10000)		$+504260.272 + 131.813821 \cdot T - 40.68801 \cdot T \cdot \ln(T) - 6.38357 \cdot 10^{-4} \cdot T^2$ $+ 1.79125333 \cdot 10^{-8} \cdot T^3 + 71496950 \cdot T^{-1}$
GZR2G		
(298–3600)		$+892794.963 - 14.4120751 \cdot T - 37.13672 \cdot T \cdot \ln(T) - 3.2039655 \cdot 10^{-4} \cdot T^2$ $- 4.30605167 \cdot 10^{-9} \cdot T^3 + 85422.15 \cdot T^{-1}$
(3600–6000)		$+874148.858 + 9.34917918 \cdot T - 39.33356 \cdot T \cdot \ln(T) - 0.001019669 \cdot T^2$ $+ 6.09799667 \cdot 10^{-8} \cdot T^3 + 14065805 \cdot T^{-1}$
GTI3O5		
(298–450)		$-2493574.81 - 73.26557 \cdot T + 23.9073342 \cdot T \cdot \ln(T) - 0.420155188 \cdot T^2$ $+ 1.34740141 \cdot 10^{-4} \cdot T^3$
(450–5000)		$-2508055.23 + 925.801 \cdot T - 158.99208 \cdot T \cdot \ln(T) - 0.0251 \cdot T^2$

TDB 3. Table of the optimized thermodynamic description for the Mg–Mn–Zr–O system (J/mol)

Phase	Sublattice model	Optimized parameters
Gas	(Mg, MgO, Mg ₂ , O, O ₂ , O ₃ , Mn, MnO, MnO ₂)	${}^0G_{\text{Mg}} = F13284T + R \cdot T \cdot \ln(P);$ ${}^0G_{\text{MgO}} = F13320T + R \cdot T \cdot \ln(P);$ ${}^0G_{\text{Mg}_2} = F13297T + R \cdot T \cdot \ln(P);$ ${}^0G_{\text{O}_2} = F14375T + R \cdot T \cdot \ln(P);$ ${}^0G_{\text{O}_3} = F14415T + R \cdot T \cdot \ln(P);$ ${}^0G_{\text{Mn}} = F13413T + R \cdot T \cdot \ln(P);$ ${}^0G_{\text{MnO}} = F13428T + R \cdot T \cdot \ln(P);$ ${}^0G_{\text{MnO}_2} = F13435T + R \cdot T \cdot \ln(P);$
Ionic Liquid	(Mg ⁺² , Mn ⁺² , Zr ⁺⁴) ₁ (O ⁻² , MnO _{3/2} , Va) ₁	${}^0G_{\text{Mg}+2:\text{Va}}^{\text{IonicLiquid}} = \text{GMGLIQ};$ ${}^0G_{\text{Mg}+2:\text{O}-2}^{\text{IonicLiquid}} = 2 \cdot \text{GMGOLIQ};$ ${}^0G_{\text{Mn}+2:\text{Va}}^{\text{IonicLiquid}} = \text{GLIQMN};$ ${}^0G_{\text{Mn}+2:\text{O}-2}^{\text{IonicLiquid}} = 2 \cdot \text{GMNOLIQ};$ ${}^0G_{\text{MnO}_3/2}^{\text{IonicLiquid}} = 0.5 \cdot \text{GLMN2O}_3;$ ${}^0G_{\text{Zr}+4:\text{Va}}^{\text{IonicLiquid}} = \text{GZRLIQ};$ ${}^0G_{\text{Zr}+4:\text{O}-2}^{\text{IonicLiquid}} = 2 \cdot \text{GZRO2LIQ};$ ${}^0L_{\text{Mg}+2:\text{O}-2,\text{Va}}^{\text{IonicLiquid}} = +182000 + 26.8 \cdot T;$ ${}^0L_{\text{Mn}+2:\text{O}-2,\text{Va}}^{\text{IonicLiquid}} = +129519;$ ${}^1L_{\text{Mn}+2:\text{O}-2,\text{Va}}^{\text{IonicLiquid}} = -45459;$ ${}^0L_{\text{Mg}+2:\text{O}-2,\text{MnO}_3/2}^{\text{IonicLiquid}} = -33859;$ ${}^0L_{\text{Mg}+2,\text{Mn}+2:\text{Va}}^{\text{IonicLiquid}} = +19125 + 12.5 \cdot T;$ ${}^0L_{\text{Mn}+2:\text{Va},\text{MnO}_3/2}^{\text{IonicLiquid}} = +110000;$ ${}^0L_{\text{Mg}+2:\text{O}-2,\text{MnO}_3/2}^{\text{IonicLiquid}} = -110000;$ ${}^0L_{\text{Mg}+2:\text{Va},\text{MnO}_3/2}^{\text{IonicLiquid}} = +110000;$ ${}^0L_{\text{Mg}+2,\text{Mn}+2:\text{O}-2}^{\text{IonicLiquid}} = +0;$ ${}^0L_{\text{Mn}+2,\text{Zr}+4:\text{O}-2}^{\text{IonicLiquid}} = -45000;$ ${}^0L_{\text{Zr}+4:\text{O}-2,\text{Va}}^{\text{IonicLiquid}} = +75166.0715 - 55.2382004 \cdot T;$ ${}^1L_{\text{Zr}+4:\text{O}-2,\text{Va}}^{\text{IonicLiquid}} = +39057.4913;$ ${}^0L_{\text{Mn}+2,\text{Zr}+4:\text{Va}}^{\text{IonicLiquid}} = -73668.72 + 30.3 \cdot T;$ ${}^1L_{\text{Mn}+2,\text{Zr}+4:\text{Va}}^{\text{IonicLiquid}} = -1991.63;$ ${}^0L_{\text{Zr}+4:\text{O}-2,\text{MnO}_3/2}^{\text{IonicLiquid}} = +19000;$ ${}^0L_{\text{Mg}+2,\text{Zr}+4:\text{O}-2}^{\text{IonicLiquid}} = -68195.5443;$ ${}^1L_{\text{Mg}+2,\text{Zr}+4:\text{O}-2}^{\text{IonicLiquid}} = +35835.397;$ ${}^0L_{\text{Mg}+2,\text{Mn}+2:\text{Va}}^{\text{IonicLiquid}} = +19125 + 12.5 \cdot T;$ ${}^0L_{\text{Zr}+4,\text{Mg}+2:\text{Va}}^{\text{IonicLiquid}} = +14003.84 + 29.34205 \cdot T;$
BCC	(Mg,Mn,Zr) ₁ (O,Va) ₃	${}^0G_{\text{Mg:Va}}^{\text{BCC}} = \text{GMGBCC};$ ${}^0G_{\text{Mg:O}}^{\text{BCC}} = 0;$ ${}^0G_{\text{Mn:Va}}^{\text{BCC}} = \text{GBCCMN};$ $T_{\text{CMn:Va}}^{\text{BCC}} = -580;$ $B_{\theta\text{Mn:Va}}^{\text{BCC}} = -0.27;$ ${}^0G_{\text{Mn:O}}^{\text{BCC}} = +0;$ ${}^0G_{\text{Zr:Va}}^{\text{BCC}} = \text{GZRBCC};$ ${}^0G_{\text{Zr:O}}^{\text{BCC}} = 3 \cdot \text{GHSEROO} + \text{GZRBCC} - 52652.008;$ ${}^0L_{\text{Mn,Zr:Va}}^{\text{BCC}} = -2135.3475 - 0.13258 \cdot T;$ ${}^1L_{\text{Mn,Zr:Va}}^{\text{BCC}} = -1084;$ ${}^0L_{\text{Mg,Mn:Va}}^{\text{BCC}} = +70000;$ ${}^0L_{\text{Mg,Zr:Va}}^{\text{BCC}} = +5720.44 + 50.11642 \cdot T;$ ${}^0L_{\text{Zr:O}}^{\text{BCC}} = -1.754239 \cdot 10^6 + 336.32517 \cdot T;$
HCP	(Mg,Mn,Zr) ₁ (O,Va) _{0.5}	${}^0G_{\text{Mg:Va}}^{\text{HCP}} = \text{GHSERMG};$ ${}^0G_{\text{Mg:O}}^{\text{HCP}} = 0;$ ${}^0G_{\text{Mn:Va}}^{\text{HCP}} = \text{GHCPMN};$ $T_{\text{CMn:Va}}^{\text{HCP}} = -1620;$ $B_{\theta\text{Mn:Va}}^{\text{HCP}} = -1.86;$ ${}^0G_{\text{Mn:O}}^{\text{HCP}} = +0;$ ${}^0G_{\text{Zr:Va}}^{\text{HCP}} = \text{GHSERZR};$ ${}^0G_{\text{Zr:O}}^{\text{HCP}} = 0.5 \cdot \text{GHSEROO} + \text{GHSERZR} - 286427.906 + 43.223 \cdot T;$ ${}^0L_{\text{Mn,Zr:Va}}^{\text{HCP}} = +25000;$ ${}^0L_{\text{Mg,Mn:Va}}^{\text{HCP}} = +32985 + 2.5 \cdot T;$ ${}^0L_{\text{Mg,Zr:Va}}^{\text{HCP}} = +42063.55 + 1.01789 \cdot T;$ ${}^1L_{\text{Mg,Zr:Va}}^{\text{HCP}} = -2885.9;$ ${}^0L_{\text{Zr:O},\text{Va}}^{\text{HCP}} = -3.78766552 \cdot 10^4 + 17.2915 \cdot T;$ ${}^1L_{\text{Zr:O},\text{Va}}^{\text{HCP}} = -4471.39;$
FCC	(Mg,Mn,Zr) ₁ (O,Va) ₁	${}^0G_{\text{Mg:Va}}^{\text{FCC}} = +2600 - 0.9 \cdot T + \text{GHSERMG};$ ${}^0G_{\text{Mn:Va}}^{\text{FCC}} = \text{GFCCMN};$ $T_{\text{CMn:Va}}^{\text{FCC}} = -1620;$ $B_{\theta\text{Mn:Va}}^{\text{FCC}} = -1.86;$ ${}^0G_{\text{Zr:Va}}^{\text{FCC}} = \text{GZRFCC};$ ${}^0L_{\text{Mn,Zr:Va}}^{\text{FCC}} = -7200;$ ${}^0L_{\text{Mg,Mn:Va}}^{\text{FCC}} = +70000;$ ${}^0L_{\text{Mg,Zr:Va}}^{\text{FCC}} = +42063.55 + 1.01789 \cdot T;$ ${}^1L_{\text{Mg,Zr:Va}}^{\text{FCC}} = -2885.9;$
CBCC	(Mg,Mn,Zr) ₁ (O,Va) ₁	${}^0G_{\text{Mg:Va}}^{\text{CBCC}} = +4602.4 - 3.011 \cdot T + \text{GHSERMG};$ ${}^0G_{\text{Mn:Va}}^{\text{CBCC}} = \text{GHSERMN};$ $T_{\text{CMn:Va}}^{\text{CBCC}} = -285;$ $B_{\theta\text{Mn:Va}}^{\text{CBCC}} = -0.66;$

		${}^0G_{\text{Zr,Va}}^{\text{CBCC}} = \text{GZRCBCC};$ ${}^0L_{\text{Mn,Zr,Va}}^{\text{CBCC}} = +20000;$ ${}^0L_{\text{Mg,Mn,Va}}^{\text{CBCC}} = +70000;$ ${}^0L_{\text{Mg,Zr,Va}}^{\text{CBCC}} = +70000;$
CUB_A13	$(\text{Mg,Mn,Zr})_1(\text{Va})_1$	${}^0G_{\text{Mg,Va}}^{\text{CUB_A13}} = +\text{GHSERMG} + 5000 - 3 \cdot T;$ ${}^0G_{\text{Mn,Va}}^{\text{CUB_A13}} = \text{GMNCUB_A13};$ ${}^0G_{\text{Zr,Va}}^{\text{CUB_A13}} = \text{GZRCUB_A13};$ ${}^0L_{\text{Mn,Zr,Va}}^{\text{CUB_A13}} = -18000;$ ${}^0L_{\text{Mg,Mn,Va}}^{\text{CUB_A13}} = +70000;$ ${}^0L_{\text{Mg,Zr,Va}}^{\text{CUB_A13}} = +70000;$
C14	$(\text{Mn,Zr})_2(\text{Zr,Mn})_1$	${}^0G_{\text{Mn,Zr}}^{\text{C14}} = -95954.93 + 427.95342 \cdot T - 0.009295 \cdot T^2 - 77.2627 \cdot T \cdot \ln(T) + 243248.5 \cdot T^{-1};$ ${}^0G_{\text{Zr,Mn}}^{\text{C14}} = +95954.93 - 427.95342 \cdot T + 0.009295 \cdot T^2 + 77.2627 \cdot T \cdot \ln(T) - 243248.5 \cdot T^{-1} + 95000;$ ${}^0G_{\text{Zr,Zr}}^{\text{C14}} = +3 \cdot \text{GHSERZR} + 80000;$ ${}^0G_{\text{Mn,Mn}}^{\text{C14}} = +3 \cdot \text{GHSERMN} + 15000;$
Halite	$(\text{Mg}^{+2}, \text{Mn}^{+2}, \text{Mn}^{+3}, \text{Zr}^{+4}, \text{Va})_1(\text{O}^{-2})_1$	${}^0G_{\text{Mg}^{+2},\text{O}^{-2}}^{\text{Halite}} = \text{GMGOSOL};$ ${}^0G_{\text{Mn}^{+2},\text{O}^{-2}}^{\text{Halite}} = \text{GMN1O1};$ ${}^0G_{\text{Mn}^{+3},\text{O}^{-2}}^{\text{Halite}} = -21884 + 22.185 \cdot T + \text{GMN1O1};$ ${}^0G_{\text{Va},\text{O}^{-2}}^{\text{Halite}} = +0;$ ${}^0G_{\text{Zr}^{+4},\text{O}^{-2}}^{\text{Halite}} = +\text{GZRO2C} + 130000 + 11.5266 \cdot T;$ ${}^0L_{\text{Mn}^{+2},\text{Mn}^{+3},\text{O}^{-2}}^{\text{Halite}} = -42105;$ ${}^1L_{\text{Mn}^{+2},\text{Mn}^{+3},\text{O}^{-2}}^{\text{Halite}} = +46513;$ ${}^0L_{\text{Mg}^{+2},\text{Mn}^{+2},\text{O}^{-2}}^{\text{Halite}} = +11000;$ ${}^0L_{\text{Mg}^{+2},\text{Mn}^{+3},\text{O}^{-2}}^{\text{Halite}} = +50000;$ ${}^0L_{\text{Mg}^{+2},\text{Mn}^{+3},\text{Zr}^{+4},\text{O}^{-2}}^{\text{Halite}} = +0;$ ${}^0L_{\text{Mg}^{+2},\text{Mn}^{+2},\text{Zr}^{+4},\text{O}^{-2}}^{\text{Halite}} = -200000;$
Alpha-Spinel	$(\text{Mg}^{+2}, \text{Mn}^{+2}, \text{Mn}^{+3})_1(\text{Mg}^{+2}, \text{Mn}^{+2}, \text{Mn}^{+3}, \text{Va})_2(\text{Mg}^{+2}, \text{Mn}^{+2}, \text{Va})_2(\text{O}^{-2})_4$	${}^0G_{\text{Mn}^{+2},\text{Mn}^{+2},\text{Va},\text{O}^{-2}}^{\text{Alpha-Spinel}} = +\text{GA22V};$ $T_{\text{CMn}^{+2},\text{Mn}^{+2},\text{Va},\text{O}^{-2}}^{\text{Alpha-Spinel}} = +43.1;$ ${}^0G_{\text{Mn}^{+3},\text{Mn}^{+2},\text{Va},\text{O}^{-2}}^{\text{Alpha-Spinel}} = +\text{GA32V};$ $T_{\text{CMn}^{+3},\text{Mn}^{+2},\text{Va},\text{O}^{-2}}^{\text{Alpha-Spinel}} = +43.1;$ ${}^0G_{\text{Mn}^{+2},\text{Mn}^{+3},\text{Va},\text{O}^{-2}}^{\text{Alpha-Spinel}} = +\text{GA23V};$ $T_{\text{CMn}^{+2},\text{Mn}^{+3},\text{Va},\text{O}^{-2}}^{\text{Alpha-Spinel}} = +43.1;$ ${}^0G_{\text{Mn}^{+3},\text{Mn}^{+3},\text{Va},\text{O}^{-2}}^{\text{Alpha-Spinel}} = +\text{GA33V};$ $T_{\text{CMn}^{+3},\text{Mn}^{+3},\text{Va},\text{O}^{-2}}^{\text{Alpha-Spinel}} = +43.1;$ ${}^0G_{\text{Mn}^{+2},\text{Va},\text{Va},\text{O}^{-2}}^{\text{Alpha-Spinel}} = +\text{GA2VV};$ $T_{\text{CMn}^{+2},\text{Va},\text{Va},\text{O}^{-2}}^{\text{Alpha-Spinel}} = +43.1;$ ${}^0G_{\text{Mn}^{+3},\text{Va},\text{Va},\text{O}^{-2}}^{\text{Alpha-Spinel}} = +\text{GA3VV};$ $T_{\text{CMn}^{+3},\text{Va},\text{Va},\text{O}^{-2}}^{\text{Alpha-Spinel}} = +43.1;$ ${}^0G_{\text{Mg}^{+2},\text{Mn}^{+3},\text{Va},\text{O}^{-2}}^{\text{Alpha-Spinel}} = +\text{GAM3V};$ ${}^0G_{\text{Mg}^{+2},\text{Mn}^{+2},\text{Va},\text{O}^{-2}}^{\text{Alpha-Spinel}} = +\text{GAM2V};$ ${}^0G_{\text{Mg}^{+2},\text{Va},\text{Va},\text{O}^{-2}}^{\text{Alpha-Spinel}} = +\text{GAMVV};$ ${}^0G_{\text{Mg}^{+2},\text{Mg}^{+2},\text{Va},\text{O}^{-2}}^{\text{Alpha-Spinel}} = +\text{GAMMV};$ ${}^0G_{\text{Mn}^{+2},\text{Mg}^{+2},\text{Va},\text{O}^{-2}}^{\text{Alpha-Spinel}} = +\text{GA2MV};$ ${}^0G_{\text{Mn}^{+3},\text{Mg}^{+2},\text{Va},\text{O}^{-2}}^{\text{Alpha-Spinel}} = +\text{GA3MV};$ ${}^0G_{\text{Mn}^{+2},\text{Mn}^{+2},\text{Mn}^{+2},\text{O}^{-2}}^{\text{Alpha-Spinel}} = +\text{GA22V} + \text{AADDMN};$ $T_{\text{CMn}^{+2},\text{Mn}^{+2},\text{Mn}^{+2},\text{O}^{-2}}^{\text{Alpha-Spinel}} = +43.1;$ ${}^0G_{\text{Mn}^{+3},\text{Mn}^{+2},\text{Mn}^{+2},\text{O}^{-2}}^{\text{Alpha-Spinel}} = +\text{GA32V} + \text{AADDMN};$ $T_{\text{CMn}^{+3},\text{Mn}^{+2},\text{Mn}^{+2},\text{O}^{-2}}^{\text{Alpha-Spinel}} = +43.1;$ ${}^0G_{\text{Mn}^{+2},\text{Mn}^{+3},\text{Mn}^{+2},\text{O}^{-2}}^{\text{Alpha-Spinel}} = +\text{GA23V} + \text{AADDMN};$ $T_{\text{CMn}^{+2},\text{Mn}^{+3},\text{Mn}^{+2},\text{O}^{-2}}^{\text{Alpha-Spinel}} = +43.1;$ ${}^0G_{\text{Mn}^{+3},\text{Mn}^{+3},\text{Mn}^{+2},\text{O}^{-2}}^{\text{Alpha-Spinel}} = +\text{GA33V} + \text{AADDMN};$ $T_{\text{CMn}^{+3},\text{Mn}^{+3},\text{Mn}^{+2},\text{O}^{-2}}^{\text{Alpha-Spinel}} = +43.1;$ ${}^0G_{\text{Mn}^{+2},\text{Va},\text{Mn}^{+2},\text{O}^{-2}}^{\text{Alpha-Spinel}} = +\text{GA2VV} + \text{AADDMN};$ $T_{\text{CMn}^{+2},\text{Va},\text{Mn}^{+2},\text{O}^{-2}}^{\text{Alpha-Spinel}} = +43.1;$ ${}^0G_{\text{Mn}^{+3},\text{Va},\text{Mn}^{+2},\text{O}^{-2}}^{\text{Alpha-Spinel}} = +\text{GA3VV} + \text{AADDMN};$ $T_{\text{CMn}^{+3},\text{Va},\text{Mn}^{+2},\text{O}^{-2}}^{\text{Alpha-Spinel}} = +43.1;$ ${}^0G_{\text{Mg}^{+2},\text{Mn}^{+3},\text{Mn}^{+2},\text{O}^{-2}}^{\text{Alpha-Spinel}} = +\text{GAM3V} + \text{AADDMN};$ ${}^0G_{\text{Mg}^{+2},\text{Mn}^{+2},\text{Mn}^{+2},\text{O}^{-2}}^{\text{Alpha-Spinel}} = +\text{GAM2V} + \text{AADDMN};$ ${}^0G_{\text{Mg}^{+2},\text{Va},\text{Mn}^{+2},\text{O}^{-2}}^{\text{Alpha-Spinel}} = +\text{GAMVV} + \text{AADDMN};$ ${}^0G_{\text{Mg}^{+2},\text{Mg}^{+2},\text{Mn}^{+2},\text{O}^{-2}}^{\text{Alpha-Spinel}} = +\text{GAMMV} + \text{AADDMN};$ ${}^0G_{\text{Mn}^{+2},\text{Mg}^{+2},\text{Mn}^{+2},\text{O}^{-2}}^{\text{Alpha-Spinel}} = +\text{GA2MV} + \text{AADDMN};$ ${}^0G_{\text{Mn}^{+3},\text{Mg}^{+2},\text{Mn}^{+2},\text{O}^{-2}}^{\text{Alpha-Spinel}} = +\text{GA3MV} + \text{AADDMN};$ ${}^0G_{\text{Mn}^{+2},\text{Mn}^{+2},\text{Mg}^{+2},\text{O}^{-2}}^{\text{Alpha-Spinel}} = +\text{GA22V} + \text{BADDMG};$ ${}^0G_{\text{Mn}^{+3},\text{Mn}^{+2},\text{Mg}^{+2},\text{O}^{-2}}^{\text{Alpha-Spinel}} = +\text{GA32V} + \text{BADDMG};$ ${}^0G_{\text{Mn}^{+2},\text{Mn}^{+3},\text{Mg}^{+2},\text{O}^{-2}}^{\text{Alpha-Spinel}} = +\text{GA23V} + \text{BADDMG};$ ${}^0G_{\text{Mn}^{+3},\text{Mn}^{+3},\text{Mg}^{+2},\text{O}^{-2}}^{\text{Alpha-Spinel}} = +\text{GA33V} + \text{BADDMG};$ ${}^0G_{\text{Mn}^{+2},\text{Va},\text{Mg}^{+2},\text{O}^{-2}}^{\text{Alpha-Spinel}} = +\text{GA2VV} + \text{BADDMG};$ ${}^0G_{\text{Mn}^{+3},\text{Va},\text{Mg}^{+2},\text{O}^{-2}}^{\text{Alpha-Spinel}} = +\text{GA3VV} + \text{BADDMG};$ ${}^0G_{\text{Mg}^{+2},\text{Mn}^{+3},\text{Mg}^{+2},\text{O}^{-2}}^{\text{Alpha-Spinel}} = +\text{GAM3V} + \text{BADDMG};$ ${}^0G_{\text{Mg}^{+2},\text{Mn}^{+2},\text{Mg}^{+2},\text{O}^{-2}}^{\text{Alpha-Spinel}} = +\text{GAM2V} + \text{BADDMG};$ ${}^0G_{\text{Mg}^{+2},\text{Va},\text{Mg}^{+2},\text{O}^{-2}}^{\text{Alpha-Spinel}} = +\text{GAMVV} + \text{BADDMG};$ ${}^0G_{\text{Mg}^{+2},\text{Mg}^{+2},\text{Mg}^{+2},\text{O}^{-2}}^{\text{Alpha-Spinel}} = +\text{GAMMV} + \text{BADDMG};$ ${}^0G_{\text{Mn}^{+2},\text{Mg}^{+2},\text{Mg}^{+2},\text{O}^{-2}}^{\text{Alpha-Spinel}} = +\text{GA2MV} + \text{BADDMG};$ ${}^0G_{\text{Mn}^{+3},\text{Mg}^{+2},\text{Mg}^{+2},\text{O}^{-2}}^{\text{Alpha-Spinel}} = +\text{GA3MV} + \text{BADDMG};$

TDB3-3

		${}^0L_{\text{Mn}+2,\text{Zr}+4,*}^{\text{C-ZrO}_2} = -29547.46;$ ${}^1L_{\text{Mn}+2,\text{Zr}+4,*}^{\text{C-ZrO}_2} = -35288.51;$ ${}^0L_{\text{Mn}+3,\text{Zr}+4,*}^{\text{C-ZrO}_2} = -15461;$ ${}^0L_{\text{Mg}+2,\text{Zr}+4,*}^{\text{C-ZrO}_2} = +2550.15;$ ${}^0L_{\text{Mg}+2,\text{Mn}+2,\text{Zr}+4,*}^{\text{C-ZrO}_2} = -70000;$ ${}^0L_{\text{Mg}+2,\text{Mn}+3,\text{Zr}+4,*}^{\text{C-ZrO}_2} = -20000;$
M2O3C	$(\text{Mg}^{+2}, \text{Mn}^{+3})_2(\text{O}^{-2}, \text{Va})_3(\text{O}^{-2}, \text{Va})_1$	${}^0G_{\text{Mn}+3,\text{O}-2,\text{O}-2}^{\text{M2O3C}} = +\text{GMN2O3} + \text{GHSEROO} + 15.87691 \cdot T + 100000;$ ${}^0G_{\text{Mn}+3,\text{Va},\text{O}-2}^{\text{M2O3C}} = +\text{GMN2O3} - 2 \cdot \text{GHSEROO} + 15.87691 \cdot T + 100000;$ ${}^0G_{\text{Mn}+3,\text{O}-2,\text{Va}}^{\text{M2O3C}} = +\text{GMN2O3};$ ${}^0G_{\text{Mn}+3,\text{Va},\text{Va}}^{\text{M2O3C}} = +\text{GMN2O3} - 3 \cdot \text{GHSEROO};$ ${}^0G_{\text{Mg}+2,\text{O}-2,\text{O}-2}^{\text{M2O3C}} = +2 \cdot \text{GMGOSOL} + 2 \cdot \text{GHSEROO} + 45.87691 \cdot T + 120000;$ ${}^0G_{\text{Mg}+2,\text{Va},\text{O}-2}^{\text{M2O3C}} = +2 \cdot \text{GMGOSOL} - 1 \cdot \text{GHSEROO} + 45.87691 \cdot T + 120000;$ ${}^0G_{\text{Mg}+2,\text{O}-2,\text{Va}}^{\text{M2O3C}} = +2 \cdot \text{GMGOSOL} + \text{GHSEROO} + 30 \cdot T + 20000;$ ${}^0G_{\text{Mg}+2,\text{Va},\text{Va}}^{\text{M2O3C}} = +2 \cdot \text{GMGOSOL} + 2 \cdot \text{GHSEROO} + 30 \cdot T + 20000;$
MnO	$(\text{Mg})_1(\text{O})_2$	${}^0G_{\text{Mn},\text{O}}^{\text{MnO}} = +\text{GMN1O2};$
Mg6MnO8	$(\text{Mg}^{+2})_6(\text{Mn}^{+4})_1(\text{O}^{-2})_8$	${}^0G_{\text{Mg}+2,\text{Mn}+4,\text{O}-2}^{\text{Mg6MnO8}} = +\text{GMG6MNO8};$
Functions	(Temperature limits)	
GHSEROO		
	(298–1000)	$-3480.87 - 25.503038 \cdot T - 11.136 \cdot T \cdot \ln(T) - 0.005098888 \cdot T^2 + 6.61846 \cdot 10^{-7} \cdot T^3 - 38365 \cdot T^{-1}$
	(1000–3300)	$-6568.763 + 12.65988 \cdot T - 16.8138 \cdot T \cdot \ln(T) - 5.95798 \cdot 10^{-4} \cdot T^2 + 6.781 \cdot 10^{-9} \cdot T^3 + 262905 \cdot T^{-1}$
	(3300–6000)	$-13986.728 + 31.259625 \cdot T - 18.9536 \cdot T \cdot \ln(T) - 4.25243 \cdot 10^{-4} \cdot T^2 + 1.0721 \cdot 10^{-8} \cdot T^3 + 4383200 \cdot T^{-1}$
GO2GAS		
	(298–1000)	$-6961.74451 - 76729.7484 \cdot T^{-1} - 51.0057202 \cdot T - 22.2710136 \cdot T \cdot \ln(T) - 0.0101977469 \cdot T^2 + 1.32369208 \cdot 10^{-6} \cdot T^3;$
	(1000–3300)	$-13137.5203 + 525809.556 \cdot T^{-1} + 25.3200332 \cdot T - 33.627603 \cdot T \cdot \ln(T) - 0.00119159274 \cdot T^2 + 1.35611111 \cdot 10^{-8} \cdot T^3;$
	(3300–6000)	$-27973.4908 + 8766421.4 \cdot T^{-1} + 62.5195726 \cdot T - 37.9072074 \cdot T \cdot \ln(T) - 8.50483772 \cdot 10^{-4} \cdot T^2 + 2.14409777 \cdot 10^{-8} \cdot T^3;$
GHSERMG		
	(298–923)	$-8367.34 + 143.677875 \cdot T - 26.1849782 \cdot T \cdot \ln(T) + 4.858 \cdot 10^{-4} \cdot T^2 - 1.393669 \cdot 10^{-6} \cdot T^3 + 78950 \cdot T^{-1}$
	(923–3000)	$-14130.185 + 204.718543 \cdot T - 34.3088 \cdot T \cdot \ln(T) + 1.038192 \cdot 10^{+28} \cdot T^{-9}$
GMGBCC		
	(298–3000)	$+3100 - 2.1 \cdot T + \text{GHSERMG}$
GMGLIQ		
	(298–923)	$+8202.243 - 8.83693 \cdot T + \text{GHSERMG} - 8.0176 \cdot 10^{-20} \cdot T^7$
	(923–3000)	$+8690.316 - 9.392158 \cdot T + \text{GHSERMG} - 1.038192 \cdot 10^{+28} \cdot T^{-9}$
GMGOSOL		
	(298–1700)	$-619428.502 + 298.253571 \cdot T - 47.4817 \cdot T \cdot \ln(T) - 0.00232681 \cdot T^2 + 4.5043 \cdot 10^{-8} \cdot T^3 + 516900 \cdot T^{-1}$
	(1700–3100)	$-655489.818 + 528.597187 \cdot T - 78.3772 \cdot T \cdot \ln(T) + 0.0097344 \cdot T^2 - 8.60338 \cdot 10^{-7} \cdot T^3 + 8591550 \cdot T^{-1}$
	(3100–5000)	$-171490.159 - 1409.43369 \cdot T + 163.674142 \cdot T \cdot \ln(T) - 0.044009535 \cdot T^2 + 1.374896 \cdot 10^{-6} \cdot T^3 - 1.72665403 \cdot 10^{+8} \cdot T^{-1}$
	(5000–5100)	$-722412.718 + 617.657452 \cdot T - 84 \cdot T \cdot \ln(T)$
GMGOLIQ		
	(298–1700)	$-549098.33 + 275.724634 \cdot T - 47.4817 \cdot T \cdot \ln(T) - 0.00232681 \cdot T^2 + 4.5043 \cdot 10^{-8} \cdot T^3 + 516900 \cdot T^{-1}$
	(1700–2450)	$-585159.646 + 506.06825 \cdot T - 78.3772 \cdot T \cdot \ln(T) + 0.0097344 \cdot T^2 - 8.60338 \cdot 10^{-7} \cdot T^3 + 8591550 \cdot T^{-1}$
	(2450–3100)	$+9110429.75 - 42013.7634 \cdot T + 5298.548 \cdot T \cdot \ln(T) - 1.30122485 \cdot T^2 + 5.8262601 \cdot 10^{-5} \cdot T^3 - 3.24037416 \cdot 10^9 \cdot T^{-1}$
	(3100–5100)	$-632664.468 + 589.239555 \cdot T - 84 \cdot T \cdot \ln(T)$
GMGOA		
	(298–6000)	-16500
GMGOB		
	(298–6000)	$+ \text{GMGOSOL} + \text{GMN2O3} + 15890 - 5.473 \cdot T$
GMGMN2O3B		
	(298–6000)	$+ \text{GMN2O3} + 192300 - 193.8 \cdot T + 0.05 \cdot T^2$
GMGMN2OB		
	(298–6000)	$+0.142857143 \cdot \text{GMGOB}$
DMNMG		
	(298–6000)	$+0$
LMGMN2O4		
	(298–6000)	$+0$

KMGMN2O4	(298–6000)	+40000
GHSERMN	(298–1519) (1519–2000)	$-8115.28 + 130.059 \cdot T - 23.4582 \cdot T \cdot \ln(T) - 0.00734768 \cdot T^2 + 69827 \cdot T^{-1}$ $-28733.41 + 312.2648 \cdot T - 48 \cdot T \cdot \ln(T) + 1.656847 \cdot 10^{30} \cdot T^{-9}$
GBCCMN	(298–1519) (1519–2000)	$-3235.3 + 127.85 \cdot T - 23.7 \cdot T \cdot \ln(T) - 0.00744271 \cdot T^2 + 60000 \cdot T^{-1}$ $-23188.83 + 307.7043 \cdot T - 48 \cdot T \cdot \ln(T) + 1.265152 \cdot 10^{30} \cdot T^{-9}$
GFCCMN	(298–1519) (1519–2000)	$-3439.3 + 131.884 \cdot T - 24.5177 \cdot T \cdot \ln(T) - 0.006 \cdot T^2 + 69600 \cdot T^{-1}$ $-26070.1 + 309.6664 \cdot T - 48 \cdot T \cdot \ln(T) + 3.86196 \cdot 10^{30} \cdot T^{-9}$
GHCPMN	(298–1519) (1519–2000)	$-4439.3 + 133.007 \cdot T - 24.5177 \cdot T \cdot \ln(T) - 0.006 \cdot T^2 + 69600 \cdot T^{-1}$ $-27070.1 + 310.7894 \cdot T - 48 \cdot T \cdot \ln(T) + 3.86196 \cdot 10^{30} \cdot T^{-9}$
GMNCUB_A13	(298–1519) (1519–2000)	$+2314.88 + 5.936 \cdot T - 1.4203 \cdot T \cdot \ln(T) + 0.00151409 \cdot T^2 + 442 \cdot T^{-1} + \text{GHSERMN}$ $+442.65 - 0.9715 \cdot T + 2.3107229 \cdot 10^{30} \cdot T^{-9} + \text{GHSERMN}$
GLIQMN	(298–1519) (1519–2000)	$+17859.91 - 12.6208 \cdot T + \text{GHSERMN} - 4.41929 \cdot 10^{-21} \cdot T^7$ $-9993.9 + 299.036 \cdot T - 48 \cdot T \cdot \ln(T)$
GMNO	(298–6000)	$-402478 + 259.356 \cdot T - 46.835 \cdot T \cdot \ln(T) - 0.00385 \cdot T^2 + 212922 \cdot T^{-1}$
GMN1O1	(298–6000)	$-402478 + 259.356 \cdot T - 46.835 \cdot T \cdot \ln(T) - 0.00385 \cdot T^2 + 212922 \cdot T^{-1}$
GMNOLIQ	(298–6000)	$+ \text{GMN1O1} + 43947 - 20.628 \cdot T$
GMN1O2	(298–6000)	$-545091 + 395.379 \cdot T - 65.277 \cdot T \cdot \ln(T) - 0.007803 \cdot T^2 + 664955 \cdot T^{-1}$
GMN2O3	(298–6000)	$-998618 + 588.619 \cdot T - 101.956 \cdot T \cdot \ln(T) - 0.018844 \cdot T^2 + 589055 \cdot T^{-1}$
GLMN2O3	(298–6000)	$+2 \cdot \text{GMN1O1} + \text{GHSEROO} - 64953 + 43.144 \cdot T$
GGMN2O3A	(298–6000)	$+ \text{GMN2O3} + 240000 - 211.8 \cdot T + 0.05 \cdot T^2$
GMGMN2OA	(298–6000)	$+0.142857143 \cdot \text{GMGOB} + 0.142857143 \cdot \text{GMGOA}$
GAMN3O4	(298–6000)	$-1439700 + 892.2 \cdot T - 154.748 \cdot T \cdot \ln(T) - 0.017408 \cdot T^2 + 986139 \cdot T^{-1}$
GMN3O4B	(298–6000)	$+15270 + 7 \cdot T$
GMNFE2O4	(298–6000)	$-182450 + 133 \cdot T - 23.099 \cdot T \cdot \ln(T) - 0.0014 \cdot T^2 + 124000 \cdot T^{-1}$
JMNFE2O4	(298–6000)	+28000
GMNFE2OA	(298–6000)	$+ \text{GMNFE2O4} + 4900 - 1.9 \cdot T$
JMNFE2OA	(298–6000)	+JMNFE2O4
GAFE3O4	(298–6000)	+GFE3O4 +1000
GMG6MNO8	(298–6000)	$-4248980 + 2053.2 \cdot T - 3.38699409 \cdot 10^2 \cdot T \cdot \ln(T) - 2.10611451 \cdot 10^{-2} \cdot T^2$ $+2.94011814 \cdot 10^6 \cdot T^{-1}$
GHSERZR	(130–2128) (2128–6000)	$-7827.595 + 125.64905 \cdot T - 24.1618 \cdot T \cdot \ln(T) - 0.00437791 \cdot T^2 + 34971 \cdot T^{-1}$ $-26085.921 + 262.724183 \cdot T - 42.144 \cdot T \cdot \ln(T) - 1.342896 \cdot 10^{31} \cdot T^{-9}$
GZRBCC	(130–2128) (2128–6000)	$-525.539 + 124.9457 \cdot T - 25.607406 \cdot T \cdot \ln(T) - 3.40084 \cdot 10^{-4} \cdot T^2 - 9.729 \cdot 10^{-9} \cdot T^3$ $+25233 \cdot T^{-1} - 7.6143 \cdot 10^{-11} \cdot T^4$ $-4620.034 + 1.55998 \cdot T + \text{GHSERZR} + 1.4103476 \cdot 10^{32} \cdot T^{-9}$

GZRFCC	(298–6000)	+7600 –0.9·T+GHSERZR
GZRCBCC	(298–2128) (2128–3000)	–3225.3947 +125.64905·T –24.1618·T·ln(T) –0.00437791·T ² +34971·T ^{–1} –21483.721 +262.72415·T –42.144·T·ln(T) –1.342895·10 ³¹ ·T ^{–9}
GZRCUB_A13	(298–2128) (2128–3000)	–296.395 +125.64905·T –24.1618·T·ln(T) –0.00437791·T ² +34971·T ^{–1} –18554.721 +262.72418·T –42.144·T·ln(T) –1.342895·10 ³¹ ·T ^{–9}
GZRLIQ	(130–2128) (2128–6000)	+18147.69 –9.080812·T+GHSERZR +1.6275·10 ^{–22} ·T ⁷ –8281.26 +253.812609·T –42.144·T·ln(T)
GZRO2M	(298–6000)	–1126163.54 +424.890806·T –69.3875137·T·ln(T) –0.00375880141·T ² +683000·T ^{–1}
GZRO2T	(298–6000)	+5468 –4·T+GZRO2M
GZRO2C	(298–6000)	+10336 –4·T+GZRO2T
GZRO2LIQ	(298–6000)	+87027 –29.17432·T+GZRO2C
NSPINEL	(298–6000)	+GMGOSOL +GCRUND –27600 –62·T +9·T·LN(T)
ISPINEL	(298–6000)	+NSPINEL +51600 –39·T
GCRUND	(298–600) (600–1500) (1500–3000)	–1707351.3 +448.021092·T –67.4804·T·ln(T) –0.06747·T ² +1.4205433·10 ^{–5} ·T ³ +938780·T ^{–1} –1724886.06 +754.856573·T –116.258·T·ln(T) –0.0072257·T ² +2.78532·10 ^{–7} ·T ³ +2120700·T ^{–1} –1772163.19 +1053.4548·T –156.058·T·ln(T) +0.00709105·T ² –6.29402·10 ^{–7} ·T ³ +12366650·T ^{–1}
NASPINEL	(298–3000)	+NSPINEL +10000;
GGAMMA	(298–600) (600–1500) (1500–3000)	–1689977.34 +469.458181·T –70.5452·T·ln(T) –0.070794·T ² +1.491345·10 ^{–5} ·T ³ +981165·T ^{–1} –1708389.72 +791.591946·T –121.754·T·ln(T) –0.0075467·T ² +2.89573·10 ^{–7} ·T ³ +2222750·T ^{–1} –1758861.74 +1110.41976·T –164.253·T·ln(T) +0.00775305·T ² –6.8247·10 ^{–7} ·T ³ +13162750·T ^{–1}
GAGAMMA	(298–6000)	+GGAMMA +10000
NSPFEAL	(298–6000)	–287500 +136·T –22.1991·T·ln(T) –0.001867857·T ² +223844·T ^{–1}
SPJ2A	(298–6000)	+65800
BFE3O4	(298–3000)	+46826 –27.266·T
GFE3O4	(298–3000)	–161731 +144.873·T –24.9879·T·ln(T) –0.0011952256·T ² +206520·T ^{–1}
G22V	(298–6000)	+7·GFE3O4 +BFE3O4
G2AV	(298–6000)	+7·NSPFEAL
G_22B	(298–6000)	+21·GMNFE2O4 +2·JMNFE2O4 –14·GFE3O4 +2·BFE3O4
GB_JK	(298–6000)	+0.142857143·GAMN3O4 +0.142857143·GMN3O4B
KMN3O4B	(298–6000)	+26210 –17.46·T
REFSPAAV	(298–6000)	+1.5·G2AV –0.5·G22V +0.5·SPJ2A

DGREC	(298–3000)	+108000
REFAAVA	(298–6000)	+REFSPAAV +10000
GA_JK	(298–6000)	+0.142857143·GAMN3O4
JAMN3O4	(298–6000)	+95000
G_33A	(298–6000)	+10.5·GA_JK +JAMN3O4 –10.5·GMNFE2O4 –JMNFE2O4 +7·GAFE3O4 –BFE3O4
GA_MG	(298–6000)	GB_MG
GA_MN	(298–6000)	+8·GGMN1O1A +4·G_33A –42·GA_JK –4·JAMN3O4 +4·R·T·ln(2)
GA22V	(298–6000)	+21·GA_JK +2·JAMN3O4 –2·G_33A
GA32V	(298–6000)	+14·GA_JK +2·JAMN3O4 –G_33A
GA23V	(298–6000)	+7·GA_JK
GA33V	(298–6000)	+G_33A
GA2VV	(298–6000)	+8·GGMN2O3A –6·G_33A +7·GA_JK +12·R·T·ln(6) –10·R·T·ln(5)
GA3VV	(298–6000)	+8·GGMN2O3A –5·G_33A +12·R·T·ln(6) –10·R·T·ln(5)
IMGMN	(298–6000)	+GAM3V +1.72277926·10 ⁴ +4.42887530·T
GAMMV	(298–6000)	GBMMV
GAMVV	(298–6000)	GBMVV
GAM2V	(298–6000)	+GAM3V +GA32V –GA33V
GAM3V	(298–6000)	+GMN2MGO4
GA2MV	(298–6000)	+GA3MV +GA22V –GA23V
GA3MV	(298–6000)	+2·IMGMN –GA33V +4·R·T·ln(2)
GGMN1O1A	(298–6000)	+GMN1O1 +58500 –11·T
AADDMN	(298–6000)	+8·GGMN1O1A +4·G_33A –42·GA_JK –4·JAMN3O4 +4·R·T·ln(2)
MSPINEL	(298–6000)	+GMGOSOL +58000 –18·T
BADDMG	(298–6000)	+8·MSPINEL –2·NSPINEL –4·ISPINEL –23.0527167 +4·REFSPAAV
GGMN1O1B	(298–6000)	+GMN1O1 +41500 –10.25·T
BADDMN	(298–6000)	–2·G_22B +8·GGMN1O1B +4·R·T·ln(2)
GMGZ RVA	(298–6000)	+4·GMGOSOL +2·GZRO2C +30000 +23.05244·T –GBMMV
GMNZ RVA	(298–6000)	+4·GMN1O1 +2·GZRO2C +70000 +23.05244·T –GB22V
GMN2MGO4	(298–6000)	–1629500 +983.45·T –166.1·T·ln(T) +2.97·10 ^{–4} ·T ² +1470000·T ^{–1}

GBMMV	(298–6000)	+NSPINEL +2·ISPINEL +23.0527167·T –2·REFSPAAY
GB22V	(298–6000)	+G_22B
GB23V	(298–6000)	+7·GB_JK
GB24V	(298–6000)	+14·GB_JK –G_22B +KMN3O4B
GBMVV	(298–6000)	+8·GGAMMA +NSPINEL +44.9543481·T +DGREC –6·REFSPAAY
GB2VV	(298–6000)	+8·GGMN2O3B –56·GB_JK +3·G_22B –3·KMN3O4B +12·R·T·ln(6) –6·R·T·ln(3) –4·R·T·ln(2);
GBM3V	(298–6000)	+GMN2MGO4 +52000 –18·T;
F13320T	(298–500)	+20088.935 +57.8131812·T –41.59562·T·ln(T) +0.020256165·T ² –1.10843517·10 ^{–5} ·T ³ +147497.95·T ^{–1}
	(500–800)	+55632.3032 –532.855703·T +51.361·T·ln(T) –0.08730415·T ² +1.2172605·10 ^{–5} ·T ³ –2387726.5·T ^{–1}
	(800–1100)	+15232.3188 –103.535483·T –10.94431·T·ln(T) –0.045568·T ² +7.08342667·10 ^{–6} ·T ³ +2434495·T ^{–1}
	(1100–1800)	–95453.5569 +949.198341·T –161.1372·T·ln(T) +0.04478888·T ² –3.083445·10 ^{–6} ·T ³ +17692215·T ^{–1}
	(1800–3900)	+57603.9158 +20.4842916·T –37.72359·T·ln(T) +2.619384·10 ^{–4} ·T ² –4.91653667·10 ^{–8} ·T ³ –18117370·T ^{–1}
	(3900–8000)	+42627.5732 +17.6963681·T –36.55545·T·ln(T) –0.001102706·T ² +3.13090167·10 ^{–8} ·T ³ –1887194·T ^{–1}
	(8000–10000)	–58764.2849 +233.649462·T –61.25933·T·ln(T) +0.001492504·T ² –1.85976333·10 ^{–8} ·T ³ +73112200·T ^{–1}
F13284T	(298–1900)	+136346.96 –4.82603167·T –20.78595·T·ln(T) –9.778455·10 ^{–8} ·T ² +131004.76 +25.2078895·T –24.73039·T·ln(T) +0.001300831·T ² –8.09592167·10 ^{–8} ·T ³ +1361843·T ^{–1}
	(1900–2700)	+108558.443 +123.736524·T –37.20356·T·ln(T) +0.004390735·T ² –2.24912·10 ^{–7} ·T ³ +8958715·T ^{–1}
	(2700–3640)	+137405.469 +24.8050173·T –25.1271·T·ln(T) +0.002179723·T ² –1.502275·10 ^{–7} ·T ³ –3744678·T ^{–1}
	(3640–5400)	+453901.917 –789.444217·T +70.54811·T·ln(T) –0.010649025·T ² +1.716475·10 ^{–7} ·T ³ –1.996814·10 ⁸ ·T ^{–1}
	(5400–9200)	–320526.4 +427.791915·T –63.73726·T·ln(T) –2.847232·10 ^{–4} ·T ² +2.15099667·10 ^{–8} ·T ³ +6.39436·10 ⁸ ·T ^{–1}
	(9200–10000)	
F13297T	(298–1900)	+265944.946 –87.7878521·T –20.93983·T·ln(T) +1.552631·10 ^{–4} ·T ² –2.450615·10 ^{–8} ·T ³ –152571.35·T ^{–1}
	(1900–3100)	+60639.4722 +1067.97947·T –172.7914·T·ln(T) +0.05046705·T ² –3.17995833·10 ^{–6} ·T ³ +52217650·T ^{–1}
	(3100–3800)	+1258706.77 –3439.78878·T +385.2094·T·ln(T) –0.06477725·T ² +1.27170267·10 ^{–6} ·T ³ –4.2909405·10 ⁸ ·T ^{–1}
	(3800–4800)	+3667699.34 –11556.5772·T +1374.666·T·ln(T) –0.24531065·T ² +7.44476833·10 ^{–6} ·T ³ –1.5282495·10 ⁹ ·T ^{–1}
	(4800–6000)	–5340467.97 +12291.2038·T –1438.848·T·ln(T) +0.1458377·T ² –2.76687·10 ^{–6} ·T ³ +3.8878475·10 ⁹ ·T ^{–1}
F13413T	(298–1575)	+276164.054 –34.4987551·T –20.786·T·ln(T);
	(1575–2100)	+275547.585 –29.248057·T –21.52064·T·ln(T) +3.819474·10 ^{–4} ·T ² –3.66030333·10 ^{–8} ·T ³ +95180.95·T ^{–1} ;
	(2100–2400)	+274521.741 –16.384493·T –23.35302·T·ln(T) +0.0013469965·T ² –1.18903067·10 ^{–7} ·T ³ ;
F13428T	(298–900)	+151356.092 –24.1662503·T –31.02229·T·ln(T) –0.005519525·T ² +8.47063667·10 ^{–7} ·T ³ +97921.9·T ^{–1}
	(900–4100)	+146503.882 +29.4389958·T –38.90434·T·ln(T) +4.8722855·10 ^{–4} ·T ² –5.46958333·10 ^{–8} ·T ³ +687003.5·T ^{–1}
	(4100–6000)	+163891.797 +1.2422565·T –35.94693·T·ln(T) +6.220655·10 ^{–4} ·T ² –7.949125·10 ^{–8} ·T ³ –12461235·T ^{–1}
F13435T	(298–700)	+9095.11832 –9.18675114·T –36.92694·T·ln(T) –0.01944391·T ² +3.43552·10 ^{–6} ·T ³ +201368.45·T ^{–1}
	(700–2000)	–4061.05443 +167.414545·T –63.68895·T·ln(T) +0.004964408·T ² –7.80481667·10 ^{–7} ·T ³ +1423101·T ^{–1} ;

	(2000–3900)	$+74138.972 - 312.782575 \cdot T + 0.1646534 \cdot T \cdot \ln(T) - 0.01801756 \cdot T^2$
	(3900–6000)	$+7.59669 \cdot 10^{-7} \cdot T^3 - 16355180 \cdot T^{-1}$ $-269662.306 + 860.503282 \cdot T - 143.1466 \cdot T \cdot \ln(T) + 0.008591745 \cdot T^2$ $-1.67854167 \cdot 10^{-7} \cdot T^3 + 1.388169 \cdot 10^8 \cdot T^{-1}$
<hr/>		
F14375T	(298–600)	$-6965.21532 - 50.5304315 \cdot T - 22.3649 \cdot T \cdot \ln(T) - 0.00990912 \cdot T^2$ $+1.20026583 \cdot 10^{-6} \cdot T^3 - 77535.75 \cdot T^{-1}$
	(600–1000)	$-8807.78237 - 26.3126811 \cdot T - 25.99933 \cdot T \cdot \ln(T) - 0.00694323 \cdot T^2$ $+8.04195333 \cdot 10^{-7} \cdot T^3 + 90022.35 \cdot T^{-1}$
	(1000–2300)	$-15052.1241 + 39.5601504 \cdot T - 35.57101 \cdot T \cdot \ln(T) - 3.708985 \cdot 10^{-4} \cdot T^2$ $-4.80521167 \cdot 10^{-8} \cdot T^3 + 860271.5 \cdot T^{-1}$
	(2300–4100)	$-8823.65673 + 3.71926228 \cdot T - 30.85139 \cdot T \cdot \ln(T) - 0.0019495235 \cdot T^2$ $+5.02773 \cdot 10^{-8} \cdot T^3 - 670976 \cdot T^{-1}$
	(4100–6000)	$-7013.9736 + 6.93103034 \cdot T - 31.38542 \cdot T \cdot \ln(T) - 0.001656954 \cdot T^2$ $+3.47421833 \cdot 10^{-8} \cdot T^3 - 3177110 \cdot T^{-1}$
	(6000–8400)	$+26556.5297 - 81.8606432 \cdot T - 20.93747 \cdot T \cdot \ln(T) - 0.0030562285 \cdot T^2$ $+6.90690167 \cdot 10^{-8} \cdot T^3 - 22459590 \cdot T^{-1}$
	(8400–12000)	$-414379.34 + 627.760535 \cdot T - 99.46439 \cdot T \cdot \ln(T) + 0.003184458 \cdot T^2$ $-2.42980333 \cdot 10^{-8} \cdot T^3 + 4.4363345 \cdot 10^8 \cdot T^{-1}$
	(12000–16000)	$-286534.147 + 496.228104 \cdot T - 85.70049 \cdot T \cdot \ln(T) + 0.002546952 \cdot T^2$ $-1.90235667 \cdot 10^{-8} \cdot T^3 + 2.2612925 \cdot 10^8 \cdot T^{-1}$
	(16000–20000)	$+169868.379 + 75.3492467 \cdot T - 42.13511 \cdot T \cdot \ln(T) + 6.93379 \cdot 10^{-4} \cdot T^2$ $-4.19646667 \cdot 10^{-9} \cdot T^3 - 6.73131 \cdot 10^8 \cdot T^{-1}$
<hr/>		
F14415T	(298–500)	$+134848.008 - 131.223611 \cdot T - 12.03048 \cdot T \cdot \ln(T) - 0.05275305 \cdot T^2$ $+1.2029595 \cdot 10^{-5} \cdot T^3 - 102360.9 \cdot T^{-1}$
	(500–800)	$+125218.595 + 47.4797409 \cdot T - 40.81794 \cdot T \cdot \ln(T) - 0.0137036 \cdot T^2$ $+1.90056833 \cdot 10^{-6} \cdot T^3 + 514086.5 \cdot T^{-1}$
	(800–1200)	$+116301.963 + 157.624133 \cdot T - 57.26249 \cdot T \cdot \ln(T) - 1.3629415 \cdot 10^{-4} \cdot T^2$ $-2.12367333 \cdot 10^{-7} \cdot T^3 + 1426255 \cdot T^{-1}$
	(1200–1600)	$+76721.1518 + 503.834314 \cdot T - 106.002 \cdot T \cdot \ln(T) + 0.0266356 \cdot T^2$ $-2.98006167 \cdot 10^{-6} \cdot T^3 + 7474120 \cdot T^{-1}$
	(1600–2100)	$+48905.4457 + 717.33371 \cdot T - 135.3917 \cdot T \cdot \ln(T) + 0.040276715 \cdot T^2$ $-4.15597833 \cdot 10^{-6} \cdot T^3 + 12338385 \cdot T^{-1}$
	(2100–2500)	$+520719.833 - 1837.33582 \cdot T + 198.1425 \cdot T \cdot \ln(T) - 0.06465645 \cdot T^2$ $+2.04255167 \cdot 10^{-6} \cdot T^3 - 1.129672 \cdot 10^8 \cdot T^{-1}$
	(2500–3100)	$+1271313.19 - 5388.12786 \cdot T + 652.5156 \cdot T \cdot \ln(T) - 0.18701485 \cdot T^2$ $+8.22613333 \cdot 10^{-6} \cdot T^3 - 3.456718 \cdot 10^8 \cdot T^{-1}$
	(3100–3500)	$-58819.7904 - 242.069298 \cdot T + 12.85911 \cdot T \cdot \ln(T) - 0.05022045 \cdot T^2$ $+2.73771 \cdot 10^{-6} \cdot T^3 + 1.7323845 \cdot 10^8 \cdot T^{-1}$
	(3500–4100)	$-1865873.5 + 6082.45586 \cdot T - 762.2686 \cdot T \cdot \ln(T) + 0.0976441 \cdot T^2$ $-2.554365 \cdot 10^{-6} \cdot T^3 + 9.636295 \cdot 10^8 \cdot T^{-1}$
	(4100–4800)	$-1603985.97 + 5364.29063 \cdot T - 677.2357 \cdot T \cdot \ln(T) + 0.08557655 \cdot T^2$ $-2.24026833 \cdot 10^{-6} \cdot T^3 + 8.14364 \cdot 10^8 \cdot T^{-1}$
	(4800–5800)	$-54953.3125 + 1260.31667 \cdot T - 193.0202 \cdot T \cdot \ln(T) + 0.018228555 \cdot T^2$ $-4.819375 \cdot 10^{-7} \cdot T^3 - 1.158314 \cdot 10^8 \cdot T^{-1}$
	(5800–6000)	$-189639.743 + 1510.18103 \cdot T - 221.0511 \cdot T \cdot \ln(T) + 0.02063245 \cdot T^2$ $-5.15334667 \cdot 10^{-7} \cdot T^3$
<hr/>		

